

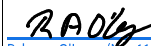


Murujuga Rock Art Monitoring Program: Monitoring Studies Report 2023

Technical Report on Monitoring Studies completed from March 2022 to March 2023.

Prepared for the Department of Water and Environmental Regulation and the Murujuga Aboriginal Corporation

Prepared by: Julian Alfing, Seamus Anderson, Adrian Baddeley, Kathryn Barker, David Belton, Katelyn Boase, Arne Bredin, Kimbra Bridges, Matthew Campbell, Francesca Cary, Aaron Cavosie, Carmelo Chippalone, Marco Coolen, Noel Cressie, Thomas Di Loreto, Katy Evans, John Fairweather, Ronald Fellows-Smith, Kliti Grice, Monica Gumulya, Petra Helmholtz, Toni Hannelly, Carmen Harris, Stephanie Hogg, Alex Holman, Peter Hopper, Laura Horan, Melanie Johnston-Hollitt, Andrew King, Katherine Landwehr, David Lynch, Dan Marrable, Ruby Marsden, Carlo Martinotti, Ryan Mead-Hunter, Abraj Mohomed, Benjamin Mullins, Nishafa Nazahir, Mawutorli Nyarku, Rebecca O’Leary, Calvin Pang, Suman Rakshit, Will Rickard, Bettina Schaefer, Robert Slater, Sebastian Stanley, Tommaso Tacchetto, Stefano Tenuta, Andrew Thorn, Taylor Tufto, Arun Veluchamy, Hridya Vijay, Brad Zhang.

Doc No	Current Rev	Revision Date	Checked By	Approved By
COPP-21065-REP-G-101	0	10/11/2023	B. Mullins	R. O’Leary
			 Ben Mullins (Nov 11, 2023 12:10 GMT+8)	 Rebecca O’Leary (Nov 11, 2023 11:50 GMT+8)

Revision history

Revision No	Date	Revision Reason
A	12/04/2023	Preliminary for review
B	23/04/2023	Internal review comments incorporated
C	27/04/2023	Technical review by Lead Statistician
D	03/05/2023	Issued for Customer review
E	20/10/2023	Update per review comments
0	10/11/2023	Issued for use with peer review close out comments addressed

The data associated with this report is available on request from the Department of Water and Environmental Regulation.

The information contained in this report is copyright the Department of Water and Environmental Regulation (DWER) WA, except for prior art (background IP) of Calibre, Curtin University and subcontractors. No part of the report may be reproduced or transmitted in any form by any means including, without limitation, electronic, photocopying, recording, or otherwise, without the prior written permission of DWER. No information embodied in the report which is not already in the public domain shall be communicated in any manner whatsoever to any third party without the prior written consent of DWER. While Calibre, Curtin University and subcontractors consider that the information and opinions given in this work are sound, all parties must rely upon their own skill and judgement when making use of it. Calibre, Curtin University and subcontractors do not make any representation or warranty, expressed or implied, as to the accuracy or completeness of the information contained in this report and assumes no responsibility for the accuracy or completeness of such information. Calibre, Curtin University and subcontractors will not assume any liability to anyone for any loss or damage arising out of the provision of this report.

Executive summary

The Murujuga Rock Art Monitoring Program (**MRAMP**) will develop a series of Environmental Quality Criteria (**EQC**) and an Environmental Quality Management Framework (**EQMF**) for the ongoing management of the Murujuga region, with a focus on air quality.

This document presents a summary of data collection, laboratory studies and analysis undertaken within the first year of scientific studies since approval of the Program's Monitoring Studies Data Collection and Analysis (**MSDCA**) Plan in March 2022 and the formal commencement of the first fieldwork campaign. This report is not intended to be a stand-alone document, rather it is intended to be read in conjunction with the Conceptual Model, MSDCA Plan and detailed methodology statements for component studies as referenced throughout.

The experimental program was approved by the Murujuga Aboriginal Corporation (MAC) Elders, including the rock art panels selected for study and the locations for all other works, including (non-art-containing) rock sample collection, air quality monitoring locations, etc. All works on or near rock art panels are limited to non-invasive methods. A comprehensive heritage survey was conducted at all proposed study locations, to ensure no impact to any heritage sites would occur. All necessary approvals were sought and obtained from the (WA) Department of Lands and Heritage (**DPLH**) and other relevant government authorities. Invasive methods such as rock sample collection were limited to sites without rock art or artefacts. Bulk material for chamber studies or rock cubes were collected from disturbed areas on existing industry leases, such as quarries and mining/salt leases, where possible. Surplus rocks and sample material will be repatriated to Murujuga when no longer required for studies, in consultation with the MAC Elders.

Between March 2022 and March 2023 (the first year of studies), four fieldwork campaigns comprising 18 weeks duration in total were undertaken. Fieldwork included monitoring 54 rock art panels and 64 sample rocks across the five rock types found in the study area, previously selected in the MSDCA development phase and approved by the **MAC** Elders for inclusion in the Program. Field campaigns resulted in over 21,600 measurements of rock art condition (spectral/colour measurement), along with 1,037 surface elemental measurements using x-ray fluorescence (**pXRF**), and 2,594 surface electrochemical measurements (pH, Eh, Cl) combined.

In addition to the above, 484 samples were collected of rock patina, lichen and soil for detailed microbial sequencing and analysis (patina, lichen, soil) and elemental analysis (soil). Twenty nine representative vegetation samples were also collected for biomass organic chemical analyses and chamber combustion studies.

The 64 sample rocks have subsequently been removed from Country to Curtin University as planned, sub-sampled, and processed for ongoing organic chemistry and geochemical analysis, both of which are well underway. Partial results of geological/geochemical analyses are presented in this report, with the majority of the multi-year laboratory studies (including microbial, organics and chamber studies) ongoing.

In addition to the above field and laboratory work, the deployment and commissioning of 18 solar powered "passive" air quality and weather monitoring stations (**AQMs**) has been completed, along with 3 powered AQMs and the installation of additional equipment into a further (3rd party) AQM (Figure ES-1). Results from the first months of passive air quality monitoring are presented in this document. Real time (low-power/cost) air quality sensor data is not presented here as the sensors are still undergoing calibration based on passive sampler and reference-grade powered monitor data. High resolution spatial mapping was undertaken, which will permit the

computational fluid dynamics (CFD) studies (also in-progress) to better estimate rock surface exposure at the study sites.

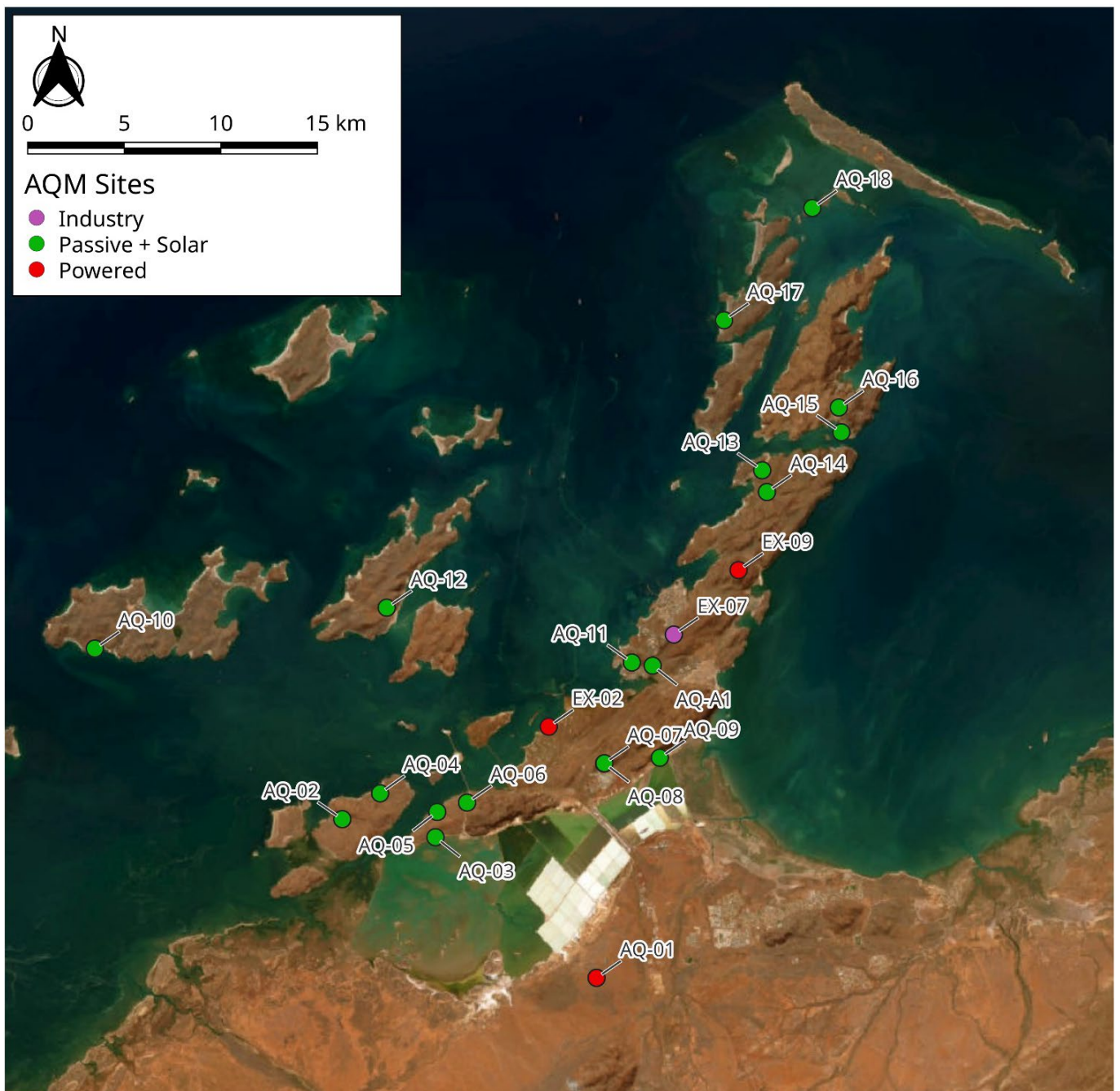


Figure ES-1: Air Quality Monitor (AQM) deployment

Many component studies remain in-progress, therefore this report presents progress to-date for most components. Likewise, statistical data analysis and synthesis is ongoing, with novel techniques being applied on an ongoing basis to enable a greater understanding of data collected. It is well known that statistical power increases with data quantity and also temporal duration, therefore these data from year 1 will also be continually reanalysed as additional data becomes available. Likewise, a transition from modelled to measured air quality data in analyses during the second year of studies will increase confidence in predictions.

Given that rock and rock-art surface monitoring necessarily commenced before the installation of the new AQMs and the new rock(art) surface measurement data generated spans only 12 months to date, statistical dose-response studies have at present been limited to comparing spatial gradients in field measurements with spatial gradients in modelled air quality data. The determination of EQCs has also been somewhat confounded by the fact that rainfall patterns (Figure ES-2) were atypical during the first year of fieldwork, with the first (wet season) campaign being unusually dry and hot, and the second (dry season) campaign being unusually wet in the preceding week.

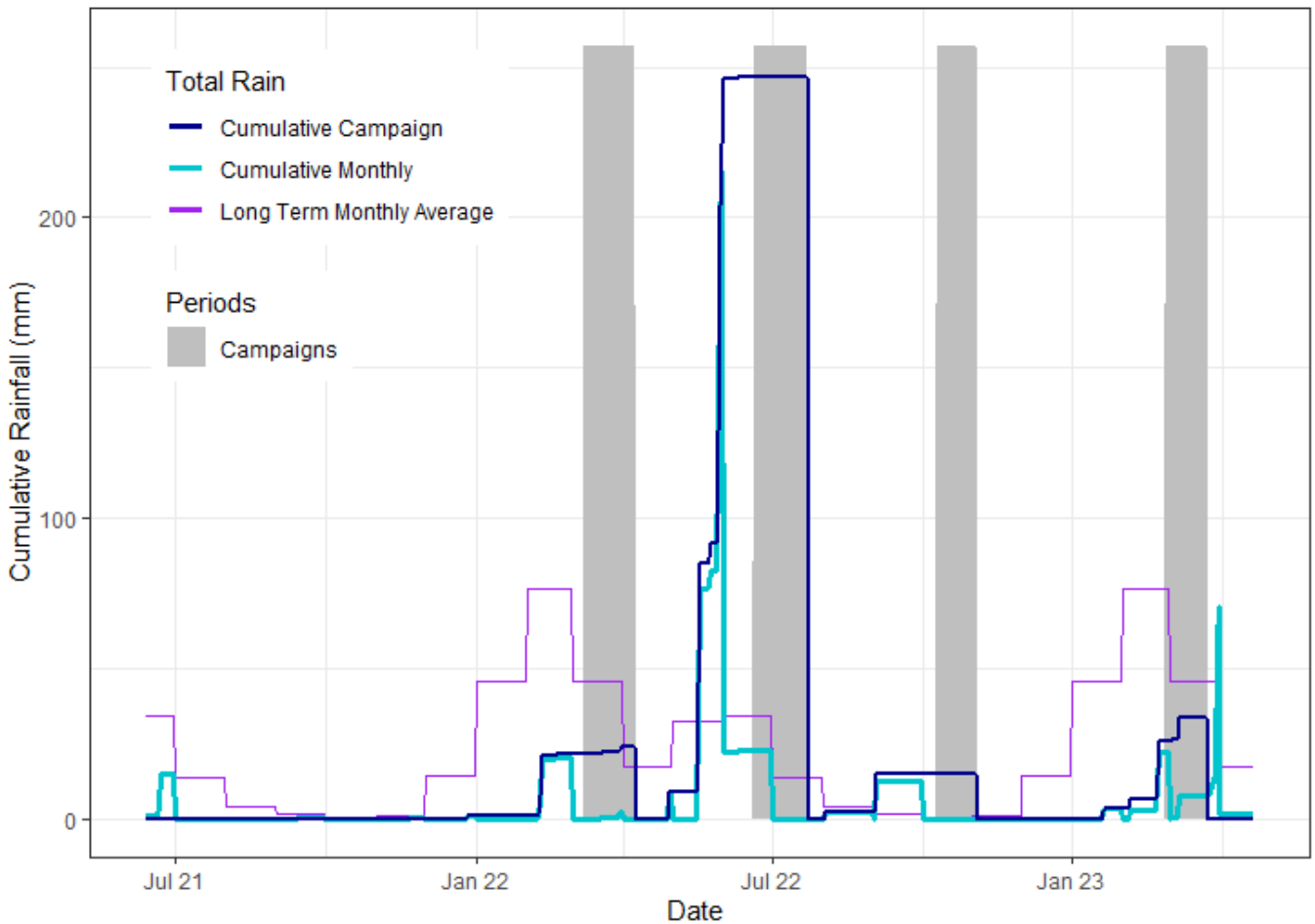


Figure ES-2: Fieldwork campaigns and Rainfall

Summary of key findings to date

The spectral measurement of rock art condition remains a promising approach, now that the issues of relocation (repositioning the probe each return visit) and shading identified from previous work appear to have largely been resolved. Detailed criteria have been developed and presented in this report to identify any sources of error or non-repeatability in the measurements. It is planned to apply these in real-time in future campaigns to ensure that all collected measurements can be utilised in analyses. The spectroscopy approach is likely best suited to monitor long term change rather than short term or seasonal responses, therefore data from additional measurement campaigns are required before it is meaningful to examine correlations between these measurements and air quality.

The geological and mineralogical studies have identified important compositional and structural/morphological trends in the rock surface/patina region. As expected, some features are related to rock type whereas others show consistent trends across rock type and are therefore likely due to environmental conditions. Detailed quantitative statistical analysis of the results are yet to be undertaken, however these studies appear to be a promising source

of key information to fully understand the system and processes occurring at Murujuga. Key minerals which may be early indicators of accelerated weathering have been identified.

Some spatial trends in electrochemical parameters and elemental composition have been found. Spatial trends are also appearing with many measured air pollutants, which generally support trends in the prior air quality (CAMx) modelling studies. Spatial correlations have been determined between the pH dataset in campaign one and modelled air quality parameters, however further work is required before determination of any causal relationships and subsequent development of EQCs. Specifically, spatial correlations were found between pH and previously modelled spatial pattern of nitrogen dioxide (NO₂), sulphur dioxide (SO₂) ozone (O₃), ammonia (NH₃) and particulate matter PM₁₀. It should be noted that the methods applied to date are unable to distinguish between air pollutants with sufficiently similar spatial patterns (for example, spatial gradients of NO₂ and SO₂ are near identical apart from regions where traffic sources are dominant). Furthermore:

- The observed relationships for the first two air pollutants (NO₂ and SO₂) and the campaign one pH data are the inverse of what would be expected for a simple acid-deposition hypothesis. This unexpected negative association does not take account of other variables which may have been involved; it is purely an empirical association observed in the exploratory phase of data analysis; however, it merits close attention.
- Ozone is a secondary air pollutant.
- PM₁₀ needs to be investigated as to whether it may act as a primary pollutant or a carrier for specific chemical species.

Further work and more field and chamber exposure study data (see Section 4.4) is therefore required in order to understand confounders and mechanistic relationships before EQCs can be developed.

The researchers are confident that the current approaches are appropriate overall in terms of techniques and statistical power and the in-progress studies will provide information to enable true mechanistic relationships to be confirmed or otherwise. Given the unseasonably low rainfall in year 1, it is proposed that field measurement campaigns be repeated in year 2 at the same frequency and timing as in year 1, with the full number of rock-art monitoring sites stratified between campaigns. A specific focus will also be given to campaigns during dry times and the mechanisms which may occur in the atmosphere or on the rock surface during those times, namely – understanding the high(er) pH values found during campaign 1 and the inverse relationship with acid-forming gases found, as well as exploring possible sources of direct emission of basic compounds or alternate pathways for secondary atmospheric pollutants during very hot and dry times – for example, the formation of basic instead of acidic compounds from gases such as SO₂ and NO₂.

Contents

Executive summary	ES-1
Summary of key findings to date	ES-3
1 Introduction	22
1.1 Background	22
1.2 Objectives of the MRAMP monitoring studies	22
1.3 Scope of this report	23
1.3.1 Inclusions	23
1.3.2 Exclusions	24
1.4 Abbreviations and definitions	25
1.4.1 Abbreviations	25
1.4.2 Chemical terms	27
1.4.3 Glossary	27
1.4.4 Site and sample numbering nomenclature	31
2 Study methodologies, verification of competency, and quality assurance	33
2.1 Elaboration of methodologies described in the MSDCA Plan	33
2.2 Personnel and verification of competency	34
2.3 Quality assurance	36
2.3.1 Air quality monitoring	36
2.3.2 Fieldwork	36
2.3.3 Laboratory analysis	37
3 Monitoring studies undertaken in the field	39
3.1 Field monitoring generally	39
3.1.1 Location of field monitoring sites	39
3.1.2 Summary of year 1 field campaigns	40
3.1.3 Weather conditions during the study period	40
3.2 Vegetation collection fieldwork	42
3.2.1 Objectives	42
3.2.2 Methodology	42
3.2.3 Fieldwork outcomes	42
3.3 Inorganic geochemistry fieldwork	45
3.3.1 Objectives	45
3.3.2 Methodology	45

3.3.3	Fieldwork outcomes	46
3.4	Microbiome collection fieldwork	49
3.4.1	Objectives	49
3.4.2	Methodology	49
3.4.3	Fieldwork outcomes	50
3.5	Surface change analysis (spectroscopy) fieldwork	53
3.5.1	Objectives	53
3.5.2	Methodology	53
4	Laboratory analysis of field samples	55
4.1	Organic geochemistry laboratory analysis.....	55
4.1.1	Objectives	55
4.1.2	Methodology	55
4.1.3	Work to date.....	55
4.2	Geology and inorganic geochemistry laboratory analysis	58
4.2.1	Objectives	58
4.2.2	Methodology	58
4.2.3	Geological mapping	58
4.2.4	Thin section preparation	61
4.2.5	Macro and micro characterisation	62
4.2.6	Scanning electron microscopy and energy dispersive x-ray spectroscopy analysis.....	67
4.2.7	Geochemical characterisation	77
4.2.8	Comparison with previous work.....	83
4.2.9	Preliminary findings from inorganic geochemistry analysis to date	85
4.3	Microbiome laboratory analysis	87
4.3.1	Objectives	87
4.3.2	Methodology	87
4.3.3	Work to date.....	87
4.4	Chamber exposure (accelerated degradation) testing	88
4.4.1	Objectives	88
4.4.2	Methodology	88
4.4.3	Work to date.....	88
5	Air quality monitoring network establishment and operation.....	93
5.1.1	Objectives	93
5.1.2	Methodology	93
5.1.3	AQM network outline	93

5.1.4	Passive AQM sites.....	95
6	Spatial mapping and surface modelling.....	99
6.1	Objectives.....	99
6.2	Spatial mapping.....	99
6.2.1	Scope of mapping	99
6.2.2	Methodology	99
6.2.3	Global navigation satellite system (GNSS) datum point.....	100
6.2.4	Local RTK control survey.....	103
6.2.5	Drone processing.....	104
6.2.6	Summary and issues	106
6.2.7	Completed site summary.....	106
6.3	Computational fluid dynamics (CFD) surface modelling.....	107
6.3.1	Objectives	107
6.3.2	Geometry and computer model.....	107
6.3.3	Meteorology and emissions data	107
6.3.4	Nesting of models.....	107
6.3.5	Interpretation of results	108
6.3.6	Progress and resources.....	108
7	Statistical analysis of combined (dose/response) data.....	109
7.1	Field colour measurements	109
7.1.1	Field campaigns and colour measurement	109
7.1.2	JAZ instrument.....	109
7.1.3	Typical spectral response	110
7.1.4	Initial validation of data.....	111
7.1.5	Data handling.....	112
7.1.6	Objectives of analysis	112
7.1.7	CIELAB perceptual colours.....	112
7.1.8	Generalised additive modelling.....	113
7.1.9	Analysis Results.....	113
7.2	Inorganic geochemistry - pH, Eh, Cl	134
7.2.1	Background.....	134
7.2.2	pH observations.....	135
7.2.3	Chloride (Cl ⁻) observations.....	142
7.2.4	Oxidation-reduction potential (ORP) observations.....	145
7.2.5	Multivariate association between pH, ORP and Cl.....	147

7.3	Inorganic geochemistry – pXRF.....	149
7.3.1	Background.....	149
7.3.2	Redundancy analysis.....	149
7.3.3	Ratios of pairs of elements.....	152
7.4	Passive samplers.....	156
7.4.1	Background.....	156
7.4.2	Selection experiment.....	156
7.4.3	Validation experiment.....	156
7.4.4	Field monitoring samples.....	157
7.5	Ramboll model (time averages).....	162
7.5.1	Background.....	162
7.5.2	Data.....	163
7.5.3	Spatial Analysis.....	163
7.6	Spatial dose response - pH versus Ramboll model.....	168
7.6.1	Correlations between pollution exposure and rock condition.....	168
7.6.2	Data extraction and processing.....	168
7.6.3	pH plotted against average gas concentration in the relevant season.....	169
7.6.4	Ramboll gas concentration predictions.....	171
7.6.5	Results for mean gas predictions over different periods.....	173
7.6.6	Results for maximum gas concentrations.....	174
7.6.7	Results for pH versus gases by rock type for campaign 1.....	175
7.7	Spatial dose response - pH versus weather and time.....	177
7.7.1	Validation of pH observations.....	177
7.7.2	Campaign impacts.....	177
7.7.3	Impact of temperatures on pH observations.....	179
7.7.4	Impact of rainfall on pH observations.....	180
7.8	Key findings from statistical analysis.....	180
7.8.1	Field measurement of colour.....	180
7.8.2	Inorganic chemistry: physico-chemical parameters (pH, Eh, Cl).....	181
7.8.3	Inorganic chemistry: pXRF.....	181
7.8.4	Passive air quality samplers.....	182
7.8.5	Ramboll model.....	182
7.8.6	Dose-response analysis.....	182
8	Progress towards interim EQCs.....	183
8.1	Introduction.....	183

8.2	Development of EQCs	183
8.3	Spatial vs temporal relationships.....	184
8.4	Correlation versus causation.....	185
8.5	Further steps to the development of EQCs	186
9	Key outcomes overall from the first year of scientific studies.....	187
10	References	189

Appendices

Appendix A:	Drone images and processing.....	A-1
Appendix A-1	Introduction	A-2
Appendix A-2	Site AQ02	A-4
Appendix A-3	Site AQ03	A-10
Appendix A-4	Site AQ04	A-16
Appendix A-5	Site AQ05	A-22
Appendix A-6	Site AQ06	A-28
Appendix A-7	Sites AQ07 and AQ08 (adjoined)	A-34
Appendix A-8	Site AQ10	A-40
Appendix A-9	Site AQ11	A-46
Appendix B:	Spectroscopy operational parameters	B-1
Appendix B-1	Spectrometer operation	B-2
Appendix B-2	Target selection and re-establishment.....	B-4
Appendix B-3	The influence of external stray light.....	B-10
Appendix B-4	Probe angle.....	B-14
Appendix B-5	Probe distance	B-17
Appendix B-6	Instrument precision	B-19
Appendix C:	TIMA analysis results	C-1
Appendix C-1	TIMA analysis precis	C-2
Appendix C-2	Granophyre.....	C-3
Appendix C-3	Gabbro	C-60
Appendix C-4	Granite.....	C-84
Appendix C-5	Dolerite	C-87
Appendix C-6	Basalt	C-93

List of Figures

Figure ES-1:	Air Quality Monitor (AQM) deployment.....	2
Figure ES-2:	Fieldwork campaigns and Rainfall	3
Figure 3-1:	Map of field monitoring sites.....	39
Figure 3-2:	Timing of field campaigns and rainfall (data source: BOM Station ID 004083 – Karratha Aero)	41
Figure 3-3:	Mean, maximum and minimum daily air temperatures during the study period (data source: BOM Station ID 004083 – Karratha Aero).....	41
Figure3-4:	Vegetation collection sites.....	43
Figure 4-1:	Example of a sample rock processed: (a) in the field (b) as received (c) after rock surface has been removed.	56
Figure 4-2:	Amount of rock surface collected. Bar graph shows the number of samples with the amount of material obtained. Pie graph displays the distribution of masses obtained.	56
Figure 4-3:	Example of organic extract of various rock surfaces.	57
Figure 4-4:	Examples of ongoing geological mapping. Top: aerial photograph of a portion of West Intercourse Island with granophyre lithology indicated around three monitored rock art panels. Bottom: aerial photograph of the area surrounding the rock art panel RS16-GBR. The shaded polygon indicates the distribution of gabbro in the surrounding of the rock art site location.	60
Figure 4-5:	Thin section preparation stages. (a) Cross-section selection. (b) Embedding into epoxy. (c) Fresh cut of the sample after epoxy impregnation. Black lines indicate billet dimensions. (d) Polished thin section.....	61
Figure 4-6:	Summary of granophyre modal analyses obtained by TIMA. The TIMA database comprises mineral end-members rather than solid solution phases so the table should be read noting that, for example, anorthite represents Ca-rich feldspars and orthoclase represents K-feldspars. A: Major phases; B: Minor phases.....	65
Figure 4-7:	Crossed polarised image of clinopyroxene showing the typical twinning.....	66
Figure 4-8:	Summary of gabbro modal analyses obtained from TIMA. The TIMA database comprises mineral end-members rather than solid solution phases so the table should be read bearing in mind that, for example, anorthite represents Ca-rich feldspars and orthoclase represents K-feldspars.	67
Figure 4-9:	SEM-BSE image of the matrix of granophyre sample EX02_GPH. In the image is possible to distinguish a vermicular granophyric intergrowth between quartz (darker) and K-feldspar (lighter grey). The brightest phases represent Fe-Ti oxides.	68
Figure 4-10:	SEM-SE image taken from sample EX08_GPH. This image shows the formation of patina (left) on top of the weathered granophyre texture (void-rich area formed by dissolution of K-feldspar). Quartz within the less weathered rock to the right shows higher relief, because it is harder than the patina.	69
Figure 4-11:	Close-up SEM-BSE image of patina from granophyre sample RS11_GPH showing discontinuous contorted layers of patina above quartz crystals. The bright particles within the patina are Fe-Ti oxides.	70

Figure 4-12:	SEM-BSE images. (top left) Rock patina on top of modified granophyric intergrowth of quartz and K-feldspar. (top right) close up of top-left image. The voids are inferred to form by dissolution of feldspar. (bottom left) Close-up detail of circular particles with a fibrous groundmass, tentatively attributed to biological activity. (bottom right) Close-up image of particle aggregates surrounded by an Fe-enriched layer.	71
Figure 4-13:	EDS compositional maps of an area of the patina shown at the top left of the image. Elements Mn, Al, Fe and P are heterogeneously distributed, and the patina comprises distinct Al, Fe, Mn, and P rich layers. The widespread distribution of S is consistent with the presence of biological material.	72
Figure 4-14:	SEM-BSE images from sample AQ16_GBR. The top images display a single crystal of clinopyroxene with dissolution patterns localised along the cleavage direction of the mineral. Bottom images show a portion of patina (left) developed in the cavity formed by the dissolution of former clinopyroxene. Bottom right image shows a close-up of the patina arrangement between relict portions of clinopyroxene. This image emphasises the different topography of the granophyre and gabbro surfaces, and the different distribution of patina on those different surfaces.	73
Figure 4-15:	Large area EDS map of a portion of the patina from sample AQ09_GBR. Top left shows the BSE image of the investigated area. The map is acquired over a relict phase of clinopyroxene. Chemical heterogeneities are mostly observed for Mg, Na, Fe and Mn. Mn is mostly enriched at the top of the area that comprises the patina. A rim of enriched Na is visible for the surrounding plagioclase.	74
Figure 4-16:	Large area SEM-BSE image of patina in sample EX02_GPH. Images at BSE reveal a compositional contrast (brighter and lighter areas) and a thin-layered structure within the patina. Brighter particles in the patina are Fe-Ti oxides.	76
Figure 4-17:	XRD analysis plot for granophyre sample rock EX02_GPH. The mineral database for the XRD software holds patterns for mineral end-members rather than for the solid solutions found in the rocks. Thus, for example, albite represents sodic plagioclase, microcline represents K-feldspar, and chamosite represents chlorite.	78
Figure 4-18:	XRD analysis plot for granophyre sample rock AQ13_GPH. The mineral database for the XRD software holds patterns for mineral end-members rather than for the solid solutions found in the rocks. Thus, for example, albite represents sodic plagioclase, microcline represents K-feldspar, and chamosite represents chlorite. Indianite is a polymorph of anorthite, and represents calcic plagioclase.	79
Figure 4-19:	XRD analysis plot for gabbro sample rock AQ03_GBR. . The mineral database for the XRD software holds patterns for mineral end-members rather than for the solid solutions found in the rocks. Thus, for example, albite represents sodic plagioclase, actinolite represents Al-poor amphibole, and clinchlore represents chlorite.	80
Figure 4-20:	XRD analysis plot for basalt sample rock RS04_BAS. The mineral database for the XRD software holds patterns for mineral end-members rather than for the solid solutions found in the rocks. Thus, for example, albite represents sodic plagioclase, actinolite represents Al-poor amphibole, clinchlore represents chlorite, and sanidine represents an unknown K-feldspar, potentially a low-temperature alteration phase.	81
Figure 4-21:	Cross section of the granophyre sample EX02_GPH showing the three-layer structure of the rock from Donaldson (2011). Scale bar is 20 -mm.	83
Figure 4-22:	Photomicrograph in plane-polarized light of gabbro sample AQ16_GBR. In the centre of the image a crystal of clinopyroxene (augite) is replaced by chlorite (pale green). Biotite (dark brown) is also present.	85

Figure 4-23:	Photomicrograph in plane-polarized light of granite sample RS02_GRT showing sericitized plagioclase (light brown). A coronitic texture of chlorite (and biotite?) surrounding plagioclase of the rock is also visible.....	85
Figure 4-24:	Preliminary chamber exposure test sample arrangement.....	89
Figure 4-25:	Mean pH measured over time (minutes) for four rock types and for distilled/deionised (DI) water alone. With (a) pre and (b) post exposure to exhaust from combustion of a 50/50 diesel/condensate mixture; (c) pre and (d) post exposure to diesel exhaust. Dots and solid lines are the mean pH values and the shaded area is mean \pm standard deviation.	90
Figure 4-26:	Boxplot of pH for initial pH (start) and final pH (end) measurements for control and condensate rock samples, one boxplot for each rock type and distilled/deionised (DI) water; post 1hr exposure to condensate exhaust.....	91
Figure 4-27:	Boxplot of pH for initial pH (start) and final pH (end) measurements for control and diesel rock samples, one boxplot for each rock type and distilled/deionised (DI) water; post 1hr exposure to diesel exhaust.....	92
Figure 5-1:	MRAMP AQM network and status as at April 2023, with existing industry monitors also shown.....	95
Figure 5-2:	Passive AQM (AQ12) showing key components of the monitoring system. Ronald Fellows-Smith and MAC Ranger Kasziem Bin Sali shown post installation of electronics.....	96
Figure 7-1:	Typical data file format from the JAZ instrument.....	109
Figure 7-2:	AQ02_GPH art panel colour measurements for Target 1 (10 replicates).....	111
Figure 7-3:	Example of invalide JAZ data file – P values of zero.	114
Figure 7-4:	Example of invalid JAZ data file – positive P value with negative numerator (S-D) and denominator (R-D).	114
Figure 7-5:	Art panel AQ09_GPH: (a) wavelength (nm) versus % reflectance with different colour dot for the four campaigns (where orange is campaign 1, blue campaign 2, pink campaign 3 and green campaign 4) only for target 1 (all other targets have a similar trend); (b) boxplot of L* values from CIELAB for each campaign; (c) boxplot of a* values from CIELAB for each campaign; (d) boxplot of b* values from CIELAB for each campaign.....	117
Figure 7-6:	Art panel EX06_GPH: (a) wavelength (nm) versus % reflectance with different colour dot for the four campaigns (where orange is campaign 1, blue campaign 2, pink campaign 3 and green campaign 4) only for target 1 (all other targets have a similar trend); (b) boxplot of L* values from CIELAB for each campaignand for all targets; (c) boxplot of a* values from CIELAB for each campaign; (d) boxplot of b* values from CIELAB for each campaign.....	118
Figure 7-7:	Art panel AQ11_GPH: (a) wavelength (nm) versus % reflectance with different colour dot for the four campaigns (where orange is campaign 1, blue campaign 2, pink campaign 3 and green campaign 4) only for target 10 (all other targets have a similar trend); (b) boxplot of L* values from CIELAB for each campaignand for all targets; (c) boxplot of a* values from CIELAB for each campaign; (d) boxplot of b* values from CIELAB for each campaign.....	119
Figure 7-8:	Art panel EX05_GPH wavelength (nm) versus % reflectance with different colour dots for the four campaigns. The ten panels correspond to the 10 targets.	120
Figure 7-9:	Wavelength (nm) versus % reflectance for: (a) exponential trend AQ07_GRT target 10; (b) “s” curve AQ10_GPH target 2; (c) “s” curve with a tail at the bottom AS01_DOL target	

	3; (d) s curve with wiggly shape and sharp peak at end AQ04_GPH target 7; (e) sharp peak AQ05_GPH target 1.....	121
Figure 7-10:	Art panel AQ 10_GPH wavelength (nm) versus % reflectance with different colour dots for the four campaigns. The ten panels correspond to the 10 targets.....	122
Figure 7-11:	Art panel AQ 10_GPH wavelength (nm) versus % reflectance with different colour dots for the four campaigns, where data from campaign 4 was re-measured. The ten panels correspond to the 10 targets.	123
Figure 7-12:	Art panel AQ10_GPH boxplot of L, a and b for each campaign; where campaign 4 m1 is the first measurement and campaign 4 m2 is the second measurement.....	124
Figure 7-13:	Art panel AQ10_GPH: (a) percentage of P values (% reflectance) that are negative between the visible spectrum (380 to 780 nm wavelength); (b) percentage of P values that are negative between all wavelengths; (c) percentage of wavelengths where the S value is less than D and R is less than D (labelled S invalid) only for wavelengths in the visible spectrum; (d) percentage of wavelengths where the S value is less than D and R is less than D for all wavelengths.	125
Figure 7-14:	Art panel AQ10_GPH reflection count versus wavelength for (a) campaign 1 target 3 and (b) campaign 4 target 3. The red points indicate that the S (spectrum) value is less than D (dark) and R (reference) is less than D. These two figures correspond to the top right panel in Figure 7-10.	125
Figure 7-15:	Art panel RS04_GBR: (a) wavelength (nm) versus % reflectance with different colour dot for the four campaigns (where orange is campaign 1, blue campaign 2, pink campaign 3 and green campaign 4) only for target 10 (all other targets have a similar trend); (b) boxplot of L* values from CIELAB for each campaign and for all targets; (c) boxplot of a* values from CIELAB for each campaign; (d) boxplot of b* values from CIELAB for each campaign.....	126
Figure 7-16:	Art panel RS04_GBR GAM fit of wavelength (nm) versus reflectance (%), with one curve for each target in each campaign. Solid coloured lines are the predicted reflectance for each campaign and the grey shaded area is the 95% prediction intervals.	128
Figure 7-17:	Art panel AQ03_DOL GAM fit of wavelength (nm) versus reflectance (%) one curved fitted for each campaign. Solid coloured lines are the predicted reflectance for each campaign and the grey shaded area is the 95% prediction intervals.	129
Figure 7-18:	Art panel AQ10_GPH GAM fit of wavelength (nm) versus reflectance (%) one curved fitted for each campaign. Solid coloured lines are the predicted reflectance for each campaign and the grey shaded area is the 95% prediction intervals. Where campaign 4 m1 is the first measurement and campaign 4 m2 is the second measurement.	130
Figure 7-19:	Art panel AQ11_GPH GAM fit of wavelength (nm) versus reflectance (%) one curved fitted for each campaign. Solid coloured lines are the predicted reflectance for each campaign and the grey shaded area is the 95% prediction intervals.	131
Figure 7-20:	Art panel RS04_GBR GAM fit of wavelength (nm) versus reflectance (%) one curved fitted for each campaign. Solid coloured lines are the predicted reflectance for each campaign and the grey shaded area is the 95% prediction intervals.	132
Figure 7-21:	Boxplots of pH by campaign	135
Figure 7-22:	Boxplots of pH by rock type for each campaign	136
Figure 7-23:	pH observations against calendar date (campaign 1).....	137

Figure 7-24:	pH measurements, shown as dots with colour representing pH value, mapped at the spatial locations of the sample rocks. Campaign 1 only.	139
Figure 7-25:	Spatially interpolated pH values. Colour map overlaid with contour lines. The blue line represents the Karratha coastline. The grey polygon is Legendre Island.	141
Figure 7-26:	Boxplots of Cl ⁻ by campaign. Note logarithmic scale.	142
Figure 7-27:	Boxplots of Cl ⁻ by rock type for different campaigns. Note logarithmic scale.	143
Figure 7-28:	Spatially smoothed chloride ion (Cl ⁻) concentration. Colour map overlaid with contour lines. The blue line represents the Karratha coastline. The grey polygon is Legendre Island.	144
Figure 7-29:	Boxplots of ORP by different campaigns.	145
Figure 7-30:	Boxplots of ORP by rock type for different campaigns.	145
Figure 7-31:	Spatially interpolated ORP colour map overlaid with contour lines. (The blue line represents the Karratha coastline. The grey polygon is Legendre island).	146
Figure 7-32:	Campaign 2 pairwise scatter plots between pH, ORP and log Cl (“Cl_log”). Where the panels above the diagonal show the correlation between two variables; panels on the diagonal show the histogram of each variable; panels below the diagonal show a scatter plot between two variables.	147
Figure 7-33:	Campaign 3 pairwise scatter plots between pH, ORP and log Cl (“Cl_log”). Where the panels above the diagonal show the correlation between two variables; panels on the diagonal show the histogram of each variable; panels below the diagonal show a scatter plot between two variables.	148
Figure 7-34:	Campaign 4 pairwise scatter plots between pH, ORP and log Cl (“Cl_log”). Where the panels above the diagonal show the correlation between two variables; panels on the diagonal show the histogram of each variable; panels below the diagonal show a scatter plot between two variables.	148
Figure 7-35:	Redundancy ordination for the fitted model of chemical species from the pXRF associated with rock type in campaign 1. Percentage in parentheses is the percentage of total variation explained by the fitted model.	150
Figure 7-36:	Redundancy ordination for the fitted model of chemical species from the pXRF associated with rock type in campaign 2. Percentage in parentheses is the percentage of total variation explained by the fitted model.	150
Figure 7-37:	Redundancy ordination for the fitted model of chemical species from the pXRF associated with rock type in campaign 3. Percentage in parentheses is the percentage of total variation explained by the fitted model.	151
Figure 7-38:	Redundancy ordination for the fitted model of chemical species from the pXRF associated with rock type in campaign 4. Percentage in parentheses is the percentage of total variation explained by the fitted model.	151
Figure 7-39:	Redundancy ordination for the fitted model of chemical species from the pXRF associated with rock type and different campaigns.	152
Figure 7-40:	Boxplots of SiO ₂ : Ti by rock type and campaign.	153
Figure 7-41:	Spatial smoothing of SiO ₂ :Ti ratio in granophyre (GPH) overlaid contours of actual SiO ₂ :Ti.	154
Figure 7-42:	Rock types of the sample rocks.	155

Figure 7-43:	Investigation of potential ‘device effect’ in campaign 1. Boxplots of SiO ₂ :Ti by device manufacturer (Left) and manufacturer of device used at each site (Right).	155
Figure 7-44:	Boxplots of gas concentration observations for the validation experiment for 11 samples collected over a month at the air quality measuring station AQA1: (a) NO ₂ , (b) SO ₂ , (c) NH ₃ , (d) O ₃ , and (e) HNO ₃	157
Figure 7-45:	Scatter plots of passive sample gas concentration by air quality station for November 2022 (blue points), December 2022 (red points) and January 2023 (green points): (a) NO ₂ ; (b) SO ₂ (log concentration); (c) NH ₃ ; (d) O ₃ ; and (e) HNO ₃ (log concentration). Stations are ordered by mean NO ₂ concentration (lowest to highest).	160
Figure 7-46:	Boxplots showing passive sampling gas concentration results across the 17 air quality monitoring stations for November 2022, December 2022, and January 2023: (a) NO ₂ ; (b) log SO ₂ ; (c) NH ₃ ; (d) O ₃ , and (e) log HNO ₃	162
Figure 7-47:	Annual average NO ₂	163
Figure 7-48:	Annual maximum NO ₂	163
Figure 7-49:	Annual average SO ₂	164
Figure-7-50:	Annual maximum SO ₂	164
Figure 7-51:	Annual average NH ₃	164
Figure 7-52:	Annual maximum NH ₃	164
Figure 7-53:	Annual average HNO ₃	165
Figure 7-54:	Annual maximum HNO ₃	165
Figure 7-55:	Annual average HCl	165
Figure 7-56:	Annual maximum HCl	165
Figure 7-57:	Annual average Na	166
Figure 7-58:	Annual Maximum Na	166
Figure 7-59:	Annual average H ₂ SO ₄	166
Figure 7-60:	Annual maximum H ₂ SO ₄	166
Figure 7-61:	Annual average CO	166
Figure 7-62:	Annual maximum CO	166
Figure 7-63:	Annual average N ₂ O ₅	167
Figure 7-64:	Annual maximum N ₂ O ₅	167
Figure 7-65:	Annual average O ₃	167
Figure 7-66:	Annual maximum O ₃	167
Figure 7-67:	Measurements of pH for each locality (including replicates) versus the mean (or log mean) of gas concentrations by campaign: (a) log mean SO ₂ concentration; (b) log mean NO ₂ concentration; (c) mean O ₃ concentration; (d) mean HCl concentration; (e) mean HNO ₃ concentration; and (f) mean calculated particulate matter PM ₁₀ concentration.	171
Figure 7-68:	Boxplot of monthly gas concentrations overall monitored art panels comparing Ramboll estimates of gases for current (2014) and future (2030) emissions for: (a) log concentration of SO ₂ ; (b) log HCl; (c) log NH ₃ . The log scale makes the ranges more readable but introduces a number of lower outliers. For HCl and NH ₃ , the overall range is from the 2nd to the 100th percentile to remove long tails of outliers that are less than 0.1.	173

Figure 7-69:	pH versus the predicted annual mean gas concentration or maximum gas concentration by campaign: (a) log annual mean concentration of SO ₂ ; (b) annual mean concentration of HCl; (c) SO ₂ log maximum concentration over each campaign period; (d) O ₃ maximum concentration over each campaign period; (e) SO ₂ log maximum concentration over a year; and (f) O ₃ maximum concentration over a year.	174
Figure 7-70:	pH versus predicted mean gas prediction by rock type for campaign 1: (a) log mean SO ₂ concentration; (b) log mean NH ₃ concentration; (c) mean O ₃ concentration; and (d) mean calculated PM ₁₀	176
Figure 7-71:	Measurements of Mn (from pXRF device) for each locality (including replicates) and campaign versus the log mean NO ₂ concentration	176
Figure 7-72:	pH observations at each location versus days since the start of each campaign.....	178
Figure 7-73:	Scatter plots showing pH observations for each site in relation to temperature: (a) wet bulb temperature; (b) air temperature (or dry bulb temperature); (c) daily maximum temperature; and (d) daily minimum temperature. These temperatures were recorded at BOM Karratha Aero Station ID 004083 within a 15 minute period of the actual measurement being made.....	179
Figure 7-74:	pH versus days since rainfall at Karratha Aero: a) since any rain and b) since substantial rain greater than 30 mm.....	180
Figure 8-1:	Example of a dose-response curve. Theoretical NOAEL, Acceptable, Action and Exceedance levels are shown, as are data points and a dose-response curve.	183
Figure A-1:	Site AQ02 mapping position uncertainties	A-6
Figure A-2:	Site AQ02 mapping resolution	A-7
Figure A-3:	Site AQ02 orthoimage.....	A-8
Figure A-4:	Site AQ02 digital elevation model	A-9
Figure A-5:	Site AQ03 mapping position uncertainties	A-12
Figure A-6:	Site AQ03 mapping resolution	A-13
Figure A-7:	Site AQ03 orthoimage.....	A-14
Figure A-8:	Site AQ03 digital elevation model	A-15
Figure A-9:	AQ04 mapping position uncertainties	A-18
Figure A-10:	Site AQ04 mapping resolution	A-19
Figure A-11:	Site AQ04 orthoimage.....	A-20
Figure A-12:	Site AQ04 digital elevation model	A-21
Figure A-13:	AQ05 mapping position uncertainties	A-24
Figure A-14:	Site AQ05 mapping resolution	A-25
Figure A-15:	Site AQ05 orthoimage.....	A-26
Figure A-16:	Site AQ05 digital elevation model	A-27
Figure A-17:	AQ06 mapping position uncertainties	A-30
Figure A-18:	Site AQ06 mapping resolution	A-31
Figure A-19:	Site AQ06 orthoimage.....	A-32
Figure A-20:	Site AQ06 digital elevation model	A-33
Figure A-21:	AQ07 and AQ08 mapping position uncertainties	A-36

Figure A-22:	Site AQ07 and AQ08 mapping resolution	A-37
Figure A-23:	Site AQ07 and AQ08 orthoimage.....	A-38
Figure A-24:	Site AQ07 and AQ08 digital elevation model	A-39
Figure A-25:	Site AQ10 mapping position uncertainties.....	A-42
Figure A-26:	Site AQ010 mapping resolution.....	A-43
Figure A-27:	Site AQ10 orthoimage.....	A-44
Figure A-28:	Site AQ10 digital elevation model	A-45
Figure A-29:	Site AQ11 mapping position uncertainties.....	A-48
Figure A-30:	Site AQ11 mapping resolution.....	A-49
Figure A-31:	Site AQ11 orthoimage.....	A-50
Figure A-32:	Site AQ11 digital elevation model	A-51
Figure B-1:	Mini weather station at left mounted on a rock close to the study site. A thermal image at right records three points with interpolation to all parts of the rock surface.	B-3
Figure B-2:	A gridded RS site, with grid cells chosen at random.....	B-5
Figure B-3:	Comparison of two grid cells at an RS site and a more freely selected EX site.	B-6
Figure B-4:	Targets from the corresponding cells in Figure in macro view, as observed through the positioning screen.....	B-6
Figure B-5:	An abridged sequence of images that locate the grid cell on the whole rock, leading to the final macro images of the probe and light source. Note that the first macro image has stray light entering, blocked out prior to taking a reading.	B-7
Figure B-6:	MAC Ranger Kasziem bin Sali aligns the spectrometer probe by comparing the macro features visible on the active camera at left with the reference location viewed on the static image in the right- hand phone.....	B-8
Figure B-7:	Test setup to record the influence of an external light source on the spectral reflectance from a white marble tile.	B-11
Figure B-8:	Reflectance spectra of the JAZ spectrometer’s xenon light source and that of the external LED interference light source	B-12
Figure B-9:	The influence of the LED is imperceptible at 23 Lux but begins to re-shape the spectrum at 50 Lux onwards. Key: Red LED, Blue 0 Lux, Violet 23 Lux, Green 50 Lux, Upper trace 202 Lux.....	B-13
Figure B-10:	Schematic of the CAD calculation of beam angle and light reflection into the sensor.	B-14
Figure B-11:	Extract from the 3-D vector plot of CIELab values at probe angles 0-50°, viewed on the L and a axes.	B-15
Figure B-12:	A 2D snapshot of the spectral response at distances from 1-11 mm for the surface.....	B-17
Figure B-13:	Site RS 11 Target 1 illustrating the difference between a 3 mm and 8 mm target area in terms of chromatic homogeneity.	B-18
Figure B-14:	Precision data for the three previously employed instruments. The grid is set at 5 L*a*b* units. It is clear from this graphic that only the ASD instrument is precise enough to draw colour change conclusions of any significance. None of them can confidently discern $\Delta E = 2$	B-20
Figure B-15:	A snapshot of the repeatability of the JAZ spectrometer together with data for the Pico smartphone attachment.....	B-23

Figure C-1:	Panorama image of granophyre sample rock AQ02_GPH.....	C-3
Figure C-2:	BSE image of granophyre sample rock AQ02_GPH	C-3
Figure C-3:	Phase map of granophyre sample rock AQ02_GPH	C-4
Figure C-4:	Modal analysis of granophyre sample rock AQ02_GPH	C-4
Figure C-5:	Element map of granophyre sample rock AQ02_GPH.....	C-5
Figure C-6:	Grain size distribution of granophyre sample rock AQ02_GPH.....	C-5
Figure C-7:	Panorama image of granophyre sample rock AQ04_GPH.....	C-6
Figure C-8:	BSE image of granophyre sample rock AQ04_GPH	C-6
Figure C-9:	Phase map of granophyre sample rock AQ04_GPH	C-7
Figure C-10:	Modal analysis of granophyre sample rock AQ04_GPH	C-7
Figure C-11:	Element map of granophyre sample rock AQ04_GPH.....	C-8
Figure C-12:	Grain size distribution of granophyre sample rock AQ04_GPH.....	C-8
Figure C-13:	Panorama image of granophyre sample rock AQ05_GPH.....	C-9
Figure C-14:	BSE image of granophyre sample rock AQ05_GPH	C-9
Figure C-15:	Phase map of granophyre sample rock AQ05_GPH	C-10
Figure C-16:	Modal analysis of granophyre sample rock AQ05_GPH	C-10
Figure C-17:	Element map of granophyre sample rock AQ05_GPH.....	C-11
Figure C-18:	Grain size distribution of granophyre sample rock AQ05_GPH.....	C-11
Figure C-19:	Panorama image of granophyre sample rock AQ06_GPH.....	C-12
Figure C-20:	BSE image of granophyre sample rock AQ06_GPH	C-12
Figure C-21:	Phase map of granophyre sample rock AQ06_GPH	C-13
Figure C-22:	Modal analysis of granophyre sample rock AQ06_GPH	C-13
Figure C-23:	Element map of granophyre sample rock AQ06_GPH.....	C-14
Figure C-24:	Grain size distribution of granophyre sample rock AQ06_GPH.....	C-14
Figure C-25:	Panorama image of granophyre sample rock AQ08_GPH.....	C-15
Figure C-26:	BSE image of granophyre sample rock AQ08_GPH	C-15
Figure C-27:	Phase map of granophyre sample rock AQ08_GPH	C-16
Figure C-28:	Modal analysis of granophyre sample rock AQ08_GPH	C-16
Figure C-29:	Element map of granophyre sample rock AQ08_GPH.....	C-17
Figure C-30:	Grain size distribution of granophyre sample rock AQ08_GPH.....	C-17
Figure C-31:	Panorama image of granophyre sample rock AQ09_GPH.....	C-18
Figure C-32:	BSE image of granophyre sample rock AQ09_GPH	C-18
Figure C-33:	Phase map of granophyre sample rock AQ09_GPH	C-19
Figure C-34:	Modal analysis of granophyre sample rock AQ09_GPH	C-19
Figure C-35:	Element map of granophyre sample rock AQ09_GPH.....	C-20
Figure C-36:	Grain size distribution of granophyre sample rock AQ09_GPH.....	C-20
Figure C-37:	Panorama image of granophyre sample rock AQ13_GPH.....	C-21

Figure C-38:	BSE image of granophyre sample rock AQ13_GPH	C-21
Figure C-39:	Phase map of granophyre sample rock AQ13_GPH	C-22
Figure C-40:	Modal analysis of granophyre sample rock AQ13_GPH	C-22
Figure C-41:	Element map of granophyre sample rock AQ13_GPH.....	C-23
Figure C-42:	Grain size distribution of granophyre sample rock AQ13_GPH.....	C-23
Figure C-43:	Panorama image of granophyre sample rock AQ14_GPH.....	C-24
Figure C-44:	BSE image of granophyre sample rock AQ14_GPH	C-24
Figure C-45:	Phase map of granophyre sample rock AQ14_GPH	C-25
Figure C-46:	Modal analysis of granophyre sample rock AQ14_GPH	C-25
Figure C-47:	Element map of granophyre sample rock AQ14_GPH.....	C-26
Figure C-48:	Grain size distribution of granophyre sample rock AQ14_GPH.....	C-26
Figure C-49:	Panorama image of granophyre sample rock EX02_GPH.....	C-27
Figure C-50:	BSE image of granophyre sample rock EX02_GPH	C-27
Figure C-51:	Phase map of granophyre sample rock EX02_GPH	C-28
Figure C-52:	Modal analysis of granophyre sample rock EX02_GPH	C-28
Figure C-53:	Element map of granophyre sample rock EX02_GPH.....	C-29
Figure C-54:	Grain size distribution of granophyre sample rock EX02_GPH.....	C-29
Figure C-55:	Panorama image of granophyre sample rock EX03_GPH.....	C-30
Figure C-56:	BSE image of granophyre sample rock EX03_GPH	C-30
Figure C-57:	Phase map of granophyre sample rock EX03_GPH	C-31
Figure C-58:	Modal analysis of granophyre sample rock EX03_GPH	C-31
Figure C-59:	Element map of granophyre sample rock EX03_GPH.....	C-32
Figure C-60:	Grain size distribution of granophyre sample rock EX03_GPH.....	C-32
Figure C-61:	Panorama image of granophyre sample rock EX05_GPH.....	C-33
Figure C-62:	BSE image of granophyre sample rock EX05_GPH	C-33
Figure C-63:	Phase map of granophyre sample rock EX05_GPH	C-34
Figure C-64:	Modal analysis of granophyre sample rock EX05_GPH	C-34
Figure C-65:	Element map of granophyre sample rock EX05_GPH.....	C-35
Figure C-66:	Grain size distribution of granophyre sample rock EX05_GPH.....	C-35
Figure C-67:	Panorama image of granophyre sample rock EX06_GPH.....	C-36
Figure C-68:	BSE image of granophyre sample rock EX06_GPH	C-36
Figure C-69:	Phase map of granophyre sample rock EX06_GPH	C-37
Figure C-70:	Modal analysis of granophyre sample rock EX06_GPH	C-37
Figure C-71:	Element map of granophyre sample rock EX06_GPH.....	C-38
Figure C-72:	Grain size distribution of granophyre sample rock EX06_GPH.....	C-38
Figure C-73:	Panorama image of granophyre sample rock EX08_GPH.....	C-39
Figure C-74:	BSE image of granophyre sample rock EX08_GPH	C-39

Figure C-75:	Phase map of granophyre sample rock EX08_GPH	C-40
Figure C-76:	Modal analysis of granophyre sample rock EX08_GPH	C-40
Figure C-77:	Element map of granophyre sample rock EX08_GPH.....	C-41
Figure C-78:	Grain size distribution of granophyre sample rock EX08_GPH.....	C-41
Figure C-79:	Panorama image of granophyre sample rock EX09_GPH.....	C-42
Figure C-80:	BSE image of granophyre sample rock EX02_GPH	C-42
Figure C-81:	Phase map of granophyre sample rock EX09_GPH	C-43
Figure C-82:	Modal analysis of granophyre sample rock EX09_GPH	C-43
Figure C-83:	Element map of granophyre sample rock EX09_GPH.....	C-44
Figure C-84:	Grain size distribution of granophyre sample rock EX09_GPH.....	C-44
Figure C-85:	Panorama image of granophyre sample rock RS01_GPH.....	C-45
Figure C-86:	BSE image of granophyre sample rock RS01_GPH	C-45
Figure C-87:	Phase map of granophyre sample rock RS01_GPH	C-46
Figure C-88:	Modal analysis of granophyre sample rock RS01_GPH	C-46
Figure C-89:	Element map of granophyre sample rock RS01_GPH.....	C-47
Figure C-90:	Grain size distribution of granophyre sample rock RS01_GPH.....	C-47
Figure C-91:	Panorama image of granophyre sample rock RS04_GPH.....	C-48
Figure C-92:	BSE image of granophyre sample rock RS04_GPH	C-48
Figure C-93:	Phase map of granophyre sample rock RS01_GPH	C-49
Figure C-94:	Modal analysis of granophyre sample rock RS04_GPH	C-49
Figure C-95:	Element map of granophyre sample rock RS04_GPH.....	C-50
Figure C-96:	Grain size distribution of granophyre sample rock RS04_GPH.....	C-50
Figure C-97:	Panorama image of granophyre sample rock RS05#1_GPH.....	C-51
Figure C-98:	BSE image of granophyre sample rock RS05#1_GPH	C-51
Figure C-99:	Phase map of granophyre sample rock RS05#1_GPH	C-52
Figure C-100:	Modal analysis of granophyre sample rock RS05#1_GPH	C-52
Figure C-101:	Element map of granophyre sample rock RS05#1_GPH.....	C-53
Figure C-102:	Grain size distribution of granophyre sample rock RS05#1_GPH.....	C-53
Figure C-103:	Panorama image of granophyre sample rock RS06_GPH.....	C-54
Figure C-104:	BSE image of granophyre sample rock RS06_GPH	C-54
Figure C-105:	Phase map of granophyre sample rock RS06_GPH	C-55
Figure C-106:	Modal analysis of granophyre sample rock RS06_GPH	C-55
Figure C-107:	Element map of granophyre sample rock RS06_GPH.....	C-56
Figure C-108:	Grain size distribution of granophyre sample rock RS06_GPH.....	C-56
Figure C-109:	Panorama image of granophyre sample rock RS11_GPH.....	C-57
Figure C-110:	BSE image of granophyre sample rock RS11_GPH	C-57
Figure C-111:	Phase map of granophyre sample rock RS11_GPH	C-58

Figure C-112:	Modal analysis of granophyre sample rock RS11_GPH	C-58
Figure C-113:	Element map of granophyre sample rock RS11_GPH.....	C-59
Figure C-114:	Grain size distribution of granophyre sample rock RS11_GPH.....	C-59
Figure C-115:	Panorama image of gabbro sample rock AQ03_GBR	C-60
Figure C-116:	BSE image of gabbro sample rock AQ03_GBR.....	C-60
Figure C-117:	Phase map of gabbro sample rock AQ03_GBR.....	C-61
Figure C-118:	Modal analysis of gabbro sample rock AQ03_GBR.....	C-61
Figure C-119:	Element map of gabbro sample rock AQ03_GBR.....	C-62
Figure C-120:	Grain size distribution of gabbro sample rock AQ03_GBR	C-62
Figure C-121:	Panorama image of gabbro sample rock AQ09_GBR	C-63
Figure C-122:	BSE image of gabbro sample rock AQ09_GBR.....	C-63
Figure C-123:	Phase map of gabbro sample rock AQ09_GBR.....	C-64
Figure C-124:	Modal analysis of gabbro sample rock AQ09_GBR.....	C-64
Figure C-125:	Element map of gabbro sample rock AQ09_GBR.....	C-65
Figure C-126:	Grain size distribution of gabbro sample rock AQ09_GBR	C-65
Figure C-127:	Panorama image of gabbro sample rock AQ16_GBR	C-66
Figure C-128:	BSE image of gabbro sample rock AQ16_GBR.....	C-66
Figure C-129:	Phase map of gabbro sample rock AQ16_GBR.....	C-67
Figure C-130:	Modal analysis of gabbro sample rock AQ16_GBR.....	C-67
Figure C-131:	Element map of gabbro sample rock AQ16_GBR	C-68
Figure C-132:	Grain size distribution of gabbro sample rock AQ16_GBR	C-68
Figure C-133:	Panorama image of gabbro sample rock EX04_GBR	C-69
Figure C-134:	BSE image of gabbro sample rock EX04_GBR.....	C-69
Figure C-135:	Phase map of gabbro sample rock EX04_GBR.....	C-70
Figure C-136:	Modal analysis of gabbro sample rock EX04_GBR.....	C-70
Figure C-137:	Element map of gabbro sample rock EX04_GBR	C-71
Figure C-138:	Grain size distribution of gabbro sample rock EX04_GBR	C-71
F Figure C-139:	Panorama image of gabbro sample rock EX09_GBR	C-72
Figure C-140:	BSE image of gabbro sample rock EX09_GBR.....	C-72
Figure C-141:	: Phase map of gabbro sample rock EX09_GBR.....	C-73
Figure C-142:	Modal analysis of gabbro sample rock EX09_GBR.....	C-73
Figure C-143:	Element map of gabbro sample rock EX09_GBR	C-74
Figure C-144:	Grain size distribution of gabbro sample rock EX09_GBR	C-74
Figure C-145:	Panorama image of gabbro sample rock RS02_GBR	C-75
Figure C-146:	BSE image of gabbro sample rock RS02_GBR.....	C-75
Figure C-147:	Phase map of gabbro sample rock RS02_GBR.....	C-76
Figure C-148:	Modal analysis of gabbro sample rock RS02_GBR.....	C-76

Figure C-149:	Element map of gabbro sample rock RS02_GBR	C-77
Figure C-150:	Grain size distribution of gabbro sample rock RS02_GBR	C-77
Figure C-151:	Panorama image of gabbro sample rock RS10_GBR	C-78
Figure C-152:	BSE image of gabbro sample rock RS10_GBR.....	C-78
Figure C-153:	Phase map of gabbro sample rock RS10_GBR.....	C-79
Figure C-154:	Modal analysis of gabbro sample rock RS10_GBR.....	C-79
Figure C-155:	Element map of gabbro sample rock RS10_GBR	C-80
Figure C-156:	Grain size distribution of gabbro sample rock RS10_GBR	C-80
Figure C-157:	Panorama image of gabbro sample rock RS16_GBR	C-81
Figure C-158:	BSE image of gabbro sample rock RS16_GBR.....	C-81
Figure C-159:	Phase map of gabbro sample rock RS16_GBR.....	C-82
Figure C-160:	Modal analysis of gabbro sample rock RS16_GBR.....	C-82
Figure C-161:	Element map of gabbro sample rock RS16_GBR	C-83
Figure C-162:	Grain size distribution of gabbro sample rock RS16_GBR	C-83
Figure C-163:	Panorama image of granite sample rock RS02_GRT	C-84
Figure C-164:	BSE image of granite sample rock RS02_GRT	C-84
Figure C-165:	Phase map of granite sample rock RS02_GRT	C-85
Figure C-166:	Modal analysis of granite sample rock RS02_GRT.....	C-85
Figure C-167:	Element map of granite sample rock RS02_GRT	C-86
Figure C-168:	Grain size distribution of granite sample rock RS02_GRT	C-86
Figure C-169:	Panorama image of dolerite sample rock EX08_DOL	C-87
Figure C-170:	BSE image of dolerite sample rock EX08_DOL.....	C-87
Figure C-171:	Phase map of dolerite sample rock EX08_DOL.....	C-88
Figure C-172:	Modal analysis of dolerite sample rock EX08_DOL	C-88
Figure C-173:	Element map of dolerite sample rock EX08_DOL.....	C-89
Figure C-174:	Grain size distribution of dolerite sample rock EX08_DOL.....	C-89
Figure C-175:	Panorama image of dolerite sample rock RS05_DOL	C-90
Figure C-176:	BSE image of dolerite sample rock RS05_DOL.....	C-90
Figure C-177:	Phase map of dolerite sample rock RS05_DOL.....	C-91
Figure C-178:	Modal analysis of dolerite sample rock RS05_DOL	C-91
Figure C-179:	Element map of dolerite sample rock RS05_DOL.....	C-92
Figure C-180:	Grain size distribution of dolerite sample rock RS05_DOL.....	C-92
Figure C-181:	anorama image of basalt sample rock AQ12_BAS.....	C-93
Figure C-182:	BSE image of basalt sample rock AQ12_BAS	C-94
Figure C-183:	Phase map of basalt sample rock AQ12_BAS	C-94
Figure C-184:	Modal analysis of basalt sample rock AQ12_BAS.....	C-95
Figure C-185:	Element map of basalt sample rock AQ12_BAS	C-95

Figure C-186:	Grain size distribution of basalt sample rock AQ12_BAS	C-96
Figure C-187:	Panorama image of basalt sample rock RS09_BAS.....	C-97
Figure C-188:	BSE image of basalt sample rock RS09_BAS	C-97
Figure C-189:	Phase map of basalt sample rock AQ12_BAS	C-98
Figure C-190:	Modal analysis of basalt sample rock RS09_BAS.....	C-98
Figure C-191:	Element map of basalt sample rock RS09_BAS	C-99
Figure C-192:	Grain size distribution of basalt sample rock RS09_BAS	C-99
Figure C-193:	Panorama image of basalt sample rock RS12_BAS.....	C-100
Figure C-194:	BSE image of basalt sample rock RS12_BAS	C-100
Figure C-195:	Phase map of basalt sample rock RS12_BAS	C-101
Figure C-196:	Modal analysis of basalt sample rock RS12_BAS.....	C-101
Figure C-197:	Element map of basalt sample rock RS12_BAS	C-102
Figure C-198:	Grain size distribution of basalt sample rock RS12_BAS	C-102

List of Tables

Table 1-1:	General abbreviations and definitions	25
Table 1-2:	Chemical terms	27
Table 1-3:	Glossary.....	27
Table 1-4:	Study site nomenclature.....	31
Table 1-5:	Abbreviation codes for sample rock types	32
Table 2-1:	Component study methodologies	33
Table 2-2:	MRAMP component study contributing team members	34
Table 3-1:	Summary of field campaigns undertaken in the first year of studies.....	40
Table 3-2:	Representative vegetation samples collected	44
Table 3-3:	Number of pH, Eh, Cl and pXRF measurements on rock art panels taken for each campaign by site type.	46
Table 3-4:	Number of pH, Eh, Cl and pXRF measurements on sample rocks taken for each campaign by site type.....	47
Table 3-5:	Number of pH, Eh, Cl and pXRF measurements taken on rock art panels for each campaign by rock type.....	47
Table 3-6:	Number of pH, Eh, Cl and pXRF measurements on sample rocks taken for each campaign by rock type.	48
Table 3-7:	Campaign 1 microbiome sample collection summary.....	50
Table 3-8:	Campaign 2 microbiome sample collection summary.....	51
Table 3-9:	Number of spectroscopic measurements taken for each campaign by rock type	54
Table 3-10:	Number of spectroscopic measurements taken for each campaign by site type	54
Table 4-1:	Total organic carbon of different rock types (by weight %)	57
Table 4-2:	Geological mapping status for MRAMP study sites.....	59
Table 4-3:	Mineral modes for granophyre samples based on TIMA analysis.....	63
Table 4-4:	Compilation of identified minerals among the analysed XRD samples.....	82
Table 4-5:	Indicative Peak Exposure levels attainable combusting diesel or diesel-KGP condensate	89
Table 5-1:	AQM network design outline.....	94
Table 5-2:	Passive AQM sampler deployment and receipt of laboratory analysis results	98
Table 6-1:	Coordinates and Uncertainty of the Datum Point for the AQ and EX sites. Note sigmas are in metres, and reported as 95% confidence interval	101
Table 6-2:	Differences between report SSMs coordinates either through using it as a Datum point or taking a RTK check shot to the SSM from the site Datum point. The values are in metres.....	103
Table 7-1:	Percentage of two or more campaigns that have the same trend line.....	127

Table 7-2:	GAM results for the model fitted to each art panel and one curve fitted to each campaign. Where the same GAM result number for a particular art panel, indicates no difference in the campaigns and a similar curve.	133
Table 7-3:	The total number of samples, number of samples below the detection limit, and samples with valid detections for each gas species and each month.	161
Table B-1:	Target reocation validation using the feature/camera method (02 March 2022).	B-9
Table B-2:	Target reocation validation using the grid sheet method (02 March 2022).	B-9
Table B-3:	Repeat target relocation measurements after reapplying the grid sheet (02 March 2023)	B-9
Table B-4:	Target relocation validation of a vertical surface using the grid sheet (04 March 2022).....	B-10
Table B-5:	Target relocation validation of a vertical surface using the feature/camera method (04 March 2022).....	B-10
Table B-6:	Colour difference calculation for 20 spectra on the one target using the Konica Minolta colorimeter.	B-21
Table B-7:	ΔE comparison of 13 repeated spectra on CSIRO Site 1 Spot 1 using ASD data provided by DWER..	B-22
Table B-8:	ΔE calculation for 20 reference spectra form the JAZ spectrometer. The highest colour variation is $\Delta E = 1.1$	B-24
Table B-9:	Summary statistic for the 20 JAZ reference spectra.....	B-25

1 Introduction

1.1 Background

The Murujuga Rock Art Monitoring Program (**MRAMP**) will develop a series of Environmental Quality Criteria (**EQC**) and an Environmental Quality Management Framework (**EQMF**) for the ongoing management of the Murujuga region, with a focus on air quality.

This document presents a summary of data collection, laboratory studies and analysis undertaken within the first year of scientific studies since approval of the Program's Monitoring Studies Data Collection and Analysis (**MSDCA**) Plan in March 2022 and the formal commencement of the first fieldwork campaign. This report is not intended to be a stand-alone document, rather it is intended to be read in conjunction with the Conceptual Model, MSDCA Plan and detailed methodology statements for component studies as references throughout.

The MSDCA Plan requires a multi-year scientific research program, and as such many components remain in progress with results not yet available. Likewise, results from external laboratory analyses (such as analysis of passive air quality samples) are still being received for samples collected during the first year. Statistical data analysis is ongoing as data is received. Section 1.3 summarises the works completed and included or excluded from this report.

1.2 Objectives of the MRAMP monitoring studies

From Section 1.3 of the MSDCA Plan (Curtin, 2022), the main research goals of the current phase of the MRAMP studies are to:

1. Accurately measure the colour and surface texture of rocks across the Murujuga region, establish baseline values for a long-term monitoring program, identify important differences in colour or surface texture which may be associated with accelerated (anthropogenic) weathering, and develop criteria for assessing weathering rates.
2. Identify and characterise the minerals, inorganic and organic chemicals, and microbes present on the rock surface and in the sub-layers, which are relevant to the appearance and integrity of the petroglyphs or may be involved in accelerating or preventing the degradation of the petroglyphs.
3. Determine which atmospheric pollutants are present in industrial (e.g. port, shipping and local industry) and natural emissions (e.g. marine aerosols, emissions from bushfires) on Murujuga, and which are capable of causing degradation of, or change in, the petroglyphs.
4. Under controlled laboratory conditions with small samples of rock, measure the effect of a known amount of pollutant chemical on the constituents of the rock surface and sub-layers.
5. Measure the concentration of atmospheric pollutants to which rocks are exposed, across the Murujuga region.
6. Identify the weather conditions, environmental conditions and industrial output conditions which are likely to pose the greatest risk of degradation to petroglyphs.
7. Calculate the timescales over which changes are predicted to occur, and thresholds of pollutants giving rise to accelerated change.

8. Identify sentinel variables (“canary in the coal mine”) which can be observed in the field and which can serve as indicators (EQC) of increased risk of degradation.
9. Determine if soil monitoring will inform some processes or measurements on the rock surface.
10. To utilise world-leading statistical design, methodology, and analysis techniques.
11. Link all of the evidence in the studies above to reach rigorous scientific conclusions and provide a rigorous evidence base for the Conceptual Model and the EQMF and the Monitoring Program as a whole.

The studies phase of the Program involves measuring and studying many things which will not be part of the final monitoring phase of the Program, but which must be understood to demonstrate links between the environmental variables and the impacts on the petroglyphs.

1.3 Scope of this report

This report summarises all work completed during the first year of the monitoring studies following approval of the MSDCA Plan in March 2022. Works still in progress are reported as such and results will be forthcoming in subsequent reports and included in statistical analyses coincident with their completion.

1.3.1 Inclusions

Activities undertaken during the first year of studies and reported on here are described following.

Fieldwork

Overall fieldwork:

- Four fieldwork campaigns were undertaken totalling approximately 18 weeks duration in all. Fieldwork involved monitoring 54 rock art panels and 64 sample rocks across the five rock types found in the study area.
- All available results from this work are presented in this document.

Spectrometry:

- 21,600 spectral/colour measurements of rock art condition are reported on and analysed in detail.

Field X-Ray Fluorescence:

- 1,037 surface elemental measurements using x-ray fluorescence (pXRF) were collected and analysed.

Electrochemical measurements:

- 2,594 surface electrochemical measurements (pH, Eh, Cl) were taken and are analysed in detail and examined for any correlation with air quality estimates. Fewer Eh and Cl measurements were taken in campaign one, due to faulty probes, which could not be replaced during the campaign, otherwise 1,037 measurements each of pH, Eh, Cl would have been obtained.

Microbiome:

- Two campaigns were undertaken with collection of triplicate patina samples from each sample rock in each campaign. These samples will be sequenced using 16S rRNA and ITS amplicon sequencing as well as metagenomic and metatranscriptomic sequencing.

- Proximal soil and/or lichen samples were also collected where present in the immediate vicinity (approximately 5 m radius) of the sample rock. 16S rRNA and ITS amplicon sequencing will be done on both the lichen and soil samples, and lichen samples will have metagenomic and metatranscriptomic sequencing.
- Plate cultures of bacteria and fungi were also prepared. These samples are still being sequenced using 16S rRNA and ITS amplicons and analysed.

Geology samples:

- 64 rock samples were collected as well as 30 proximal soil samples where undisturbed soil was present in the immediate vicinity (approximately 5 m radius) of the sample rock.

Vegetation samples:

- Samples of all major vegetation types (both native and weed species) were collected for organic chemical analysis and for use in chamber exposure studies.

Spatial mapping:

- Spatial mapping was completed for all sites with a planned or existing AQM (AQ and EX sites) which contain one of the 54 rock art panels being observed in the Program.
- Processed mapping is presented.

AQM deployment:

- Deployment and commissioning of 18 solar powered “passive” air quality and weather monitoring stations (AQMs) is well advanced and will be completed by the time this report is published.
- The deployment of an additional three powered AQMs and planning for installation of Program equipment in an existing industry AQM is well underway.
- The first months of passive air quality monitoring is presented in this document.

Laboratory Analysis

- Patina samples from all sample rocks have been collected and processed for organic geochemistry analysis.
- Thin sections from all sample rocks have been prepared for mineralogical and inorganic geochemical analysis. Partial results are presented here.
- Preliminary chamber exposure studies have been undertaken and are presented here.

1.3.2 Exclusions

The MSDCA Plan encompasses a research program of several years’ duration. As such, at the end of the first year of studies, some activities have not yet reached the point where sufficient data is available for meaningful analysis.

- Real time (low-cost) air quality sensor data is not presented as the sensors are still undergoing calibration based on the IVL laboratory passive sampler data.
- Passive sampler results are presented for the first four months of operation. Results exclude volatile organic compound (VOC) samples, which are still with the laboratory for analysis. Only one month of Deposition sampler data is available, therefore it is not presented.

- Data from passive sampler validation studies is likewise presented apart from VOC results.
- Organic chemistry analysis is not yet complete and not presented.
- Microbiome sequencing and analysis is not yet complete and not presented.
- Vegetation characterisation is not yet complete and not presented.
- Synthesis of prior (industry) monitoring data with year 1 studies results is ongoing and not yet included.

These data will be included in subsequent reports and analysis.

1.4 Abbreviations and definitions

1.4.1 Abbreviations

The abbreviations listed in Table 1-1 are used throughout this report.

Table 1-1: General abbreviations and definitions

Abbreviations	Definition
AHD	Australian height datum
AL	Action level
AQM	Air quality monitoring / air quality monitor
ASD	Analytical spectral devices (spectrophotometer)
AUSPOS	Online GPS Processing Service
BDL	Below detection limit
BOM	Bureau of Meteorology
BSE	Backscattered electron
BYK	BYK-Gardner spectrophotometer
CIELAB	Commission Internationale de l'Éclairage (International Commission on Illumination) L*a*b colour space. (Also CIE Lab or CIE L*a*b).
CSIRO	Commonwealth Scientific and Industrial Research Organisation
DNA	Deoxyribonucleic acid
DSM	Digital surface model
DTM	Digital terrain model
DWER	Department of Water and Environmental Regulation (Western Australia)
EBSD	Electron backscatter diffraction
EDA	Exploratory data analysis
EDM	Electronic distance measurement
EDS	Energy dispersive x-ray spectroscopy
Eh	Via oxidation reduction potential (ORP)
EL	Exceedance level
EQC	Environmental quality criteria
EQMF	Environmental quality management framework
GC-irMS	gas chromatography – isotope ratio mass spectrometry

Abbreviations	Definition
GC-MS	Gas chromatography – mass spectrometry
GNSS	Global navigation satellite systems
IDA	Initial data analysis
ITS	Internal transcribed spacer (genomic marker)
JAZ	Portable spectrometer
KGP	Karratha Gas Plant
KM	Konica Minolta
LOD	Limit of detection
MAC	Murujuga Aboriginal Corporation
MAG	Metagenome assembled genome
MGA2020	Map Grid of Australia 2020
MRAMP (the Program)	Murujuga Rock Art Monitoring Program
MSDCA Plan	Monitoring Studies Data Collection and Analysis Plan
NATA	National Association of Testing Authorities
NOAEL	No observed adverse effect level (NOAEL)
OM	Ongoing monitoring
ORP	Oxidation reduction potential (mV)
pH	Negative logarithm to base 10 of the hydrogen ion activity (dimensionless)
PM _{2.5, 10}	Particulate matter < 2.5 and <10 microns (µm) aerodynamic diameter, respectively
QA/QC	Quality assurance and quality control
RNA	Ribonucleic Acid
RTK	Real time kinematic (processing)
SAB	Sabouraud agar
SEM	Scanning electron microscope / scanning electron microscopy
SOA	Secondary organic aerosol
SRG	Stakeholder Reference Group
SSM	State survey marker
STRM	Shuttle Radar Topography Mission
TIMA	Tescan Integrated Mineral Analyser
TOC	Total organic carbon
ToF-SIMS	Time-of-flight secondary ion mass spectrometry
TSA	Trypton soy agar
UAV	Unmanned aerial vehicle
ULSD	Ultra-low sulphur diesel
VOC	Volatile organic compound
WA-OIGC	Western Australia Organic and Isotope Geochemistry Centre
wt%	Percentage by weight
XRD	X-ray diffraction
(p)XRF	(portable) X-ray fluorescence

1.4.2 Chemical terms

The following standard chemical abbreviations have been used in this report.

Table 1-2: Chemical terms

Term	Name	Term	Name
Al	Aluminium	NO	Nitric oxide
Ba	Barium	NO ₂	Nitrogen dioxide
Bi	Bismuth	NO _x	Oxides of Nitrogen (NO + NO ₂)
Ca	Calcium	N ₂ O ₅	Dinitrogen pentoxide
Cl / Cl ⁻	Chlorine / chloride	O ₃	Ozone
CO	Carbon monoxide	P	Phosphorous
CO ₂	Carbon dioxide	Pu	Plutonium
Cu	Copper	Rb	Rubidium
DCM:MeOH	Dichloromethane : methanol	S	Sulphur
Fe	Iron	SiO ₂	Silica
Fe ₃ O ₄	Magnetite	SO ₂	Sulfur dioxide
Fe ₂ O ₃	Hematite	SO _x	Oxides of Sulphur (SO ₂ + SO ₃)
Hg	Mercury	Th	Thorium
Mg	Magnesium	Ti	Titanium

1.4.3 Glossary

Table 1-3: Glossary

Term	Definition
Anthropogenic	From human activity. In the context of this research anthropogenic includes human impact, including industrial, transport, tourism, site management, and all other impact that can be attributed to human activity. It can also be considered to include distal or global human activity which may impact the natural environment through changes in climate.
Barcoding gene	A gene that is shared by a group of organisms but differs in the genetic code between species because of evolutionary changes. Sequencing analysis of these genes in environmental samples can reveal evolutionary differences between the organisms within the group. This makes it possible to classify organisms that cannot be distinguished based on morphological features.
Biofilm	A biofilm growing on a surface typically comprises a syntrophic (feeding together) consortium of microbial cells that are embedded in a slimy extracellular matrix that is composed of extracellular polymeric substances (EPSs). The organisms that live close together can “communicate” with each other (share nutrients, exchange genes to make them immune to antibiotics etc.). In some cases a biofilm can comprise of a single species of microbial cells, however is not common in environmental contexts.
Biomarkers	Organic compounds produced from natural degradation of biochemicals produced by living organisms. The structure of a biomarker can sometimes be linked to a biochemical produced by a specific organism or group of organisms, while others are more general. They are known as “molecular fossils” as they can be used to infer the presence of certain organisms in ancient environments.

Term	Definition
Bioweathering	The degradation of mineral/rock surfaces through the combined action multiple biological and physiochemical factors. Some examples include organic/inorganic acid production, physical alterations from hyphae growing into rock surfaces and metabolic processes resulting in the release of minerals from the rock.
Boxplot	The middle line (inside the box) is the median (50% of the data); the lower bound of the box is the lower quartile (first 25% of the data) and upper bound of the box is the third (75% of the data) quartile; “whiskers” (values at which the horizontal lines stop) are approximately 95% confidence interval; data points greater or lesser than the termination of the whiskers are outliers.
Chemolithoautotrophic	Organisms that are able to utilise atmospheric carbon dioxide as a carbon source and utilizes inorganic compounds as an energy source.
Culturally Important Place	A Place, area of land/sea, in the landscape nominated by Traditional Owners
Culturally Important Site	A specific location, such as a rock waterhole etc., within the landscape. Such sites may or may not lie within a Culturally Important Place.
Cumulative campaign	Cumulative values of a parameter during a MRAMP field measurement campaign, commencing on the first day of measurements until the final day of continuous (weekdays) measurement. Typically, three-five week duration.
Cumulative monthly	Cumulative values of a parameter during a calendar month.
Dispersion	The spreading out of emissions from a localised source (e.g. industry stack, wildfire) over a wide area due to the effect of wind.
Eh-pH	A parameter which indicates the stability of mineral or chemical systems based on the activity of hydrogen ions (pH) and electrons (Eh). These are often compared using an Eh-pH diagram (Pourbaix diagram).
End Member	A pure chemical compound (/mineral) component entering into solid solution with other pure chemical compounds to form a series of minerals.
Endolithic lichens	Lichens that grow in rocks. Lichens were originally thought to occur through a symbiotic relationship of fungi and photosynthetic algae or cyanobacteria, it is currently understood that yeast and other bacterial species can also be present in the lichen consortium.
Environmental Quality Criteria (EQC)	Scientifically based limits of “acceptable” change within an EQMF.
Environmental Quality Management Framework (EQMF)	A framework to guide the assessment and management of activities related to a particular environmental value.
Environmental Quality Objective (EQO)	A specific management goal for a designated part of the environment that signals the level of environmental quality needed to protect the environmental value of an EQMF.
Environmental Value (EV)	A beneficial use or an ecosystem health condition which requires protection from the effects of emissions or environmental harm.
Eukarya	Members of the domain Eukarya—called eukaryotes—have membrane-bound organelles (including a nucleus containing genetic material) and are represented by five kingdoms: Plantae, Protista, Animalia, Chromista, and Fungi.
Extracellular polymeric substances (EPS)	EPS consists of a variety of macromolecules that are secreted by bacteria in the environment to make biofilms.
Fermentation	The microbial enzymatic degradation of organic matter (e.g. carbohydrates) into short-chain fatty acids (notably acetic, propionic and butyric acids) that can lower the pH of the patina.
Gene transcription	The active expression of a gene that produces an RNA copy. This can be a structural component such as ribosomal RNA that make up the ribosomes. Functional gene products are messenger RNA, which is translated into proteins within the ribosomes. Transcripts are

Term	Definition
	indicative that the cell was alive and possibly active at the time of sampling since RNA is much more insatiable and prone to degradation than DNA. DNA survives much longer in the environment.
Heterotrophs	Heterotrophic bacteria and fungi that derive energy from organic compounds.
Hypolithic	Microbial communities that colonize and grow below the rock surface where they are protected against UV damage and desiccation.
MAGs	Metagenome Assembled Genomes. This technique combines short environmental DNA sequences (metagenomes) to build genomes of key species present in the microbiome. Expressed genes (metatranscriptome) that are sequenced in parallel can be mapped against the assembled genomes to link these processes with the key species involved in patina formation and/or degradation.
Metabolic pathways	A metabolic pathway is a linked series of chemical reactions occurring within a cell. The reactants, products, and intermediates of an enzymatic reaction are known as metabolites, which are modified by a sequence of chemical reactions catalysed by enzymes. The genes involved in the individual enzymatic processes as part of the metabolic pathways and the active expression of these genes will be identified through respectively metagenomics and metatranscriptomics as defined below.
Metagenomics	The study of sequenced genetic material in environmental samples. Depending on sequence depth, this can reveal a holistic overview of the relative abundance of all microbial genes present. In our study this refers to microbial genes that encode for enzymes involved in processes leading to patina formation and/or degradation.
Metatranscriptomics	The study of microbial gene expression in environmental samples. Depending on sequence depth, this can reveal a holistic overview of the relative abundance of all actively expressed microbial genes present. In our study this refers to actively expressed microbial genes that encode for enzymes involved in processes leading to patina formation and/or degradation. Owing to the short-lived survival of gene transcripts in the environment, their presence is indicative of an active role in these processes
Microbial metabolites	Breakdown products or compounds that the microbial communities use as energy sources, for growth and other cellular processes.
Microbiome	An integrated community of micro-organisms (bacteria, archaea, unicellular eukaryotes and fungi) occupying a particular habitat.
Microcolonial fungi	Colonies of fungi growing on rock surfaces. They are highly resistant against desiccation and ultraviolet damage.
Mineral Assemblages	Presence and abundance of mineral species in a given spatial region (either across the rock surface or from the rock surface to the “fresh” rock below the outer weathered rind.
Murujuga	Traditional name for Burrup Peninsula and surrounding islands of the Dampier Archipelago.
Murujuga Rock Art Monitoring Program (MRAMP)	Overall program of work to be conducted to 2026. Includes Initial studies to inform the design of the ongoing monitoring framework, as well as the development of EQCs and the EQMF.
Ongoing monitoring	The ongoing monitoring refers to the longer-term monitoring program to be jointly run by MAC and DWER once this program of works is complete (expected to commence from 2026). Also referred to as “long term monitoring”.
Ordination	This is a group of statistical approaches to visualise how much microbial communities differ between samples by projecting the distances in a multidimensional space. The closer the dots in the graph, the more related they are and vice versa. This can also show if communities are significantly different between sample categories such as between rock types.
Organic geochemistry	The study of organic compounds in the environment, including in rocks, sediments, soils, petroleum, aquatic environments and the atmosphere. Organic geochemistry studies the

Term	Definition
	origin of organic compounds, their transportation processes, and the alteration they undergo in the environment, over time scales ranging from the present day to hundreds of millions of years ago.
Patina	In the Murujuga context the texture and colour of the rock surface is referred to as a patina. This is a deliberately broad definition, which encompasses other characterisation such as rock varnish or desert varnish including any biota which may be present on the rock surface. The patina has been shown to form over a depletion zone, referred to as the crust, which generally has a lighter appearance than both the patina and the underlying rock. An engraving is formed by breaking through the naturally formed patina to expose the lighter crust beneath. There may be cases where the engraving has exposed the underlying rock, which may result in a darker engraved channel.
Petroglyph	Literally “rock mark”, the term describes any cultural marking into a rock surface. The marks can be produced by a range of techniques, including pecking, pounding, incising, scratching or abrading, or a combination of two or more techniques. Techniques such as scratching can be very shallow (<1 mm), while pecking can be from 1mm to more than 100mm deep. All petroglyphs at Murujuga are Culturally Important.
Photoautotrophs	Photoautotrophs are organisms that can make their own energy using light and carbon dioxide via the process of photosynthesis. Examples are cyanobacteria and green algae, known to colonise rock surfaces. Photoautotrophs are considered primary producers since their biomass can be consumed by heterotrophs (defined above) as a source of carbon and energy.
Photolysis	The process by which molecules are broken into small fragments by exposure to sunlight (typically UV radiation).
Photospectrometry	An instrumental technique for measuring the chromatic reflectance of a surface by scanning at frequencies that cover the visible spectrum and beyond. Photospectrometry provides both a single value colour designation and spectral data that can indicate non-chromatic change. The technique has been applied to both the measurement of change and the characterization of unknown minerals and compounds.
Primary producers	See definition of “photoautotrophs”.
Quartile	The quartiles are three numbers which divide the population or data values into four equal segments. The first quartile is a number that lies above one-quarter of the population and below three-quarters of the population. The second quartile is the median, lying above half of the population and below the other half of the population. The third quartile lies above three-quarters of the population and below one-quarter.
Secondary Organic Aerosol (SOA)	Solid organic molecules produced in the atmosphere by the reaction of smaller, gaseous organic molecules with oxygen (and often ozone and UV / OH radicals).
Stable isotopes	Atoms of the same element which contain a different number of neutrons in the nucleus. Most elements consist of more than one stable isotope, the ratios of which can be measured using specialised instrumentation. Stable isotope ratios in organic compounds are affected by the processes of formation and alteration, hence their measurement gives information on source and alteration history.
Weathered rind	The outer portion of the rock that is sufficiently close to the surface to have interacted with oxygen or other environmental conditions. This layer is significantly thicker than the layer forming the patina and has different colouration to the underlying fresh rock (core).

Term	Definition
Weathering	<p>In the Murujuga context the concepts of weathering are differentiated as natural weathering and accelerated (/anthropogenic) weathering, which MAC would prefer is referred to as degradation. However, these effects may be difficult to decouple.</p> <p><u>Natural Weathering</u>: the alteration of a rock surface through natural agents such as the impacts of temperature cycles, microbial activity, and interactions with water and aerosols/gases released by the surrounding terrestrial and marine environments. Weathering can be subtractive (erosion) or additive (mineralization or accretion).</p> <p><u>Accelerated weathering</u>: degradation due to anthropogenic activity and not be considered as natural weathering.</p>

1.4.4 Site and sample numbering nomenclature

Study sites

Study sites are generally identified with an alphanumeric code in the format:

AABB

where:

- AA is a two-letter code indicating the type of study site as described in Table 1-4.
- BB is a two-digit sequential number derived from the study design outputs (MSDCA Plan Appendix I and Appendix II).

The exception to the standard nomenclature is study site “AQA1”, which was added to the program during the course of the first year of scientific studies and designates the MAC Office AQM.

Table 1-4: Study site nomenclature

Site code	Numbering	Count	Name	Descriptor
AQ	01 to 18	18	Air quality	Study squares where new MRAMP air quality monitors are being installed.
AQA	1	1	Air quality additional	Designation given to the location of the initial field prototype AQM installed at the MAC Office.
AS	01 to 02	2	Additional sample	Study squares providing targeted samples of rare rock types.
EX	01 to 09	9	Existing (AQM)	Study squares with existing industry air quality monitors.
RS	01 to 18	18	Representative sample	Study squares without AQMs, where field observations and sample collection occur to form a rigorous representative sample of the entire Murujuga region.
Total		48		

Sample rocks

Sample rocks are identified with an alphanumeric code in the format:

AABB_CCC

where:

- AA is a two-letter code indicating the type of study site as described in Table 1-5.
- BB is a two-digit sequential number derived from the study design outputs (MSDCA Plan Appendix I and Appendix II).
- CCC is the rock type as defined in Table 1-5

It should be noted that all sample rock locations and subsequent sampling/removal were approved both by the Murujuga Aboriginal Corporation and its Circle of Elders and the Western Australia Department of Lands and Heritage under Section 10 regulations. A separate heritage report was prepared to demonstrate that the sample rocks and associated activities would not impact cultural heritage values and were sufficiently far removed from any rock art or artefact sites.

Table 1-5: Abbreviation codes for sample rock types

Rock type code	Descriptor
BAS	Basalt
DOL	Dolerite
GBR	Gabbro
GPH	Granophyre
GRT	Granite

Rock art panels

Rock art panels will be referred to in the same manner as the host rock. Where a study square includes more than one rock art panel on the same rock type a numeral will be added after the rock type to differentiate between the art panels (e.g. RS10_GBR1).

Studies on rock art panels underwent the same approval process as above. All work on or near rock art panels is limited to non-invasive techniques, such as photography/spectrometry, pH/Eh/Cl and pXRF.

2 Study methodologies, verification of competency, and quality assurance

2.1 Elaboration of methodologies described in the MSDCA Plan

General scientific methodologies for each of the component studies are described in the relevant section of the MSDCA Plan. For quality assurance purposes, more detailed methodology statements were developed for each component study to ensure that techniques were applied repeatedly and consistently by all team members.

These methodologies are version-controlled documents and specify key controls such as:

- A detailed breakdown of the work sequence to be undertaken for each task or activity.
- Equipment and consumables required.
- Training required.
- Other related reference documents.
- Risk and safety management requirements.

Table 2-1 lists the component study methodologies and their status. Owing to the multi-year nature of the research program, methodologies for some work areas are still being developed in consultation with internal and external subject matter experts.

Table 2-1: Component study methodologies

Document Reference	Title	Status	Primary Author
COPP21065-PRO-G-101	Preparation of Rock Cubes for AQMs	Rev 2, IFU	R. Mead-Hunter
COPP21065-PRO-G-102	Passive Air Quality Monitoring (AQM) Installation and Commissioning	Rev 2, IFU	R. Mead-Hunter
COPP21065-PRO-G-103	Passive Air Quality Monitoring (AQM) Sample Collection, Maintenance and Context Observations	Rev 3, IFU	R. Mead-Hunter
COPP21065-PRO-G-104	Powered AQM Instrumentation Installation and Commissioning	DEV	R. Mead-Hunter
COPP21065-PRO-G-105	Unmanned Aerial Vehicle and Spatial Mapping	Rev 2, IFU	D. Belton
COPP21065-PRO-G-106	Inorganic Monitoring (pH and Portable X-Ray Fluorometer)	Rev 3, IFU	K. Evans
COPP21065-PRO-G-107	Microbiome Field Sampling	Rev 2, IFU	M. Coolen
COPP21065-PRO-G-108	Post Cyclone Procedures and Checklist	Rev 2, IFU	R. Mead-Hunter
COPP21065-PRO-G-109	Vegetation Sample Collection	Rev 2, IFU	K. Grice
COPP21065-PRO-G-110	Photospectrometric Colour Change Measurement	Rev 3, IFU	A. Thorn
COPP21065-PRO-G-112	Microbiome Laboratory Analysis	Rev 2, IFU	M. Coolen
COPP21065-PRO-G-113	Organic Geochemistry of Rock Surfaces, Dust and Particulates	Rev 2, IFU	K. Grice
COPP21065-PRO-G-114	Inorganic Geochemistry Laboratory Analysis	Rev 2, IFU	K. Evans
COPP21065-PRO-G-115	Sample Rock Collection	Rev 2, IFU	T. Tacchetto

Document Reference	Title	Status	Primary Author
COPP21065-PRO-G-116	Plutonium Isotope Testing	DEV	K. Evans
COPP21065-PRO-G-117	Chamber Exposure Studies	Rev 2, IFU	B. Mullins
COPP21065-SPE-G-100	Air Quality Monitoring Station Control Functional Specification	Rev 1, IFU	R. Mead-Hunter

Notes: IFU = issued for use
DEV = under development

2.2 Personnel and verification of competency

A training matrix has been developed for each method to ensure that all personnel undertaking field and laboratory tasks are sufficiently trained by experienced practitioners. All methods have been broken-down into key steps for competency verification, and the matrix is signed and dated once a team member is deemed competent in a methodology or methodology step.

The scientific lead for each component study (or their nominated delegate) has been assigned the responsibility of verifying that each of their team members can apply the methodology techniques to undertake the required work.

Table 2-2 lists team members contributing to each of the component studies.

Table 2-2: MRAMP component study contributing team members

Name	Project Role	Activities Undertaken
Prof Ben Mullins	Program Scientific Lead	Study design and coordination, air quality research
Kimbra Bridges	Project Manager	Project management, report editing
Air quality		
Dr Ryan Mead-Hunter	Air quality monitoring component study lead	Air quality monitoring
Dr Arne Bredin	Senior Research Fellow	AQM design and real time monitoring
Dr Mawutorli Nyarku	Research Fellow	Passive sampling and AQM fabrication
Dr Kathryn Landwehr	Research Fellow	Chamber studies
Dr Andrew King	CFD Lead	Computational fluid dynamics
Dr Monica Gumulya	Researcher	Computational fluid dynamics
Thomas Di Loreto	Research Assistant	AQM fabrication
Ronald Fellows-Smith	Electronics Technician	AQM construction and installation
Laura Horan	Electronics Technician	AQM construction and installation
Robert Slater	Electronics Technician	AQM construction and installation
Dr David Lynch	ChemCentre Inorganics Lead	Analytical chemistry
Inorganic geochemistry		
Prof Katy Evans	Geology Lead	Design and coordination of geology studies
Dr Tommaso Tacchetto	Research Fellow	Geology field and laboratory studies
Prof Will Rickard	JDLC Deputy Director	Inorganic analysis
Dr Aaron Cavosie	Geologist	Geology fieldwork

Name	Project Role	Activities Undertaken
Stefano Tenuta	Geologist	Geology fieldwork
Ruby Marsden	Geologist	Geology fieldwork
Francesca Cary	Geologist	Geology fieldwork
Julian Alfing	Geologist	Geology fieldwork
John Fairweather	Geologist	Geology fieldwork
Carmen Harris	Geologist	Geology fieldwork
Seamus Anderson	Geologist	Geology fieldwork
Organic geochemistry		
Prof Kliti Grice FAA	Organic geochemistry Lead	Design and coordination of geochemistry studies
Dr Bettina Schaefer	Research Fellow	Representative vegetation sample collection, organic geochemistry laboratory studies
Dr Alex Holman	Research Fellow	Organic geochemistry laboratory studies
Dr Peter Hopper	Research Fellow	Organic geochemistry laboratory studies
Carmelo Chippalone	Research Fellow	Organic geochemistry laboratory studies
Sebastian Stanley	Research Fellow	Organic geochemistry laboratory studies
Microbiology		
Prof Marco Coolen	Geomicrobiology lead	Design and coordination of geomicrobiology studies, geomicrobiology fieldwork
Katelyn Boase	Research Fellow	Geomicrobiology field and laboratory work
Dr Matthew Campbell	Research Fellow	Geomicrobiology fieldwork
Hridya Vijay	Research Assistant	Geomicrobiology fieldwork
Spatial mapping		
Dr David Belton	Spatial Scientist	Spatial mapping
Dr Petra Helmholz	Spatial Scientist	Spatial mapping
Spectroscopy		
Andrew Thorn	Spectrometry Lead	Spectrometry design and fieldwork
Data science		
Prof Melanie Johnson-Hollitt	CIC Director	Computational science lead
Dr Dan Marrable	Lead Data Scientist	Computational scientist
Dr Carlo Martinotti	Data Scientist	Data science / engineering
Calvin Pang	Data Scientist	AQM dashboard
Arun Veluchamy	Project Coordinator	Project administration and data scientist
Dr Kathryn Barker	Project Coordinator	Project administration and data scientist
Statistical Methodology and Data Analysis		
Prof Adrian Baddeley FAA	Statistics Lead	Design and coordination of statistical analysis
Prof Noel Cressie FAA	Statistics Co-Lead	Design and coordination of statistical analysis
Dr Rebecca O'Leary	Senior Research Fellow	Statistical design and analysis
Dr Stephanie Hogg	Research Fellow	Statistical analysis
Dr Brad Zhang	Research Fellow	Statistical analysis
Dr Suman Rakshit	Senior Research Fellow	Statistical analysis

Name	Project Role	Activities Undertaken
Abraj Mohamed	Research Fellow	Statistical analysis
Nishafa Nazahir	Research Assistant	Data entry
Administration		
Dr Toni Hannelly	Fieldwork Coordinator	Report compilation and technical editing, fieldwork coordination
Taylor Tufto	Project Administrator	Project administration and report editing

2.3 Quality assurance

Extensive calibration, validation and quality assurance controls have been developed for all measurements and study components. These are detailed in the respective methodologies.

Some of the key protocols are summarised below:

2.3.1 Air quality monitoring

Passive sampler deployment occurs in duplicate at each AQM and utilises multiple field blanks as per best practice. Samples are analysed by IVL (Sweden) under equivalent certification to the Australian National Association of Testing Authorities (**NATA**).

Deposition samples are analysed by the NATA-accredited ChemCentre following their chain of custody, documented blank, calibration and validation protocols for each method. Distilled water used in the methods has been obtained from the ChemCentre. Blank samples of distilled/deionised water are returned with each set of measurements.

Powered AQMs use reference grade instruments, operated in compliance with relevant AS3080 and USEPA standards, which undergo automated zero and span calibrations at a minimum of once per day. The data collected from these instruments with the co-located passive samplers will be used by the statistical team to develop robust region- and climate-specific calibration for the low power samplers in the passive AQMs.

2.3.2 Fieldwork

Microbiology field sample collection utilised the highest quality certified DNA-free collection media. Field (air) blanks and collection media were collected and retained for culturing and/or sequencing as appropriate to verify no contamination had occurred.

Spectrometry methods utilise thin films with known properties to undertake instrument calibrations at least once per rock art panel. The statisticians have developed a set of rigorous protocols and criteria for quality assurance and quality control (**QA/QC**) checking of data. These protocols will be automated and applied in the field in real-time.

The pXRF instrument used for geological fieldwork contains an internal calibration standard and is calibrated each time it powers on. In addition, standard reference materials are measured twice per day and the results are recorded.

The equipment used for pH/Eh/Cl measurement is calibrated at least twice per day using known reference solutions. Distilled water is replaced regularly.

2.3.3 Laboratory analysis

All laboratory measurements utilise blanks and reference standards as per best practice. All instruments and equipment are serviced and calibrated according to manufacturer's protocols.

QA/QC of SEM microanalysis data

Scanning electron microscopy (**SEM**) is an analytical technique used to obtain high-resolution images and elemental analyses of a sample's surface. QA/QC is an essential aspect of SEM microanalysis data analysis to ensure that the data obtained is reliable and accurate.

Some steps considered for the QA/QC of SEM microanalysis data:

- Instrument calibration

The SEM instrument must be calibrated regularly to ensure the accuracy of the data. Calibration includes the electron beam energy, beam current, and magnification. Instrumentation used in this study is regularly calibrated and analysis conditions are standardised.

- Sample preparation

Proper sample preparation is crucial for obtaining accurate and reliable data. Samples are cleaned to remove any surface contamination and handled with care to avoid any alteration.

- Reproducibility

To ensure the reproducibility of the data, it is important to perform multiple measurements of the same sample or replicate measurements of different samples under the same experimental conditions.

- Data Analysis

The SEM microanalysis data are analysed using appropriate statistical methods to identify significant differences between the samples. The data should also be validated using complementary techniques such as ToF-SIMS, X-ray diffraction or XRF.

- Quality control

To ensure the quality of the data, the SEM microanalysis data are required to be checked for outliers, systematic errors, and other sources of variability. The data will be reviewed by experts in the field to identify any potential issues or limitations.

In conclusion, QA/QC is a critical step in the SEM microanalysis data analysis process. Following these steps will help to ensure the accuracy, reliability, and reproducibility of the data, leading to more confident conclusions and interpretations.

QA/QC of Time-of-flight secondary ion mass spectrometry (ToF-SIMS) data

Time-of-flight secondary ion mass spectrometry (**ToF-SIMS**) is an analytical technique used to investigate the surface chemistry and molecular structure of a sample. QA/QC is an essential aspect of ToF-SIMS data analysis to ensure that the data obtained are reliable and accurate.

Some steps considered for the QA/QC of ToF-SIMS data:

- Instrument calibration

To ensure the accuracy of the data, the ToF-SIMS instrument is calibrated regularly. Calibration includes the checking and optimising the mass accuracy, mass resolution, and primary ion intensity.

- Sample preparation:

Appropriate sample preparation is crucial for obtaining accurate and reliable ToF-SIMS data. Samples will be carefully cleaned to remove any surface contamination and will be stored under clean, dry conditions to minimise any atmospheric alteration.

- Reproducibility

To ensure the reproducibility of the data, it is important to perform multiple measurements of the same sample or replicate measurements of different samples under the same experimental conditions.

- Data normalisation

Normalisation is necessary to eliminate variations in signal intensity due to differences in sample conductivity, chamber vacuum, instrument sensitivity, and primary ion dose. Normalisation is achieved by dividing the signal by the total ion current.

- Data analysis

- The ToF-SIMS data will be analysed using appropriate statistical methods to identify significant differences between the samples. The data will be validated using complementary techniques, such as SEM, XRD and EDS. Ions in the mass spectrum will be identified using values from internationally recognised databases and peer reviewed literature.

- Quality control

To ensure the quality of the data, the ToF-SIMS data will be checked for outliers, systematic errors, and other sources of variability. The data will be reviewed by experts in the field to identify any potential issues or limitations.

In conclusion, QA/QC is a critical step in the ToF-SIMS data analysis process. Following these steps will help ensure the accuracy, reliability, and reproducibility of the data, leading to more confident conclusions and interpretations.

3 Monitoring studies undertaken in the field

3.1 Field monitoring generally

3.1.1 Location of field monitoring sites

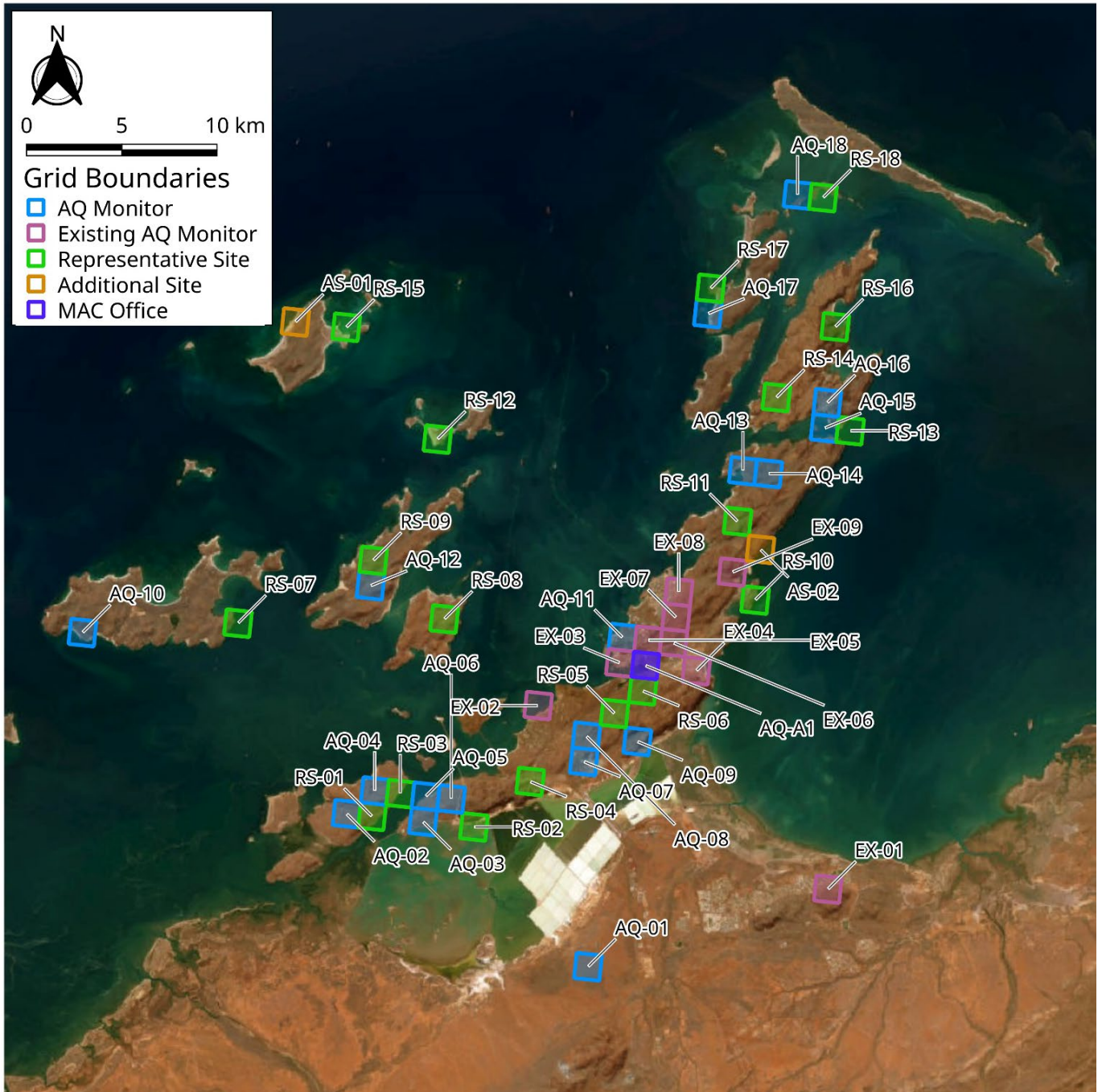


Figure 3-1: Map of field monitoring sites

Figure 3-1 shows the location of field monitoring sites arising from the site selection process undertaken previously during development of the MSDCA Plan. All sites and artifacts included in the Program were approved by the Murujuga Aboriginal Corporation’s Circle of Elders prior to commencement of the monitoring studies.

3.1.2 Summary of year 1 field campaigns

Table 3-1 outlines the four fieldwork campaigns included in the first year of monitoring studies. These dates were selected to correspond with wet, dry and shoulder seasons to create an understanding of the effect of seasonal changes.

Table 3-1: Summary of field campaigns undertaken in the first year of studies

Campaign number.	Dates	Inorganic geology	Colour monitoring	Organic Microbiome	Vegetation Collection	Spatial mapping
1	07 Mar - 08 Apr 2022	Y	Y	Y	Y	-
2	20 Jun - 29 Jul 2022	Y	Y	Y	Y	Y
3	03 Oct - 28 Oct 2022	Y	Y	-	-	Y
4	27 Feb - 24 Mar 2023	Y	Y	-	-	-

Table 3-1 does not include installation and commissioning of air quality monitors (AQMs) or changeover of AQM samplers. This information is provided as part of the air quality monitoring discussion in Section 5.

3.1.3 Weather conditions during the study period

Weather conditions are relevant because some of the quantities measured in the field are very likely to be affected by the presence of rainwater and salt aerosol, and by temperature before and during the field visit. These include physicochemical measurements (pH, Eh, Cl) and possibly the spectroscopic measurements.

Figure 3-2 shows the historic and actual rainfall alongside the field campaign dates during the field campaigns, for Karratha Aerodrome. Campaign 1 was preceded by a long dry spell, while it rained substantially during campaign 2. Figure 3-3 shows the historic average temperature patterns and the actual temperatures during the field campaigns (using weekly averages of the daily minimum and maximum temperatures). Temperatures were broadly consistent with the long-term averages except that the dry spell before campaign 1 was also somewhat hotter than usual.

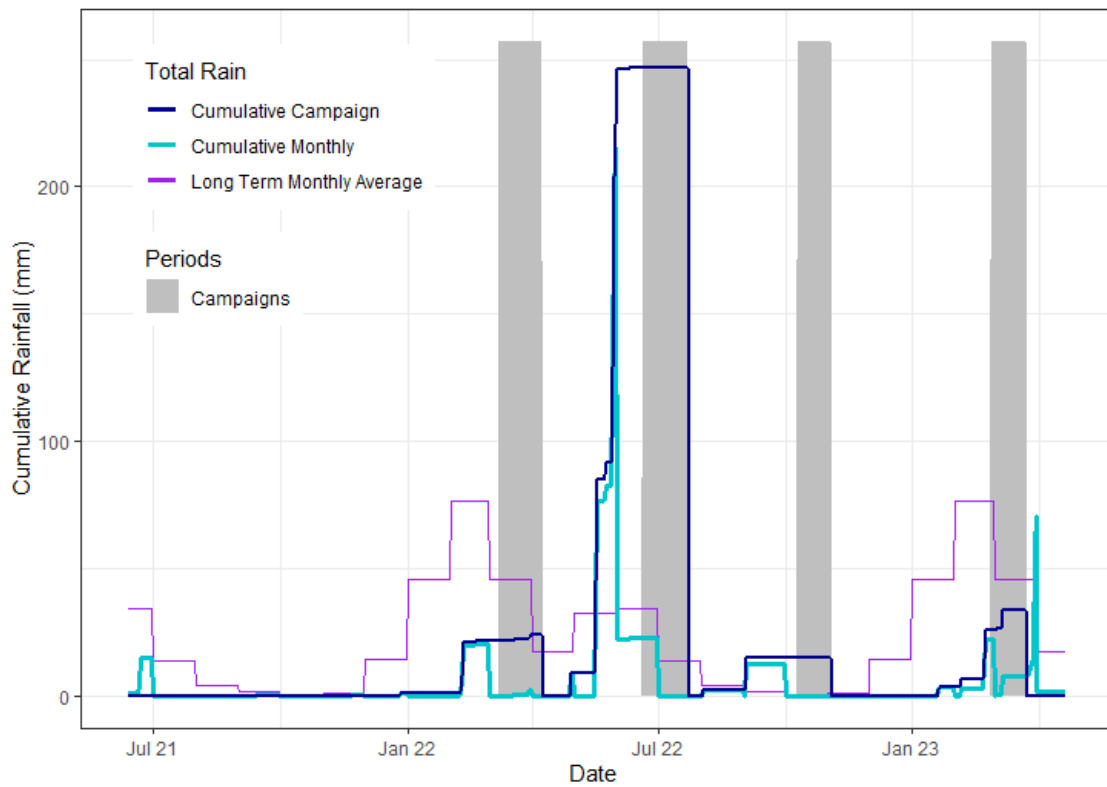


Figure 3-2: Timing of field campaigns and rainfall (data source: BOM Station ID 004083 – Karratha Aero)

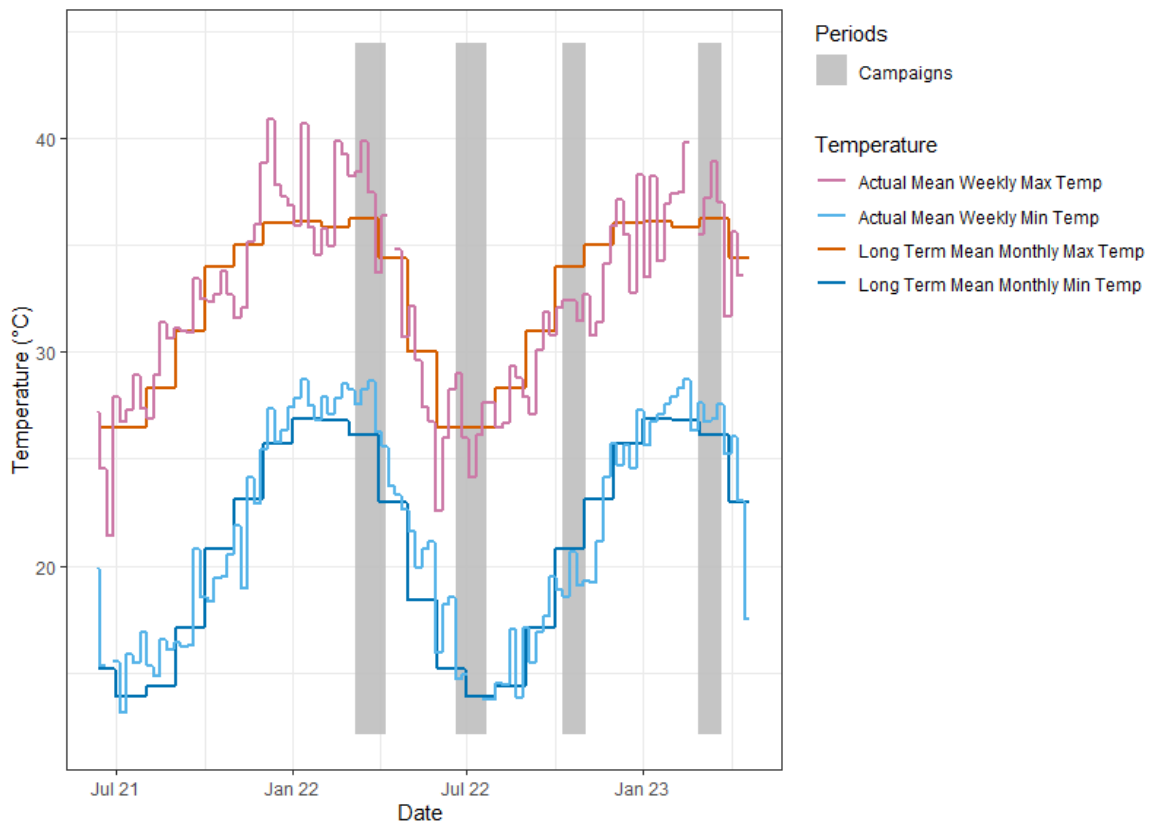


Figure 3-3: Mean, maximum and minimum daily air temperatures during the study period (data source: BOM Station ID 004083 – Karratha Aero)

3.2 Vegetation collection fieldwork

3.2.1 Objectives

To achieve the overarching Program objectives it is important to be able to differentiate between natural and anthropogenic emissions. One source of natural emissions is biogenic volatile organic compounds (**VOCs**), which are emitted by plants during hot weather and through their combustion products (soot, gases, etc) during burning. For this reason, a selection of the dominant native and introduced vegetation has been collected for use in isotopic, organic, and chamber combustion studies.

3.2.2 Methodology

Vegetation collection took place during the first two field campaigns in accordance with the component study methodology statement:

- COPP21065-PRO-G-109 Vegetation Sample Collection.

3.2.3 Fieldwork outcomes

Approximately 10 L volume of each of the species in Table 3-2 were collected from the locations listed and shown on the map in Figure3-4. These samples are stored in climate-controlled conditions in appropriate storage bags pending analysis.

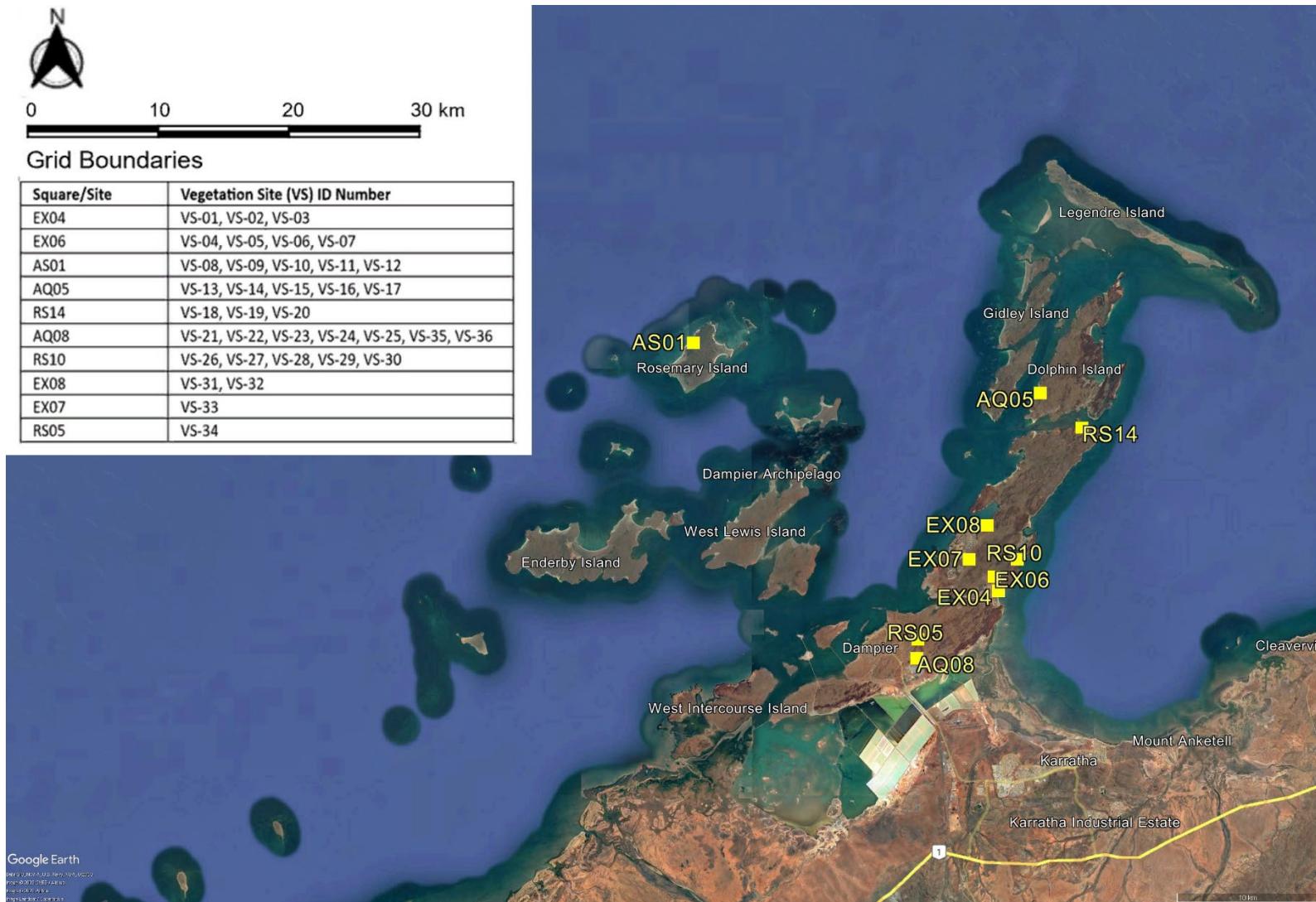


Figure3-4: Vegetation collection sites

Table 3-2: Representative vegetation samples collected

ID Number	Site	Date	Time	Name/Species
VS-01	EX04	21/03/2022	1:54 PM	Mangrove
VS-02	EX04	21/03/2022	2:01 PM	Beach spinifex
VS-03	EX04	21/03/2022	2:09 PM	Mangrove
VS-04	EX06	21/03/2022	2:23 PM	Saltbush
VS-05	EX06	21/03/2022	2:36 PM	Acacia pyrophillea (bush lolly)
VS-06	EX06	21/03/2022	2:46 PM	Snakewood
VS-07	EX06	21/03/2022	1:07 PM	Gum tree white bark
VS-08	AS01	22/03/2022	7:57 AM	Caper Bush Bajila
VS-09	AS01	22/03/2022	8:08 AM	Weeping Gymnanthera
VS-10	AS01	22/03/2022	8:52 AM	Acacia wirewood
VS-11	AS01	22/03/2022	9:02 AM	Acacia stellaticeps
VS-12	AS01	22/03/2022	8:47 AM	Spinifex
VS-13	AQ05	23/03/2022	8:57 AM	Kurrajong tree
VS-14	AQ05	23/03/2022	9:12 AM	Terminalia supranitifolia
VS-15	AQ05	23/03/2022	9:27 AM	Acacia pyrophillea (bush lolly)
VS-16	AQ05	23/03/2022	9:47 AM	Acacia sp.
VS-17	AQ05	23/03/2022	1:25 PM	Soap wattle
VS-18	RS14	23/03/2022	1:25 PM	Hibiscus/ cotton wood
VS-19	RS14	23/03/2022	1:42 PM	Acacia sp.
VS-20	RS14	23/03/2022	1:51 PM	Acacia sp.
VS-21	AQ08	25/03/2022	12:05 PM	Acacia sp.
VS-22	AQ08	25/03/2022	12:34 PM	to be identified
VS-23	AQ08	25/03/2022	12:50 PM	Gum tree dark bark
VS-24	AQ08	25/03/2022	1:06 PM	Gum tree white bark
VS-25	AQ08	25/03/2022	2:30 PM	Dry wood of Kurrajong Tree
VS-26	RS10	30/03/2022	3:30 PM	Spinifex
VS-27	RS10	30/03/2022	3:45 PM	Spinifex
VS-28	RS10	30/03/2022	4:00 PM	Spinifex
VS-29	RS10	30/03/2022	4:30 PM	Spinifex
VS-30	RS10	30/03/2022	4:45 PM	Spinifex
VS-31	EX08	25/08/2022	11:00 AM	Kapok bush
VS-32	EX08	26/08/2022	11:05 AM	Kapok bush
VS-33	EX07	27/08/2022	11:20 AM	Euphorbia
VS-34	RS05	28/08/2022	11:40 AM	Buffel grass
VS-35	AQ08	29/08/2022	11:50 AM	Pasa flora
VS-36	AQ08	30/08/2022	11:55 AM	Unknown vine

The vegetation collected is considered sufficient to capture the spectrum of genera present at Murujuga and the likely biogenic emissions. The study team is very grateful to both the MAC Rangers and local DBCA staff for their assistance with species identification.

3.3 Inorganic geochemistry fieldwork

3.3.1 Objectives

From Section 1.5 of the MSDCA Plan, the objectives of the inorganic geochemistry investigations are to:

1. Characterise the mineralogy and mineral compositions of the fresh rock, weathered rind, and patina for the granophyre, gabbro, dolerite, granite and basalt rock types from a range of settings including high and low exposure to industry emissions and differences in exposure to rain and wind.
2. Determine the mineralogy for these systems at thermodynamic equilibrium using thermodynamic calculations and use best practice approaches to estimate the timescales of change, based upon measured reaction rates, reaction mechanisms, and the results of other component studies (organic, microbiome, field observations, weathering experiments).
3. Compare the expected and observed mineralogy for sites with different exposure to anthropogenic emissions to (a) obtain proof-of-concept for the thermodynamic calculations; (b) investigate the presence of statistically significant differences among the sites and relate these to industry emissions.
4. Use the observations and calculations to identify components of the mineralogy that are most sensitive to industrial emissions and that can act as early indicators of change (EQC) and devise a monitoring strategy that will form part of the EQMF and ongoing monitoring (OM) Program.

3.3.2 Methodology

Inorganic geochemistry fieldwork in the four field campaigns involved:

1. Performing an elemental surface analysis of the selected sample rocks and rock art panels using a portable x-ray Fluorescence (**pXRF**) device.
2. Measuring the Eh-pH and chloride ion levels on the surface of the selected sample rocks.

During the second field campaign conducted in June-July 2022, sample rocks were removed from country and transported to Curtin University for in-depth destructive testing and analysis.

Further information on inorganic geochemistry field methodologies can be found in Section 3.2.4 of the MSDCA Plan and the following component study methodology statements:

- COPP21065-PRO-G-106 Inorganic Monitoring (pH and Portable X-Ray Fluorometer)
- COPP21065-PRO-G-115 Sample Rock Collection

Variations from planned methodology

The Bruker Tracer 5G pXRF was selected as the desired instrument for the fieldwork due to the broad suite of elements it can measure. A single Bruker Tracer 5G was purchased and utilised for campaigns 2-4, however could not be manufactured in time for campaign 1 and an identical model hire instrument was used instead. This instrument suffered an x-ray tube failure mid-campaign and was replaced by a second identical model instrument. Therefore, three instruments of the same model have been utilised across the campaigns. This

variable does not appear to have influenced results, however, has been noted and accounted for in analyses where possible. To avoid misunderstanding we emphasise that the analysis did not assume that the different individual instruments gave identical results. The analysis allowed for the possibility that the different individual instruments gave different results. The exploratory analysis did not find any evidence of a difference.

The second round of microbiome sampling and sample rock collection was undertaken in campaign 2 rather than the campaign 3 as originally planned. This was due in part to the favourable cooler weather conditions for carrying heavy rocks. Additionally, the desired sampling protocol of one set of microbiome samples in dry weather and one set post-rainfall was achieved with collection of sample rocks in campaign 2 (albeit with rainfall patterns reversed from a typical year).

3.3.3 Fieldwork outcomes

Table 3-3 to Table 3-6 summarise the number of inorganic geochemistry observations taken during the year field campaigns.

Table 3-3: Number of pH, Eh, Cl and pXRF measurements on rock art panels taken for each campaign by site type.

Campaign no.	Site type	Number of measurements on rock art			
		pH	ORP (Eh)	Chloride	pXRF
1	AQ	69	0	36	66
	AS	6	0	6	12
	EX	27	0	21	30
	RS	53	12	35	62
2	AQ	66	66	66	66
	AS	9	9	9	9
	EX	27	27	27	27
	RS	60	60	60	60
3	AQ	66	66	66	66
	AS	9	9	9	9
	EX	27	27	27	27
	RS	60	60	60	60
4	AQ	69	69	69	69
	AS	9	9	9	9
	EX	27	27	27	27
	RS	60	60	60	60

Table 3-4: Number of pH, Eh, Cl and pXRF measurements on sample rocks taken for each campaign by site type.

Campaign no.	Site type	Number of measurements on sample rocks			
		pH	ORP (Eh)	Chloride	pXRF
1	AQ	66	2	36	63
	AS	6	0	6	12
	EX	24	0	24	30
	RS	81	10	49	87
2	AQ	63	63	63	63
	AS	9	9	9	9
	EX	27	27	27	27
	RS	87	87	87	87

Table 3-5: Number of pH, Eh, Cl and pXRF measurements taken on rock art panels for each campaign by rock type

Campaign no.	Site type	Number of measurements on rock art panels			
		pH	ORP (Eh)	Chloride	pXRF
1	BAS	11	2	9	12
	DOL	15	0	12	15
	GBR	39	3	20	36
	GPH	87	7	54	98
	GRT	3	0	3	9
2	BAS	12	12	12	12
	DOL	15	15	15	15
	GBR	39	39	39	39
	GPH	90	90	90	90
	GRT	6	6	6	6
3	BAS	12	12	12	12
	DOL	15	15	15	15
	GBR	39	39	39	39
	GPH	90	90	90	90
	GRT	6	6	6	6
4	BAS	12	12	12	12
	DOL	15	15	15	15
	GBR	39	39	39	39
	GPH*	93	93	93	93
	GRT	6	6	6	6

Note: * indicates a repeat measurement on one rock art panel.

Table 3-6: Number of pH, Eh, Cl and pXRF measurements on sample rocks taken for each campaign by rock type.

Campaign no.	Site type	Number of measurements on sample rocks			
		pH	ORP (Eh)	Chloride	pXRF
1	BAS	18	1	10	18
	DOL	21	0	21	21
	GBR	36	3	18	36
	GPH	87	8	60	93
	GRT	15	0	6	21
2	BAS	18	18	18	18
	DOL	24	24	24	24
	GBR	33	33	33	33
	GPH	93	93	93	93
	GRT	18	18	18	18

The field observations of elemental composition using pXRF provide essential information about the rock surfaces that is valuable in the overall analysis and informative for many of the other component studies. Exploratory data analysis of pXRF results is reported in Section 7.3. The pXRF results collected in campaigns 1 to 4 may be sufficient for the study, depending on whether a degradation-related signal can be recognised through the noise of natural variability and instrument precision. Further statistical analysis will be used to establish the signal:noise ratio.

The field observations of physico-chemical parameters (pH, Eh, Cl) reveal interesting spatial trends but also reveal the presence of sources of variability and potential bias, as discussed in Section 7.2. Further field observations are required, in particular to investigate the effect of weather events.

In addition, there are concerns around pH and comparisons of our pH measurements with those of previous studies, that relate to three main issues:

1. The lengthy time taken for equilibration with the rock, so that the pH measured by this study and previous studies is at best, a measure of only the most rapid reactions between water and rock, and at worst, a measure of the pH of distilled/deionised water equilibrated with CO₂ (around 5.6).
2. Previous methods used inconsistent amounts of water. The methods state “a few drops” which, while having the advantage of maximising the concentrations of any rock-derived solutes, leads inevitably to issues in summer when small amounts of water evaporate instantly, and potentially leading to a seasonal bias on results. Further, the use of small amounts of water on hot rocks leads to constantly changing concentrations as the water evaporates which exacerbates the issues with equilibration noted above.
3. Previously stated trends based on Bednarik and coworkers, and used by Smith, Black and others, do not show a good understanding of the fundamentals of water-atmosphere interactions. For example, rainwater in arid areas is stated to have had a pH of 6.8 in previous studies, but rainwater should actually be around 5.6 because the rain equilibrates with CO₂ in the atmosphere to form a weak carbonic acid. The small number of analyses of pH values of 6.8 (8 analyses) were made in the 1970s, and it is acknowledged that lightning-derived ammonium might be increasing the pH of those samples. It’s a concern that so many subsequent workers have used these data without checking the validity of the source.

Our methods avoid the problems inherent in 2., but the issue of what, exactly, is measured remains. It is likely that the measured pH relates to a subset of the rock–fluid interactions that control stability, and include mineral–fluid, microbiome–fluid, and air- or dew-deposited species–fluid interactions. The systems that reach partial equilibrium in the two minutes of pH measurement may vary seasonally.

Soil samples were collected for inorganic geochemistry studies where the sample rocks were located near undisturbed soil that could be a potential sample for plutonium (Pu) analysis, where Pu is to be used as an indicator of weathering. Soil samples are stored at the MAC office until the analysis protocols and laboratory being engaged to undertake the work have been finalised.

Fieldwork for the first year of studies was undertaken in accordance with the study design specified in Section 3 of the MSDCA Plan. Some data are missing, due to failures of ORP(Eh) and Cl probes, as summarised in Table 3-3 to Table 3-6 above. It cannot yet be determined whether the missing data for these physico-chemical parameters will have an impact on the analysis and outcomes. While there is a well-developed statistical methodology for dealing with missing data, the main concern is that these measurements are affected by seasonally varying weather, and measurements are missing for the driest season monitored to date season. Accordingly, the statistical team recommends that the upcoming second year of fieldwork should include field visits on four different occasions at the same time as those undertaken in the first year. Overall, the studies are on track to achieve the MSDCA Plan objectives.

3.4 Microbiome collection fieldwork

3.4.1 Objectives

The purpose of the microbiome fieldwork is to acquire material for use in laboratory microbiome testing (see Section 4.3).

3.4.2 Methodology

Microbiome fieldwork took place in the first two field campaigns and involved collecting microbiome samples for later laboratory analysis.

Further information on microbiome field methodologies can be found in Section 3.3.3 of the MSDCA Plan and the component study methodology statement:

- COPP21065-PRO-G-107 Microbiome Field Sampling.

Soil samples were collected as per MSDCA Plan Section 3.3.3(i) using the same method as for lichen and other relevant opportunistic samples proximal to study rocks to support the microbial analysis.

Variations from planned methodology

Alterations from the planned microbiome study design in the MSDCA Plan are as follows:

1. The patina and the weathering rind layer were sampled together. The surface of the rock was wet with sterile molecular grade water and a sterilised DREMEL[®] tool was used to create a paste of the surface of the rock, which includes the patina and up to a maximum of 1 mm of the weathering rind.
2. Preserving the patina samples in a liquid nitrogen dewar on site was not viable due to logistical challenges. Instead, samples (including patina, soil, and lichen samples) were immediately submerged into DNA/RNA Shield solution (ZymoResearch) on site, kept on ice in the field, and stored in a -20°C freezer at the MAC office, until transported to Curtin University in a liquid nitrogen dewar. The DNA/RNA Shield solution guarantees the integrity of DNA and RNA at room temperature for up to 7 days and at -20°C indefinitely.
3. Cultivation of microbes from the rock patina was completed by using a sterile swab to sample the patina, and immediately inoculating onto Trypton Soy Agar (**TSA**) plates and Sabouraud agar (**SAB**) plates to

cultivate rock surface bacteria and fungi, respectively, which were incubated at room temperature at the MAC office and stored at –20°C once microbial growth was visible. Controls were also taken by holding a sterile swab for 30 seconds in the air and inoculating onto the TSA and SAB plates. By freezing the SAB and TSA plates further cultivation of the microbes is not viable however DNA extraction of colonies to understand what microbes were actively growing on the rock surface is possible.

3.4.3 Fieldwork outcomes

Patina samples were taken in triplicate per sample rock and a total of 491 samples were collected.

Table 3-7 and Table 3-8 summarise the number and type of samples (rock patina, soil, lichen and rock surface swabs) collected during campaigns 1 and 2 respectively. A total of 464 microbiome samples were collected in the field.

Table 3-7: Campaign 1 microbiome sample collection summary

Site ID	Granophyre	Gabbro	Dolerite	Granite	Basalt	Soil sample	Lichen	Rock surface swab
AQ01	-	-	-	-	-	-	-	-
AQ02	3	-	-	-	-	1	-	-
AQ03	3	3	-	-	-	1	-	-
AQ04	-	-	-	-	-	-	-	-
AQ05	3	-	3	-	-	1	1	-
AQ06	3	-	-	-	-	1	-	-
AQ07	3	-	-	3	-	1	1	-
AQ08	3	-	-	-	-	-	-	-
AQ09	3	3	-	-	-	1	-	-
AQ10	3	-	-	3	-	-	-	-
AQ11	3	-	-	-	-	-	-	-
AQ12	-	-	-	-	3	-	2	-
AQ13	3	-	-	-	-	-	-	-
AQ14	-	-	-	-	-	-	-	-
AQ15	-	3	-	-	-	1	-	-
AQ16	-	3	-	-	-	1	-	-
AQ17	3	-	-	-	-	3	1	-
AQ18	3	-	-	-	-	-	-	-
EX01	-	-	-	-	-	-	-	-
EX02	3	-	-	-	-	1	-	-
EX03	3	-	-	-	-	1	-	-
EX04	-	3	-	-	-	-	-	-
EX05	3	-	-	-	-	1	1	-
EX06	3	-	-	-	-	-	1	-
EX07	3	-	-	-	-	-	-	-
EX08	3	-	-	-	-	-	-	-

Site ID	Granophyre	Gabbro	Dolerite	Granite	Basalt	Soil sample	Lichen	Rock surface swab
EX09	3	3	-	-	-	1	1	-
RS01	3	-	-	-	-	1	-	-
RS02	-	3	-	3	-	1	1	-
RS03	3	-	-	3	-	2	-	-
RS04	3	3	3	-	-	-	-	-
RS05	6	-	3	-	-	-	-	-
RS06B	3	-	-	-	-	-	-	-
RS07	-	-	-	-	3	-	-	-
RS08	-	-	3	-	3	2	-	-
RS09	-	-	3	-	3	-	-	-
RS10	-	3	-	-	-	-	-	-
RS11	3	-	-	-	-	1	-	-
RS12	-	-	-	-	3	-	-	-
RS13	-	3	-	3	-	2	2	-
RS14	3	-	3	-	-	-	-	-
RS15	-	-	-	-	3	-	2	-
RS16	-	6	-	-	-	3	-	-
RS17	3	-	-	-	-	-	-	-
RS18	3	-	-	-	-	-	-	-
AS01	-	-	3	-	-	1	1	-
AS02	-	-	3	3	-	2	-	-

Table 3-8: Campaign 2 microbiome sample collection summary

Site ID	Granophyre	Gabbro	Dolerite	Granite	Basalt	Soil sample	Lichen	Surface swab
AQ01	-	-	-	-	-	-	-	-
AQ02	3	-	-	-	-	1	-	-
AQ03	3	3	-	-	-	2	-	-
AQ04	3	-	-	-	-	-	-	-
AQ05	3	-	3	-	-	-	-	-
AQ06	3	-	-	-	-	-	-	-
AQ07	3	-	-	3	-	2	-	-
AQ08	3	-	-	-	-	1	-	-
AQ09	-	3	-	-	-	-	-	-
AQ10	3	-	-	-	-	1	-	-
AQ11	3	-	-	-	-	-	-	-
AQ12	-	-	-	-	3	1	-	-
AQ13	3	-	-	-	-	1	-	-

Site ID	Granophyre	Gabbro	Dolerite	Granite	Basalt	Soil sample	Lichen	Surface swab
AQ14	3	-	-	-	-	1	-	-
AQ15	-	3	-	-	-	-	1	-
AQ16	-	3	-	-	-	1	-	-
AQ17	3	-	-	-	-	1	-	-
AQ18	3	-	-	-	-	1	-	-
EX01	-	-	-	-	-	-	-	-
EX02	3	-	-	-	-	1	-	-
EX03	3	-	-	-	-	-	-	1
EX04	-	3	-	-	-	-	-	-
EX05	3	-	-	-	-	-	-	-
EX06	3	-	-	-	-	-	1	-
EX07	3	-	-	-	-	1	-	1
EX08	3	-	-	-	-	-	-	-
EX09	3	3	-	-	-	1	-	1
RS01	2	-	-	-	-	-	-	1
RS02	-	3	-	3	-	4	1	-
RS03	4	-	-	3	-	1	-	1
RS04	3	3	3	-	-	1	1	-
RS05	6	-	3	-	-	3	-	3
RS06B	3	-	-	-	-	-	-	-
RS07	-	-	-	-	3	-	-	-
RS08	-	-	3	-	3	1	1	1
RS09	3	-	3	-	3	2	-	-
RS10	-	3	-	3	-	-	-	2
RS11	3	-	-	-	-	1	-	-
RS12	-	-	-	-	3	1	1	-
RS13	-	3	-	3	-	-	-	2
RS14	3	-	2	-	-	-	1	2
RS15	-	-	-	-	3	-	1	1
RS16	-	3	-	-	-	-	-	1
RS17	3	-	-	-	-	1	-	1
RS18	3	-	-	-	-	-	-	1
AS01	-	-	-	-	-	-	-	-
AS02	-	-	3	-	-	-	-	-

Soil samples were collected for microbiology studies where the sample rocks were located near soil. This is to understand any correlations between soil and rock surface microbiome.

3.5 Surface change analysis (spectroscopy) fieldwork

3.5.1 Objectives

From Section 1.7 of the MSDCA Plan, the objectives of the spectroscopy investigations are to:

1. Accurately measure the colour, texture and elemental composition of selected rock surfaces across Murujuga.
2. Study the secondary reflectance characteristics to monitor chemical change, anticipating future colour change.
3. Capture the broad surface elemental distribution to understand colour change across whole surfaces to correlate with and inform spot measurements.
4. Establish baseline values for a long-term monitoring program.
5. Identify important differences or changes in colour, surface texture and elemental composition which may be associated with degradation of appearance or condition.
6. Develop deeper understanding of variation in elemental composition across the rock surface and its relationship to colour and texture.
7. Develop criteria for assessing degradation of appearance or condition.
8. Ensure that the study data provide information required by other component studies (such as the precise spatial location of each observation).

3.5.2 Methodology

Spectroscopy fieldwork in the four field campaigns involved:

1. Spectroscopic measurement of ten targets at each site
2. In-field management of spectral files
3. Gathering of environmental and condition data at each site, including comprehensive photographic record of the site and its context.

Further information on spectroscopy field methodologies can be found in Section 3.2.3 of the MSDCA Plan and the component study methodology statement:

- COPP21065-PRO-G-110 Photospectrometric Colour Change Measurement.

Variations from planned methodology

A detailed assessment of possible sources of variability in the spectroscopy methodology and how these were practically addressed in the field is included in Appendix B:

Fieldwork outcomes

Table 3-9 and Table 3-10 summarise the number of spectroscopic measurements recorded in each fieldwork campaign so far, broken down by rock type and by site type.

The fieldwork also involved the testing and development of the field protocol to ensure that valid data are produced. Each recorded spectrum was initially validated in the field by checking the validity of the CIELAB colour

values reported by the instrument, as described in Appendix B:. Invalid measurements were repeated, where possible. Field technique was modified several times during the campaigns to reduce the frequency of invalid measurements, for example, by improving the cooling of the device, as described in Appendix B:.

The recorded spectral data were saved to individual files and later shared with the statistical team. These data were subjected to close scrutiny and further validation steps, as reported in Section 7.1. Exploratory data analysis is also reported in Section 7.1. Further conclusions are reported in Section 9.

Table 3-9: Number of spectroscopic measurements taken for each campaign by rock type

Campaign no.	Rock type				
	Granophyre	Gabbro	Dolerite	Granite	Basalt
1	3,562	1,530	594	208	470
2	3,602	1,542	651	215	504
3	3,656	1,519	612	213	466
4	3,288	1,531	581	208	475

Table 3-10: Number of spectroscopic measurements taken for each campaign by site type

Campaign no.	Study square type			
	AQ	AS	EX	RS
1	2,596	348	1,090	2,330
2	2,585	374	1,064	2,491
3	2,635	359	1,032	2,440
4	2,472	330	935	2,346

4 Laboratory analysis of field samples

4.1 Organic geochemistry laboratory analysis

4.1.1 Objectives

From Section 1.4 of the MSDCA Plan, the objectives of the organic geochemistry investigations are to:

1. Measure the molecular and stable isotopic composition of organics from all sources, including natural emissions (terrestrial vegetation, fire), anthropogenic emissions (shipping, traffic, industry) and organics present in the host rocks (including rock dust from iron ore transport), to produce a detailed characterisation of organic emissions in the Murujuga region. Including determination of the occurrence and magnitude of seasonal variations in emissions.
2. Measure the molecular and stable isotopic composition of organics deposited on rock surfaces and in soils, to link organics on rock surfaces to the various emission sources, and determine which sources contribute the highest quantity of organics to the surface deposition.
3. Identify any organics that are likely to affect weathering of rock art, e.g. by affecting growth of microorganisms (in conjunction with microbiome expert(s)) or interaction with specific minerals (in conjunction with inorganic geochemist(s)).
4. Understand confounding factors introduced by (reported) changed fire management regimes approximately coinciding with the commencement of industrial activity on the Burrup.

4.1.2 Methodology

Organic geochemistry laboratory methodologies are described in Section 3.3.3 of the MSDCA Plan and the component study methodology statement:

- COPP21065-PRO-G-113 Organic Geochemistry of Rock Surfaces, Dust and Particulates

4.1.3 Work to date

Sixty-four field sample rocks were received in September 2022 following collection in field campaign 2, and the surface removal of the sample rocks was completed in December 2022. Figure 4-1 provides an example of a typical sample rock in-situ in the field through to removal of its outer surface.

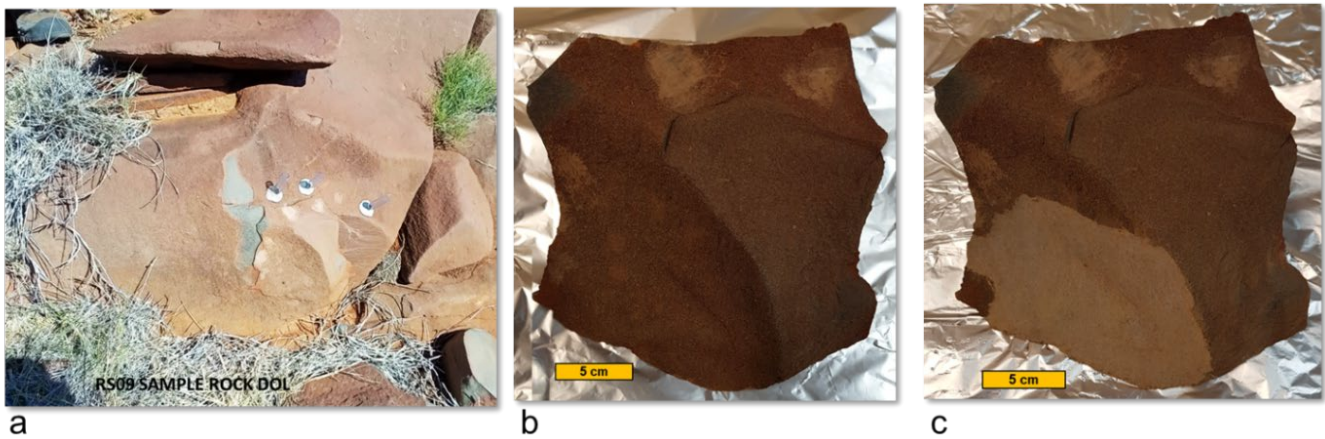


Figure 4-1: Example of a sample rock processed: (a) in the field (b) as received (c) after rock surface has been removed.

Seventy surface samples were obtained in total. The additional six samples were taken either when:

- The sample rock consisted of multiple rock pieces (e.g., AQ05_DOL),
- Sufficient material was available (e.g., RS15_BAS), or
- Extra pieces of rock patina could be removed (e.g., RS08_DOL).

The aim was to collect a minimum of approximately 10 g of rock surface for each sample to ensure a sufficient yield of total bitumen extract. This was only possible for 64% of the samples. For 19% of the sample rocks the recovered amount ranged between 5 and 10 g, and for the remaining 17% of field sample rocks, less than 5 g of surface material was obtained (Figure 4-2).

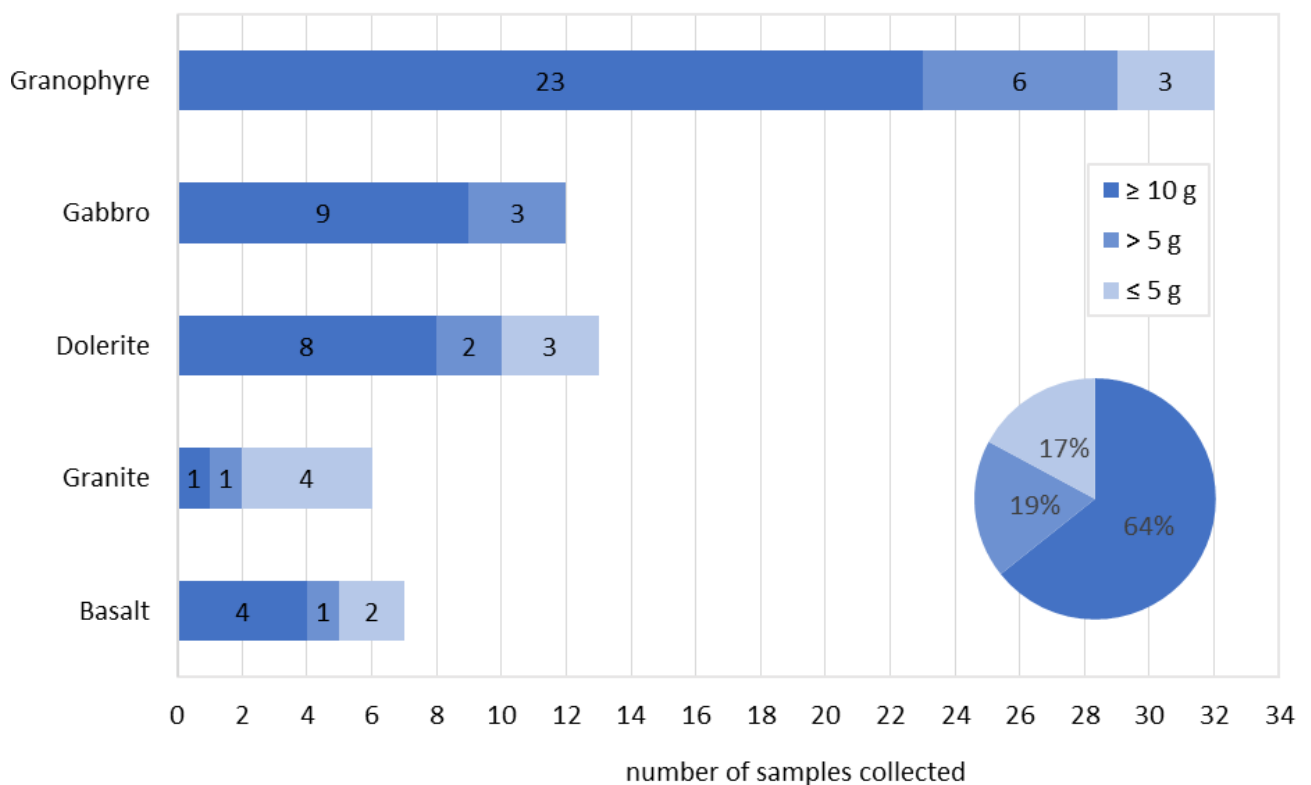


Figure 4-2: Amount of rock surface collected. Bar graph shows the number of samples with the amount of material obtained. Pie graph displays the distribution of masses obtained.

The target sample weight of 10 g was conservative. It was determined from an initial trial in which samples of approximately 5 g of material were used. Assay results were obtained from these samples, but some were detected with low levels or low reliability. For enhanced quality of the analysis, it was decided to double the sample mass for the full study, giving a target weight of 10 g. A full set of results can nevertheless be obtained from smaller samples, and the study will extract all samples where at least 3 g of material was collected. Only 5 samples fall below this threshold.

All samples were analysed for total organic carbon (TOC) using an Elementar soli TOC[®] instrument operated by Curtin’s Soil and Landscape Science Group. The TOC of all the samples was in general low and ranged between 0.04 to 1 wt %, averaging 0.24 wt%. Table 4-1 shows TOC of the different rock types separated into two categories (less than 0.3 and between 0.3 to 1 wt%).

Table 4-1: Total organic carbon of different rock types (by weight %)

Rock Type	Total organic carbon (wt %)	
	< 0.3	> 0.3 ≤ 1
Granophyre (%)	84	16
Gabbro (%)	58	42
Dolerite (%)	69	31
Basalt (%)	100	0
Granite (%)	67	33

The pulverised surface samples were Soxhlet extracted for 72 h with dichloromethane:methanol solvent (DCM:MeOH, 9:1 vol./vol.). The sample extractions are still in progress with 40 samples extracted to date. Examples of recovered organic extract for different rock types are shown in Figure 4-3.



Figure 4-3: Example of organic extract of various rock surfaces.

After the extractions are completed, the extracts obtained will be fractionated and analysed by gas chromatography-mass spectrometry (GC-MS) for organic composition. Isotopic values will be determined by gas chromatography – isotope ratio mass spectrometry (GC-irMS), as per the procedures in Appendix 1 of the Organic Geochemistry of Rock Surfaces, Dust and Particulates Methodology (COPP21065-PRO-G-113).

At the time of writing, the laboratory procedures are ongoing. They appear to be on track to achieve the objectives of this component study. The key point is that the organic chemical composition of the patina is still largely unknown, so that this component study involves elements of exploratory investigation. Its results will influence and support the other component studies, especially the study of the microbiome of the rock surface.

4.2 Geology and inorganic geochemistry laboratory analysis

4.2.1 Objectives

Objectives of the inorganic geochemistry laboratory work have already been described in Section 3.3 of this report as part of the fieldwork summary.

4.2.2 Methodology

Inorganic geochemistry laboratory methodologies are described in Section 3.3.2 of the MSDCA Plan and the component study methodology statement:

- COPP21065-PRO-G-114 Inorganic Geochemistry Laboratory Analysis.

4.2.3 Geological mapping

The geological mapping aims to produce a detailed geological background of the lithologies outcropping in the immediate surroundings where the rock art panels are localised and to closely evaluate the contact relationships between different rock types. These larger-scale observations will then be correlated with results obtained from laboratory analyses in thin sections to quantify processes and/or mineral distributions observed at the micro and nano scale.

The ongoing geological mapping consists of recording the lithology and geological boundaries outcropping within approximately 50 m of each rock art site. Lithological information is recorded on the fieldwork tablet by using the open-source app FieldMove developed by Petroleum Experts Limited. The obtained polygons can be then visualized on map visualization software, such as Google Earth (see Figure 4-4).

Currently, the team has completed spatial geological mapping of 28 sites (see Table 4-2). The remaining sites are characterised by a more complex network of lithological boundaries that are difficult to resolve with the current available aerial open-source images (e.g., Google Earth). Where available, the team aims to complete the geological mapping of these sites by using the high-resolution aerial images produced by the spatial mapping team of the project. These images will allow a better recognition and a more accurate localisation of complex geological boundaries.

Table 4-2: Geological mapping status for MRAMP study sites

Site name	Geological map	Site name	Geological map	Site name	Geological map	Site name	Geological map
AQ01	N/A – no sample	RS01_GPH	Completed	EX01	N/A – no sample	AS01_DOL	To be completed
AQ02_GPH	Completed	RS02_GBR	To be completed	EX02_GPH	To be completed	AS02_DOL	To be completed
AQ03_GBR	To be completed	RS03_GPH	To be completed	EX03_GPH	Completed		
AQ03_GPH	To be completed	RS04_GBR	Completed	EX04_GBR	Completed		
AQ03_DOL	To be completed	RS04_GPH	Completed	EX05_GPH	Completed		
AQ04_GPH	Completed	RS05_GPH	Completed	EX06_GPH	Completed		
AQ05_GPH	To be completed	RS06_GPH	Completed	EX07_GPH	Completed		
AQ06_GBR	Completed	RS07_BAS	To be completed	EX08_GPH	To be completed		
AQ06_GPH	Completed	RS08_DOL	To be completed	EX09_GBR	Completed		
AQ07_GPH	To be completed	RS08_BAS	To be completed	EX09_GPH	To be completed		
AQ07_GRT	To be completed	RS09_DOL	To be completed				
AQ08_GPH	To be completed	RS09_BAS	To be completed				
AQ09_GBR	Completed	RS10_GBR#4	Completed				
AQ09_GPH	To be completed	RS10_GBR#10	Completed				
AQ10_GPH	To be completed	RS11_GPH	To be completed				
AQ11_GPH	Completed	RS12_BAS	To be completed				
AQ12_BAS	To be completed	RS13_GBR	To be completed				
AQ13_GPH	Completed	RS14_GPH	To be completed				
AQ14_GPH	Completed	RS15_BAS	To be completed				
AQ15_GBR	Completed	RS16_GBR	Completed				
AQ16_GBR	Completed	RS17_GPH	Completed				
AQ17_GPH	Completed	RS18_GPH	Completed				
AQ18_GPH	Completed						

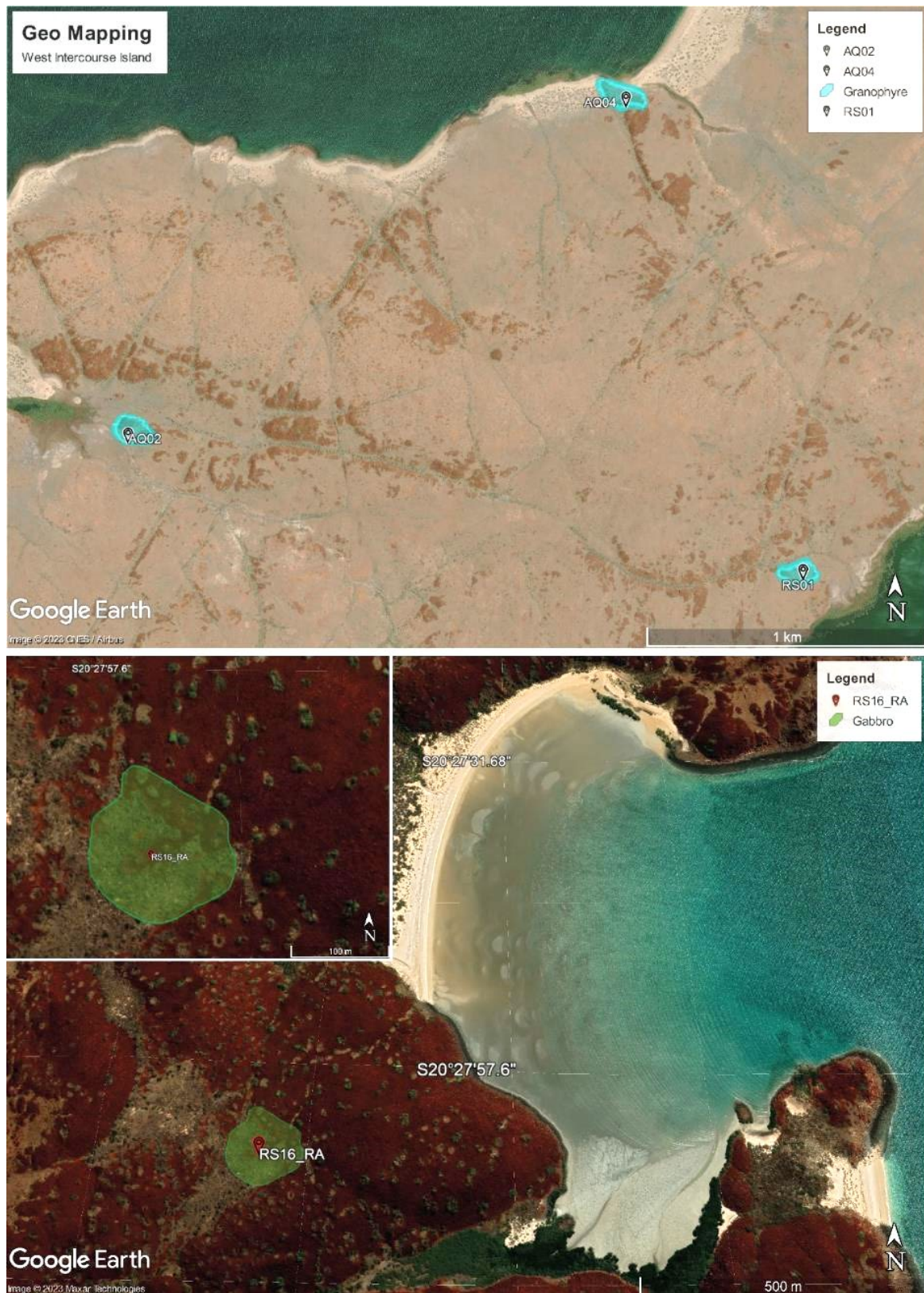


Figure 4-4: Examples of ongoing geological mapping. Top: aerial photograph of a portion of West Intercourse Island with granophyre lithology indicated around three monitored rock art panels. Bottom: aerial photograph of the area surrounding the rock art panel RS16-GBR. The shaded polygon indicates the distribution of gabbro in the surrounding of the rock art site location.

4.2.4 Thin section preparation

Thin sections of the 64 rock samples collected during field campaign 2 were prepared. Representative cross-sections through the patina, weathered rind and fresh rock of the various samples were obtained from those portions of the samples that had not been contaminated from microbial sampling and patina removal for organic studies (Figure 4-5a).

These were embedded into epoxy resin for 48 hours to consolidate the patina of the samples (Figure 4-5b). This procedure reduces the loss of fragile material during further cutting of the sample to conventional rock billets size.

Samples were then cut to form a billet with a surface area of approximately 44 mm x 24 mm (Figure 4-5c) and posted to Adelaide Petrographic for the production of polished thin sections (Figure 4-5d).

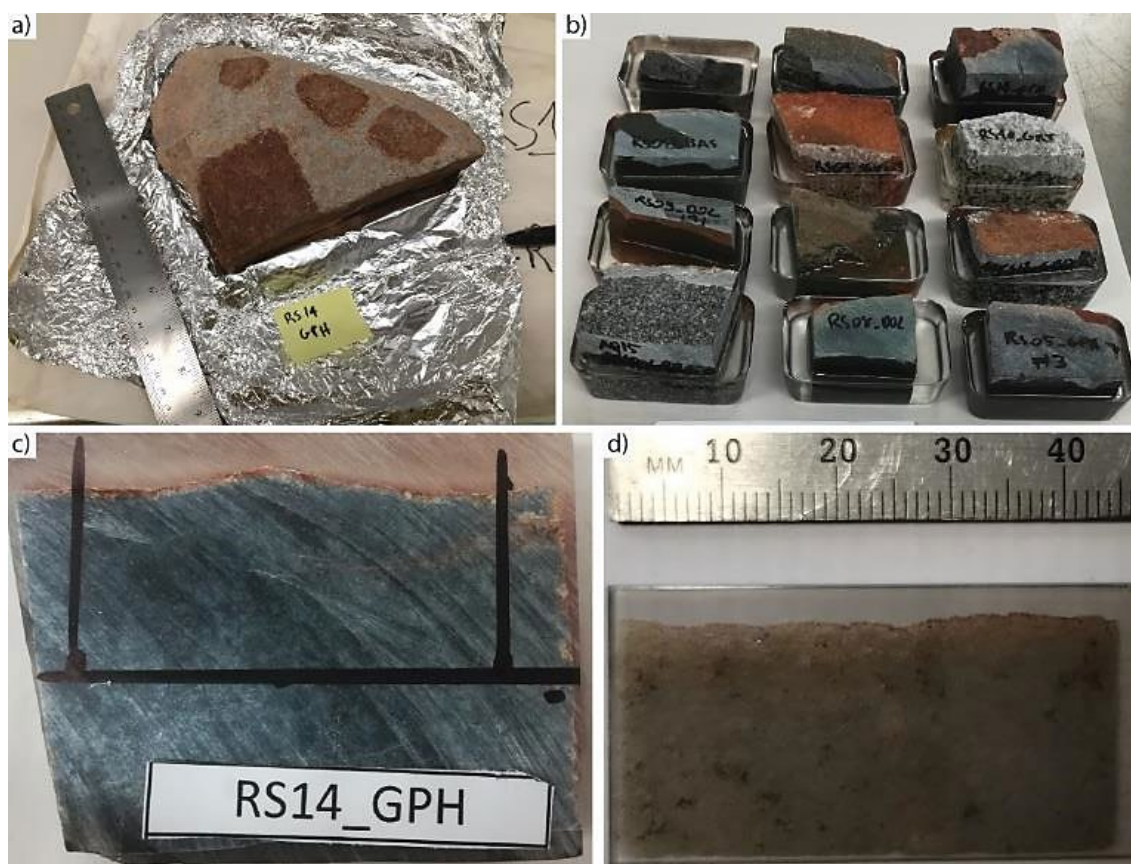


Figure 4-5: Thin section preparation stages. (a) Cross-section selection. (b) Embedding into epoxy. (c) Fresh cut of the sample after epoxy impregnation. Black lines indicate billet dimensions. (d) Polished thin section.

All billets for thin section slides have been prepared and 33 polished thin sections have been returned from Adelaide Petrographic. The remaining 30 billets are currently at Adelaide Petrographic. One sample, RS15_BAS, was insufficiently consolidated to produce a petrographic thin section because polishing would not be possible. For this sample, XRD analyses will provide an efficient characterisation.

4.2.5 Macro and micro characterisation

The 33 available thin sections have been investigated by optical microscopy and Tescan Integrated Mineral Analyser (**TIMA**) to obtain maps of the distribution of the different mineral phases and to quantify their abundances (i.e., mineral mode).

TIMA analysis images are provided in Appendix C:

Granophyre

The term granophyre is used to describe a fine-grained intrusive felsic rock that is characterised by the textural intergrowth of quartz and alkali feldspar (K-feldspar). Generally, the composition of a granophyre is similar to that of granite. The finer grain size, compared to the majority of intrusive rocks, derives from crystallisation during relatively rapid cooling, which forms smaller grains than the larger crystals in granite which cooled more slowly. Granophyric textures are thought to result from crystallisation close to the SiO₂ – feldspar eutectic. However, granophyric textures need not reflect a particularly fast cooling rate. Instead, they record near simultaneous crystallization of the two major minerals that form the greatest portion of the rock. The SiO₂-rich magmas that form granophyre are also prone to delayed crystal nucleation preceding very rapid crystal growth, a result of the very strong network-structure of silica-rich liquids.

In the observed samples, granophyre is fine-grained, holocrystalline, aphanitic and porphyritic. The mineral assemblage is dominated by quartz (40-50 wt.%), albitic plagioclase (20-30 wt.%) and alkali feldspar (orthoclase, 15-20 wt.%) where larger subhedral phenocrysts of plagioclase define the porphyritic texture of the rock. Minor phases are chlorite, clinopyroxene, biotite and epidote (Figure 4-6, Table 4-3). Amphibole and calcic plagioclase may be present. Accessory Fe and Ti-oxides such as hematite/magnetite and ilmenite occur in variable amounts. Because of the nature of the energy dispersive x-ray spectroscopy (**EDS**), it is not possible to distinguish between magnetite and hematite during the analyses. This information must be acquired by complementary methods such as reflected light, electron backscatter diffraction (**EBS**D), Raman, or XRD.

At a microstructural level, the texture of the rock is strongly characterised by the occurrence of granophyric intergrowth between quartz and alkali feldspar (see Section 4.2.6 on SEM analysis). Among the observed samples, these vary from acicular to radial aggregates. The radial texture (as seen for example in Appendix C Figure C-38 and Figure C-39 for sample rock AQ13_GPH) is characterised by circular aggregates of quartz and alkali feldspar, with quartz crystals projecting towards the plagioclase-rich matrix of the rock. This texture resembles spherulitic structures observed in basalts. The spheroidal texture may be record quench devitrification formed relatively shortly after magma cooling.

The acicular texture is mostly defined by elongated prisms of quartz within a groundmass of alkali feldspar (as seen in Appendix C Figure C-86 and Figure C-87 for sample rock RS01_GPH). Interestingly, quartz often occurs as a groundmass anhedral mineral within the same sample. Tridymite is the hexagonal high-temperature polymorph of quartz and can occur in volcanic rocks with a characteristic acicular habit (e.g., Egli et al., 2008). The elongated quartz may originally have formed as tridymite.

Murujuga Rock Art Monitoring Program
Monitoring Studies Report 2023

Table 4-3: Mineral modes for granophyre samples based on TIMA analysis.

Phases	AQ02_GPH	AQ04_GPH	AQ05_GPH	AQ06_GPH	AQ08_GPH	AQ09_GPH	AQ13_GPH	AQ14_GPH	EX02_GPH	EX03_GPH	EX05_GPH	EX06_GPH	EX08_GPH	EX09_GPH	RS01_GPH	RS04_GPH	RS05_GPH#	RS06_GPH	RS11_GPH
Quartz	46.13	43.45	41.25	39.22	46.1	51.29	50.99	50.08	44.95	43.33	50.86	40.65	49.85	55.32	41.64	42.16	42.81	51.53	40.49
Albite	29	26.55	30.93	32.53	25.78	25.3	22.03	29.54	24.66	30.32	18.81	30.66	28.1	20.83	25.41	28.62	31.71	22.2	28.16
Orthoclase	16.35	19.13	14.17	13.81	13.28	12.61	13.59	8.48	17.93	10.58	10.05	17.12	9.57	11.76	19.79	15.58	13.61	14.17	17.34
Biotite	2.32	4.36	2.44	6.55	2.09	2.42	3.01	4.3	4.46	1.79	4.77	1.65	3.06	4.59	3.57	3	4.63	3.02	2.78
Chlorite - Clinocllore	1.86	3.85	7.37	4.34	1.49	1.33	1.33	4.1	1.96	1.51	0.89	0.23	3.74	1.05	3.26	3.14	2.31	1.3	3.51
Epidote	1.26	0.05	0.25	0.02	6.19	5.7	3.33	0.15	0.89	3.37	2.03	1.17	2.08	4.36	0.65	4.47	1.26	3.77	0.84
Hematite/Magn etite	1.62	1.21	1.3	0.95	0.57	0.11	2.86	2.1	2.31	2.48	2.74	7.91	2.6	0.15	2.26	0.99	2.28	1.84	2.11
Anorthite	0.01	0	0.01	0	0.06	0.02	0.03	0	1.25	3.9	7.25	0.02	0.01	0.05	0.07	0.06	0.02	0.03	0.15
Ilmenite	0.75	0.37	1.03	0.74	0.95	0.35	0.6	0.26	0.65	0.44	1.18	0.17	0.31	0.28	1.73	1.16	0.56	0.41	1.42
Amphibole	0.14	0.15	0.39	0.13	2.84	0.44	0.91	0.24	0.17	1.67	0.15	0.06	0.29	0.45	0.22	0.32	0.15	1.32	1.62
Varnish	0.07	0.33	0	0.25	0.12	0.06	0.49	0.34	0.2	0.03	0.56	0.04	0.08	0.76	0.73	0.17	0.31	0.21	0.63
Titanite	0.31	0.34	0.65	0.54	0.2	0.22	0.05	0.05	0.15	0.16	0.02	0.01	0.04	0.08	0.21	0.25	0.08	0.04	0.35
Muscovite	0	0.1	0.07	0.69	0.01	0.02	0.26	0.23	0.08	0.04	0.32	0.22	0.15	0.08	0.15	0.02	0.05	0.04	0.34
Kaolinite	0	0.03	0	0.05	0	0.01	0.2	0.08	0.01	0	0.22	0.01	0.02	0.16	0.04	0.01	0.05	0.01	0
Calcite	0.13	0	0	0	0.21	0	0.03	0	0.17	0	0	0	0.02	0.01	0.07	0	0.01	0	0
Clinopyroxene	0	0	0	0	0	0	0.14	0	0	0.32	0	0	0	0	0	0	0	0.07	0.13
Apatite	0.02	0.02	0.08	0.11	0.01	0.01	0	0	0.01	0.01	0	0.02	0.01	0	0.06	0.03	0.01	0	0.07
Rutile	0.01	0.02	0.02	0.01	0	0	0	0	0	0	0	0	0	0	0.04	0	0	0	0.02
Ankerite	0.01	0	0.01	0	0.01	0	0	0	0.01	0	0	0	0	0	0.02	0	0	0	0
Baryte	0	0	0	0	0	0	0.01	0	0	0	0	0	0	0	0	0	0.02	0	0

Murujuga Rock Art Monitoring Program
Monitoring Studies Report 2023

Phases	AQ02_GPH	AQ04_GPH	AQ05_GPH	AQ06_GPH	AQ08_GPH	AQ09_GPH	AQ13_GPH	AQ14_GPH	EX02_GPH	EX03_GPH	EX05_GPH	EX06_GPH	EX08_GPH	EX09_GPH	RS01_GPH	RS04_GPH	RS05_GPH#	RS06_GPH	RS11_GPH
Wollastonite	0	0	0	0	0.01	0	0	0	0	0	0	0	0	0	0.01	0	0	0	0
Pyrite	0	0	0	0	0	0.03	0	0	0	0	0	0	0	0	0	0	0	0	0
[Unclassified]	0.01	0.03	0.01	0.03	0.04	0.07	0.12	0.03	0.11	0.04	0.14	0.06	0.09	0.05	0.08	0.02	0.11	0.05	0.04
The rest	0	0	0.01	0	0.01	0	0	0	0	0.01	0	0	0	0	0	0	0.01	0	0
Total	100																		

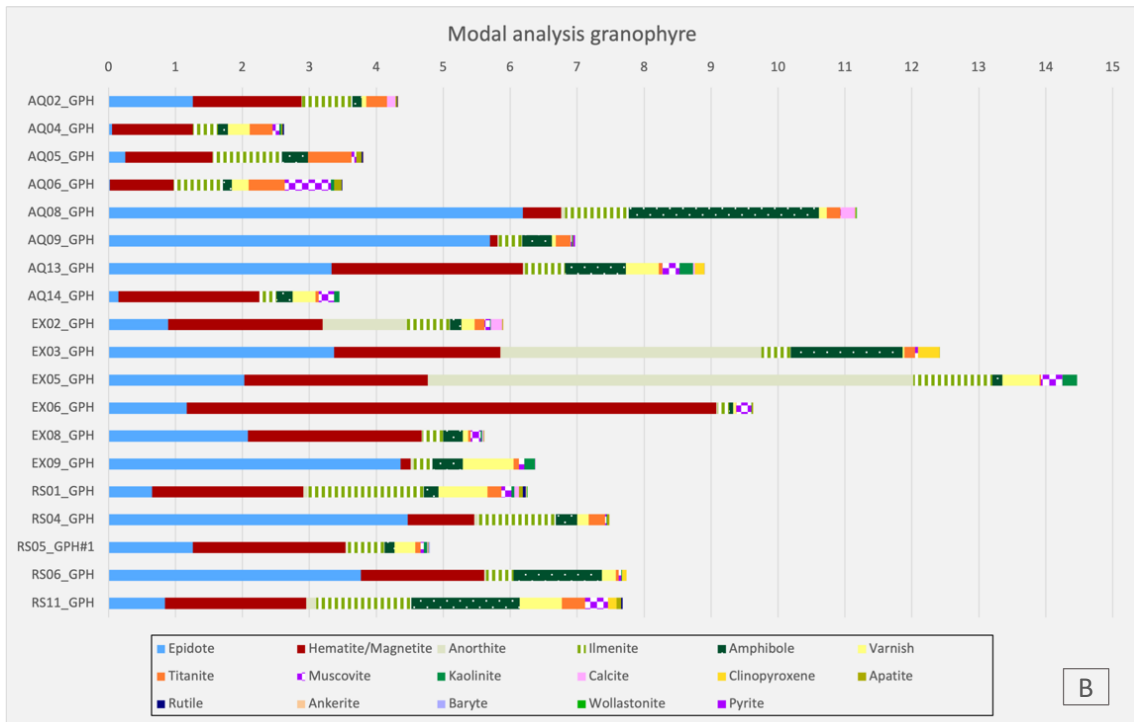
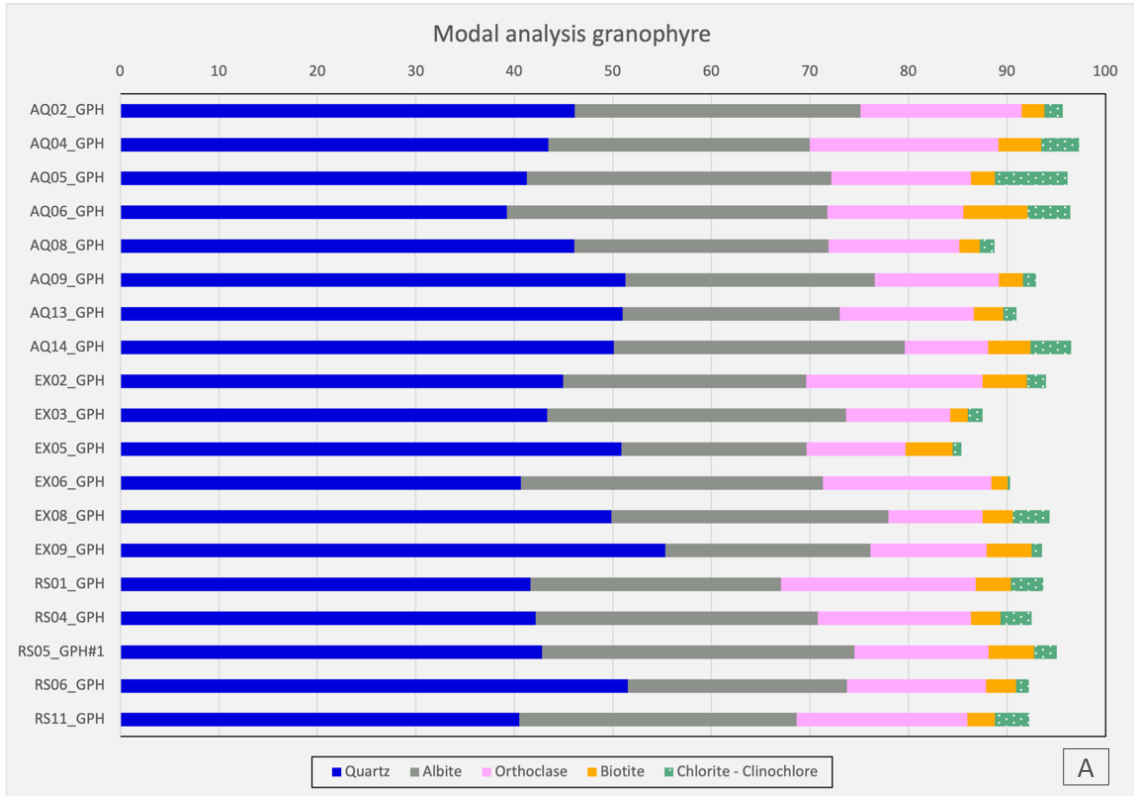


Figure 4-6: Summary of granophyre modal analyses obtained by TIMA. The TIMA database comprises mineral end-members rather than solid solution phases so the table should be read noting that, for example, anorthite represents Ca-rich feldspars and orthoclase represents K-feldspars. A: Major phases; B: Minor phases

Gabbro

Gabbro is a coarse-grained mafic intrusive rock mostly composed of calcium-rich plagioclase (labradorite) and pyroxenes. Generally, the pyroxene is mostly clinopyroxene (augite) although orthopyroxenes are also present in most samples. The formation of gabbro can be associated with both in-situ crystallisation of pyroxene and plagioclase, or as part of a layered intrusion formed by the accumulation of pyroxene and plagioclase from a crystallising magma. The main difference between gabbro and granophyre lithologies is their composition. Gabbro is much more mafic than granophyre, meaning that it has a lower SiO₂ content.

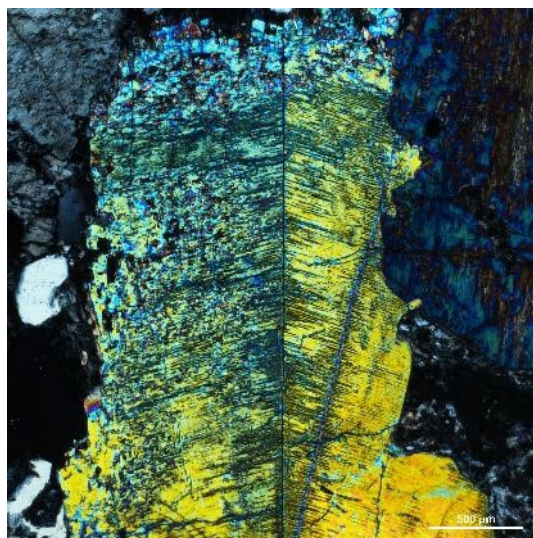


Figure 4-7: Crossed polarised image of clinopyroxene showing the typical twinning.

The gabbro at Murujuga is coarse-grained, holocrystalline and phaneritic. In this report no distinction is made between gabbro and quench gabbro, although the much coarser grain size of the quench gabbro is noted and a brief description and discussion is presented here. The gabbro referred to as ‘quench gabbro’ consists of elongate skeletal grains, up to 30 cm long, and occurs at the contact between the gabbro and the older granite. The textures are similar to spinifex textures, which form when a magma is cooled below the temperature at which a mineral appears on the liquidus without that mineral nucleating. When the mineral finally nucleates, growth is rapid and forms large skeletal crystals, similar to those seen at Murujuga. It is likely that this formation mechanism is the reason that the very coarse-grained gabbro is referred to as ‘quench gabbro’.

Clinopyroxene is generally the largest and most common mineral within the gabbros. It shows characteristic twinning parallel to the direction of elongation of ragged prismatic grains and high birefringence (Figure 4-7). The mineral assemblage is mostly composed of clinopyroxene (ca. 40 wt.%), Ca-rich feldspar (10-40 wt.%), orthopyroxene (10-20 wt.%) and quartz (10-15 wt.%) as shown in Figure 4-8. The minor phases comprise chlorite, amphibole, albitic plagioclase, epidote and muscovite. The Fe- and Ti-bearing oxides occur in various amounts.

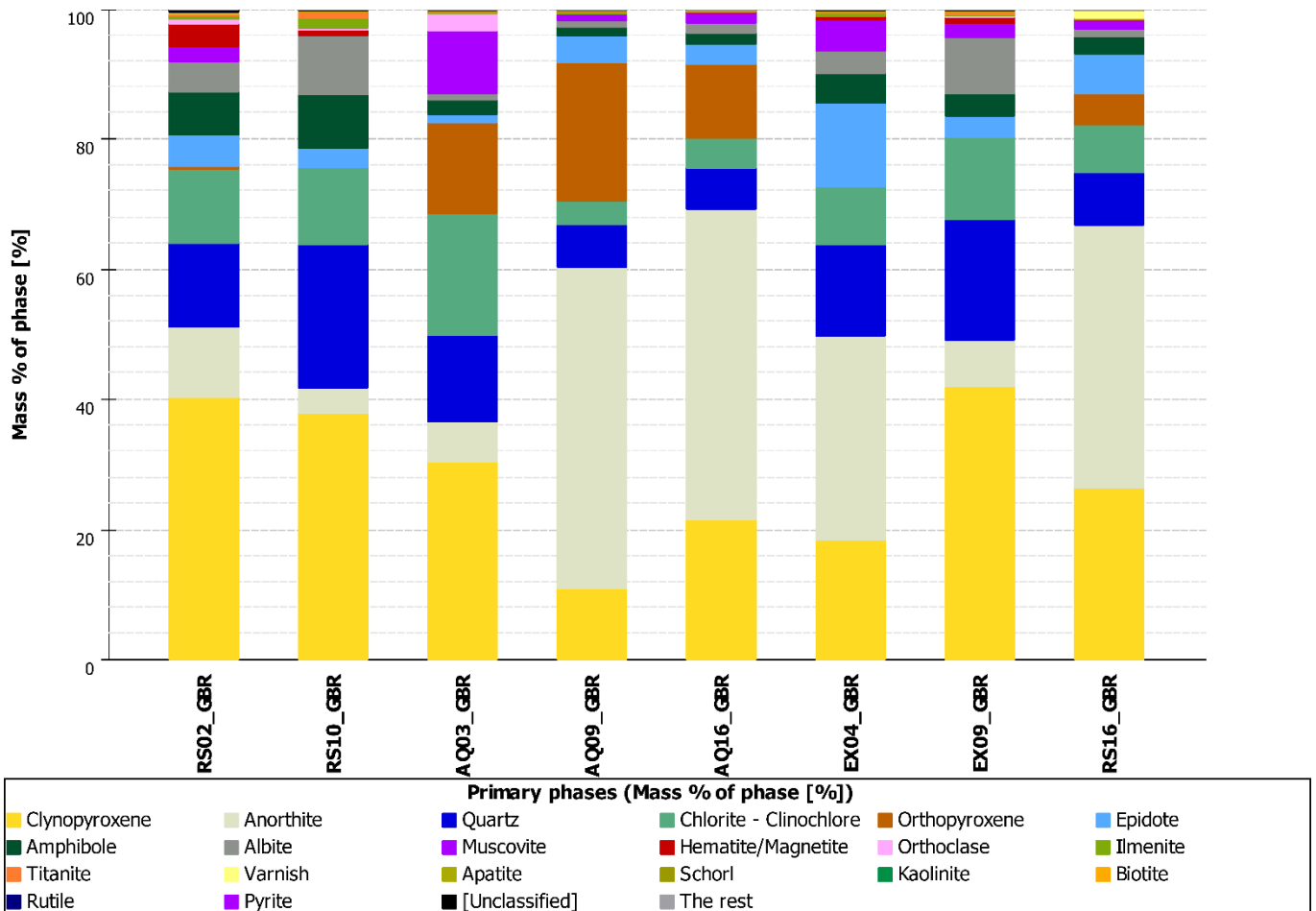


Figure 4-8: Summary of gabbro modal analyses obtained from TIMA. The TIMA database comprises mineral end-members rather than solid solution phases so the table should be read bearing in mind that, for example, anorthite represents Ca-rich feldspars and orthoclase represents K-feldspars.

4.2.6 Scanning electron microscopy and energy dispersive x-ray spectroscopy analysis

Five samples have been inspected using scanning electron microscopy (SEM). The objective of this work is to identify the microstructural relationship amongst the minerals of the patina, and between the patina and underlying rock layers.

The results include high-resolution BSE (Backscattered electrons) images of the patina, within which areas with high average atomic number appear paler, in contrast to darker areas with lower average atomic number, and EDS images that show the distribution of key elements on maps obtained for areas of interest. The following representative samples are divided by lithology.

Granophyre

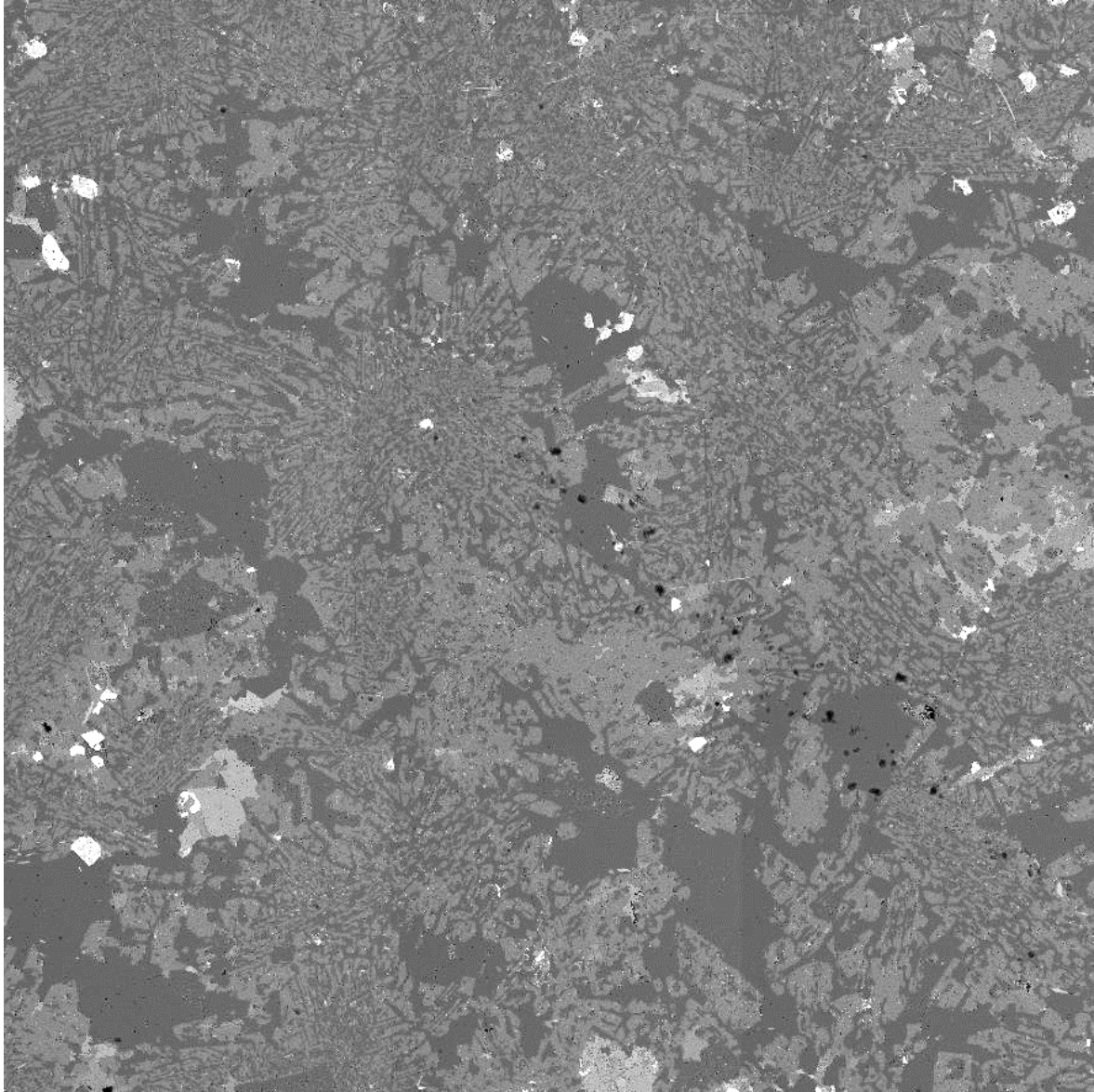


Figure 4-9: SEM-BSE image of the matrix of granophyre sample EX02_GPH. In the image is possible to distinguish a vermicular granophyric intergrowth between quartz (darker) and K-feldspar (lighter grey). The brightest phases represent Fe-Ti oxides.

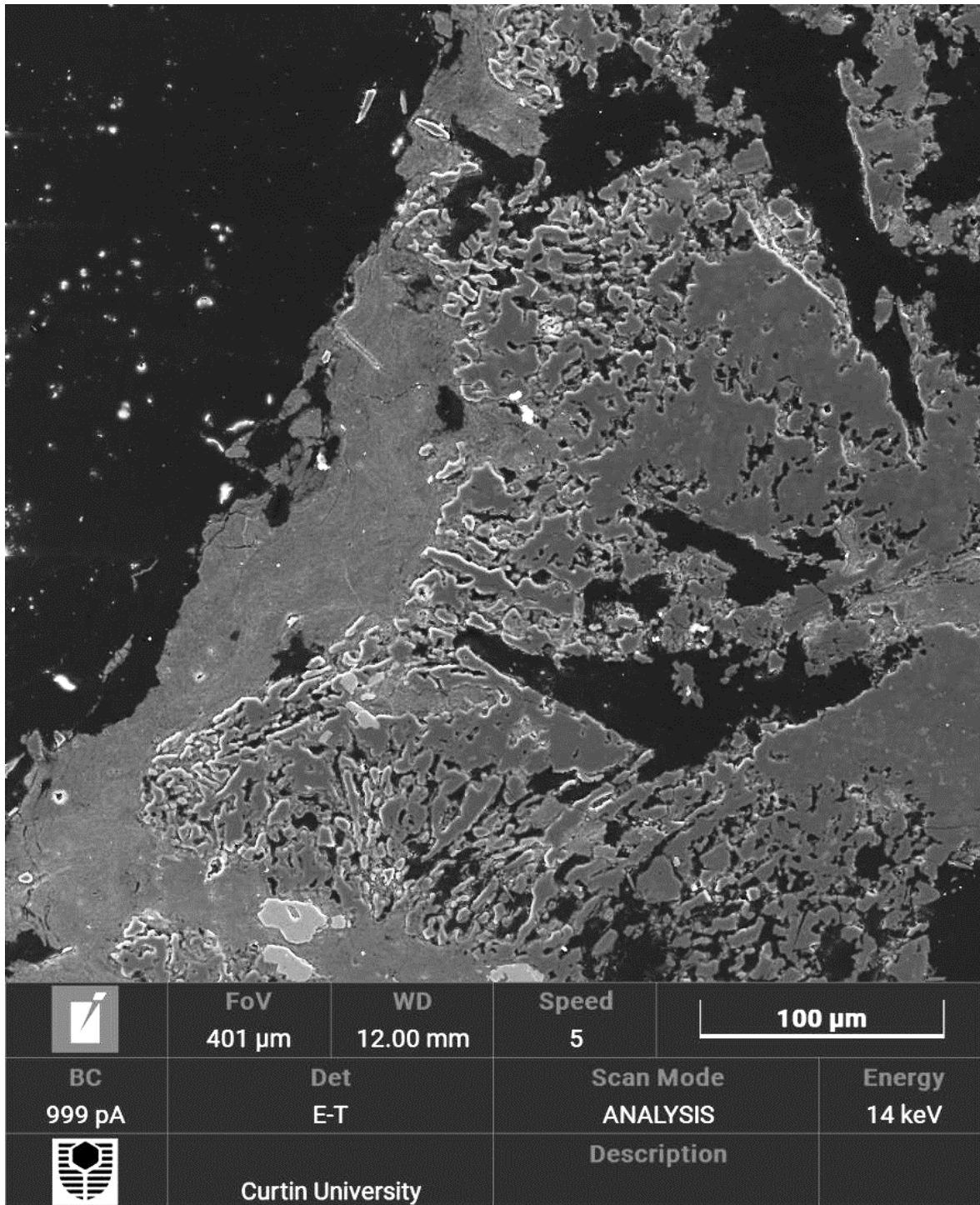


Figure 4-10: SEM-SE image taken from sample EX08_GPH. This image shows the formation of patina (left) on top of the weathered granophyre texture (void-rich area formed by dissolution of K-feldspar). Quartz within the less weathered rock to the right shows higher relief, because it is harder than the patina.

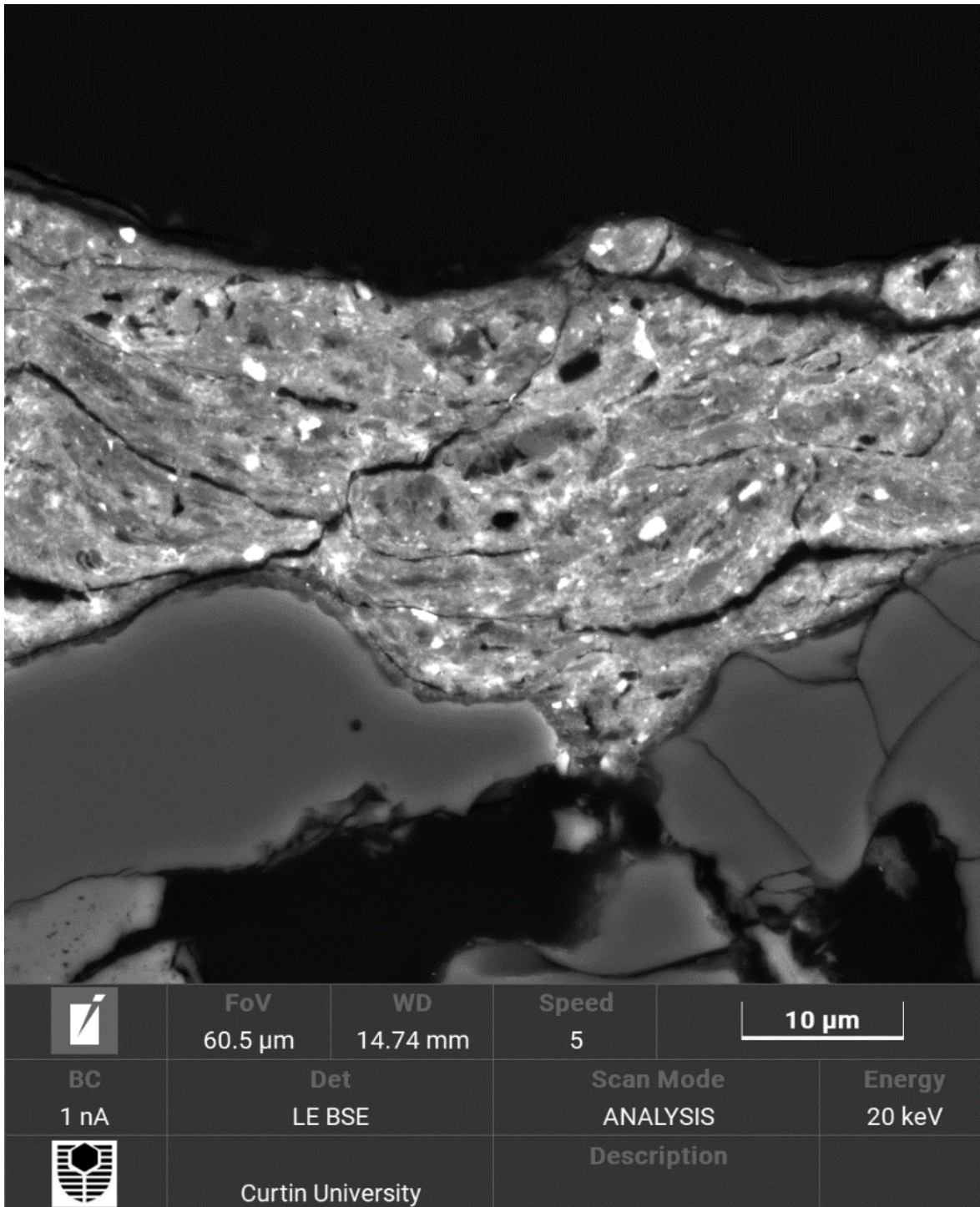


Figure 4-11: Close-up SEM-BSE image of patina from granophyre sample RS11_GPH showing discontinuous contorted layers of patina above quartz crystals. The bright particles within the patina are Fe-Ti oxides.

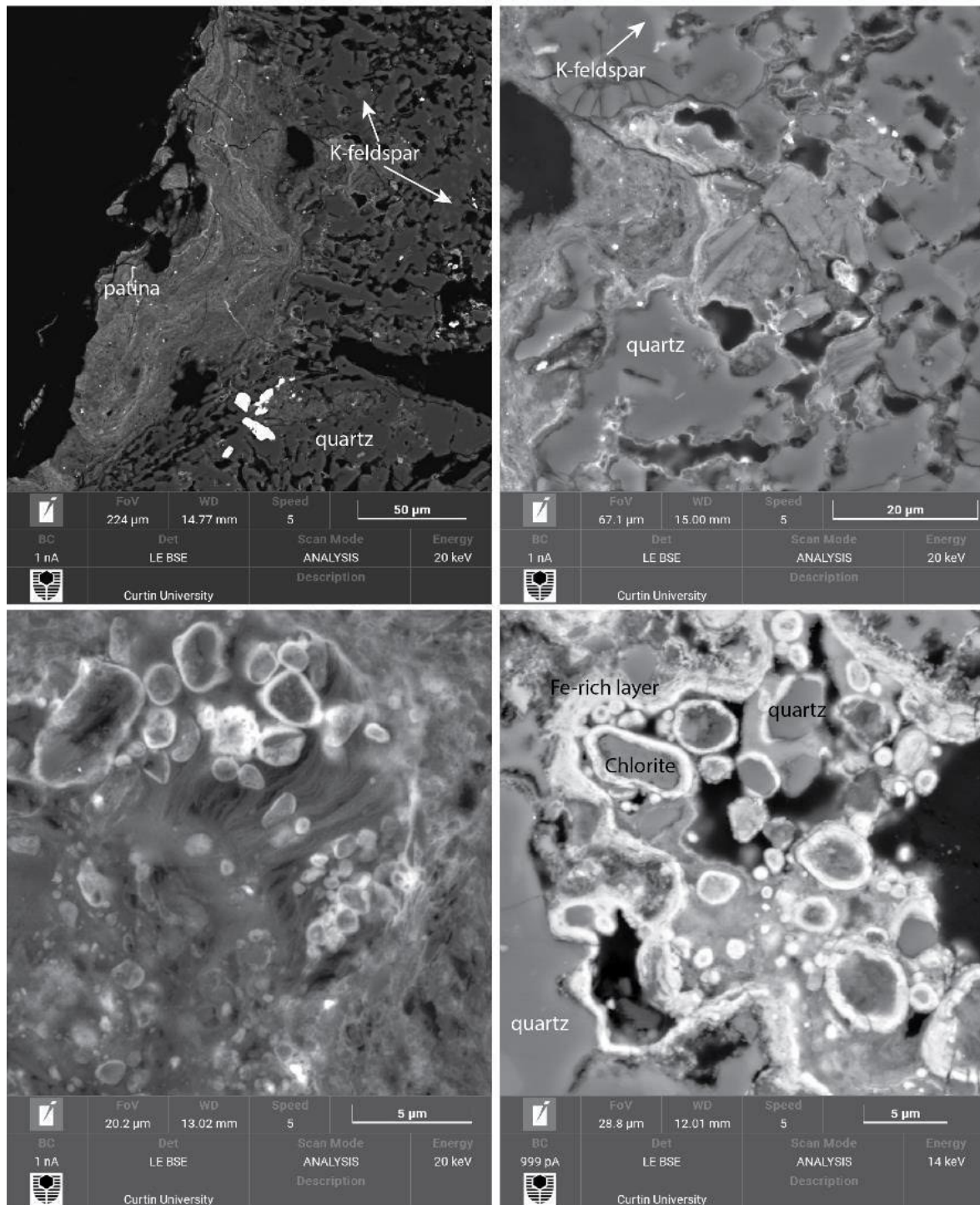


Figure 4-12: SEM-BSE images. (top left) Rock patina on top of modified granophyric intergrowth of quartz and K-feldspar. (top right) close up of top-left image. The voids are inferred to form by dissolution of feldspar. (bottom left) Close-up detail of circular particles with a fibrous groundmass, tentatively attributed to biological activity. (bottom right) Close-up image of particle aggregates surrounded by an Fe-enriched layer.

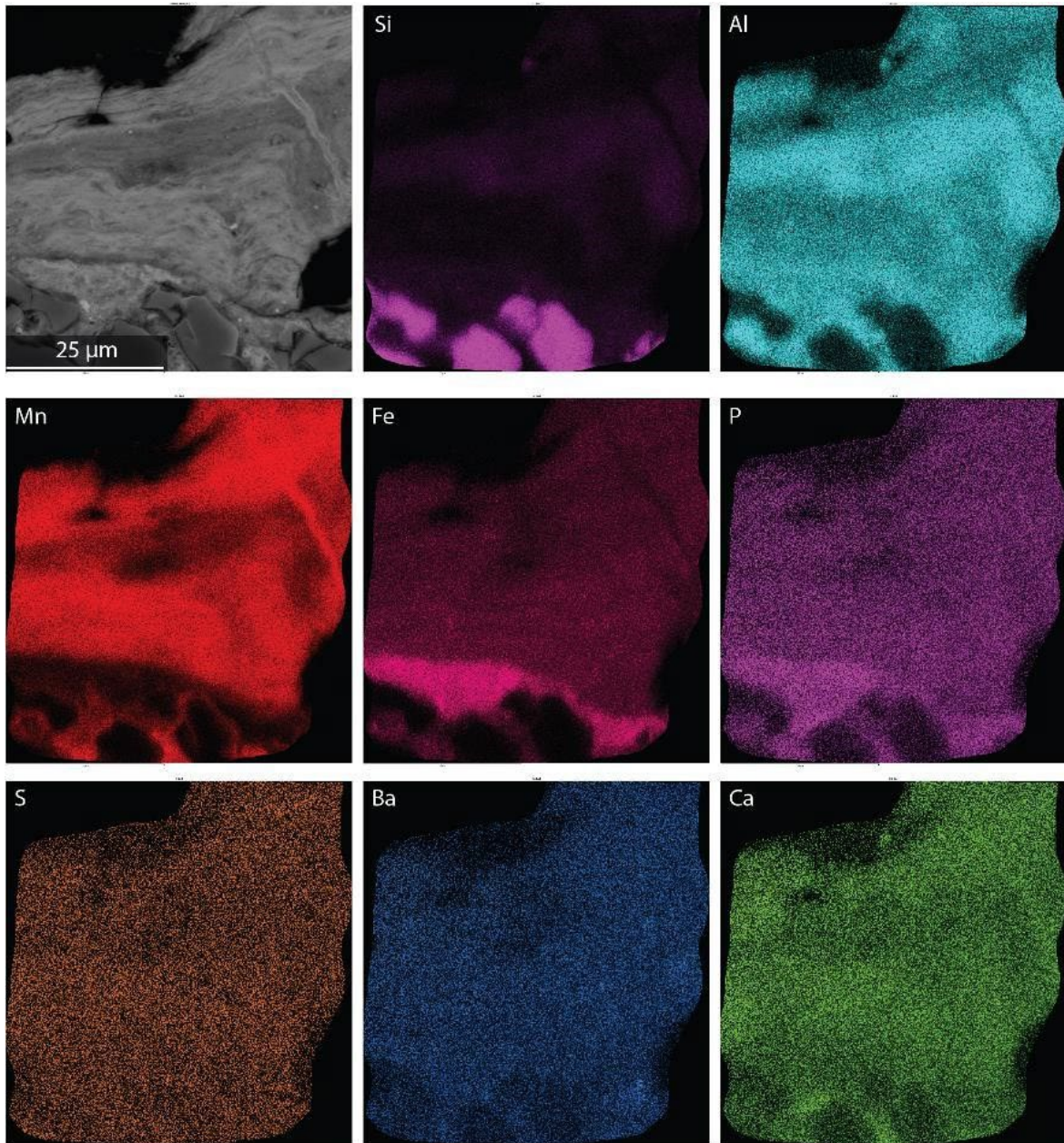


Figure 4-13: EDS compositional maps of an area of the patina shown at the top left of the image. Elements Mn, Al, Fe and P are heterogeneously distributed, and the patina comprises distinct Al, Fe, Mn, and P rich layers. The widespread distribution of S is consistent with the presence of biological material.

Gabbro

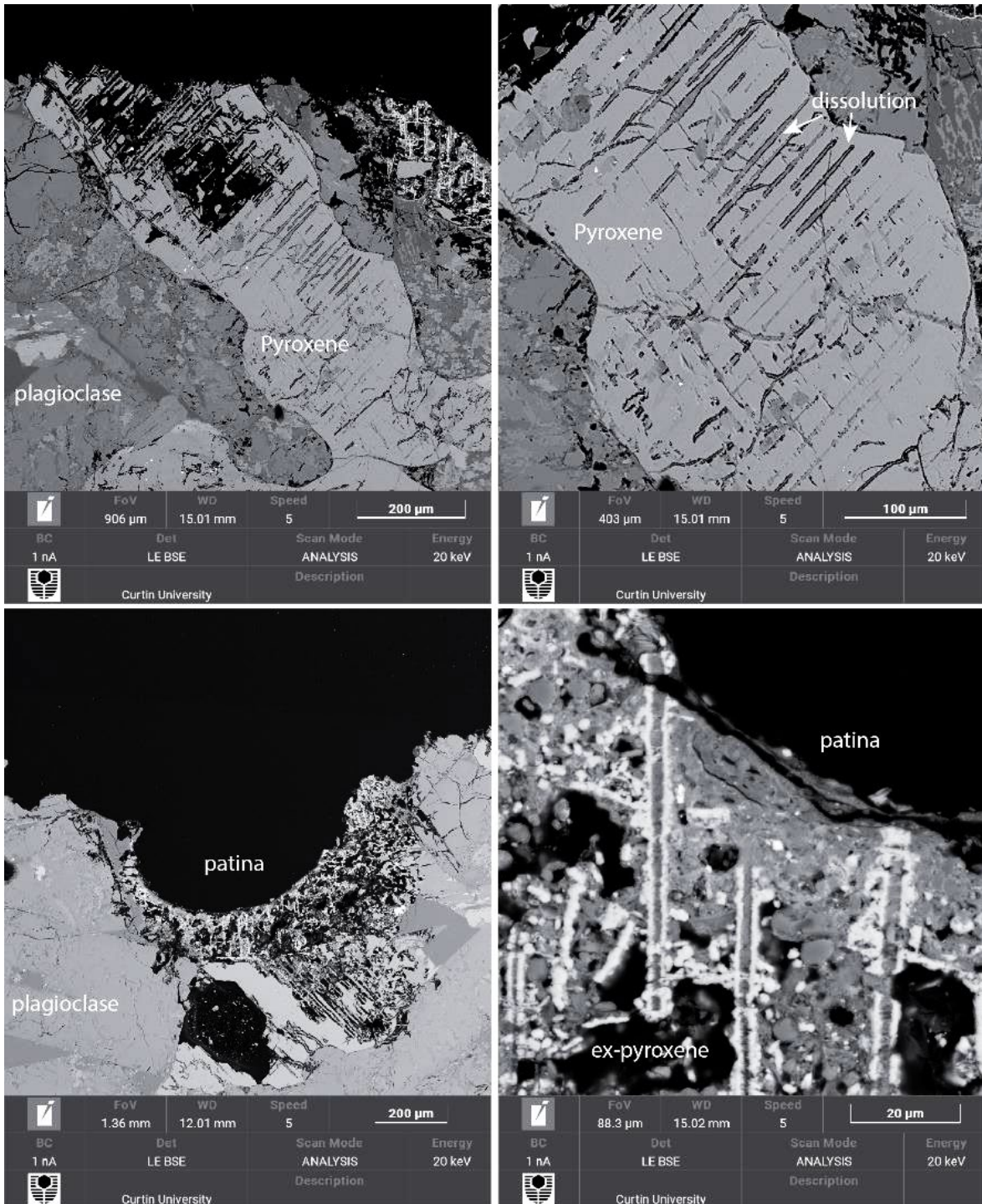


Figure 4-14: SEM-BSE images from sample AQ16_GBR. The top images display a single crystal of clinopyroxene with dissolution patterns localised along the cleavage direction of the mineral. Bottom images show a portion of patina (left) developed in the cavity formed by the dissolution of former clinopyroxene. Bottom right image shows a close-up of the patina arrangement between relict portions of clinopyroxene. This image emphasises the different topography of the granophyre and gabbro surfaces, and the different distribution of patina on those different surfaces.

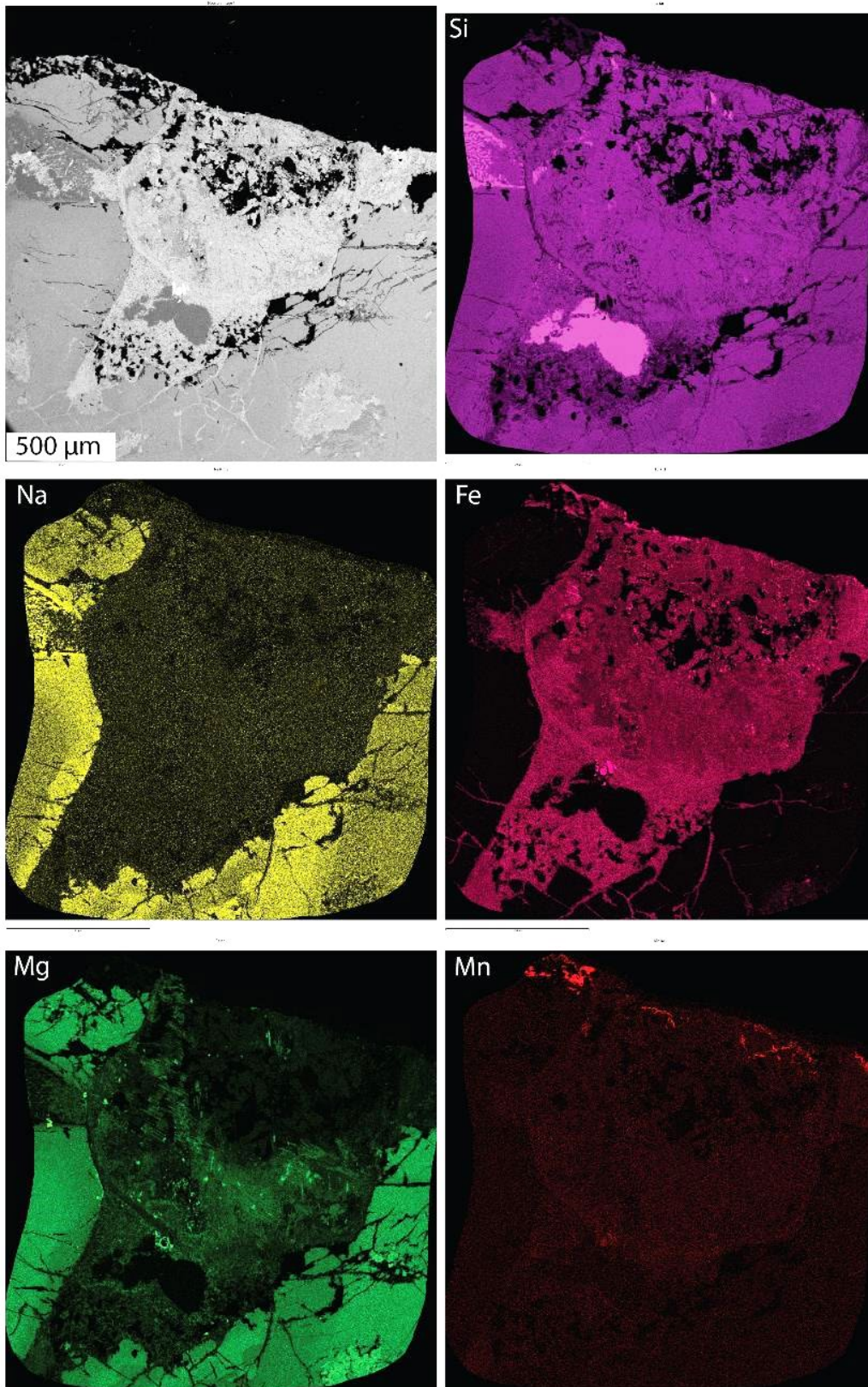


Figure 4-15: Large area EDS map of a portion of the patina from sample AQ09_GBR. Top left shows the BSE image of the investigated area. The map is acquired over a relict phase of clinopyroxene. Chemical heterogeneities are mostly observed for Mg, Na, Fe and Mn. Mn is mostly enriched at the top of the area that comprises the patina. A rim of enriched Na is visible for the surrounding plagioclase.

Patina

Scanning electron microscopy allowed further investigation of the microscale texture of the patina on granophyre and gabbro. High-resolution backscattered electron images show the patina is internally characterised by a very fine-layered internal structure. These features are consistent with descriptions of rock varnish (i.e., desert varnish, e.g., Neumann et al., 2022).

Patina appears to develop within those portions of the rocks characterised by a higher level of porosity. For example, in the case of granophyre, patina formation seems to be related to the preferential dissolution of alkali feldspar within the granophyric intergrowth. Similarly, in the gabbro, the patina is localised in regions characterised by the dissolution of former clinopyroxenes.

In the case of granophyre, K-feldspar is more susceptible to weathering-related alteration than quartz. Similarly in the gabbro, pyroxene is more affected by dissolution than plagioclase within the same rock. This is particularly visible in the EDS compositional maps presented previously. These observations, therefore, suggest the presence of a microstructural control of the minerals (and their composition) to the formation of preferential sites for patina development. Moreover, considering the nature of the lithologies, it is therefore reasonable to be expecting a wide variation of rock patina thicknesses among the different rock types (Figure 4-10 to Figure 4-13).

The results obtained from TIMA and SEM reveal the presence of compositional variations within the analysed rocks. In particular, at the thin section scale, TIMA plots for Fe, Mg and Ca distributions (Figure 4-6 and Figure 4-8) display a general trend of Fe enrichment from the fresh rock towards the patina for most of the lithologies. This is particularly visible for gabbro where this variation can also be observed at the scale of the same grain (e.g., sample RS02_GBR). At the microscale level, SEM-EDS mapping reveals compositional variations between layers of the rock patina. Different lithologies are clearly associated with different element distributions, but there is no evidence, so far, of compositional difference among the patina found in different rock types. However, examination of rocks not yet fully characterised may alter this preliminary conclusion.

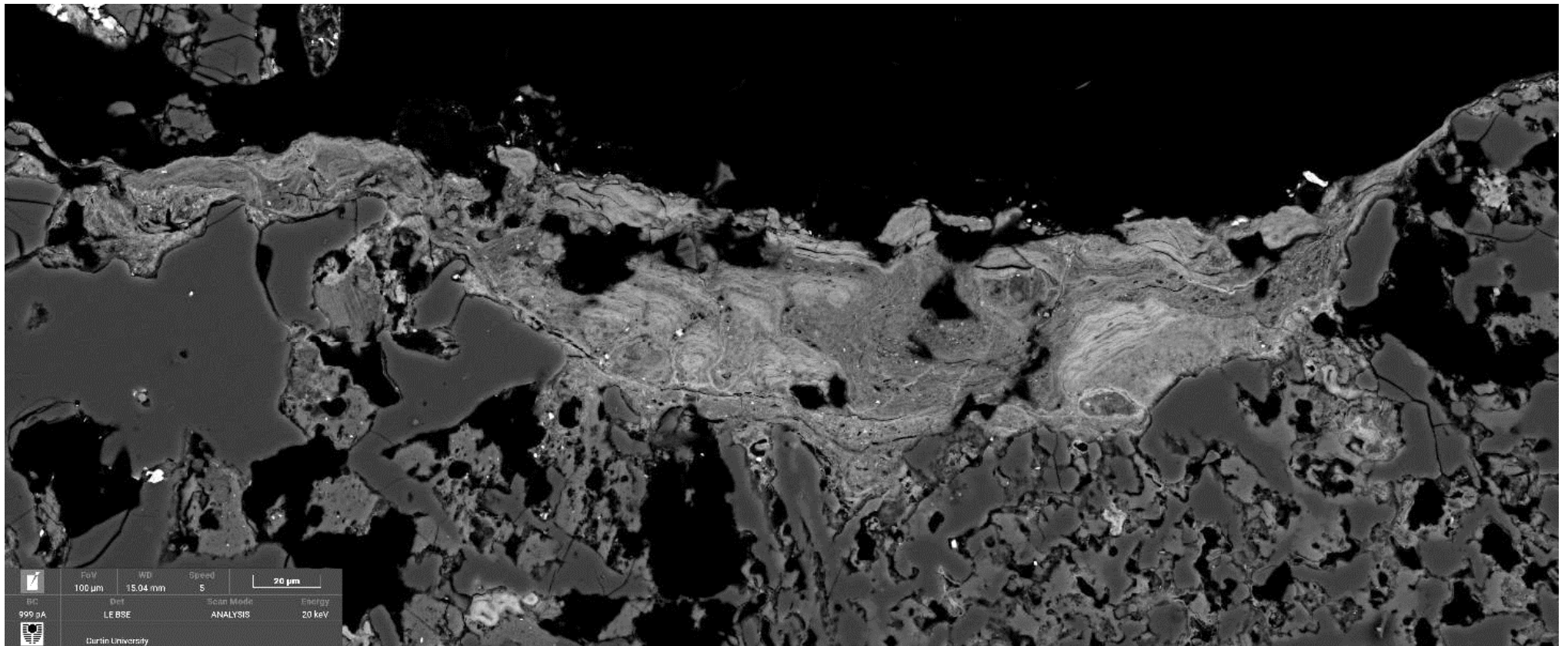


Figure 4-16: Large area SEM-BSE image of patina in sample EX02_GPH. Images at BSE reveal a compositional contrast (brighter and lighter areas) and a thin-layered structure within the patina. Brighter particles in the patina are Fe-Ti oxides.

4.2.7 Geochemical characterisation

X-ray diffraction (XRD)

Diffraction patterns obtained from XRD analysis are derived from the interaction between the incident X-rays and minerals and they are dependent on mineral composition and the location of atoms within unit cells. The identification of mineral phases within the powdered material is performed by matching the obtained spectrum with a database of reference minerals. In this case, the obtained spectra are post-processed by using DIFFRAC.EVA software and matched with PDF4+ database available at the laboratory facility.

The procedure undertaken for the preparation of XRD samples is described in the Inorganic Geochemistry Laboratory Analysis methodology (COPP21065-PRO-G-114). Here, the results obtained from the preliminary XRD analysis of four samples are shown. For each sample, the data are graphically presented as a whole diffraction pattern with overlapping matched mineral phases.

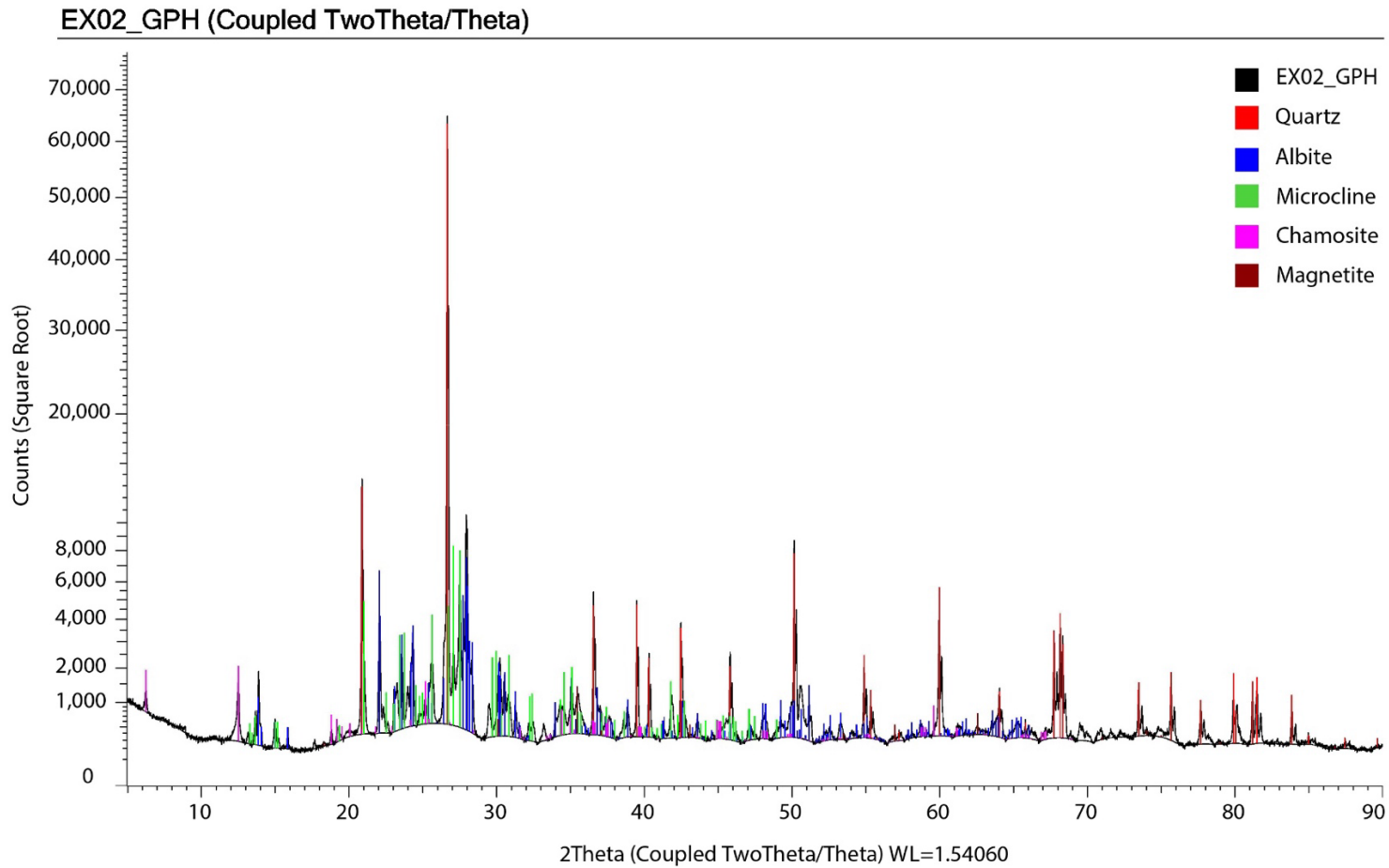


Figure 4-17: XRD analysis plot for granophyre sample rock EX02_GPH. The mineral database for the XRD software holds patterns for mineral end-members rather than for the solid solutions found in the rocks. Thus, for example, albite represents sodic plagioclase, microcline represents K-feldspar, and chamosite represents chlorite.

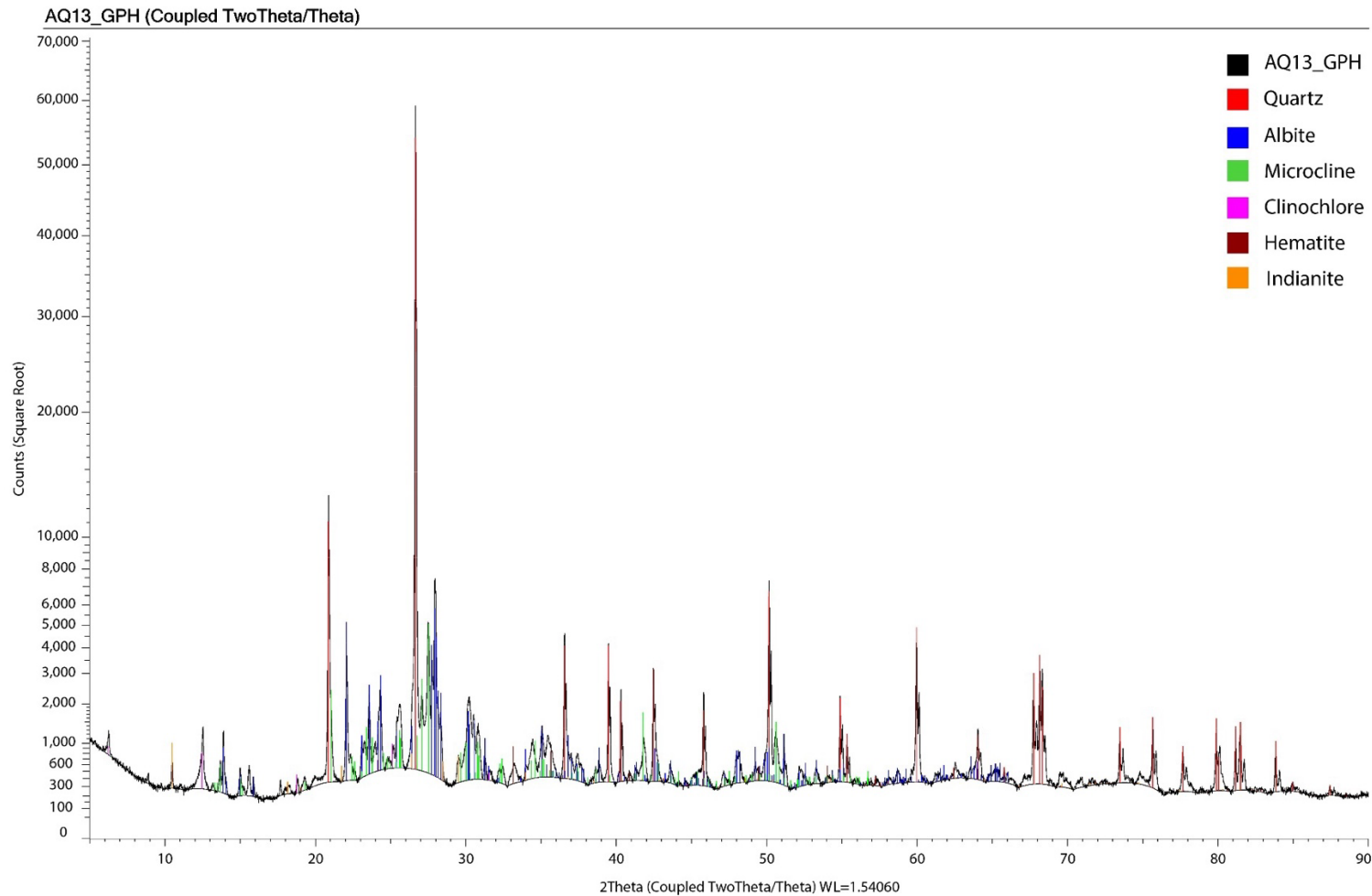


Figure 4-18: XRD analysis plot for granophyre sample rock AQ13_GPH. The mineral database for the XRD software holds patterns for mineral end-members rather than for the solid solutions found in the rocks. Thus, for example, albite represents sodic plagioclase, microcline represents K-feldspar, and chamosite represents chlorite. Indianite is a polymorph of anorthite, and represents calcic plagioclase.

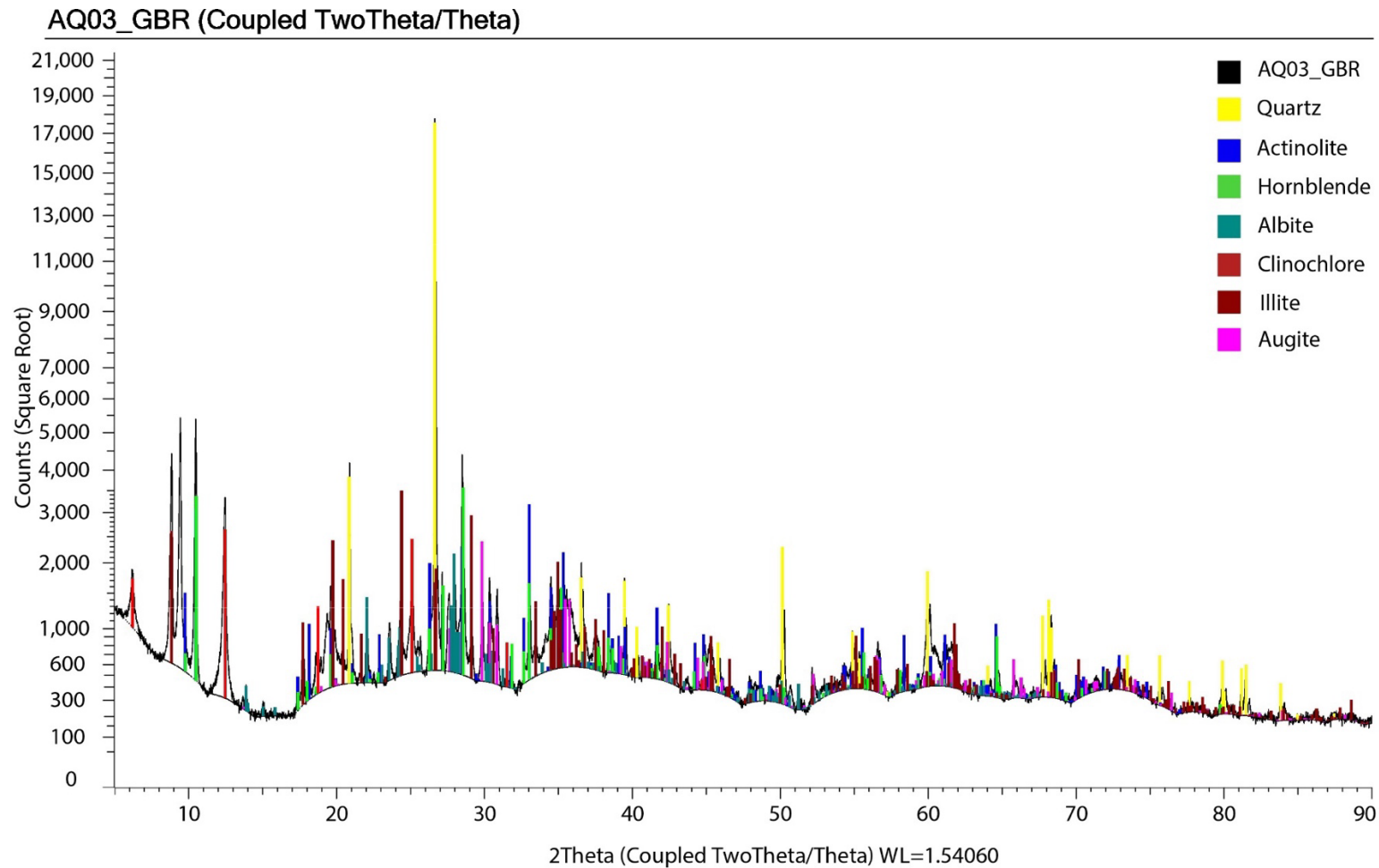


Figure 4-19: XRD analysis plot for gabbro sample rock AQ03_GBR. . The mineral database for the XRD software holds patterns for mineral end-members rather than for the solid solutions found in the rocks. Thus, for example, albite represents sodic plagioclase, actinolite represents Al-poor amphibole, and clinchllore represents chlorite

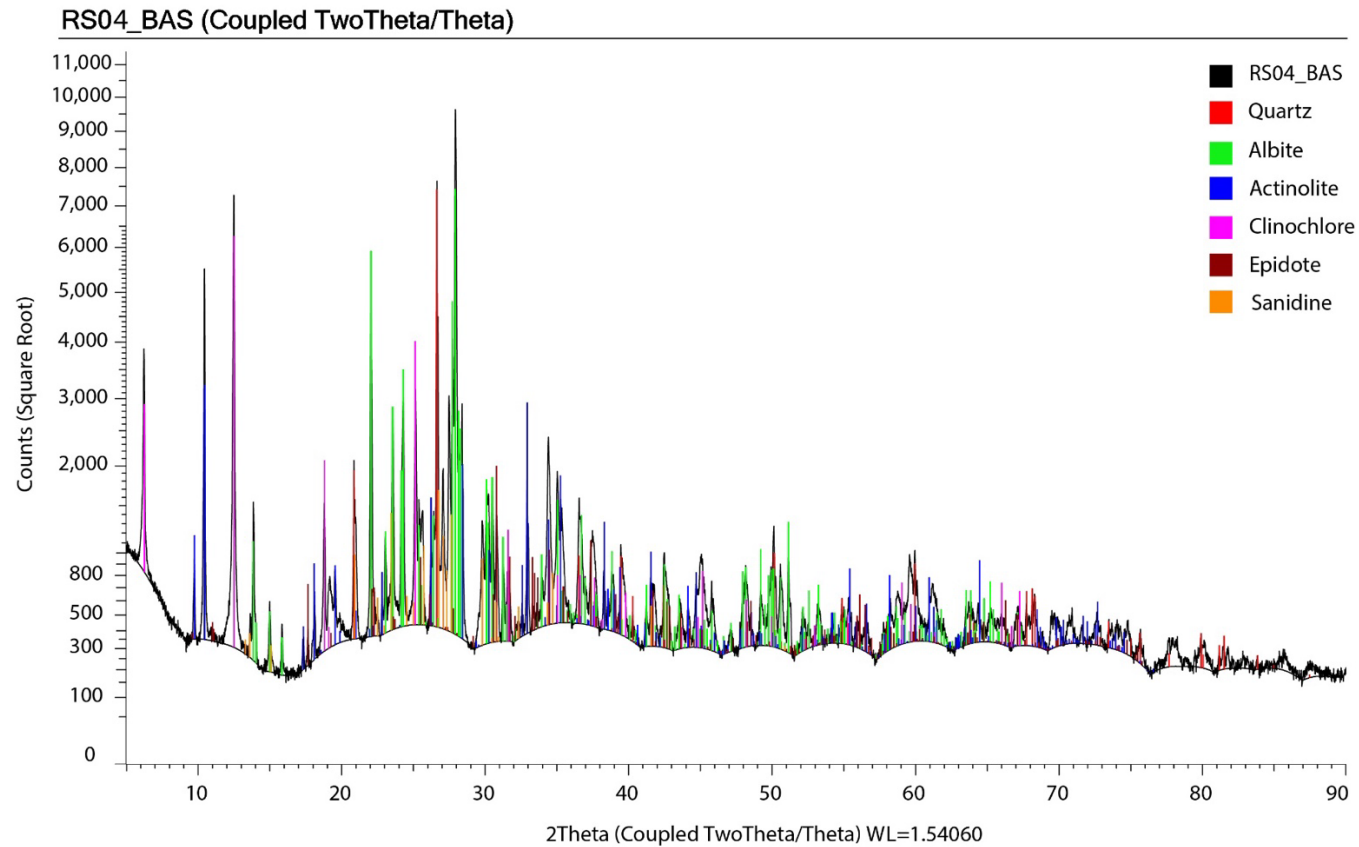


Figure 4-20: XRD analysis plot for basalt sample rock RS04_BAS. The mineral database for the XRD software holds patterns for mineral end-members rather than for the solid solutions found in the rocks. Thus, for example, albite represents sodic plagioclase, actinolite represents Al-poor amphibole, clinchlore represents chlorite, and sanidine represents an unknown K-feldspar, potentially a low-temperature alteration phase.

Table 4-4: Compilation of identified minerals among the analysed XRD samples.

Mineral Name	Formula	Sample name			
		AQ03_GBR (gabbro)	AQ13_GPH (granophyre)	EX02_GPH (granophyre)	RS04_BAS (basalt)
Quartz	(SiO ₂)	Present	Present	Present	Present
Albite	NaAlSi ₃ O ₈	Present	Present	Present	Present
Microcline	KAlSi ₃ O ₈		Present	Present	
Sanidine	KAlSi ₃ O ₈				Present
Anorthite	Ca(Al ₂ Si ₂ O ₈)		Present		
Epidote	Ca ₂ Al ₂ O(AlFe)OH(Si ₂ O ₇)(SiO ₄)				Present
Chamosite	(Fe,Mg) ₅ Al(Si ₃ Al)O ₁₀ (OH,O) ₈			Present	
Clinocllore	(Mg,Fe) ₅ Al(Si ₃ Al)O ₁₀ (OH) ₈	Present	Present		Present
Actinolite	Ca ₂ (Mg _{4.5-2.5} Fe _{0.5-2.5})Si ₈ O ₂₂ (OH) ₂	Present			Present
Hornblende	Ca ₂ (Mg, Fe, Al) ₅ (Al, Si) ₈ O ₂₂ (OH, F) ₂	Present			
Augite	(Ca,Mg,Fe) ₂ Si ₂ O ₆	Present			
Illite	K _{1.5-1} Al ₄ (Si _{6.5-7} Al _{1.5-1}) ₂₀ (OH) ₄	Present			
Magnetite	Fe ₃ O ₄			Present	
Hematite	Fe ₂ O ₃		Present		

Note: The mineral database for the XRD software holds patterns for mineral end-members rather than for the solid solutions found in the rocks. Thus, for example, albite represents sodic plagioclase, actinolite represents Al-poor amphibole, clinchlore represents chlorite, and sanidine represents an unknown K-feldspar, potentially a low-temperature alteration phase.

Minerals identified within the studied samples are mainly silicates. The most common phases detected are quartz, albite, which represents sodic plagioclase, microcline, which represents K-feldspar and chamosite/clinchlore, which represent chlorite. Clay minerals (illite) and Fe-oxides (hematite and magnetite) are also found. The mineral formulae are for the mineral end-members and do not take into account solid solution or ion charge state.

Albite, together with **anorthite**, is part of the plagioclase solid-solution where albite is the Na-end-member of the solid solution and anorthite is the Ca-end-member. The feldspars are fundamental constituents of crustal rocks such as those investigated here. **Microcline** is the low-temperature polymorph of the alkali feldspars (K-feldspars), whereas **sanidine** represents a high-temperature K-feldspar polymorph. While microcline is generally found within intrusive rocks (i.e., slow cooling rates), sanidine is more characteristic of rapidly cooled volcanic rocks, although it would not normally be expected in a basalt, and here may represent a low-temperature alteration phase. Similarly, the quartz noted in sample RS04 is surprising for this SiO₂-poor lithology and may have formed during alteration on the seafloor or during weathering.

Clinochlore and **chamosite** both belong to the chlorite mineral group representing the Mg and Fe end-members respectively. Chlorite minerals are hydrous silicates and they are found in igneous rocks as an alteration product of other mafic minerals (e.g., pyroxenes). They are often found in association with micas and amphiboles.

Actinolite and **hornblende** both belong to the amphibole mineral group. Because of the wide range of possible chemical substitutions within their chemical formula, amphiboles can crystallise with a wide range of bulk chemistries. Here, actinolite describes Al-poor Ca-Mg-Fe amphiboles whereas hornblende is a general term to indicate Al-rich calcic amphiboles.

Augite is an Al-rich clinopyroxene. Pyroxenes are the most abundant group of Fe-Mg silicates and fundamental constituents of gabbros.

Epidote is a group of hydrous silicates formed by hydrous alteration of plagioclase or mafic minerals such as pyroxene. It is particularly common in altered basalts or gabbros.

Illite is a potassium-bearing clay-mineral and it is quite similar to the muscovite. Illite forms by alteration (sericitization) of pre-existing minerals such as micas or feldspars.

Magnetite (Fe_3O_4) and **hematite** (Fe_2O_3) are both Fe-oxides. Magnetite is an Fe end-member within the spinel group. It is very common as an accessory mineral in igneous rocks. Hematite is common in igneous rocks of granitic composition or as an alteration of Fe-bearing minerals (e.g., pyroxenes and olivine).

4.2.8 Comparison with previous work

The work by Donaldson (2011) presents a conceptual model for the Murujuga rocks of a three-layer structure patina, weathered rind and fresh rock (Figure 4-21).



Figure 4-21: Cross section of the granophyre sample EX02_GPH showing the three-layer structure of the rock from Donaldson (2011). Scale bar is 20 -mm.

In the Conceptual Model, the **patina** represents the outermost part of the rock in contact with the air. SEM images indicate that the patina is of variable thickness but generally less than $100\ \mu\text{m}$ (Figure C-3 to Figure C-9), discontinuous, and internally characterized by a heterogeneous layered structure. Within these layers, there is a heterogeneous distribution of brighter particles of various grainsizes. These are mostly interpreted as Fe- and Ti-oxides (i.e., magnetite, hematite, ilmenite). In addition, EDS compositional mapping of the patina has revealed compositional variations within the internal layers. These heterogeneities are mostly visible for Fe, Mn and Al (Figure C-5). Other commonly enriched elements within the patina are P, S, Ti, Ca and Ba (Figure C-5). Based on the EDS maps, these enrichments are interpreted to represent heterogeneously distributed Fe- and Mn-oxides and hydroxides, apatite and clay minerals.

The **weathered rind** comprises the lighter region of transition between the patina of the rock and the fresh rock underneath (e.g., Figure 4-21). Among the investigated samples, this layer varies in thickness from $<1\ \text{mm}$ up to ca. 5 mm and it appears more developed within the granophyre. In thin sections, the weathered rind is characterised by high porosity and increase in the modal abundances of sheet silicates (e.g., kaolinite and illite). However, the source of the orangish/light-brown colour is less clear. The **fresh rock** represents the inner portion of the rock structurally underlying the weathered rind.

Field and microscopy observations from this study are not consistent with Donaldson's model (2011) in many cases. The patina is commonly discontinuous and shows contorted layering that extends over a few hundred microns to a few millimetres. Moreover, the transition from the paler "weathered rind" to the "fresh rock" appears gradational rather than distinct. The visual transition between pale orange rind and darker interior is difficult to relate to an obvious or systematic variation in the mineral phases. The reason for this, in detail, has not been established yet, but it may relate to the iron oxidation within existing minerals.

In geology, the term fresh rock refers to a rock (or a portion of it) that has not been affected by alteration processes since the time of its crystallisation. However, rocks outcropping at Murujuga all show some degree of alteration by weathering or hydrothermal activity.

Weathering alteration relates to physical disintegration and chemical decomposition that occur within a rock exposed to the surface induced by climate or biological processes. This type of alteration is visible in the observed samples by the development of porosity within the first millimetres of the rock (i.e., weathered rind) and the cleavage-related alteration of the clinopyroxene in the gabbros.

In contrast, hydrothermal alteration involves interaction between rocks and fluids at temperatures of 150–350°C and the formation of hydrous minerals such as chlorite and biotite from anhydrous minerals formed as the original magma cooled to form rock. For example, within the gabbro, optical microscopy has revealed widespread chlorite which replaces pyroxene within the gabbro (Figure 4-22). Hydrothermal alteration is also recorded by plagioclase within granite sample RS02 which is sericitized, a common alteration process of feldspar minerals (Figure 4-23).

Hence, based on the current observations, it is clear that the term **fresh rock** is not appropriate to describe the inner portion of the rocks at Murujuga. We suggest the term "**fresher rock**" as a more appropriate terminology. Some of the rock–patina systems fit well, on the macro-scale, with Donaldson's model. However, others do not, and the relatively large number of samples that we have been fortunate enough to collect and study means that we are able to see a greater range of the natural variation than that available to Donaldson. It is unlikely that the differences relate to sampling methodologies or sample preparation because some of the samples do show a structure similar to that observed by Donaldson. The differences are revealed by techniques that Donaldson did not use.

In addition, the use of scanning electron microscopy, element analysis by energy dispersive spectroscopy, and other micrometre-scale techniques, has revealed features that Donaldson would not have been able to see, and it is the information from these techniques that form the basis for a revised conceptual model, which is still under construction. Therefore, we consider our revision of the model to be additive rather than replacive, with respect to Donaldson's work.

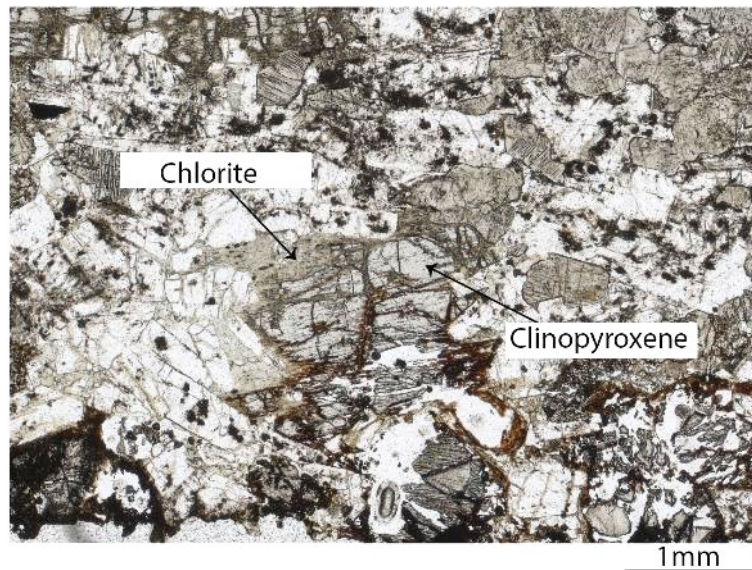


Figure 4-22: Photomicrograph in plane-polarized light of gabbro sample AQ16_GBR. In the centre of the image a crystal of clinopyroxene (augite) is replaced by chlorite (pale green). Biotite (dark brown) is also present.



Figure 4-23: Photomicrograph in plane-polarized light of granite sample RS02_GRT showing sericitized plagioclase (light brown). A coronitic texture of chlorite (and biotite?) surrounding plagioclase of the rock is also visible.

4.2.9 Preliminary findings from inorganic geochemistry analysis to date

The following preliminary findings are noted:

1. The patina is a discontinuous layer that shows a generally sharp contact against the rock below it.
2. The weathered rind is not very different in mineralogy from the underlying portions of the rock except for visual (colour difference) and textural (porosity) variations, and the presence of kaolinite and illite.
3. There is no sharp transition between the weathered rind and the interior of the rock (fresher rock).
4. The fresher rock is characterised by the presence of both hydrothermal and weathering alteration. Hydrothermal alteration is characterised by the formation of chlorite and sericite at the expense of pre-existing clinopyroxene and feldspars of the rocks. Weathering alteration in this zone is characterised by some porosity formation below the colour-defined weathered rind.

5. The patina shows micron-scale variations in the concentration of Fe, Mn, Al, and P, and weathering has induced some changes in the Fe-content of the weathered rind. This compositional profile is mostly evident in gabbro where Fe is mostly enriched in the first few millimetres of the rock.
6. The patina consists of a complex layered structure consistent with textures reported for rock varnish from arid environments elsewhere. This finding is consistent with those of Neumann et al, (2022).
7. Chemically the patina shows compositional variation, mostly obviously for Fe and Mn.
8. Minerals within the fresher rock provide microstructural control on the topology and distribution of patina. For example, in the gabbro, the patina is rooted onto altered clinopyroxene crystals (Figure 4-14), whereas on the granophyre, the patina is located above quartz that shows vermicular porosity formation related to dissolution of granophyric K-feldspar. For both rock types, the processes of porosity formation are likely to be different and have implications for the stability of the patina. For example, higher porosity might lead to patina instability and consequent flaking.

These preliminary findings raise some unanswered questions that will be investigated as the research progresses into the second year of studies:

1. What are the organic/amorphous components in the patina and what controls its chemical stability? This work will be undertaken in collaboration with the organic and microbiome component study teams.
2. What factors control the development and stability of the patina (e.g., pH, moisture, Eh)?
3. What is the distribution and role of trace elements undetected by EDS analyses?
4. What are the physical and mineralogical changes that generate the visual colour transition in the weathered rind?
5. It is clear that the distribution of minerals within the patina is complex and includes a range of different Fe, Al, and Mn bearing oxides and hydroxides. Which of these minerals buffer the pH and Eh? And how relevant are considerations of thermodynamic equilibrium to these dynamic systems?

4.3 Microbiome laboratory analysis

4.3.1 Objectives

From Section 1.6 of the MSDCA Plan, the objectives of the microbiome investigations are to:

1. Use advanced molecular biological approaches to characterise:
 - a) Microbial community composition associated with rock patina and the underlying weathered rind. This answers the question “who is there?”
 - b) Diversity and relative abundance of functional genes involved in microbial processes and pathways that may contribute to stabilising or bio-deteriorating (bio-weathering) the rock patina are present: This answers the question “what are they potentially doing?”
 - c) Characterise which of these functional genes are expressed to functional gene transcripts that can potentially be translated into functional proteins/enzymes that carry out these processes.
2. Use advanced bioinformatics tools to:
 - d) Build metagenome assembled genomes (**MAGs**) from the shotgun metagenome dataset of objective 1b and map the functional gene transcripts from objective 1c to the MAGs. This will reveal all sequenced genes belonging to the same species that were expressed at the time of sampling.
 - e) Determine the number of mutations that occurred post-mortem in the assembled metagenomic bins (from objective 2a) to distinguish between microbial taxa that have been preserved in the patina as ancient DNA vs. those that represent modern taxa represent. Since this DNA damage increases with time it may be possible to determine the order in which these taxa died.
 - f) to estimate the growth rate of the patina associated microbial communities by measuring genome replication rates from shotgun metagenomic bins without the need for cultivation.

4.3.2 Methodology

Microbiome laboratory methodologies are described in Section 3.3.3 of the MSDCA Plan and the component study methodology statement:

- COPP21065-PRO-G-112 Microbiome Laboratory Analysis

Variations from planned methodology

18S rRNA amplicon sequencing has been excluded from the methodology. The rationale for excluding this is due to the redundancy/overlap of data generated from both ITS and 18S sequencing. These regions are both designed to identify eukaryotic organisms and the ITS amplicon sequencing gives superior taxonomic clarity to fungal microbes and thus is the better candidate.

4.3.3 Work to date

All DNA and RNA extractions from the collected field samples have been completed. DNA and RNA concentrations extracted varied between samples, all of which have been successfully amplified for the bacterial and archaeal 16S rRNA and fungal ITS genes. Sequencing data of the 16S rRNA gene and the ITS gene is currently being generated by the Australian Genomics Research Foundation (**AGRF**) and the data should be available to us for analysis between April and May 2023. After analysis, selection of appropriate samples will be undertaken for metagenomic and metatranscriptomic studies.

While waiting for the amplicon sequencing to be completed by AGRF, cDNA will be generated from the RNA samples for sequencing of the 16S rRNA genes and ITS gene to determine the living microbial communities on the rock at the time of sampling. ITS and 16S sequencing are both approximately 50% complete at time of preparing this report.

Substantial growth of fungi and bacteria was observed on the TSA and SAB plates. Researchers are currently waiting for a biosafety cabinet to be installed into the WA-OIGC laboratory so the microbial plates can be handled safely before commencing DNA extractions.

4.4 Chamber exposure (accelerated degradation) testing

4.4.1 Objectives

From Section 2.2.6 and 3.4 of the MSDCA Plan, the objective of the chamber exposure testing is to ensure that a dose-response relationship for (elevated) air pollutant concentrations can be established. It remains possible that the current level of anthropogenic emissions at Murujuga may not have a measurable impact on the rock art – or an effect below the level of measurement accuracy and precision inherent in field work. If that is the case, no field study of any size will result in a statistically significant outcome. For this reason, chamber studies are vital to give the project certainty in its ability to establish EQC levels. The chamber studies will consider as broad a range of parameters as possible, however will be focused on (a) physicochemical weathering of the rock and measurement of any by-products or results of such weathering and (b) exposure concentrations which may reduce the “health” or growth rates of the most abundant components of the microbiome. Noting that the studies in (b) will include analysis of abiotic products as in (a), in order to account for biotic/abiotic interactions.

4.4.2 Methodology

Information on the planned chamber exposure methodologies can be found in Section 3.4 of the MSDCA Plan. Laboratory work in this area during the first year of scientific studies has focussed on detailing the chamber exposure methodology in the MSDCA Plan to develop the component study methodology statement:

- COPP21065-PRO-G-117 Chamber Exposure Studies.

Experiments with direct exposure to cooled emissions will also expose the rock samples to high humidity/mist deposition produced as a result of cooling combustion emissions which contain significant water vapour. For dry deposition/exposure scenarios, the exhaust stream can be passed through a diffusion dryer or desiccant chamber. Conversely, water mists to simulate mist deposition can be introduced directly to the chamber inlet, with or without air pollutant exposures. Likewise, UV lamps can be utilised during exposures to permit the generation of secondary photocatalysed chemicals, or post exposure in an additional weathering chamber.

4.4.3 Work to date

Preliminary chamber exposures have been conducted using diesel and diesel/condensate exhaust to finalise exposure protocols and determine maximum exposure rates obtainable from the experimental apparatus. This work has allowed a full series of exposures to be planned in consultation with the statistical team and component study subject matter experts, with reference to previous relevant works (e.g. Neumann et al., 2022). In addition to pre-post exposure/weathering measurements similar to Neumann et al. (2022), microbiome characterisation pre and post exposure via confocal microscopy is planned.

The exposure method undertaken to-date has utilised pieces of patinated rock with dimensions 12.5 mm W x 12.5 mm L x 25 mm H, located in 37 mm cell culture dishes as shown in Figure 4-24.

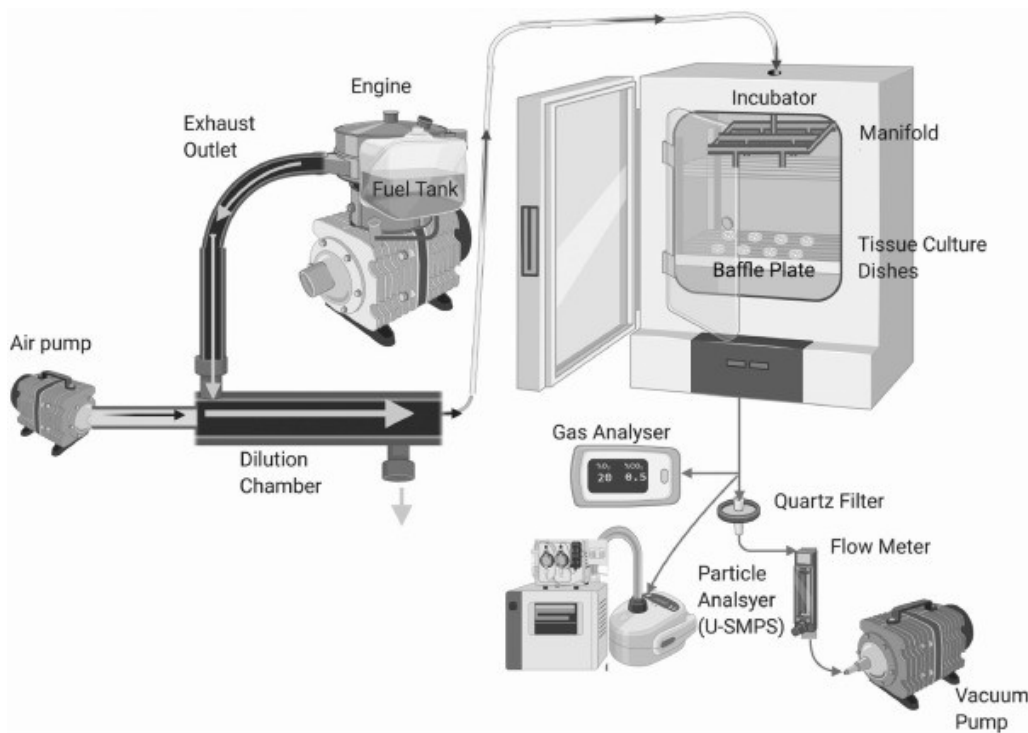


Figure 4-24: Preliminary chamber exposure test sample arrangement.

In order to reduce the number of experiments required, multi (air pollutant)-species exposures will be conducted (e.g., from combustion exhaust or biomass burning), with the possibility of single species exposures at a later date.

Current exposures have been for 1 hr only, with pre and post pH measurement only. More sophisticated analysis such as confocal microscopy will be utilised for further tests to image microbiome composition and health pre and post testing. Inductively Coupled Plasma – Optical Emission Spectroscopy (ICP-OES) and related techniques will be used to measure dissolution by-products from the rock and patina surface post exposure. Other techniques such as Raman and other spectroscopy/microscopy methods will be applied to measure rock surface chemistry and topography post exposure. Optimum incubation periods post measurement are yet to be determined however for the inorganic processes, multiple 1hr exposures, followed by 23 hr incubation periods appears most appropriate.

Table 4-5 shows indicative maximum exposure levels which could be obtained from the apparatus during preliminary tests using Ultra Low Sulphur Diesel (**ULSD**) conforming to the Australian Fuel Quality Standard (2019) and a 50/50 mix of ULSD and Karratha Gas Plant (**KGP**) condensate held by Curtin from previous work.

Table 4-5: Indicative Peak Exposure levels attainable combusting diesel or diesel-KGP condensate

Species	Level	Unit
CO ₂	3-5	%
CO	300-400	ppm
NO _x	100-200	ppm
NO	180-140	ppm
NO ₂	40-60	ppm
SO ₂	15-30	ppm

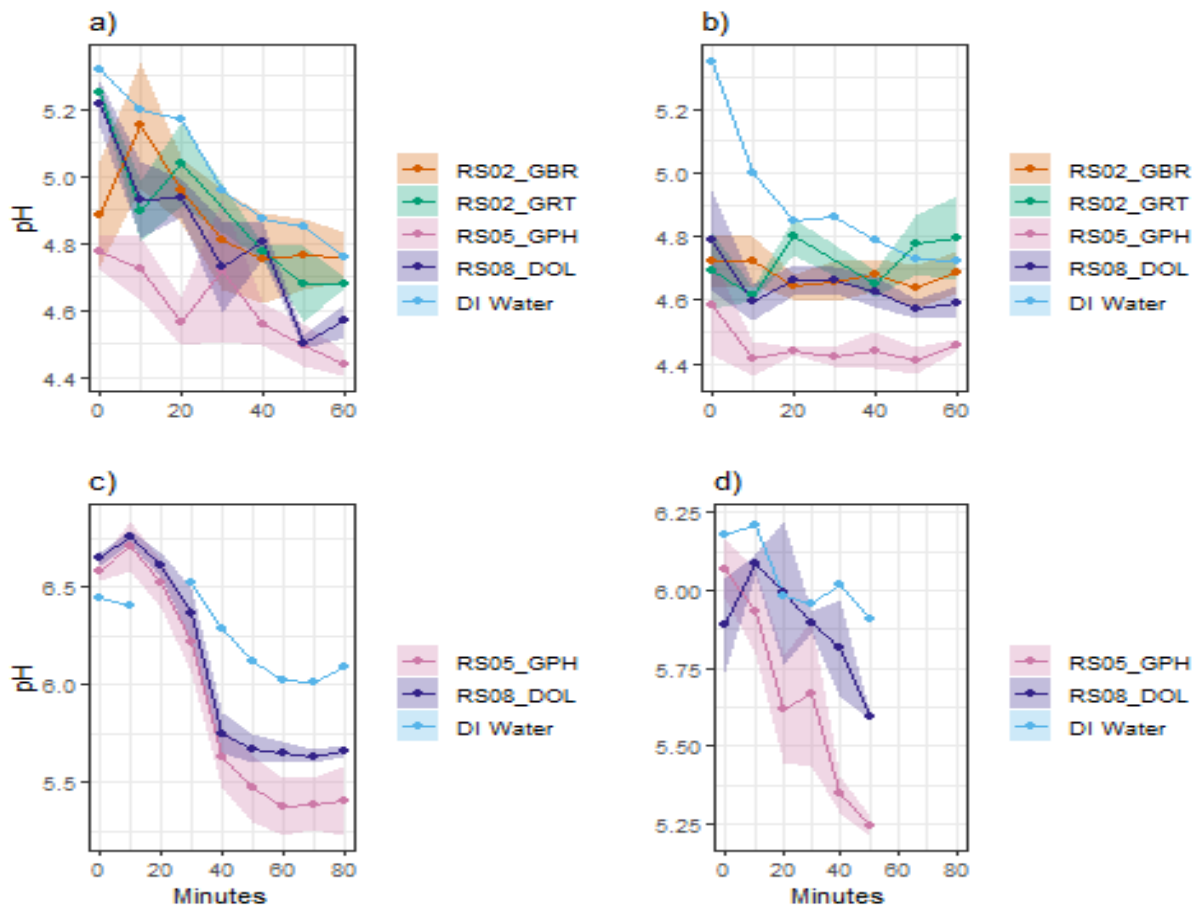


Figure 4-25: Mean pH measured over time (minutes) for four rock types and for distilled/deionised (DI) water alone. With (a) pre and (b) post exposure to exhaust from combustion of a 50/50 diesel/condensate mixture; (c) pre and (d) post exposure to diesel exhaust. Dots and solid lines are the mean pH values and the shaded area is mean \pm standard deviation. The experiment in (d) was terminated earlier than others as it was one of the first conducted and appropriate time points/durations had not yet been determined. The protocol for the chamber studies, has since been revised and finalised for the year two studies.

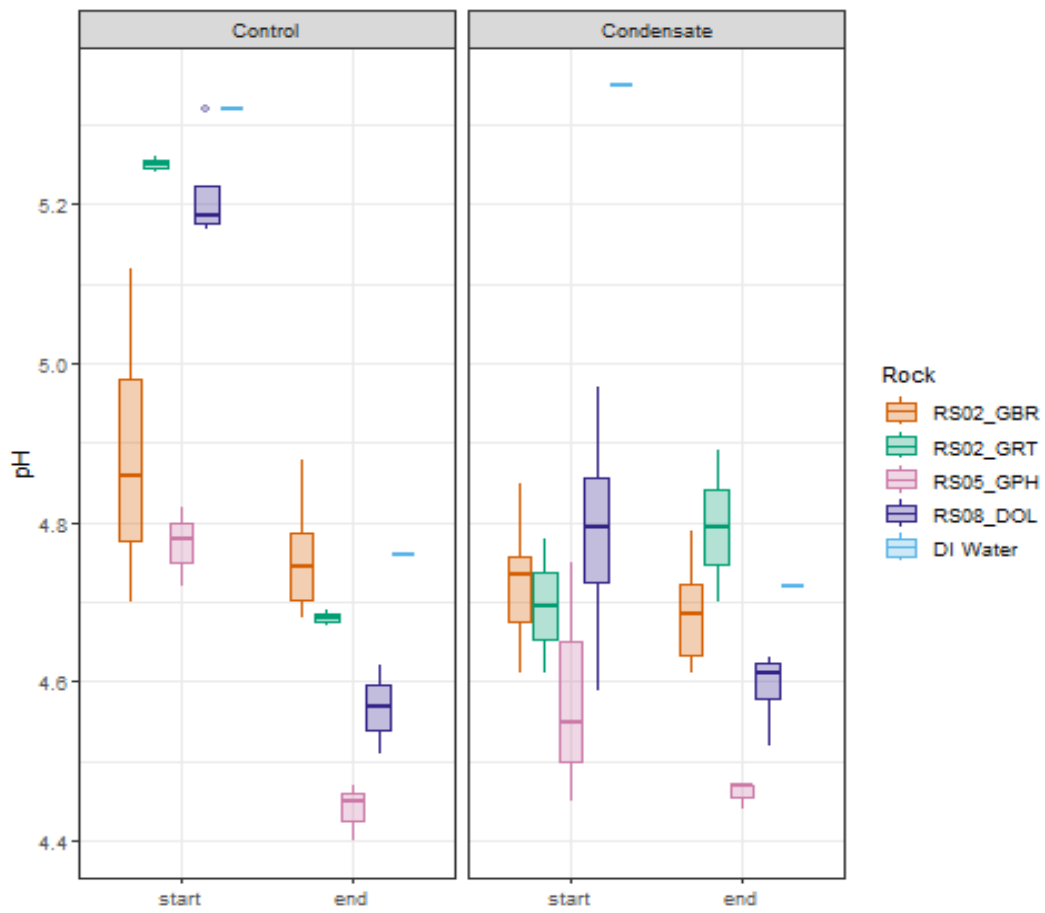


Figure 4-26: Boxplot of pH for initial pH (start) and final pH (end) measurements for control and condensate rock samples, one boxplot for each rock type and distilled/deionised (DI) water; post 1hr exposure to condensate exhaust.

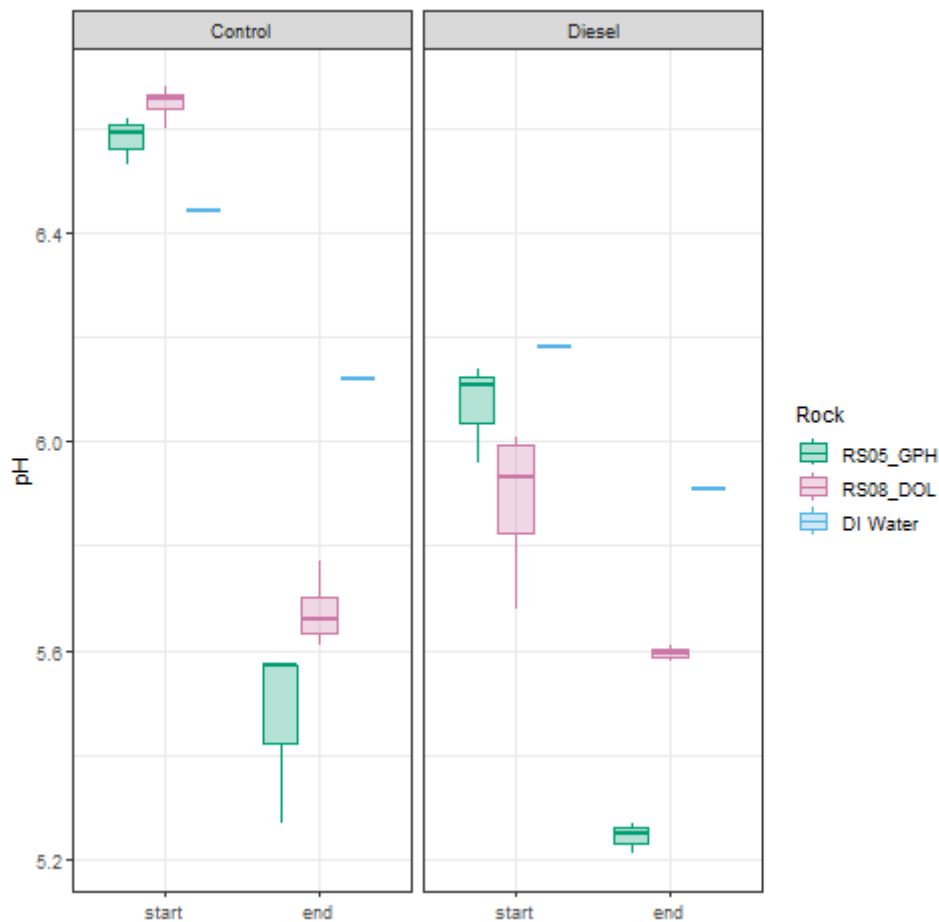


Figure 4-27: Boxplot of pH for initial pH (start) and final pH (end) measurements for control and diesel rock samples, one boxplot for each rock type and distilled/deionised (DI) water; post 1hr exposure to diesel exhaust.

Figure 4-25 to Figure 4-27 show the results of preliminary pH measurements following a 1 hr exposure. Pre and post pH tests were conducted using the immersed method developed by Aho and Weaver (2006).

It can be seen that the exposed rocks are initially much more acidic than the control rocks, however at the end the solution pH is equivalent. The pH trends over time are similar to those in Aho and Weaver (2006). A similar process may occur in the field, however this cannot yet be determined. Both the tests by ourselves and by Aho and Weaver (2006) used a similar volume of water to the volume of rock, permitting significant dilution and or aqueous reactions to occur. It is possible that these chamber pH tests can inform the optimisation of field pH measurements with respect to measurement duration and distilled/deionised water volume. Future experiments will extend to understanding the reaction chemistry occurring, examining microbial health pre and post experiment and incorporating photocatalytic effects and other likely reactants such as NaCl. The research team is confident that this method will permit the development of dose response curves for all relevant species identified through field studies.

5 Air quality monitoring network establishment and operation

5.1.1 Objectives

As described in Section 1.8 of the MSDCA Plan, the objectives of the air quality monitoring network are to deploy and maintain appropriate air quality monitoring equipment at appropriate spatial locations such that the air quality across all of the Murujuga region can be determined.

5.1.2 Methodology

The AQM network includes both passive monitors (with low voltage solar power), and mains powered AQMs to provide accurate real-time monitoring data where existing power infrastructure can be accessed.

The AQMs were designed and sited according to AS3580 where applicable. In order to meet all relevant National Code of Construction standards, the enclosures housing the equipment and relevant components were designed and certified to AS4100; AS1170; AS3600; AS1554; and AS1252. The AQMs have been designed to visually blend into the environment as far as possible, and thus were manufactured from weathering steel for installation sites near rock outcrops or finished with a sand-coloured paint at sites in or near coastal dunes. Figure 5-2 shows a weathering steel AQM. AQM deployment has been undertaken using the lowest impact means possible for each of the sites.

The following documents provide further information on the methodologies relevant to AQM installation and deployment:

- COPP21065-PRO-G-102 Passive Air Quality Monitoring (AQM) Installation and Commissioning
- COPP21065-PRO-G-103 Passive Air Quality Monitoring (AQM) Sample Collection, Maintenance and Context Observations
- COPP21065-PRO-G-104 Powered AQM Instrumentation Installation and Commissioning
- COPP21065-SPE-G-100 Air Quality Monitoring Station Control Functional Specification

5.1.3 AQM network outline

Table 5-1 outlines the AQM network arising from the MSDCA Plan and Figure 5-1 shows the current AQM status. Information on the design of the AQM network is provided in Appendix 2 of the MSDCA Plan.

Table 5-1: AQM network design outline

AQ sites	MRAMP AQM type	EX sites	MRAMP AQM type
AQA1	Passive	EX01	*
AQ01	Powered	EX02	Powered
AQ02	Passive	EX03	*
AQ03	Passive	EX04	*
AQ04	Passive	EX05	*
AQ05	Passive	EX06	*
AQ06	Passive	EX07	MRAMP equipment in existing powered industry AQM
AQ07	Passive	EX08	*
AQ08	Passive	EX09	Powered
AQ09	Passive		
AQ10	Passive		
AQ11	Passive		
AQ12	Passive		
AQ13	Passive		
AQ14	Passive		
AQ15	Passive		
AQ16	Passive		
AQ17	Passive		
AQ18	Passive		

Note: In addition to the AQM network being deployed as part of the MRAMP, industry AQM data is being obtained for inclusion in the Program’s air quality analysis for sites indicated with an asterisk.

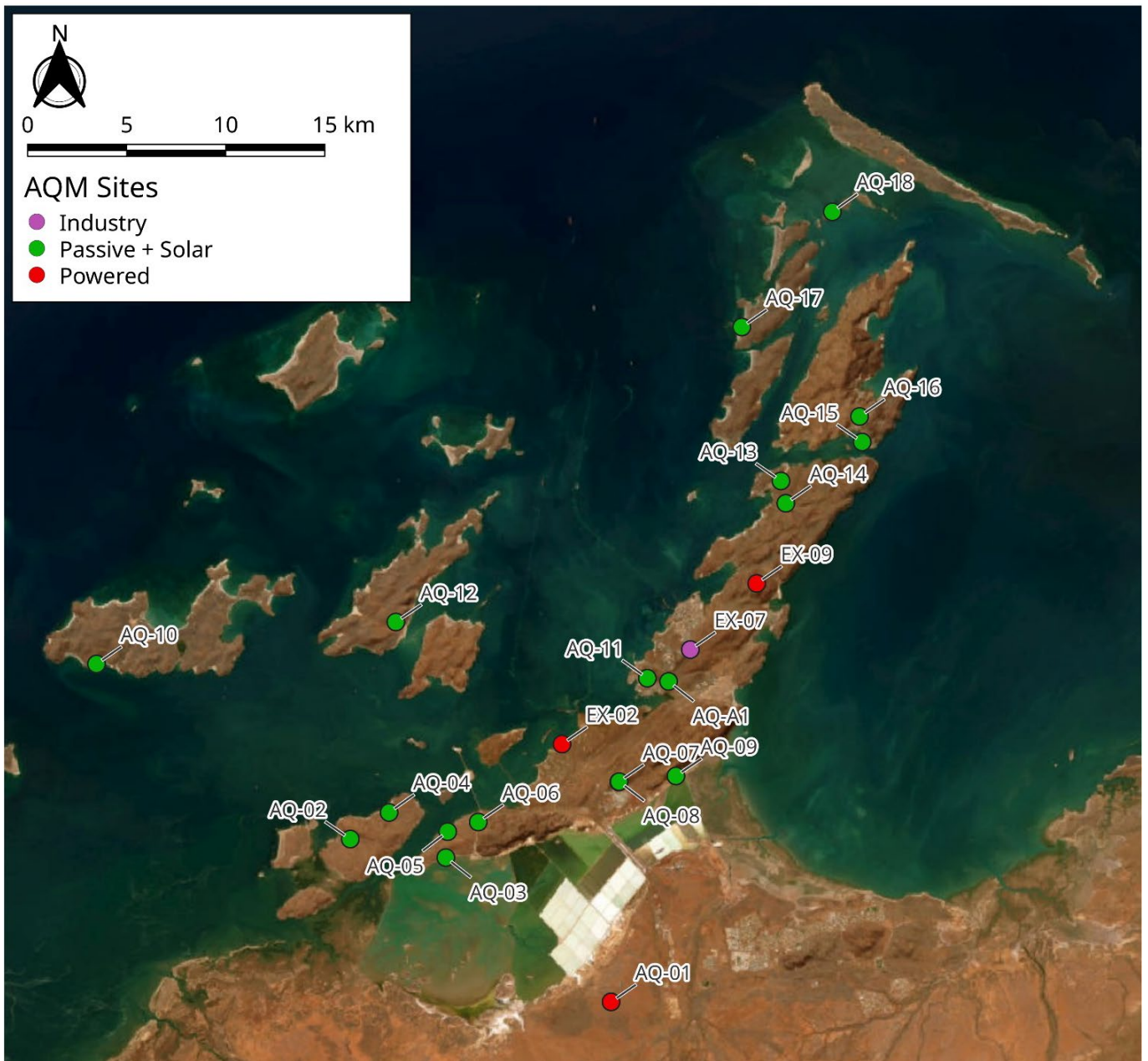


Figure 5-1: MRAMP AQM network and status as at April 2023, with existing industry monitors also shown.

5.1.4 Passive AQM sites

As can be seen from Figure 5-2, the passive AQMs consist of a complete, high-quality weather station, real-time samplers for NO, NO₂, NH₃, CO₂ and PM_{0.3-10}, deposition sampler, and passive samplers. The real time air quality sensors are low power items which will primarily be used to give information on transient peaks in air quality. Data from these instruments are recorded continuously, with average values (or total values for the rain gauge) transmitted every 5 minutes via the 4G LTE GSM network, as well as being logged locally as a backup. Various system telemetry and system health status information is also transmitted at 5 minute intervals.

The pneumatic mast is programmed to retract if wind speed reaches 80 km/h, which generally only occurs during cyclonic conditions.



Figure 5-2: *Passive AQM (AQ12) showing key components of the monitoring system. Ronald Fellows-Smith and MAC Ranger Kasziem Bin Sali shown post installation of electronics*

The passive AQMs include duplicate passive samplers for NO₂, SO₂, O₃, HNO₃, NH₃ and VOCs, as well as a triple-collector deposition sampler after AS3580.10. As detailed in the MSDCA Plan, the three bucket deposition sampler is a novel design with separate collectors for dry, wet and mist/dew events. The protocol for the sampler to move between buckets is given in COPP21065-SPE-G-100. Validation against the AS3580.10 total flask standard will be performed post completion of AQM deployment.

Passive sampler validation studies

In order to select the most appropriate passive sampler, three different types of passive samplers were trialled in a cross-validation study in 2022 to determine the best option for the given conditions. The three options assessed were:

- Gradko International (UK): sampler and laboratory analysis
- IVL (Sweden): sampler + analysis
- Radiello (Italy): samplers only, with analysis performed at the ChemCentre, Perth

IVL in Sweden were found to be the most suitable, based on the limit of detection (**LOD**) over the suite of species. Outcomes of the validation study are documented in COPP21065-REP-G-100 Passive Sampling Tube Evaluation and Testing Report.

A second study of between-sampler variability was conducted using 11 IVL replicates for each species, based on peer-review feedback of report COPP21065-REP-G-100, with VOC results pending. Results from the available validation and field monitoring passive sampler data to-date are presented and discussed in Section 7.4.

Passive sample collection

Passive sample tubes are scheduled to be changed over at four weekly intervals, and this has occurred on the following dates:

- 5-6 December 2022
- 9-11 January 2023
- 6-8 February 2023
- 8-10 March 2023
- 2-5 April 2023

In December 2022 the number of samplers deployed was reduced to ten AQMs as shown in Table 5-2 due to issues with supply logistics as delivery of samplers was delayed due to customs clearance.

Laboratory results have been received for all species of passive samples collected from December 2022 through to February 2023 with the exception of VOCs. There was a ten week turnaround on laboratory analysis for the initial samples, including a four week closure over the Christmas-New Year period. It is expected future results will be returned in a shorter time frame now that logistics have been streamlined with IVL.

Available passive sampler results are presented and discussed in Section 7.4. Deposition sampler results are not presented in this report as only one set of results is currently available. Real time sensor data is also not presented as the sensors require calibration to local conditions, which will be performed for all data collected, primarily based on passive sampler data once a sufficient body is available. CO₂ and PM sensors will be calibrated using data from the reference grade instruments to be installed in the powered AQMs. These will also add additional calibration data for the other low-cost/power sensors.

Table 5-2: *Passive AQM sampler deployment and receipt of laboratory analysis results*

Month	Nov 2022		Dec 2022		Jan 2023		Feb 2023		Mar 2023		Apr 2023	
AQM ID	Passive	Deposition										
AQ-01												
AQ-02	PR		PR		PR		WL		WL	WL	Dep	Dep
AQ-03	PR				PR		WL	R	WL	WL	Dep	Dep
AQ-04	PR				PR		WL		WL	WL	Dep	Dep
AQ-05	PR				PR		WL		WL		Dep	
AQ-06	PR		PR		PR		WL		WL	WL	Dep	Dep
AQ-07												
AQ-08	PR		PR		PR		WL	R	WL	WL	Dep	Dep
AQ-09	PR				PR		WL			WL	Dep	Dep
AQ-10	PR				PR		WL		WL		Dep	
AQ-11	PR		PR		PR		WL	R	WL		Dep	Dep
AQ-12	PR		PR		PR		WL		WL		Dep	
AQ-13	PR		PR		PR		WL		WL	WL	Dep	Dep
AQ-14	PR				PR		WL		WL		Dep	
AQ-15	PR		PR		PR		WL	R	WL		Dep	Dep
AQ-16	PR		PR		PR		WL	R	WL		Dep	
AQ-17	PR		PR		PR		WL		WL		Dep	
AQ-18	PR		PR		PR		WL		WL		Dep	
AQ-A1							WL	R	WL		Dep	Dep
EX-02												
EX-09												

PR: Partial Results

WL: With Laboratory

R: Results

Dep: Deployed

6 Spatial mapping and surface modelling

6.1 Objectives

It is important to understand how environmental and air quality parameters measured at the AQMs relate to the exposures at the rock(art) surfaces being studied. For all sites containing both AQMs monitors and rock art or sample rocks included in the study design (i.e. all AQ and EX sites except for AQ01 and EX01), it was deemed essential to:

1. Map the topography of the sites, incorporation of a region around each sample rock and rock art panel and the AQM location.
2. Triangulate and fill in the mapping between each of (1) and include any nearby features likely to be major air flow paths.

Following the field mapping, processed topographies are provided to the computational fluid dynamics (**CFD**) team to develop meso-scale models of airflow in the regions above the study targets. This will provide improved determination of pollutant exposures at the rock surface.

6.2 Spatial mapping

6.2.1 Scope of mapping

The targeted sites for three dimensional (**3D**) modelling were AQ02-AQ18, the MAC office (AQA1), and EX02-09. Most of the data capture for these sites was based on an area approximately 250 m² around the air quality monitor, and the rock art and sample rocks included in the study square. In some cases, multiple study squares were joined together, and in others some had to have extended capture areas due to the terrain. While most sites could be captured over a single flight campaign, some had to be split up over different campaigns due to the size, schedule of other field activities, or restrictions from local industries or CASA controlled airspace.

To date, all sites have been flown and data captured. Nine sites (AQ02-AQ08, and AQ10-AQ11) have been fully processed and processed surfaces uploaded to Cloudstor. Data processing for other sites is ongoing.

Site mapping is being processed and established:

- horizontally in Map Grid of Australia 2020 (**MGA2020**) Zone 50 coordinates, with the horizontal datum in Easting and Northings), and
- vertically in orthometric height datum for Australia (**AHD**).

6.2.2 Methodology

Spatial mapping was undertaken according to the prescribed methodology, using a Phantom 4 Pro and a Phantom 4 RTK drone.

- COPP21065-PRO-G-105 Unmanned Aerial Vehicle and Spatial Mapping

6.2.3 Global navigation satellite system (GNSS) datum point

The first part of the field capture for each site was to establish a datum point on site. After processing, this served as a known point with well defined coordinates, so the rest of the survey could be completed relative to this point. In most cases, this was a newly established point located adjacent to the AQM and was installed as a short star picket or steel spike in the ground that will be permanent for the duration of the Program. A GNSS receiver (in this case a Trimble R10) was set up over the mark, and data was captured for a duration of at least two hours to be post-processed by AUSPOS, with a nominal accuracy of approximately 20 mm horizontally, and 200 mm vertically to the AHD (approximate 80 mm to the ellipsoid height).

In some cases, existing State Survey Marks (**SSMs**) established by Landgate were located nearby the AQM sites. Since these have previously defined coordinates (with known uncertainties), they were either adopted instead of establishing a datum point (with a two-hour AUSPOS still completed to check the point and allow for comparison of results) or used as a check-point in the real time kinematic (**RTK**) survey (again to allow for a comparison).

After returning from the field, the raw GNSS observations were uploaded to the AUSPOS after a period of two weeks. AUSPOS is an online post-processing service operated by Geoscience Australia which processes the point using reference stations around Australia to give coordinates and uncertainties for marks observed by GNSS. It recommends that least two hours of observations are captured to get centimetre-level results (although only a minimum of one hour is required). The reason for the delay in post-processing was to allow for the use of precise satellite ephemeris to increase accuracy of the results.

The final values for the datum points are presented in Table 6-1 below. The table contains the site, the date, occupation, and coordinates. These are presented in MGA2020 for horizontal values, and in the ellipse and orthometric (AHD) heights for the vertical value. Also reported are the 95% confidence regions for each mark based on the propagation of errors through the AUSPOIS processing method. It can be seen that the ellipsoid height is slightly better in terms of the AHD, due to the extra uncertainty of converting from ellipsoid height to orthometric height introduced by the geoid model required for the conversion. Table 6-2 shows the results of the checks completed between processing the observations from different days, or from the reported values of the SSMs from Landgate. Most are within 95% confidence intervals reported from the AUSPOS processing report. All datum points have been surveyed and processed, apart from EX07 which is tied into EX08.

Table 6-1: Coordinates and Uncertainty of the Datum Point for the AQ and EX sites. Note sigmas are in metres, and reported as 95% confidence interval

Info			Coordinates				95% confidence interval			
Site	Date	Occupation	Easting (m)	Northing (m)	Ellipsoid Ht (m) (h)	AHD Ht (m) (H)	E	N	h	H
AQ02	4/07/2022	1hr 59m 30s	459525.073	7711460.888	-0.318	7.007	0.013	0.016	0.051	0.213
AQ03	23/06/2022	2hr 51m 00s	464345.785	7710524.565	-3.316	3.972	0.023	0.014	0.055	0.201
AQ04	4/07/2022	2hr 01m 30s	461486.151	7712803.855	-3.996	3.267	0.017	0.015	0.063	0.212
AQ05	21/06/2022	2hr 03m 30s	464451.168	7711835.669	-1.699	5.555	0.019	0.02	0.062	0.204
AQ06	21/06/2022	1hr 49m 30s	465983.135	7712327.107	15.12	22.354	0.016	0.017	0.069	0.201
AQ07-08	28/06/2022	2hr 48m 30s	473091.259	7714348.639	69.754	76.938	0.014	0.013	0.045	0.17
AQ09	30/06/2022	3hr 50m 00s	475962.375	7714646.331	-1.204	5.978	0.015	0.015	0.052	0.174
AQ10	5/07/2022	2hr 03m 30s	446726.447	7720297.835	-1.104	6.082	0.017	0.017	0.061	0.224
AQ11	20/06/2022	2hr 59m 30s	474521.431	7719575.352	32.62	39.668	0.014	0.014	0.044	0.173
AQ12	7/07/2022	1hr 55m 30s	461821.556	7722410.904	10.734	17.612	0.103	0.029	0.132	0.248
AQ13	22/06/2022	2hr 37m 00s	481250.757	7729528.996	8.135	14.933	0.014	0.014	0.049	0.195
AQ14	22/06/2022	1hr 49m 00s	481506.856	7728404.126	16.957	23.778	0.016	0.019	0.071	0.199
AQ15	7/07/2022	2hr 47m 00s	485356.878	7731491.5	-1.852	4.927	0.013	0.012	0.039	0.197
AQ15	7/07/2022	0hr 59m 00s	485356.855	7731491.506	-1.956	4.823	0.135	0.05	0.19	0.271
AQ15	26/10/2022	2hr 13m 00s	485356.887	7731491.523	-1.819	4.96	0.021	0.015	0.056	0.201
AQ16	6/07/2022	1hr 59m 30s	485221.213	7732785.423	2.863	9.614	0.016	0.015	0.061	0.204
AQ17	29/06/2022	1hr 41m 00s	479290.308	7737300.864	8.263	14.916	0.024	0.02	0.093	0.221
AQ18	6/07/2022	1hr 59m 30s	483849.304	7743109.507	-1.464	5.126	0.014	0.016	0.052	0.215
AQA1 (MAC Office)	20/06/2022	2hr 02m 30s	475589.167	7719412.026	6.185	13.239	0.018	0.016	0.064	0.178
EX02	27/06/2022	2hr 35m 30s	469814.422	7716005.543	8.069	15.197	0.02	0.015	0.064	0.184
EX03	28/10/2022	2hr 03m 30s	474302.366	7719126.336	11.507	18.569	0.023	0.017	0.063	0.178
EX04	24/06/2022	2hr 57m 30s	478597.325	7718196.335	1.989	9.075	0.023	0.019	0.073	0.184

Murujuga Rock Art Monitoring Program
Monitoring Studies Report 2023

Info			Coordinates				95% confidence interval			
Site	Date	Occupation	Easting (m)	Northing (m)	Ellipsoid Ht (m) (h)	AHD Ht (m) (H)	E	N	h	H
EX05	24/06/2022	2hr 18m 30s	475962.892	7719787.388	16.255	23.297	0.015	0.018	0.058	0.177
EX06	27/06/2022	2hr 35m 00s	477041.351	7719930.687	32.133	39.169	0.018	0.016	0.06	0.179
EX07	16/01/2023	TBA	TBA	TBA	TBA	TBA	TBA	TBA	TBA	TBA
EX08	28/06/2022	1hr 58m 30s	477378.559	7722168.416	33.717	40.689	0.013	0.016	0.049	0.179
EX09	1/07/2022	2hr 09m 30s	481033.282	7724674.952	19.433	26.343	0.018	0.015	0.053	0.189
EX09 (Valley)	8/07/2022	2hr 50m 00s	480039.185	7723193.169	20.297	27.244	0.012	0.014	0.05	0.185
EX09 (Mt Wongama)	28/10/2022	2hr 45m 00s	480036.009	7724289.752	112.054	118.973	0.02	0.017	0.066	0.192

Table 6-2: Differences between report SSMs coordinates either through using it as a Datum point or taking a RTK check shot to the SSM from the site Datum point. The values are in metres.

Location	Notes on check	Δ Easting	Δ Northing	Δ Ell Ht	Δ Ortho Ht
AQ07-08	Repeat 25/10/2022 (session 1)	-0.01	0.015	0.043	0.043
AQ07-08	Repeat 25/10/2022 (session 2)	0	-0.011	0.061	0.061
AQ09	Repeat 24/10/2022	0.009	0.005	0.044	0.044
AQ15	Repeat same day (session 2)	-0.01	0.015	-0.104	-0.104
EX02	Setup on SSM Harbour Mound	-0.003	-0.005	-0.063	-0.08
EX03	Check shot to D141	-0.013	0.003	0.031	0.031
EX06	Setup on SSM Dampier 140	0.007	0.01	-0.007	-0.007
EX08	Setup on SSM Dampier 148	-0.014	0.002	0.044	0.044

6.2.4 Local RTK control survey

A local RTK survey was conducted for picking up the rock art and sample locations, and the control used for the georeferencing of the drone images and producing the 3D model of the surrounding areas. RTK was performed by setting up a base station over a known point, and then using a GNSS rover to pick up the required points in the area. To get accurate coordinates of the desired points, the rover was set up over the point. It then uses the satellite observations and the known coordinates of the base to correct the errors in the observations at the rover, and to calculate a relative vector between the base and rover, and hence to calculate the coordinates at the rover from this.

In this case two Trimble R10s were used with a Trimble TC3/TC5 controller to observe the base and the required points. The base was set up over the datum point, using a tripod, and a height offset between the receiver and the point was applied. The rover was set up over the required points for pick-up using a fixed pole (and level bubble to ensure correct height and verticality over the point). The points included the rock art panel and sample rock locations and the unmanned aerial vehicle (UAV) drone targets. To increase precision and to cancel out movement of the rover on the pole (due to wind or ability to hold it steady), at least five epochs (observations) were taken at each point. The point was re-observed if excessive movement was observed. The exact relative uncertainty for the control points is reported in the summary for the ground control points in the later sections for the processed sites, but most of the values are substantially under 20 mm for the horizontal, and 50 mm for the vertical (reported at 1 standard deviation).

The true datum coordinates were unknown at this stage because there was no control or know points on the site originally. Instead, an arbitrary coordinate was assumed to be the datum mark on site (approximately estimated using raw GNSS observations with +/-10 m accuracies) and this coordinate was entered into the base (from the raw unprocessed GNSS reported coordinates). An arbitrary coordinate was applied because a selected surveyed point using two-hour GNSS observations would need to be processed using the online service AUSPOS run by Geoscience Australia, thus would have delayed the RTK survey by at least two weeks. The RTK survey was then conducted relatively from this arbitrary coordinate. To correct for this, once the datum point for the site has been processed and determined, a block shift between the arbitrary and post-processed coordinates are calculated and applied to all the RTK points to align them to their correct coordinates. The final uncertainty of these points will then be the uncertainty of the base combined with the uncertainty of the RTK observation (and these will then propagate into the final solution).

In addition, the RTK required line of sight for the rover to receive the required information from the base. Where this was not achievable, two solutions were implemented:

- The first was to establish another (secondary) datum point on the site and process it in a similar manner to the main datum point using AUSPOS (and, if able, to check the difference between the points using RTK).
- The second was to use the Trimble Infill option (which was used later in the campaign). This allowed for the observations of the rover to be stored, and post-processed later to calculate the RTK solution. The issue with this is that the current uncertainties cannot be monitored in the field.

All the RTK surveys have been completed for the sites. The block shifts have been calculated for sites AQ02 to AQ02, and AQ10 to AQ11 (others have been completed, but are still awaiting verification with the drone processing). While most rock art and sample locations were also observed using RTK, it appears that some sites were not picked up using RTK. The coordinates can be derived from the processed drone data (with similar accuracies).

6.2.5 Drone processing

In order to create the 3D model of the surrounding area, there are three main steps:

- setting up control to geo-reference the images
- flying the area and capturing the images with sufficient overlap
- processing the images and control together to create a 3D geo-referenced model.

Two drones were used over the campaign. They were a Phantom 4 Pro and a Phantom 4 RTK, both with a 20 mega pixel (13.2 mm) sensor, and a focal length of 8.8 mm (24 mm at 35 mm equivalent frame size). The RTK drone has an RTK receiver built in to help geo-locate each image, while the Phantom 4 Pro relies purely on the ground control for geo-referencing.

Control

The ground control is used to help align the images and solve all the interior camera parameters, including the focal length, principal point offsets, and lens distortions, as well as geo-reference the 3-D model into MGA2020 zone 50 + AHD coordinate system. In this case the ground control used were white crosses on the ground (made from corflute with a bolt holding them through the centre as a temporary and non-permanent mark). These were picked up with RTK as described in the previous section. In order to ensure a good registration of the images, the targets were distributed around the entire scene and throughout the middle. This was observed over most sites as regions captured outside areas covered by the targets could suffer from unchecked propagation of uncertainties (extrapolation effects). Also, if targets were missing from the centre of the region, then a warping effect could be present in the middle (due to insufficient coverage in the modelling and the middle bowing either up or down). This only happened for AQ03 and AQ06 due to missing targets in the centre of a long narrow corridor, and to AQ18 where the opportunity to capture the whole island was undertaken instead of the region local to the AQM. To help mitigate this, a pre-calibration of the camera was applied (to solve for the interior camera parameters) to strengthen the model. In later flights (such as AQ15), the RTK drone was used to solve for the location of the images without the reliance on such control (other control was still used as a check).

Flight

Once the targets were in place, flights were then conducted. The ideal parameters of the flight consisted of flight pattern that would enable at least 70% overlap between images and a ground sample distance of approximately 0.02 metres. This varied due to the terrain heights, the time allowed for the flight due to battery limitations, environmental effects such as wind, and scheduling to fit in with other activities. Where batteries and scheduling allowed, two flights at differing altitudes were conducted to improve overlap and the strength of the final model. In areas with a large elevation variability, the overlapping flights were conducted with the camera off nadir (with

the camera pointing 15 degrees off down axis). This helped to ensure the better coverage of gullies and hills and strengthen the final production of the model (such as AQ07-AQ08).

Adjustment

Once the images were captured, and the control was adjusted and corrected, the images were processed using the Bentley software ContextCapture. A project for each site was created, and the images and control were imported into the software. For the first pass, the keypoints (feature points) in the images were extracted and matched between images to create an initial alignment and solve for the initial interior parameters (calibration parameters for the focal length, offsets, and lens distortions) and exterior camera parameters (relative location and orientation between the images). At this stage the processing relied on the raw GPS coordinates of the drone; the calibration parameters can be inaccurate and can introduce errors (such as wrapping or positional errors) without the control information or the pre-calibrated parameters. However, at this step it is used to identify regions of poor overlap, missing information, and to aid in the initial control identification and alignment.

From this set of parameters, the control points in the images are identified. The adjustment is then reprocessed, this time constraining the final solution to the control. Because the external control is present, the calibration parameters can be solved more accurately (as the projection of the image control points onto the 3D object space's control coordinates can be used to solve the camera model more accurately), and the final adjustment is georeferenced by constraining the final solution to the known 3D values of the control. The solution is inspected to see if the calibration parameters agree with the pre-calibrated results, if the errors between the re-projection of the key points in the image to the calculated 3D points are small, and the errors between the object and model control coordinates are acceptable. Where the RTK drone was used, the image locations are already solved and can be constrained to georeference the model instead of using the control (although normally either one is used to check the other, or a combination is used).

Production

Once this is done, the production of the 3-D data is completed. This comes in the form of three products:

- The first is a 3D point cloud where a dense reconstruction is performed. Here, the adjusted alignment is used and matching pixels between images are projected into 3D to create discrete points. This is done for all images to create a 3D point cloud. This can have some errors due to mismatches between pixels and some smoothing effects, but in most cases is considered to be the raw 3D data generated for the model. This can then be meshed, filtered, and modelled further for the air flow modelling portion of the project. Care should be taken, as the points generated at the edge can suffer in accuracy due to a low number of overlapping pixels, and poor geometry between the images and the points being generated.
- The second product is a 2.5D digital surface/elevation model (DSM/DTM). In this case the elevation over the 2-D area (highest and lowest point) is calculated over a 2D grid. The grid is georeferenced and produces as a TIF image, with each grid cell/pixel size equating to the nominal ground-sampling distance (of approximately 0.02 metre resolution). The value of each cell/pixel is the calculated elevation value from the points in that cell, and the final TIF represents a 2.5D model of the terrain surface. This is a projection of the elevation onto a 2D reference system and hence it does lose some of the 3D information (such as terrain overhangs for example).
- The last product produced is a 2D ortho-rectified image mosaic. This is created by projecting all the RGB or colour information of the images onto the digital surface (from the previous step). These projected (or ortho-rectified) images are then blended into a continuous 2D image over the entire region.

6.2.6 Summary and issues

Some issues were encountered during the field and post-processing activities:

- The first is that the Phantom 4 Pro would not consistently produce the same image format due to a software issue (changed between native 3:2 to 4:3 format). This required the images to be cropped to a consistent 4:3 image size for processing, with no effect on the camera model, parameters, or solution, apart from a slight change in potential overlap. This overlap was accounted in the flight planning to ensure the overlap was done for the worst-case scenario in resolution.
- The other issue was the presence of water (normally where the flights were along beaches). Because the surface of the water was moving, and the refractive effect of light travelling through the water was not accounted for, the data created over the water was erroneous. This needs to be removed from the final digital model production, a task which is still ongoing.

At this stage, sites AQ02-AQ08, and AQ10-AQ11 have been fully processed, with the others in various stages of completion. In addition, sites such as AQ09, AQ15 and EX09 cover a much larger area than other sites due to relative positions of the AQM, art panel(s) and sample rock(s), with data captured over several days and modalities. This means that incorporating these into a single model is challenging, and testing is being undertaken to see if it is preferable to separate out the captures and modalities and process them separately, or whether they can be combined into a single adjustment model.

6.2.7 Completed site summary

A summary of information from fully processed sites is included in Appendix A: This includes:

- A summary of capture data
- Position uncertainties table
- Generated tie points
- Control points
- Position uncertainty figure
- A figure showing resolution of the final 3D model
- A low resolution orthographic mosaics of the area captured
- A digital elevation model (DEM) snapshot.

6.3 Computational fluid dynamics (CFD) surface modelling

6.3.1 Objectives

As described in Section 4.5. of the MSDCA Plan, the objective of the computational fluid dynamics (CFD) modelling is to assist interpretation of the field-based air quality monitoring studies. CFD is advantageous in this aspect as it allows an area of interest (such as AQM site, or rock art site) to be studied at a finer spatial or temporal resolution relative to previous modelling (Ramboll, 2021) or that which can be achieved by the MRAMP AQMs alone. The CFD modelling will be used either pre-emptively, in the case where local features (either terrain, or emissions) are identified as a possible future source of uncertainty in a measurement, or post-hoc, where a measurement shows an unexpected trend.

In these cases, a virtual model of the site can be constructed with different emissions and weather scenarios simulated to determine quantitatively and/or qualitatively the level of uncertainty in a measurement or impact.

It is important to note that the objective of the CFD modelling is for it to support the MRAMP air quality monitoring as an additional tool for interpretation. The CFD results will not feed directly into the EQCs but will allow the statistical team to reduce measurement uncertainties by testing and assessing particular localised impacts.

6.3.2 Geometry and computer model

The CFD models require detailed geometry and emission sources to be available. For the required geometries, data at the coarsest scale (approximately 30 m) is available from the Shuttle Radar Topography Mission (**SRTM**). This is supplemented by 1 m resolution data from Landgate (acquired in 2020, and available to the MRAMP project), and still finer resolution data acquired in the spatial mapping component of the studies (refer to Section 6.2 previously). The coarser geometries will be used to fill gaps in the finer models (i.e., Landgate data to supplement the spatial mapping data, and SRTM data to supplement the Landgate data). The CFD process requires this geometry to be discretised in three dimensions to allow tracking of the airflow and any chemical species through the model.

6.3.3 Meteorology and emissions data

To complete the CFD modelling, suitable meteorological and emissions data is required as inputs to the model. Predominantly the meteorological inputs to the CFD model will be matched to the site conditions as recorded by the AQM network, however the CFD model may also be set up to match infrequent events that may occur but have not been recorded during the campaign. Data on emissions sources will primarily be obtained from the emissions inventory prepared by Ramboll (2021), supplemented by local observations and measurements, or updated emissions inventory data.

6.3.4 Nesting of models

The CFD model is computationally intensive, and it is not feasible to model the whole of Murujuga at the resolution captured by the spatial mapping program. However, data at this scale is required as an input to the more localised models. To support this, a CFD investigation will initially use a coarse model of Murujuga to capture larger scale weather features and more distant emission sources. These will then be used to provide inputs to the more localised models.

6.3.5 Interpretation of results

The CFD model returns high fidelity data under carefully controlled input conditions. The model set-up, and consequent interpretation of the results, depends on which uncertainty is being investigated. For example, if an AQM is sited within a gorge, the sensitivity to wind direction on its recordings can be quantitatively assessed by simulating the small changes in wind direction and measuring exposure. Alternatively, by adding or removing a particular local emission source its impact can be quantified by comparing exposures before and after. This type of investigation is generally not possible to do in situ.

6.3.6 Progress and resources

The tools for processing and creating the CFD models (geometries and emissions) have been developed and tested. The fieldwork component of the spatial mapping programme has only recently completed, and the processing to obtain the high-resolution data to feed into the CFD models is ongoing. Computational resources have been allocated by the Pawsey Supercomputing Centre to support the project, and the first model runs will be undertaken in the near future.

7 Statistical analysis of combined (dose/response) data

7.1 Field colour measurements

7.1.1 Field campaigns and colour measurement

The study design calls for repeated measurement of the colour of rock surfaces at exactly the same locations during successive field visits. During the site selection process, the researchers and Rangers identified 54 rock panels across Murujuga that would be measured in this way. On each rock panel there are 10 designated ‘targets’ (precise positions on the panel). The study design requires that each target be measured repeatedly at each visit, yielding at least 10 replicate measurements of each target on each visit.

7.1.2 JAZ instrument

Rock surface colour is measured using a JAZ spectrophotometer. The instrument provides its results as data files (with a .jaz filename extension) which can be analysed using the commercial software package OceanInsight. The package can display reflectivity spectra as graphical plots and can convert a spectrum to perceptual colour coordinates (L^* , a^* , b^* values, described in Section 7.1.7).

For more penetrating analysis, the ability to analyse the spectral data directly was required. Accordingly, the statistical team and colleagues from the Curtin Institute for Computation have investigated the structure of the JAZ data files. These are simply text files with a “.jaz” filename extension. The typical appearance of these files is shown below.

```
Jaz Data File
+++++
Date: Thu Mar 02 14:33:00 2023
User: jaz
Dark Spectrum Present: Yes
Reference Spectrum Present: Yes
Processed Spectrum Present: Yes
Spectrometers: JAZA1682
Integration Time (usec): 37000 (JAZA1682)
Spectra Averaged: 1 (JAZA1682)
Boxcar Smoothing: 0 (JAZA1682)
Correct for Electrical Dark: No (JAZA1682)
Strobe/Lamp Enabled: Yes (JAZA1682)
Correct for Detector Non-linearity: No (JAZA1682)
Correct for Stray Light: No (JAZA1682)
Number of Pixels in Processed Spectrum: 2048
>>>>Begin Processed Spectral Data<<<<<
W      D      R      S      P
189.513458  0.000000  0.000000  0.000000  0.000000
189.969238  0.000000  0.000000  0.000000  0.000000
190.424988  655.350037  743.483276  714.105530  66.666664
190.880707  723.144836  677.948303  693.767090  65.000000
191.336411  668.908997  702.806396  684.727783  46.666668
191.792068  777.380676  709.585876  711.845703  96.666664
192.247711  770.601196  784.160156  680.208130  -666.666687
192.703308  729.924316  711.845703  689.247437  225.000000
193.158890  784.160156  716.365356  786.419983  -3.333333
193.614426  750.262756  752.522583  797.719177  2100.002686
194.069946  763.821716  775.120850  736.703796  -240.000000
194.525436  786.419983  831.616577  716.365356  -154.999786
194.980896  718.625183  775.120850  729.924316  20.000000
```

Figure 7-1: Typical data file format from the JAZ instrument

The original manufacturer of the JAZ instrument has been acquired by another company, and the instrument is now discontinued from production and sale. The technical manual is still available online, but expert support is no longer available. Consequently, some of the following statements represent the statistical team's best knowledge or interpretation of the available information, rather than being authoritative statements from the manufacturer.

The data files contain columns labelled W, D, R, S and P. The statistical team's interpretation of the manual is that:

- W represents the wavelength of light in nanometres (nm)
- D is the dark field photon count for this wavelength
- R is the reference (illumination) photon count
- S is the sample sensed photon count
- P is the processed (calculated) reflectivity for this wavelength.

The wavelength values are fractional (rather than integer) values and are not the same sequence of wavelength values in different data files. The team's best explanation is the following:

- The sensor is a linear array of pixels, indexed by the numbers 1 to 2,048.
- Each pixel receives photons of light of a particular wavelength.
- Wavelength increases as the pixel index increases. However, the precise correspondence between pixel index and wavelength is not constant, because it is affected by the internal state of the device (especially by its temperature).
- When the device is recalibrated, the correspondence between pixel index and wavelength is estimated using a cubic regression, and the coefficients of the regression are stored internally.
- Data files provide the current estimated wavelength value for each pixel.

That is, the data files are not 'raw' but internally adjusted data. Recalibration changes this internal adjustment.

Future, definitive analysis of these data will need to take into account the presence of errors in the wavelength values themselves, and the change points in time when the device is recalibrated. These effects are ignored in the current exploratory analysis which treats the wavelengths as accurate values.

The manual states that the reflectivity (at each wavelength) is calculated:

$$P = (S - D)/(R - D) \times 100$$

and this formula agrees with direct calculation in the data files.

7.1.3 Typical spectral response

The plot in Figure 7-2 below shows a typical example dataset. It is a superposition of 10 different curves which represent the 10 replicate measurements of spectral response from a particular target in field campaign 1. The 10 replicate curves are very similar and numerically close together. This pattern is repeated in most of the data, giving a degree of confidence that the spectral measurements are reproducible.

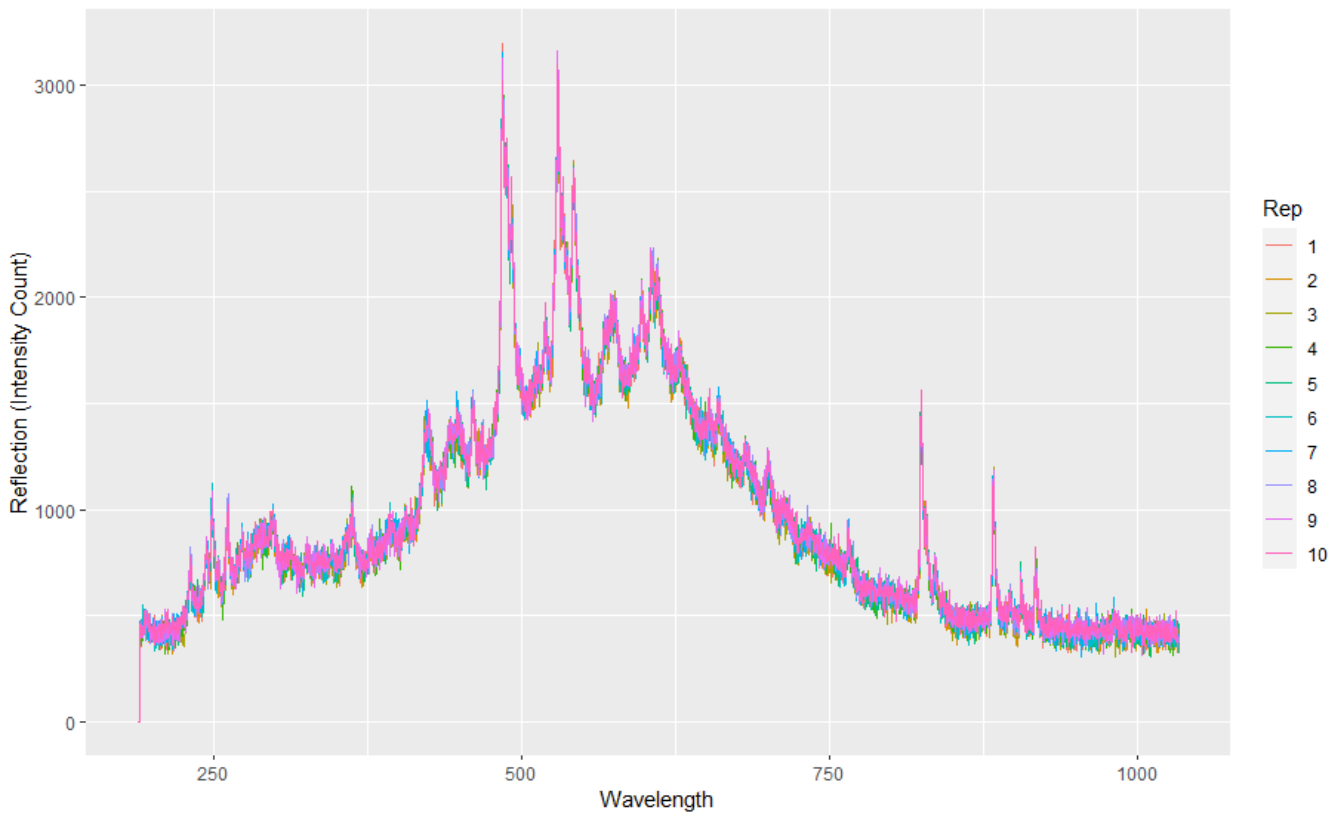


Figure 7-2: AQ02_GPH art panel colour measurements for Target 1 (10 replicates)

7.1.4 Initial validation of data

The JAZ data files provide the photon counts D, R, S and the calculated reflectivity P for a wide range of wavelengths from about 180 to 1030 nm. The visible spectrum is usually taken to be the range between 380 and 780 nm, so the JAZ data reach quite far into the ultraviolet (wavelengths shorter than 380 nm) and infrared (wavelengths longer than 780 nm) bands.

Photon counts at the extreme wavelengths are expected to be more highly variable, due to factors including low illumination, thermal noise, and sensor-sensitivity limitations.

An initial check on the validity of each colour measurement was performed during the fieldwork campaigns (typically each evening, at least for field campaign 4) by converting each spectrum to CIELAB perceptual colour coordinates (L^* , a^* , b^*) and checking whether the coordinate values are within the permitted ranges. A negative value of lightness L^* is interpreted as implying that the data are invalid. Observations deemed invalid at this stage may be revisited and repeated.

In this analysis of the spectral data it was found that some JAZ data files included cases where (at least for some of the extreme wavelengths) the sample sensor count S is less than the dark field count D, and/or the reference illuminant count R is less than D. Physical considerations suggest that $S > D$ and $R > D$ but these can be violated if noise is sufficiently high. When both $S < D$ and $R < D$ then P will still be positive and the calculated CIELAB values could well be within the required limits and would not indicate invalid data. Hence, this analysis rejects as invalid some of the JAZ results that passed the initial validity checks in the field.

P is the reflectance and should range between 0% and 100%. In this analysis it was identified that some art panels in at least one campaign had a calculated reflectance P that was either negative or greater than 100%. This is physically implausible and should probably be rejected as invalid.

In response to these issues, the fieldwork procedure was revised to include much more effective cooling of both ends of the JAZ device and more frequent re-calibration of the device. After the first campaign, the spectrometer was placed in a cooler box on top of a freezer cube and block of ice (as described in Appendix B-1). In the fourth campaign, due to the extreme heat, an additional freezer cube was placed in the lid of the cooler box.

7.1.5 Data handling

The colour measurements provide a moderately large amount of data in a structured design: 54 rock art panels, 10 targets per panel, at least 10 replicates per target, and currently four field campaigns in the first year or studies, making 25,427 spectral measurements (.jaz files: see Table 3-9 and Table 3-10 for the number of measurements taken for each campaign by rock type and site type). Each spectral measurement has 2,048 wavelengths and 5 parameters [W, D, R, S, P], resulting in 10,240 data points per spectral measurement, and a total of over 220 million data values. This calls for reasonably efficient and well-structured software coding.

Statistical analysis was performed using the statistical analysis and graphics platform 'R'. Scripts in the R language that were used to perform the analyses will be available at a later date.

7.1.6 Objectives of analysis

The ultimate objective of analysis is to model the rate of change in rock surface colour over time as a function of the level of exposure to pollutants. Colour changes may be defined either as perceptible changes in the colour visible to the human eye, or as detectable changes in the full spectral signature of reflection from the rock surface. It is conceivable that changes may be detectable in the full spectral signature, and therefore measurable in this study, long before they are visible to the human eye. Accordingly, there are two types of analysis that should be performed, based on the perceptual colour and on the full spectral signature, respectively.

In this initial examination of the data, the main objectives are to check that the data are valid, and to evaluate sources of variability in the data, in order to confirm that the study design has sufficient power to detect changes in colour.

7.1.7 CIELAB perceptual colours

Perceptual colour is calculated by transforming the spectra to the L^* , a^* , b^* coordinates defined by the CIE (Commission International de l'Eclairage) international standard (CIELAB). In brief, L^* represents lightness, a^* represents the balance between red and green, and b^* represents the balance between blue and yellow. The advantage of the L^* , a^* , b^* coordinates over other coordinate systems such as R, G, B is that CIELAB is device independent and perceptually uniform (meaning that a given value of numerical change in the coordinates represents the same amount of perceptible change in colour).

To calculate the CIELAB coordinates in R code, the wavelengths were restricted to the visible range (380-780 nm wavelength). The data were converted to a common grid of integer wavelengths by linear interpolation (Becker et al. 1988) using the "as.spec" function from the pavo R package. Next, each spectral response was converted to tristimulus (X, Y, Z) values using the function "spectra2XYZ" function from the colorscience R package. The range of illuminant wavelengths (look-up table) that applied was the CIE 1964 10-degree table. Lastly, the tristimulus values were converted into CIELAB coordinates using the "XYZ2Lab" function, with illuminant set to D65 (daylight at 6,500

degrees K) and the observer set to 10 degrees. The CIELAB values that were calculated in R were checked against the results from the Spectra Suite software (Ocean Optics Inc.).

In this initial analysis, the CIELAB coordinates were used as a simplified summary of colour, and as a cross-check on the validity of the data.

7.1.8 Generalised additive modelling

The full spectral response of a rock surface can be plotted as a curve giving the percentage reflectivity as a function of the wavelength of light. Figure 7-14 shows two examples. Sharp peaks are often seen in these curves and may be attributable to the presence of certain minerals in the rock. A full multivariate analysis of these data will be performed later. For the moment, the objective is to decide whether the data are valid and to estimate sources of variability. For this purpose, the spectral responses were provisionally treated as smooth curves.

Generalised additive models (**GAMs**) with fixed and/or random effects were applied to find smooth trends in the relationship between wavelength and percent reflectance. The main advantage of GAM analysis is that it models linear and complex non-linear relationships automatically and does not require transformations (Hastie and Tibshirani 1990; Wood 2017). Two such models were fitted to the data.

The first model fitted a smooth curve to the spectral responses, separately for each target on each selected art panel in each campaign, yielding a total of four curves for each target (one curve for each campaign) and 40 curves for each rock art panel (one curve for each target in each campaign). Roughly speaking, each curve is a smoothed average of the 10 replicate measurements of colour at a specific target in a specific campaign.

The second model fitted a smooth curve to the spectral responses, separately for each rock art panel in each campaign, yielding a total of four curves for each panel (one curve for each campaign). Each curve is a smoothed average of the 40 measurements of colour taken over all targets on the given rock in a given campaign.

In the second model, a random effects term was fitted for the replicates within each target, by using a smooth term with $bs = 're'$. This term captures the variability between replicates and is important for evaluating the study design.

The basis dimension of each smoothing term was tested using a "GAM.check" function. However, the exact value of the dimension is generally not critical as long as it is large enough to ensure there are sufficient degrees of freedom to characterise the underlying 'truth' well (Wood 2017). To select the best model, the following goodness of fit measures were calculated for each model: R-squared, deviance explained, and AIC t. Since the dataset was exceedingly large, GAMs were fitted in R (R Core Team 2020) using the 'bam' function from the 'mgcv' library (Wood 2017). Note that if a campaign had a percent reflectance less than -1,000% and/or greater than 1,000% then it was excluded from the GAM analysis.

7.1.9 Analysis Results

Data acceptance and validation

A few JAZ files were unusable. Three files were empty; several files were corrupted; and a few files contained only the columns W and S. These were all discarded because it is not possible to calculate reflectivity from this information.

Spectra which failed the initial validation check (namely for which L^* was negative) were rejected.

Amongst the remaining spectral data files, there were numerous anomalies in the values of calculated reflectivity P. These are listed below.

1. Values of P ranged from -172% to 241% throughout the dataset.
2. In a few cases, the value of P was zero, when either S = D or R = D, an example of which is shown in Figure 7-3 below.

W	D	R	S	P	target	rep	Site	Campaign
824.5007	1893.736	6784.002	1893.736	0	9	6	RS04_GBR	2
824.891	1855.318	6865.356	1855.318	0	6	11	RS04_GBR	2
825.6715	1875.657	5507.2	1875.657	0	3	8	RS04_GBR	2
882.7677	1844.019	3780.692	1844.019	0	3	3	RS04_GBR	2
957.0293	1895.995	1895.995	1498.266	0	1	1	RS04_GBR	2
957.0293	1895.995	1895.995	1462.109	0	1	10	RS04_GBR	2
957.0293	1895.995	1895.995	1448.55	0	1	11	RS04_GBR	2

Figure 7-3: Example of invalide JAZ data file – P values of zero.

3. If both the numerator (S-D) and denominator (R-D) were negative, this resulted in a positive value of P. This occurred in some cases as shown in Figure 7-4.

W	D	R	S	S - D	R - D	P	target	rep	Site	Campaign
764.8956	1450.809	3294.829	1667.753	216.9435	1844.019	11.76471	6	6	4 RS04_GBR	4
973.9196	1439.51	1401.093	1434.99	-4.519653	-38.41699	11.76473	6	6	5 RS04_GBR	4
610.6853	1477.927	12688.93	2797.667	1319.739	11211	11.77182	6	6	7 RS04_GBR	4

Figure 7-4: Example of invalid JAZ data file – positive P value with negative numerator (S-D) and denominator (R-D).

4. Calculated reflectance P was less than -1,000% and/or greater than 1,000% in eight instances. Four of these art panels had a negative L* value. The percent reflectance ranged from about -350,000% to at least 60,000%. For example, Figure 7-5a shows that AQ09_GRT had a huge range in percent reflectance values for field campaign 2 in target 1, while all other targets had a similar trend. The L* values for AQ09_GRT were about -18,000 (Figure 7-5b). The other three art panels that had this problem were AQ12_BAS in field campaign 3, EX02_GPH in field campaign 1, and RS10_GBR2 in field campaign 2.
5. Another four art panels had a big positive number range in percent reflectance for one campaign, which resulted in a positive L* value. For example, EX06_GPH ranged from -32,000 to 72,000% reflectance (Figure 7-6a) in campaign 1 for target 1, with all other targets having a similar trend. The L* values for EX06_GPH were about 175 (Figure 7-6b).
6. The wavelength vs percent reflectance line was highly irregular, in six cases. For example, the plot line for rock art panel AQ11_GPH in campaign 1 is very wiggly and mostly less than 0% reflectance (Figure 7-7a). Note that Figure 7-7a only displays target 10, but targets 5 to 10 all have a similar irregular trend line. The L* value from CIELAB were mostly negative for field campaign 1 (Figure 7-7b).
7. For a given target in a given campaign, the spectral response curves are expected to be very similar. However, in ten cases, there were multiple distinct spectral curves for the same target in the same campaign. Figure 7-8 shows an example of the multiple curves for rock art panel EX05_GPH, in which target 6 has three curves and target 9 has two curves. Another example, Figure 7-9d shows two curves for art panel AQ04_GPH target 7. Possible explanations include re-calibration of the device half-way through measuring a target, and failure to re-position the device in exactly the same place.
8. Greater than 100% reflectance occurs in some cases. There are five types of curves which produce greater than 100% reflectance and yield positive values of L*:
 - a) Exponential trend – at the beginning of the visible spectrum (380 nm) the percent reflectance is similar to other campaigns. About half-way along the visible spectrum the percent reflectance starts increasing exponentially. This has occurred three times. For example, art panel AQ07_GRT target 10 (Figure 7-9a).

- b) “s” curve – At the beginning of the visible spectrum (380 nm) the percent reflectance is similar to other campaigns. However, about half-way along the visible spectrum the percent reflectance starts increasing and goes above 150%, this has occurred six times. For example, with respect to rock art panel AQ10_GPH target 2 (Figure 7-9b and Figure 7-10) and target 3 (Figure 7-10) there is a large increase in the reflectance after 550 nm and at the end of the visible spectrum the reflectance is 200%. The other targets also have an increase in the reflectance but they only increase to about 100%. However, the L* values from CIELAB for field campaign 4 are all positive (Figure 7-12).

The statistical team requested the fieldwork team revisit rock art panel AQ10 at the end of field campaign 4. Figure 7-11 shows the wavelength versus percent reflectance for all ten targets for the second measurement; clearly the second measurements are “correct” since these follow similar trend to the other three campaigns but the line is very flat for all four targets.

For the L* values from CIELAB for the second measurement about half of the replicates have a negative L* (Figure 7-12). Therefore, Mr Thorn would deem the second measurements from field campaign 4 had failed because L* is negative, but the statistician team would only deem that the first measurements from campaign 4 had failed because percent reflectance is greater than 100%.

- c) “s” curve with a tail at the bottom – At the beginning of the visible spectrum (380 nm) the percent reflectance starts around 80% and has a sharp drop to almost 0%, then about half-way along the visible spectrum the percent reflectance starts increasing and goes above 100%. This has occurred three times. For example, for rock art panel AS01_DOL target 3 (Figure 7-9c).
- d) “s” curve with highly irregular line and a sharp peak at the end. This trend is similar to b) the “s” curve, but around 650 nm wavelength the trend is irregular and has a sharp peak at the end of the visible spectrum. This has occurred once, for rock art panel AQ04_GPH target 7, shown in Figure 7-9d.
- e) sharp peak – from 380 to 700 nm wavelength the trend is similar to other campaigns, but after 700 nm there are a few squiggles and a sharp peak at the end of the visible spectrum. This has occurred once, for rock art panel AQ05_GPH target 1, shown in Figure 7-9e.

9. Negative reflectance and negative L*. At the beginning of the visible spectra the reflectance is around 0%, at around 600 nm wavelength the percent reflectance has a sharp decreasing trend. This has occurred at 50% of art panels, for at least one campaign per art panel. Thus, this suggests values below 0% cannot be disregarded and maybe a typical trend for rocks at Murujuga. Possible explanations include bioluminescence of microorganisms on the rock surface.

For example, for art panel AQ10_GPH for the first three campaigns, the percent reflectance goes below zero after around 600 nm wavelengths (Figure 7-10). Figure 7-12 shows that for campaign 1 and 2 some replicates had negative L* values. Also campaign 4 measurement 2 has about half the replicates with a negative L* (Figure 7-12).

Another example occurs with art panel RS04_GBR, with Figure 7-15a showing the sharp decreasing trend for field campaign 2 and the Figure 7-15b boxplot of L* values shows that for field campaign 2 almost all L* values were negative.

For each target in each campaign a ‘failure index’ was calculated which is the percentage of visible wavelengths (380-780 nm) for which all 10 replicate measurements yielded a negative value of reflectivity P. Boxplots of these failure index values for each campaign are shown in Figure 7-13a. Figure 7-13b shows the corresponding boxplots when wavelengths are not restricted to the visible spectrum. These two panels suggest that there has been progressive improvement in the reliability of the spectral measurements over the four field campaigns. In campaign 4, all the failure index values are zero (Figure

7-13a), meaning that none of the calculated reflectivity values P were negative between 380 to 780 nm in all ten replicates, and only a few spectra included any negative reflectivity values in any wavelengths (Figure 7-13b). In contrast, for campaign 1, the median percentage is more than 50% (Figure 7-13a), meaning that more than half of all targets in campaign 1 yielded spectra in which more than 50% of visible wavelengths had negative values of reflectivity P from all 10 replicate measurements. The median percentage is more than 75% in Figure 7-13b, meaning that more than half of all targets in campaign 1 yielded spectra in which more than 75% of all wavelengths had negative values of reflectivity P in all 10 replicate measurements.

The boxplots in Figure 7-13c and Figure 7-13d were very similar to Figure 7-13a and Figure 7-13b respectively. Figure 7-13c shows the percentage of wavelengths where the S (spectrum) value is less than D (dark) and R (reference) is less than D for only for wavelengths in the visible spectrum; and Figure 7-13d is overall wavelengths. There are a few occasions when both $S-D$ and $R-D$ are negative, but P is positive. However, as the criteria S value is less than D and R is less than D for these occasions it is deemed invalid.

Figure 7-14 shows two specific examples in which the calculated reflectivity spectrum (plotted as a black line) is annotated by indicating those wavelengths where the data are invalid (indicated by red dots).

The AQ, EX and AS art panel target locations were selected by the fieldwork team based on readily recognisable features (to enable relocation) and to provide a diverse range of both lighter and darker surfaces for observation (Appendix B:). In contrast, RS art panels were selected randomly to capture all sources of variability. However, as detailed above there were problems in both the freely selected and randomly selected rock art panels.

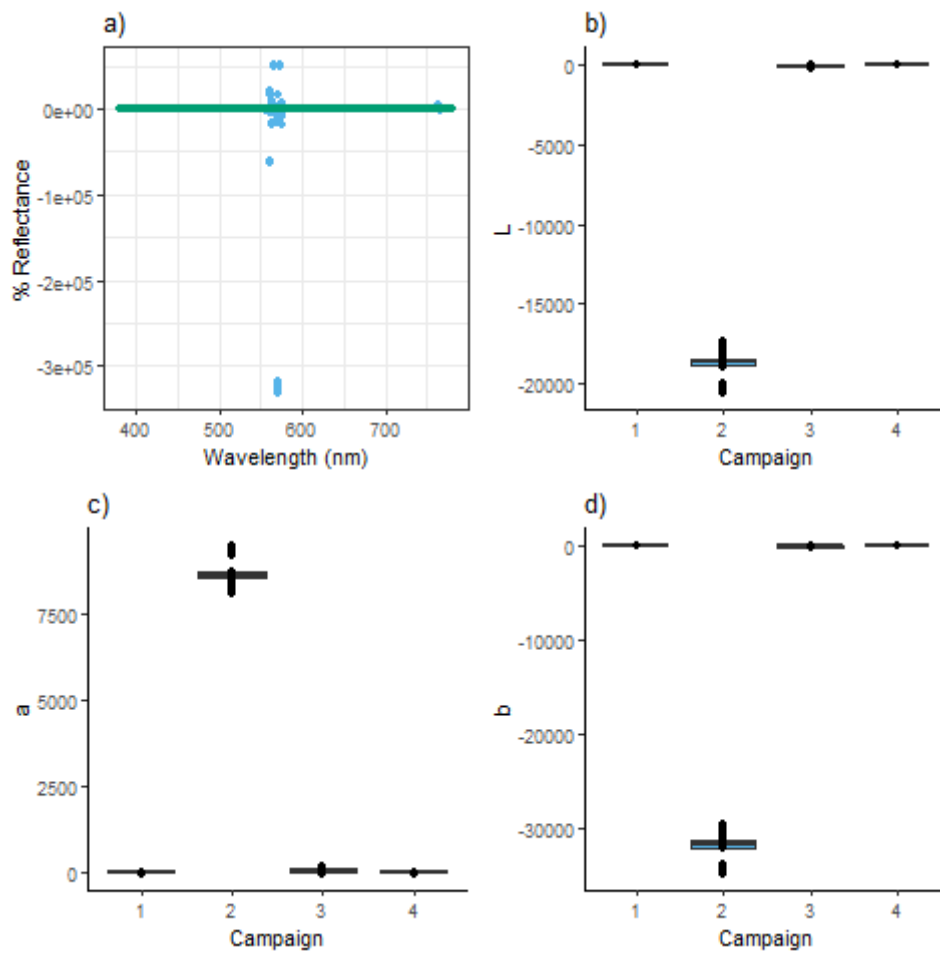


Figure 7-5: Art panel AQ09_GPH: (a) wavelength (nm) versus % reflectance with different colour dot for the four campaigns (where orange is campaign 1, blue campaign 2, pink campaign 3 and green campaign 4) only for target 1 (all other targets have a similar trend); (b) boxplot of L* values from CIELAB for each campaign; (c) boxplot of a* values from CIELAB for each campaign; (d) boxplot of b* values from CIELAB for each campaign.

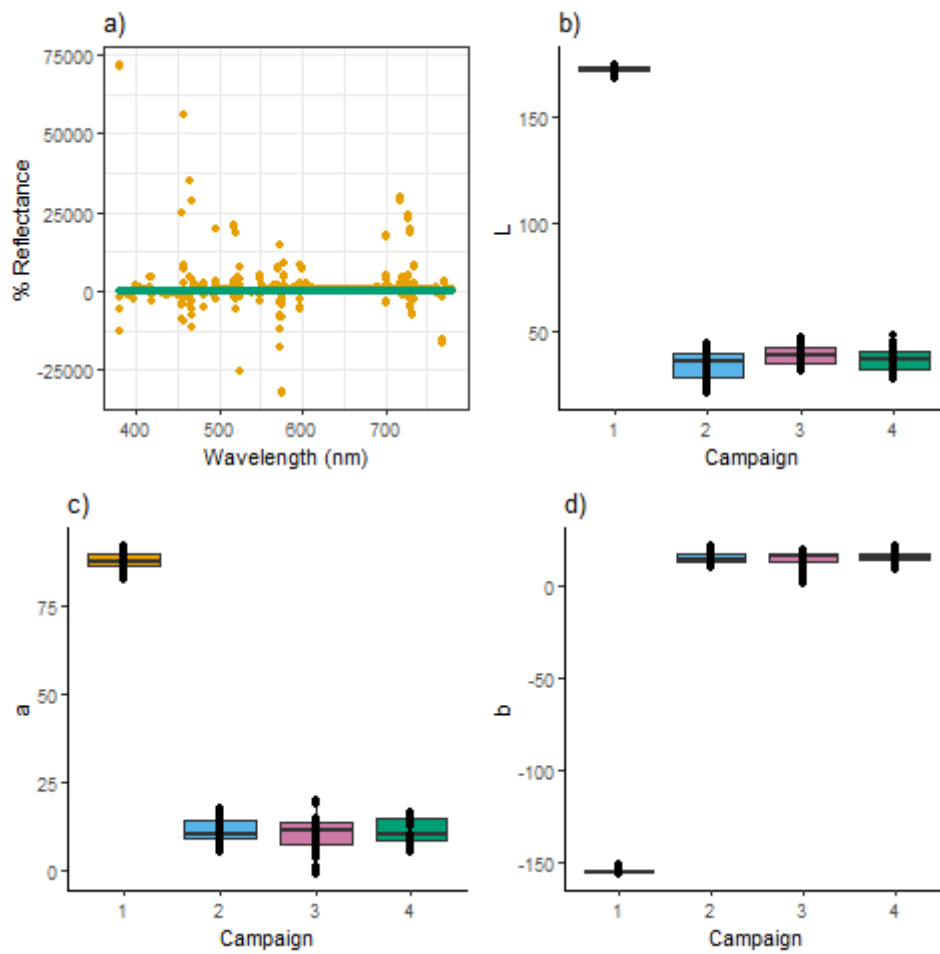


Figure 7-6: Art panel EX06_GPH: (a) wavelength (nm) versus % reflectance with different colour dot for the four campaigns (where orange is campaign 1, blue campaign 2, pink campaign 3 and green campaign 4) only for target 1 (all other targets have a similar trend); (b) boxplot of L* values from CIELAB for each campaign and for all targets; (c) boxplot of a* values from CIELAB for each campaign; (d) boxplot of b* values from CIELAB for each campaign.

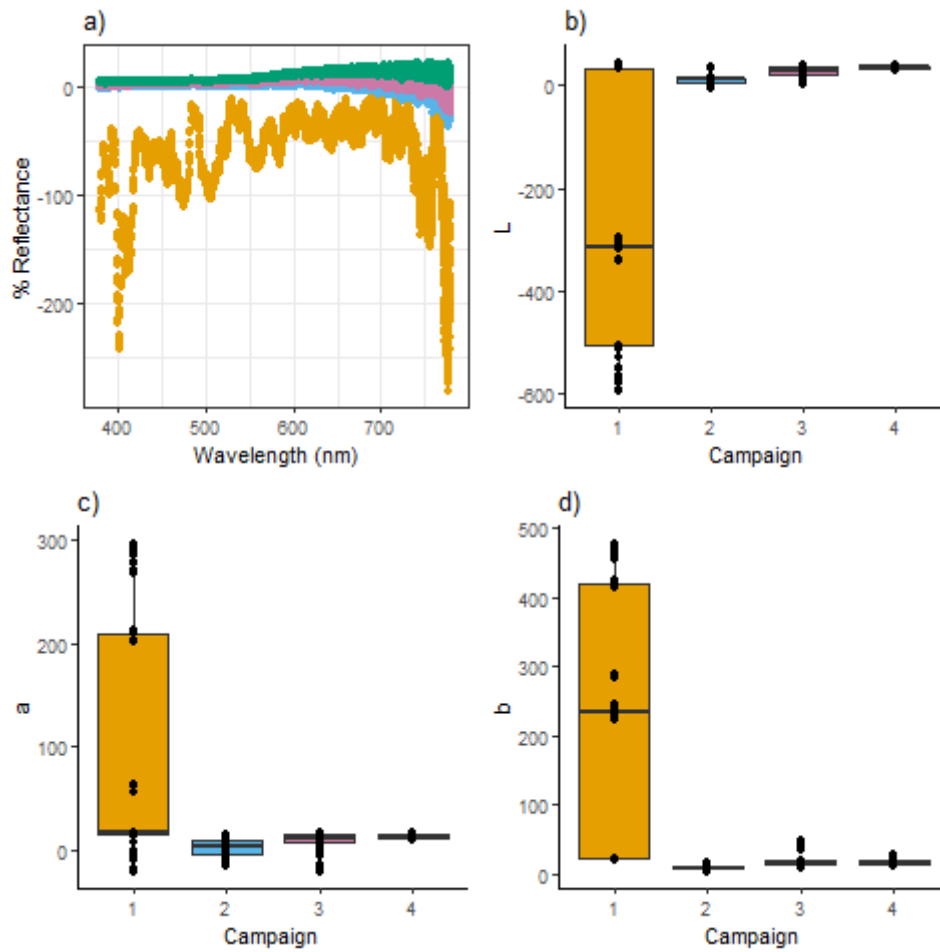


Figure 7-7: Art panel AQ11_GPH: (a) wavelength (nm) versus % reflectance with different colour dot for the four campaigns (where orange is campaign 1, blue campaign 2, pink campaign 3 and green campaign 4) only for target 10 (all other targets have a similar trend); (b) boxplot of L* values from CIELAB for each campaign and for all targets; (c) boxplot of a* values from CIELAB for each campaign; (d) boxplot of b* values from CIELAB for each campaign

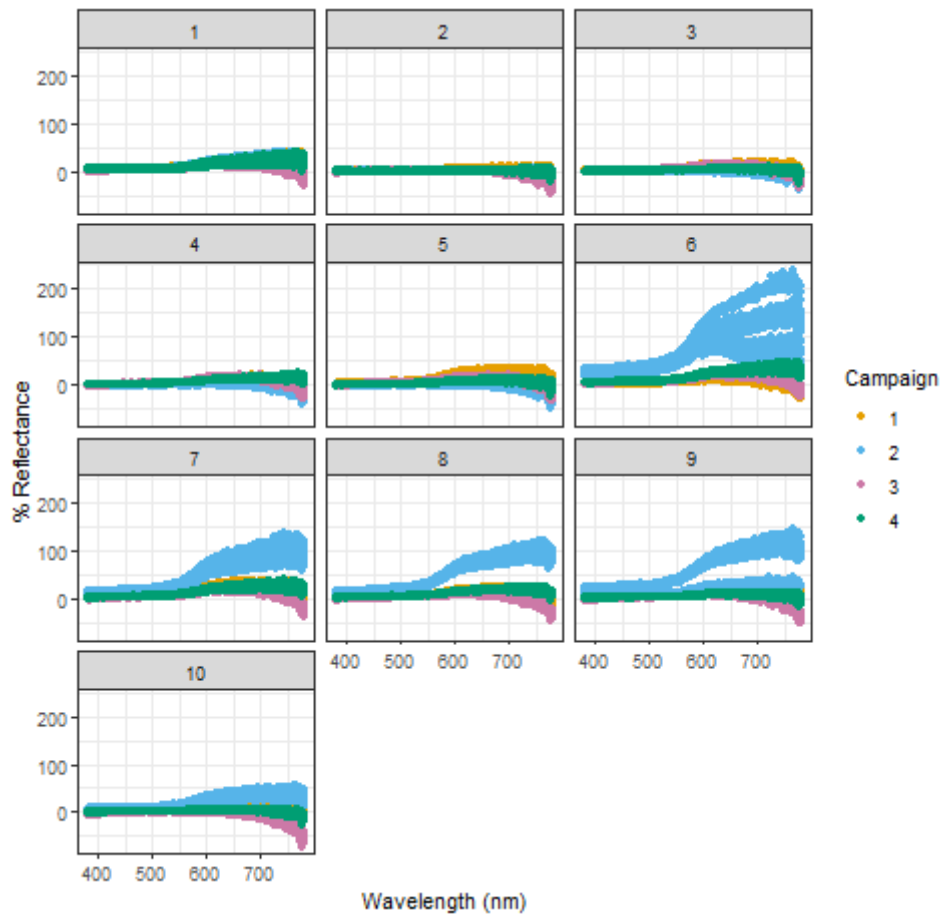


Figure 7-8: Art panel EX05_GPH wavelength (nm) versus % reflectance with different colour dots for the four campaigns. The ten panels correspond to the 10 targets.

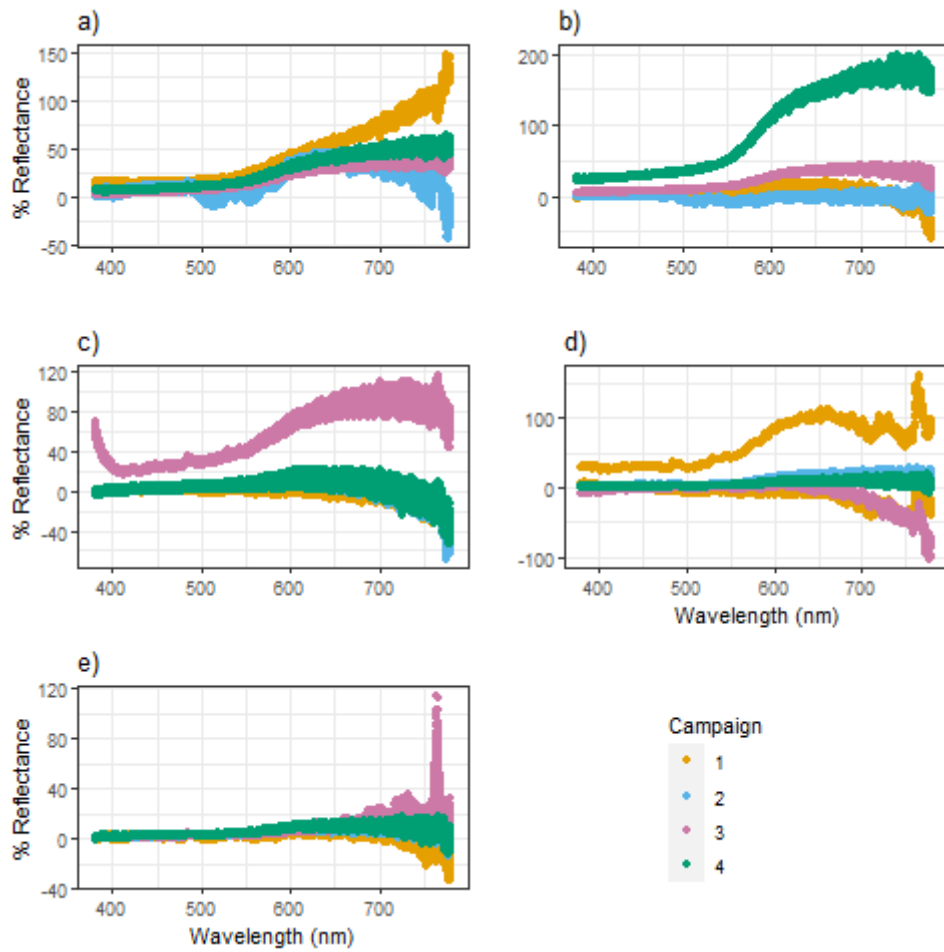


Figure 7-9: Wavelength (nm) versus % reflectance for: (a) exponential trend AQ07_GRT target 10; (b) “s” curve AQ10_GPH target 2; (c) “s” curve with a tail at the bottom AS01_DOL target 3; (d) s curve with wiggly shape and sharp peak at end AQ04_GPH target 7; (e) sharp peak AQ05_GPH target 1.

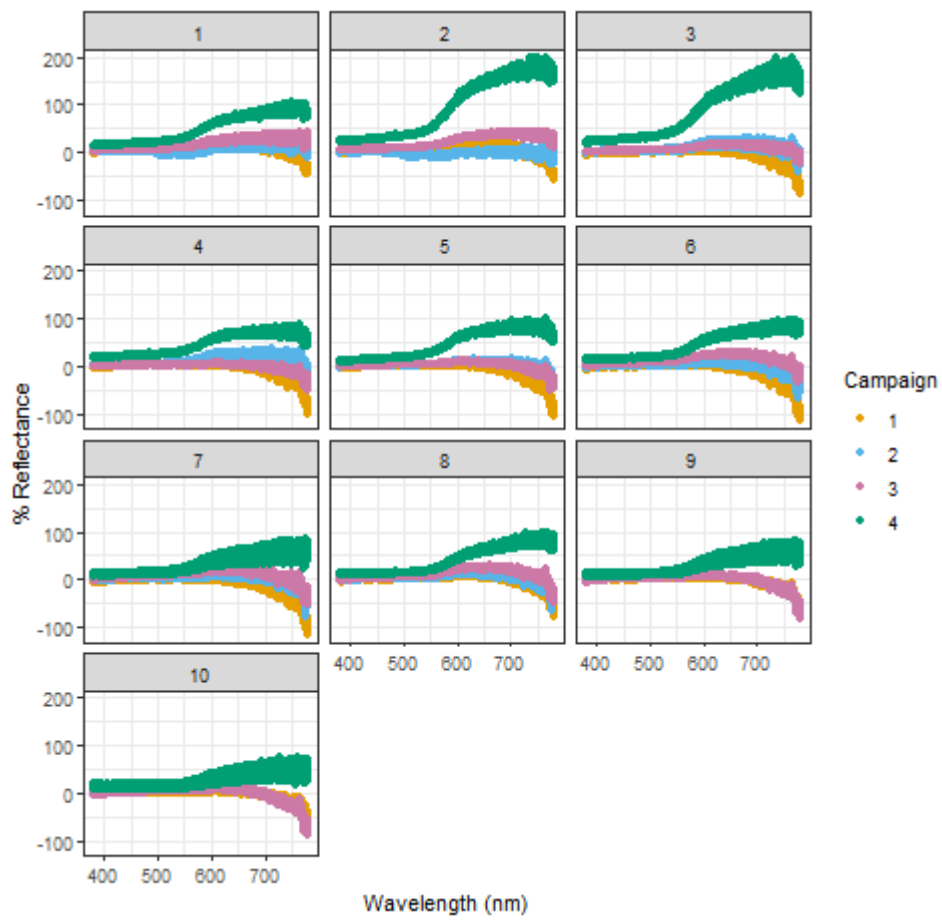


Figure 7-10: Art panel AQ 10_GPH wavelength (nm) versus % reflectance with different colour dots for the four campaigns. The ten panels correspond to the 10 targets.

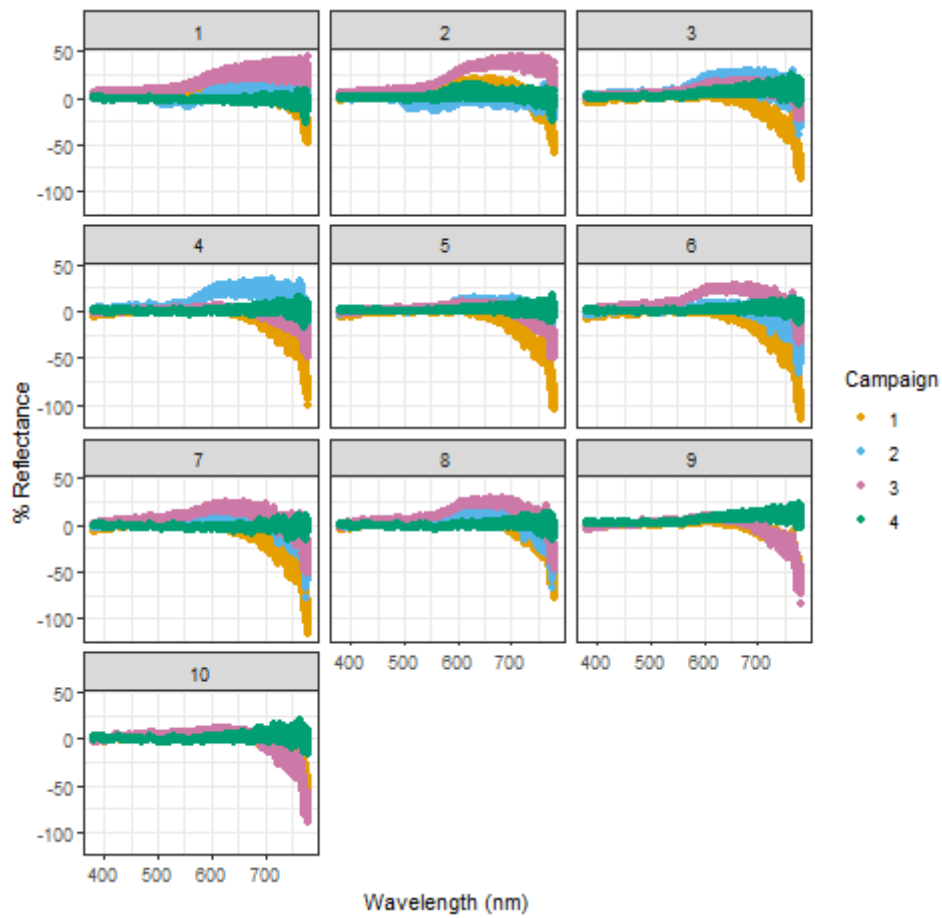


Figure 7-11: Art panel AQ 10_GPH wavelength (nm) versus % reflectance with different colour dots for the four campaigns, where data from campaign 4 was re-measured. The ten panels correspond to the 10 targets.

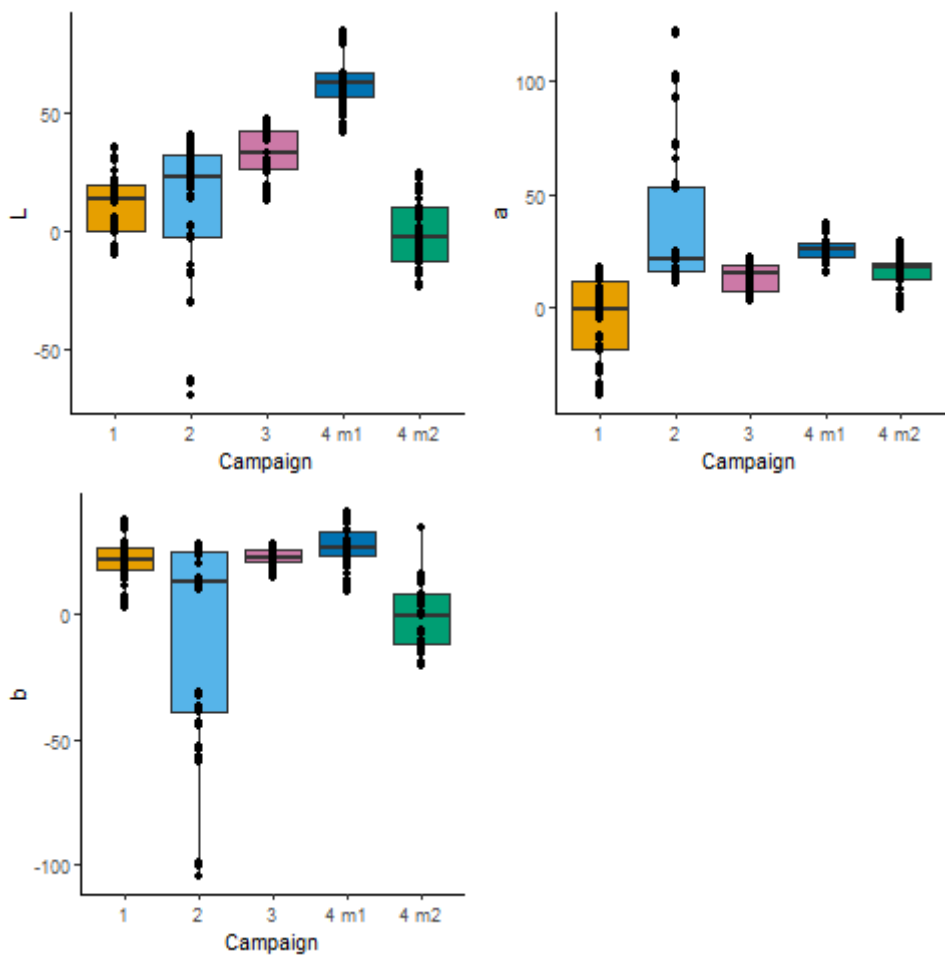


Figure 7-12: Art panel AQ10_GPH boxplot of L, a and b for each campaign; where campaign 4 m1 is the first measurement and campaign 4 m2 is the second measurement.

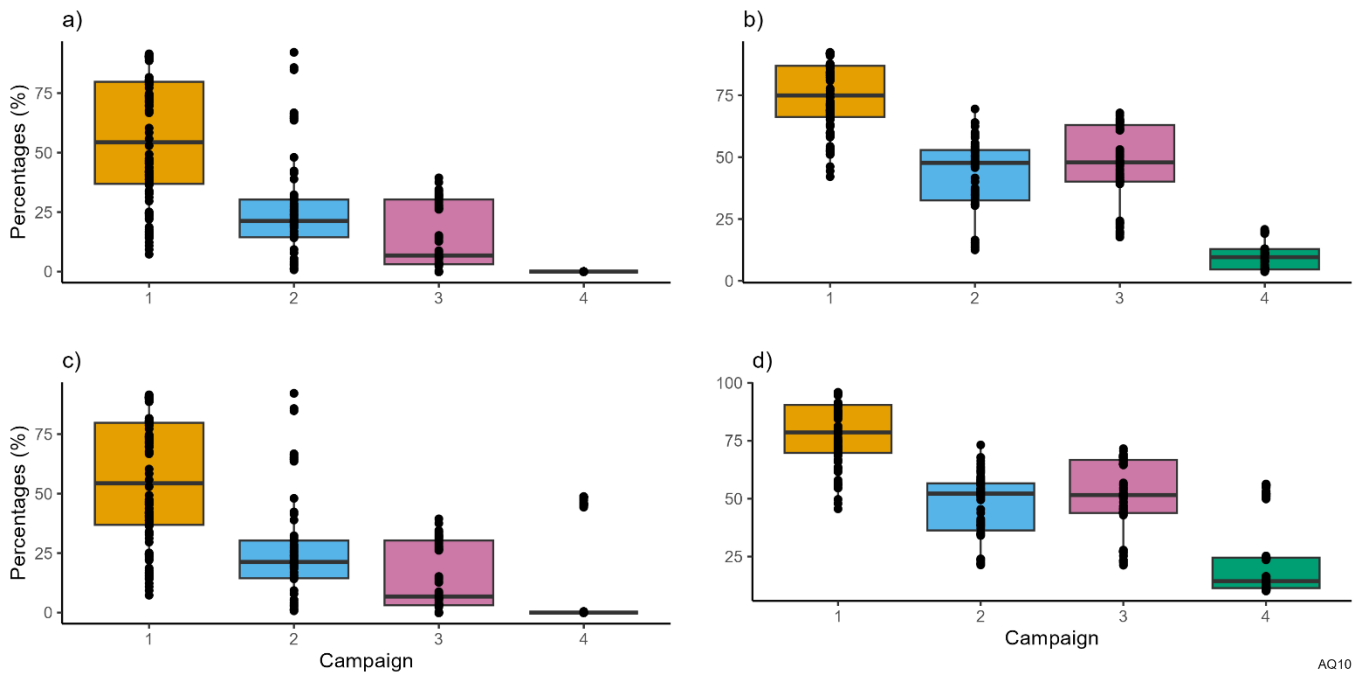


Figure 7-13: Art panel AQ10_GPH: **(a)** percentage of P values (% reflectance) that are negative between the visible spectrum (380 to 780 nm wavelength); **(b)** percentage of P values that are negative between all wavelengths; **(c)** percentage of wavelengths where the S value is less than D and R is less than D (labelled S invalid) only for wavelengths in the visible spectrum; **(d)** percentage of wavelengths where the S value is less than D and R is less than D for all wavelengths.

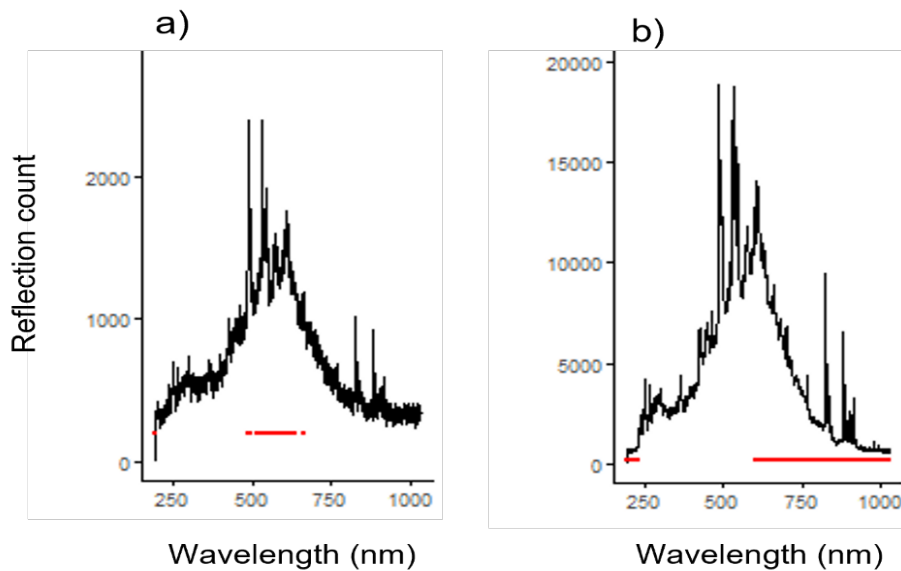


Figure 7-14: Art panel AQ10_GPH reflection count versus wavelength for **(a)** campaign 1 target 3 and **(b)** campaign 4 target 3. The red points indicate that the S (spectrum) value is less than D (dark) and R (reference) is less than D. These two figures correspond to the top right panel in Figure 7-10.

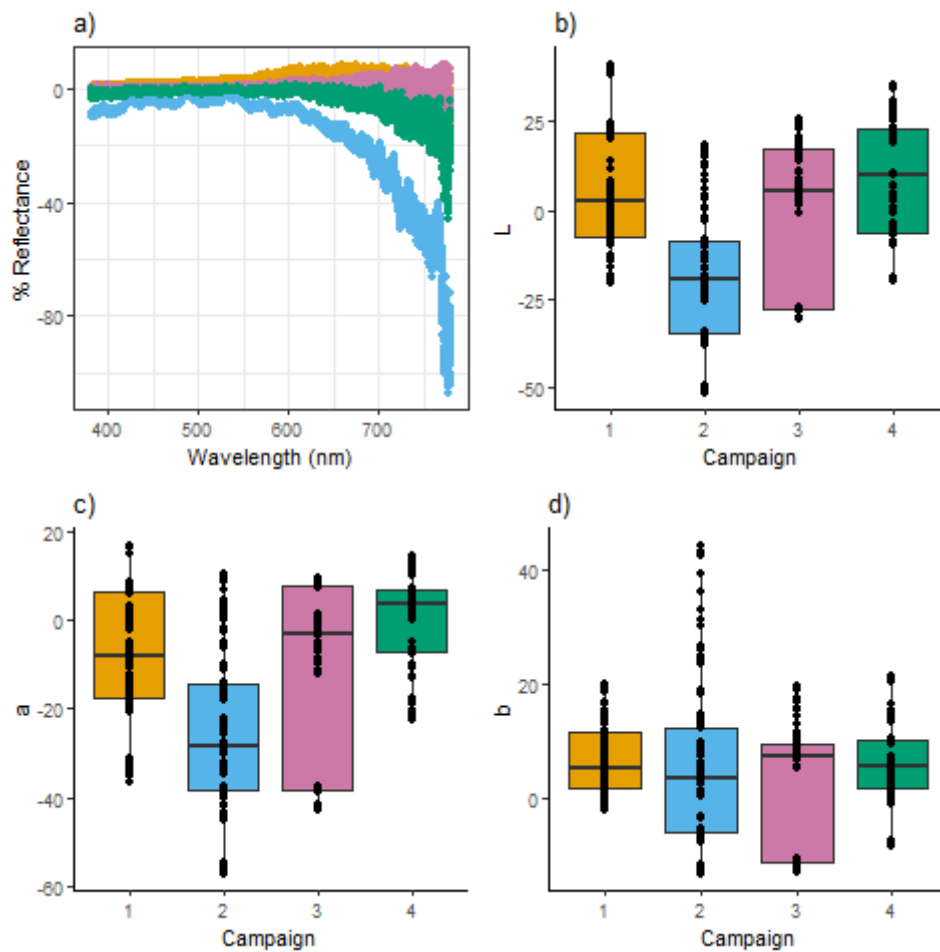


Figure 7-15: Art panel RS04_GBR: **(a)** wavelength (nm) versus % reflectance with different colour dot for the four campaigns (where orange is campaign 1, blue campaign 2, pink campaign 3 and green campaign 4) only for target 10 (all other targets have a similar trend); **(b)** boxplot of L* values from CIELAB for each campaign and for all targets; **(c)** boxplot of a* values from CIELAB for each campaign; **(d)** boxplot of b* values from CIELAB for each campaign

Smooth trend models

Two generalised additive mixed models (GAMs) were used in an exploratory analysis to examine the trend in percent reflectance over the visible wavelengths for each art panel.

First, a GAM was fitted to each target in each campaign for each art panel (i.e., one model for each art panel), thus resulting in 40 curves fitted for each art panel. For example, Figure 7-16 shows the 40 curves fitted for RS04_GBR. For campaign 1, most targets have a similar decreasing trend after around 600 nm, except one target has an “s” shaped curve. For campaign 2, all the targets have a similar trend, and after 600 nm the percent reflectance has a large decrease. Almost all targets for campaigns 3 and 4 have a similar decreasing trend after 600 nm. One target in campaign 3 has a linear increasing trend.

Another GAM was performed for each art panel that fitted one trend line to each campaign. Only 7.41% of the 54 rock art panels had the same trend over all four campaigns (see Table 7-1). For example, for AQ03_DOL, all four campaigns started around 0% reflectance at the beginning of the visible spectrum (380 nm), there was a peak around 625 nm of about 10% reflectance, then the reflectance decreased to zero or about -5% (Figure 7-17).

The percentage of art panel that had a similar trend for campaigns 1 to 3 was 11.11 %; campaigns 1, 3 and 4 was 9.26%; and campaigns 2 to 4 was 14.81% (Table 7-1).

For example, for campaigns 1 to 3, AQ10_GPH had similar trends lines, with all three campaigns starting around 0%, a gentle increase to around 650 nm then a decreasing trend (Figure 7-18). The first measurement of campaign 4 had a similar trend at the beginning of the visible spectrum, but shifted up by starting around 15%, but at 550 nm had a big increase in reflectance to almost 100% at the end of the visible spectrum (780 nm) (see the dark blue line in Figure 7-18). The second measurement for campaign 4 had an almost flat trend for the whole visible spectrum, with the reflectance around 0 to 5% (Figure 7-18 green line). Another example, AQ11_GPH had a similar trend for campaigns 2 to 4 but campaign 1 was very different trend (Figure 7-19).

Figure 7-20 shows that for RS04_GBR that campaigns 1, 3 and 4 had a very similar trend. For campaign 2 the trend line was shifted higher than the other campaigns between 380 nm and 600 nm wavelengths, after which there was a larger decreasing trend than the other three campaigns.

Table 7-2 displays which campaigns are the same and have a similar curve for each art panel.

Table 7-1: Percentage of two or more campaigns that have the same trend line.

Comparison	Percent
all the same	7.41%
C1, C2 and C3	11.11%
C1, C3 and C4	9.26%
C2, C3 and C4	14.81%
C1 and C2	12.96%
C2 and C3	12.96%
C3 and C4	7.41%
C2 and C4	9.26%

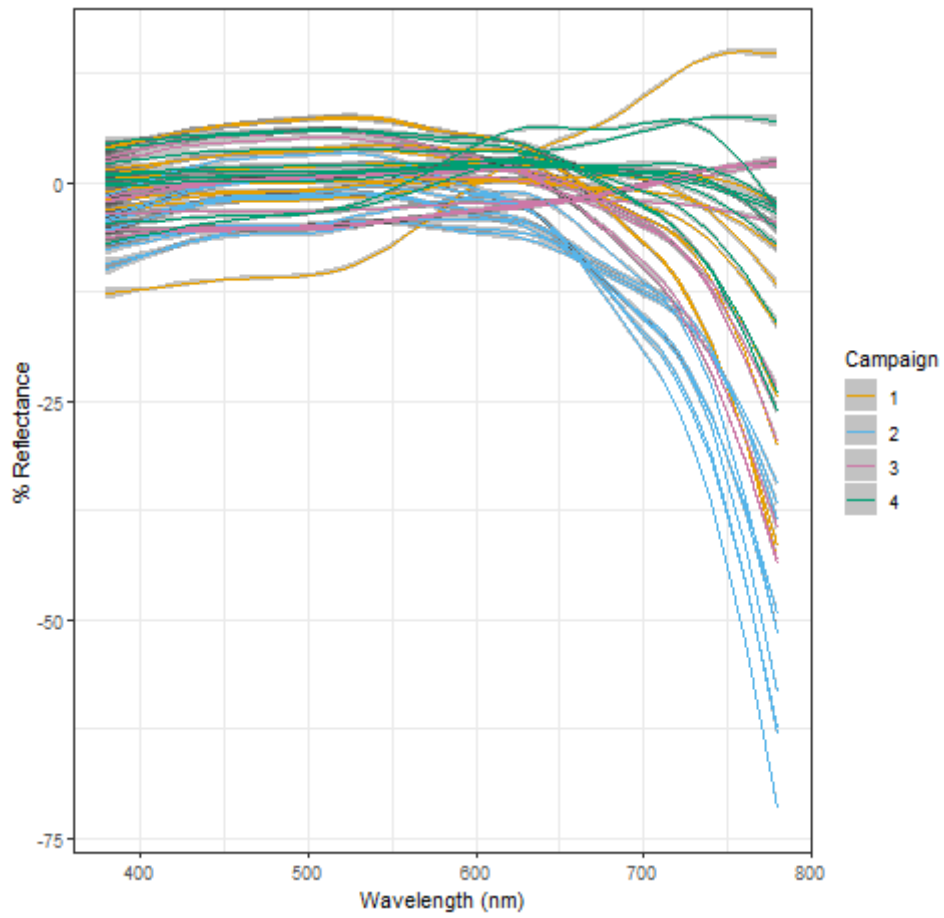


Figure 7-16: Art panel RS04_GBR GAM fit of wavelength (nm) versus reflectance (%), with one curve for each target in each campaign. Solid coloured lines are the predicted reflectance for each campaign and the grey shaded area is the 95% prediction intervals.

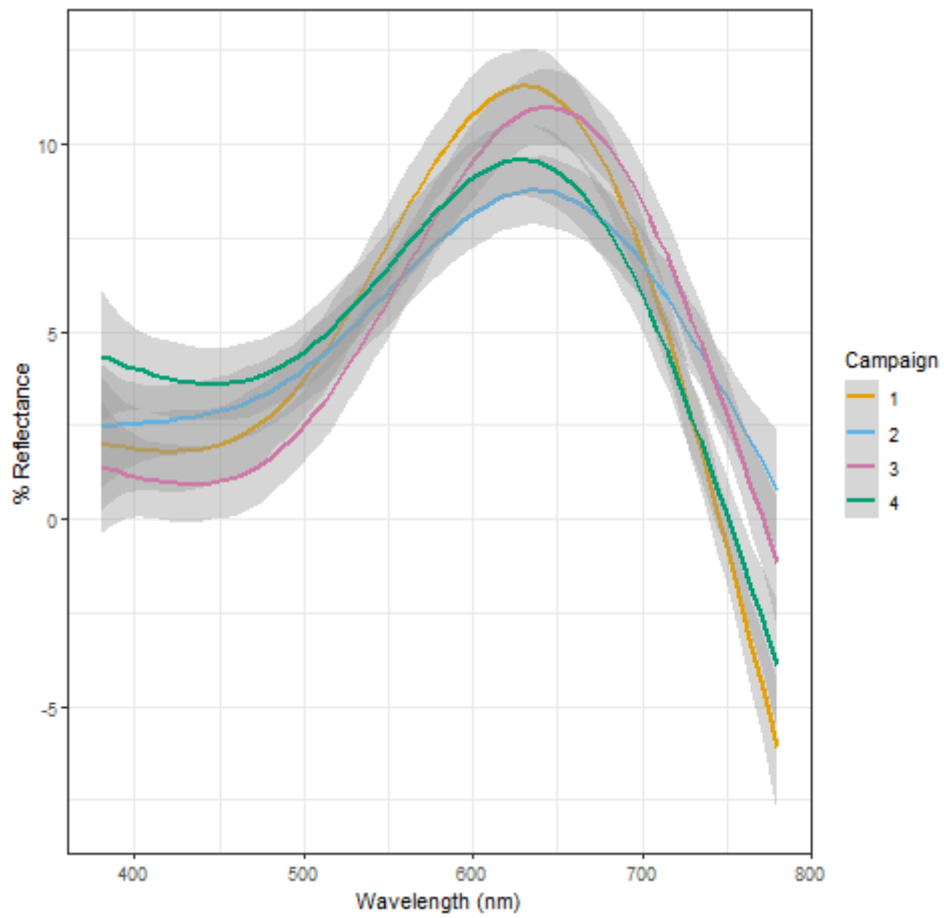


Figure 7-17: Art panel AQ03_DOL GAM fit of wavelength (nm) versus reflectance (%) one curved fitted for each campaign. Solid coloured lines are the predicted reflectance for each campaign and the grey shaded area is the 95% prediction intervals.

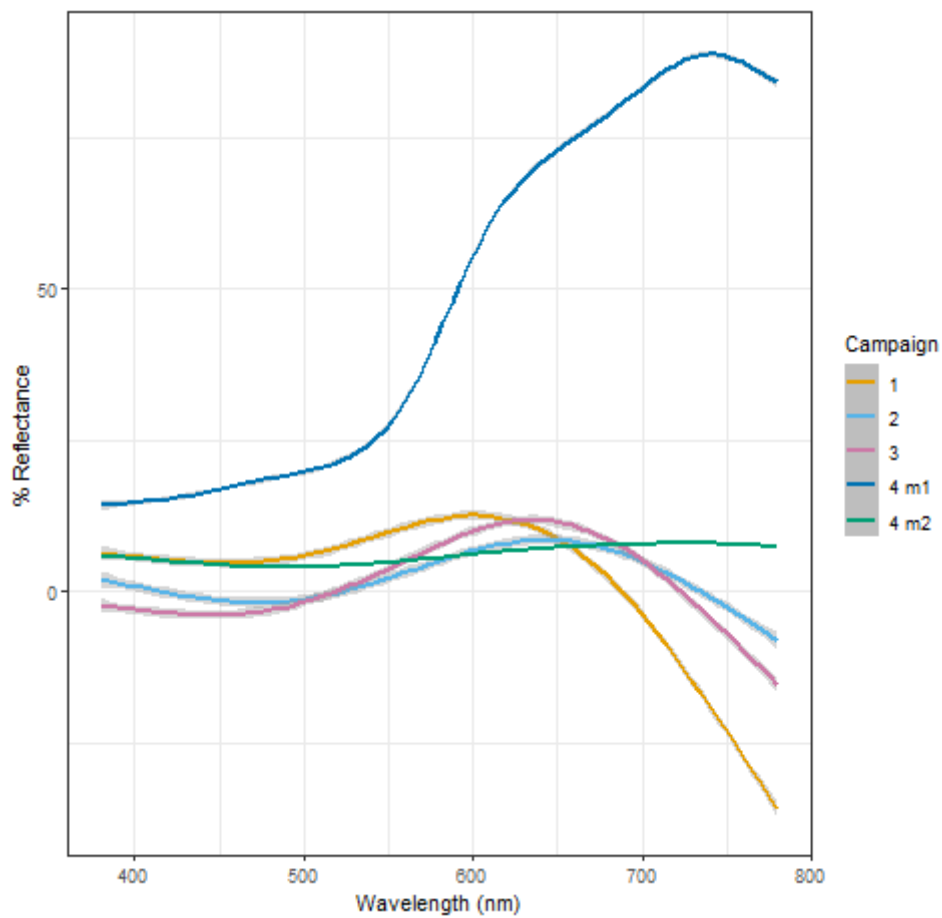


Figure 7-18: Art panel AQ10_GPH GAM fit of wavelength (nm) versus reflectance (%) one curved fitted for each campaign. Solid coloured lines are the predicted reflectance for each campaign and the grey shaded area is the 95% prediction intervals. Where campaign 4 m1 is the first measurement and Campaign 4 m2 is the second measurement.

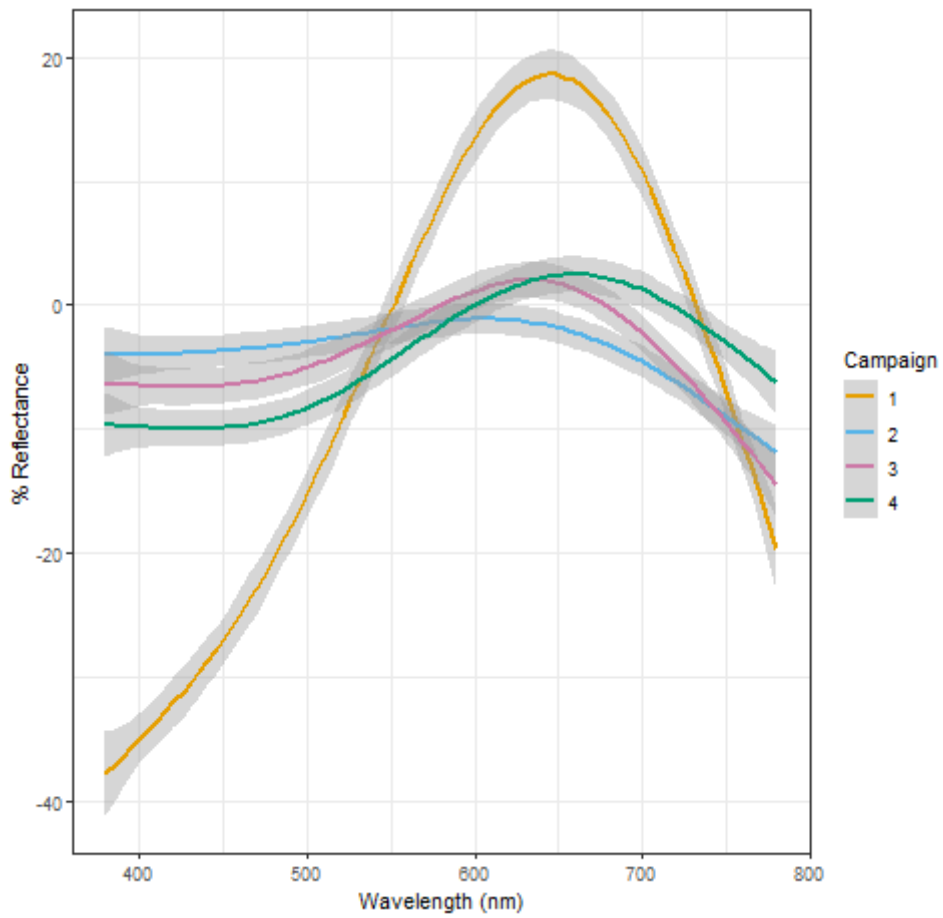


Figure 7-19: Art panel AQ11_GPH GAM fit of wavelength (nm) versus reflectance (%) one curved fitted for each campaign. Solid coloured lines are the predicted reflectance for each campaign and the grey shaded area is the 95% prediction intervals.

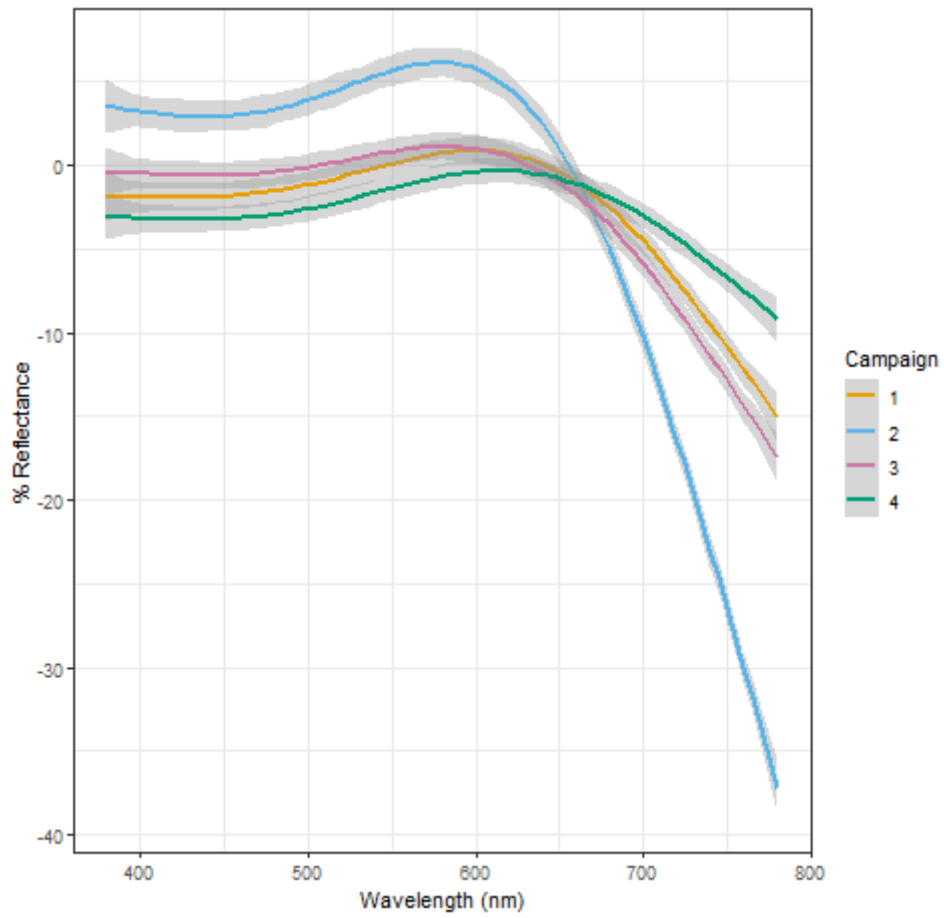


Figure 7-20: Art panel RS04_GBR GAM fit of wavelength (nm) versus reflectance (%) one curved fitted for each campaign. Solid coloured lines are the predicted reflectance for each campaign and the grey shaded area is the 95% prediction intervals.

Table 7-2: GAM results for the model fitted to each art panel and one curve fitted to each campaign. Where the same GAM result number for a particular art panel, indicates no difference in the campaigns and a similar curve.

Site	Campaign 1	Campaign 2	Campaign 3	Campaign 4
AQ02_GPH	1	2	2	3
AQ03_GBR	1	2	2	2
AQ03_GPH	1	2	1	3
AQ03_DOL	1	1	1	1
AQ04_GPH	1	1	2	3
AQ05_GPH	1	NA	2	3
AQ06_GPH	1	2	3	4
AQ06_GBR	1	2	3	3
AQ07_GRT	1	1	1	2
AQ07_GPH	1	2	3	3
AQ08_GPH	1	2	2	2
AQ09_GBR	1	2	2	2
AQ09_GPH	1	NA	1	1
AQ10_GPH	1	1	1	2
AQ10_GPH (m2)	1	1	1	2
AQ11_GPH	1	2	2	2
AQ12_BAS	1	2	NA	1
AQ13_GPH	1	2	1	1
AQ14_GPH	1	2	2	2
AQ15_GBR	1	2	2	2
AQ16_GBR	1	1	1	1
AQ17_GPH	1	2	3	4
AQ18_GPH	1	2	2	3
AS01_DOL	1	1	2	3
AS02_GRT	1	1	2	1
AS02_DOL	1	2	1	1
EX02_GPH	NA	NA	1	NA
EX03_GPH	1	1	2	2
EX04_GBR	1	1	1	1
EX05_GPH	1	2	1	1
EX06_GPH	NA	1	1	1
EX07_GPH	1	1	1	2
EX08_GPH	1	1	1	1
EX09_GPH	1	1	1	2
EX09_GBR	1	1	2	1
RS01_GPH	1	1	2	3
RS02_GBR	1	2	NA	3
RS03_GPH	1	2	1	3

Site	Campaign 1	Campaign 2	Campaign 3	Campaign 4
RS04_GPH	NA	1	2	NA
RS04_GBR	1	2	1	1
RS05_GPH	NA	1	2	2
RS06_GPH	1	1	NA	1
RS07_BAS	1	2	3	4
RS08_BAS	1	1	1	2
RS08_DOL	1	2	2	3
RS09_BAS	1	2	3	2
RS09_DOL	1	2	3	1
RS10_GBR1	1	2	3	2
RS10_GBR2	1	NA	1	2
RS11_GPH	1	2	3	2
RS13_GBR	1	1	2	2
RS14_GPH	1	2	3	2
RS16_GBR	1	2	3	2
RS17_GPH	1	2	3	4
RS18_GPH	1	2	2	2

Note: (a) m2 denotes the second measurement taken at this site.

7.2 Inorganic geochemistry - pH, Eh, Cl

7.2.1 Background

During the study design phase, The Murujuga Rock Art Stakeholder Reference Group (**SRG**) suggested that the study design be extended to include measurement of pH on rock surfaces. This proposal is in response to some recent scientific literature, which advanced the hypothesis that industrial output could damage the Murujuga rock surfaces by deposition of gases which form acidic or basic solutions on the rock surface, with sufficient strength to erode the patina.

The study design was extended to include measurement of pH (negative value of $\log_{10} [H^+]$ where the activity of the hydrogen ion is measured on the moles per litre scale), Eh (via oxidation-reduction potential ORP) and Chloride ion (Cl^-) concentration. The field technique is described in Section 3.2.2.

In each field campaign, pH, ORP and Cl^- concentration were measured at each sample rock, with three replicate measurements per rock at each visit, except that Cl^- concentration and ORP were not measured in campaign 1 due to an instrument breakdown.

The results of the initial data analysis (IDA) and exploratory data analysis (EDA) of these inorganic geochemical data are reported here. IDA aims to identify any technical problems and indications of invalid results. EDA investigates evidence for any association between pH/Eh/Cl and explanatory variables. In particular, EDA should evaluate whether rock type could have an effect on typical pH/Eh readings (perhaps because of differences in mineral composition and surface texture).

7.2.2 pH observations

Figure 7-21 shows boxplots of the observations of pH for each campaign. The median pH observed in campaign 1 is close to the neutral pH value of 7, while the subsequent campaigns have pH values that are quite acidic. For comparison, acid rain has a pH around 4.3. The variability of pH observations is also much higher in campaign 1 than in the subsequent campaigns.

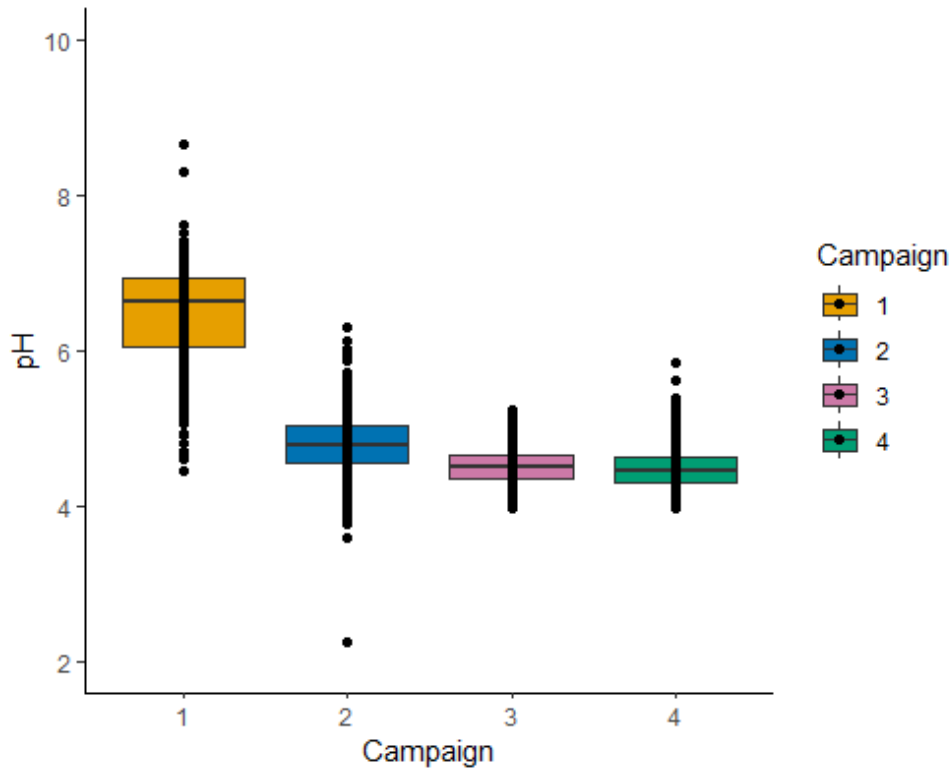


Figure 7-21: Boxplots of pH by campaign

Figure 7-22 shows boxplots of the pH observations from each campaign, broken down by Rock Type. The panel for campaign 1 suggests that there may be differences in pH between different rock types, and in any case, that rock type should be retained as an explanatory variable in the analysis. The subsequent campaigns did not support this so strongly.

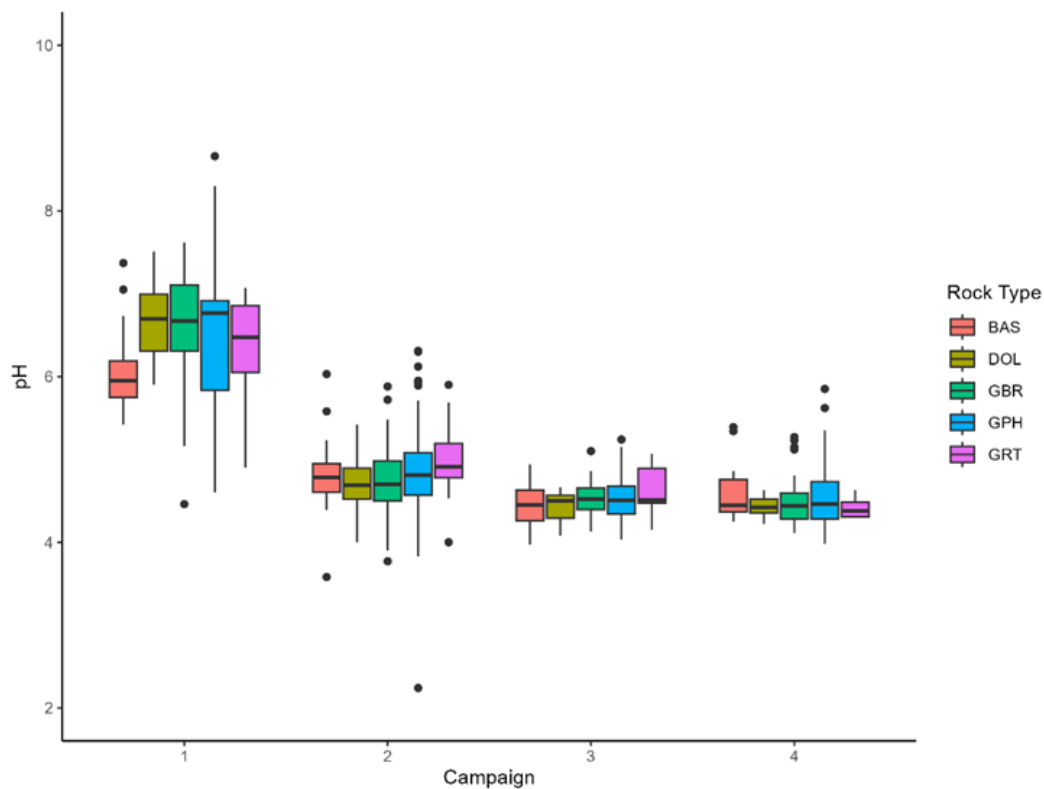


Figure 7-22: Boxplots of pH by rock type for each campaign

The difference in average pH between the campaigns has several possible explanations, which should be investigated:

- a) there could be a seasonal effect on pH related to temperature, rainfall and other environmental factors. It has been hypothesised (Bednarik 2007) that large rainfall events have a large effect on the pH of rock surfaces. campaign 1 was preceded by a long dry period, whereas campaigns 2-4 were preceded by, or took place during, rain.
- b) the first campaign was the first field trial of the pH-measurement technique and it could have been affected by changes in the technique due to the operator's learning curve, revision of the technique, equipment changes, equipment failure, deterioration of reagents and other factors.

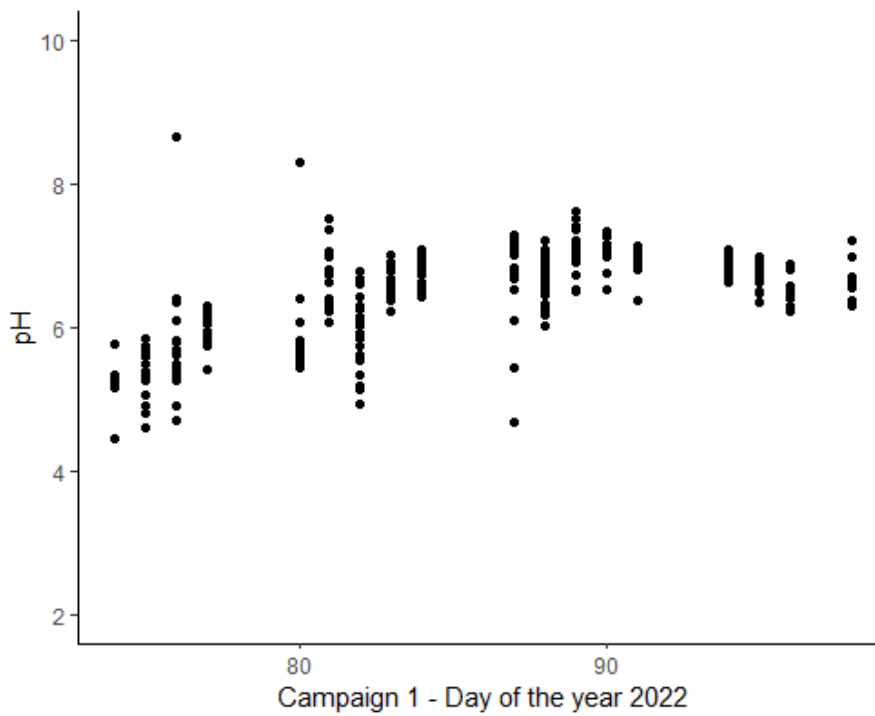


Figure 7-23: pH observations against calendar date (campaign 1)

Some support for hypothesis (b) is provided by Figure 7-23 showing pH measurements in campaign 1 plotted against calendar date. There is a slight suggestion of a trend over time. This is not conclusive evidence for (b) because the successive observations are not replicates; the apparent trend could be an artefact of the sequence of sites that were visited.

One possible explanation for a trend over time is that there was an unexpected shortage of distilled/deionised water during campaign 1, so that field workers were obliged to take distilled/deionised water from containers that may have been opened hours earlier for use at a previous site. Exposure to air permits CO₂ to diffuse into the water, reducing its pH. This is consistent with the trend observed over time. A more detailed analysis will need to be conducted.

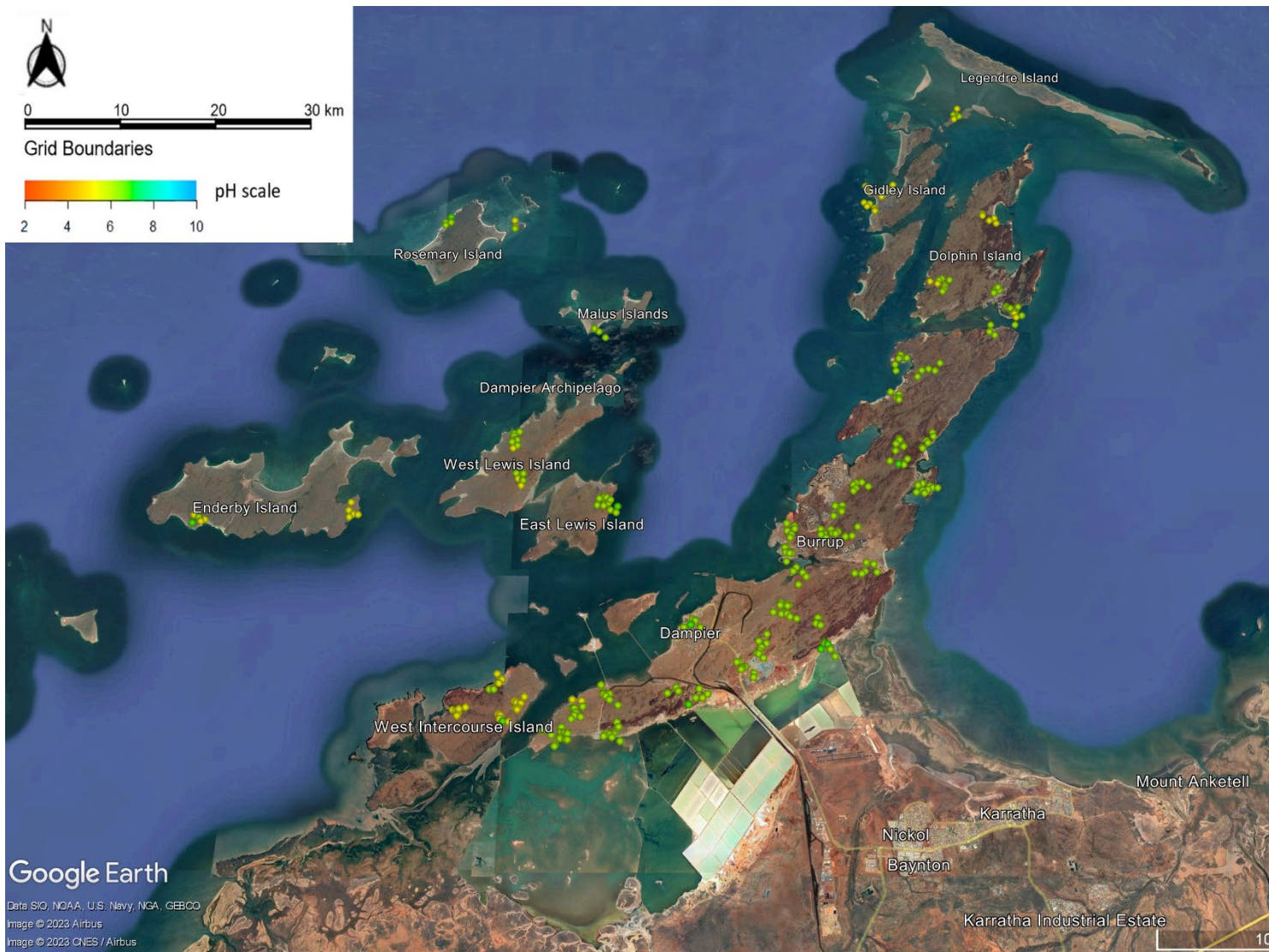


Figure 7-24 shows the pH measurements from campaign 1 plotted as coloured dots at their actual spatial locations on Murujuga, coloured according to the pH value. There were replicate observations at each location, and these have been visually separated on the plot by randomly displacing (jittering) the locations.

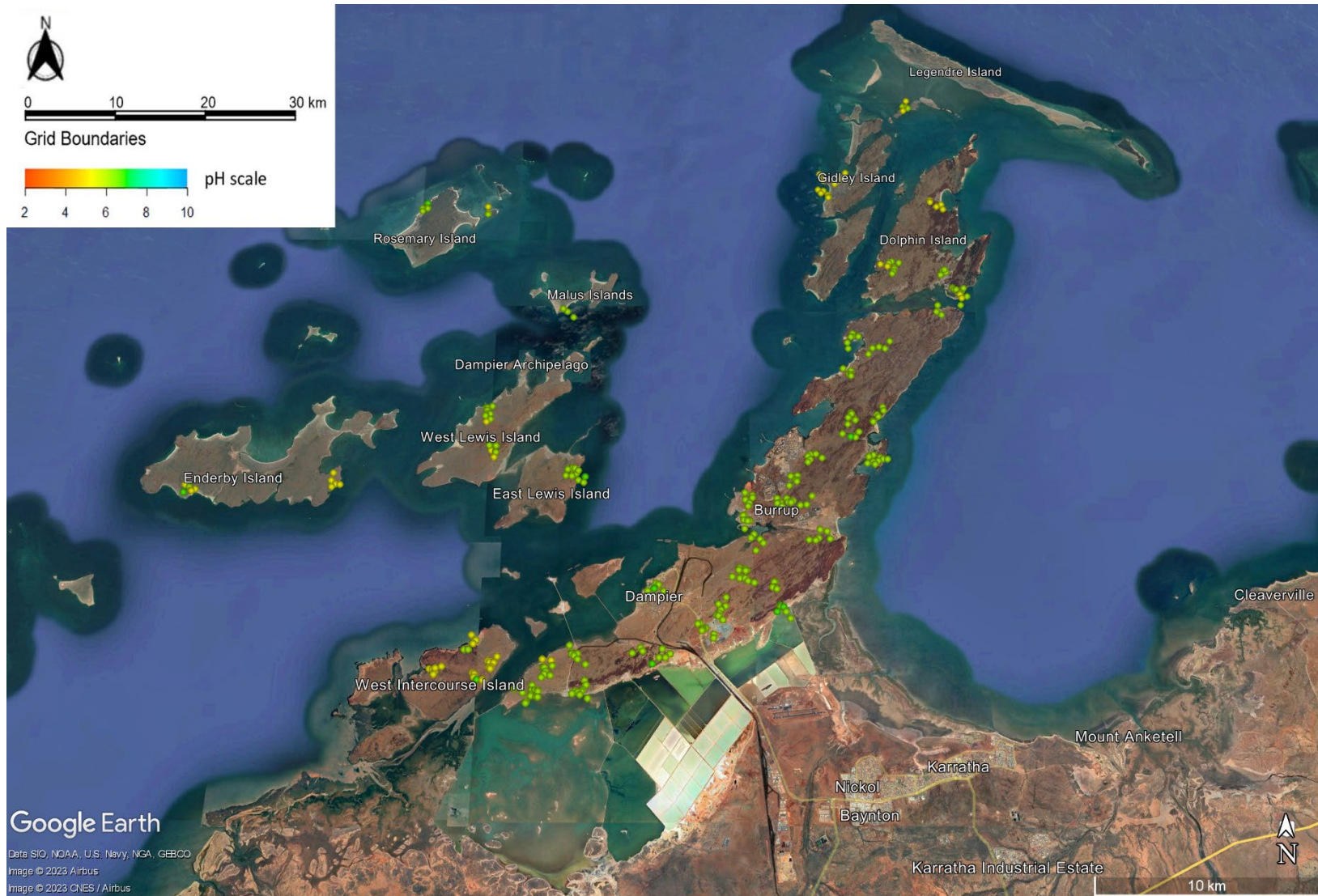


Figure 7-24: pH measurements, shown as dots with colour representing pH value, mapped at the spatial locations of the sample rocks. Campaign 1 only.

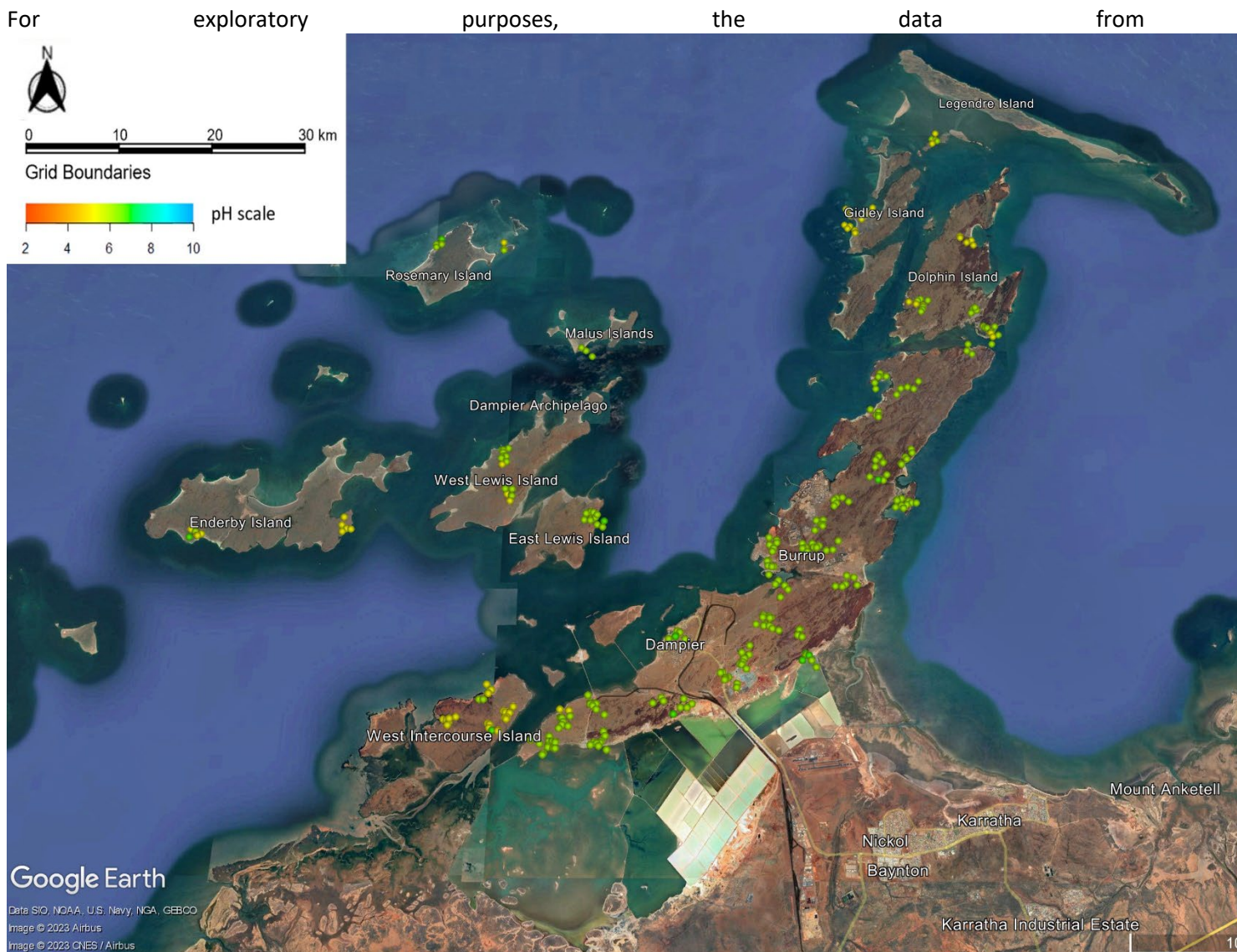


Figure 7-24 were spatially interpolated to give a pH value at every location on Murujuga. Figure 7-25 shows the results of spatial interpolation of the pH data using Nadaraya-Watson kernel smoothing. For reference, the blue line in this figure follows the main coastline, and the grey polygon is Legendre Island. The colour map used in each of the four panels is the same and is the standard colour representation of pH values, as shown at the bottom of Figure 7-25. The colours show immediately that the interpolated pH from campaign 1 is closer to the neutral value of 7 (represented as green) while the interpolated pH values from other campaigns are relatively acidic (represented as yellow to orange). To show finer detail, contour lines are superimposed on each plot using a different choice of contour levels for each panel. The panel for campaign 1 suggests a spatial ‘trend’ insofar as the pH measurements from the middle of the peninsula were close to 7, while relatively acidic values close to 5 were obtained in the north and south-west of the study area.

Spatial interpolation was also performed using kriging and spatial copula techniques, yielding quite similar results.

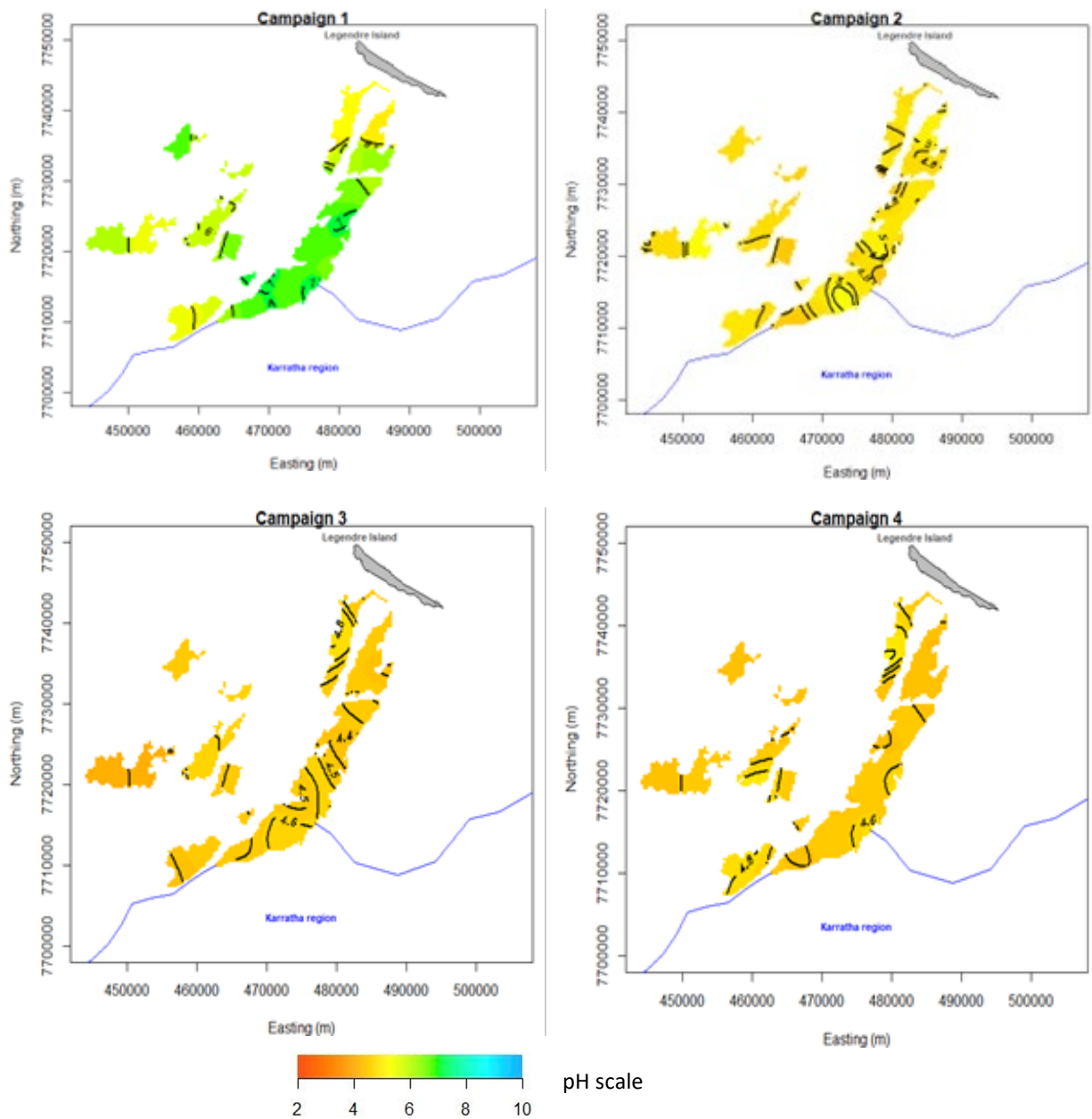


Figure 7-25: Spatially interpolated pH values. Colour map overlaid with contour lines. The blue line represents the Karratha coastline. The grey polygon is Legendre Island.

The spatial trend in mean pH is about 1 pH unit difference, being strongest in the data from campaign 1. A true trend could be a result of spatially varying environmental effects such as dryness and rainfall, or spatially varying mineralogical composition. An apparent trend could also be an artefact of the smoothing technique, although it persisted across the different choices of technique that were tried.

These findings suggest that:

1. Seasonal/weather effects could be substantial. This needs to be evaluated using observations over more time periods. The second year of studies should include four campaigns during the four different seasons. These campaigns do not need to visit every site on every occasion, but the four campaigns should be designed so that a reliable estimate of seasonal effect can be calculated, as well as estimates of other effects.

2. For the data analysis of the combined (pooled) set of observations from all campaigns, it would be prudent to repeat each analysis with and without the data from campaign 1.
3. Possible dependence of pH on rock type, and on spatially-varying explanatory variables, should be included in the analysis.

7.2.3 Chloride (Cl⁻) observations

Chloride ion concentration (in parts per million) was measured at each rock in triplicate, starting from campaign 2, because of a device breakdown in campaign 1.

Histograms of the recorded values of Cl⁻ concentration show that they vary over several orders of magnitude and have a highly skewed distribution. Accordingly, a logarithmic transformation was used to analyse these data.

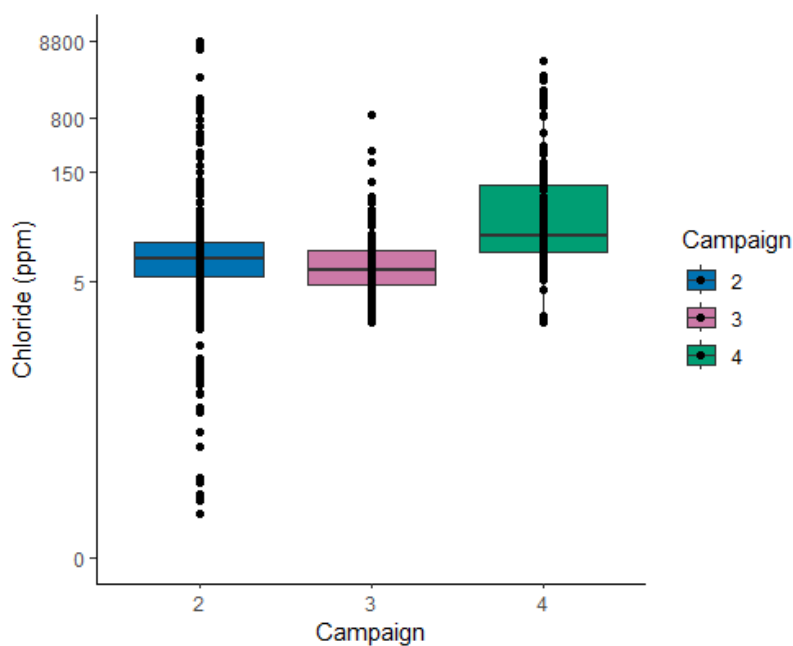


Figure 7-26: Boxplots of Cl⁻ by campaign. Note logarithmic scale.

Figure 7-26 shows boxplots of Cl⁻ concentration from each of the campaigns 2, 3 and 4 using a logarithmic scale. The first and third quartiles (see Table 1-3 for the definition of quartile) are about 5 to 20 ppm in campaigns 2 and 3, and about 20 to 100 ppm in campaign 4. The median Cl⁻ concentration is higher in campaign 4 than in campaigns 2 and 3.

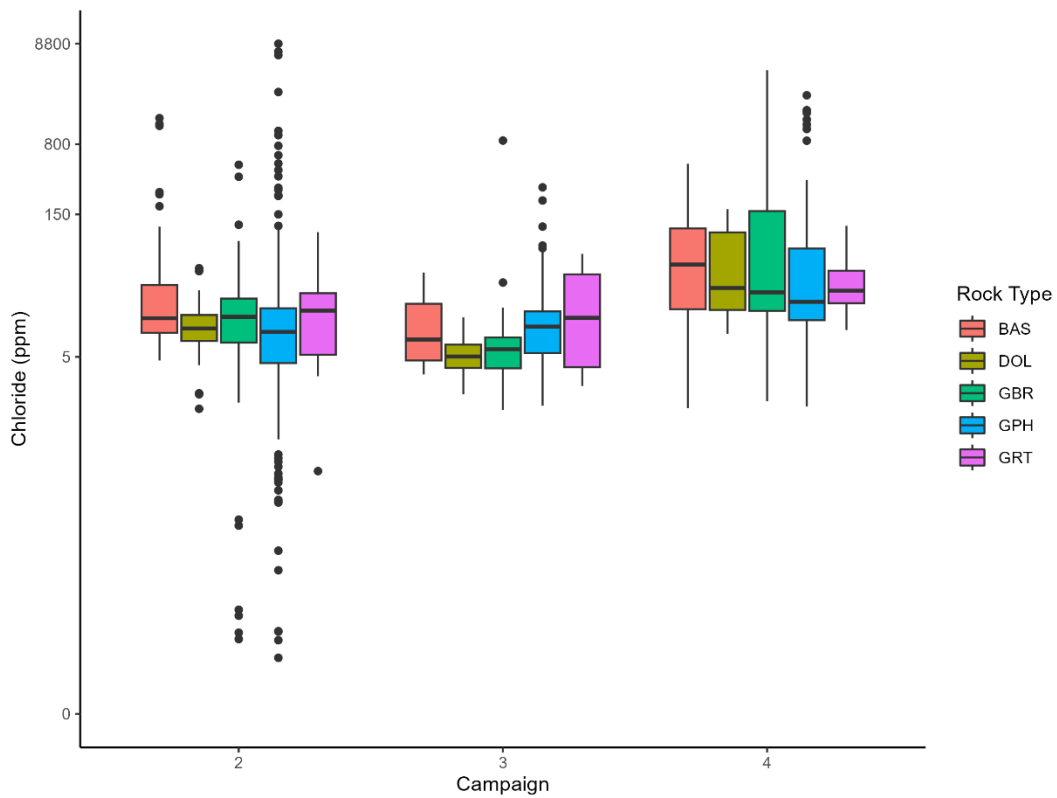


Figure 7-27: Boxplots of Cl⁻ by rock type for different campaigns. Note logarithmic scale.

Figure 7-27 shows the same data broken down by rock type. Note that in campaign 2 the median Cl⁻ values are similar for each rock type. However, many extreme Cl⁻ values (very low and high) are observed in the granophyre and also gabbro rock types. The basalt rocks showed some higher Cl⁻ values. In campaign 3, the medians are not as similar for each rock type as in campaign 2. However, some extreme Cl⁻ values are again observed in granophyre and gabbro rock types. In campaign 4, many extreme Cl⁻ values are observed in gabbro and granophyre rock types.

Overall, analysis showed a tendency for gabbro and granophyre rocks to have a more extreme range of Cl⁻ values.

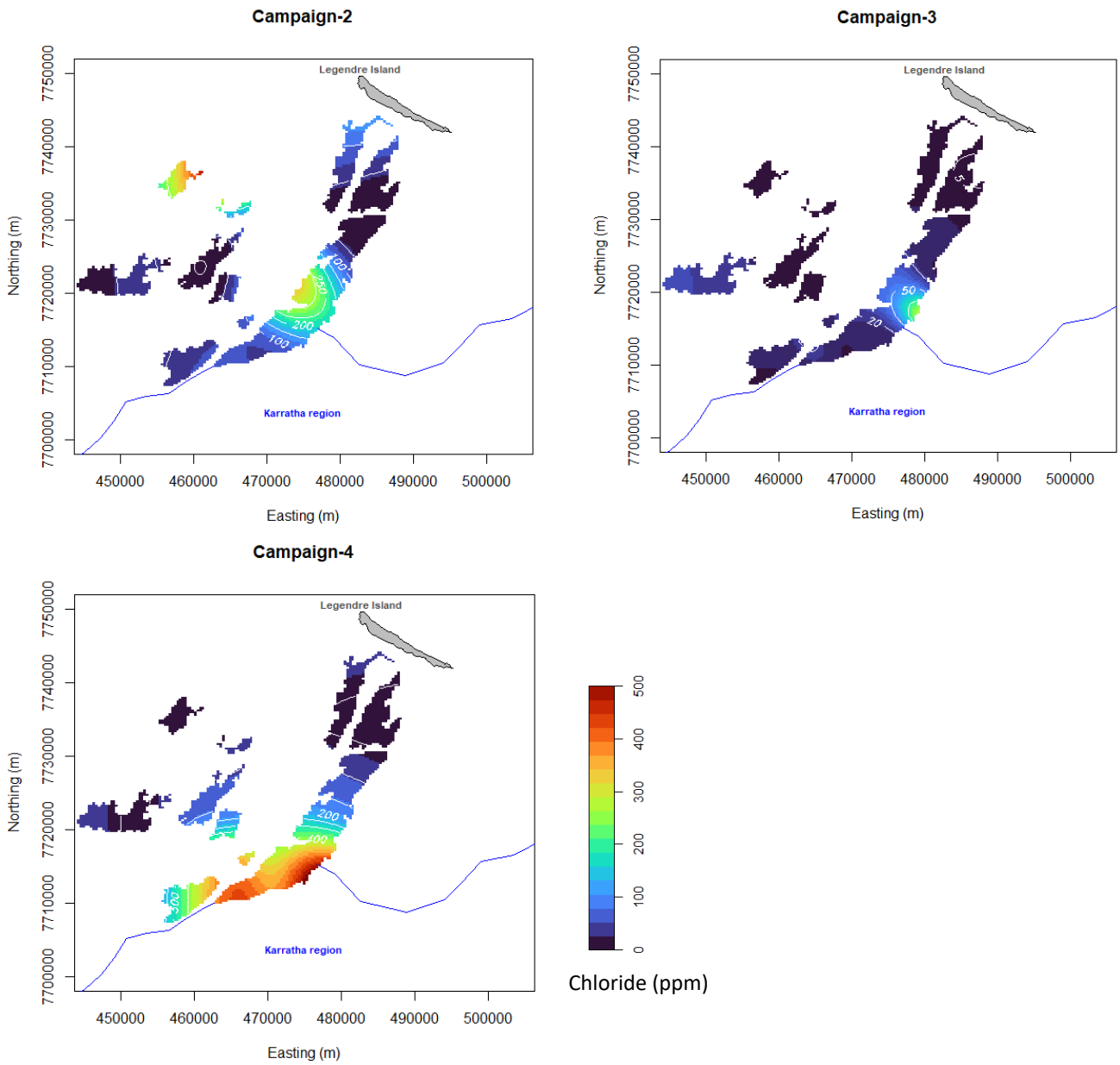


Figure 7-28: Spatially smoothed chloride ion (Cl⁻) concentration. Colour map overlaid with contour lines. The blue line represents the Karratha coastline. The grey polygon is Legendre Island.

Figure 7-28 shows a spatial interpolation of the Cl⁻ concentration values, using Nadaraya-Watson spatial smoothing on a logarithmic scale. Lower Cl⁻ values correspond to blue colours. Higher interpolated values of Cl⁻ concentration are observed in the areas around Karratha, Dampier and Rosemary Island. More complex interpretations are not warranted by the data at this stage.

7.2.4 Oxidation-reduction potential (ORP) observations

Owing to the failure of an instrument probe, ORP data were only measured from campaign 2 onwards.

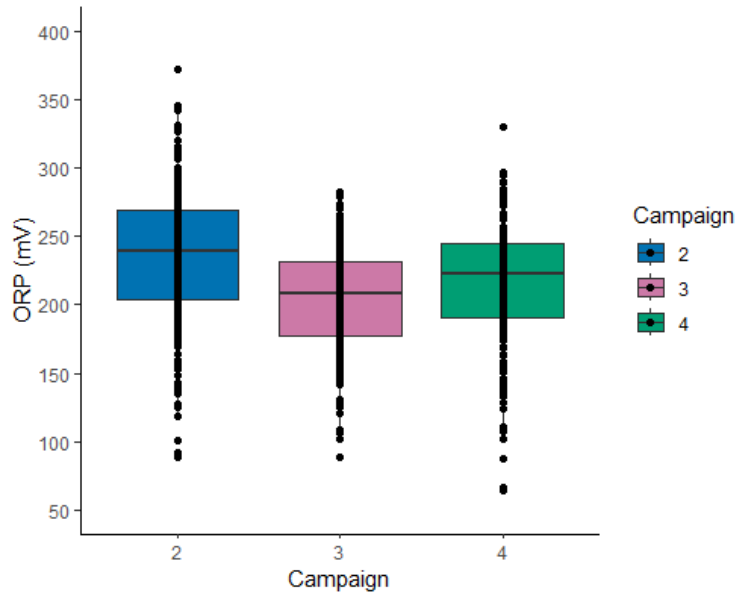


Figure 7-29: Boxplots of ORP by different campaigns.

Figure 7-29 shows boxplots of the ORP values from each campaign. Values range between 80-400 mV with quartiles at about 200, 250 and 300 mV, suggesting good approximation by a normal distribution for exploratory purposes. Values observed in campaign 3 are slightly lower than those observed in campaigns 2 and 4.

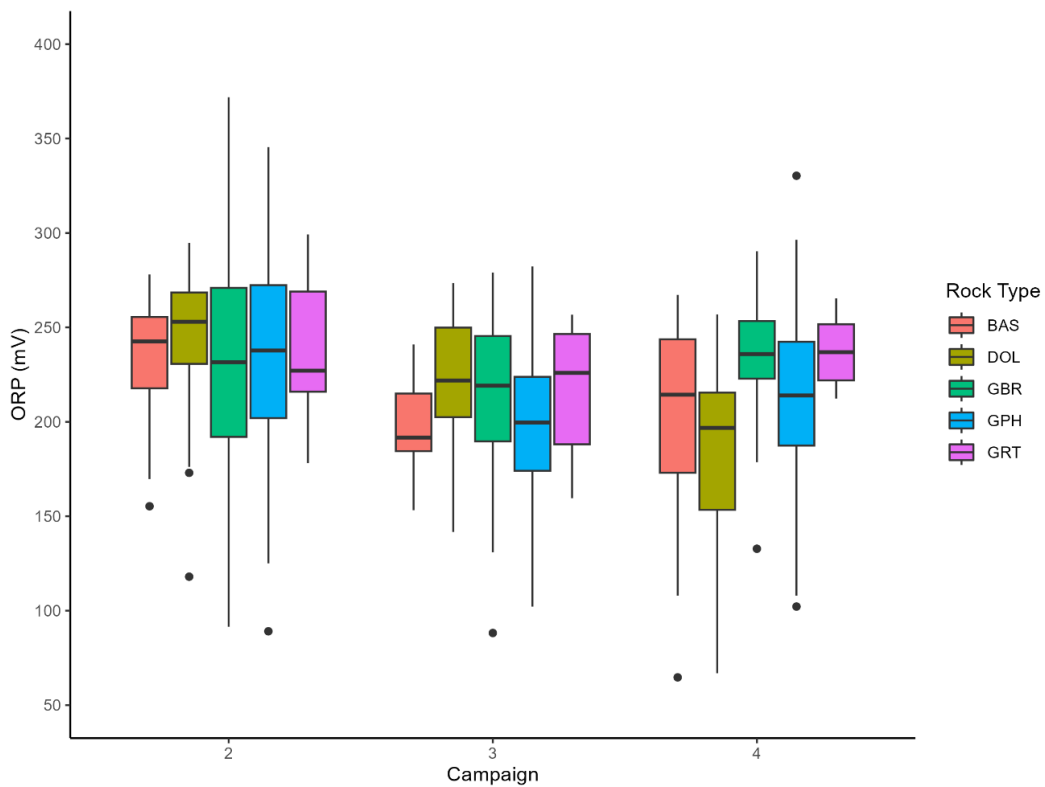


Figure 7-30: Boxplots of ORP by rock type for different campaigns.

Figure 7-30 shows boxplots of ORP values broken down by rock type. Again, the values observed in campaign 3 tend to be slightly lower than those observed in campaigns 2 and 4 for each rock type. Owing to the variability of the data, more complex interpretations are not warranted by the data at this stage.

Figure 7-31 shows spatially interpolated ORP values, again using Nadaraya-Watson smoothing on a logarithmic scale.

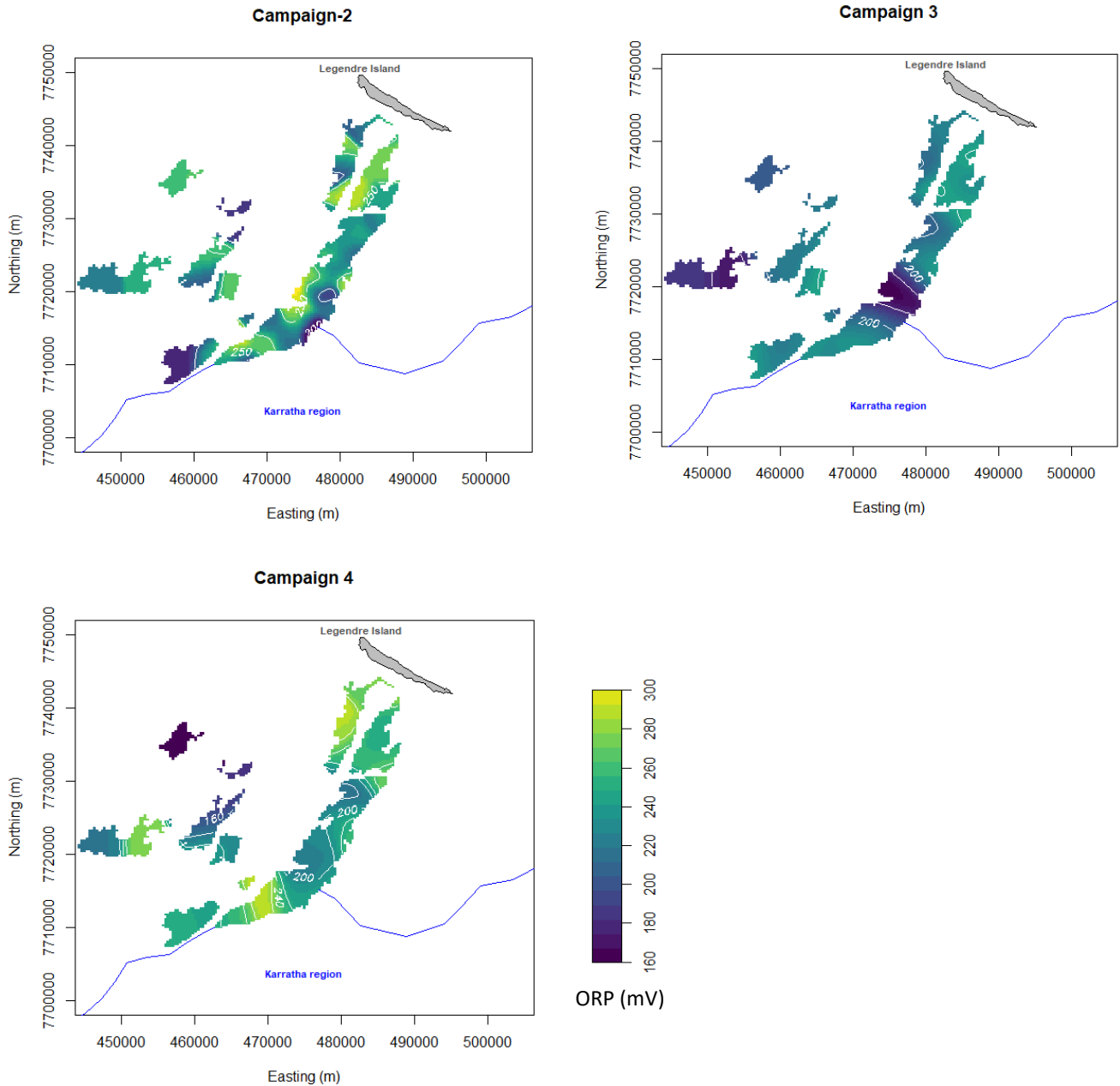


Figure 7-31: Spatially interpolated ORP colour map overlaid with contour lines. (The blue line represents the Karratha coastline. The grey polygon is Legendre island).

7.2.5 Multivariate association between pH, ORP and Cl

No evidence of association between the values of pH, ORP and Cl measured at the same site was found.

Figure 7-32 to Figure 7-34 show a scatterplot matrix for investigating relationships between pH, ORP and the decimal logarithm of Cl concentration for campaign 2, 3 and 4. The upper right panels in these figures show the corresponding Pearson correlation for the samples.

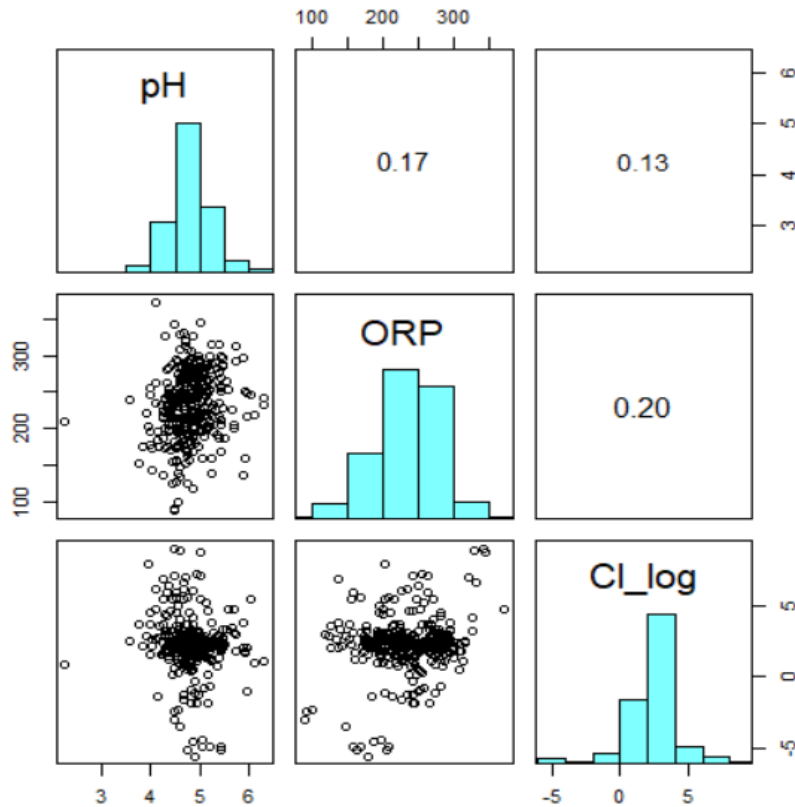


Figure 7-32: Campaign 2 pairwise scatter plots between pH, ORP and log Cl (“Cl_log”). Where the panels above the diagonal show the correlation between two variables; panels on the diagonal show the histogram of each variable; panels below the diagonal show a scatter plot between two variables.

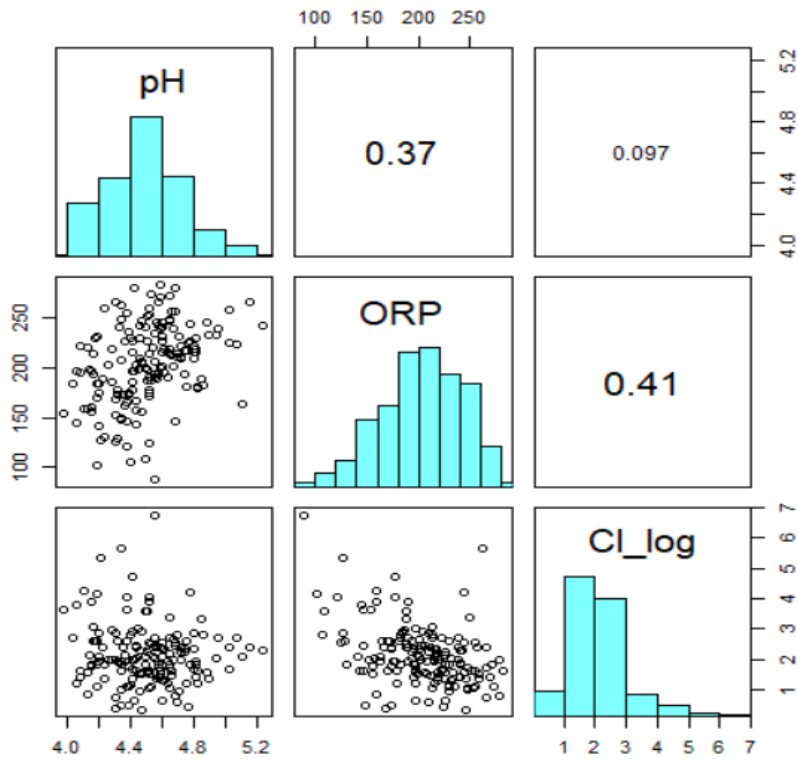


Figure 7-33: Campaign 3 pairwise scatter plots between pH, ORP and log Cl (“Cl log”). Where the panels above the diagonal show the correlation between two variables; panels on the diagonal show the histogram of each variable; panels below the diagonal show a scatter plot between two variables.

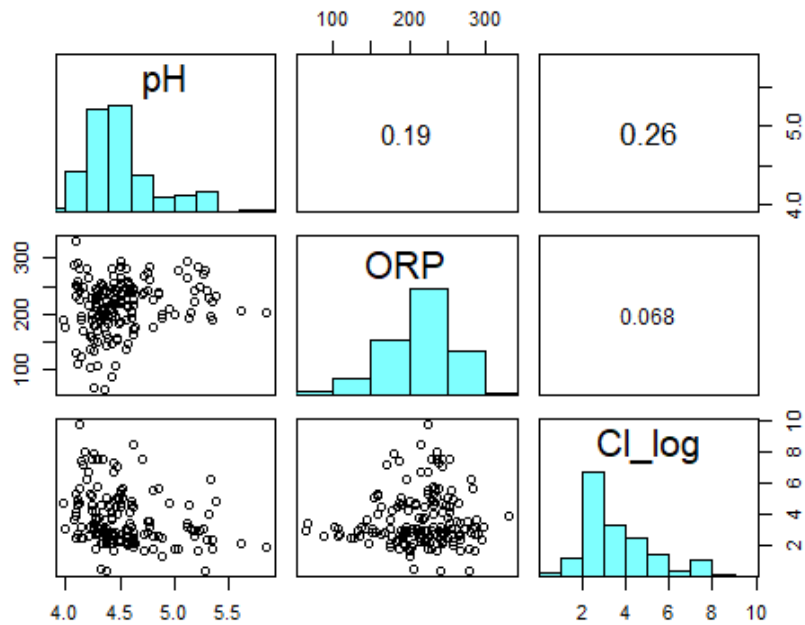


Figure 7-34: Campaign 4 pairwise scatter plots between pH, ORP and log Cl (“Cl_log”). Where the panels above the diagonal show the correlation between two variables; panels on the diagonal show the histogram of each variable; panels below the diagonal show a scatter plot between two variables.

7.3 Inorganic geochemistry – pXRF

7.3.1 Background

Mineral composition of individual rocks is assayed in the field using a portable X-ray Fluorescence (pXRF) device. Each pXRF reading is a list of elemental abundances in percent or ppm, computed by an internal device algorithm from the device's measured fluorescence spectrum, and presented to the user on the screen of the device. Some models allow for download of the pXRF readings into electronic files.

The maximum depth, or range of depths, of pXRF analysis is not known. The vendors state an approximate depth of X-ray penetration of 5 mm, but lower energy X-rays penetrate less far, so the measured composition includes contributions from the patina, weathered rind, and fresher rock, with a weighting towards elements with higher atomic number, which fluoresce higher energy X-rays, with increasing depth. Therefore, it is reasonable to assume that, unless the rock surface is freshly cut, the pXRF measures a weighted average of the compositions of the patina, weathered rind and interior fresh rock. Unfortunately, the variable porosity and density complicates the relationship between layer thickness and signal strength for any individual analyte, and it is not straightforward to deconvolute the spectra in a quantitative way.

Replicate readings on a standard dolerite target block are variable, but they tend to be proportional between replicates, so that ratios of estimated element abundances seem to be stable between replicates. Readings for heavier elements tend to be more stable.

In this study, pXRF data serve as an explanatory variable in the analysis (i.e., it is not the intention to analyse or model the spatially-varying mineralogy). Nonetheless, this is challenging multivariate data which requires careful study. Only some exploratory results are presented only.

7.3.2 Redundancy analysis

Redundancy Analysis (RDA) is a multivariate counterpart of linear regression combined with some features of principal component analysis. It can be used to explore potential relationships between multivariate predictors and multivariate response variables. (Legendre & Legendre, 2012)

The pXRF readings were subjected to RDA using the rock-type labels (encoded as dummy variables) as explanatory variables and pXRF element abundances as the response variables. This exploratory analysis is reasonable because rock types are defined partially by their geochemistry, so that it would be expected to see strong associations between particular rock types and particular elements.

Figure 7-35 shows the RDA triplot for the pXRF and rock-type data from campaign 1. The horizontal and vertical axes are the principal components in the RDA analysis and capture about 50% of the variation. Blue arrows correspond to the various elements identified by the pXRF device, and red labels correspond to the rock labels. The triplot indicates that granophyre was positively correlated with high levels of Thorium (Th) and Rubidium (Rb) and negatively correlated with Copper (Cu), for example. Dolerite was positively correlated with Titanium (Ti), Bismuth (Bi) and Mercury (Hg).

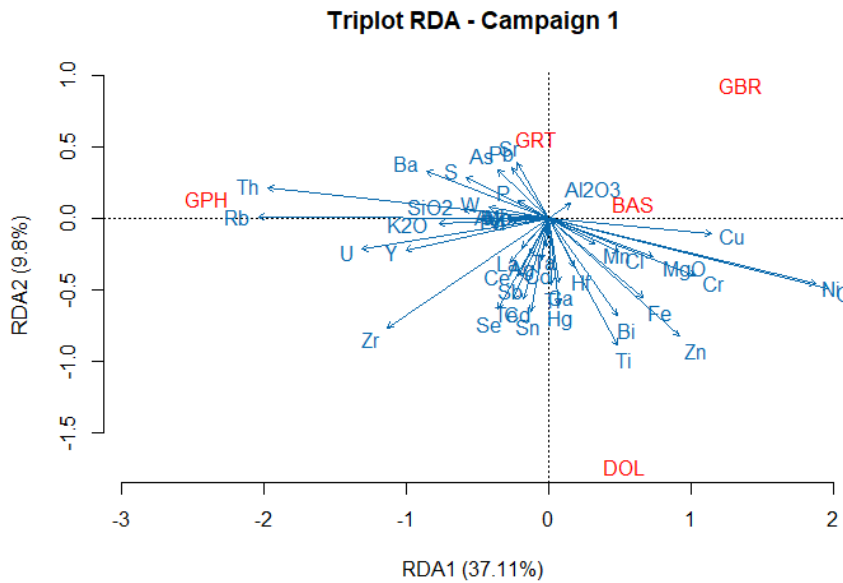


Figure 7-35: Redundancy ordination for the fitted model of chemical species from the pXRF associated with rock type in campaign 1. Percentage in parentheses is the percentage of total variation explained by the fitted model.

Figure 7-36 to Figure 7-38 show similar triplots for the data obtained from campaigns 2 to 4. Rocks are unlikely to have changed their composition from one campaign to another, except that some minerals in the surface layers might dissolve in water and be gradually removed over time. These plots are mainly of use for cross-checking the internal consistency of the technique. The results in Figure 7-35 to Figure 7-38 are broadly consistent. The vertical axes (second principal component scores) in Figure 7-37 and Figure 7-38 are reversed relative to those in Figure 7-35 and Figure 7-36, which is quite normal because the sign of a principal component is not well defined in the mathematical sense.

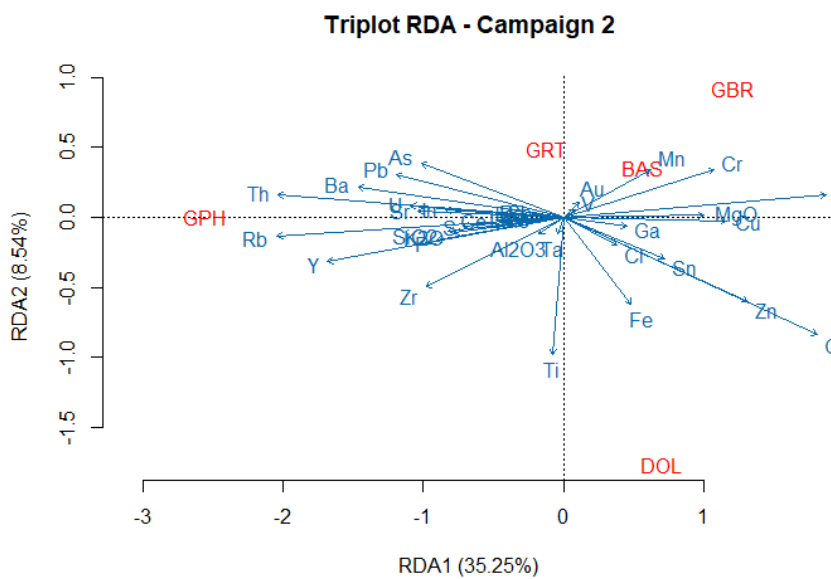


Figure 7-36: Redundancy ordination for the fitted model of chemical species from the pXRF associated with rock type in campaign 2. Percentage in parentheses is the percentage of total variation explained by the fitted model.

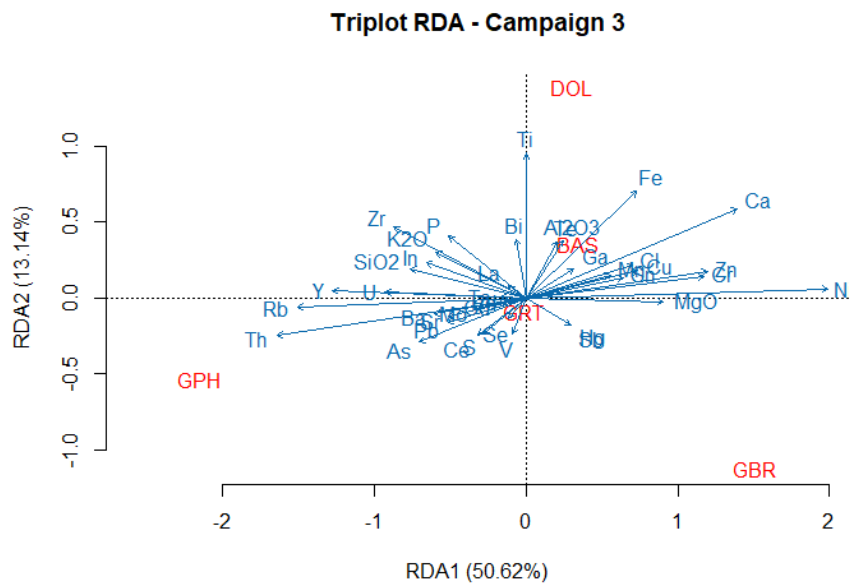


Figure 7-37: Redundancy ordination for the fitted model of chemical species from the pXRF associated with rock type in campaign 3. Percentage in parentheses is the percentage of total variation explained by the fitted model.

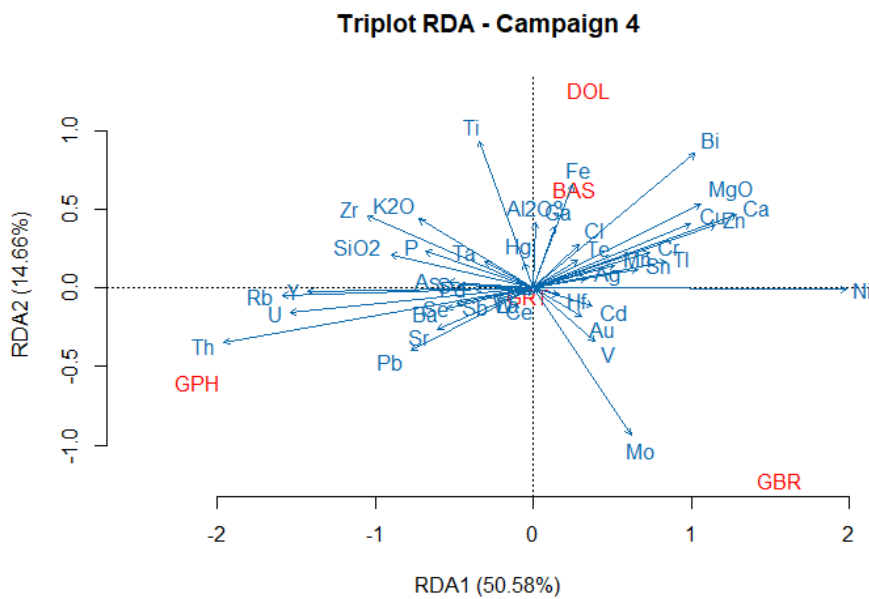


Figure 7-38: Redundancy ordination for the fitted model of chemical species from the pXRF associated with rock type in campaign 4. Percentage in parentheses is the percentage of total variation explained by the fitted model.

Figure 7-39 shows a triplot for the pooled pXRF data from all four campaigns, adding the campaign number as an explanatory variable. It does not suggest a difference between campaigns. However, this does suggest that the pXRF data was positively correlated between campaign 1 and 4, also between campaign 2 and 3.

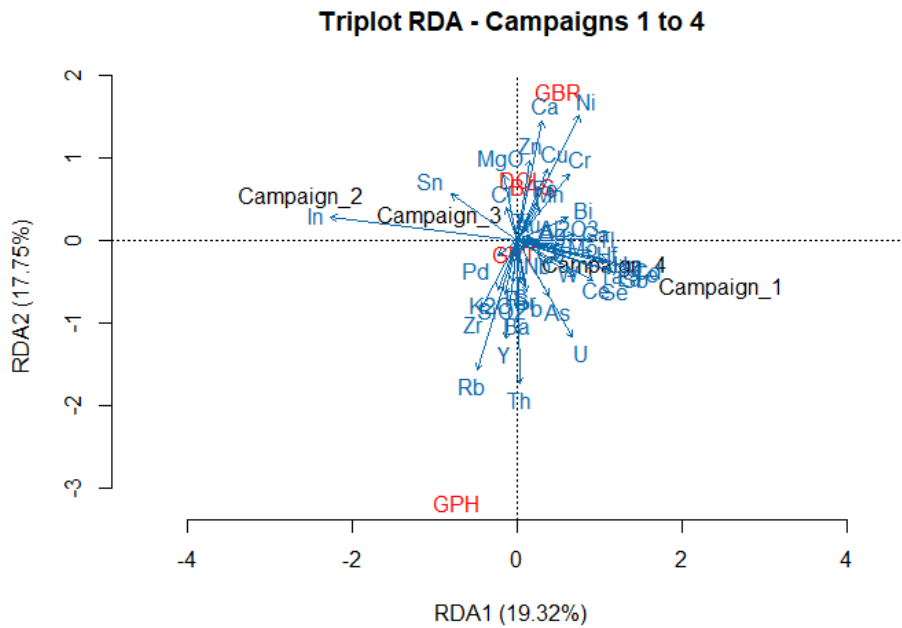


Figure 7-39: Redundancy ordination for the fitted model of chemical species from the pXRF associated with rock type and different campaigns.

7.3.3 Ratios of pairs of elements

A possibly more informative analysis is to compute, separately for each pXRF assay, the ratio of the abundances of two chosen elements, for example, the ratio of silica (SiO₂) to titanium (Ti) abundance. Geoscientists often use broad classifications of rock types according to the proportions of elements, for example, the division of igneous rocks into ‘mafic’ and ‘felsic’ rocks is based on the proportion of silica.

In this field data, rock type labels were determined by visual macroscopic inspection of the rocks and the geological context, rather than by laboratory petrographic analysis. Nevertheless, it is expected that the element percentages assayed by the pXRF device would be consistent with the element percentages predicted according to the rock-type labels assigned. This is confirmed in Figure 7-40, which shows boxplots of the ratio of silica to titanium, broken down by rock type and by campaign. Note the logarithmic scale on the vertical axis.

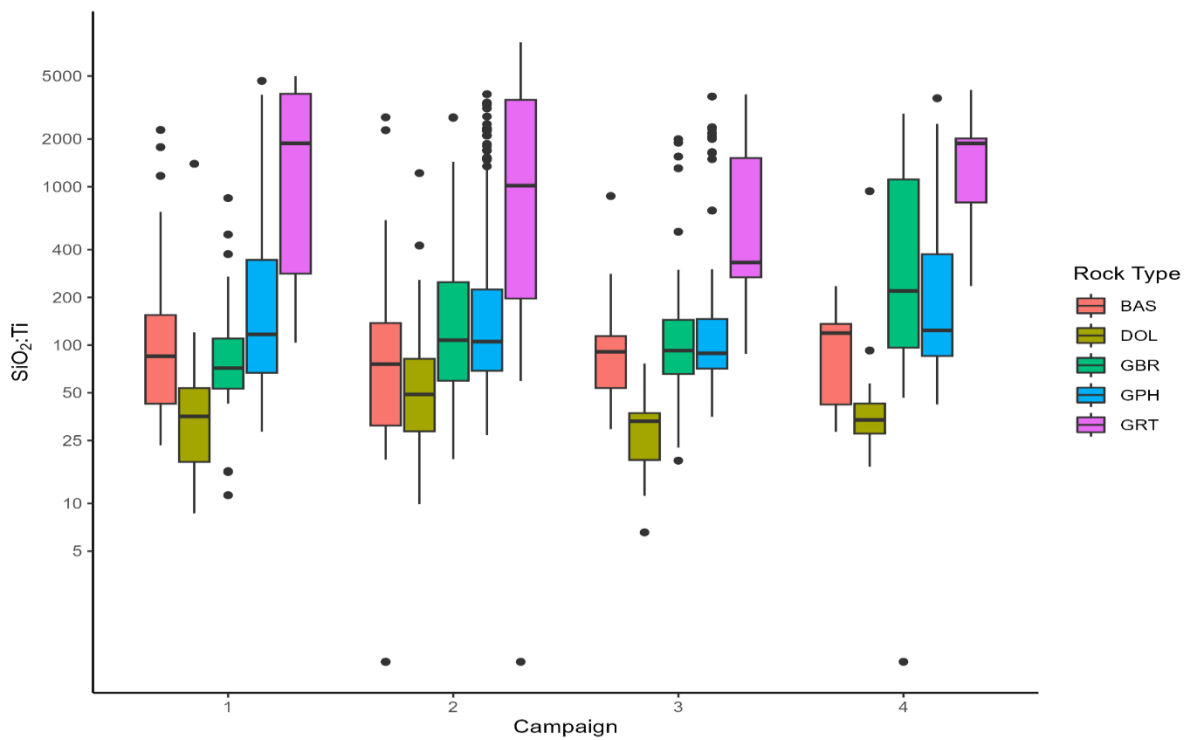


Figure 7-40: Boxplots of SiO₂: Ti by rock type and campaign

A more useful analysis is to investigate variability in the element ratios within a particular rock type, across the Murujuga landscape. Continuous gradual variation in the proportions of elements is expected, even within a specific type of rock.

Figure 7-41 shows spatially interpolated values of the ratio of silica to titanium, for rocks classified as Granophyre only, calculated from the pXRF data from campaigns 1 to 4. (Assayed values of SiO₂ and Ti lower than 50 ppm, and missing values, were reset to 50 ppm). The individual ratios exhibited considerable variation and a strongly skewed distribution, so the interpolation was performed on a logarithmic scale. A standard-error calculation has not yet been performed.

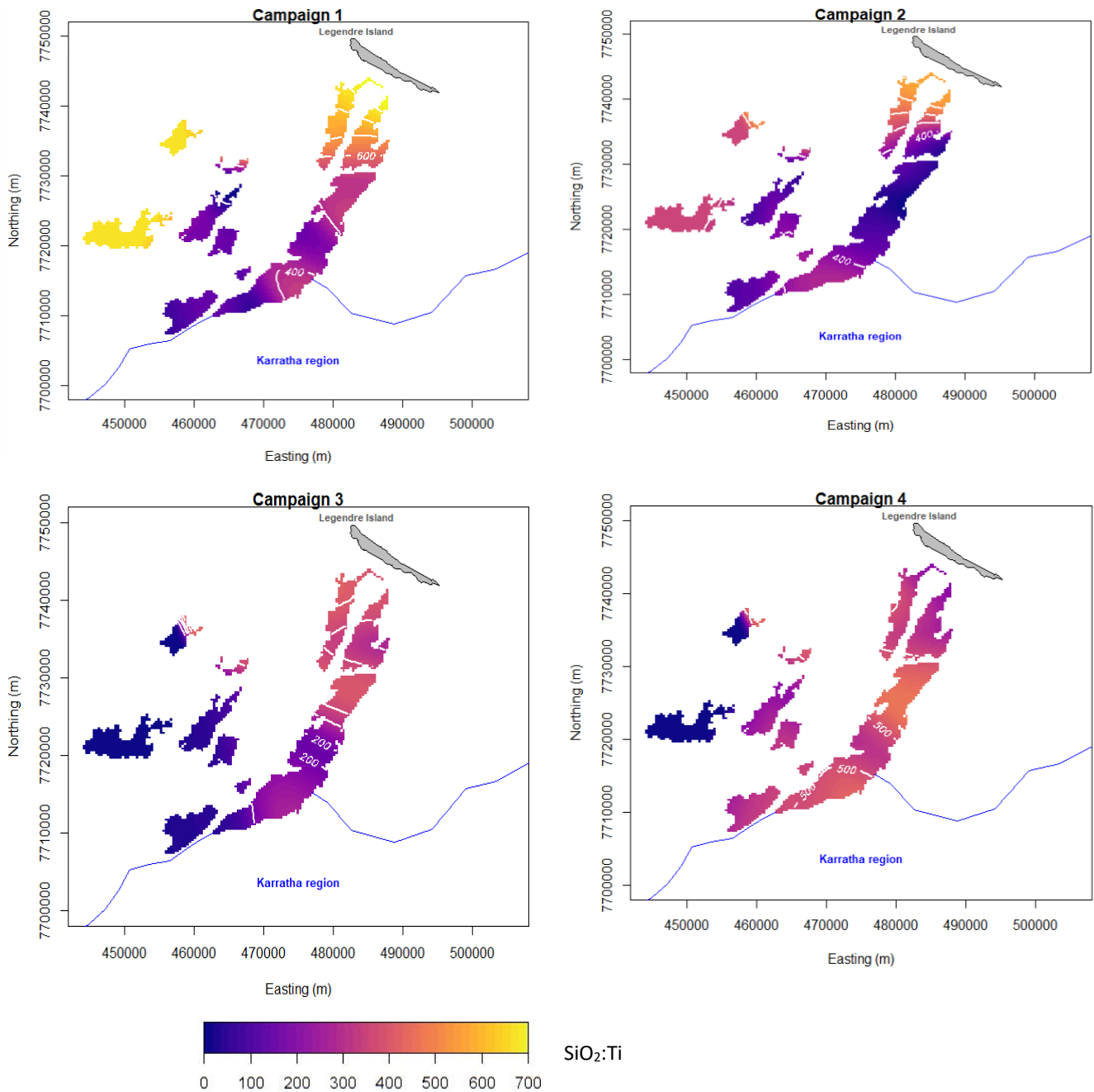


Figure 7-41: Spatial smoothing of SiO₂:Ti ratio in granophyre (GPH) overlaid contours of actual SiO₂:Ti.

The panel for campaign 1 shows substantially higher values of the ratio of silica to titanium in the north (Gidley and Dolphin islands) and west (Enderby and Rosemary islands) parts of Murujuga. The panel for campaign 2 again shows quite high values in the north (Gidley and Dolphin islands) but not as high as in campaign 1. There is inconsistency between campaigns 1-2 and 3-4 insofar as the interpolated ratios are very low in campaigns 3 and 4 in the west (Enderby and Rosemary islands) compared to campaigns 1 and 2. Overall, campaign 4 yields substantially higher values than campaign 3.

There are several confounding factors in the spatial analysis. Firstly, the spatial distribution of the different rock types themselves is uneven: Figure 7-42 shows the rock type labels for the sample rocks. Another potential source of confounding is that campaign 1 employed two pXRF devices from different manufacturers (Bruker and Olympus)

at different sites. Figure 7-43 shows a boxplot of the SiO₂:Ti ratios broken down by device manufacturer, and a spatial map of the sites where each device was used.

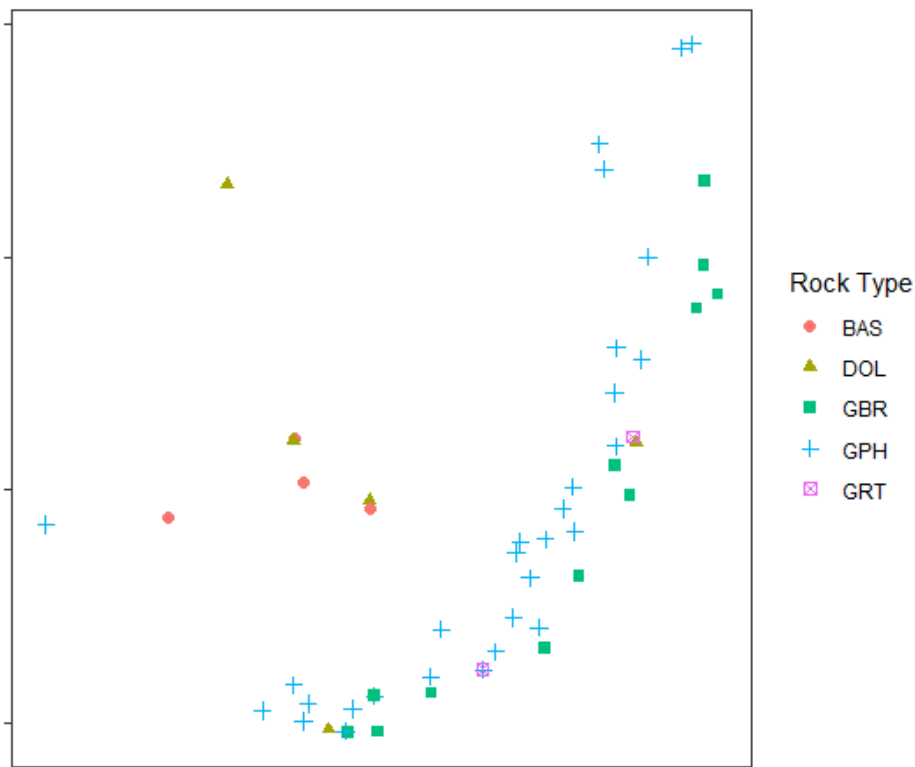


Figure 7-42: Rock types of the sample rocks.

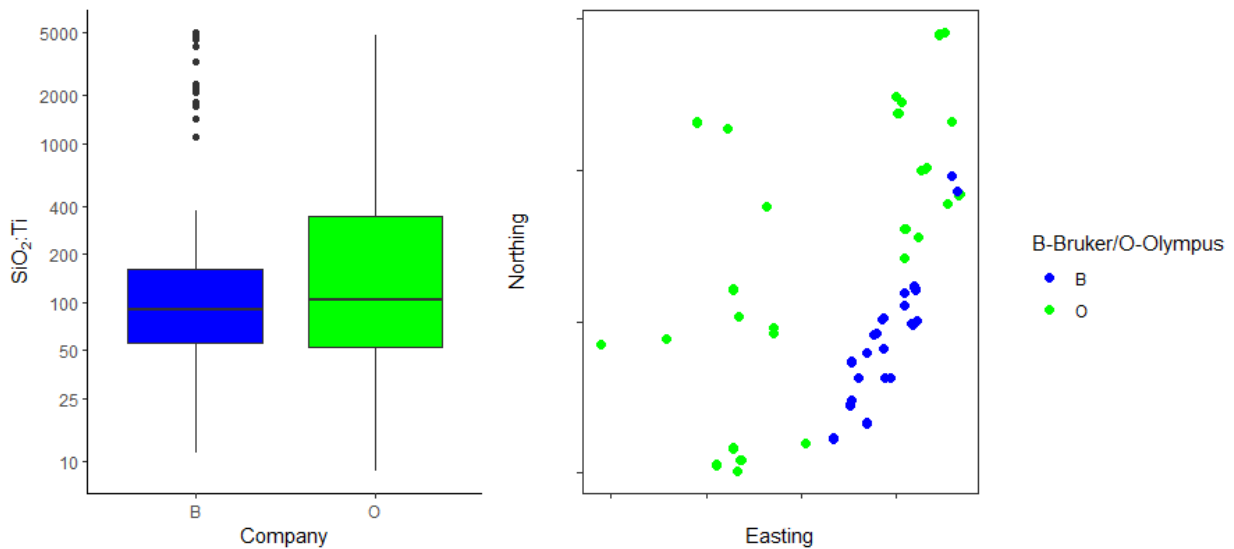


Figure 7-43: Investigation of potential 'device effect' in campaign 1. Boxplots of SiO₂:Ti by device manufacturer (Left) and manufacturer of device used at each site (Right).

While Figure 7-43 does not suggest a bias due to differences between the devices, the anomalously high values of SiO₂:Ti recorded in the north and west in campaign 1 were recorded using the Olympus device.

7.4 Passive samplers

7.4.1 Background

Passive samplers are small cylindrical tubes which are placed so that they are exposed to the atmosphere and accumulate gas molecules by chemical deposition ('fly trap'). After a specified exposure time in the field, the tubes are retrieved and sent to a laboratory for analysis.

The analysis report from one sample tube gives the assayed concentration of one gas species (with or without the label BDL denoting Below Detection Limit), together with brief remarks on the condition of the tube.

7.4.2 Selection experiment

An initial experiment was conducted to choose between three different brands of passive sampler. The design of this experiment and the results were reported in COPP21065-REP-G-100 Passive Sampling Tube Evaluation and Testing Report (July 2022).

This initial experiment considered many different gas species and allowed only limited replication per brand per gas species. The experimental design (developed by the statistical team) aimed to avoid the most likely types of confounding. Additional results for some of the brands of sampler tube were available from another study conducted by industry.

Conclusions of the selection experiment were the following. There was unequivocal support for choosing the IVL brand of sampler tube. This was consistent with results obtained by industry. The results for all three brands showed very high relative error, which may be attributable to the low concentrations of many of the gas species relative to industrial city environments.

7.4.3 Validation experiment

Expert reviewers commented on the high relative error in the results of the brand selection experiment and recommended that this be investigated further. The Statistical Team agreed. The high variability, together with the small number of replicates per brand per gas species, implied that the results of the selection experiment did not provide adequate information about the variability and statistical distribution of typical passive sampler assay results to be expected on Murujuga.

Accordingly, the Statistical Team recommended that the experiment be repeated using the same experimental design but using IVL brand only. This would provide 11 samples for each gas (i.e., three times as much replication as in the selection experiment).

This validation experiment was conducted, and the sample tubes were sent to the IVL laboratory in Sweden in late 2022. Processing normally takes several months. Results for five gases have been returned: NO₂, SO₂, NH₃, O₃ and HNO₃.

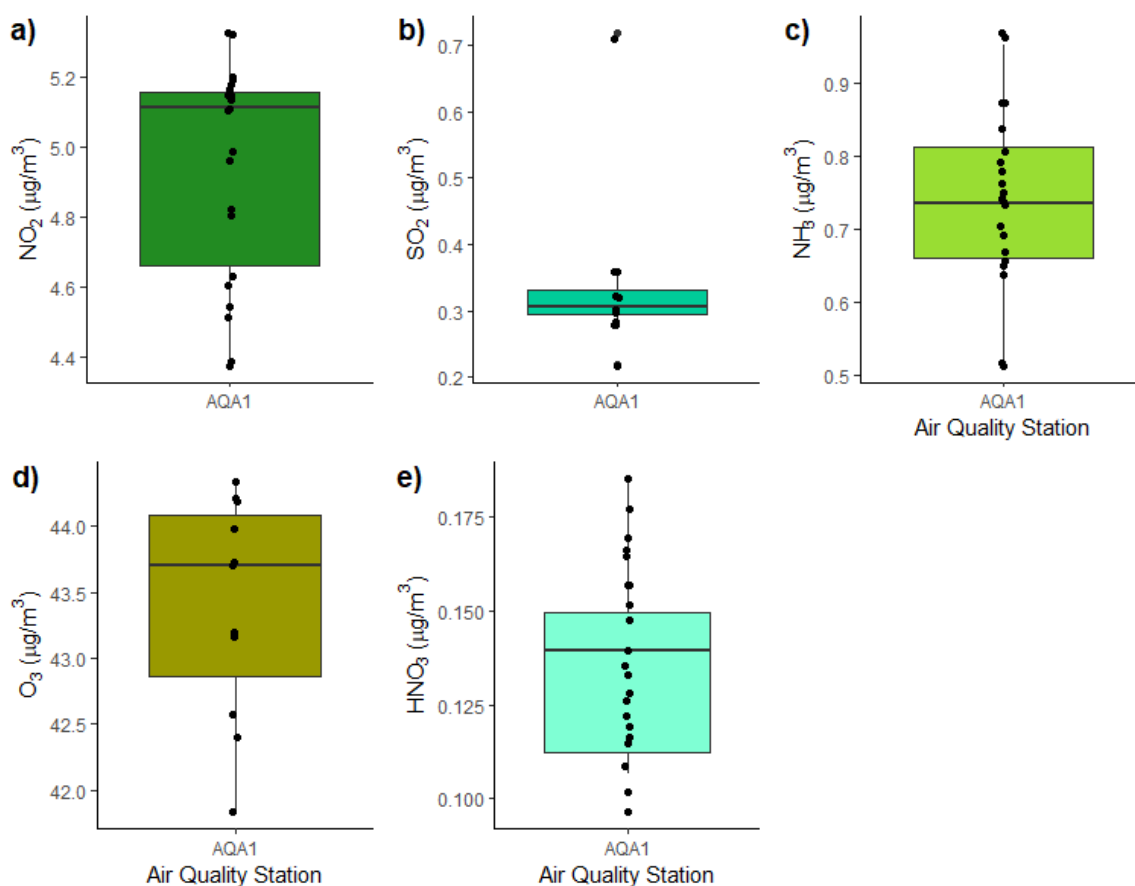


Figure 7-44: Boxplots of gas concentration observations for the validation experiment for 11 samples collected over a month at the air quality measuring station AQA1: (a) NO₂, (b) SO₂, (c) NH₃, (d) O₃, and (e) HNO₃.

Figure 7-44 shows boxplots of the observed concentrations of NO₂, SO₂, NH₃, O₃ and HNO₃ obtained for the validation experiment. NO₂ observations vary between 4.4 and 5.3 micrograms per cubic metre, with a range of approximately 0.9 which is small relative to the median value of 5.1. The distribution may be slightly skewed with a tail of lower values and the median close the upper quartile. SO₂ observations vary between 0.7 and 0.2 with a median value of approximately 0.3. Most observations are quite closely grouped but there are two possible outliers much higher than the median value. The distribution has a distinct right skew and the range is the same order of magnitude as the median value. The NH₃ observations show a fairly symmetrical distribution. Observations vary between 0.5 and 1, with a range of 0.5, which is the same order of magnitude as the median value of 0.75. Observed concentrations of O₃ vary between 41.5 and 44.5 with a median of 44.7. The range is an order of magnitude less than the median and the distribution has a slight left skew. HNO₃ observations vary between 0.075 and 0.2 with a median of 0.14. The range of observations is of the same order of magnitude as the median value with a mild skew.

These initial results suggest that the statistical distribution of NO₂, SO₂, NH₃, O₃ and HNO₃ assay results are well characterised.

7.4.4 Field monitoring samples

As envisaged in the original study design, passive sampler tubes have now been placed at 17 air quality monitoring stations, with two samplers for each gas species at each site. Sampler tubes are collected monthly and sent to the IVL laboratory in Sweden for analysis.

The turnaround time for reports from the IVL laboratory has been two months or more. So far, results are available for November 2022 through to February 2023 for NO₂, SO₂, NH₃, O₃ and HNO₃. (being all species except for VOCs).

Figure 7-45 shows the assayed gas concentrations plotted against the site label, with sites ordered by increasing value of mean NO₂ concentration.

The highest concentrations of NO₂ for each month (see Figure 7-45a) were all recorded at site AQ11, which is near the Port of Dampier (see the site map in

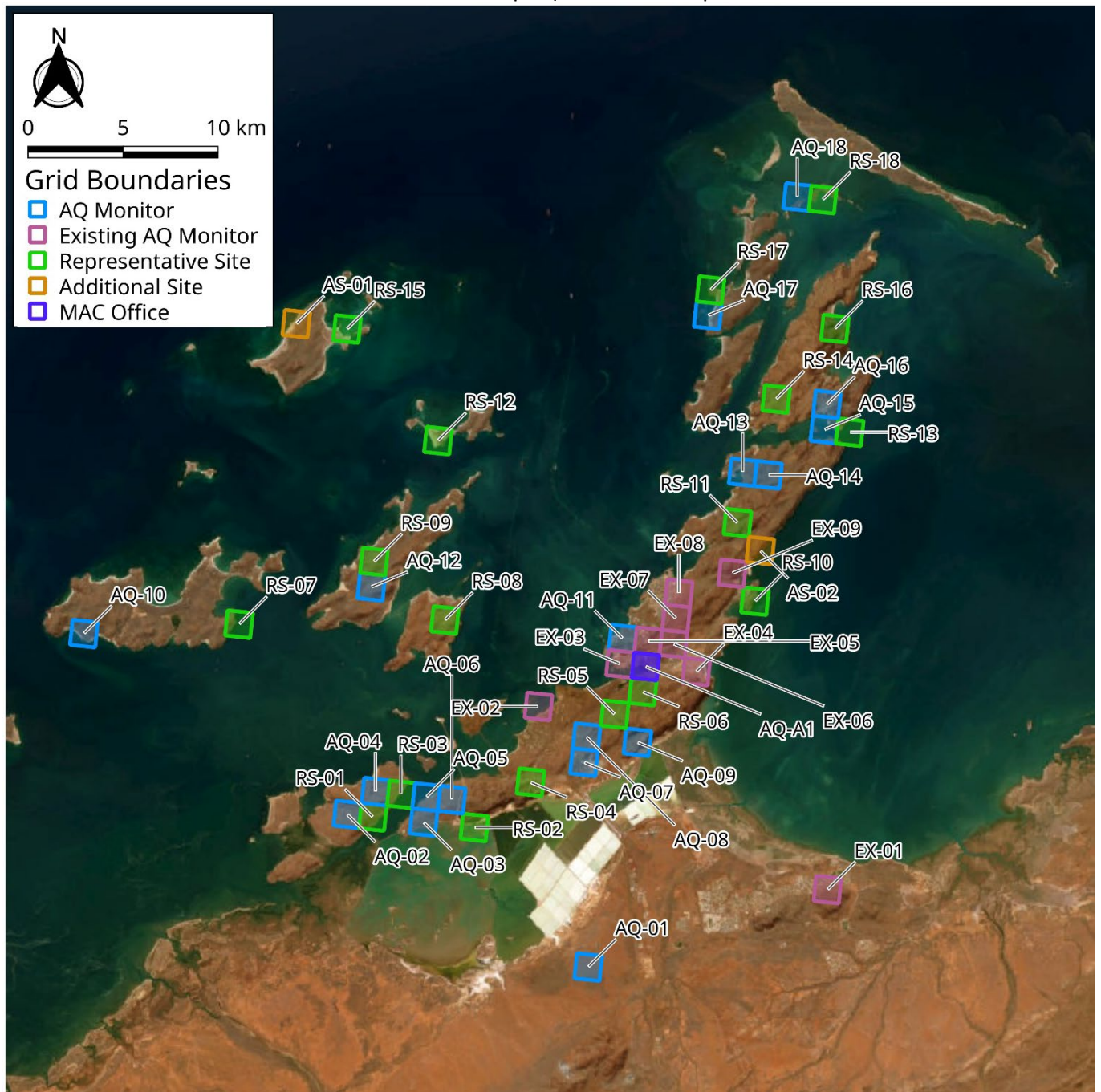


Figure 3-1 previously). The lowest concentrations of NO₂ were observed at AQ10 on Enderby Island and AQ18, north of Gidley Island, both of which are well away from the industrial area.

High SO₂ concentrations were also recorded at site AQ11 for January 2023, but in December 2022 a number of other sites (AQ10, AQ18, AQ17 and AQ04) had higher readings (Figure 7-45b). AQ10, AQ18 and AQ17 readings had relatively large differences between duplicates, while the concentrations at AQ04 were detected by both samplers. Readings in November 2022 were relatively low for all locations. There were also a number of below detection limit readings for November, as shown in Table 7-3, which were not seen in other months. There was no feedback from IVL indicating sample state or setup issues with these below detection limit samples.

Observations of NH₃ concentration were relatively low in November 2022 (Figure 7-45c), except for AQ11, with many below detection limit readings as shown in Table 7-3. These below detection limit results may reflect the generally low concentrations of NH₃ for that month. There was no feedback from IVL indicating systematic issues with these specific samples. Readings in December 2023 were slightly higher than in November, with the highest reading recorded at AQ04. In January 2023, NH₃ readings were generally higher across all sites, with the lowest concentrations recorded at AQ13, AQ16 and AQ10 which are all distant from the Port of Dampier. The highest concentration of NH₃ was recorded in January 2023 at AQ04 (West Intercourse Island)

Ozone (O₃) readings tended to exhibit an opposite trend to the SO₂, NO₂ and NH₃ gases: the lowest concentration of O₃ was recorded at AQ11 (Figure 7-45d). The highest values were at AQA18, the most northerly station, followed by other northern stations distant from the Port (AQ17, AQ16 and AQ13). AQ03 and AQ05 south and west of the Port also returned high concentrations of ozone, but neighbouring stations AQ02 and AQ04 returned low values. When concentrations of other gases were observed to increase in January 2023 across most sites, O₃ concentrations decreased across most sites; while other gases showed increases at most stations.

The highest record of HNO₃ was at AQ04 in December 2022, but the duplicate sample at AQ04 for that month was an order of magnitude lower and similar to concentrations from both replicates in November 2022. Otherwise, duplicate readings were relatively close for each station and each month. The lowest values were consistently recorded at sites AQ10, AQ15, AQ17 and AQ18. For most stations, HNO₃ observations were higher for January 2023 while December 2022 had the lowest observations.

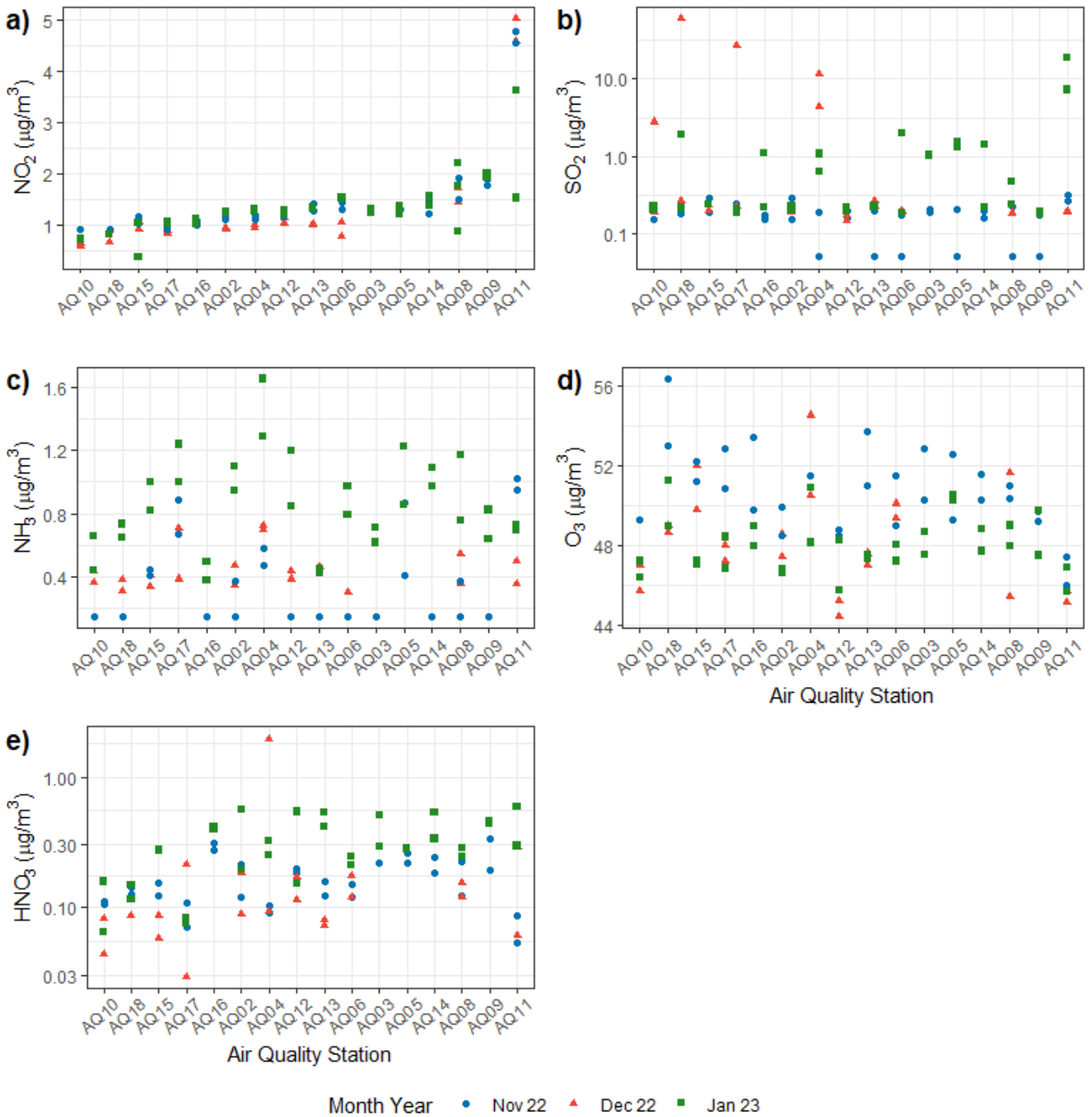


Figure 7-45: Scatter plots of passive sample gas concentration by air quality station for November 2022 (blue points), December 2022 (red points) and January 2023 (green points): (a) NO_2 ; (b) SO_2 (log concentration); (c) NH_3 ; (d) O_3 ; and (e) HNO_3 (log concentration). Stations are ordered by mean NO_2 concentration (lowest to highest).

Table 7-3: The total number of samples, number of samples below the detection limit, and samples with valid detections for each gas species and each month.

Period	Gas	Total no. samples	No. samples below detection limit	No. valid detections
Nov-22	NO ₂	32	0	32
Nov-22	NH ₃	32	20	12
Nov-22	O ₃	30	0	30
Nov-22	HNO ₃	30	0	30
Nov-22	SO ₂	32	6	26
Dec-22	NO ₂	44	0	44
Dec-22	NH ₃	44	0	44
Dec-22	O ₃	33	0	33
Dec-22	HNO ₃	33	0	33
Dec-22	SO ₂	33	0	33
Jan-23	NO ₂	32	0	32
Jan-23	NH ₃	32	0	32
Jan-23	O ₃	32	0	32
Jan-23	HNO ₃	32	0	32
Jan-23	SO ₂	31	0	31

The boxplots in Figure 7-46 show the distribution of observed concentration of each gas by month across all sites (except the air quality testing station). These plots suggest there is some monthly variation in NO₂, SO₂, NH₃, O₃, and HNO₃ with differences in range and variability of the results. Due to ranges over two orders of magnitude for SO₂ and HNO₃, these boxplots are shown on a log scale. There are outliers (points above or below the “whiskers” of approximately 95% confidence interval) in these plots unlike Figure 7-44, as might be expected from results across sites with varying gas exposure.

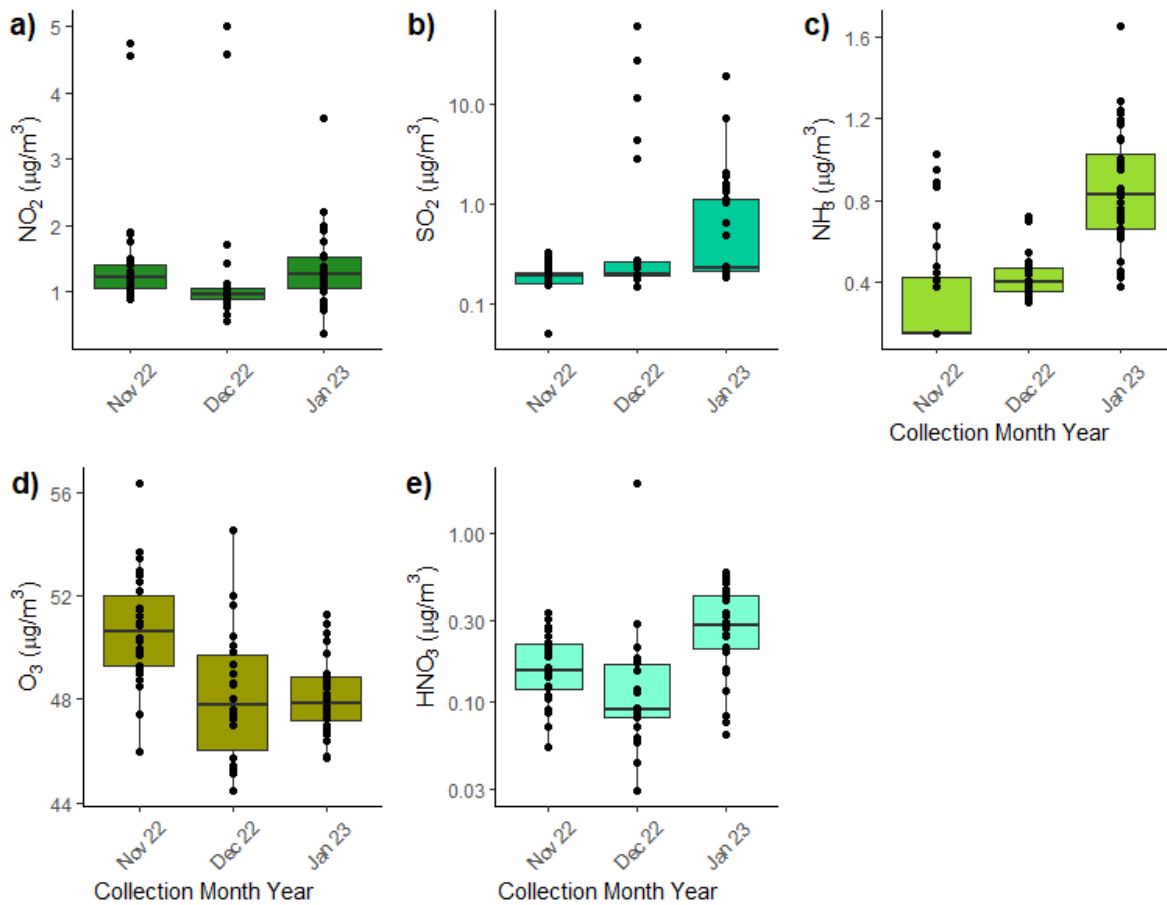


Figure 7-46: Boxplots showing passive sampling gas concentration results across the 17 air quality monitoring stations for November 2022, December 2022, and January 2023: (a) NO_2 ; (b) $\log \text{SO}_2$; (c) NH_3 ; (d) O_3 , and (e) $\log \text{HNO}_3$.

7.5 Ramboll model (time averages)

7.5.1 Background

A pivotal issue is whether there are measurably different levels of exposure to industrial output at different locations across Murujuga. Previous studies were criticised for assuming, without evidence, that some locations at Murujuga are not exposed to any industrial output and can therefore serve as "control" locations. This study relies on the expectation that there will be a spatial gradient across Murujuga in the level of exposure to industrial output, so that when the level of exposure at each location is known, a regression analysis can identify any relationship that might exist between the exposure to industrial output and the deterioration of rock condition.

Supporting evidence for the existence of such a gradient was presented in the original study design using an early version of the Ramboll data. These data are outputs of a model which incorporates meteorological inputs (actual weather observations and interpolated weather states according to a weather-forecasting model) and known or assumed sources of pollution, to predict atmospheric concentrations of various gases at a grid of spatial locations at different times.

7.5.2 Data

The Ramboll models used meteorological inputs taken from the calendar year 2014, which was considered a typical year for the weather around Murujuga. The weather forecasts were cross-checked against actual meteorological observations from 2014. Two datasets of Ramboll model outputs are available:

- for the calendar year 2014 which denotes current known sources of emissions, and
- for a hypothetical year 2030 assuming the same meteorological inputs as 2014 but with additional proposed/approved industrial facilities included.

Both the 2014 and 2030 scenarios were evaluated as part of the analysis and no differences in the relationships were found using either data set.

7.5.3 Spatial Analysis

The Ramboll data are available at grid resolutions of 1.3 km and 4km, but for statistical analyses only the 1.3 km grid data were extracted, which match the grid cells used in the MSDCA Plan study design. Gas concentrations in the model were provided in $\mu\text{mol}/\text{m}^3$ and were converted to ng/m^3 (nanograms per cubic metre) for analysis.

Concentration values for some of the gas species exhibited highly skewed distributions. Instead of averaging these values, the geometric mean was used, obtained by first taking the logarithm of the values, then calculating the average, then inverting the logarithmic transformation.

Figure 7-47 shows the annual geometric mean concentration of nitrous dioxide NO_2 in each 1.3 km cell of the Ramboll grid, calculated by averaging the Ramboll model outputs for the calendar year 2014. The high concentrations are seen near the industrial installations, the two towns of Karratha and Roebourne, and along major roads. The difference between high and low concentrations is at least one order of magnitude. Low, but not zero, concentrations are seen at the northern tip of the peninsula.



Figure 7-47: Annual average NO_2



Figure 7-48: Annual maximum NO_2

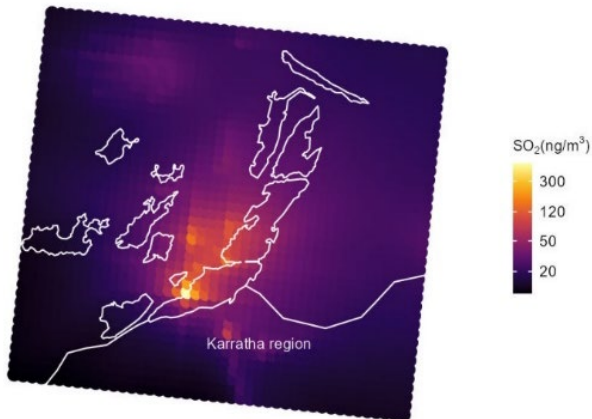


Figure 7-49: Annual average SO₂

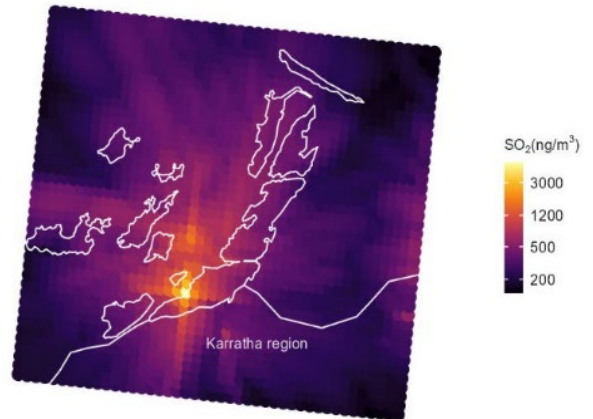


Figure-7-50: Annual maximum SO₂



Figure 7-51: Annual average NH₃



Figure 7-52: Annual maximum NH₃

Figure 7-48 shows the annual **maximum** concentration of NO₂ in each grid cell. This reveals other areas of concentration which may be associated with ship movements and with prevailing wind patterns. High and low values of maximum concentration differ by a factor of 3, suggesting that all parts of Murujuga experience substantial concentrations of NO₂ at some times during a typical year.

Figure 7-49 to Figure 7-51Figure 7-52 show the corresponding plots for sulphur dioxide SO₂ and ammonia NH₃. Within the Murujuga study area, high relative concentrations of SO₂ are focussed around the two Ramboll (2021) grid squares that span Dampier, and high relative concentrations of NH₃ are found further north in the grid squares inland from King Bay. These gradients are steeper than the gradient of NO₂, with at least an order-of-magnitude difference between high and low values of mean and maximum concentration across the peninsula. Elevated gas concentrations can also be seen near Rosemary Island and Legendre Island.

It can be observed that the geometric means and maxima plotted in the figures are not actual observations but are expected to be good approximations of the true values. The computed annual geometric mean for 2014 serves as a surrogate for the long-term average exposure over recent decades.

The main purpose of this calculation at this early stage of analysis is to check the pivotal assumption that different spatial locations across Murujuga experience measurably different exposures to the gas species of interest. The calculation appears to support this assumption.

At later stages of the study, the monitoring network will provide actual observations of gas concentrations across Murujuga, which will play an important role in the analysis.

With regard to previous studies, the calculation of average concentrations of pollutants also confirms that there are no sites on Murujuga where pollution is entirely absent. Some may argue that there are sites in the far north of the Burrup Peninsula, or at a greater distance from the sea, which are exposed only to 'background' levels of pollution, without being exposed to pollution associated with the industry on Murujuga. However, the figures displaying the annual maximum concentrations of pollutants suggest that even these remote sites experience high concentrations of pollution under some conditions. Overall these calculations support the approach taken in the current study.



Figure 7-53: Annual average HNO₃

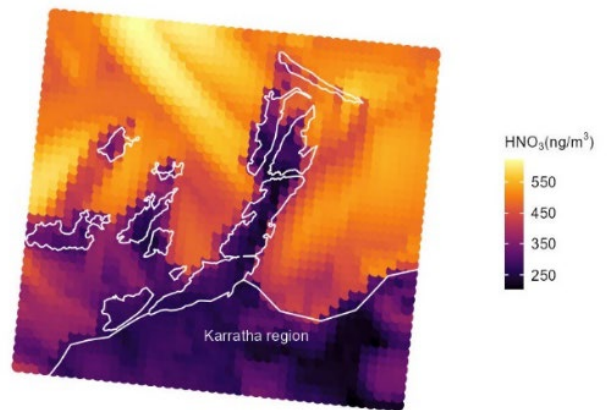


Figure 7-54: Annual maximum HNO₃

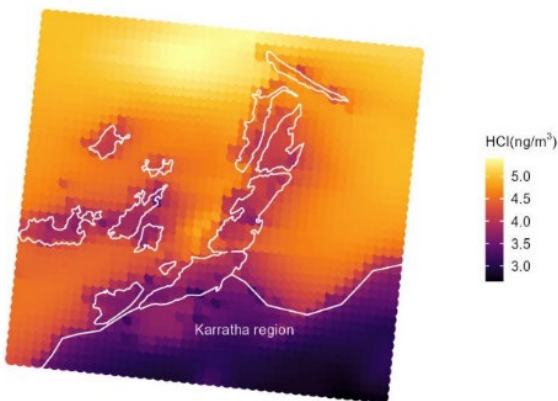


Figure 7-55: Annual average HCl

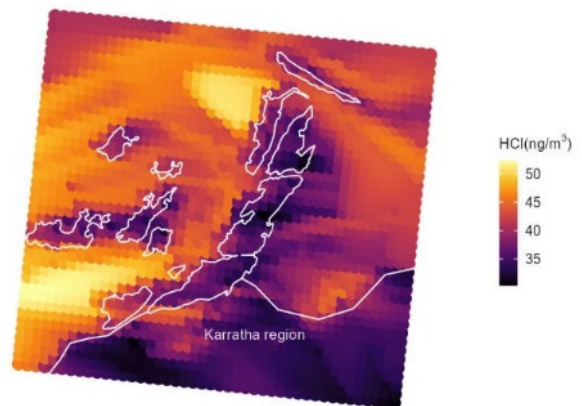


Figure 7-56: Annual maximum HCl



Figure 7-57: Annual average Na

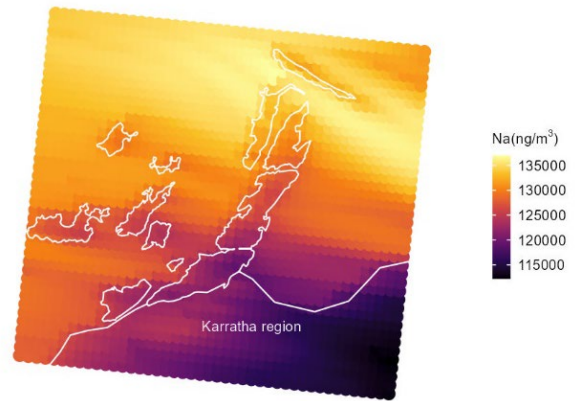


Figure 7-58: Annual Maximum Na

Figure 7-53 to Figure 7-58 show similar plots for nitric acid (HNO₃), hydrogen chloride (HCl), and sodium (Na). Elevated higher concentrations can be seen over the sea and lower concentration over land.

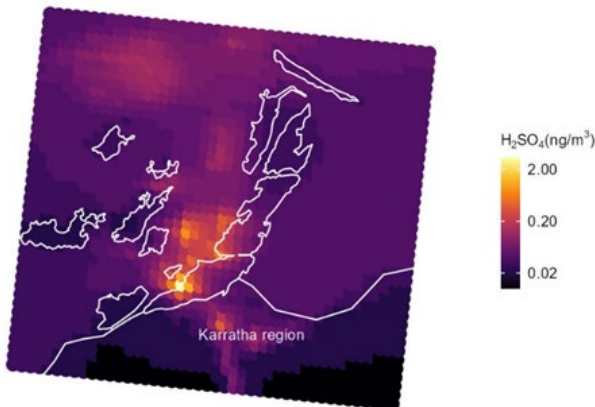


Figure 7-59: Annual average H₂SO₄

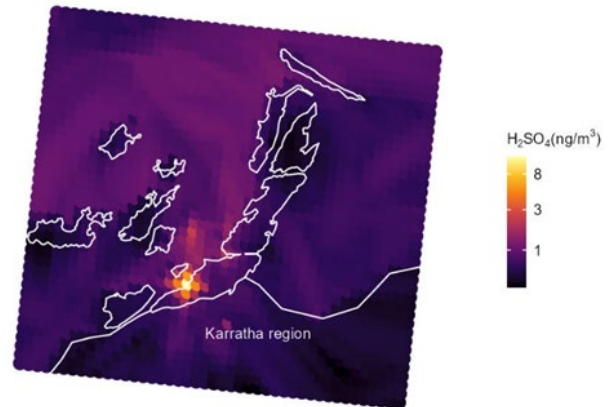


Figure 7-60: Annual maximum H₂SO₄



Figure 7-61: Annual average CO

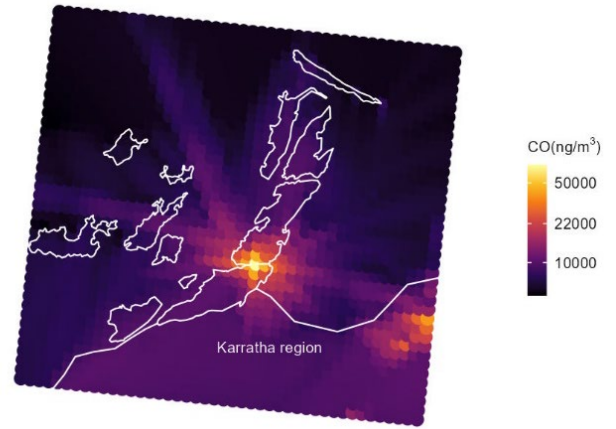


Figure 7-62: Annual maximum CO

Figure 7-59 to Figure 7-62 show similar plots for sulphuric acid (H_2SO_4) and carbon monoxide (CO). Elevated concentrations can be seen near the industrial sites.

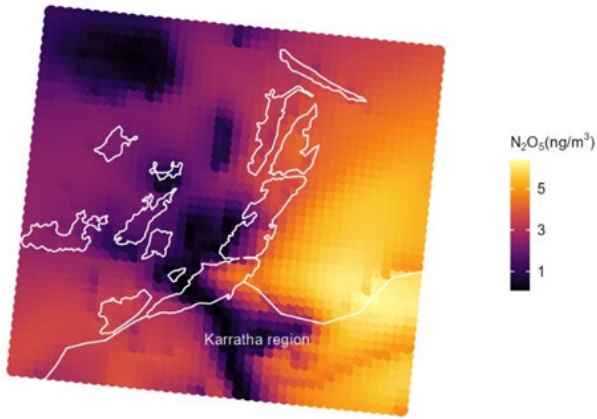


Figure 7-63: Annual average N_2O_5

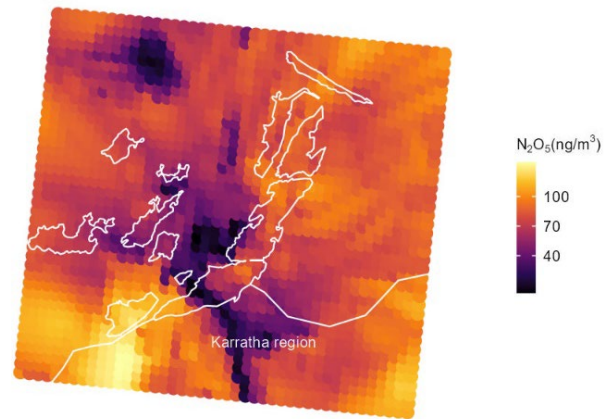


Figure 7-64: Annual maximum N_2O_5

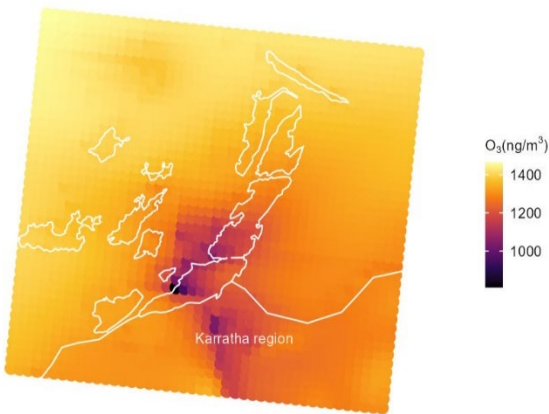


Figure 7-65: Annual average O_3

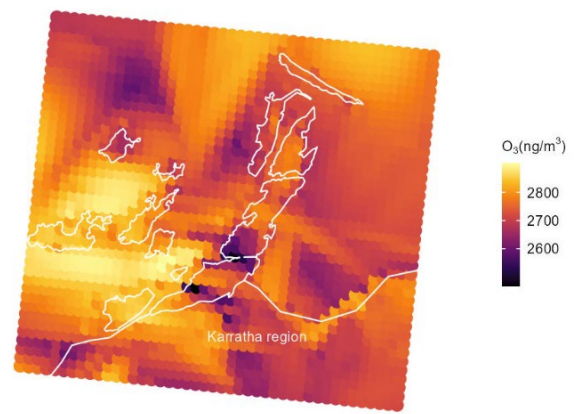


Figure 7-66: Annual maximum O_3

Figure 7-63 to Figure 7-66 show similar plots for dinitrogen pentoxide (N_2O_5) and ozone (O_3). Lower concentrations can be seen near the industrial sites.

7.6 Spatial dose response - pH versus Ramboll model

7.6.1 Correlations between pollution exposure and rock condition

The goal of the study phase of the project is to investigate possible association between the level of exposure to industrial pollution and the rate of deterioration in condition of the rock surface.

The chamber experiments are designed to identify causal relationships between gas exposure and deterioration (the 'dose-response curve'). These experiments are only in the initial stages at the time of writing.

Field monitoring of the concentration of industrial gases at the air quality monitoring sites is designed to enable us to detect any direct association between the level of exposure to pollution and the rate of deterioration in rock condition over time. However, this network of monitoring stations is still being set up, and sufficient measurements are not available for this investigation.

Until these data are available, an interim strategy is to use the existing data to calculate an indirect, surrogate index of pollution exposure and a surrogate marker of the rate of deterioration of rock condition, and to explore evidence for any association between them. The Ramboll model output data was used to calculate a surrogate for the level of **long-term** exposure to pollution at different spatial locations. Then the apparent correlations between this surrogate exposure index and the field observations of pH already obtained will be investigated, since pH levels have been proposed as a possible proxy for rock-surface deterioration.

In this section, the possible association between pH level measurements at the monitoring sites, as described previously, and exposure to different gases has been investigated.

It must be clearly understood that this interim approach is an exploratory data analysis which does not lead to rigorous conclusions. The Ramboll 'data' are not observed data, rather they are outputs of a broad-scale dispersion model of air pollution over the Murujuga and Karratha region. The pH values are not direct measures of rock degradation. Any observed correlations cannot be declared 'statistically significant' using this exploratory analysis. This interim analysis will be discarded once the full suite of data from the chamber experiments and the air quality monitoring is available.

However, the results of this exploratory analysis may guide the final definitive analysis. For example, this interim analysis may indicate which gas species are likely to be involved in the causal pathways leading to the degradation of rock patina. The final definitive analysis will combine chamber study laboratory results, air quality monitoring records, field observations on the rock surfaces, and domain-specific expert knowledge to build regression models for estimating pollution effects on the rock patina.

7.6.2 Data extraction and processing

The first step is to calculate a surrogate measure of long-term exposure to pollutants for each of the study rock art panels in the MSDCA Plan design. The Ramboll model output that is used is based on the meteorological inputs taken from the calendar year 2014 (which is regarded as a typical weather year for this region) and based on the known pollution sources (see Section 7.5.2). Two data sets from the Ramboll model outputs were extracted. The first dataset is the 2014 emissions, which simulates current emission scenarios. The second data set is the 2030 emissions, which simulates future scenario including additional proposed/approved industrial facilities. The 2030 results are presented in this analysis since these data were used to select the air quality monitoring locations.

For each rock art panel in the study, the 1.3 km grid cell containing the art panel was identified and the Ramboll model output data for this grid cell was extracted. Hourly data were extracted for the chemical species NO₂, SO₂,

NH₃, HNO₃, HCl, H₂SO₄, O₃, N₂O₅, Na, and CO. The mass density of particles PM₁₀ was calculated using the following equations (Camx User Guide 7.10)

$$PM_{2.5} = PSO_4 + PNO_3 + PNH_4 + PEC + NA + PCL + POA + SOA1 + SOA2 + SOA_3 + SOA_4 + SOPA + SOPB + FPRM + FCRS$$

$$PM_{10} = PM_{2.5} + CPRM + CCRS$$

For each gas species, the annual mean and maximum gas concentrations according to Ramboll model outputs were calculated at each art panel as a measure of long-term exposure.

Additionally, a surrogate measure of exposure in the relevant season of the year was calculated. For each field campaign in the first year of studies, the 'relevant season' was defined as the period in 2014 with the same calendar dates as the field campaign. Optionally the relevant season was expanded to include the two, four, or eight weeks prior to the start of the field campaign. The mean or maximum gas concentration according to the Ramboll model was then calculated over the relevant season.

7.6.3 pH plotted against average gas concentration in the relevant season

Figure 7-67 shows pH measurements plotted against estimated gas concentration in the relevant season. Each data point represents one pH measurement at a particular site in a particular campaign. Three measurements of pH were made at each art panel for each campaign. Each data point is coloured according to the campaign in which it was observed. The horizontal coordinate is the average gas concentration at that art panel in the relevant season, as explained above. Figure 7-67 uses the mean gas concentration over each campaign period as the seasonal measure. Some of the gas concentration values exhibit a highly skewed, roughly lognormal distribution, and thus logarithmic scales were used in some graphics to show the results more clearly.

Figure 7-67 does not suggest that pH is related to the predicted 'seasonal' gas concentration, especially for campaigns 2, 3 and 4.

Note that observations taken at the same art panel, but in different campaigns, are not plotted at the same horizontal position, because the 'relevant seasonal' gas concentration values are different. The decision to use 'relevant seasonal' gas concentration is supported by the presence of large gaps between the different coloured clouds of data points in panels (d), (e) and (f) of Figure 7-67. Each campaign revisits the same art panels as the other campaigns, so these plots indicate indirectly that there is substantial seasonal variation in the concentration of HCl, HNO₃ and PM₁₀ at the same art panels.

The data for campaign 1 (Figure 7-67 orange dots) exhibit some special features. The values of pH are much higher than in other campaigns and show greater variation. There are two pH values greater than 8: these values are thought to be anomalous, as the pH for the other two samples on the same rocks are less than or equal to 5.5. Figure 7-67 suggests that pH may increase with the mean concentration of some gases, as shown by panel (a) SO₂, panel (b) NO₂, and panel (f) PM₁₀ in campaign 1. For these plots, the relation is generally not linear and is not discernible for campaigns 2, 3 or 4. Similar relations were observed between other gases and pH including NH₃ and H₂SO₄ (SULF). Plots of these gases are not shown here. Figure 7-67c suggests that pH may tend to decrease with increasing levels of ozone (O₃) in campaign 1. Again, the relationship is not discernible in campaigns 2, 3 or 4.

Some further remarks regarding Figure 7-67 are appropriate.

- The number of observations in each campaign is not the same. The pH was measured at each location on at least one rock and from three sites on each rock. In campaigns 1 and 2, measures were made on both rocks with art and random rock samples at the same locality. During campaign 2, these sample rocks were removed for further laboratory testing, hence a smaller number of rocks were sampled in subsequent campaigns.

- Some gases show discernible seasonal variation (that is, the Ramboll-model gas concentrations change over different time periods in the year).
- Predicted Na (sodium) and HCl (hydrogen chloride) concentrations show very similar seasonal variations. Concentrations of HCl, (Figure 7-67d), are much higher for campaigns 3 and 4 than for campaign 2. pH may be slightly lower for campaigns 3 and 4 compared to campaign 2. Concentrations of these gases for campaign 1 sit between these other campaigns, however the pH for campaign 1 is markedly higher than all the other campaign periods – hence it is not possible to show there is a seasonal relationship with pH based on these gases alone.
- Figure 7-67e shows the Ramboll predicted HNO_3 concentrations exhibited seasonal differences. In this plot, HNO_3 concentrations are much lower for campaigns 2 and 3 compared to campaigns 1 and 4.
- Predicted PM_{10} and N_2O_5 concentrations also show similar seasonal variations. PM_{10} is calculated from $\text{PM}_{2.5}$ (smaller particulate matter), which is calculated from a range of gases and particle types. Figure 7-67f shows that mean predictions for the calculated PM_{10} have much a wider range of concentrations and much higher concentration values for campaign 2 than the other three campaigns.

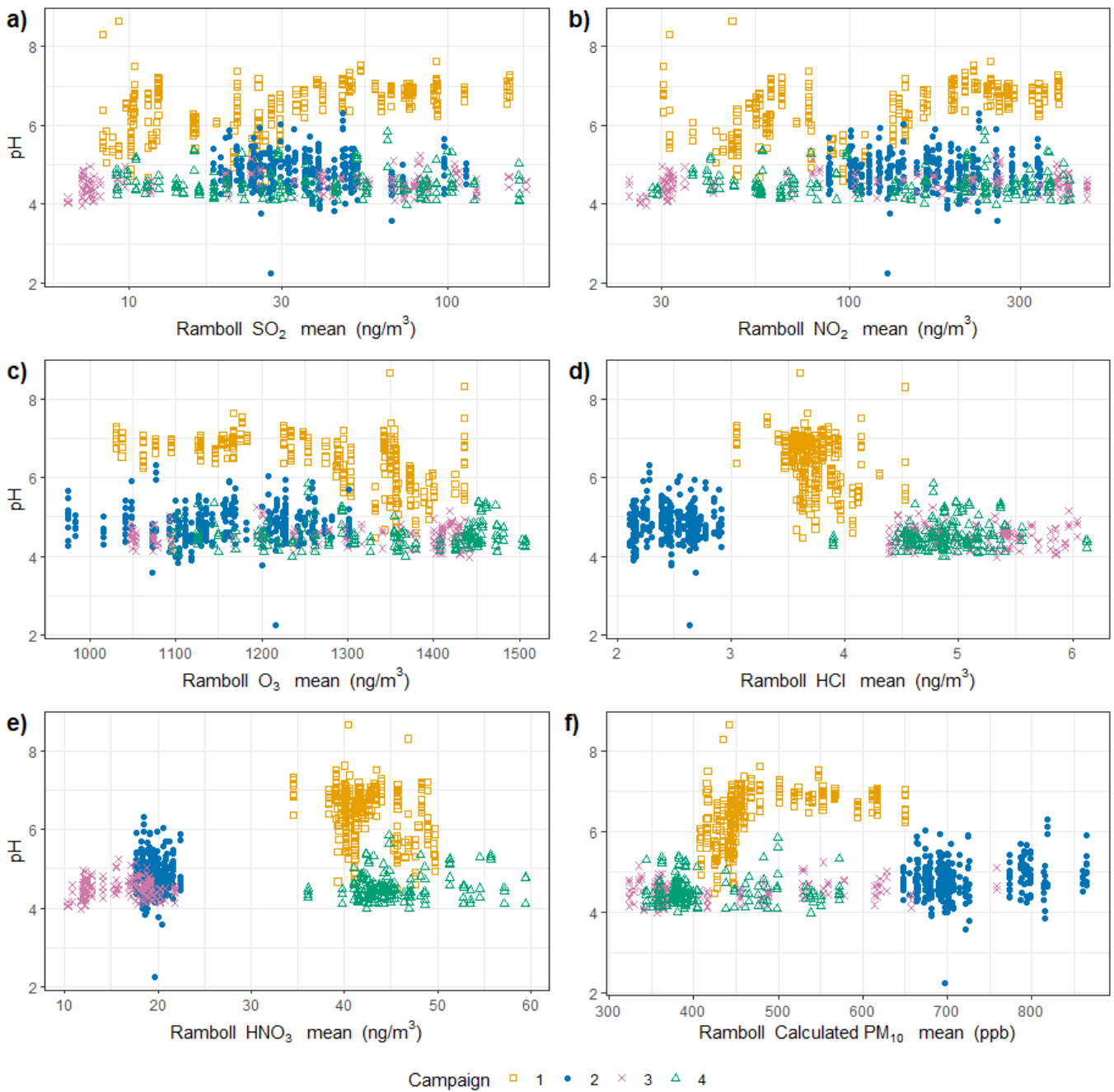


Figure 7-67: Measurements of pH for each locality (including replicates) versus the mean (or log mean) of gas concentrations by campaign: (a) log mean SO₂ concentration; (b) log mean NO₂ concentration; (c) mean O₃ concentration; (d) mean HCl concentration; (e) mean HNO₃ concentration; and (f) mean calculated particulate matter PM₁₀ concentration.

7.6.4 Ramboll gas concentration predictions

The pH dose response plots presented in this section use the Ramboll gas concentration predictions for 2030 emissions and historic weather conditions from 2014. This is the same Ramboll gas prediction used to optimise the air quality monitoring sites (refer to Appendix 2 of the MSDCA Plan). Similar plots for pH versus predicted gas dosages were also generated for the Ramboll gas prediction using the 2014 emission data and weather conditions

for 2014. Plots for the 2014 emission scenario (not included in this document) showed very little differences to those generated with the Ramboll predictions for future emissions.

The predicted gas concentrations across all art panels for current and future emissions were compared, as shown in Figure 7-68. Most gases showed only very small differences between the Ramboll estimates for the current (2014 data) and future (2030 data) scenarios. The biggest differences were for SO₂ concentrations, see Figure 7-68a, which were predicted to drop between the current 2014 and 2030 future scenarios. H₂SO₄ follows a similar pattern to SO₂.

Most gases showed small increases between the 2014 and 2030 model scenarios similar to HCl (see Figure 7-68b). There are only minor increases for each month. NH₃ had a similar range in concentration for most months, but for August to October NH₃ is higher. The boxplots for the current (2014 data) and future (2030 data) emissions of NH₃ are similar for each month. Note there are many upper outliers for all months. The statistical team conclude that using the 2030 Ramboll predictions has no effect on the pH versus gas dosage relations compared to using the 2014 estimates.

In conclusion, there is very little difference between the Ramboll predicted current and future emissions, thus resulting in both emissions scenarios having a very similar patterns for pH versus gas dosage relationships.

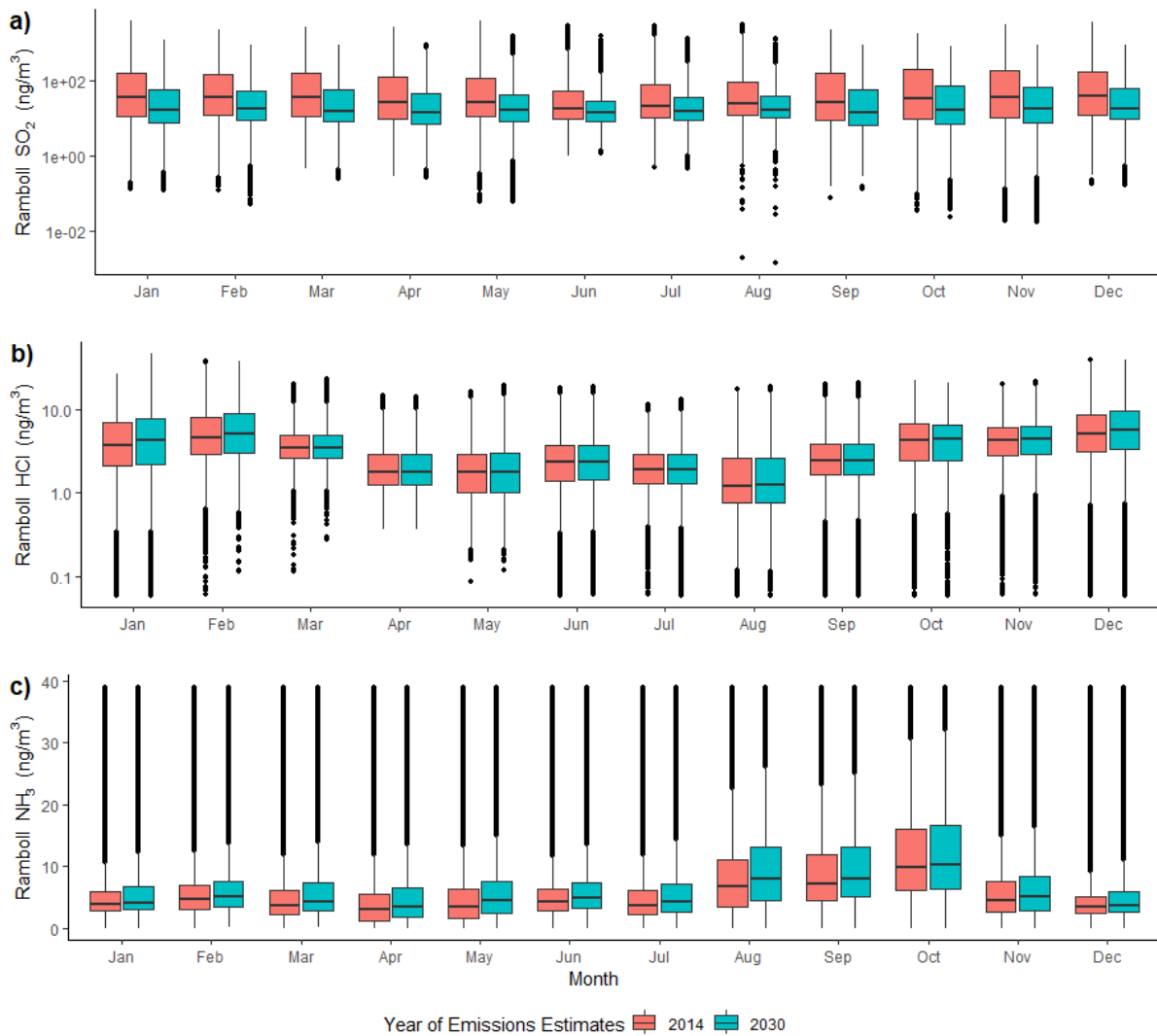


Figure 7-68: Boxplot of monthly gas concentrations overall monitored art panels comparing Ramboll estimates of gases for current (2014) and future (2030) emissions for: (a) log concentration of SO₂; (b) log HCl; (c) log NH₃. The log scale makes the ranges more readable but introduces a number of lower outliers. For HCl and NH₃, the overall range is from the 2nd to the 100th percentile to remove long tails of outliers that are less than 0.1.

7.6.5 Results for mean gas predictions over different periods

Changing the averaging period over which average gas concentrations are computed changes the mean gas concentration value but did not seem to affect the actual relationship with pH. Scatter plots of this (not shown here) simply show the same relationship transposed along the x-axis (gas concentration). Several gases showed quite small changes over these periods, but other gases, particularly those showing seasonal effects such as Na and HCl, show quite large shifts. However, the size of the shift did not affect the relationship with pH for those gases.

The relationships between pH and the predicted annual mean Ramboll gas concentration seem to give similar results to those for the predicted mean gas concentration over campaigns as shown **Error! Reference source not found**. Figure 7-69. The pH had a generally flat relationship with the predicted annual mean gas concentrations, that is the variation in pH values does not seem to be accounted for by the variations in the (predicted) gas measurements. Some slight increases or decreases of pH in relation to gas concentrations did remain for campaign

1. For example, Figure 7-69a shows some slight increases of pH with mean annual concentration for SO₂, but as before the relation is non-linear and is not discernible for other campaigns.

Predicted annual mean gas concentrations did not show the seasonal variation of the predicted mean gas concentrations for the campaigns, as shown in Figure 7-69b for HCl. The relationship with pH is relatively flat.

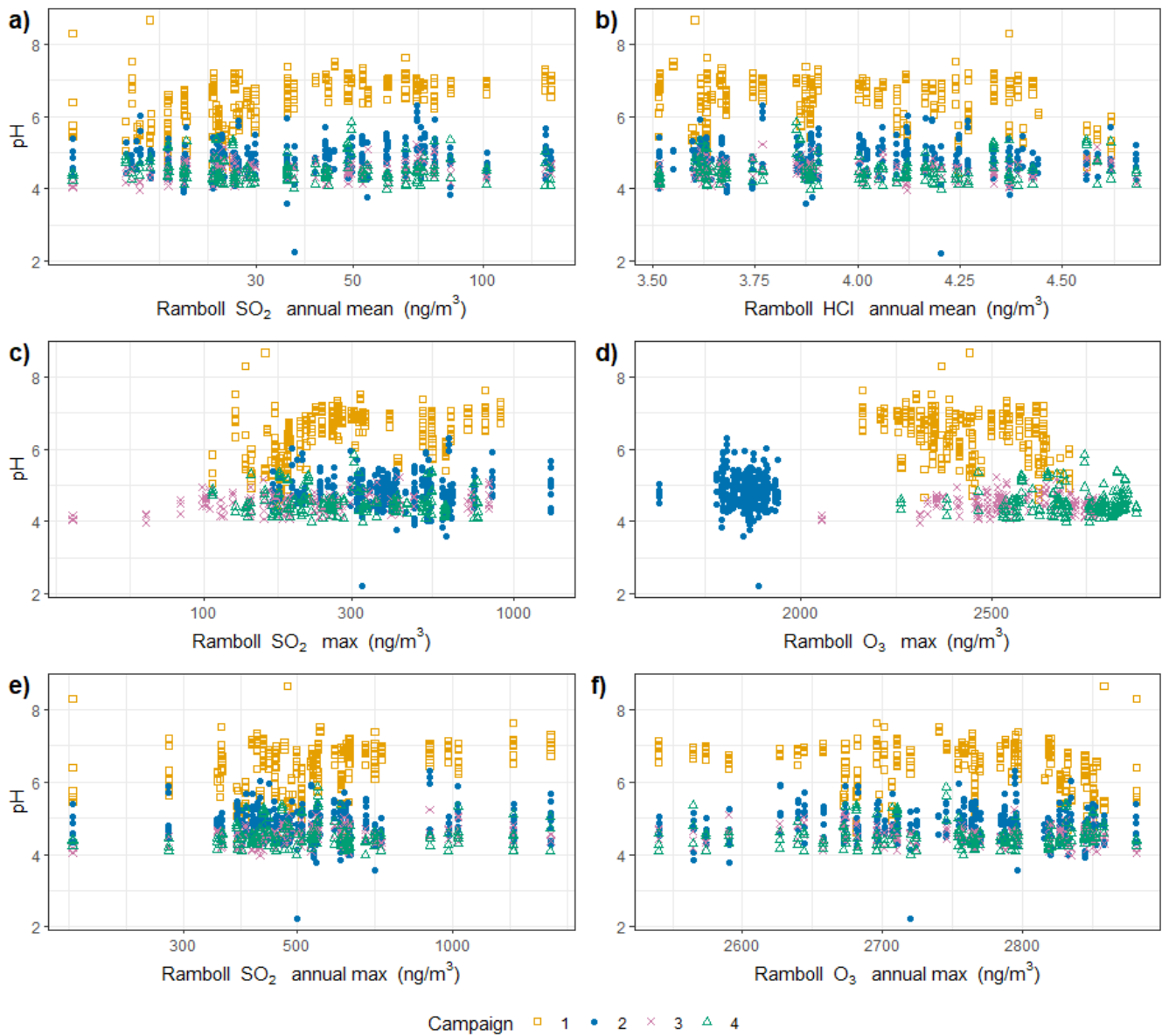


Figure 7-69: pH versus the predicted annual mean gas concentration or maximum gas concentration by campaign: (a) log annual mean concentration of SO₂; (b) annual mean concentration of HCl; (c) SO₂ log maximum concentration over each campaign period; (d) O₃ maximum concentration over each campaign period; (e) SO₂ log maximum concentration over a year; and (f) O₃ maximum concentration over a year.

7.6.6 Results for maximum gas concentrations

Figure 7-69 plots (c) to (f) show that using maximum gas concentrations as seasonal or annual rather than mean gas concentrations did not have a large effect on these generally flat relations between pH and gas concentration.

Figure 7-69a shows that the slight increase in pH for increasing SO₂ concentrations in campaign 1 seems more definite for the maximum concentration over the campaign period than for the mean concentration shown in Figure 7-67a. However, Figure 7-69d shows the decline in pH for increased concentrations of O₃ seems less linear and defined for the maximum gas concentrations.

Figure 7-69d also shows seasonal variation in the maximum O₃ concentration not shown for mean O₃ concentrations. Seasonal variations in gas concentrations seem to be sensitive to the type of summary over the campaign period. For annual maximum concentration of gas, the SO₂ trend for campaign 1 seemed quite flat in Figure 7-69e, but pH seemed to show more sustained declining trend for annual maximum O₃ (Figure 7-69f).

7.6.7 Results for pH versus gases by rock type for campaign 1

The relation between pH versus gases by rock types was also investigated, with some results for campaign 1 shown in Figure 7-70. pH for other campaigns stayed generally flat for gas concentration by rock type and are not shown here.

For campaign 1, the overall trends in pH observed for mean gas concentrations stay similar when considering pH by gas and rock type for the two more common rock samples, gabbro and granophyre. However, some increasing trends are more obvious for these two rock types. pH data for less common rock types were often too few to draw any conclusions. As noted previously, these relations are not linear and are not discernible in campaigns 2, 3 and 4.

As in Figure 7-67, pH seems to increase for several gases including SO₂, NO₂ and NH₃. Figure 7-70 plots (a), (b) and (d) shows these increasing pH trends for granophyre, but these trends are not so clear for other rock types. For instance, the relation between pH and NH₃ in Figure 7-70 b is relatively flat for the gabbro rock type with no clear increase.

Figure 7-70c shows that pH seems to decline with increasing O₃ concentration for granophyre and gabbro, but this trend is not so clear for other rock types. Several gases, including HCl, HNO₃ and N₂O₅ (not shown) have relatively flat relationship with pH. pH seems to increase more markedly with PM₁₀ for both granophyre and gabbro than other rock types in Figure 7-70d.

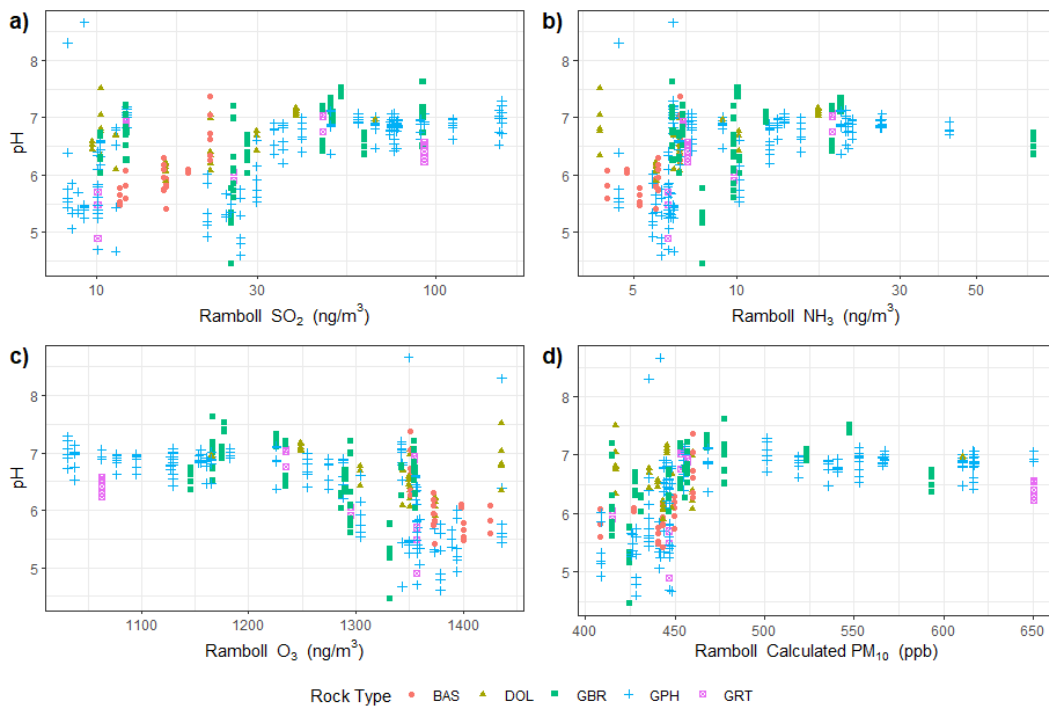


Figure 7-70: pH versus predicted mean gas prediction by rock type for campaign 1: (a) log mean SO₂ concentration; (b) log mean NH₃ concentration; (c) mean O₃ concentration; and (d) mean calculated PM₁₀.

It has been suggested that manganese (Mn) maybe the most sensitive element to acid forming pollutants. Therefore, the first assessment was to determine whether there was a correlation between Mn and NO₂. Figure 7-71 shows that for all four campaigns there was no relationship Mn and NO₂.

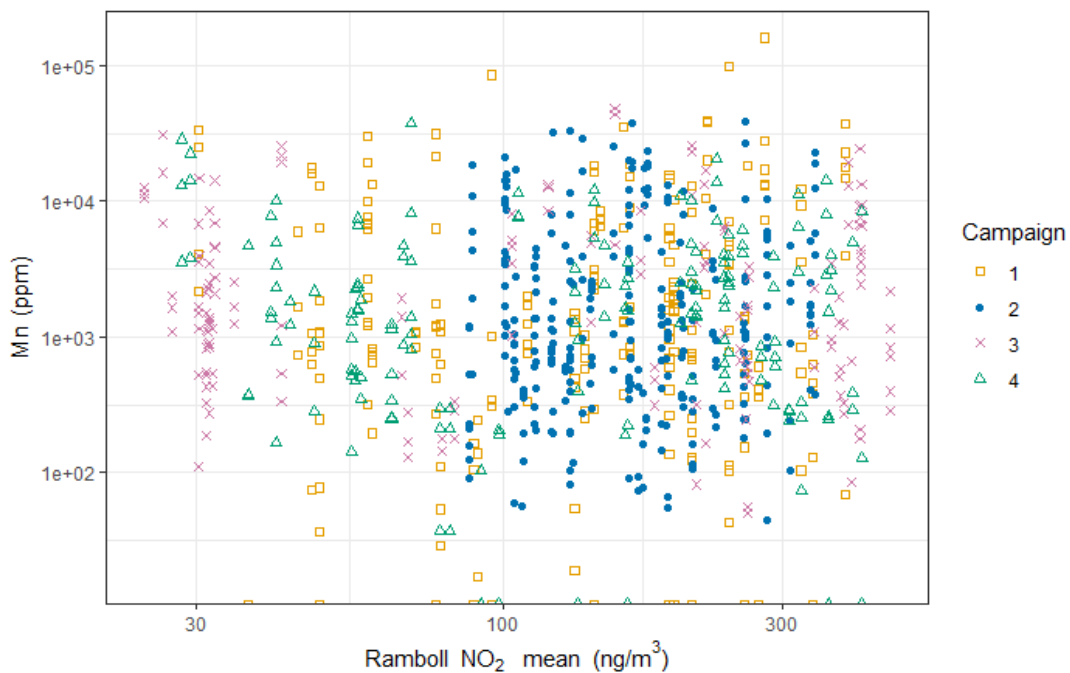


Figure 7-71: Measurements of Mn (from pXRF device) for each locality (including replicates) and campaign versus the log mean NO₂ concentration

7.7 Spatial dose response - pH versus weather and time

7.7.1 Validation of pH observations

The validity of this study rests on the validity of the field observations. It is especially important to identify any factors which could cause bias in these observations.

For the measurements of physico-chemical parameters (pH, Eh and Cl concentrations) on rock surfaces, there are several factors which could cause bias. The physical-chemical processes involved in these measurements are dependent on temperature (although the measurement device is designed to adjust for the temperature effect). The measurement procedure involves placing distilled/deionised water on the rock surface; the physical processes occurring in the solution will depend on the current wetness of the rock surface, and on recent weather. In a campaign of field measurements taking place over multiple days, the measurement technique itself can change in subtle ways, due to human factors (learning curves, differences between operators, changes in staffing) or changes in the instrumentation (electrode deterioration).

A standard check for potential sources of bias is a “lurking variable plot” in which the field observations are plotted against an external variable, such as the time of observation, which is not expected to have had any influence on the observed value. In cases where this plot unexpectedly reveals a trend in the observed values over time, for example, then this suggests that the observations depend on some factor (the ‘lurking variable’) which changes over time. Further investigation is then required.

For the field observations of pH, the main concerns are that the observations could be affected by weather and environmental conditions, or by changes in the field technique. To investigate the influence of any changes in the field technique, pH observations were plotted against date, day of the year, and day since the start of the campaign.

To investigate possible weather impacts, pH would ideally be plotted against the weather recorded at each site. However, weather observations were not available for these first four campaigns from the real-time monitoring stations. Instead, weather readings at Karratha Aerodrome (Bureau of Meteorology (BoM) weather station 004083) have been used as a proxy. The observed pH has been plotted against rain amount (both cumulative rain over various periods and days since rainfall) and temperature (wet bulb and dry bulb air temperature). This data is not yet available for campaign 4.

7.7.2 Campaign impacts

Figure 7-72 shows pH observations from each of the four campaigns, plotted against time in days since the start of the campaign. The weekly cycle of observations is clear, with gaps in measurement for each weekend. For campaigns 2, 3 and 4 there does not appear to be any trend in pH against time. However, for campaign 1 readings show a distinct increase in weeks 2 and 3 which is then maintained in weeks 4 and 5. In campaign 1, different observers made the observations for each week of the campaign, suggesting that this trend may be independent of the observers.

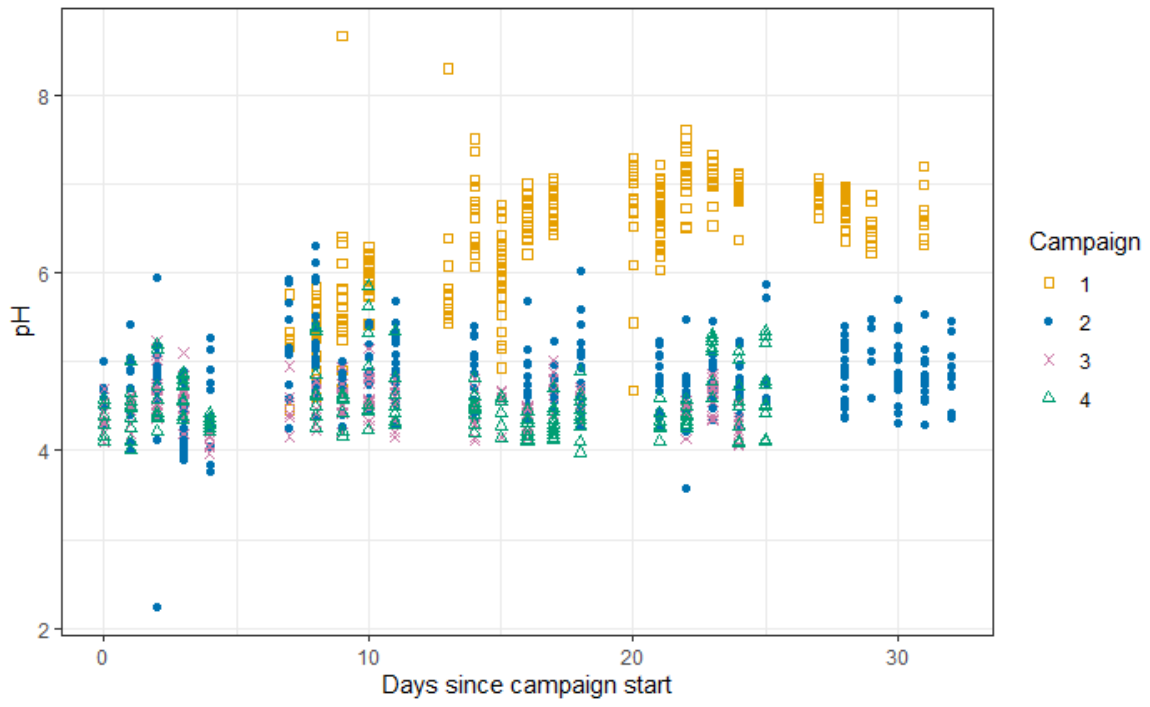


Figure 7-72: pH observations at each location versus days since the start of each campaign

7.7.3 Impact of temperatures on pH observations

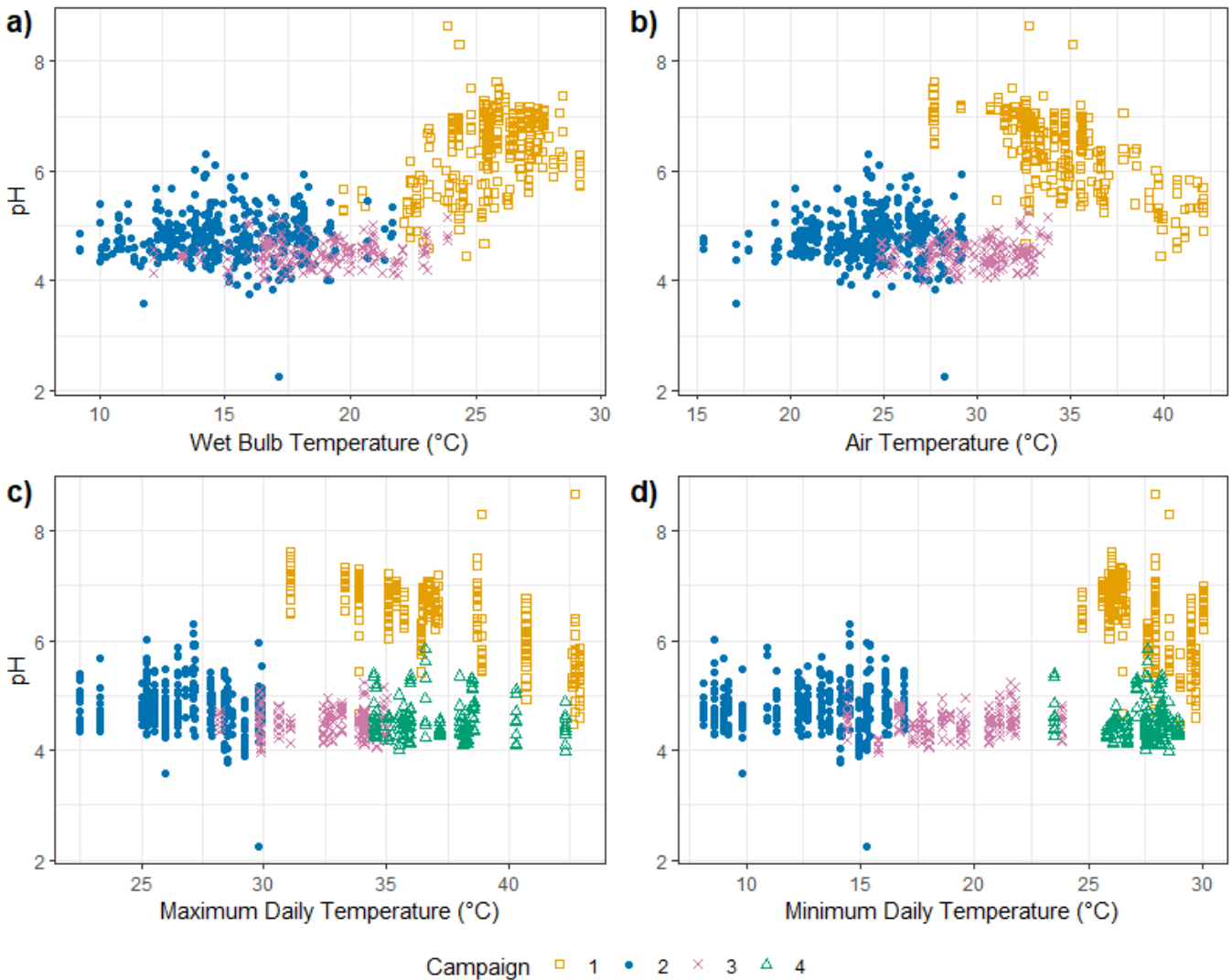


Figure 7-73: Scatter plots showing pH observations for each site in relation to temperature: (a) wet bulb temperature; (b) air temperature (or dry bulb temperature); (c) daily maximum temperature; and (d) daily minimum temperature. These temperatures were recorded at BOM Karratha Aero Station ID 004083 within a 15 minute period of the actual measurement being made.

Figure 7-73 plots (a) and (b) show pH observations against temperatures recorded at the BoM Karratha Aero weather station in the 15 minute period of the actual observation being made. Both wet bulb and air temperatures are shown. Wet bulb temperatures are made with a thermometer wrapped in damp cloth. Wet bulb temperature is related to both air temperature and humidity. The wet bulb temperature is generally lower than air temperature but increases as humidity increases towards the air temperature (BoM). For campaigns 2, 3, and 4 there is no distinct trend related to temperature. For campaign 1, there is a distinct increase in pH as the wet bulb temperature increases. Wet bulb temperatures for campaign 1 also tend to be higher than for the other campaigns. pH observations follow the opposite trend with air temperature, tending to decrease as air temperature increases. While there are differences in air temperatures in the campaigns, with campaign 3 generally hotter than campaign 2, and campaign 1 hotter than campaign 3, there is also some overlap in temperatures as well between campaigns 1 and 3. However, the trends shown in relation to air temperature for campaign 1 are not repeated in campaign 3.

Figure 7-73 plots (c) and (d) show the pH observations plotted against the daily maximum and minimum temperatures recorded at Karratha. These temperatures were used to enable inclusion of campaign 4 data, for

which other temperature statistics were not available at the time of undertaking this analysis. pH has a flat response to maximum and minimum temperatures for campaigns 2, 3 and 4. For campaign 1, pH tends to decrease as temperature rises (especially maximum temperatures), but this trend is not observed for the other campaigns, even when temperature values overlap.

Temperature was also measured in the field as the temperature of a tube of water: these measurements are not available for campaign 1 and show no correlation with pH observations for campaigns 2 to 4.

7.7.4 Impact of rainfall on pH observations

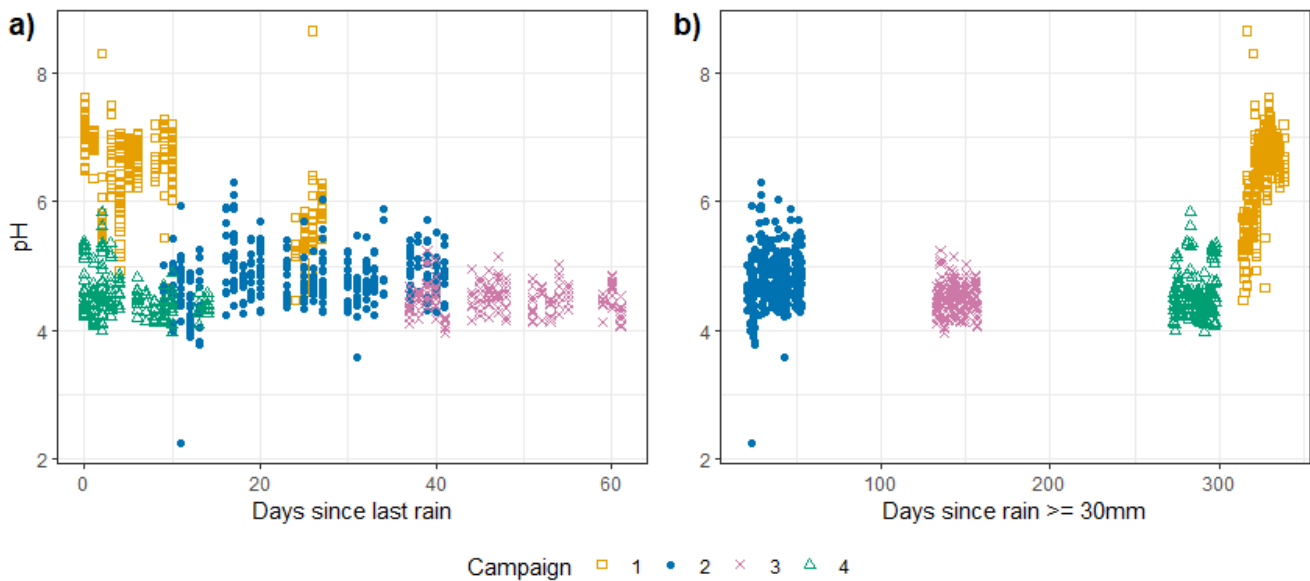


Figure 7-74: pH versus days since rainfall at Karratha Aero: a) since any rain and b) since substantial rain greater than 30 mm

Figure 7-74 shows pH plotted against the number of days since it last rained. Plot (a) shows days since any rainfall at all, including very small rainfalls of 0.4mm, while plot (b) shows days since substantial rainfall, defined here as rainfall > 30mm in a single day period. For pH since days of rain, there is no conclusive trend observable for campaigns 2, 3 and 4. For campaign 1, the pH appears to drop with increasing days since rain. However, there was a small rainfall event part way through this campaign after a dry wet season where no large rain fall event had yet occurred. For days since substantial rain, again there is no readily observable trend for campaigns 2, 3 and 4 but there is an apparent increase for campaign 1. pH was also plotted in relation to cumulative rainfall over periods prior to each campaign, but no substantive relations were observed for either four week or six-month periods prior to each campaign.

7.8 Key findings from statistical analysis

7.8.1 Field measurement of colour

The fieldwork team addressed many concerns that existed before the study began about the repeatability of procedures for colour measurement in the field. The protocol developed and adopted for this study has eliminated many of these concerns.

The fieldwork protocol also enabled researchers to detect cases in the field where the data produced by the JAZ instrument failed to meet criteria for validity of a colour measurement, and in many cases, enabled the operator to repeat the measurement. Conditions leading to high failure rates were identified, and the field protocol was modified to reduce the failure rate (for example by improved cooling of the device.).

The statistical team has closely scrutinised the data produced by the JAZ instrument in order to validate the reflectance spectrum and permit a more searching statistical analysis of colour change. Using a more stringent set of validity criteria, the team detected further issues, which were not previously reported or expected, in which the JAZ data are insufficiently consistent or otherwise fail to meet the validity criteria.

It is considered likely that further improvements to the field protocol (in particular, more effective thermal stabilisation of the device) could further reduce the proportion of measurements which fail to meet the validity criteria.

It would also be advantageous to update the JAZ instrument (which is no longer supported by the manufacturer), replacing it by its successor models which have a more accessible software interface. This would allow the statistical team and the data science team to code, and upload onto the new device, an algorithm which validates the reflectance spectrum according to the most stringent criteria. This would avoid the situation where a measurement appears to be valid in the field but subsequently fails the more stringent checks.

If a new model of spectroscopic sensor is adopted, then the statistical team strongly recommends an experiment to cross-calibrate the two models, in which both sensors are used in the field to measure the same targets.

7.8.2 Inorganic chemistry: physico-chemical parameters (pH, Eh, Cl)

There are currently several competing explanations for the differences observed between the results from the first and the subsequent fieldwork campaigns. One of the possible explanations is that weather has a strong influence on these measurements. More observations at different times of year are required to resolve this. Accordingly, the statistical team recommends that there should be four field campaigns in year 2 of the fieldwork phase. Only half of the sites need to be visited in each campaign.

Further investigation into the measurement technique is also warranted.

Setting these issues aside, and taking the Eh, pH, and Cl data at face value, the exploratory statistical analysis suggests the presence of spatial trend in the measurements. It also suggests that rock type should be treated as an explanatory variable in any analysis. No overall association between pH, Eh, and Cl concentration was observed.

7.8.3 Inorganic chemistry: pXRF

The results of element analysis in the field using pXRF are sufficient for purpose. Since it is highly plausible that patina condition and patina deterioration may depend on the rock's composition and microstructure, the pXRF results are needed mainly for use as explanatory variables. Results obtained in different campaigns are expected to be consistent, albeit subject to variability due to the instrument and the uncontrolled manual use of the device. These issues can be avoided by the use of element ratios shown to be robust by repeated analysis of the secondary standard. Initial statistical analysis confirms that the results are broadly consistent.

Vigilance is recommended when different brands or models of pXRF device are used. The limited data suggest there are systematic differences between brands. This issue can be avoided by continued use of the Bruker instrument purchased for the project and detailed cross-checking for any necessary instrument switch.

7.8.4 Passive air quality samplers

The initial validation of the IVL passive samplers is not entirely complete due to delays in laboratory processing. The provisional conclusion is that the statistical distribution of the IVL assays of the most important gas species is now well characterised, and that the passive sampler data will serve the intended purpose in the study.

7.8.5 Ramboll model

A simple analysis of the Ramboll model outputs, based on annual averages and annual maxima at each spatial location, supports the approach taken in this study, and militates against the idea of treating any site as a 'control'.

7.8.6 Dose-response analysis

A definitive analysis of the effect of pollution on rock condition is not possible (and was not envisaged to be possible) with the data collected so far.

Chamber studies in the laboratory are designed to provide evidence of cause-and-effect relationships between exposure to pollution and degradation in rock condition. These are in their early stages of development.

Field monitoring will provide direct measurements of exposure to pollution, and of changes in rock surface condition over time, and any association will then be investigated. The field monitoring stations have just been set up and are not yet returning stable streams of data.

In the meantime the statistical team has conducted a preliminary analysis comparing a surrogate measure of long term exposure (the Ramboll model output) with a proposed marker of rock surface degradation rate (the measured pH). These variables did not appear to be associated.

Observed differences between the pH measurements for campaign 1 and for the subsequent campaigns undertaken in the first year of studies need further investigation. Possible explanations include the effect of rainfall, sea spray and temperature. The statistical team recommends that there should be four fieldwork campaigns in the second year of fieldwork, in order to gain information about seasonal effects.

8 Progress towards interim EQCs

8.1 Introduction

The Murujuga Rock Art Monitoring (MRAMP) project will develop a suite of Environmental Quality Criteria (EQC), which will be combined – along with appropriate monitoring and management strategies– into an Environmental Quality Management Framework (EQMF) for Murujuga. The EQMF will be designed to ensure the rock art at Murujuga is protected from anthropogenic degradation (anthropogenically accelerated weathering) as far as practicable.

To ensure that EQCs can be determined, the current study is dual-armed, i.e., combines field experiments over a gradient of exposures and simulated exposure experiments in the laboratory. In addition, a range of laboratory experiments are underway to quantify physico-chemical and biological environments on the rocks and rock art, which will lead either to the development of new theoretical pathways for degradation, or direct evidence through the development of causal relationships across long term spatial air quality gradients.

8.2 Development of EQCs

Ideally, EQCs will be developed based on relationships initially determined in the field, with laboratory chamber experiments used to determine the “dose-response” curve for the system, permitting appropriate safety margins to be set for the various action levels.

Figure 8-1 shows an example of such a curve, with theoretical no observed adverse effect level (**NOAEL**), acceptable range, action Level (**AL**) and exceedance level (**EL**) shown.

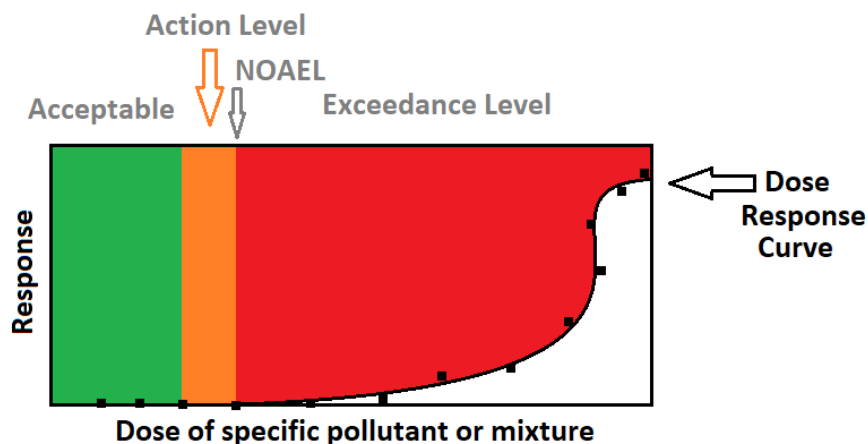


Figure 8-1: Example of a dose-response curve. Theoretical NOAEL, Acceptable, Action and Exceedance levels are shown, as are data points and a dose-response curve.

The MRAMP Head Agreement and subsequent clarifications from DWER and MAC representatives have defined degradation of the rocks and rock art to be any measurable change or acceleration of natural weathering which can be determined with an appropriate level of confidence to be due to anthropogenic activity. This excludes activities such as physical relocation of rocks or acts of vandalism, which are subject to separate management processes.

Typically, in toxicology, a NOAEL would have an appropriate safety factor added (e.g. x10 – x1000) lower than the lowest observed effect level, in order to determine a “safe” or Acceptable exposure level (i.e. a level at which there is sufficient confidence that no impacts above a natural baseline would occur). The AL would then be the range above this level but below any observed effect (e.g. at or below the NOAEL). The EL is the start of the region where effects have been observed, either in the field or the laboratory. It may be desirable to apply a larger safety factor to EQCs developed entirely using laboratory data, however this has yet to be determined.

While it is expected the EQCs will be able to be developed for all air pollutants which can produce strongly acidic or basic compounds (e.g. NO, NO₂, SO₂, etc.) it is likely that EQCs may not be able to be developed for some compounds, or the levels determined may be so far above established human health limits, it may be determined they are already captured by existing health standards and monitoring.

Another consideration is primary vs secondary air pollutants. For example, ground level ozone (O₃) is typically produced through a photocatalysed reaction between NO/NO₂ and VOCs. Therefore, EQC focus may be more appropriately placed on primary air pollutants.

Furthermore, it may be desirable to group classes of pollutant species. Toxicological effects can be additive or opposite for specific mixtures of chemicals, which may require grouping of species.

8.3 Spatial vs temporal relationships

Toxicological dose-response studies typically employ control populations to establish unequivocal dose-response curves. Unfortunately, in this case, it is not possible to conduct such an experiment without either a time machine or a 3-billion-year study, commencing with “fresh” rock surfaces, engraving them after ca. 2,999,920,000 to 2,999,999,900 years to produce petroglyphs, then exposing them to anthropogenic air pollution for the final ~60 years until the present day.

As such, aside from “accelerated” chamber studies in the laboratory (commencing with already weathered and exposed rock samples) the remaining options are:

- a) Longitudinal studies – observing if changes over time can be correlated with air pollutant levels.
- b) Spatial studies, which examine trends across spatial gradients, with a necessary assumption that such gradients have remained sufficiently constant over time.
- c) A combination of (a) and (b).

Given limitations in previous studies, at present, we are largely limited to (a) type studies, however will transition to include (b-c) type studies in year 2, incorporating prior datasets where possible (i.e. where data quality and study location permit). Furthermore, given the need to commence field (rock art) monitoring immediately following study design (MSDCA, 2022) approval, and delays in deployment of the MRAMP air quality monitoring network (mainly due to supply logistics and approval constraints), it is necessary to use the chemical dispersion modelling data (Ramboll, 2021), from a study commissioned by the WA Government, using the CAMx suite of chemical transport models, to determine any relationships at present. The CAMx model has used input data from known sources and modelled hourly pollutant concentrations and deposition over a “typical” year at 1.3 km grid resolution. Therefore, present dose-response correlations are using measured responses, however simulated “typical” dose information.

8.4 Correlation versus causation

The catch-phrase 'correlation is not causation' is often quoted as a caution against reading too much meaning into an observed correlation between variables in a study.

Under the right conditions, correlation is a useful tool for statistical analysis, and it is for this reason that correlations have been employed in this interim report. However, as the catch-phrase suggests, it is important to be cautious about the interpretation of the correlations which have been found.

First, by an effect known as Simpson's Paradox, a correlation observed between two variables X and Y may disappear when the analysis is adjusted to account for another variable Z. Alternatively if X and Y are uncorrelated, they may become correlated when the analysis is adjusted to account for Z. Because of this effect, there is no guarantee that the correlations between pairs of variables which have been found in this interim analysis will be confirmed in the final definitive statistical analysis based on all the relevant variables. This is also the reason why the definitive statistical analysis involves all variables at once.

Second, the development of EQCs must not only demonstrate a statistically significant association between dose and response variables, but also offer a plausible mechanism which gives confidence that an intervention changing the 'dose' would lead to a change in the 'response'.

From the first year's data, correlations have been found between the pH measurements taken on the rock (art) surfaces during the first campaign (campaign 1) and five (5) modelled air quality parameters, namely:

- NO₂,
- SO₂
- O₃
- NH₃
- PM₁₀

As noted previously, O₃ is a secondary air pollutant and the others are generally primary pollutants. Importantly, the expectation is that NO₂ and SO₂ generally produce acids in the environment given sufficient water and ultraviolet light to create OH radicals. However, the relationships found are the inverse of the acid deposition relationship predicted previously (e.g. Smith et al. 2022, Bednarik 2007), i.e., higher NO₂ or SO₂ results in higher pH (less acidic) instead of lower pH (more acidic). No correlation is present between the deposition predictions for the related acids in the CAMx model. One possibility is that given the period preceding campaign 1 was unseasonably dry, and field measurements also coincided with the hottest time of the year, reactions between the aforementioned gases and sea salt (NaCl) aerosol could perhaps become a dominant mechanism, resulting in less acidic or even basic compounds being formed (e.g., see Rissler et al., 2023), either in the atmosphere or on the rock surface. This would explain the significantly higher pH during campaign 1, however this mechanism is a poorly studied atmospheric phenomenon.

The NH₃ relationship follows the expected trend if the ammonia remains basic, rather than converts to the acidic ammonium (NH₄⁺) ion.

PM₁₀ is more complex, given it is a solid and composed of multiple species – primarily geogenic dust, iron ore dust, NaCl and to a lesser extent, carbonaceous matter and other compounds. Furthermore, given the substantial mass of particulate matter in the system and the lack of precipitation preceding campaign 1, it has the potential to adsorb and absorb other matter from the air. Further work is required to investigate any potential role of PM₁₀ constituent components and interactions with the rock surface – for example the potential SO₂+NaCl interaction discussed above.

A note of caution is necessary with respect to this summary of results. All combustion emissions (e.g. NO₂ and SO₂) have a similar emission and exposure concentration profile on a spatial scale. It is therefore difficult or impossible to differentiate them based on the current results. This means that EQCs must either be developed for a combination of species based on acid/base potential, or individual species based on chamber experiments. The Ramboll/CAMx model was unable to utilise a spatial (grid) resolution below 1.333 km, which inherently groups much of the industry footprint at Murujuga over 1-2 grids, and thus it is likely that much of the industrial emissions are spatially confounded in the air quality modelling outcomes used as the basis of analysis in this report.

Given the above considerations and the counter-intuitive nature of the pH/(NO₂ ; SO₂) correlations, more work is required to understand the geo/bio/chemical relationships taking place. However, it is expected that EQCs for the above species will be able to be developed in the near future.

8.5 Further steps to the development of EQCs

In general, for EQCs to be developed, the following questions must be answered:

- Is there a correlation between one or more dose variables and one or more response variables (either based on field or laboratory observations (detailed or chamber studies)?)
- Is there sufficient evidence of causation (e.g., a clear mechanism)?
- Have all relevant confounding factors been explored?
- Does the measured effect constitute a measurable change in the condition or integrity of the rock surface?

Once these questions have been answered, a dose-response curve can then be developed and EQC can be determined.

In the specific case of the relationships found to-date with pH as the response variable, the first question has been addressed, however the remaining steps are still in progress. Given the effect was only found during campaign 1, further measurements during dry seasons, or further chamber studies to confirm the mechanistic relationship, will be needed. Previous work has focused on acidification hypotheses and much of the study design has been influenced by the potential for mist deposition to concentrate air pollutants and acids on the rock surface. Given the lack of correlation during these wetter periods to date, attention must also be given to alternate chemical pathways during excessively hot and dry periods, which may become more prevalent given regional climate trends.

9 Key outcomes overall from the first year of scientific studies

This report summarises all available data and results from the MRAMP project to date.

The spectral measurement of rock art condition remains a promising approach, now that the issues of relocation and shading identified from previous work appear to have largely been resolved. Detailed criteria have been developed and presented in this report to identify any sources of error or non-repeatability in the measurements. It is planned to apply these in real time in future campaigns to ensure that all collected measurements can be utilised in analyses. The spectroscopy approach is likely best suited to monitor long term change rather than short term or seasonal responses, therefore data from additional measurement campaigns are required before it is meaningful to examine correlations between these measurements and air quality.

The geological and mineralogical studies have identified important compositional and structural/morphological trends in the surface/patina region. As expected, some features are related to rock type whereas others show consistent trends across rock type and are therefore likely due to environmental conditions. Detailed quantitative statistical analysis of the results are yet to be undertaken, however these studies appear to be a promising source of key information to fully understand the weathering system and processes occurring at Murujuga.

Some spatial trends in surface electrochemical measurements and elemental composition have been found. Spatial trends are also appearing with many air pollutants, which generally support trends in the prior air quality (CAMx) modelling studies. Spatial correlations have been determined between the pH dataset in campaign 1 and modelled air quality parameters, however further work is required before any EQCs can be developed based on these correlations. Specifically, correlations were found for nitrogen dioxide (NO₂), sulphur dioxide (SO₂) ozone (O₃), ammonia (NH₃) and particulate matter PM₁₀. It should be noted that the methods applied to date are unable to distinguish between air pollutants with sufficiently similar spatial patterns (for example, spatial gradients of NO₂ and SO₂ are near identical apart from regions where traffic sources are dominant). Furthermore:

- the observed relationships for the first two air pollutants are the reverse of what would be expected for a simple acid-deposition hypothesis;
- ozone is a secondary air pollutant, and
- PM₁₀ needs to be investigated as to whether it is a primary pollutant or a carrier for specific chemical species.

Further work and more field and chamber data are therefore required in order to understand confounders and mechanistic relationships before EQCs can be developed. Additionally, there are concerns held by the majority of the scientific team as regards the use of pH as an indicator. As shown (in Section 7.2), the method is highly susceptible to a range of factors including absorption of atmospheric CO₂ by distilled/deionised water, temperature, and other effects. It would be preferable to base the response component of any EQCs on more rigorous parameters. Work to determine such parameters, beyond potentially using pXRF measurements and field spectrometry measurements, is ongoing.

The researchers are confident that the current approaches are appropriate overall in terms of techniques and statistical power and the in-progress studies will provide information to enable true mechanistic relationships to be confirmed or otherwise. Given the unseasonably low rainfall in year 1, it is proposed that field measurement campaigns be repeated in year 2 at the same frequency and timing as in year 1, with the full number of rock-art monitoring sites stratified between campaigns (meaning that each campaign will study all AQ, EX and AS site with the RS sites randomly split across the campaigns such that each RS site is monitored once in year 2). A specific focus

will also be given to campaigns during dry times and the mechanisms which may occur in the atmosphere or on the rock surface during those times.

10 References

- Aho, K. and Weaver, T. (2006). Measuring water relations and pH of cryptogam rock-surface environments. *The Bryologist*, 109(3), 348-357. [https://doi.org/10.1639/0007-2745\(2006\)109\[348:MWRAP0\]2.0.CO;2](https://doi.org/10.1639/0007-2745(2006)109[348:MWRAP0]2.0.CO;2)
- American Society for Testing and Materials (ASTM). (2017). *Standard Practice for Obtaining Spectrophotometric Data for Object-Color Evaluation (E1164)*. <https://www.astm.org/>
- Diesel Fuel Quality Standard. (2019). *Fuel Quality Standards (Automotive Diesel) Determination 2019 (F2019L00456)*. Australian Government.
- Becker, R. A., Chambers, J. M. and Wilks, A. R. (1988). *The New S Language*. Wadsworth & Brooks/Cole.
- Bednarik, R.G. (2007). The science of Dampier rock art – Part 1, *Rock Art Research* 24(2):209-246
- Curtin University. (2022). *Murujuga Rock Art Monitoring Program: Monitoring Studies Data Collection and Analysis Plan*, Final Report prepared by Curtin University for the Department of Water and Environmental Regulation (COPP21065-PLN-G-102_0 / RES-HS-SPH-BM-62312_3). Government of Western Australia. <https://www.wa.gov.au/government/publications/murujuga-rock-art-monitoring-program-monitoring-studies-data-collection-and-analysis-plan>
- Donaldson, M. (2011). Understanding the rocks: Rock art and the geology of Murujuga (Burrup ‘Peninsula’), *Rock Art Research*, 28(1), 1-9.
- DWER (Department of Water and Environmental Regulation. (2021). *Murujuga Rock Art Monitoring Program: Conceptual Model* [Fact sheet]. Government of Western Australia. <https://www.wa.gov.au/government/publications/murujuga-rock-art-monitoring-conceptual-model>
- DIN (Deutsches Institut für Normung / German Institute for Standardisation). (2017). *Colorimetry- Part 1; Basic terms of colorimetry (5033-1)*. <https://www.din.de/>
- Egli, M; Mirabella, A; Nater, M; Alioth, L; Raimondi, S (2008). Clay minerals, oxyhydroxide formation, element leaching and humus development in volcanic soils. *Geoderma*, 143(1-2),101-114.
- Hastie, T. and Tibshirani, R. (1990). *Generalized Additive Models*. Chapman and Hall.
- International Standards Organisation (ISO). (1984). *Paints and varnishes Colorimetry Part 1: Principles (ISO 7724-1: 1984)*.
- Legendre, P. and Legendre, L. (2012). *Numerical Ecology* (3rd ed.). Elsevier.
- Markley, T., Fonteneau, L., Ramanaidou, E., Lau, D. and Alexander, D. (2014). *Burrup Peninsula Aboriginal Petroglyphs: Colour Change & Spectral Mineralogy 2004–2013* (Confidential Report t # EP143145). CSIRO.
- Neumann, J.T., Black, J.L., Hoerlé, S., Smith, B.W., Watkins, R., Lagos, M., Ziegler, A., Geisler, T. (2022). Artificial weathering of rock types bearing petroglyphs from Murujuga, Western Australia. *Heritage Science*, 10 (1), art. no. 77.
- Ramboll. (2021). *Study of the Cumulative impacts of Air Emissions in the Murujuga Airshed*, Final Report prepared by Ramboll for the Department of Water and Environmental Regulation. Government of Western Australia (18000883-14 Rev B). <https://www.der.wa.gov.au/images/documents/your->

environment/air/publications/Study-of-the-Cumulative-Impacts-of-Air-Emissions-in-the-Murujuga-Airshed-2022.pdf

- Rissler J., Preger C., Eriksson A.C., Lin J.J., Prisle N.L. and Svenningsson B. (2023). Missed evaporation from atmospherically relevant inorganic mixtures confounds experimental aerosol studies (2023) *Environmental Science and Technology*, 57 (7), 2706-2714. DOI: 10.1021/acs.est.2c06545.
- Smith, B.W., Black, J.L., Høerlé, S., Ferland, M.A., Diffey, S.M., Neumann, J.T., Geisler, T. (2022) The impact of industrial pollution on the rock art of Murujuga, Western Australia. *Rock Art Research*, 39 (1), 3-14.
- Wood S.N. (2017). *Generalized Additive Models: An Introduction with R* (2nd ed.). Chapman and Hall/CRC Press.

Appendix A: Drone images and processing

Appendix A-1 Introduction

This Appendix contains a summary of information from fully processed spatial mapping sites AQ02 to AQ08, and AQ10 to AQ11. The summary contains the following information for each site:

- Summary of capture data

This includes the drone (and camera) used, the number of images capture, the average resolution or ground sampling, and the type of control used to geo-reference the final model (and the number of control and how it was captured). Also summarised is the median number of key points per image (feature points used to match points between images), the number of tie points used in aligning the images together to create the 3D model, and the average re-projection error (error of the projected image point to the observed point). The last values are an indication of the strength of the signal and the errors in the 3D model.

- Position uncertainties table

This table documents the uncertainties in the calculated camera locations of the final adjustment. The locations are used in the projections and matching of the image points to re-create the 3D scene captured.

- Generated tie points

This table is a summary of the number of tie points used to match the image and create the 3D models. Included in this information is the total number of tie points found, the median number of images per point in the generation, the median number of points per image, and the re-projection errors (in terms of the median and RMS in pixels, and the RMS in terms of the distance of the projected tie points to the 3D object point).

- Control points

This table is a summary of the control points used to geo-reference the 3D model to the real-world location. This contains the initial accuracy of the points from the RTK pickup (relative to the base), the number of images they occur in, the errors (median and RMS) of the control in terms of the 3D model. The summaries of the 3D errors between the object point recreated from the imagery and the RTK located point are also presented. This is separated into 3D, horizontal errors, and vertical errors (with vertical errors normally being higher than horizontal errors).

- Position uncertainty figure

These figures contains the positional uncertainties of the generated tie points over the region. It gives an indication of the distribution of the tie points, and their errors and uncertainties in image matching in the adjustment. This can be used to determine some of the errors and missing information in the final 3D model.

(Figure A-1, Figure A-5, Figure A-9, Figure A-13, Figure A-17, Figure A-21, Figure A-25, and Figure A-29 for AQ02, AQ03, AQ04, AQ05, AQ06, AQ07-08, AQ10, and AQ11 respectively)

- Resolution figure

These figures show the resolution of the final 3D model, and the values over the area of capture. This is dependent on the flight parameters and the terrain that was captured.

(Figure A-2, Figure A-6, Figure A-10, Figure A-13, Figure A-18, Figure A-22, Figure A-26, and Figure A-30 for AQ02, AQ03, AQ04, AQ05, AQ06, AQ07-08, AQ10, and AQ11 respectively)

- Ortho image

These images are low-resolution orthographic mosaics depicting the area captured. This is created by projecting the images onto the terrain surface and stitching them together into a continuous mosaic.

(Figure A-3, Figure A-7, Figure A-11, Figure A-15, Figure A-19, Figure A-23, Figure A-27, and Figure A-31 for AQ02, AQ03, AQ04, AQ05, AQ06, AQ07-08, AQ10, and AQ11 respectively)

- Digital Elevation Model (DEM)

These figures are a low-resolution elevation model of the area, illustrating the changes in topology.

(Figure A-4, Figure A-8, Figure A-12, Figure A-16, Figure A-20, Figure A-24, Figure A-28, and Figure A-32 for AQ02, AQ03, AQ04, AQ05, AQ06, AQ07-08, AQ10, and AQ11 respectively)

Appendix A-2 Site AQ02

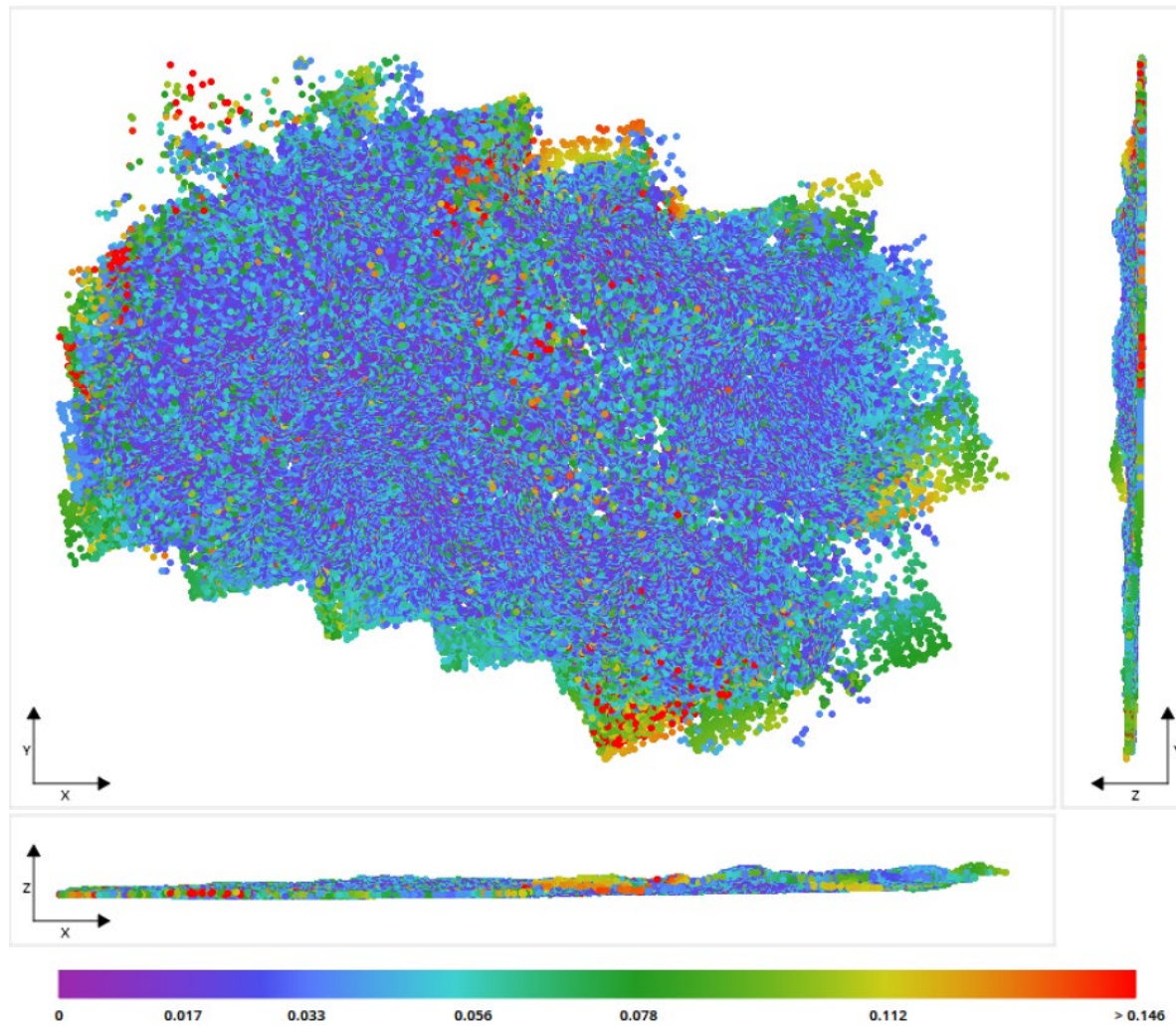
Survey parameters	
Drone	Phantom 4 Pro
Camera model	DJI FC6310
Images	558/558
Ground coverage	2405601 m ²
Average ground resolution	17.4834 mm/pixel
Geo referencing	7 control points (RTK)
Key points	Median of 49313 key points per image
Tie points	255109 points (median of 27060 points per photo)
Reprojection errors (RMS)	0.53 pixels

Position uncertainties (camera locations)			
	X (m)	Y (m)	Z (m)
Minimum	0.0018	0.0016	0.0008
Mean	0.003	0.003	0.0014
Maximum	0.0346	0.0444	0.023

Generated tie points						
Parameter	No. points	Median no. photos per point	Median no. points per photo	Median reprojection error (px)	RMS of reprojection error (px)	RMS of distances to rays (m)
Values	255109	4	2760	0.39	0.53	0.0639

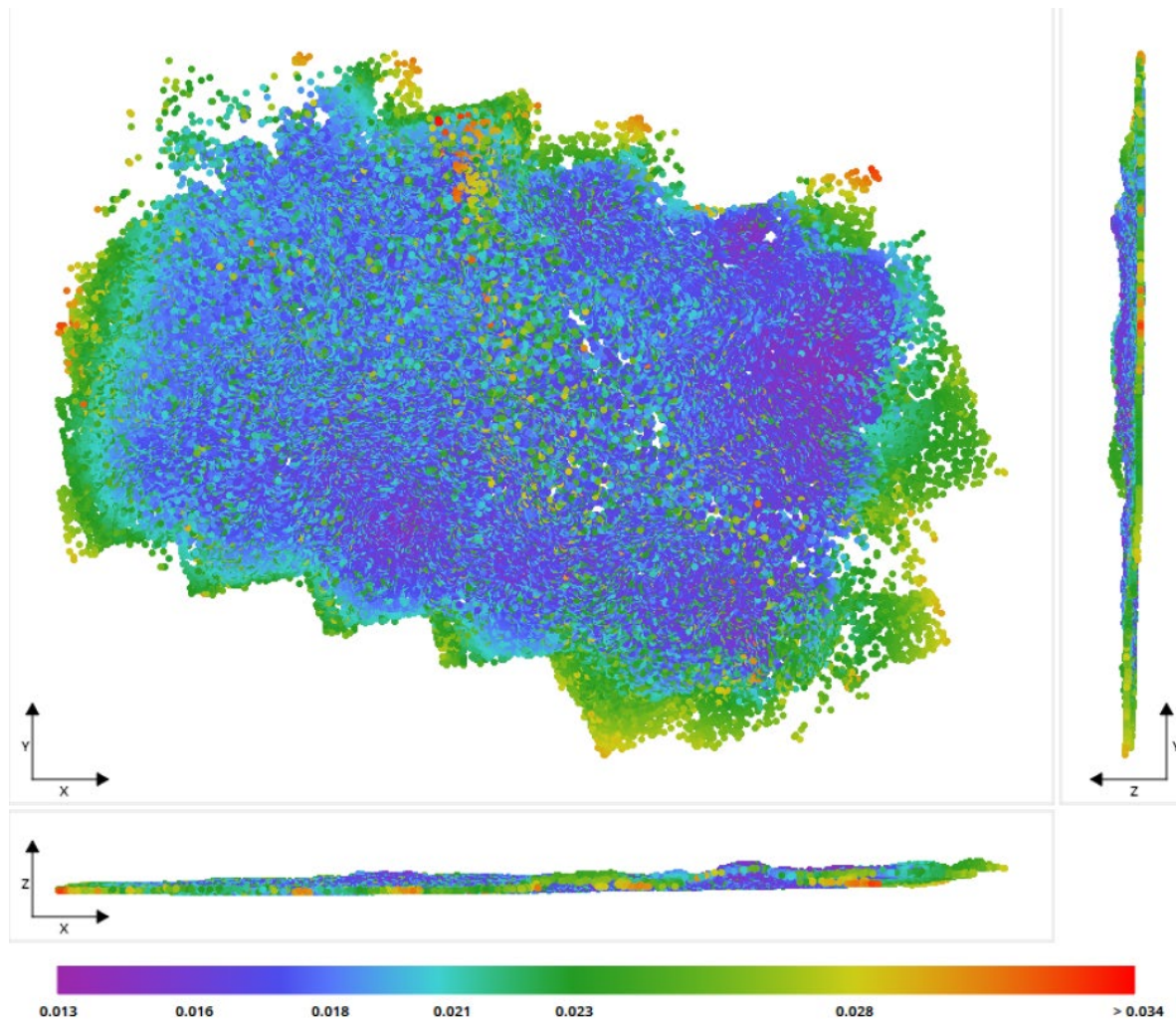
Murujuga Rock Art Monitoring Program
Monitoring Studies Report 2023

Control Points							
Name	Accuracy (m)	No. photos	RMS of reprojection error (px)	RMS of distances to rays (m)	3-D error (m)	Horizontal errors (m)	Vertical error (m)
aq02-uav01	H: 0.012 V: 0.026	16	0.6	0.051	0.0058	X: 0.0048 Y:-0.0008	0.0031
aq02-uav02	H: 0.011 V: 0.024	21	0.73	0.0629	0.0061	X:-0.0055 Y:-0.0006	-0.0027
aq02-uav03	H: 0.009 V: 0.018	40	0.64	0.0575	0.0051	X:-0.0001 Y:-0.0009	0.005
aq02-uav04	H: 0.01 V: 0.02	41	0.69	0.0808	0.0078	X: 0.0024 Y: 0.007	-0.0026
aq02-uav05	H: 0.01 V: 0.019	7	0.55	0.0793	0.0124	X: 0.0005 Y: 0.0015	0.0123
aq02-uav06	H: 0.015 V: 0.027	32	0.66	0.0693	0.0057	X:-0.0005 Y:-0.0004	-0.0057
aq02-uav07	H: 0.010 V: 0.018	21	0.59	0.0602	0.0038	X: 0.0008 Y:-0.0014	0.0035
Global RMS			0.64	0.0667	0.0072	X: 0.0029 Y:-0.0028	0.0059
Median			0.64	0.0629	0.0058	X: 0.0005 Y:-0.0006	0.0031



Position Uncertainties: Top view (XY plane), side view (ZY plane) and front view (XZ plane) displays of all tie points, with colors representing uncertainty in the individual point position. The values are in meters, with a minimum uncertainty of 0.0051 meters and a maximum of 0.6867 meters. The median position uncertainty equals 0.0335 meters.

Figure A-1: Site AQ02 mapping position uncertainties



Resolution: Top view (XY plane), side view (ZY plane) and front view (XZ plane) displays of all tie points, with colors representing resolution in the individual point position. The values are in meters/pixel, with a minimum resolution of 0.013 meters/pixel and a maximum of 0.0336 meters/pixel. The median resolution equals 0.0182 meters/pixel.

Figure A-2: Site AQ02 mapping resolution



Orthoimage

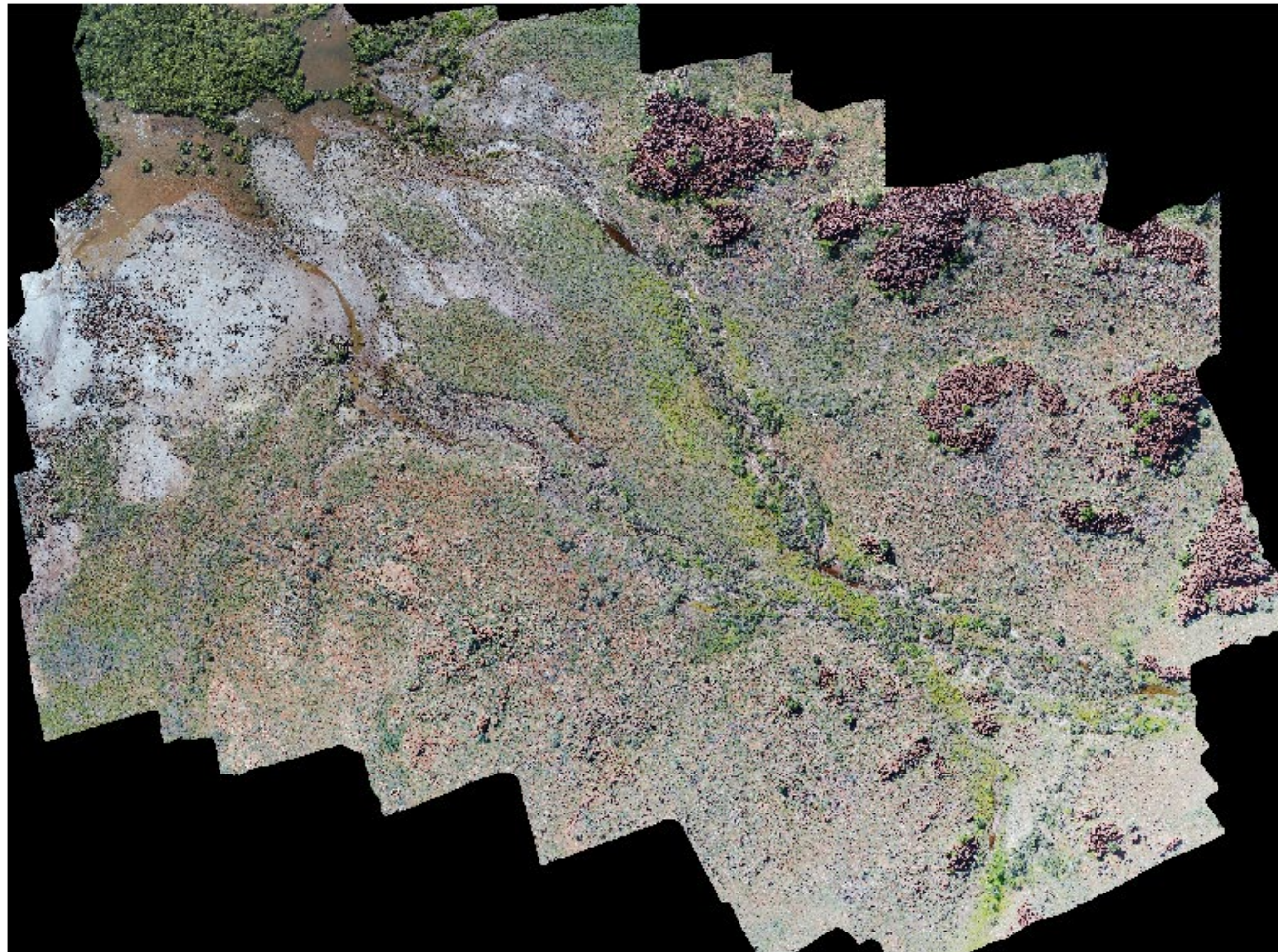


Figure A-3: Site AQ02 orthoimage

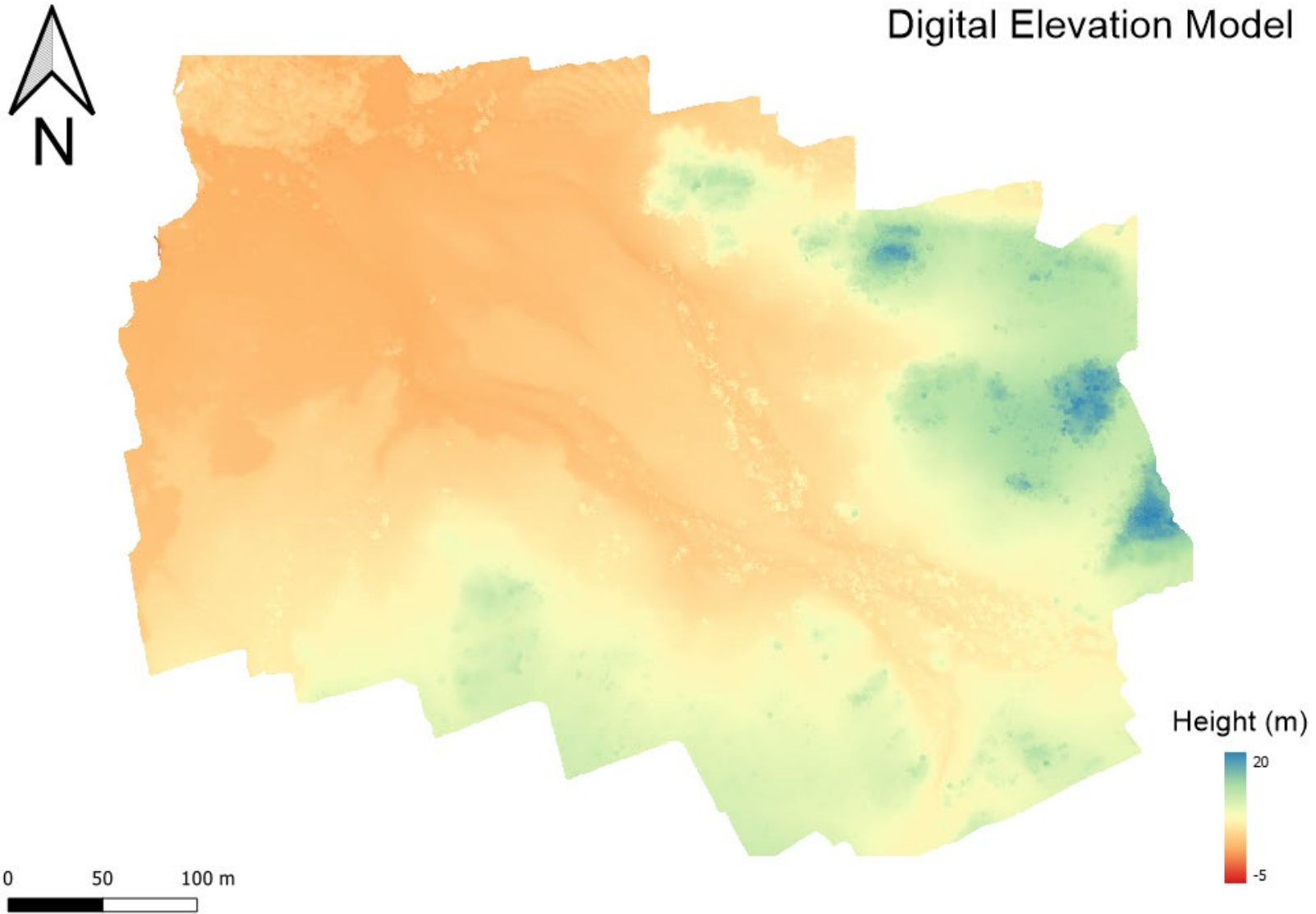


Figure A-4: Site AQ02 digital elevation model

Appendix A-3 Site AQ03

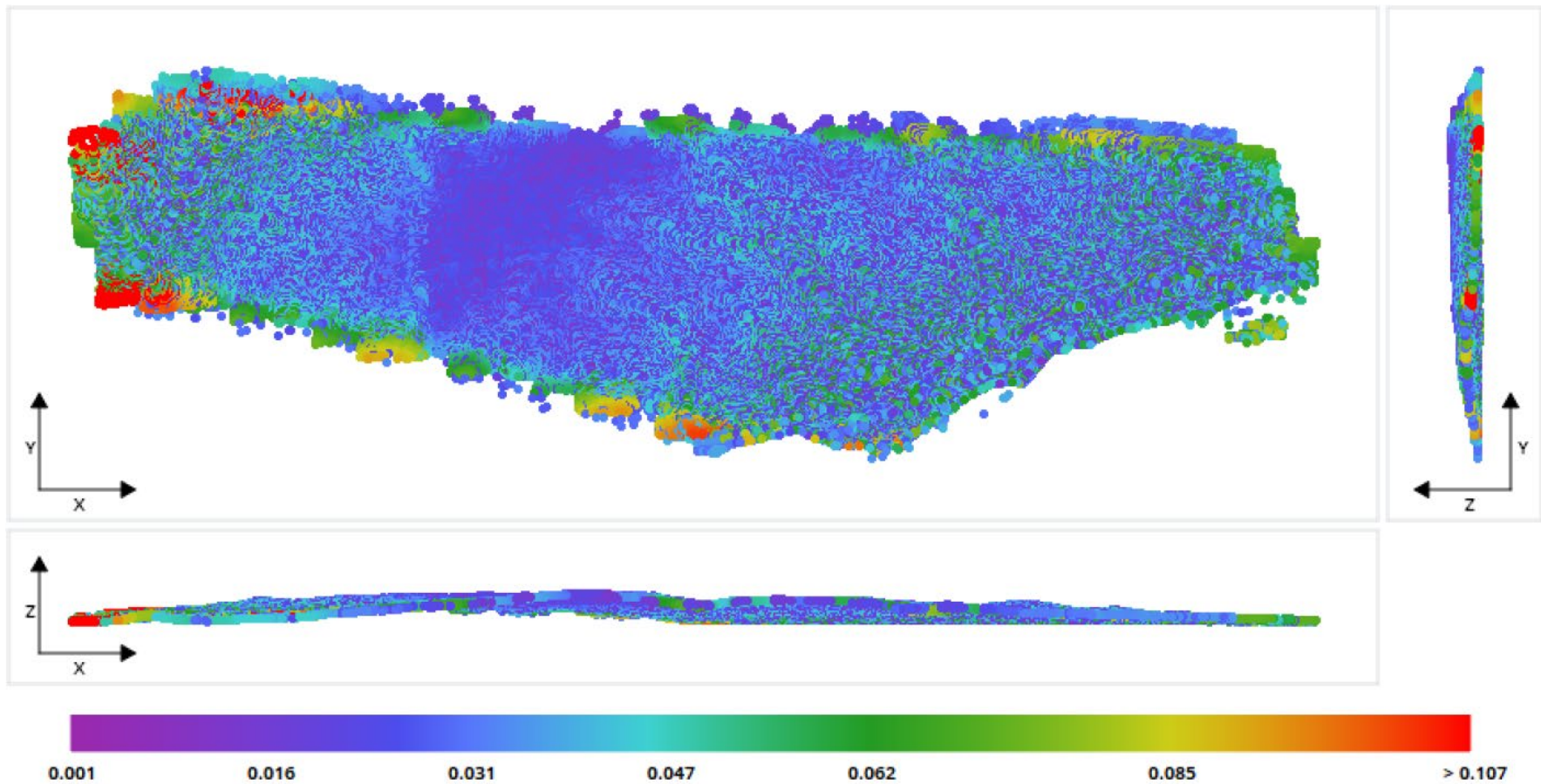
Survey parameters	
Drone	Phantom 4 Pro
Camera model	DJI FC6310
Images	895/865
Ground coverage	0.821 km ²
Average ground resolution	18.4324 mm/pixel
Geo referencing	8 control points (RTK)
Key points	Median of 48451 key points per image
Tie points	383184 points (median of 2014 points per photo)
Reprojection errors (RMS)	0.49 pixels

Position uncertainties (camera locations)			
	X (m)	Y (m)	Z (m)
Minimum	0.0020	0.0022	0.0008
Mean	0.0039	0.0052	0.0022
Maximum	0.3231	0.6447	0.5063

Generated tie points						
Parameter	No. points	Median no. photos per point	Median no. points per photo	Median reprojection error (px)	RMS of reprojection error (px)	RMS of distances to rays (m)
Values	383184	4	2014	0.35	0.49	0.0636

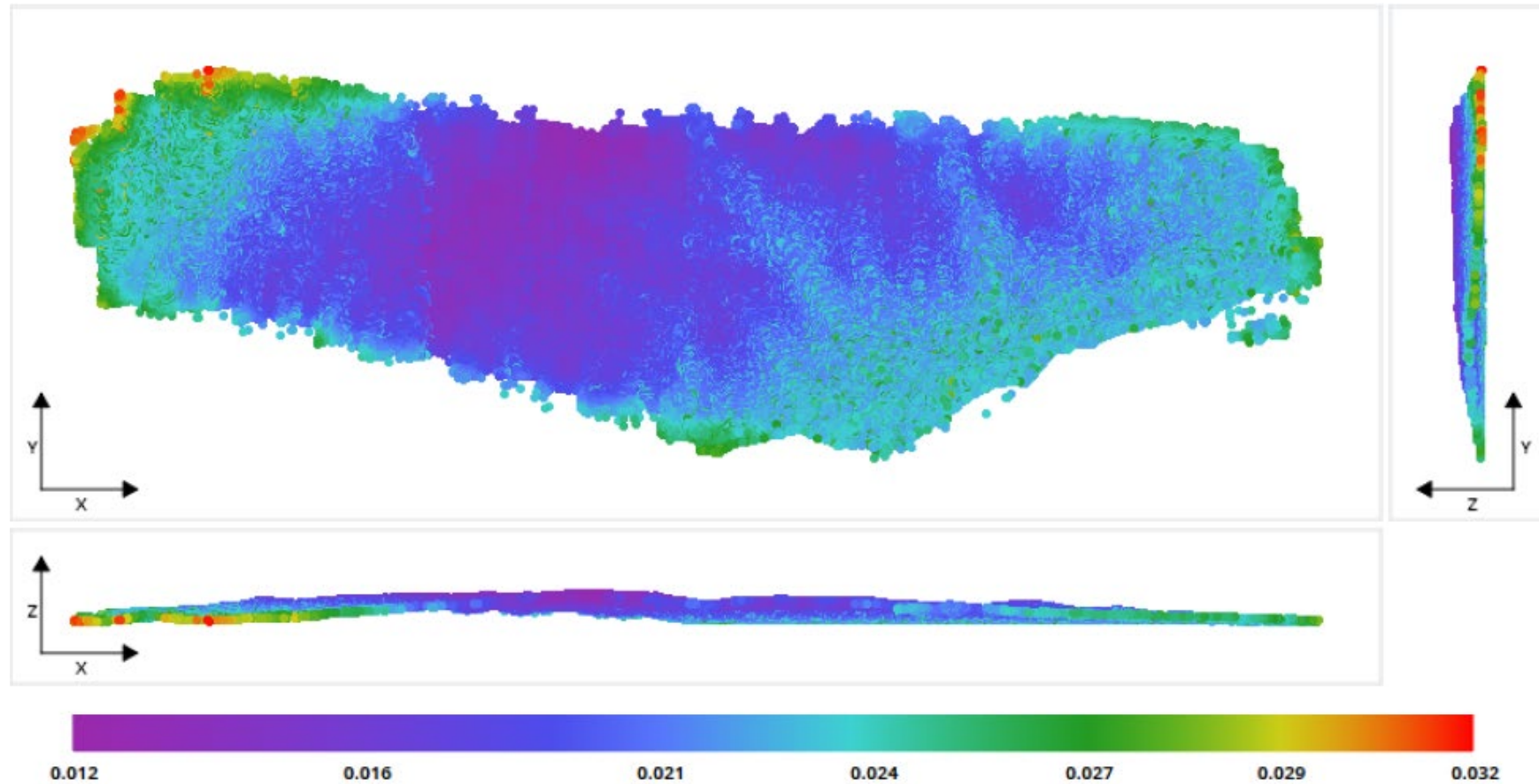
Murujuga Rock Art Monitoring Program
Monitoring Studies Report 2023

Control Points							
Name	Accuracy (m)	No. photos	RMS of reprojection error (px)	RMS of distances to rays (m)	3-D error (m)	Horizontal errors (m)	Vertical error (m)
aq03-uav01	H: 0.008 V: 0.018	17	0.45	0.0797	0.0043	X:-0.0014 Y: 0.001	0.0039
aq03-uav02	H: 0.009 V: 0.022	16	0.49	0.0791	0.004	X:-0.0010 Y: 0.0005	-0.0038
aq03-uav03	H: 0.009 V: 0.018	13	0.55	0.0717	0.0033	X: 0.0014 Y:-0.0011	-0.0028
aq03-uav04	H: 0.008 V: 0.015	11	0.44	0.0579	0.0045	X:-0.0002 Y: 0.0039	-0.0022
aq03-uav05	H: 0.006 V: 0.012	11	0.48	0.0743	0.0059	X: 0.0025 Y:-0.0046	0.0026
aq03-uav06	H: 0.017 V: 0.035	15	0.41	0.0732	0.0039	X:-0.0006 Y:-0.0032	-0.0021
aq03-uav07	H: 0.015 V: 0.03	17	0.39	0.0807	0.0059	X: 0.003 Y:-0.0011	0.0049
Aq03-uav-8	H: 0.015 V: 0.03	14	0.44	0.086	0.0032	X:-0.0019 Y: 0.0016	-0.002
Global RMS			0.46	0.0758	0.0045	X: 0.0017 Y: 0.0026	0.0032
Median			0.45	0.0791	0.0042	X:-0.0002 Y: 0.0005	-0.002



Position Uncertainties: Top view (XY plane), side view (ZY plane) and front view (XZ plane) displays of all tie points, with colors representing uncertainty in the individual point position. The values are in meters, with a minimum uncertainty of **0.0076 meters** and a maximum of **0.1783 meters**. The median position uncertainty equals **0.0314 meters**.

Figure A-5: Site AQ03 mapping position uncertainties



Resolution: Top view (XY plane), side view (ZY plane) and front view (XZ plane) displays of all tie points, with colors representing resolution in the individual point position. The values are in meters/pixel, with a minimum resolution of 0.0122 meters/pixel and a maximum of 0.0321 meters/pixel. The median resolution equals 0.0206 meters/pixel.

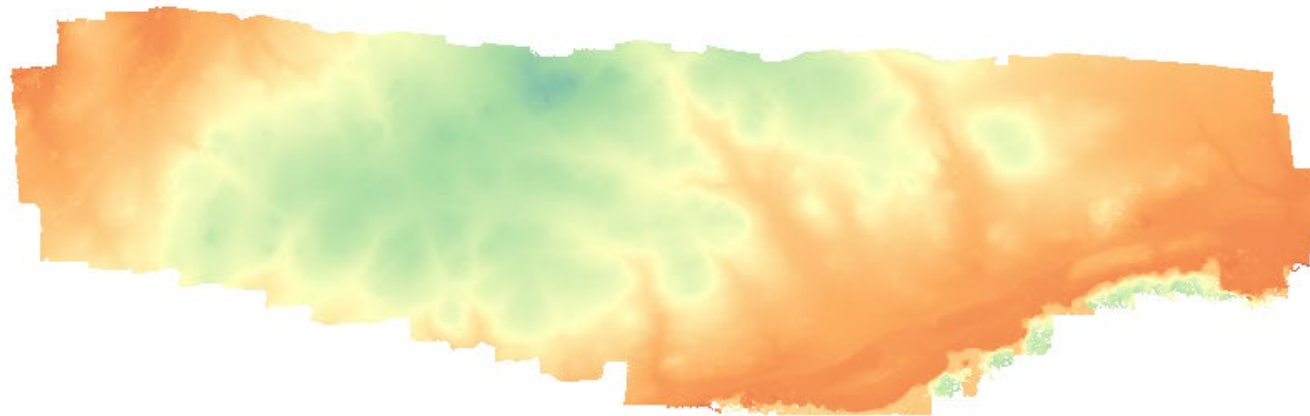
Figure A-6: Site AQ03 mapping resolution

Orthoimage



Figure A-7: Site AQ03 orthoimage

Digital Elevation Model



Height (m)



Figure A-8: Site AQ03 digital elevation model

Appendix A-4 Site AQ04

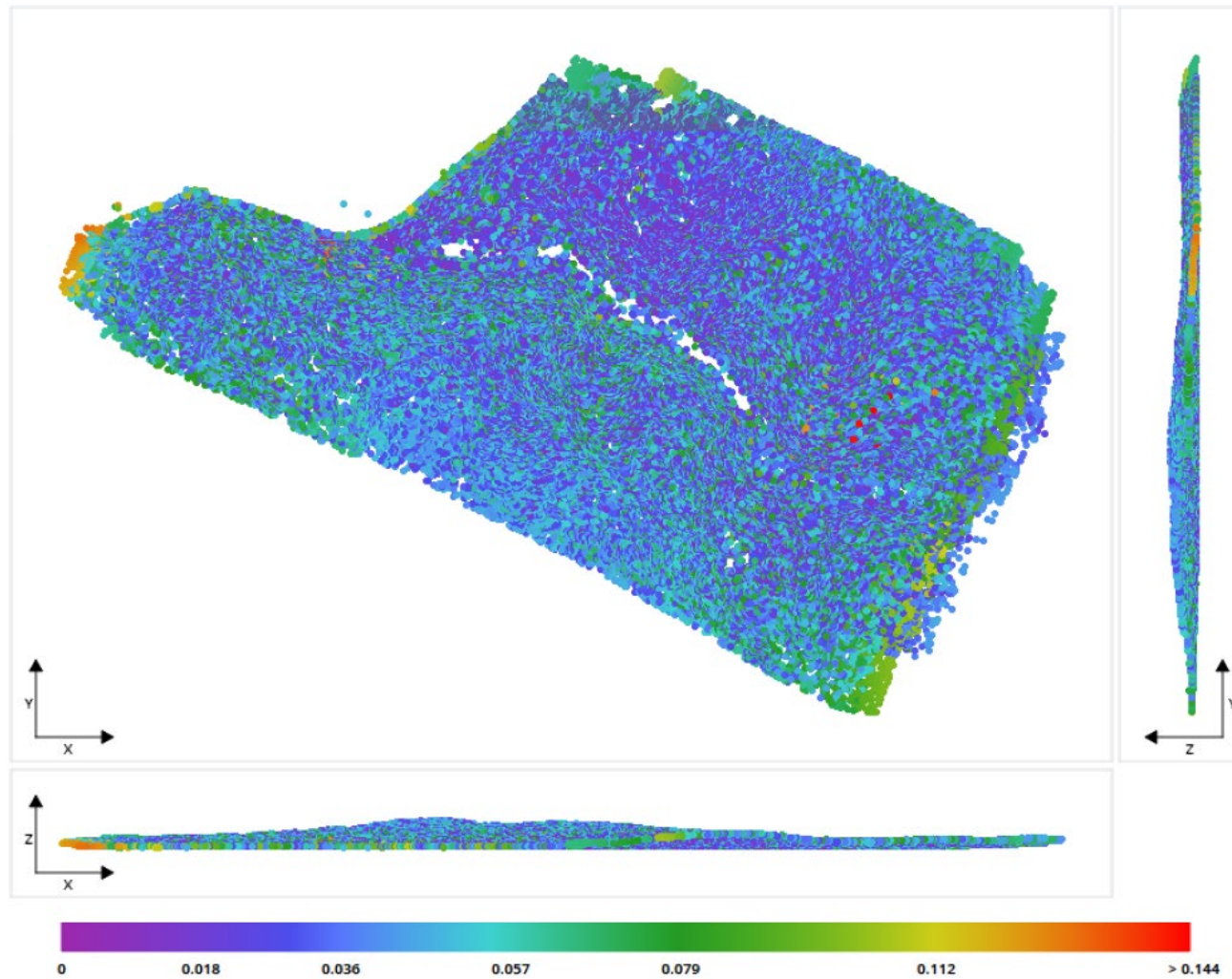
Survey parameters	
Drone	Phantom 4 Pro
Camera model	DJI FC6310
Images	373/373
Ground coverage	313790.02 m ²
Average ground resolution	19.6639 mm/pixel
Geo referencing	8 control points (RTK)
Key points	Median of 49187 key points per image
Tie points	176289 points (median of 2509 points per photo)
Reprojection errors (RMS)	0.53 pixels

Position uncertainties (camera locations)			
	X (m)	Y (m)	Z (m)
Minimum	0.0021	0.0021	0.0009
Mean	0.0033	0.0031	0.0014
Maximum	0.012	0.0127	0.0046

Generated tie points						
Parameter	No. points	Median no. photos per point	Median no. points per photo	Median reprojection error (px)	RMS of reprojection error (px)	RMS of distances to rays (m)
Values	176289	4	2509	0.39	0.53	0.06642

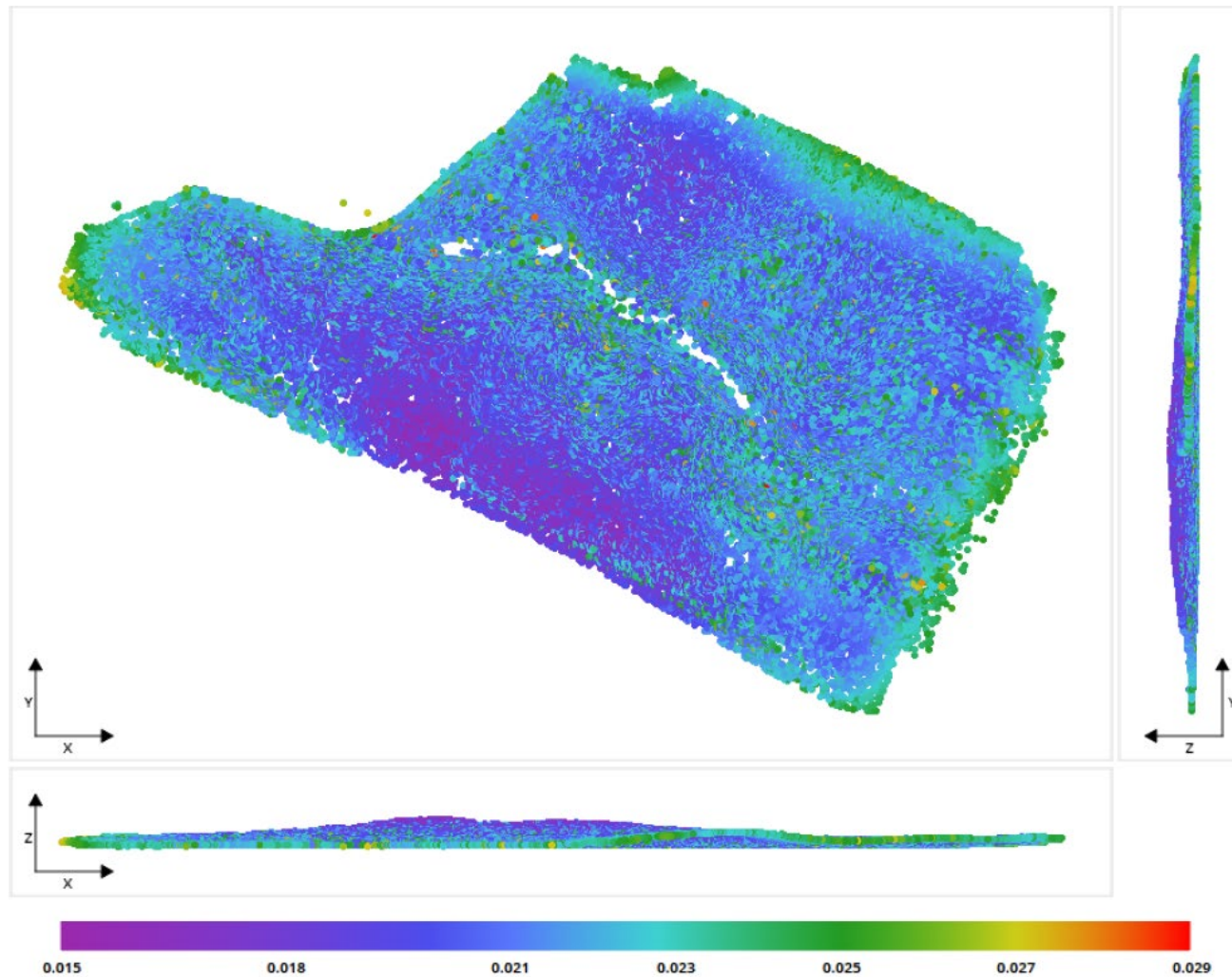
Murujuga Rock Art Monitoring Program
Monitoring Studies Report 2023

Control Points							
Name	Accuracy (m)	No. photos	RMS of reprojection error (px)	RMS of distances to rays (m)	3-D error (m)	Horizontal errors (m)	Vertical error (m)
aq04-uav01	H: 0.008 V: 0.02	25	0.65	0.0849	0.0027	X: 0.0009 Y: 0.0024	0.0009
aq04-uav02	H: 0.007 V: 0.017	18	0.54	0.0656	0.0082	X:-0.008 Y: 0.0017	0
aq04-uav03	H: 0.009 V: 0.02	18	0.69	0.0574	0.00124	X: 0.0036 Y:-0.0107	0.005
aq04-uav04	H: 0.008 V: 0.017	20	0.69	0.0619	0.0084	X: 0.0077 Y: 0.0024	0.0023
aq04-uav05	H: 0.01 V: 0.022	18	0.84	0.06	0.0136	X:-0.0126 Y: 0.005	-0.0011
aq04-uav06	H: 0.008 V: 0.017	19	0.44	0.062	0.0043	X:-0.0033 Y: 0.0027	-0.0010
aq04-uav07	H: 0.008 V: 0.017	26	0.65	0.0879	0.0031	X:-0.0016 Y:-0.0021	0.0017
aq04-uav08	H: 0.008 V: 0.016	25	0.81	0.0952	0.0122	X: 0.012 Y:-0.001	-0.0017
Global RMS			0.67	0.0732	0.0091	X: 0.0075 Y:-0.0046	0.0022
Median			0.69	0.0656	0.0084	X: 0.0009 Y: 0.0024	0.0009



Position Uncertainties: Top view (XY plane), side view (ZY plane) and front view (XZ plane) displays of all tie points, with colors representing uncertainty in the individual point position. The values are in meters, with a minimum uncertainty of 0.0069 meters and a maximum of 0.1573 meters. The median position uncertainty equals 0.0357 meters.

Figure A-9: AQ04 mapping position uncertainties



Resolution: Top view (XY plane), side view (ZY plane) and front view (XZ plane) displays of all tie points, with colors representing resolution in the individual point position. The values are in meters/pixel, with a minimum resolution of 0.015 meters/pixel and a maximum of 0.029 meters/pixel. The median resolution equals 0.0206 meters/pixel.

Figure A-10: Site AQ04 mapping resolution

Orthoimage

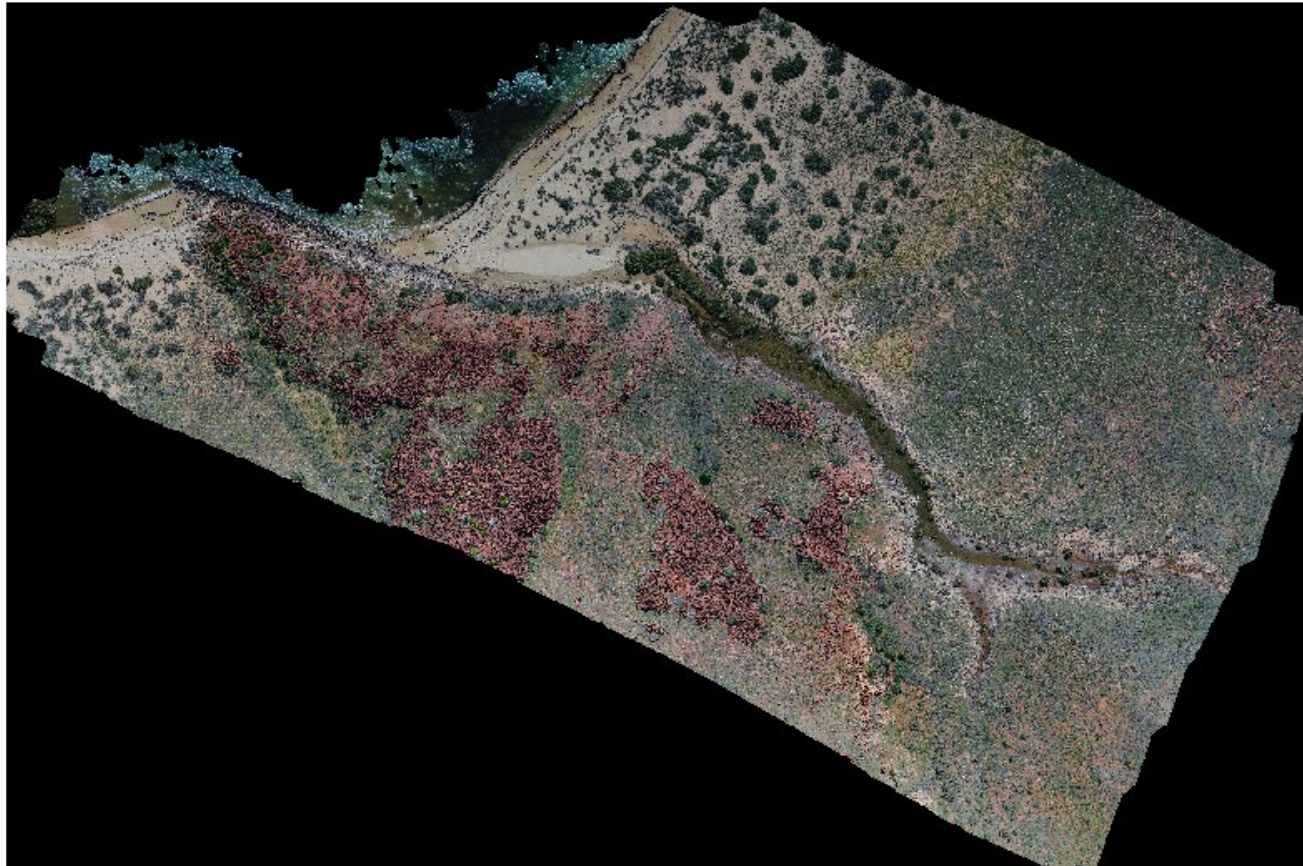
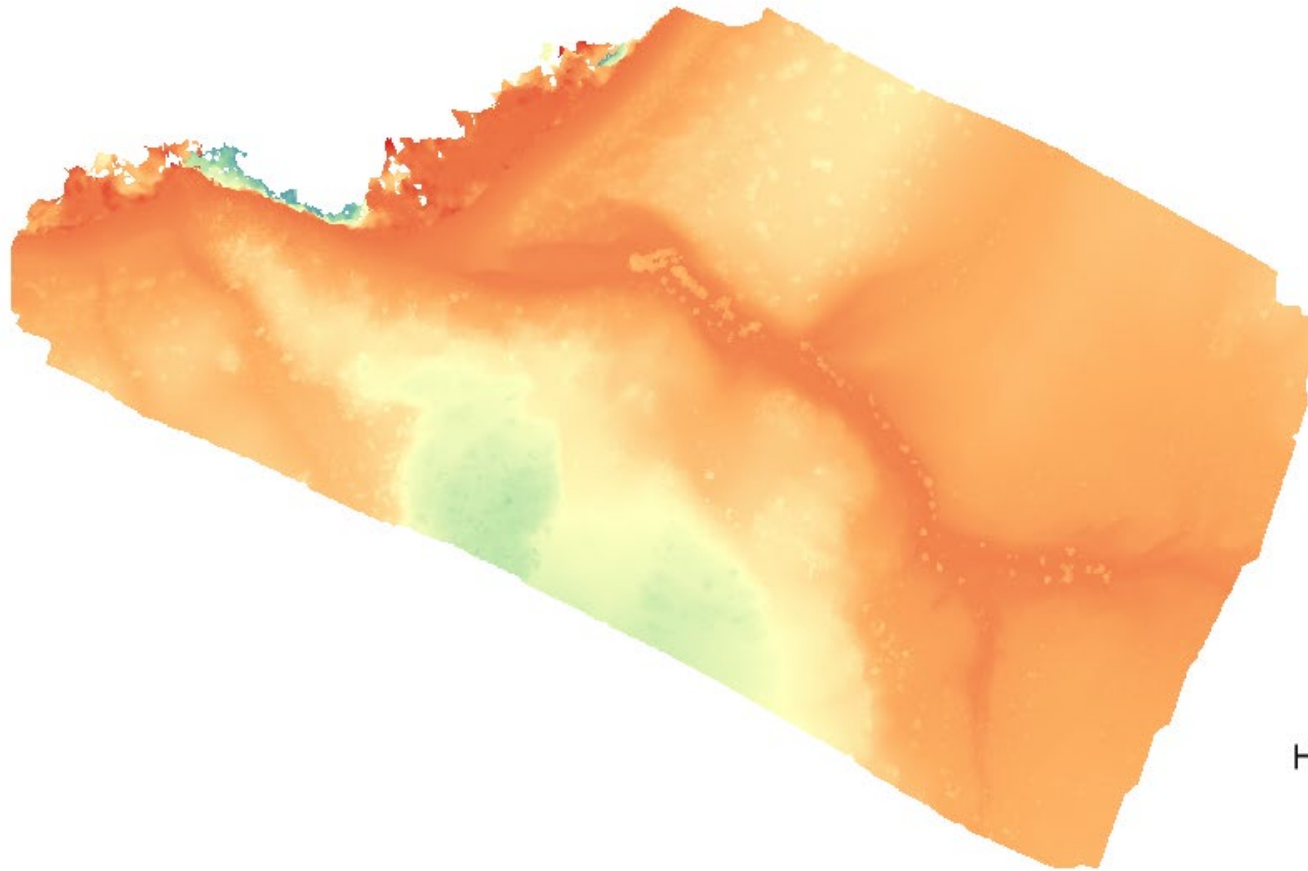


Figure A-11: Site AQ04 orthoimage



Digital Elevation Model



Height (m)



Figure A-12: Site AQ04 digital elevation model

Appendix A-5 Site AQ05

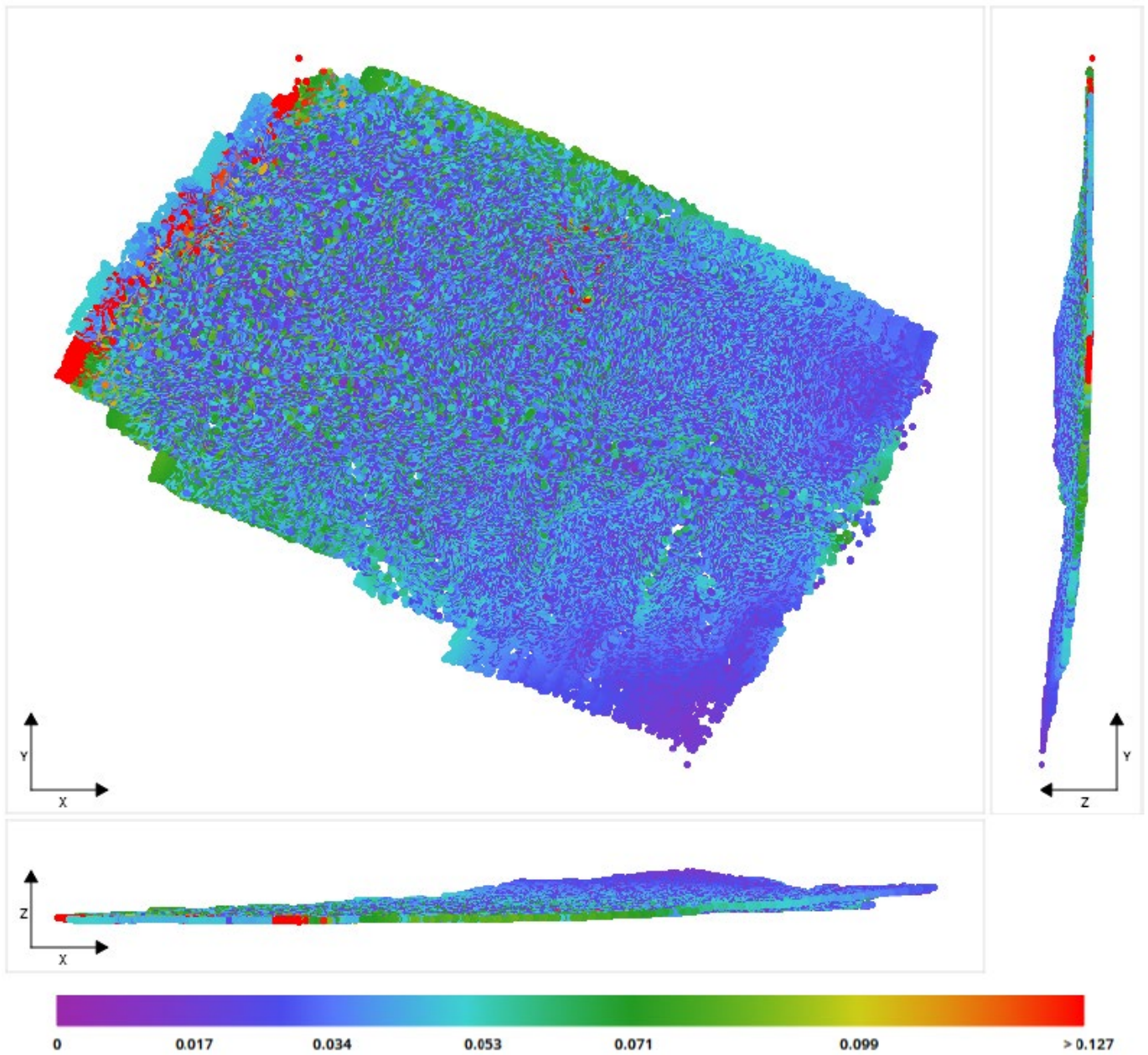
Survey parameters	
Drone	Phantom 4 Pro
Camera model	DJI FC6310
Images	584/588
Ground coverage	0.542 km ²
Average ground resolution	19.59255 mm/pixel
Geo referencing	6 control points (RTK)
Key points	Median of 49584 key points per image
Tie points	292382 points (median of 2707 points per photo)
Reprojection errors (RMS)	0.49 pixels

Position uncertainties (camera locations)			
	X (m)	Y (m)	Z (m)
Minimum	0.00228	0.00205	0.00088
Mean	0.00327	0.00304	0.00128
Maximum	0.02807	0.02021	0.01183

Generated tie points						
Parameter	No. points	Median no. photos per point	Median no. points per photo	Median reprojection error (px)	RMS of reprojection error (px)	RMS of distances to rays (m)
Values	292382	4	2707	0.36	0.49	0.07117

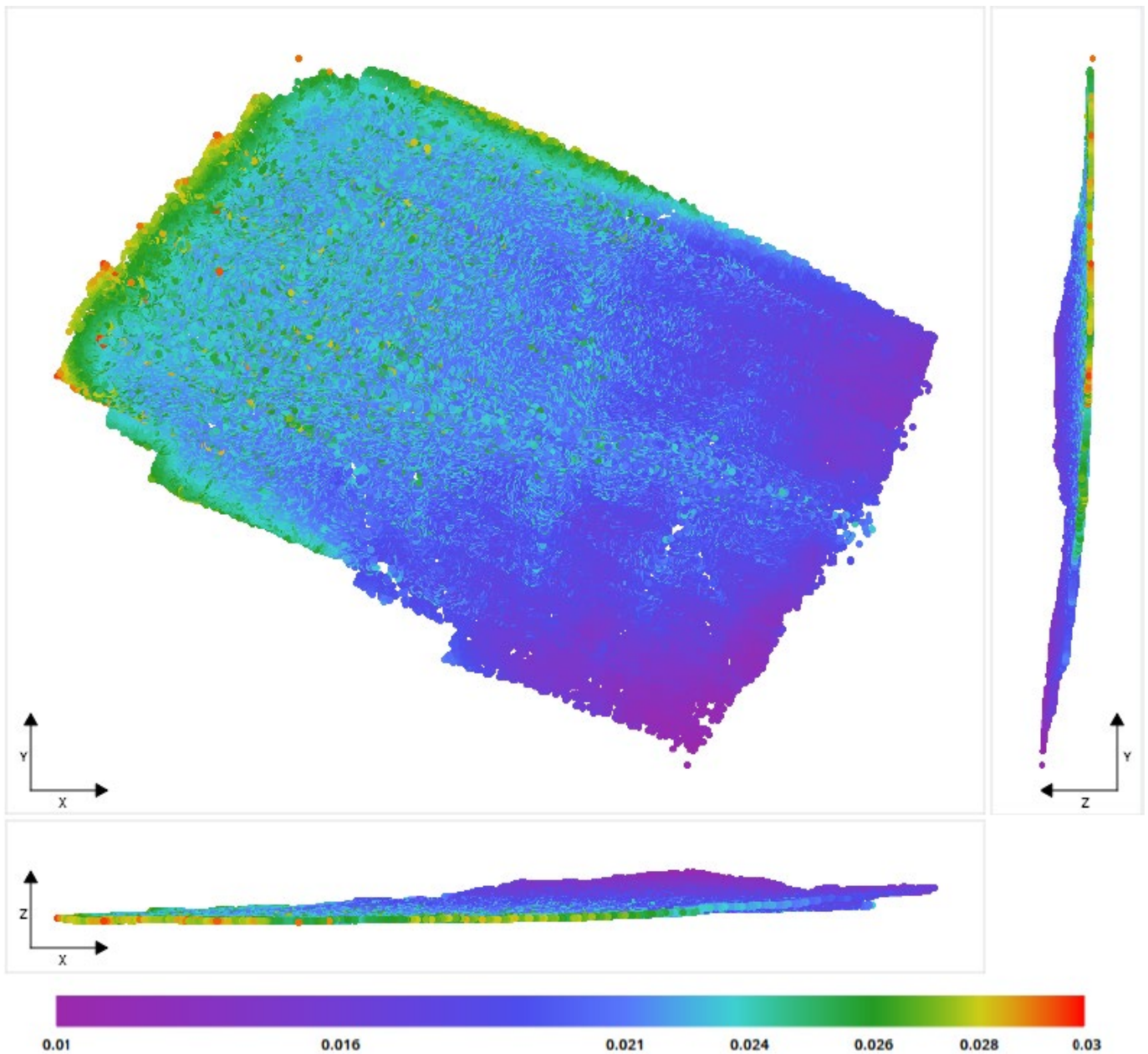
Murujuga Rock Art Monitoring Program
Monitoring Studies Report 2023

Control Points							
Name	Accuracy (m)	No. photos	RMS of reprojection error (px)	RMS of distances to rays (m)	3-D error (m)	Horizontal errors (m)	Vertical error (m)
aq05-01	H: 0.007 V: 0.021	13	0.42	0.0874	0.00529	X: 0.00275 Y: 0.00348	-0.00287
aq05-02	H: 0.016 V: 0.051	14	0.77	0.05287	0.01243	X: 0.00822 Y:-0.00919	0.00157
aq05-03	H: 0.015 V: 0.045	16	0.45	0.06944	0.00495	X:-0.00486 Y:-0.0008	0.00512
aq05-04	H: 0.011 V: 0.033	20	0.61	0.07506	0.00968	X: 0.00408 Y: 0.00874	0.00081
aq05-05	H: 0.011 V: 0.031	22	0.61	0.09459	0.00772	X:-0.00751 Y:-0.0014	0.00115
Global RMS			0.58	0.07725	0.00849	X: 0.00586 Y: 0.00593	0.00161
Median			0.61	0.07506	0.00772	X: 0.00275 Y:-0.00008	0.00081



Position Uncertainties: Top view (XY plane), side view (ZY plane) and front view (XZ plane) displays of all tie points, with colors representing uncertainty in the individual point position. The values are in meters, with a minimum uncertainty of 0.00739 meters and a maximum of 0.15929 meters. The median position uncertainty equals 0.03397 meters.

Figure A-13: AQ05 mapping position uncertainties



Resolution: Top view (XY plane), side view (ZY plane) and front view (XZ plane) displays of all tie points, with colors representing resolution in the individual point position. The values are in meters/pixel, with a minimum resolution of 0.01018 meters/pixel and a maximum of 0.03017 meters/pixel. The median resolution equals 0.02123 meters/pixel.

Figure A-14: Site AQ05 mapping resolution

Orthoimage

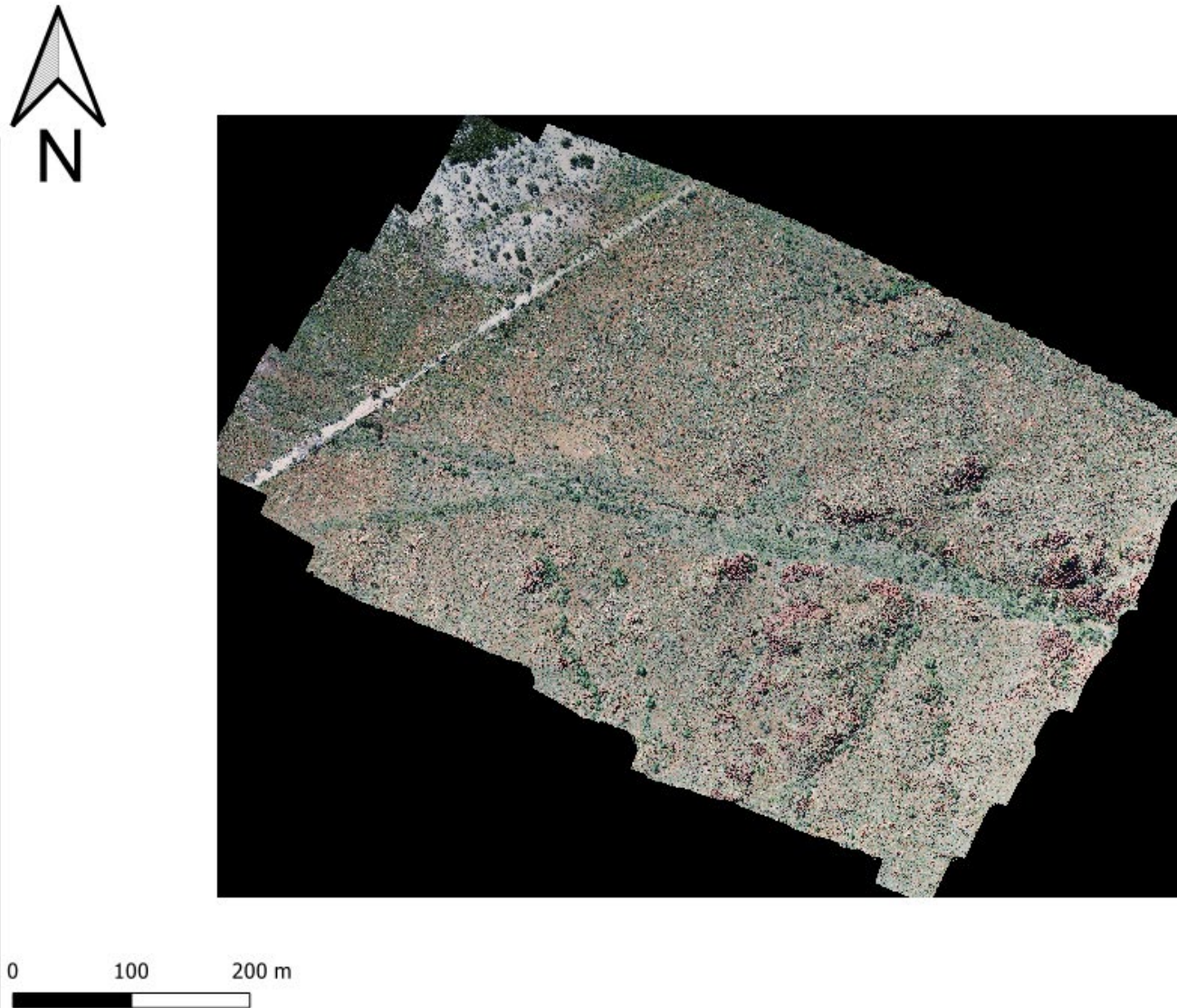
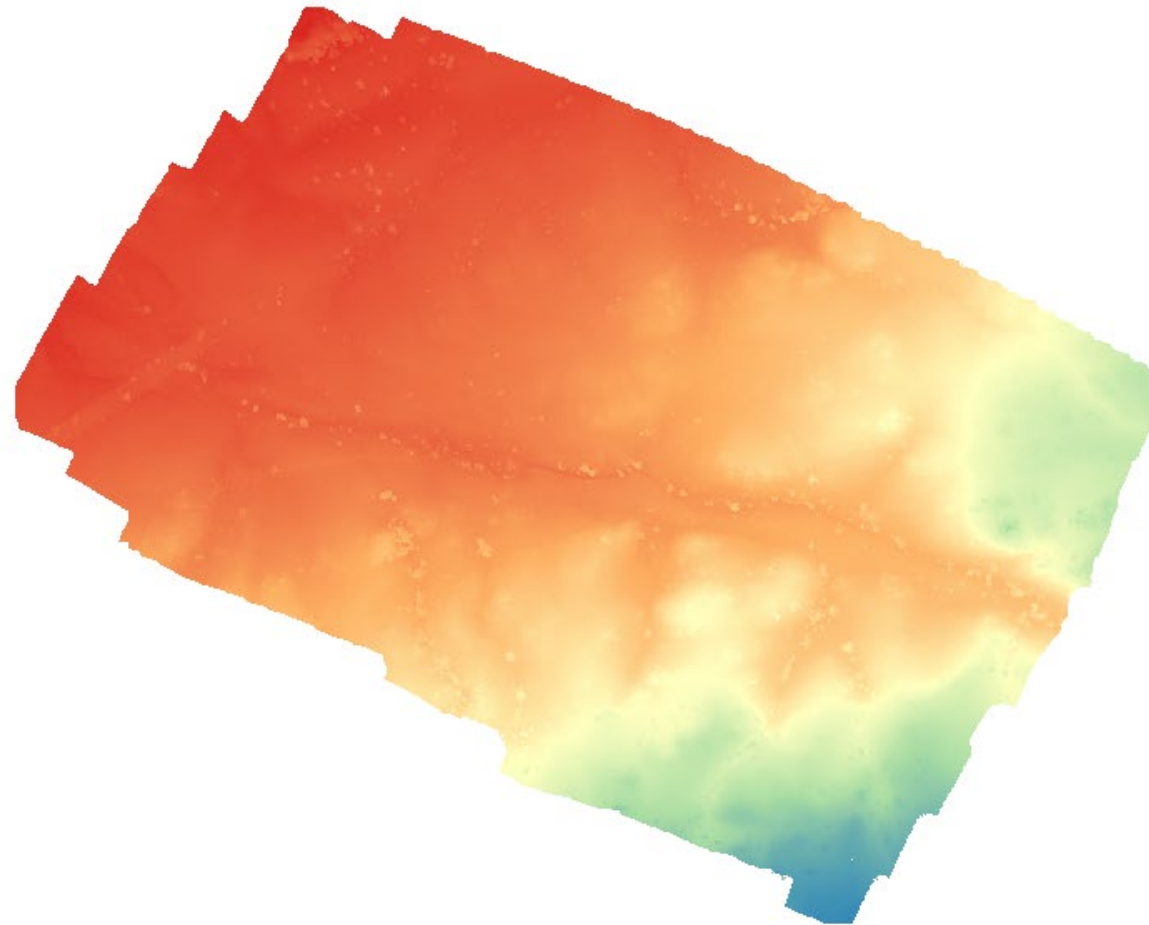


Figure A-15: Site AQ05 orthoimage



Digital Elevation Model



Height (m)



Figure A-16: Site AQ05 digital elevation model

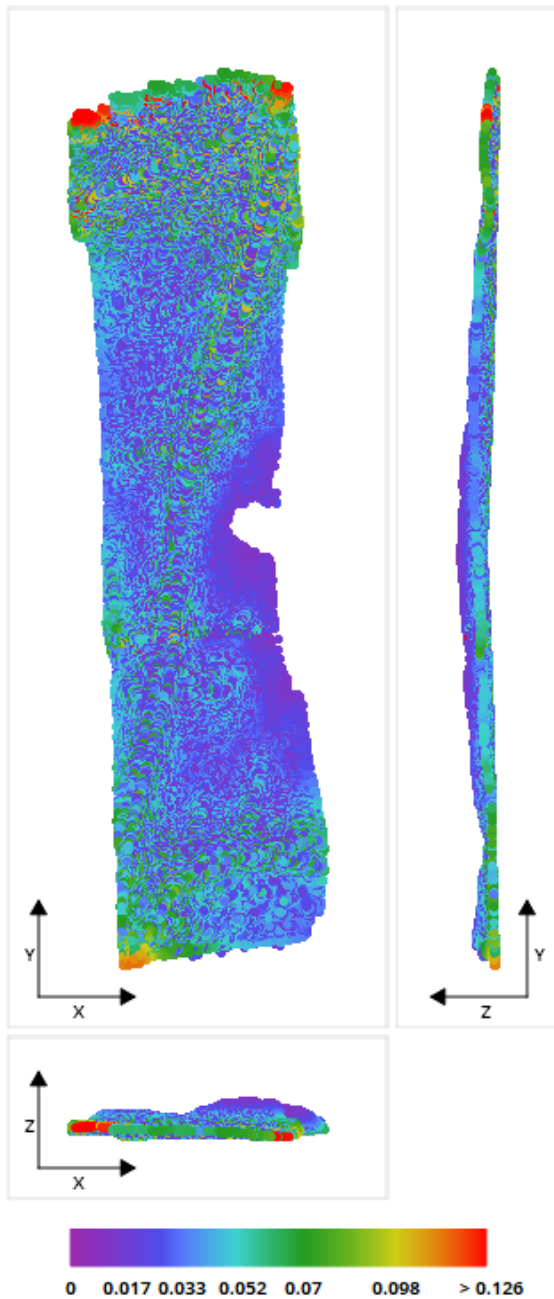
Appendix A-6 Site AQ06

Survey parameters	
Drone	Phantom 4 Pro
Camera model	DJI FC6310
Images	1182/1206
Ground coverage	0.752 km ²
Average ground resolution	18.107 mm/pixel
Geo referencing	6 control points (RTK)
Key points	Median of 49214 key points per image
Tie points	522901 points (median of 2187 points per photo)
Reprojection errors (RMS)	0.48 pixels

Position uncertainties (camera locations)			
	X (m)	Y (m)	Z (m)
Minimum	0.0017	0.00196	0.00088
Mean	0.00301	0.00333	0.00143
Maximum	0.02368	0.0231	0.01523

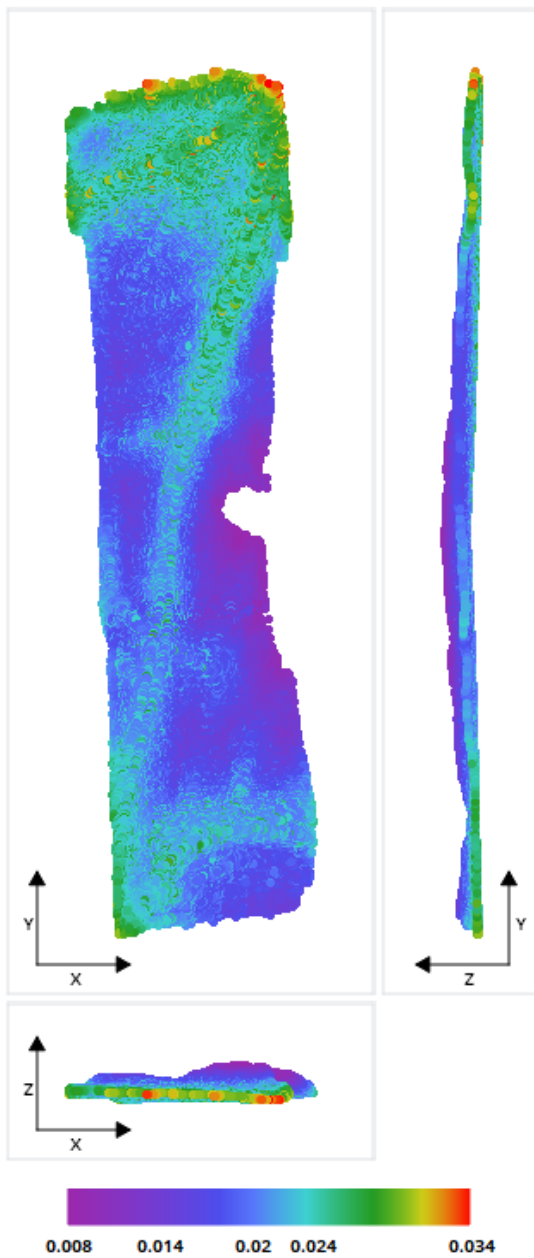
Generated tie points						
Parameter	No. points	Median no. photos per point	Median no. points per photo	Median reprojection error (px)	RMS of reprojection error (px)	RMS of distances to rays (m)
Values	522901	4	2187	0.34	0.48	0.06408

Control Points							
Name	Accuracy (m)	No. photos	RMS of reprojection error (px)	RMS of distances to rays (m)	3-D error (m)	Horizontal errors (m)	Vertical error (m)
aq06-02	H: 0.01 V: 0.022	22	0.55	0.06852	0.00514	X: 0.0033 Y: 0.00273	-0.00284
aq06-03	H: 0.01 V: 0.021	32	0.56	0.09782	0.00692	X:-0.00003 Y:-0.00656	0.00221
aq06-ro01	H: 0.006 V: 0.015	18	0.42	0.06493	0.00596	X: 0.00427 Y:-0.00044	-0.00412
aq06-ro03	H: 0.008 V: 0.019	18	0.57	0.06802	0.00764	X: -0.00019 Y: 0.00669	-0.00369
aq06-ro04	H: 0.0008 V: 0.02	15	0.54	0.0752	0.00786	X:-0.00312 Y:-0.00612	0.00383
aq06-01	H: 0.01 V: 0.022	27	0.56	0.08464	0.00302	X:-0.0011 Y: 0.00226	0.00169
Global RMS			0.54	0.07738	0.00631	X: 0.00259 Y: 0.0048	0.00319
Median			0.56	0.0752	0.00692	X:-0.00003 Y: 0.00226	0.00169



Position Uncertainties: Top view (XY plane), side view (ZY plane) and front view (XZ plane) displays of all tie points, with colors representing uncertainty in the individual point position. The values are in meters, with a minimum uncertainty of 0.00681 meters and a maximum of 0.16185 meters. The median position uncertainty equals 0.03345 meters.

Figure A-17: AQ06 mapping position uncertainties



Resolution: Top view (XY plane), side view (ZY plane) and front view (XZ plane) displays of all tie points, with colors representing resolution in the individual point position. The values are in meters/pixel, with a minimum resolution of 0.00846 meters/pixel and a maximum of 0.0337 meters/pixel. The median resolution equals 0.02006 meters/pixel.

Figure A-18: Site AQ06 mapping resolution

Orthoimage

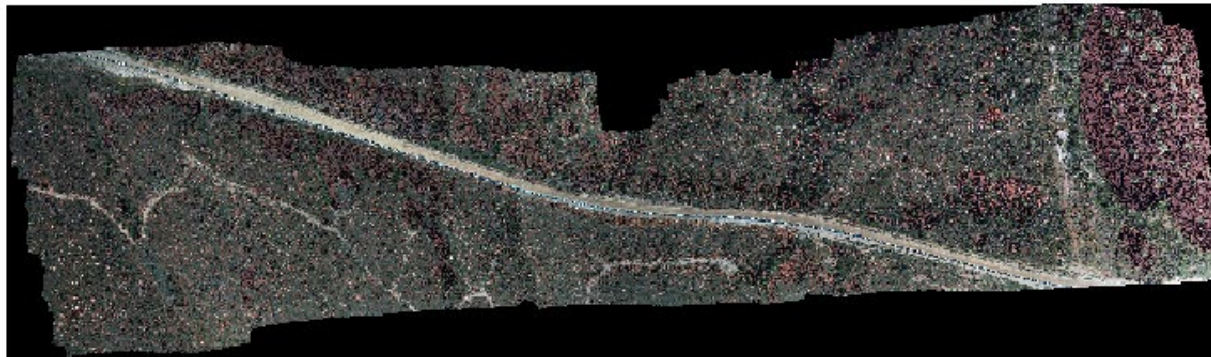
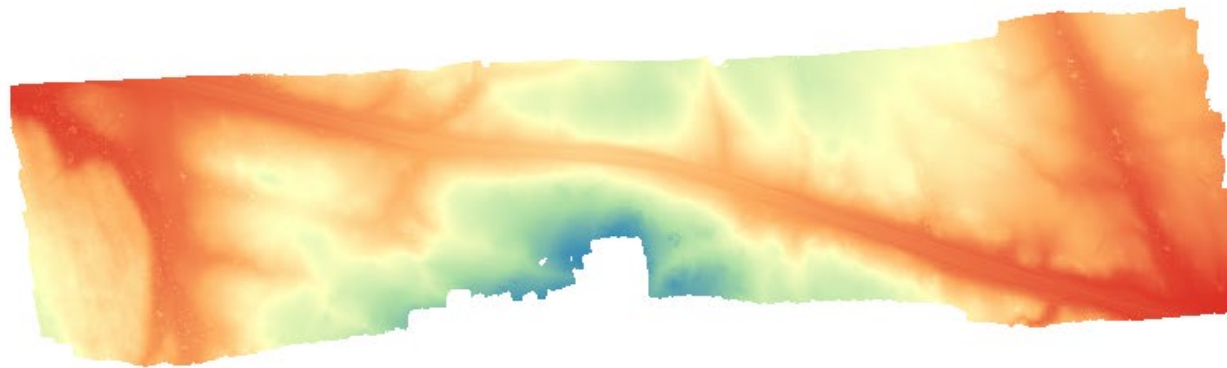


Figure A-19: Site AQ06 orthoimage

Digital Elevation Model



Height (m)



Figure A-20: Site AQ06 digital elevation model

Appendix A-7 Sites AQ07 and AQ08 (adjoined)

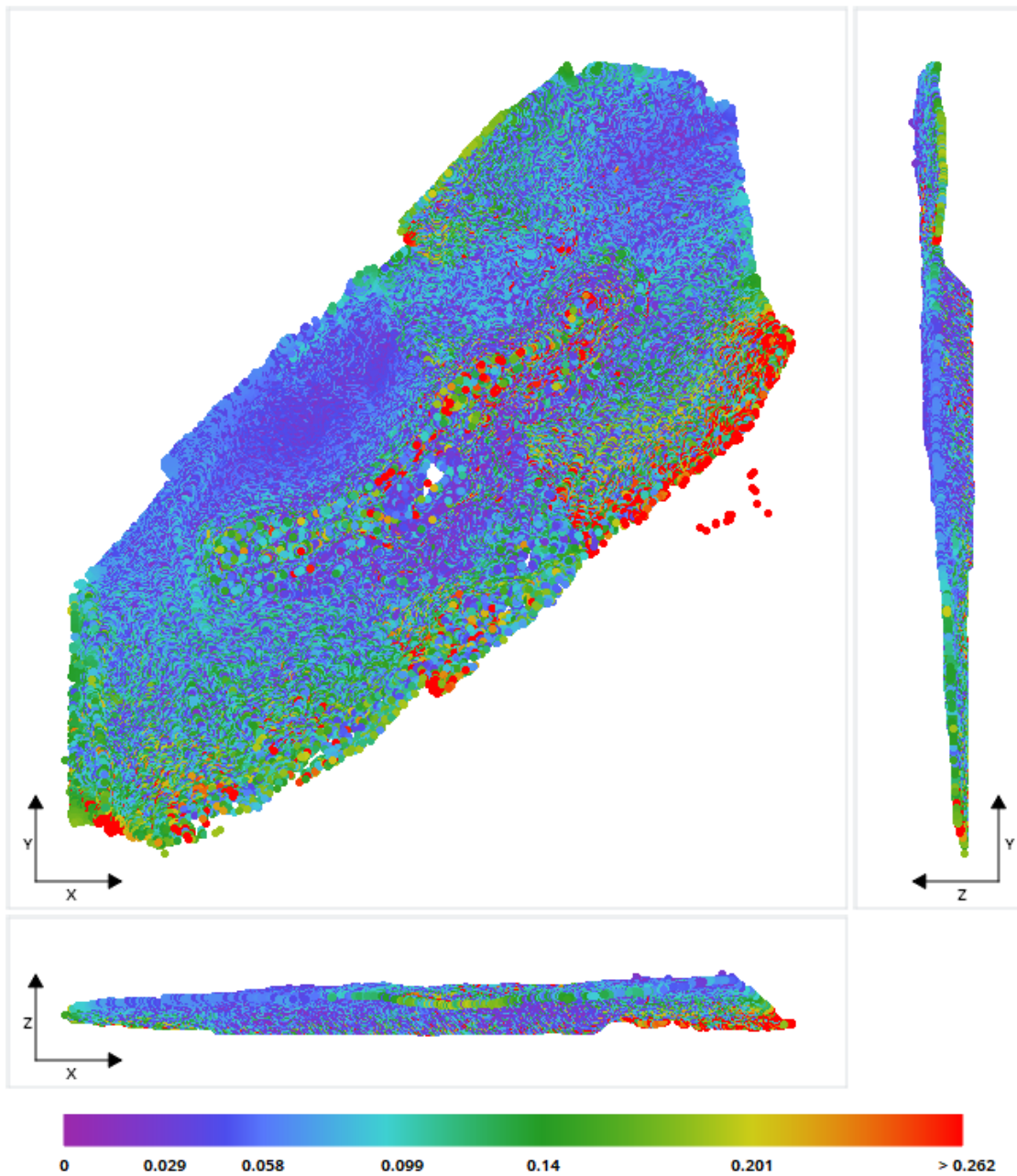
Survey parameters	
Drone	Phantom 4 RTK
Camera model	DJI FC6310R
Images	1182/2139
Ground coverage	1.566 km ²
Average ground resolution	20.423502 mm/pixel
Geo referencing	10 control points (RTK)
Key points	Median of 44758 key points per image
Tie points	1052911 points (median of 2666 points per photo)
Reprojection errors (RMS)	0.42 pixels

Position uncertainties (camera locations)			
	X (m)	Y (m)	Z (m)
Minimum	0.00084	0.00076	0.00064
Mean	0.00298	0.0028	0.00133
Maximum	0.54585	0.08446	0.04552

Generated tie points						
Parameter	No. points	Median no. photos per point	Median no. points per photo	Median reprojection error (px)	RMS of reprojection error (px)	RMS of distances to rays (m)
Values	1052911	4	2666	0.3	0.42	0.03179

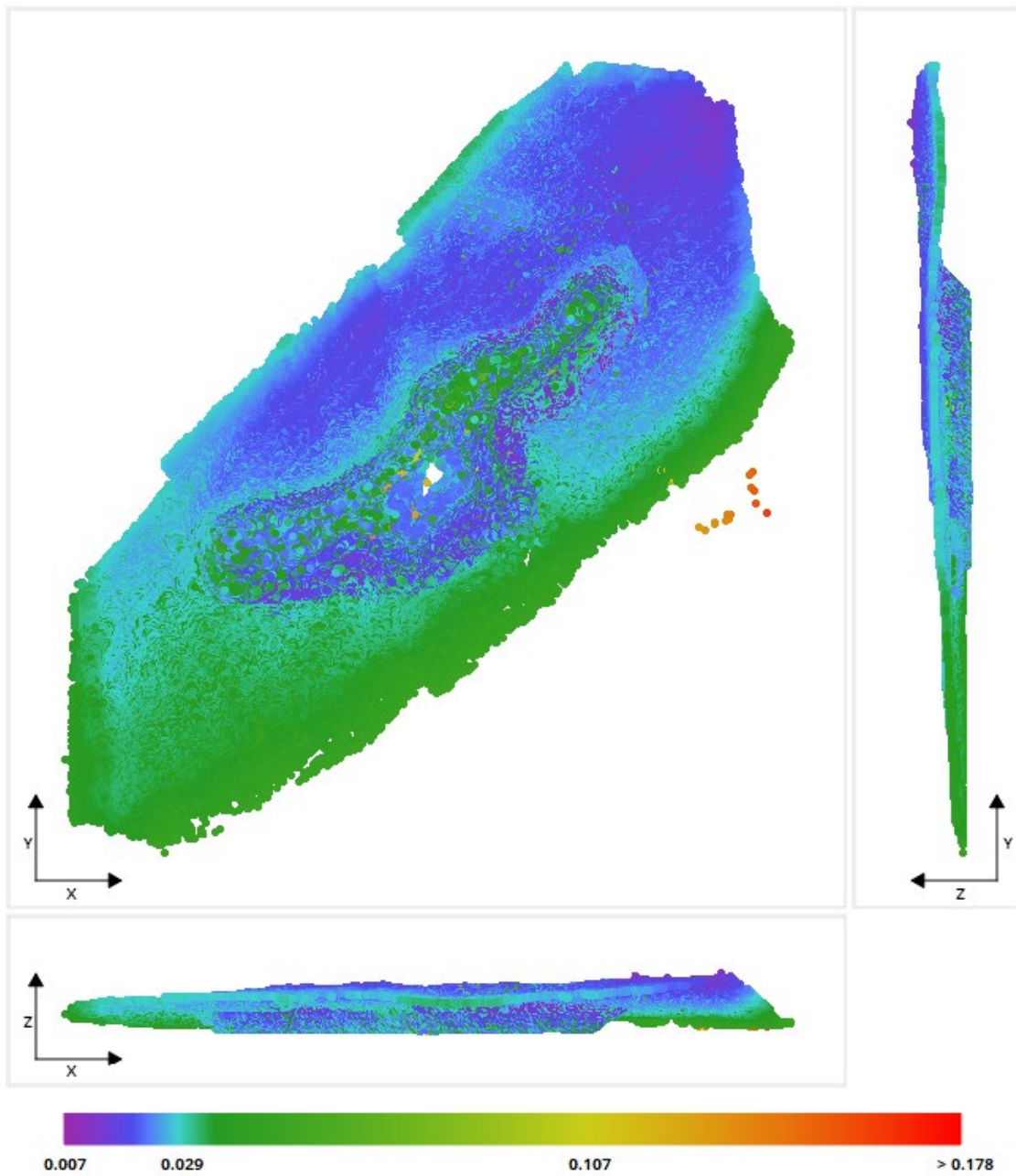
Murujuga Rock Art Monitoring Program
Monitoring Studies Report 2023

Control Points							
Name	Accuracy (m)	No. photos	RMS of reprojection error (px)	RMS of distances to rays (m)	3-D error (m)	Horizontal errors (m)	Vertical error (m)
uav-01	H: 0.009 V: 0.013	28	0.47	0.03157	0.00217	X:-0.00012 Y: 0.00113	-0.00185
uav-02	H: 0.015 V: 0.024	12	0.42	0.01261	0.00058	X:-0.00052 Y:0.000254	-0.0001
uav-03	H: 0.008 V: 0.014	39	0.35	0.02625	0.00107	X: 0.00025 Y:-0.00044	0.00094
uav-04	H: 0.018 V: 0.04	14	0.53	0.04233	0.00826	X: 0.00441 Y:-0.00507	-0.00479
uav-05	H: 0.018 V: 0.041	34	0.66	0.04744	0.00902	X:-0.00781 Y: 0.00427	-0.00144
uav-06	H: 0.018 V: 0.043	14	0.54	0.03399	0.00592	X: 0.00095 Y: 0.0045	-0.00372
uav-07	H: 0.017 V: 0.043	31	0.74	0.0429	0.00655	X:-0.00104 Y: -0.00637	0.00114
uav-08	H: 0.016 V: 0.043	29	0.52	0.03497	0.00978	X: 0.00354 Y:-0.0006	0.0091
uav-09	H: 0.017 V: 0.043	37	0.58	0.04372	0.00838	X: 0.00457 Y: 0.00366	0.006
uav-11	H: 0.007 V: 0.019	92	0.5	0.05376	0.00264	X:-0.00211 Y: 0.00143	0.00067
Global RMS			0.54	0.03861	0.00638	X: 0.00347 Y: 0.0035	0.00405
Median			0.53	0.04233	0.00655	X: 0.00025 Y: 0.00113	0.00067



Position Uncertainties: Top view (XY plane), side view (ZY plane) and front view (XZ plane) displays of all tie points, with colors representing uncertainty in the individual point position. The values are in meters, with a minimum uncertainty of 0.00406 meters and a maximum of 3.90985 meters. The median position uncertainty equals 0.05804 meters.

Figure A-21: AQ07 and AQ08 mapping position uncertainties



Resolution: Top view (XY plane), side view (ZY plane) and front view (XZ plane) displays of all tie points, with colors representing resolution in the individual point position. The values are in meters/pixel, with a minimum resolution of 0.00651 meters/pixel and a maximum of 0.17799 meters/pixel. The median resolution equals 0.02239 meters/pixel.

Figure A-22: Site AQ07 and AQ08 mapping resolution



Orthoimage



Figure A-23: Site AQ07 and AQ08 orthoimage



Digital Elevation Model

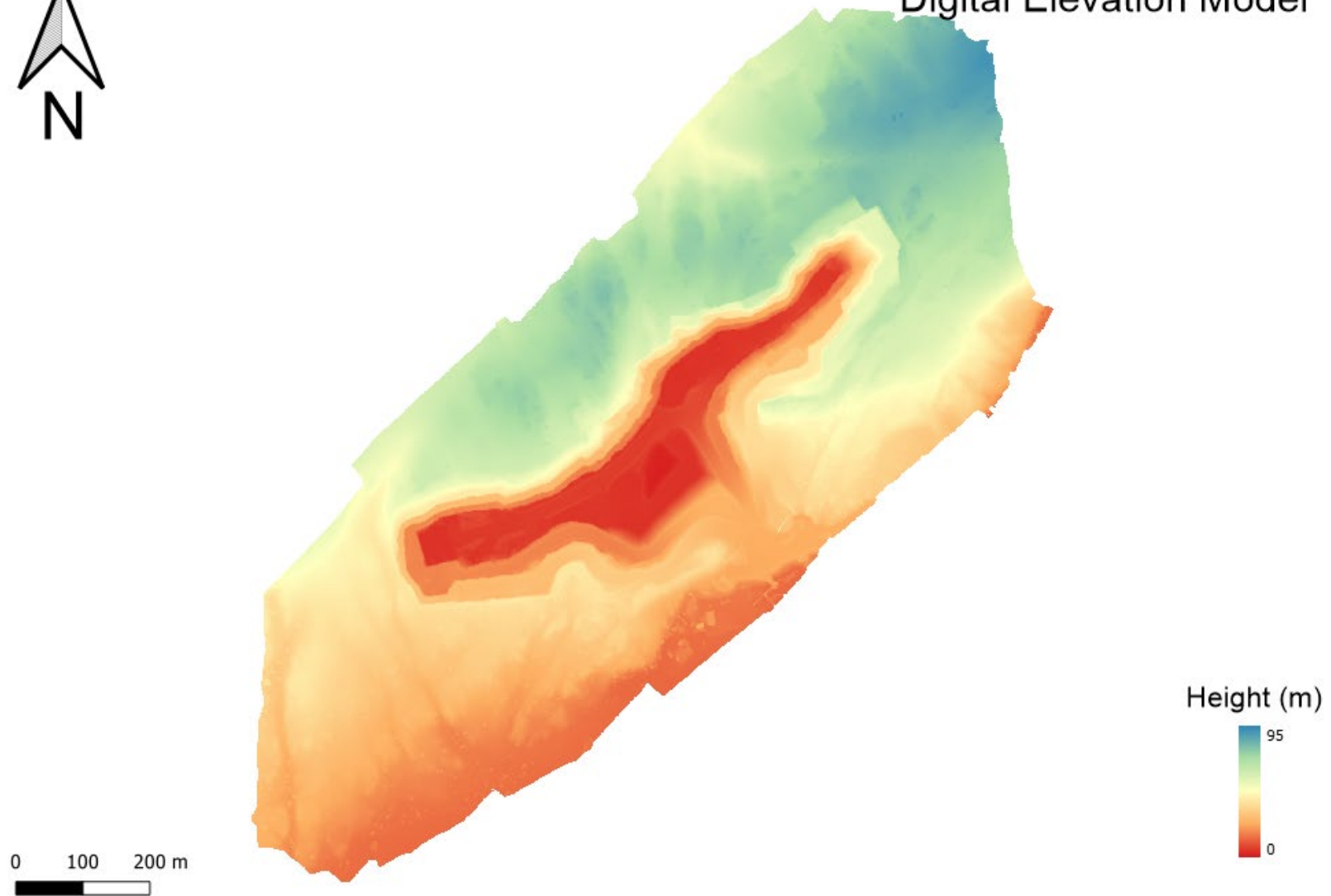


Figure A-24: Site AQ07 and AQ08 digital elevation model

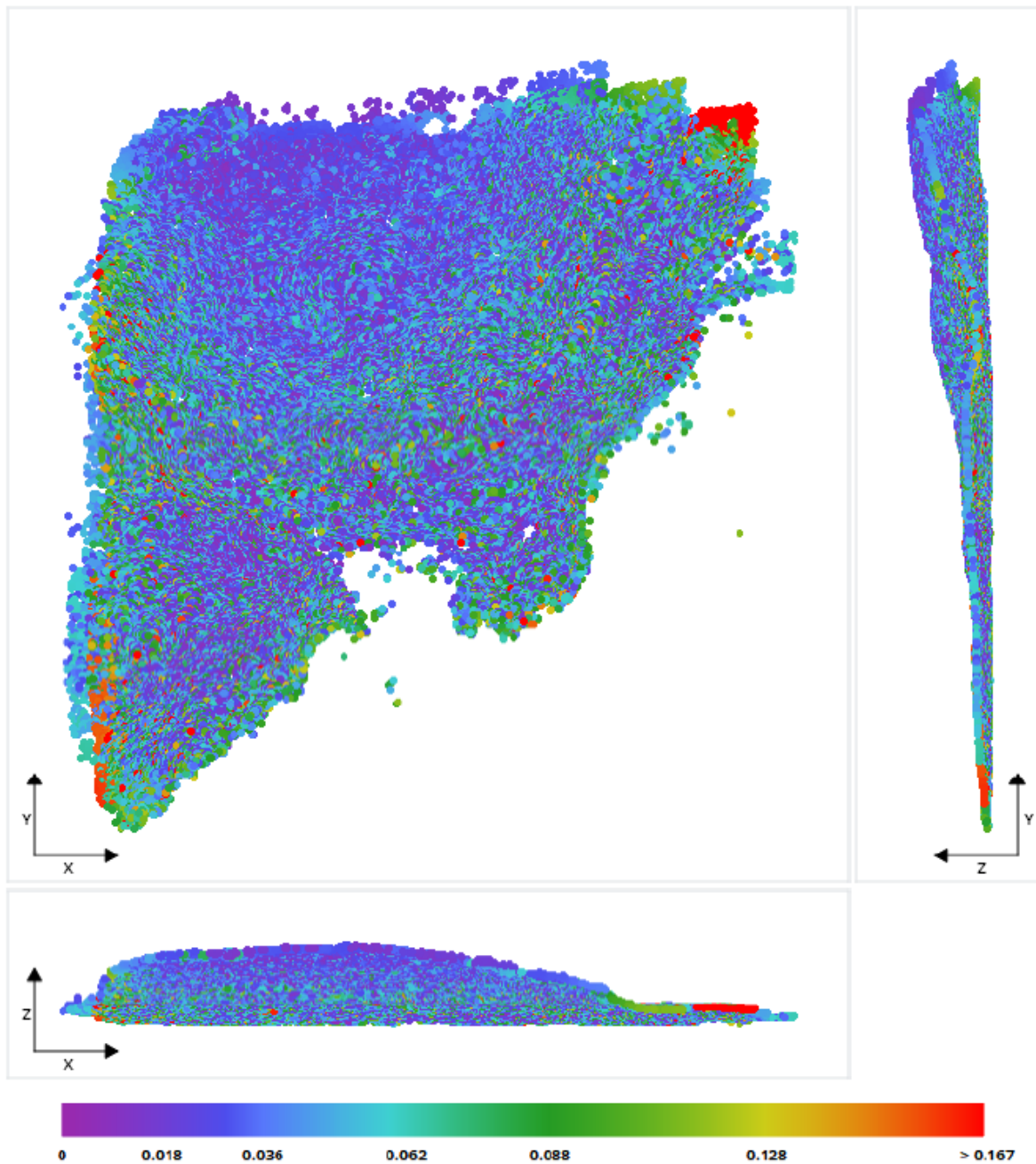
Appendix A-8 Site AQ10

Survey parameters	
Drone	DJI FC6310
Camera model	696/702
Images	232224 m ²
Ground coverage	21.31051 mm/pixel
Average ground resolution	6 control points (RTK)
Geo referencing	Median of 45698 key points per image
Key points	254559 points (median of 2719 points per photo)
Tie points	0.6 pixels
Reprojection errors (RMS)	DJI FC6310

Position uncertainties (camera locations)			
	X (m)	Y (m)	Z (m)
Minimum	0.00156	0.00144	0.00081
Mean	0.00486	0.0051	0.00251
Maximum	0.12754	20019	0.0579

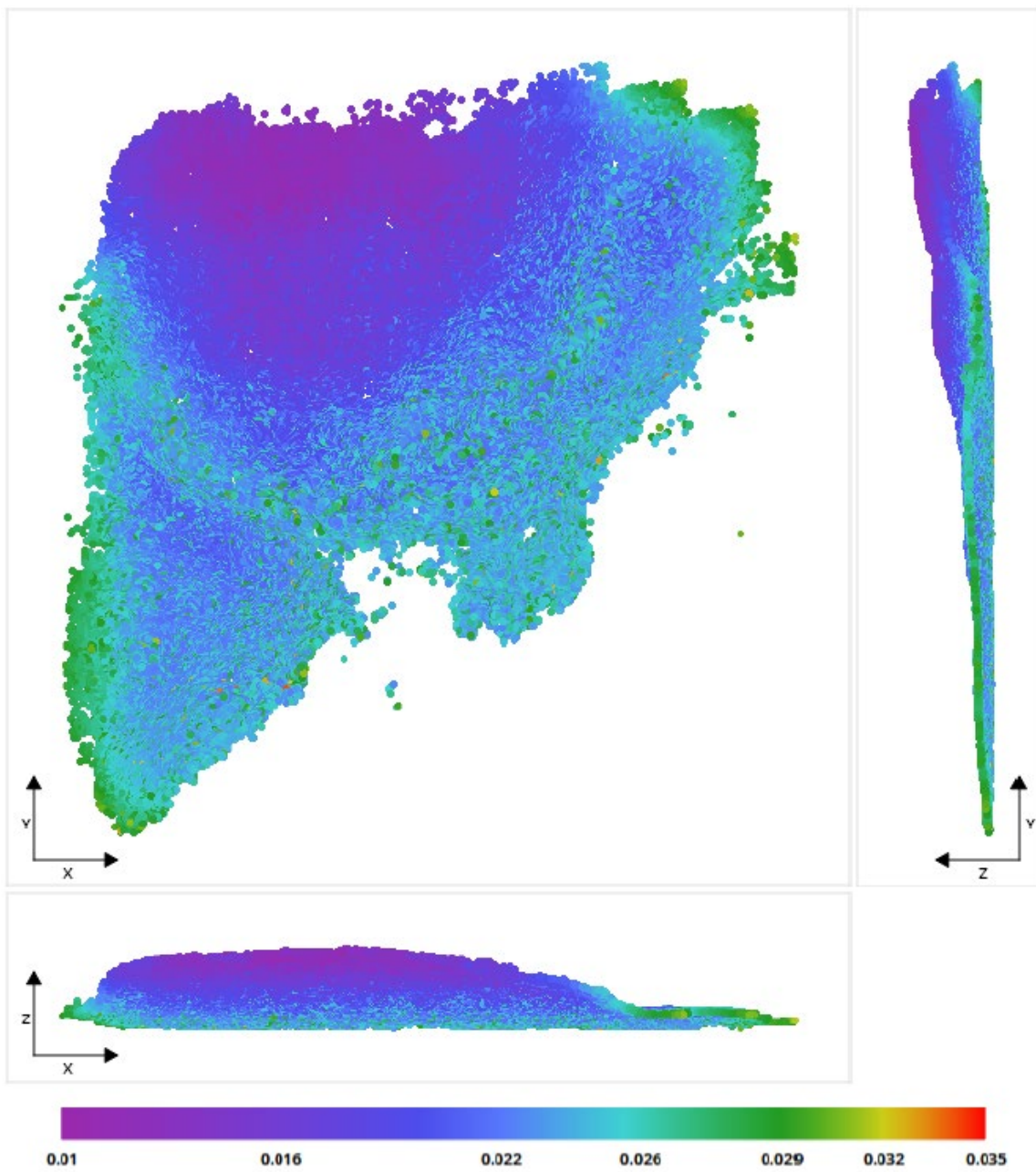
Generated tie points						
Parameter	No. points	Median no. photos per point	Median no. points per photo	Median reprojection error (px)	RMS of reprojection error (px)	RMS of distances to rays (m)
Values	254559	4	2719	0.44	0.6	0.05843

Control Points							
Name	Accuracy (m)	No. photos	RMS of reprojection error (px)	RMS of distances to rays (m)	3-D error (m)	Horizontal errors (m)	Vertical error (m)
aq10_uav01	H: 0.009 V: 0.021	30	0.82	0.05164	0.01096	X:-0.00116 Y: 0.001057	-0.00267
aq10_uav02	H: 0.013 V: 0.027	30	0.88	0.05415	0.01293	X: 0.00259 Y:-0.01166	-0.00495
aq10_uav03	H: 0.013 V: 0.028	35	0.86	0.06123	0.01392	X:-0.00564 Y: 0.00416	0.01203
aq10_uav04	H: 0.008 V: 0.018	50	0.98	0.08127	0.01096	X: 0.00506 Y:-0.00955	-0.00182
aq10_uav05	H: 0.008 V: 0.018	47	0.62	0.07212	0.00446	X: 0.00283 Y: 0.00345	-0.00012
aq10_uav06	H: 0.009 V: 0.02	64	0.68	0.07823	0.00375	X:-0.00293 Y: 0.00214	-0.00094
Global RMS			0.82	0.06742	0.01029	X: 0.0037 Y: 0.007788	0.00549
Median			0.86	0.07212	0.01096	X: 0.00259 Y: 0.00345	-0.00094



Position Uncertainties: Top view (XY plane), side view (ZY plane) and front view (XZ plane) displays of all tie points, with colors representing uncertainty in the individual point position. The values are in meters, with a minimum uncertainty of 0.00512 meters and a maximum of 0.43011 meters. The median position uncertainty equals 0.03629 meters.

Figure A-25: Site AQ10 mapping position uncertainties



Resolution: Top view (XY plane), side view (ZY plane) and front view (XZ plane) displays of all tie points, with colors representing resolution in the individual point position. The values are in meters/pixel, with a minimum resolution of 0.0101 meters/pixel and a maximum of 0.03464 meters/pixel. The median resolution equals 0.02178 meters/pixel.

Figure A-26: Site AQ010 mapping resolution



Figure A-27: Site AQ10 orthoimage

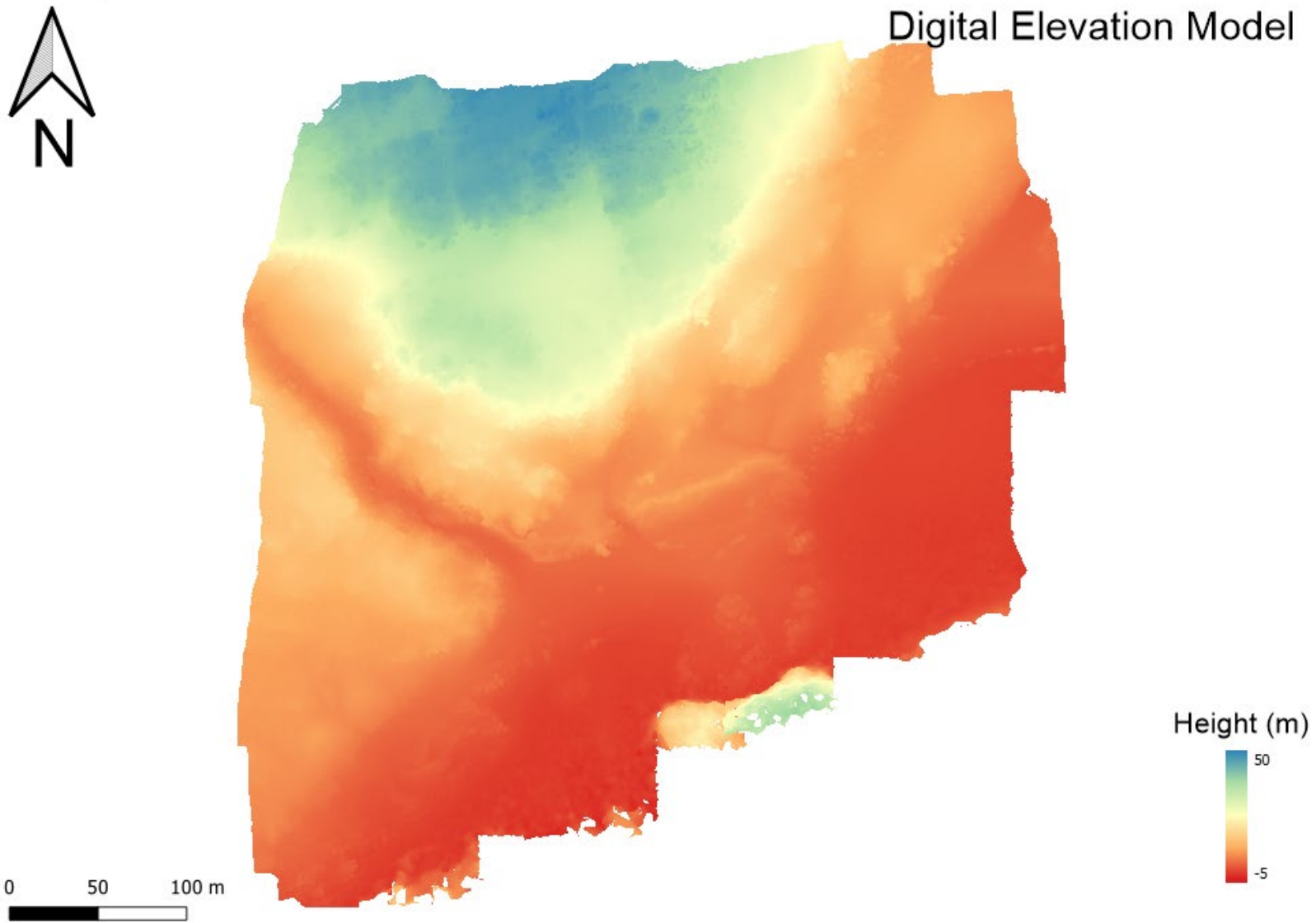


Figure A-28: Site AQ10 digital elevation model

Appendix A-9 Site AQ11

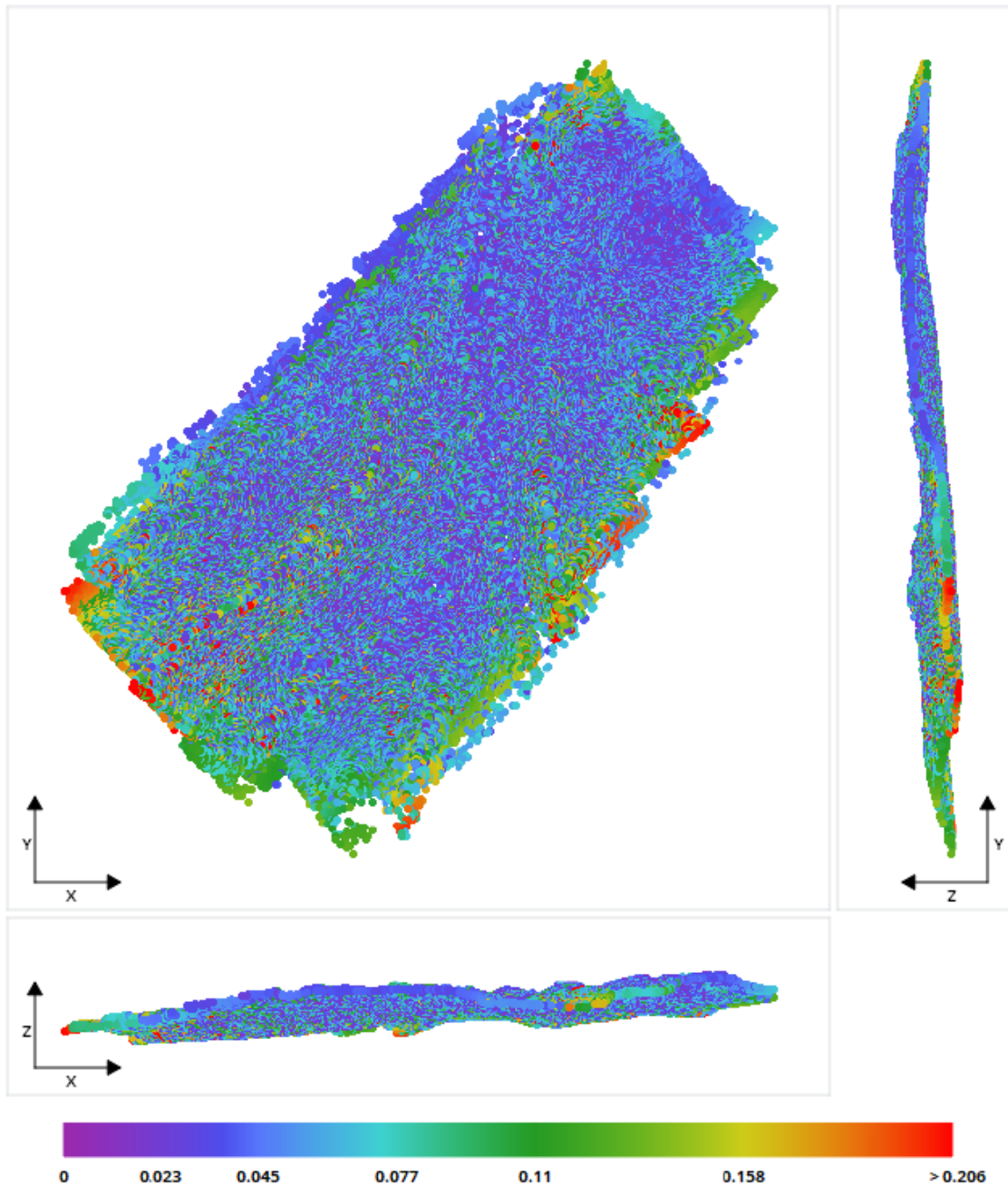
Survey parameters	
Drone	Phantom 4 Pro
Camera model	DJI FC6310
Images	891/891
Ground coverage	0.583 km ²
Average ground resolution	22.2477 mm/pixel
Geo referencing	11 control points (RTK)
Key points	Median of 45698 key points per image
Tie points	430657 points (median of 3254 points per photo)
Reprojection errors (RMS)	0.52 pixels

Position uncertainties (camera locations)			
	X (m)	Y (m)	Z (m)
Minimum	0.0017	0.0019	0.0009
Mean	0.0028	0.0028	0.0013
Maximum	0.0081	0.0094	0.003

Generated tie points						
Parameter	No. points	Median no. photos per point	Median no. points per photo	Median reprojection error (px)	RMS of reprojection error (px)	RMS of distances to rays (m)
Values	430657	4	3254	0.4	0.52	0.0765

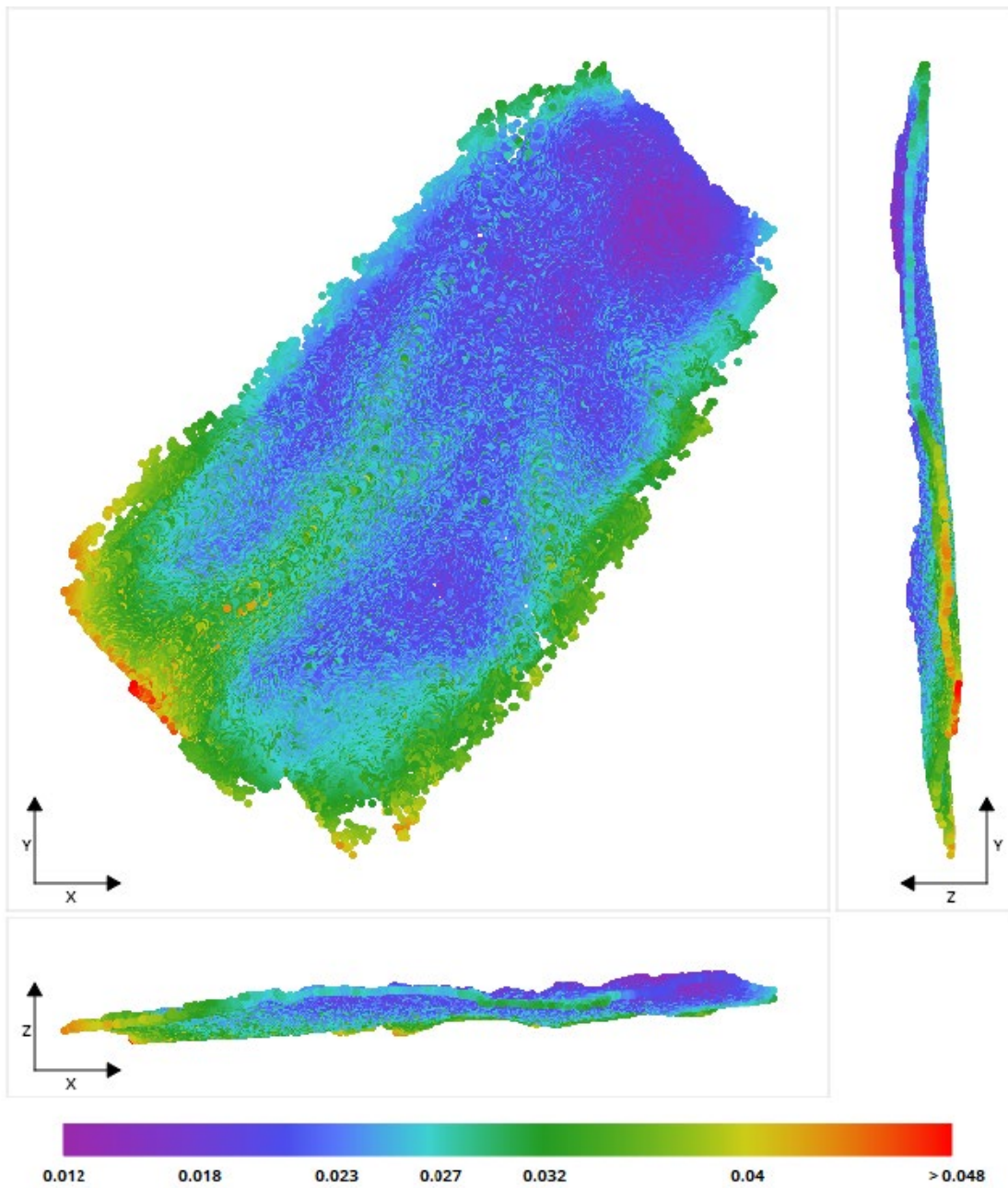
Murujuga Rock Art Monitoring Program
Monitoring Studies Report 2023

Control Points							
Name	Accuracy (m)	No. photos	RMS of reprojection error (px)	RMS of distances to rays (m)	3-D error (m)	Horizontal errors (m)	Vertical error (m)
aq-mac-uav1	H: 0.007 V: 0.015	45	0.56	0.0951	0.0034	X: 0.0009 Y: 0.0024	0.0022
aq-mac-uav2	H: 0.009 V: 0.021	24	0.55	0.0889	0.0078	X: 0.0021 Y: 0.0012	-0.0075
aq-mac-uav3	H: 0.009 V: 0.02	37	0.63	0.0955	0.0124	X: 0.0019 Y:-0.0062	0.0106
aq-mac-uav4	H: 0.009 V: 0.02	59	0.53	0.0887	0.0043	X:-0.0033 Y:-0.0027	0.0001
aq-mac-uav5	H: 0.009 V: 0.021	45	0.5	0.0815	0.005	X: 0.0021 Y:-0.0002	0.0045
aq-mac-uav6	H: 0.009 V: 0.021	76	0.49	0.0989	0.0054	X: -0.0013 Y: 0.004	-0.0034
aq-mac-uav7	H: 0.008 V: 0.017	53	0.56	0.0922	0.0049	X: 0.0037 Y:-0.0003	0.0032
aq-mac-uav8	H: 0.009 V: 0.021	32	0.42	0.0712	0.002	X: 0.0003 Y:-0.0015	0.0012
aq-mac-uav9	H: 0.009 V: 0.021	37	0.56	0.079	0.0057	X: 0.0012 Y: 0.0013	-0.0054
aq-mac-uav10	H: 0.01 V: 0.022	22	0.64	0.0815	0.0073	X:-0.0027 Y:-0.0066	-0.0017
aq-mac-uav11	H: 0.01 V: 0.022	11	0.63	0.0451	0.0092	X: 0.0004 Y: 0.0068	0.0062
Global RMS			0.56	0.0847	0.0067	X: 0.0021 Y: 0.0039	0.0051
Median			0.56	0.0887	0.0054	X: 0.0009 Y:-0.0002	0.0012



Position Uncertainties: Top view (XY plane), side view (ZY plane) and front view (XZ plane) displays of all tie points, with colors representing uncertainty in the individual point position. The values are in meters, with a minimum uncertainty of 0.0055 meters and a maximum of 0.492 meters. The median position uncertainty equals 0.0453 meters.

Figure A-29: Site AQ11 mapping position uncertainties



Resolution: Top view (XY plane), side view (ZY plane) and front view (XZ plane) displays of all tie points, with colors representing resolution in the individual point position. The values are in meters/pixel, with a minimum resolution of 0.0123 meters/pixel and a maximum of 0.0479 meters/pixel. The median resolution equals 0.0232 meters/pixel.

Figure A-30: Site AQ11 mapping resolution



Orthoimage

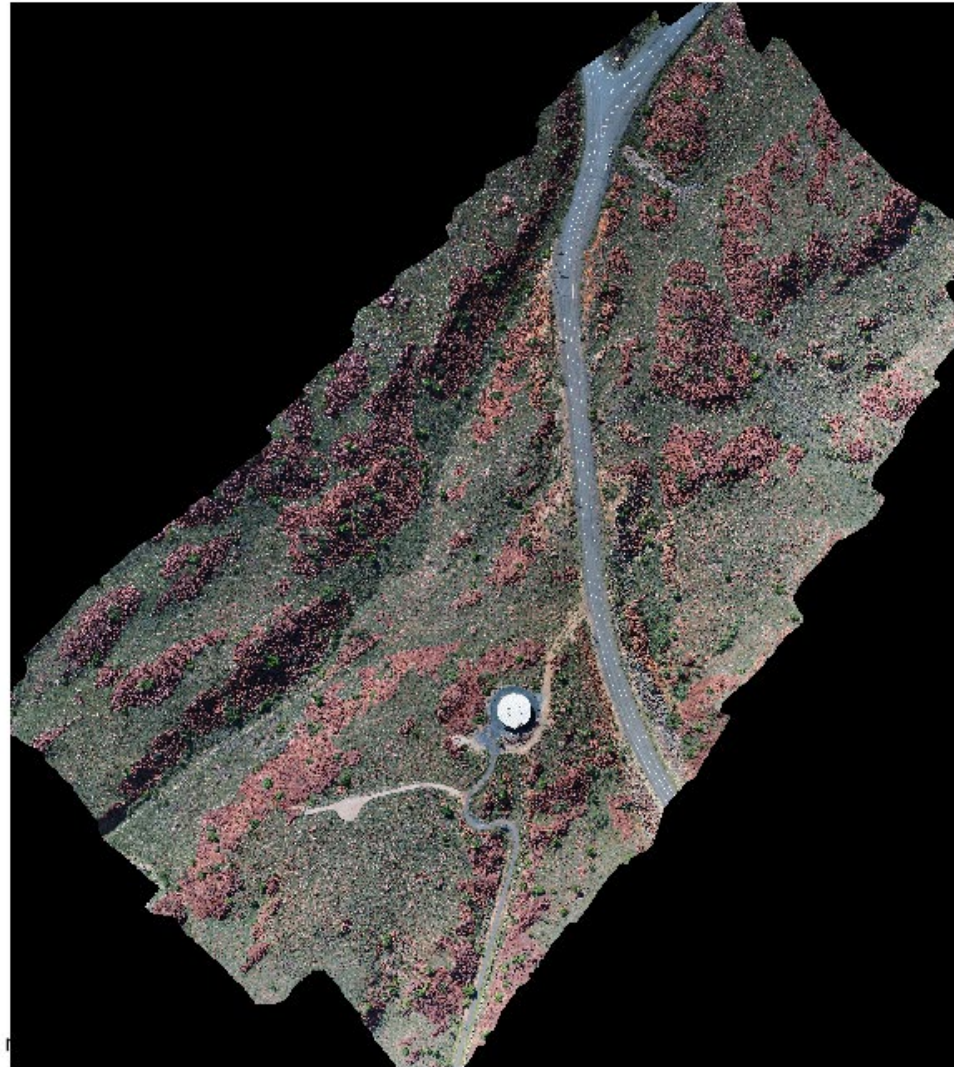
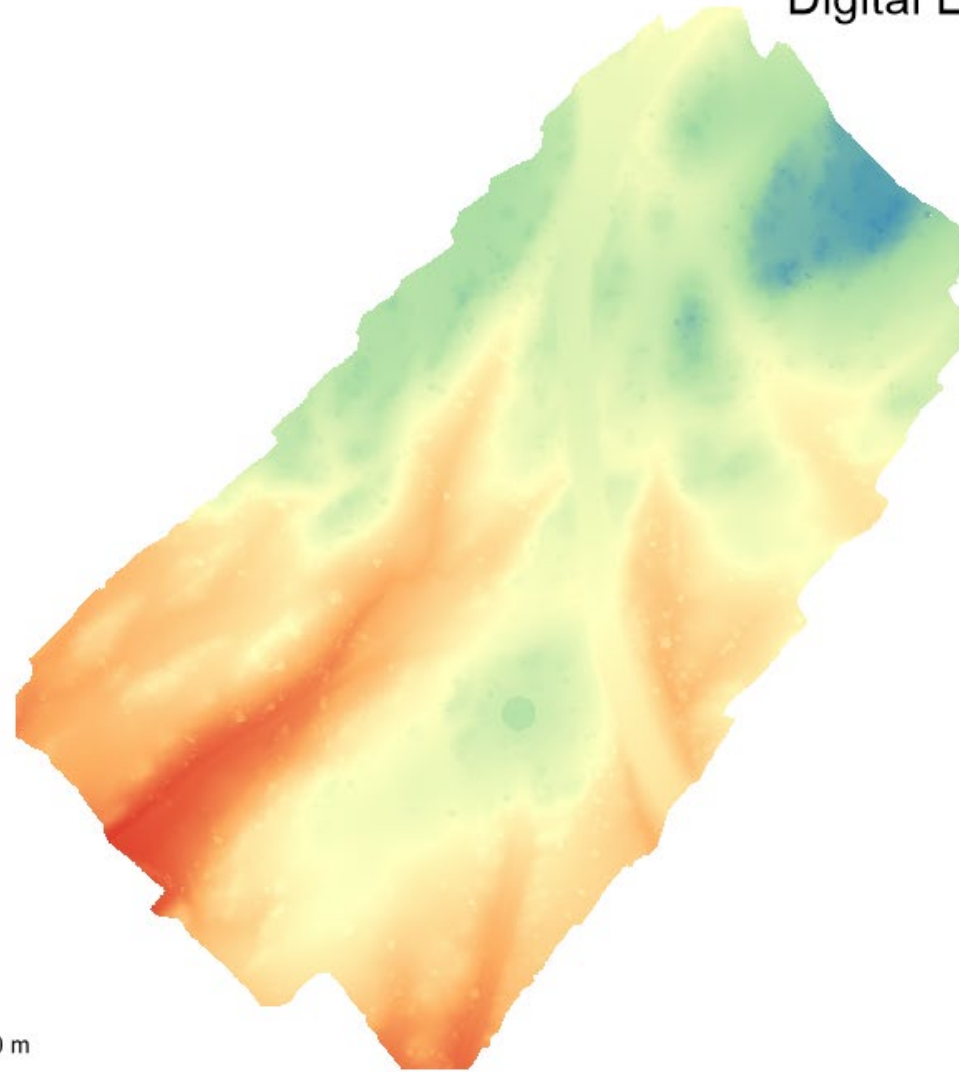


Figure A-31: Site AQ11 orthoimage



Digital Elevation Model



Height (m)

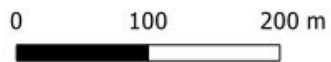
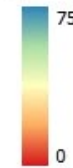


Figure A-32: Site AQ11 digital elevation model

Appendix B: Spectroscopy operational parameters

Appendix B-1 Spectrometer operation

B-1-1 Spectroscopy workflow

The following workflow has been developed, following established principles for obtaining reliable and repeatable spectra, by addressing various critical assessments of previous studies, and to ensure the collected data is transferred from the sites to the data storage repository intact.

The operating parameters of the chosen spectrometer have been evaluated together with all other means by which an error may be introduced, and the protocols adopted to mitigate such error are described.

An evaluation of all instrument variables has been undertaken in the laboratory and described in fuller detail in following sections of this appendix. The instrument variables evaluated include probe distance, probe angle, ambient temperature, rock surface temperature (thermochromism) stray light influence, humidity influence, instrument run-time stability, among other considerations.

The project has been initiated with 54 rock art surfaces, each containing ten targets (spots) to be measured ten times each. For the 35 rock art surfaces in the AQ (air quality monitoring), EX (existing air quality monitor) and AS (additional) sites, it was important to reapply the probe to exactly the same spot. The rationale for this will be discussed, together with the protocols developed in the field and implemented to achieve the most consistent results. For the 19 rock art surfaces in the RS (representative sample) sites, it was important to capture all sources of variability, and this requires a randomised selection procedure. A protocol for randomised selection of the target spots was developed in the field.

Two of the most critical parameters for maintaining consistent spectra are light exclusion (Appendix B-3) and accurate target relocation (Appendix B-2). The spectrometer itself operates under set conditions, namely within a set temperature range and calibration requirements.

B-1-2 Instrument calibration

Calibration is carried out prior to operation, as the instrument will not function without passing through this setup procedure. A number of calibration sequences have been tried, ranging from calibrating once per site, whereby 100 spectra are run sequentially, through to calibrating after each target with 10 spectra run before recalibration. The final regime adopted since the March 2023 campaign is to recalibrate after each target, with a two-minute rest prior to recalibrating and a 15-minute rest after five targets. Frequent calibration ensures better temperature-compensated calibrations, however temperature variations across the hour of acquisition do not change by more than 2-3°C.

The first campaign of operation in March 2022 revealed that the spectrometer can overheat and shut down until back within operating conditions. While the instrument is stable to 55°C the xenon lamp and battery contribute considerably to the heat load. The spectrometer has since been placed in a cool box. Thermal imaging has revealed that the lower two modules contribute to the heat generation and thus a compound cooling system has been devised. A freezer cube is set atop a block of ice and the spectrometer set onto the freezer cube. The cube remains at around 5° and this dissipates heat through the instrument. In the hot March campaign of 2023, an additional freezer cube has been placed in the lid of the cooler to remove heat from the top of the spectrometer when not being interrogated. This keeps the instrument at around or below 30° for most of the operation cycle and ensures no overheating shut-downs.

Despite these controls the instrument still malfunctions on some targets. The spectra are examined for integrity and any failed targets repeated. Such failures are a product of the hostile environment as the instrument has been regularly tested in an air-conditioned Donga environment with 200 spectra run sequentially without failure.

The spectrometer has been configured in the following manner.

- Reflectance/Transmission mode
- Xenon flash rate 100Hz, Intensity 400V, Free running
- Calibration to manufacturer's barium sulphate tile
- Placement parameters as described in Appendix B-2.

B-1-3 Environmental conditions

The instrument has been stabilised thermally, as described above, however the rock surface temperature varies for each visit. Previous work by the authors on the impact of rock temperature has demonstrated that the rock surface temperature should ideally be within $\pm 3^{\circ}\text{C}$ when recorded, however this is very difficult at different seasons. This has partly been overcome by measuring in the same months, but the most recent March 2023 campaign has illustrated how rock temperatures can vary substantially (by more than $\pm 3^{\circ}\text{C}$ at any chosen measurement time point).

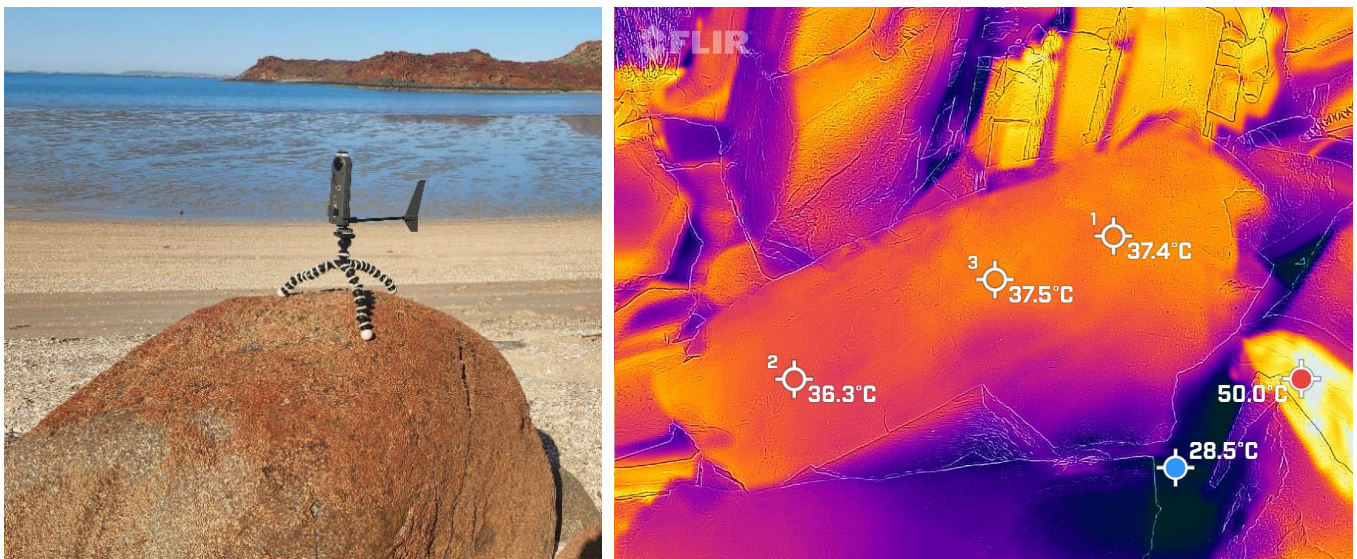


Figure B-1: Mini weather station at left mounted on a rock close to the study site. A thermal image at right records three points with interpolation to all parts of the rock surface.

To monitor the spectral recording conditions a weather station is setup near to the site to record air temperature, RH%, barometric pressure and wind speed and direction. An additional data logger is placed in the shade to give instant readings of temperature and humidity. A thermal image and infrared spot reading are taken of the surface. Owing to severe conditions, not all data is gathered but enough to be able to plot the environmental conditions under which the readings have been taken. The benefit of the thermal image is that it provides an interpolated spot reading for every target on a rock surface, should this be required.

B-1-4 Data management

The primary storage for the spectrometer is an SD card. The spectra are stored to this removable card with generic naming from 0-99 per folder. Typically, for each visit to a rock art panel, the observer creates two sub-folders of spectra under a generic head folder. On completion the card is removed from the instrument and inserted via card reader into an android phone where the generic folder is renamed to the site number. This re-labelled folder remains on the SD card for the entirety of a field campaign, ensuring that the primary physical data remain intact.

The folder is then immediately copied on-site to a local drive within the phone, ensuring that two copies of the data exist within minutes of completion. Both are vulnerable however, as a card can drop in the rocks and one phone has been smashed.

The phone is set up to automatically synchronize the data to the spectroscopist's cloud storage. The benefit of this lies in the fact that the synchronization does not need a permanent Wi-Fi connection but will upload incrementally whenever within range. In the case of the broken phone the data synchronized from within the rock to the cloud despite complete destruction of the screen. Generally, all data is uploaded to cloud storage either immediately or within a few hours, and well before returning to base. In the field synchronization is set to one way upload to avoid any possibility of reverse loading old or commonly named files.

Once on the computer the generic files are renamed to target groups T1-T10. Any extraneous files are deleted to ensure that the useable files are correctly sorted and labelled.

The final step is to create a local back up on the computer and an external storage device.

In total five copies of the data are created before final upload to the Curtin Cloudstor facility at the completion of each field campaign. Once completed the auto syncing is set to two-way to ensure that any modified files between campaigns are loaded back to the phone. These are typically edited or additional target recognition images.

Appendix B-2 Target selection and re-establishment

B-2-1 Target selection – RS sites

The 19 rock art surfaces at the RS sites were required to have target areas selected randomly. The random selection process followed these steps.

1. Whole rock surface imaged with smartphone camera.
2. Image cropped to the vertical and horizontal extents of the study surface.
3. Image gridded to produce 20 cells in one orientation. This was not always sensible on smaller surfaces. Typically, the grid provided 120 cells on larger rocks and 60 cells on smaller rocks.
4. A random number generator produced 13 numbers from the total cell count. Supplementary numbers were necessary as some cells fell on void space.
5. The random cells were marked onto the gridded image.
6. A 100 x 100 mm physical target was placed centrally over the imaged cell. The target was quartered with cotton to ultimately provided a random cell of 50 x 50 mm
7. Within that cell a target was chosen relying in recognisable features for accurate alignment purposes.

Figure B-2 illustrates the outcome of randomised selection.

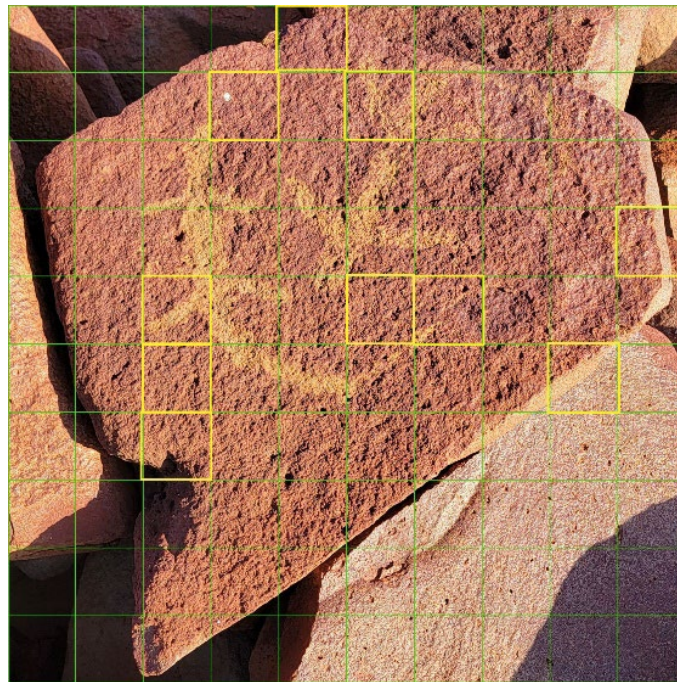


Figure B-2: A gridded RS site, with grid cells chosen at random.

B-2-2 Target Selection – AQ, EX and AS Sites

The 35 rock art surfaces at the AQ, EX and AS sites followed the same gridding process as described above, except that in step 3 it was permitted to adjust the position of the grid, and in step 4 the selection of grid cells was arbitrary. That is, researchers had free choice to select the grid cells. Selection aimed to avoid difficult placement near edges, favoured cells with readily recognisable features to enable relocation, and aimed to provide a diverse chromatic range of targets to monitor change on both lighter and darker surfaces.

B-2-3 Comparison of the two target selection methods

The target selection protocol for the AQ, EX and AS sites aims to achieve accurate target recognition and hence accurate re-registration of the probe over subsequent campaigns. The target selection protocol for the RS sites is designed to produce a representative sample of rock art surfaces on the entire peninsula and to incorporate all relevant sources of variability. Data from the AQ, EX and RS sites are expected to be more repeatable between subsequent visits.

Figure B-2 shows the ten randomly generated cells, two of which have very few identifying features and three of which have landed at the perimeter of the rock where placement of the light exclusion box becomes more difficult. Neither of these issues have been insurmountable.

Figure B-3 presents two contrasting cells, a random cell from the fully randomized target process on the left, where cell 2b has been determined. This cell is somewhat featureless making subsequent re-positioning more difficult. On the right, cell 1c has been chosen because it is surrounded by recognisable landscape reference features that can be seen with the unaided eye, together with several micro-features that allow for quick and accurate repositioning in macro view.

Figure B-4 presents the two targets from the cells in Figure B-3, viewed through the alignment screen. While the left-hand target contains sufficient alignment features, they are much harder to distinguish on a rock surface than those in the image on the right, containing features visible to the naked eye.

Of the 540 targets established in March 2022, only two could not be found in the following July campaign, one in an RS site and the other in an AQ/EX/AS site. Featureless targets contain enough features in macro view to enable precise positioning, however the process can be more time consuming.

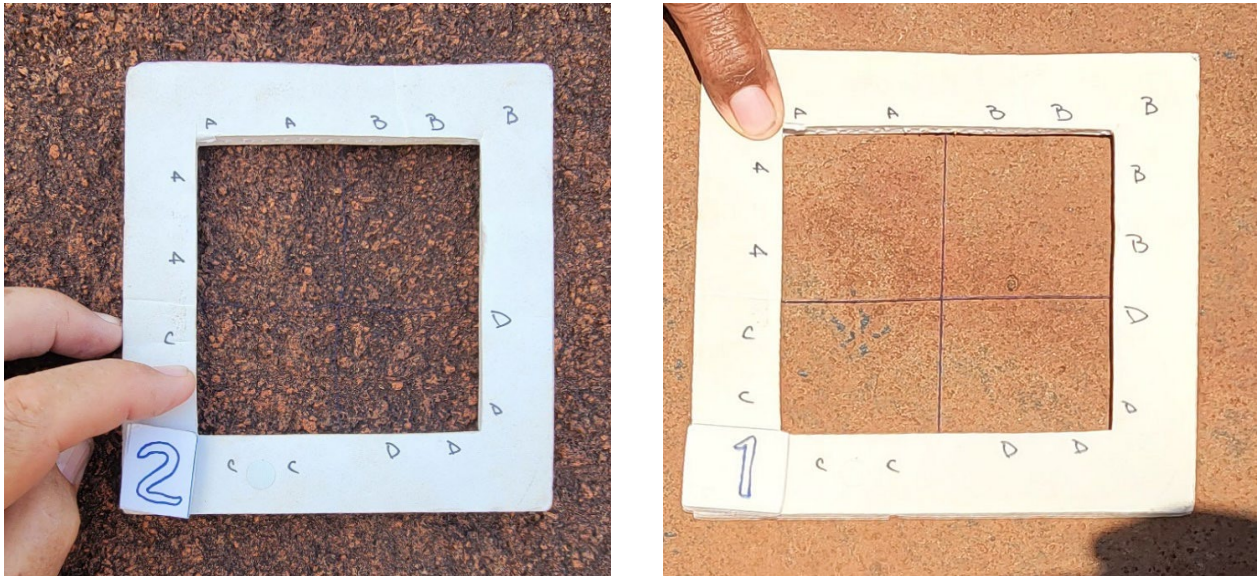


Figure B-3: Comparison of two grid cells at an RS site and a more freely selected EX site.

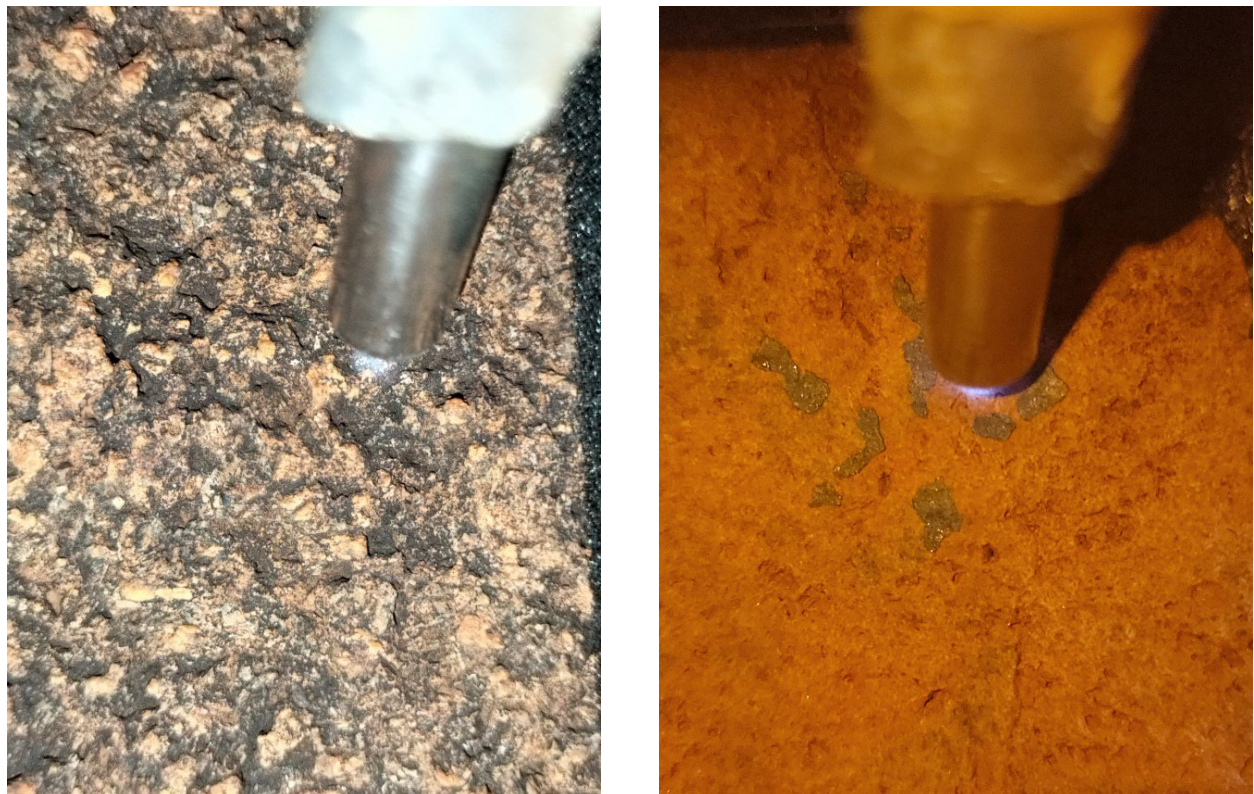


Figure B-4: Targets from the corresponding cells in Figure in macro view, as observed through the positioning screen.

B-2-4 Target re-establishment

A target is relocated through a series of images starting at the whole rock view and continuing in six to eight progressive increments to the final zoomed macro view, showing the probe position, and more importantly the light illuminating the target. Figure shows an abridged series from the whole rock surface through to macro images of the probe over the target. The macro images are achieved by a phone camera mounted to the top of the light exclusion box that holds the probe in position. A magnifier app allows the camera light to remain illuminated for positioning and imaging before being extinguished to check for light leaks and ultimately the spectroscopic reading. It is noted that light can be seen leaking in Figure . This is removed by covering the box with a black-out cloth.



Figure B-5: An abridged sequence of images that locate the grid cell on the whole rock, leading to the final macro images of the probe and light source. Note that the first macro image has stray light entering, blocked out prior to taking a reading.

By stepping through the existing image set the target is relocated. Most often this requires placing the box over the suspected target area and searching in macro mode with the light source. Heavily textured surfaces present a greater challenge as the appearance under normal and macro lighting are unrecognizable in many instances.

The probe in Figure B-5, the silver tube closest to the surface, is 6.35 mm in diameter and the light spot 4 mm across. Many of the reference landscape features at this level of magnification are 500 microns or less and it requires realignment of at least three such figures to position the probe with sufficient accuracy.

Laboratory evaluations of re-alignment accuracy are described in Appendix B-2-5, where a spatial accuracy of 0.2 mm was achieved without a reference image. The accuracy with reference images is half of that.



Figure B-6: MAC Ranger Kasziem bin Sali aligns the spectrometer probe by comparing the macro features visible on the active camera at left with the reference location viewed on the static image in the right- hand phone.

Figure B-6 shows the target alignment in process. The target is viewed through a magnifier app on the phone and compared to the previous reference image viewed on an adjacent screen. Both screens can be zoomed further to confirm sub-millimetre surface features where necessary.

This image also illustrates the nature of the light exclusion box, including the spectrometer probe entering and various foam pads blocking out light. On uneven surfaces an additional black-out cloth is applied, and the scene viewed through the phone to confirm darkness. Endoscopes have been used previously for this type of relocation but zooming a phone screen allows for views from the entire light box area (c. 70 x90 mm) to suitably sharp and close views of fine surface features, as illustrated in Figure B-5. Both light levels and zoom factors are readily adjustable on the screen. Every target is imaged for each campaign, prior to taking the spectral readings, using the 48Mp camera mounted on the box.

B-2-5 Independent validation of positioning accuracy

An independent laboratory experiment was conducted by Spatial Scientists at Curtin University to measure the accuracy with which the probe could be repositioned on a rock surface, using several candidate techniques.

The experiment was performed using a Leica TS15 1" Total Station.

Each spatial location was converted into cartesian coordinates, with the Y axis being along the direction of the laser. Since the laser was measuring using a reflectorless EDM, accuracy of measurement of the Y coordinate is approximately +/-2mm. The angular accuracy was +/- 1 arc seconds. Given the targeting and pointing error, the X and Z coordinates were measured with an accuracy of +/- 1-2mm.

Two targets were used to the side of the box. The X and Z axis are aligned to the side of the box, and the Y is perpendicular to the box. 10 repeat measurements were made of each spot. Outcomes are presented in Table B-1 to Table B-5 following.

Table B-1: Target relocation validation using the feature/camera method (02 March 2022).

Target	Mean coordinates			Sample standard deviation		
	X position (m)	Y position (m)	Z position (m)	X position (m)	Y position (m)	Z position (m)
Location 1						
Target 1	0.113877	2.30171	-0.50121	0.001294	0.000378	0.001035
Target 2	0.047863	2.291037	-0.53341	0.001384	0.002227	0.000303
Location 2						
Target 1	0.105389	2.325867	-0.50220	0.000754	0.000688	0.000515
Target 2	0.039262	2.320296	-0.53545	0.000937	0.002044	0.000445
Location 3						
Target 1	0.083875	2.274698	-0.51511	0.000416	0.000430	0.000292
Target 2	0.018598	2.267459	-0.54964	0.000767	0.001604	0.000126

Table B-2: Target relocation validation using the grid sheet method (02 March 2022).

Target	Mean coordinates			Sample standard deviation		
	X position (m)	Y position (m)	Z position (m)	X position (m)	Y position (m)	Z position (m)
Location 1						
Target 1	0.11916	2.344525	-0.50995	0.000929	0.0012	0.000845
Target 2	0.048368	2.347289	-0.53151	0.000934	0.004344	0.000684
Location 2						
Target 1	0.121472	2.217815	-0.52220	0.002097	0.000666	0.001644
Target 2	0.048944	2.229322	-0.53137	0.00116	0.005689	0.001706

Table B-3: Repeat target relocation measurements after reapplying the grid sheet (02 March 2023)

Target	Mean coordinates			Sample standard deviation		
	X position (m)	Y position (m)	Z position (m)	X position (m)	Y position (m)	Z position (m)
Location 1						
Target 1	0.118007	2.34359	-0.51121	0.001029	0.001283	0.000659
Δ to previous	-0.00115	-0.00093	-0.00127	-	-	-
Target 2	0.047071	2.347607	-0.53204	0.000815	0.004094	0.000633
Δ to previous	-0.0013	0.000317	-0.00053	-	-	-
Location 2						
Target 1	0.126472	2.217998	-0.52460	0.000467	0.00048	0.00018
Δ to previous	0.005001	0.000183	-0.00241	-	-	-
Target 2	0.052914	2.21807	-0.53418	0.000517	0.001268	0.000234

Δ to previous	0.00397	-0.01125	-0.00280	-	-	-
---------------	---------	----------	----------	---	---	---

Note: Measurements for targets at Location 1 and Location 2 should coincide with positions in Table B-2)

Table B-4: Target relocation validation of a vertical surface using the grid sheet (04 March 2022)

Target	Mean coordinates			Sample standard deviation		
	X position (m)	Y position (m)	Z position (m)	X position (m)	Y position (m)	Z position (m)
Target 1	0.077049	2.524033	-0.47557	0.001003	0.000947	0.000817
Target 2	0.077442	2.524418	-0.55001	0.001028	0.00186	0.000825

Table B-5: Target relocation validation of a vertical surface using the feature/camera method (04 March 2022)

Target	Mean coordinates			Sample standard deviation		
	X position (m)	Y position (m)	Z position (m)	X position (m)	Y position (m)	Z position (m)
Target 1	0.074471	2.451556	-0.51514	0.000602	0.000822	0.000289
Target 2	0.01791	2.409823	-0.5384	0.002074	0.001408	0.000306

Appendix B-3 The influence of external stray light.

Stray light, whether internally generated, or more pertinently from external sources, will affect the spectral reflectance response from a surface. Mixed light sources not only alter the intensity of light but in the case of metameric materials, can vastly alter the spectral response.

The aim of this study is to determine to what extent this is true, to ensure that spectra are reliable and repeatable.

An external LED light source has been introduced to contribute to the lighting regime in the range 23-9,000 Lux, with the spectrum recorded at each increment. LED has been chosen as it has a dominant emission peak distinctly different to that of the xenon light source of the spectrometer.

In the Murujuga context the sun is the main external light source. Not only does it exceed 30,000 Lux but the colour of the light varies with angle and cloud cover.

B-3-1 Test procedure

A white marble tile has been mounted at 45° to the direction of the spectrometer probe and the same angle to the external light source, fixed in a retort stand to maintain a constant geometric relationship. A light meter has been set to measure the relative level of external stray light on the tile, slightly off-set from the spectrometer light source. The LED was then positioned to provide set increments of light from 25 lux through to a maximum of 9,000 lux.

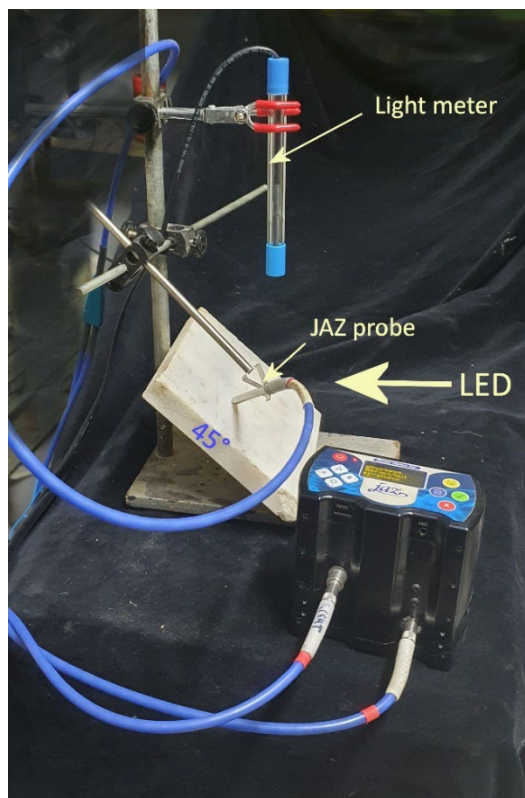


Figure B-7: Test setup to record the influence of an external light source on the spectral reflectance from a white marble tile.

B-3-2 Aim

To determine the level of external light that will alter the spectral response.

B-3-3 Result

The following series indicate the influence of stray light at various Lux levels.

Figure B-8 compares the reflectance spectra, measured on the calibration tile, of the spectrometer's xenon light source to that of the chosen external LED source to show the obvious difference in their emission spectra.

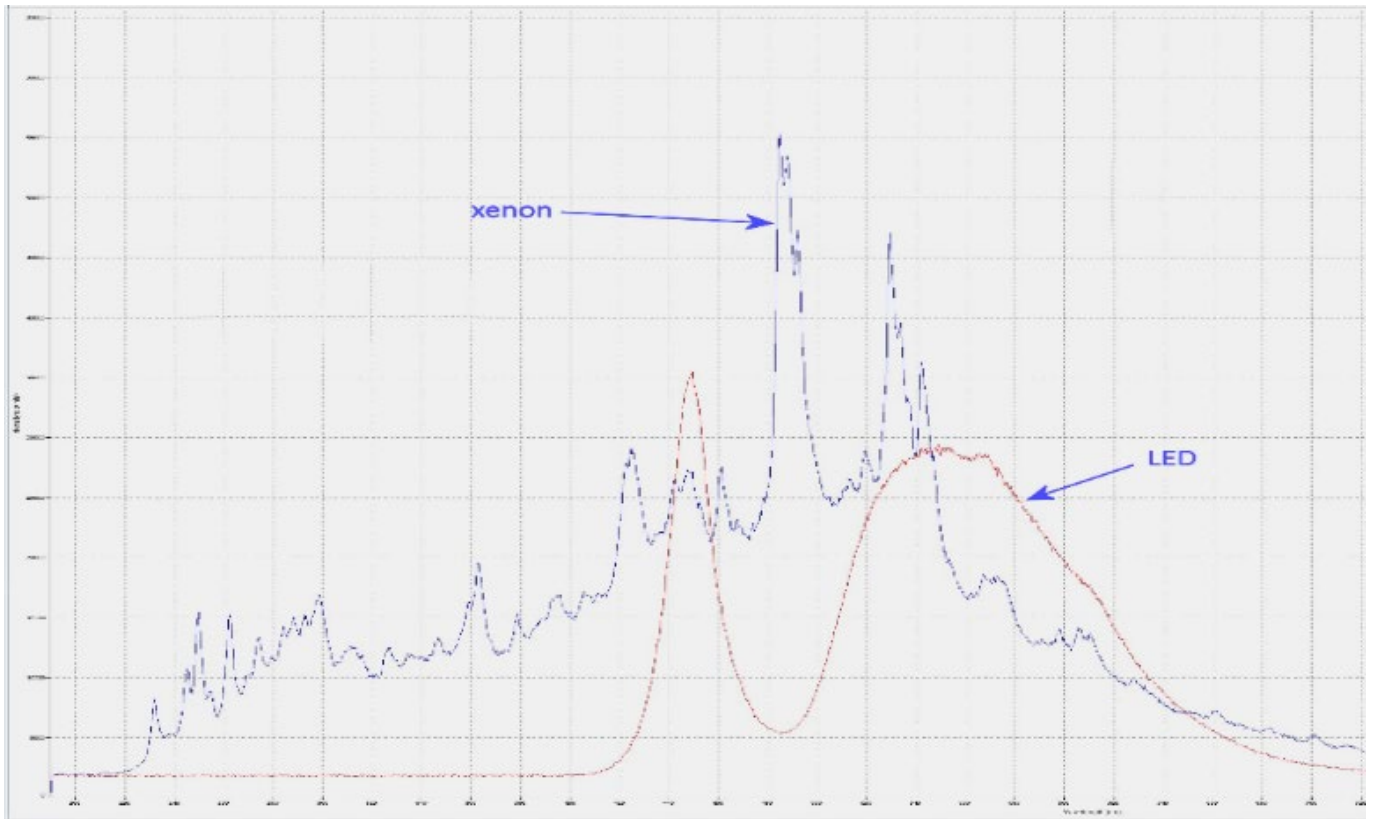


Figure B-8: Reflectance spectra of the JAZ spectrometer's xenon light source and that of the external LED interference light source

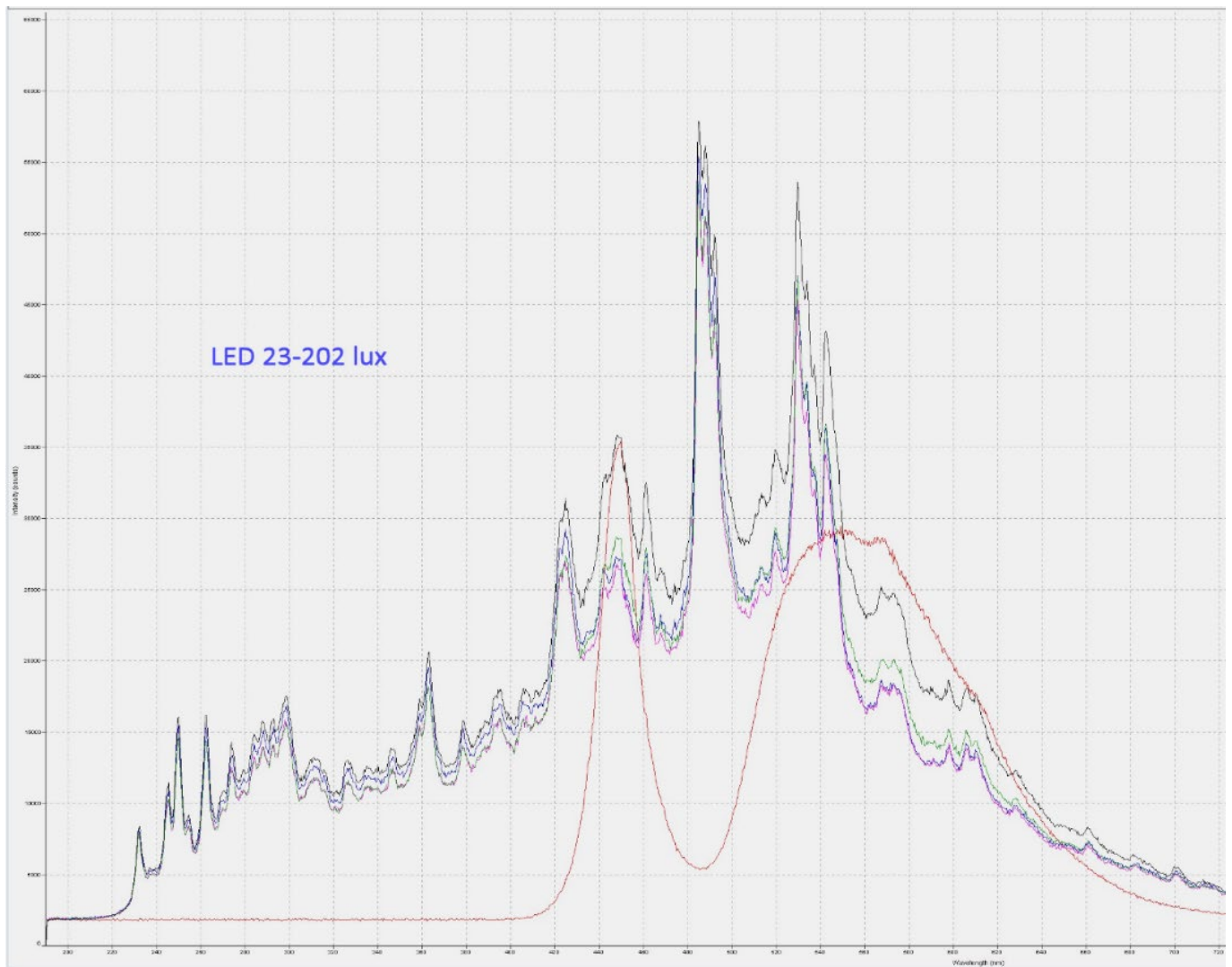


Figure B-9: The influence of the LED is imperceptible at 23 Lux but begins to re-shape the spectrum at 50 Lux onwards. Key: Red LED, Blue 0 Lux, Violet 23 Lux, Green 50 Lux, Upper trace 202 Lux.

B-3-4 Findings

In this study all light above 50 lux can be considered contributory to the reflectance spectrum. 50 lux is the equivalent of a very dimly lit room and compares to the conditions at Murujuga where 30,000+ lux are encountered every day. The issue here is not simply whether stray light contributes but that it varies in colour and intensity.

B-3-5 Methodology response

1. The probe is applied to a light exclusion box that ensures total darkness. This box also ensures the probe is maintained at a consistent angle and distance from the surface (See Appendix B-4 and Appendix B-5).
2. Once the target re-registration procedure is complete (Figure B-6) the camera light-source is extinguished, and the screen checked for stray light. Where necessary additional black-out materials are applied to augment the effectiveness of the sponge applied to the bottom of the box.

Appendix B-4 Probe angle

The inclination of the probe relative to a surface will affect spectral reflectance intensity. Standards exist for fixed light source instruments, such as the Konica Minolta colorimeter, typically specifying an 8° offset of the light source to the reflectance sensor, set perpendicular to the surface [1]. Spectrometers utilizing an optical fibre to transmit light to the surface and return the spectral intensity to the processor have no fixed geometry relative to a surface but are traditionally configured at 0° or 45° for colorimetry measurement. A typical optical fibre cluster consists of a sensor fibre surrounded by seven light transmission fibres, hence the sensor and light source are coaxial. By attaching a separate fibre bundle to the light source to that connected to the sensor, the geometry can be altered but this is generally limited to the measurement of gloss rather than colour. In this latter configuration the aim is to capture the reflected light from the source, whereas in colorimetry the opposite is the case, the surface should not reflect light back into the sensor.

Positioning the probe at 0° , that is perpendicular to the surface, ensures that reflected light is optimized, whereas at 45° there is little chance of reflection back into the sensor. There is no optical physics to justify 45° as the optimal angle, particularly when the standards for fixed instruments specify 8° .

The purpose of this study is to determine the optimal angle to set the coaxial optical fibre bundle at to minimize reflection and to provide the most reliable spectra.

B-4-1 Evaluation 1 – geometry to avoid reflectance into the sensor

The probe used for the Murujuga study consists of a central $400\ \mu\text{m}$ sensor fibre, surrounded by seven light transmission fibres of the same dimensions, with a beam angle of 25° .

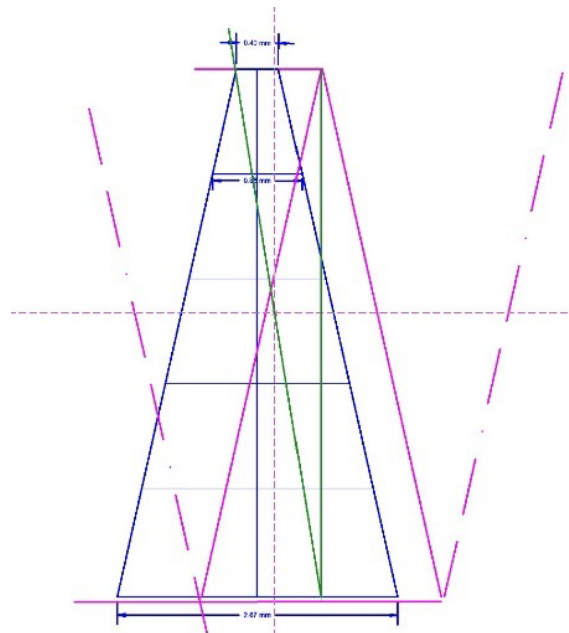


Figure B-10: Schematic of the CAD calculation of beam angle and light reflection into the sensor.

Figure B-10 presents a schematic summary of the CAD calculations on the “beam” angle of the sensor to calculate the diameter of the sensed area at various distances. This geometry is represented by blue lines. The magenta lines show beam angle of the right-hand light source for which a calculation of potential reflection back into the sensor has been derived and indicated by the green lines.

The diameter of the sensed area will be 0.4 mm at zero distance, up to 2.67mmØ at 5 mm distance. The probe has nominally been set at 5mm.

The green lines calculate the angle of probe tilt to avoid direct light reflection back into the sensor. This has been measured on the CAD model to be 9°. Any tilt angle greater than 9° will ensure there is no reflection into the sensor on a perfectly flat surface. It is interesting to note that the standard for fixed geometry instruments has been set at 8°.

These calculations are for a perfectly flat surface, which is certainly not the case for the 540 targets being measured at Murujuga. There are however a number of more or less flat glossy targets and the chosen geometry of 20° minimises reflection for these targets. More rugose target surfaces will have a combination of reflective and diffractive facets, leading to a complex and unresolvable configuration for the probe.

B-4-2 Evaluation 2 – spectral response v. probe angle

In this test a uniform matte surface has been rotated in relation to the probe, ensuring no alteration in position or distance. A matte surface has been chosen to minimise reflection. Five readings have been taken at each angle and the results plotted in vector CIE Lab space.

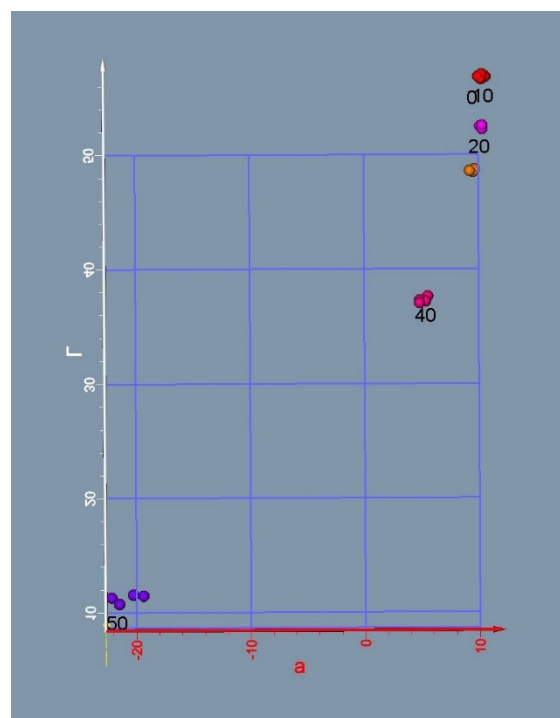


Figure B-11: Extract from the 3-D vector plot of CIE Lab values at probe angles 0-50°, viewed on the L and a axes.

Figure B-11 present a 2D view of the data with L* (lightness) on the Y axis and a* (red positive, green negative) on the X axis. The grid has been set at 10 CIE Lab units. Colour difference values, ΔE, have not been calculated but can be inferred from the vector plot from which Figure has been extracted.

The probe angle has been marked adjacent to each cluster of spectra.

B-4-3 Findings

The most important finding of this plot is the difference in CIELab units between 40° and 50°, indicating that a probe set at the conventional 45° position and varied by ±5° through surface rugosity would produce a colour variation of up to 25 units on each axis. The b* axis, not shown, varies by 10 units. The ΔE calculation for the difference between 40 and 50 degrees is ΔE = 36.7. Given that a perceptible colour difference is considered to be ΔE > 2, a ±5° variation through surface rugosity would produce erratic results.

The variation 0-10° is satisfactory, however the likelihood of reflected light augers against such a perpendicular setting. 20° has been chosen as a compromise between limiting reflection and reducing chromatic error. It can be seen that the colour shift 10-30° is approximately a quarter of the 45° setting, despite being double the angle.

B-4-4 Methodology response

The spectrometer probe angle has been set at 20°. This is achieved by embedding a holder tube into the top of the light exclusion box Figure . This controls both the angle and distance from the surface.

Appendix B-5 Probe distance

It is expected that probe distance will affect the spectral response. From the diameter of the light spot on the surface it is possible to calculate the probe distance at 5 mm, relying in the geometry illustrated in Figure B-10. This also produces a sensing area of 3 mm in diameter, aimed to coincide with the smaller sensing area of the KM instrument used in previous studies. While there is no ideal probe distance, consideration for the sensed area is an over-riding consideration. The preference in this study is to measure a smaller spot than that provided by instruments such as the Konica Minolta CM 700d that provides set measurement areas of 8mm \emptyset and 3 mm \emptyset .

B-5-1 Aim

To measure the colour at various probe distances from the surface to demonstrate the need to maintain consistency.

B-5-2 Findings

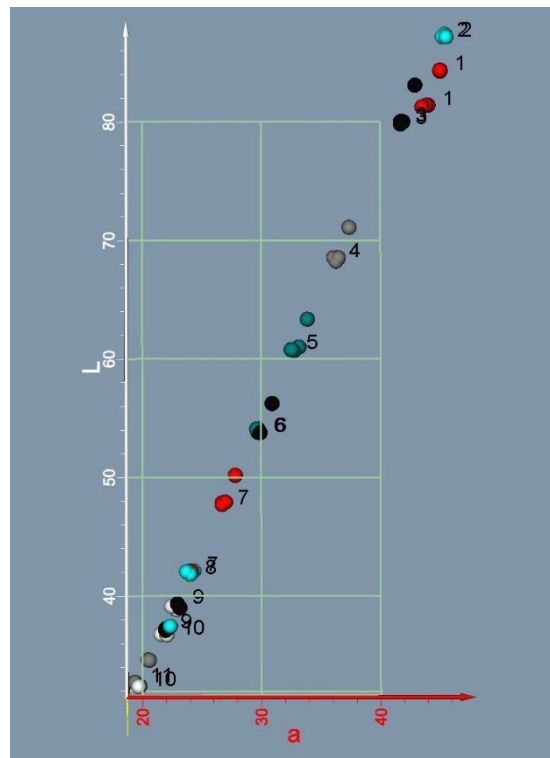


Figure B-12: A 2D snapshot of the spectral response at distances from 1-11 mm for the surface.

Figure B-12 shows a more or less linear regression in both L^* and a^* axes. It is noted however that there is less colour difference in the 8-10 mm range than in the 3-5 mm range. Probe distance is indicated adjacent to each cluster of measurements. The 5 mm probe distance chosen lies at the centre of the chart. This data illustrates one thing only, that the probe must be maintained at a uniform distance from the surface.

B-5-3 Methodology response

The probe has been set to be 5 mm from the surface, however the surface upon which the light exclusion box is placed is not flat. The distance will not always be 5 mm. To ensure that the readings in any target remain constant

the probe is positioned in the same orientation as the reference image on all occasions. Owing to the precise probe placement this ensures that the box will be at a constant distance.

B-5-4 Target size

The sensed area can be varied on the JAZ instrument simply by altering the probe distance. Fixed geometry instruments offer one, or two selectable diameters. This discussion compares the virtues of a 3 mm area and a larger area. Larger areas are favoured in industry for coloured surfaces that may be discontinuous, such as dyed woven fabrics, or where a more averaged reading is preferred. In the case of the Murujuga rocks the surfaces are either dense and smooth or highly pitted. When illuminated by the spectrometer's light source, effectively a macro ring light, the texture becomes imperceptible with only chromatic variation being apparent.

The main benefit of a larger area in the current context lies in the accuracy of re-positioning. A 1 mm shift on an 8 mm area results in a 12.5% error compared to a 33% error on a 3 mm area.

Given however that the probe re-positioning has been measured to be < 0.2mm in a context where a reference image was not used, repositioning error is not considered to be as substantial as the problems presented by a larger target area embracing a range of minerals compared to a smaller target isolating out a chromatically uniform surface. The primary objective of this research is to measure colour change; hence, it is important to be able to isolate a uniformly coloured target area. Dark inclusions may not darken to the same extent as light ones and chromatic shifts can be expected to be mineral specific. Figure illustrates the difference in surface features embraced by a 3 mm and 8 mm sensor, indicated by the green circles below the probe.

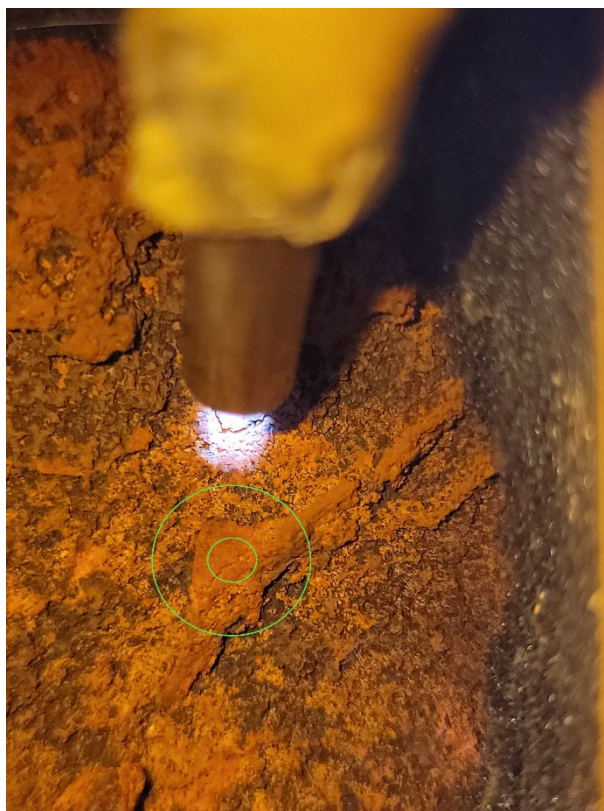


Figure B-13: Site RS 11 Target 1 illustrating the difference between a 3 mm and 8 mm target area in terms of chromatic homogeneity.

It is notable that previous research reports concluded that surface heterogeneity was the biggest factor in producing unreliable spectra (Markley et al, 2014, pg 56).

Appendix B-6 Instrument precision

The standard measure of colour difference, for colours expressed in CIELAB coordinates, is the Euclidean distance in CIELAB space, denoted ΔE . That is, ΔE is the square root of the sum of squared differences in the L^* , a^* and b^* coordinates. In previous studies the criterion for colour change was set at $\Delta E > 2$, considered to be the degree of colour difference perceptible to the viewer with average colour acuity. Figure B-10 and Figure B-11 illustrate how small a change this is. Whether this arbitrary measure of change is valid or not, it can only be substantiated if the instrument being used has a repeatable precision of $\Delta E < 2$. To establish this the Jaz spectrometer has been compared with three other instruments used in previous research and a fifth instrument, discussed for its affordability combined with tristimulus lighting that potentially could generate very reliable CIE Lab units. This latter instrument attaches to a smartphone and costs c. \$100.

B-6-1 Evaluation

Spectral data from previous research has been processed to evaluate the precision of the three instruments employed. Data has been provided by DWER, or through the project report [2] for each of the instruments.

- Konica Minolta CM 700d assumed from report wording to have operated with an 8mm window, measuring at 10 nm sample interval across the waveband 400-700 nm
- Gardner BYK colorimeter with a 4mm window and 20 nm sample interval across the spectral band 400-700 nm.
- ASD FieldSpecPro, the fibre optic sensor head can be held at any distance from the surface as or the Jaz, discussed in Appendix X.3. The sample interval is 1.4-2 nm across the 350-2500 waveband.

Markley et al (2014) provides test data for the KM and BYK instruments but not for the ASD, this field data has been used for the latter instrument.

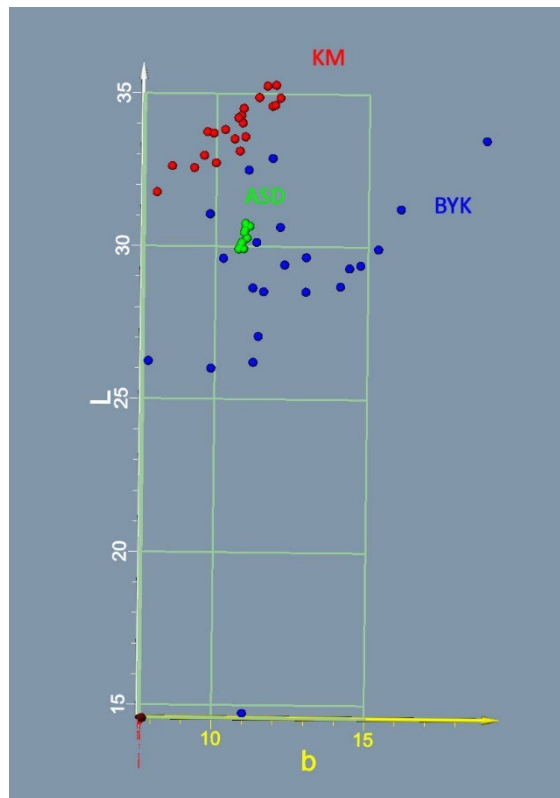


Figure B-14: Precision data for the three previously employed instruments. The grid is set at 5 L*a*b* units. It is clear from this graphic that only the ASD instrument is precise enough to draw colour change conclusions of any significance. None of them can confidently discern $\Delta E = 2$.

Figure B-14 gives a snapshot of the precision of the three instruments. It is clear that only the ASD instrument has a precision suited to the colour change parameters determined by the operators of these instruments. Detailed values for the KM instrument are presented in Table B-6. This table compares the ΔE for all 20 spectra. Cells highlighted in orange exceed the nominated $\Delta E > 2$, with the peak difference at $\Delta E = 5.5$. This instrument cannot resolve colour differences at the levels sought.

Table B-6: Colour difference calculation for 20 spectra on the one target using the Konica Minolta colorimeter.

	1	2	3	4	5	6	7	8	9	10	11	12	13	14	15	16	17	18	19	20	21
1		1.4	1.0	3.7	0.6	4.6	1.3	2.8	1.5	2.5	2.3	1.0	3.1	0.4	1.3	0.4	1.3	2.0	1.0	2.4	1.4
2			1.6	2.6	0.8	3.4	0.4	1.6	0.5	1.5	1.0	1.9	1.8	1.0	2.1	1.0	2.0	1.0	1.7	1.4	2.3
3				3.9	1.1	4.8	1.4	2.9	1.9	2.4	2.6	0.9	3.3	1.0	0.9	1.2	0.5	1.8	0.8	2.3	0.8
4					3.2	1.0	2.9	1.1	2.8	1.6	1.8	4.4	0.9	3.3	4.6	3.4	4.3	2.1	4.3	1.7	4.6
5						4.1	0.7	2.3	0.9	2.0	1.7	1.2	2.5	0.3	1.5	0.3	1.5	1.5	1.1	2.0	1.7
6							3.7	2.0	3.5	2.6	2.5	5.2	1.6	4.2	5.5	4.2	5.3	3.1	5.1	2.7	5.5
7								1.9	0.6	1.7	1.3	1.6	2.1	0.9	1.8	1.0	1.8	1.2	1.5	1.6	2.0
8									1.8	0.8	1.0	3.4	0.6	2.4	3.5	2.5	3.3	1.1	3.2	0.8	3.6
9										1.9	1.0	1.9	1.9	1.2	2.2	1.2	2.3	1.5	1.8	1.8	2.5
10											1.4	3.0	1.3	2.1	3.1	2.2	2.8	0.6	2.9	0.2	3.1
11												2.8	1.0	1.9	3.1	1.9	3.0	1.4	2.7	1.4	3.3
12													3.7	1.2	0.3	1.3	0.9	2.4	0.1	2.9	0.7
13														2.7	3.9	2.7	3.7	1.6	3.6	1.3	4.0
14															1.4	0.3	1.3	1.6	1.1	2.0	1.5
15																1.5	0.7	2.6	0.4	3.0	0.5
16																	1.5	1.8	1.2	2.2	1.7
17																		2.3	0.8	2.7	0.4
18																			2.3	0.5	2.6
19																				2.8	0.7
20																					3.0

The ASD instrument produces a much tighter cluster in Figure and this is borne out in the comparative ΔE data in Table B-7, where 13 spectra from their Site 1 Spot 1 have been compared.

Table B-7: ΔE comparison of 13 repeated spectra on CSIRO Site 1 Spot 1 using ASD data provided by DWER..

	1	2	3	4	5	6	7	8	9	10	11	12	13
1		2	1.7	0.7	2.0	0.5	0.9	0.9	1.7	0.9	1.1	1.1	2.3
2			3.1	2.4	3.2	1.5	1.9	2.8	2.1	1.4	2.7	1.3	3.4
3				1.0	0.4	1.7	1.3	1.0	3.4	2.5	0.7	1.9	0.7
4					1.3	0.9	0.8	0.4	2.4	1.6	0.5	1.3	1.7
5						2.0	1.6	1.3	3.7	2.7	0.9	2.0	0.5
6							0.8	1.2	1.9	0.8	1.2	0.7	2.2
7								1.2	2.5	1.5	1.1	0.7	1.7
8									2.5	1.8	0.5	1.7	1.7
9										1.2	2.8	2.3	4.0
10											1.9	1.2	3.0
11												1.6	1.4
12													2.2
13													

There were no off-site evaluations provided for the ASD instrument and thus site data has been used for this precision evaluation.

The table shows that while the cluster is much tighter in Figure , and that overall, the ΔE values are lower, there are still some ΔE as high as 4.0.

It should be noted that the precision of these instruments is not at fault, rather than the expectation that a $\Delta E < 2$ is measurable using such instruments. What is more important is the identification of trends towards colour alteration that can be interpreted as being caused by known external factors. An instrument with less precision will take longer to determine a trend and thus in the current 5-year program instruments lie the KM and BYK most likely will not develop trends sufficiently quickly.

B-6-2 JAZ precision

The JAZ instrument has been nominated in this research not only because it is a compact ruggedised instrument, but also its specifications. Being a fibre optic unit the target area can be varied, as described in Appendix B-4. The sample interval is 0.45 nm (a third of the ASD) and it measures in the bandwidth 190-1100, with effective spectral data being extracted in the 220-850 range. This compares with the ASD bandwidth of 350-2500, achieved by combining three light sources and two sensors. In essence the ASD contains the same photo-optical properties as the JAZ but extending the range by including an NIR configuration as separate components within the case.

The JAZ has performed relatively better than the instruments described above and can be considered a suitable instrument for identifying trends more quickly.

Figure shows a snapshot of the cluster of 10 spectra run from the JAZ onto a uniform target. It can be seen that the spectra lie within a radius of less than 2 units.

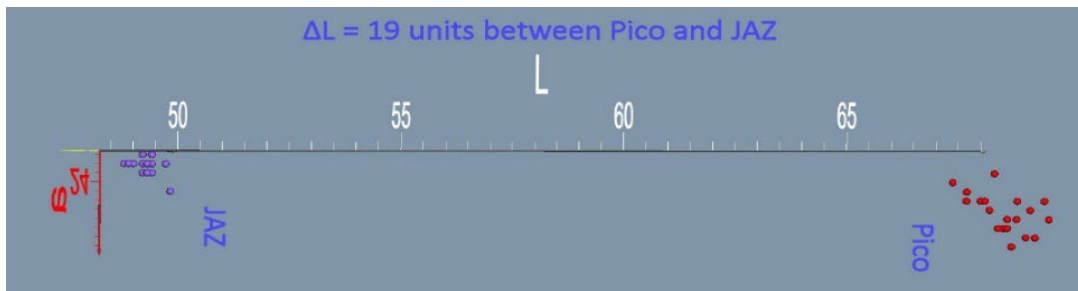


Figure B-15: A snapshot of the repeatability of the JAZ spectrometer together with data for the Pico smartphone attachment.

Table B-8: ΔE calculation for 20 reference spectra from the JAZ spectrometer. The highest colour variation is $\Delta E = 1.1$

	1	2	3	4	5	6	7	8	9	10	11	12	13	14	15	16	17	18	19	20
1		0.44	0.4	0.4	0.3	0.3	0.5	0.4	0.4	0.5	0.3	0.4	0.5	0.4	0.6	0.4	0.6	0.3	0.5	0.4
2			0.5	0.2	0.2	0.5	0.1	0.3	0.2	0.1	0.4	0.5	0.1	0.1	0.6	0.7	0.7	0.4	0.7	0.1
3				0.6	0.5	0.3	0.6	0.7	0.6	0.6	0.1	0.2	0.6	0.5	0.4	0.6	0.9	0.7	0.3	0.5
4					0.1	0.5	0.1	0.2	0.1	0.2	0.5	0.5	0.1	0.2	0.7	0.7	0.5	0.3	0.8	0.1
5						0.5	0.2	0.2	0.1	0.3	0.4	0.5	0.2	0.2	0.7	0.6	0.5	0.2	0.7	0.2
6							0.5	0.6	0.5	0.6	0.2	0.2	0.6	0.6	0.3	0.3	0.8	0.5	0.3	0.5
7								0.3	0.2	0.2	0.5	0.5	0.1	0.2	0.7	0.7	0.6	0.4	0.7	0.1
8									0.1	0.3	0.6	0.7	0.3	0.2	0.8	0.7	0.4	0.2	0.9	0.3
9										0.3	0.5	0.6	0.2	0.2	0.7	0.6	0.4	0.2	0.8	0.2
10											0.5	0.6	0.1	0.1	0.7	0.8	0.7	0.5	0.8	0.2
11												0.1	0.5	0.5	0.3	0.5	0.9	0.6	0.3	0.4
12													0.5	0.5	0.2	0.5	0.9	0.6	0.2	0.4
13														0.2	0.7	0.8	0.6	0.5	0.8	0.1
14															0.7	0.7	0.6	0.4	0.7	0.2
15																0.5	1.1	0.8	0.1	0.6
16																	0.7	0.5	0.5	0.6
17																		0.3	1.1	0.6
18																			0.8	0.4
19																				0.6

Table B-8 presents the ΔE calculations for all 20 reference spectra derived from a uniform matte tile approximating a light tan surface such as those encountered in fresh engravings at Murujuga.

The notable result is that the greatest colour difference is that between spectra 15 and 17 with a $\Delta E_{\max} = 1.1$. This compares very favourably with the results of the ASD instrument, $\Delta E_{\max} = 4.0$.

B-6-3 Findings

The JAZ is capable of discerning colour change as determined by the CSIRO threshold of $\Delta E > 2$. It is stated again that a numerical change in colour is not a measure of change, rather a trend over time needs to be identified, the magnitude of which is secondary to the trend itself. Summary statistics for the 20 JAZ spectra are presented in Table B-9, showing standard deviations of $L \cdot 0.28$, $a \cdot 0.21$, and $b \cdot 0.19$, respectively.

Table B-9: Summary statistic for the 20 JAZ reference spectra.

Parameter	L	Parameter	a	Parameter	b
Mean	67.70	Mean	24.33	Mean	26.37
Standard Error	0.06	Standard Error	0.05	Standard Error	0.04
Median	67.9	Median	24.35	Median	26.3
Mode	67.9	Mode	24.2	Mode	26.3
Standard Deviation	0.28	Standard Deviation	0.21	Standard Deviation	0.19
Sample Variance	0.08	Sample Variance	0.04	Sample Variance	0.04
Kurtosis	-1.52	Kurtosis	-0.36	Kurtosis	-0.23
Skewness	-0.53	Skewness	-0.21	Skewness	0.25
Range	0.8	Range	0.8	Range	0.7
Minimum	67.2	Minimum	23.9	Minimum	26
Maximum	68	Maximum	24.7	Maximum	26.7
Sum	1354	Sum	486.6	Sum	527.3
Count	20	Count	20	Count	20

Appendix C: TIMA analysis results

Appendix C-1 TIMA analysis precis

The results of optical microscopy observations and TIMA are summarised in this Appendix. Samples are listed according to lithology and shown with the patina layer towards the top of the image. For each sample, the following data are provided:

1. Panorama image in plane-polarized transmitted light acquired by Axio Imager.
2. TIMA electron backscattered (BSE) image.
3. TIMA mineral phase map.
4. TIMA modal analysis displaying the calculated proportions of minerals within the thin section.
5. TIMA elemental X-ray map for Fe, Mg and Ca.
6. Grain size distribution of major mineral phases contained in the thin section. This shows the frequency of each grainsize of a considered phase in micrometres.

In the TIMA results, the term:

- “Unclassified” indicates the percentage of pixels that have not been associated with a specific phase. Generally, a value < 5 wt.% is considered acceptable.
- “The rest” indicates the cumulative percentage of phases that are not shown in the current display.
- “Primary phases” in the modal analyses plots refers to phases present within the mineral library of the software and does not imply that the phases are “primary” in a geological context, where “primary” indicates that a mineral formed at the same time as the initial formation of the rock.

Appendix C-2 Granophyre

C-2-1 Sample rock AQ02_GPH



Figure C-1: Panorama image of granophyre sample rock AQ02_GPH

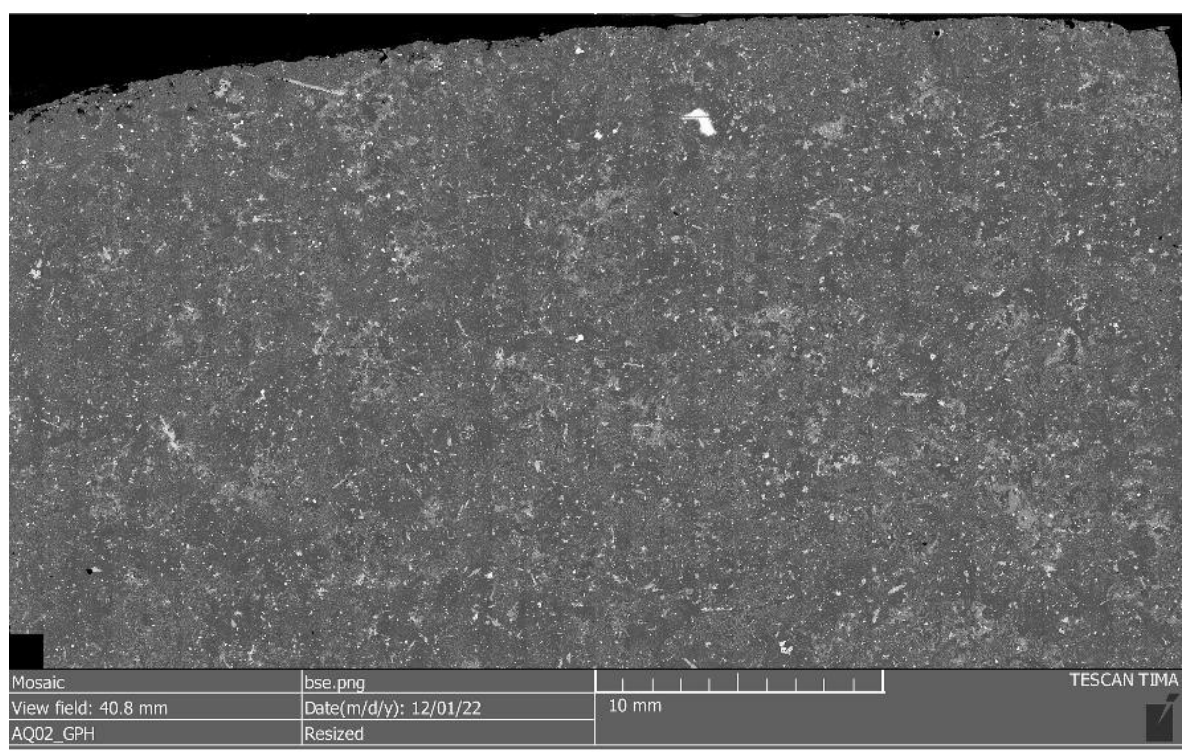


Figure C-2: BSE image of granophyre sample rock AQ02_GPH

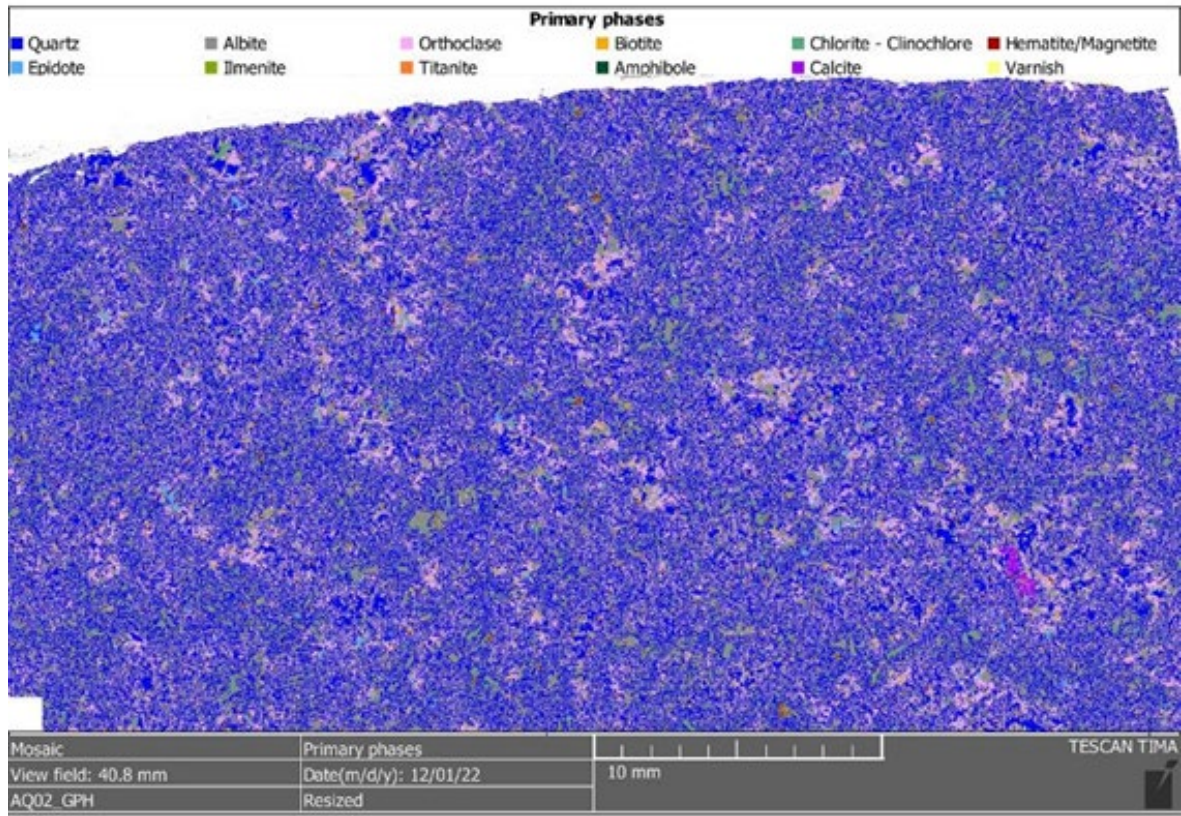


Figure C-3: Phase map of granophyre sample rock AQ02_GPH

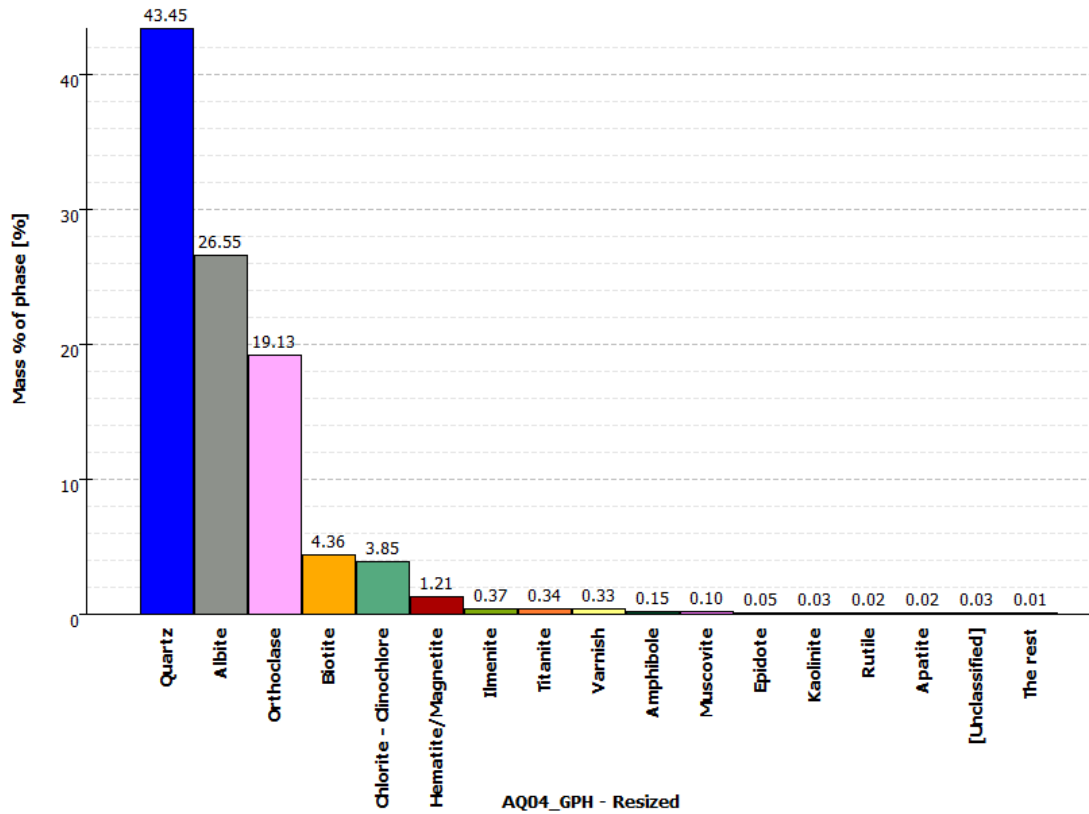


Figure C-4: Modal analysis of granophyre sample rock AQ02_GPH

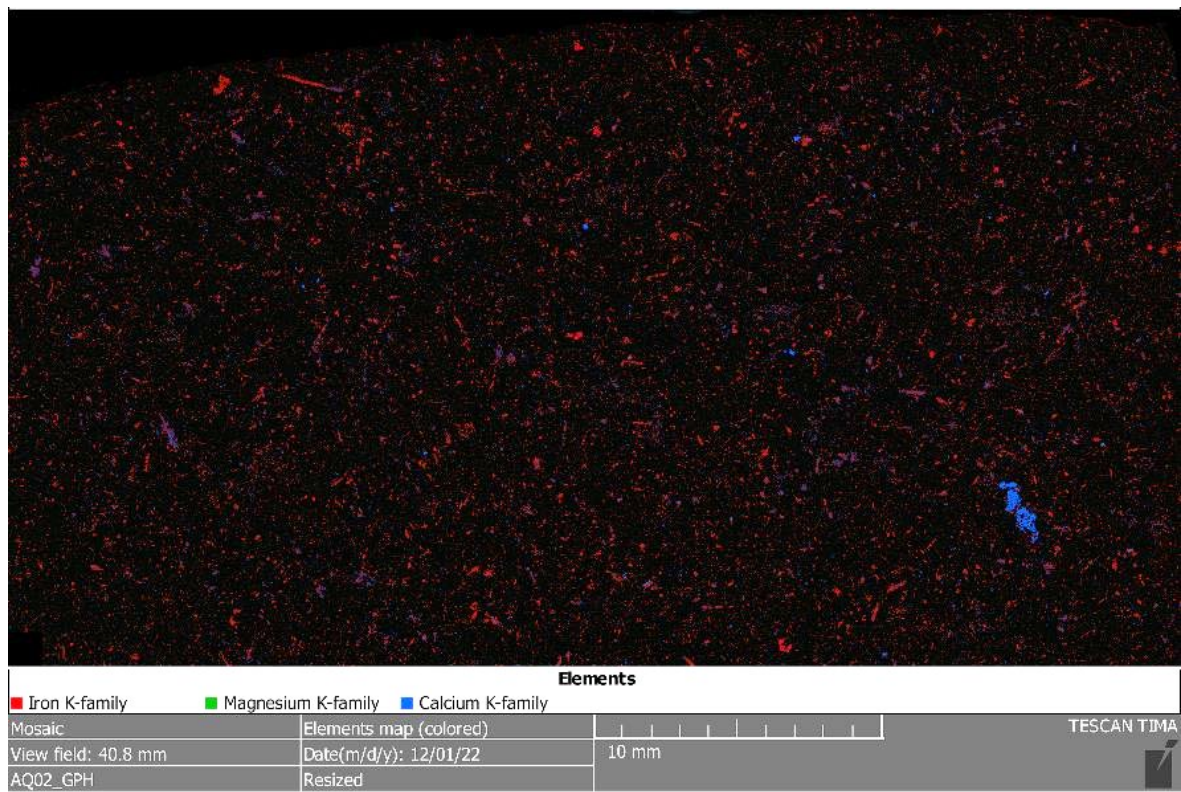


Figure C-5: Element map of granophyre sample rock AQ02_GPH

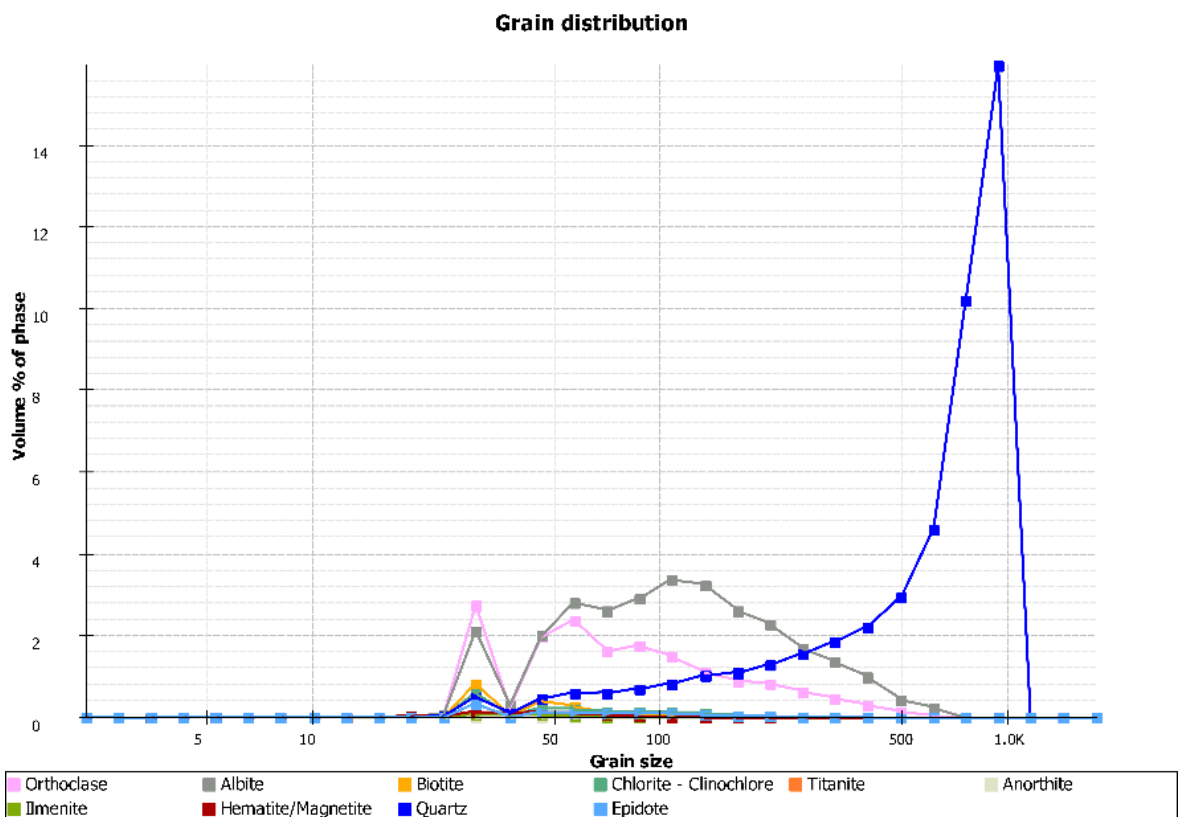


Figure C-6: Grain size distribution of granophyre sample rock AQ02_GPH

c-2-2 Sample rock AQ04_GPH



Figure C-7: Panorama image of granophyre sample rock AQ04_GPH

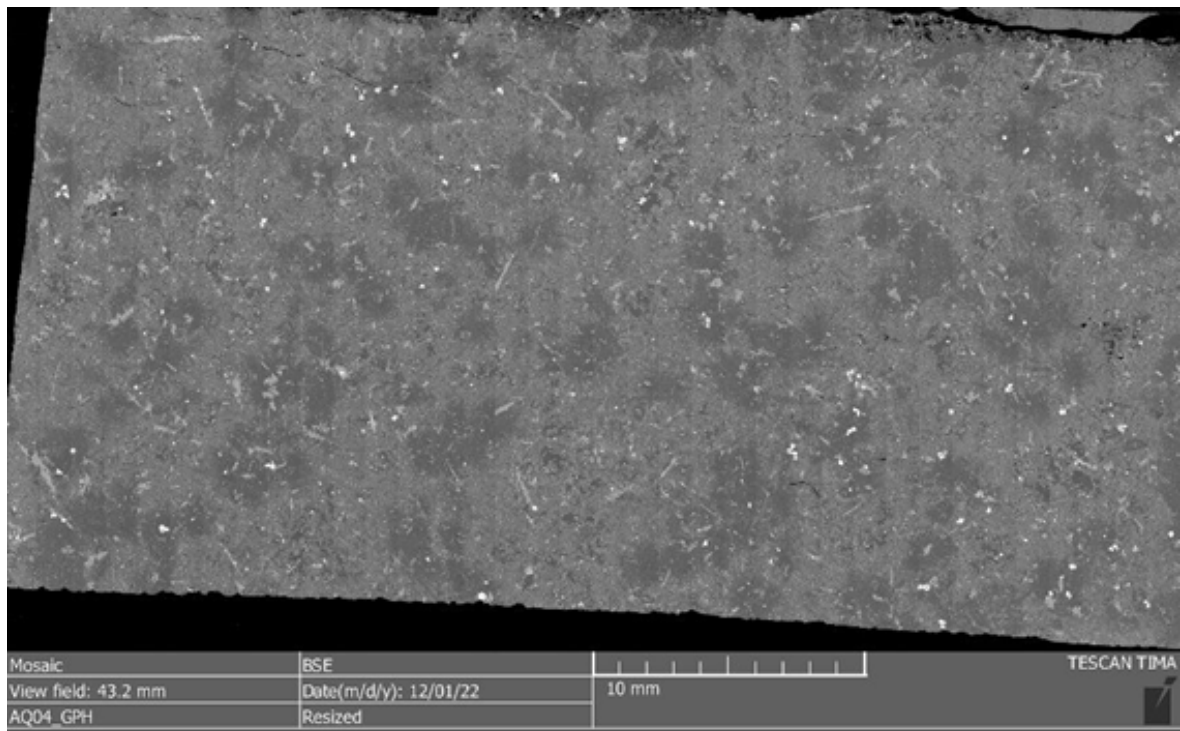


Figure C-8: BSE image of granophyre sample rock AQ04_GPH

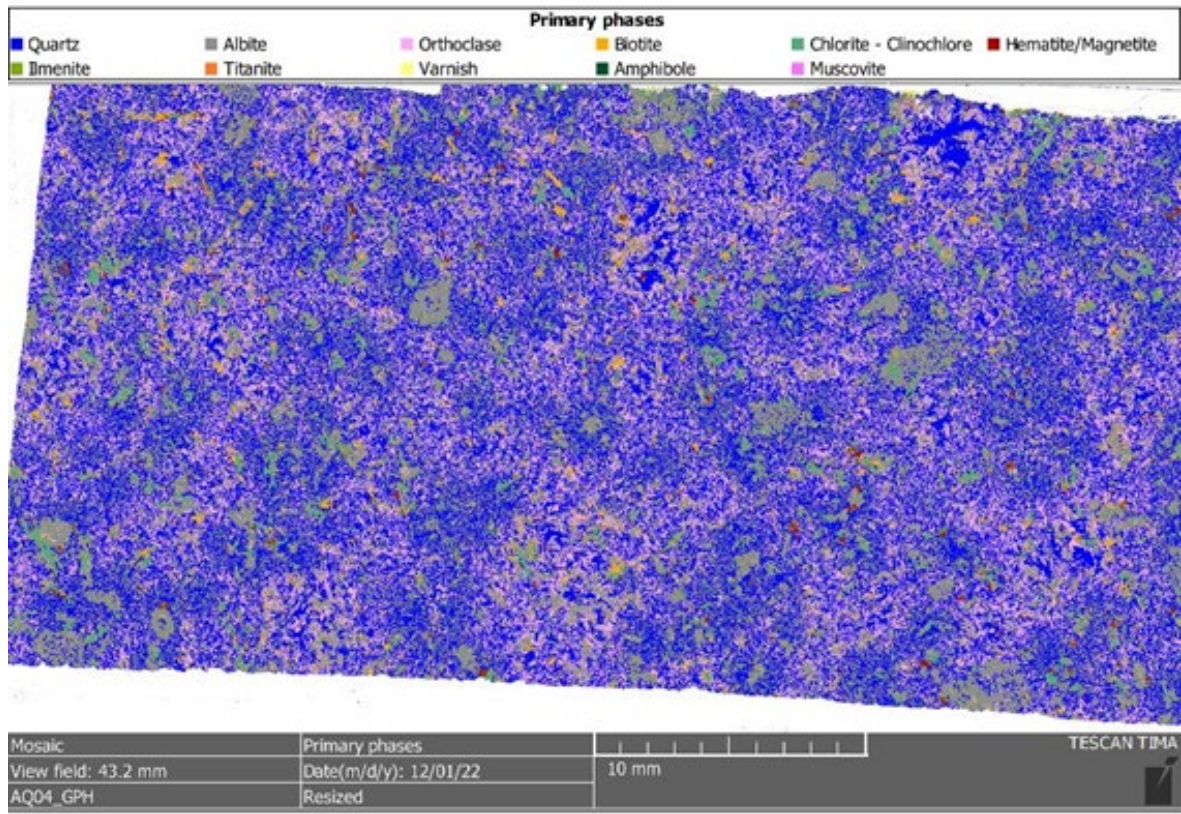


Figure C-9: Phase map of granophyre sample rock AQ04_GPH

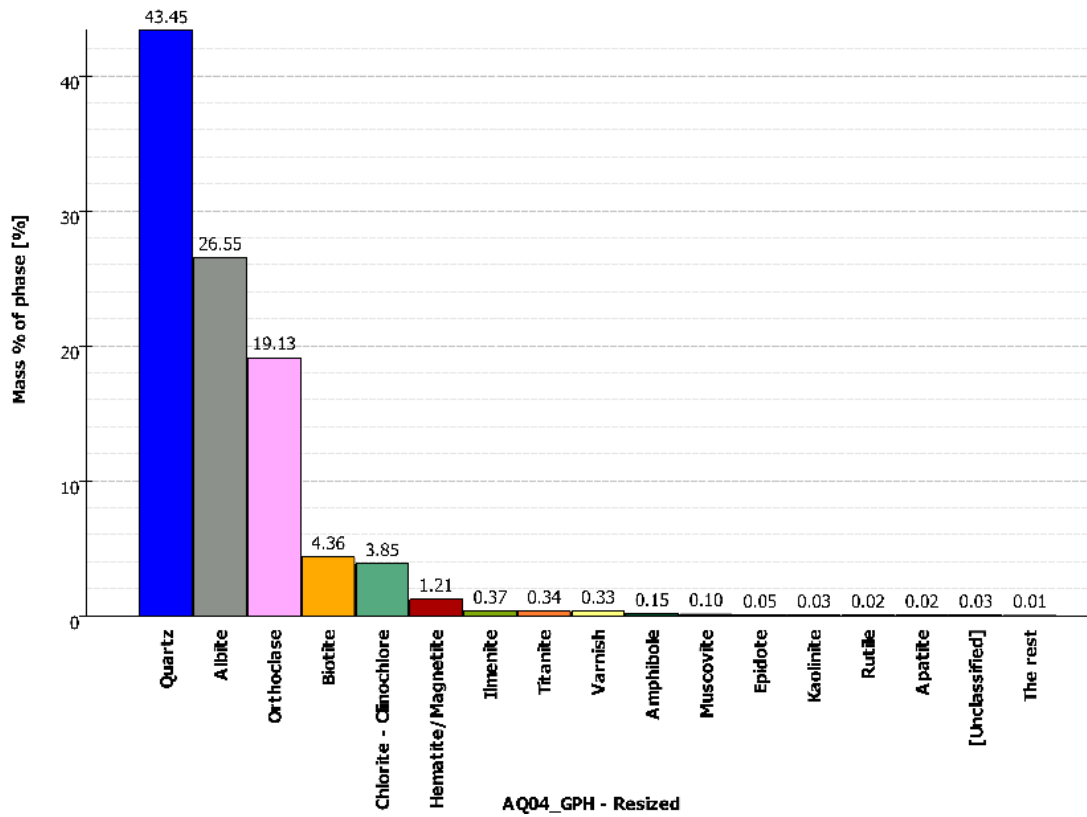


Figure C-10: Modal analysis of granophyre sample rock AQ04_GPH

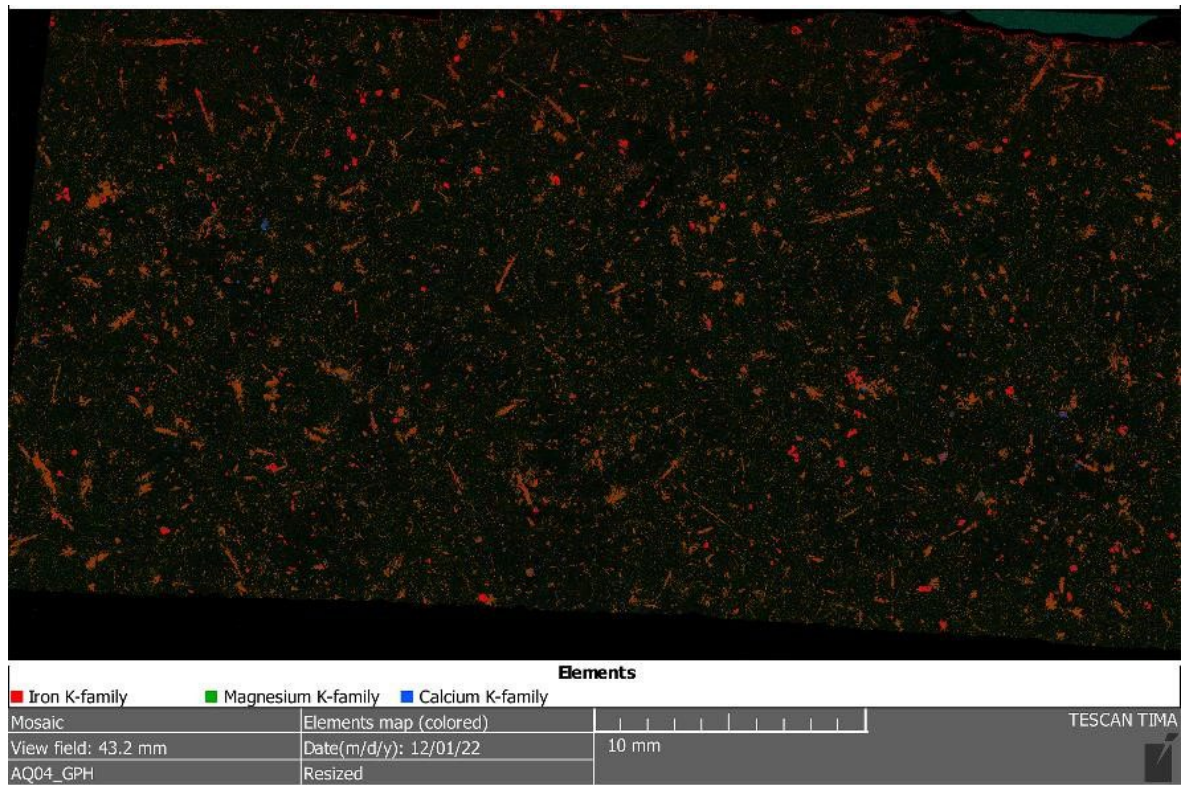


Figure C-11: Element map of granophyre sample rock AQ04_GPH

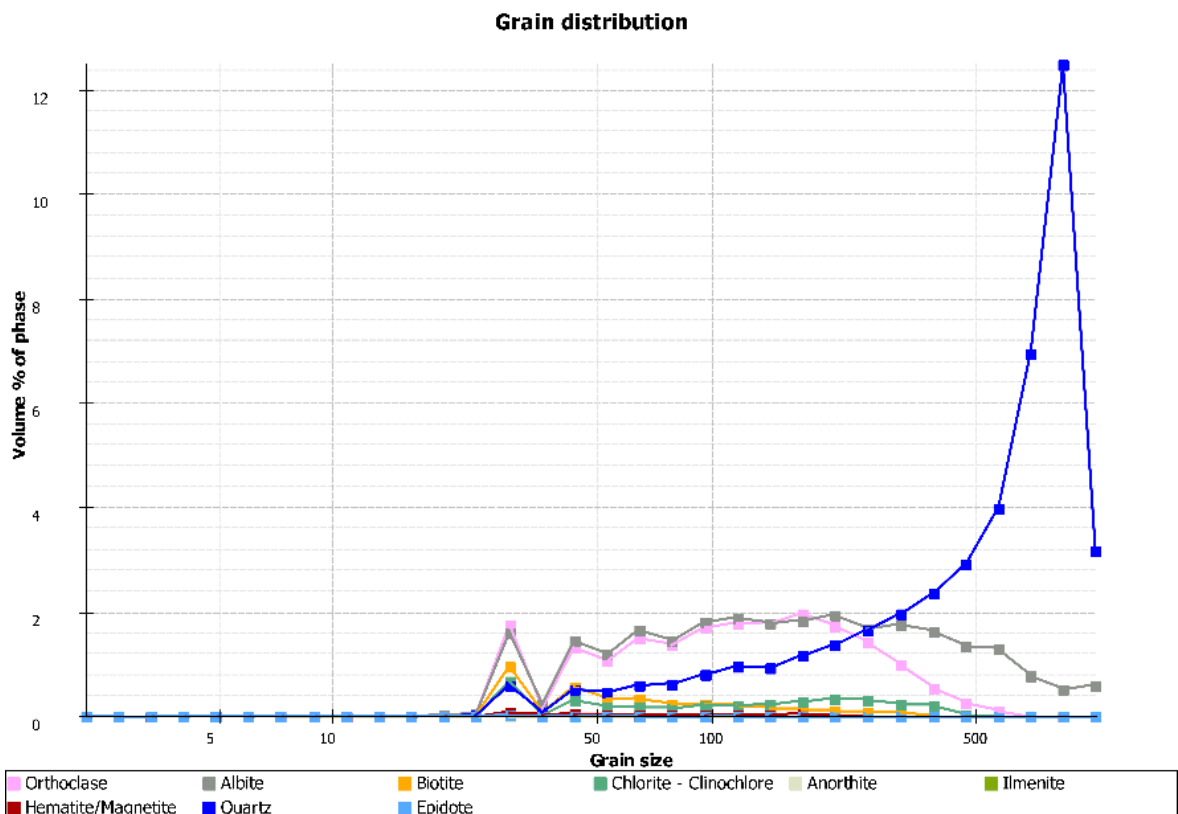


Figure C-12: Grain size distribution of granophyre sample rock AQ04_GPH

C-2-3 Sample rock AQ05_GPH



Figure C-13: Panorama image of granophyre sample rock AQ05_GPH

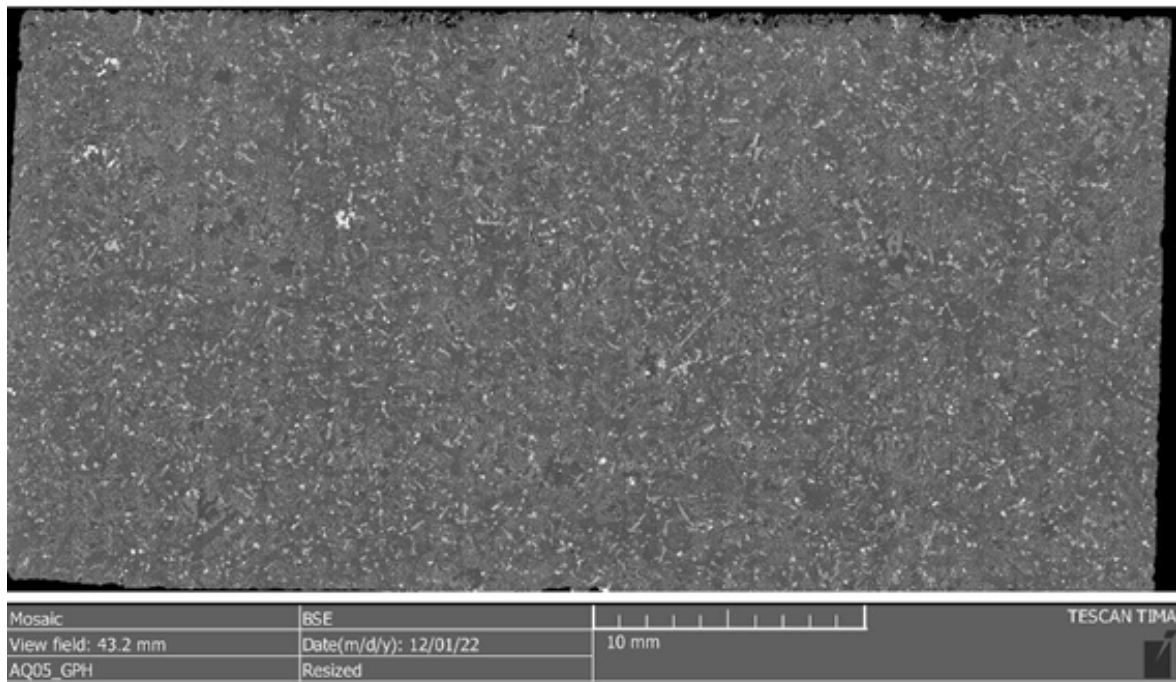


Figure C-14: BSE image of granophyre sample rock AQ05_GPH

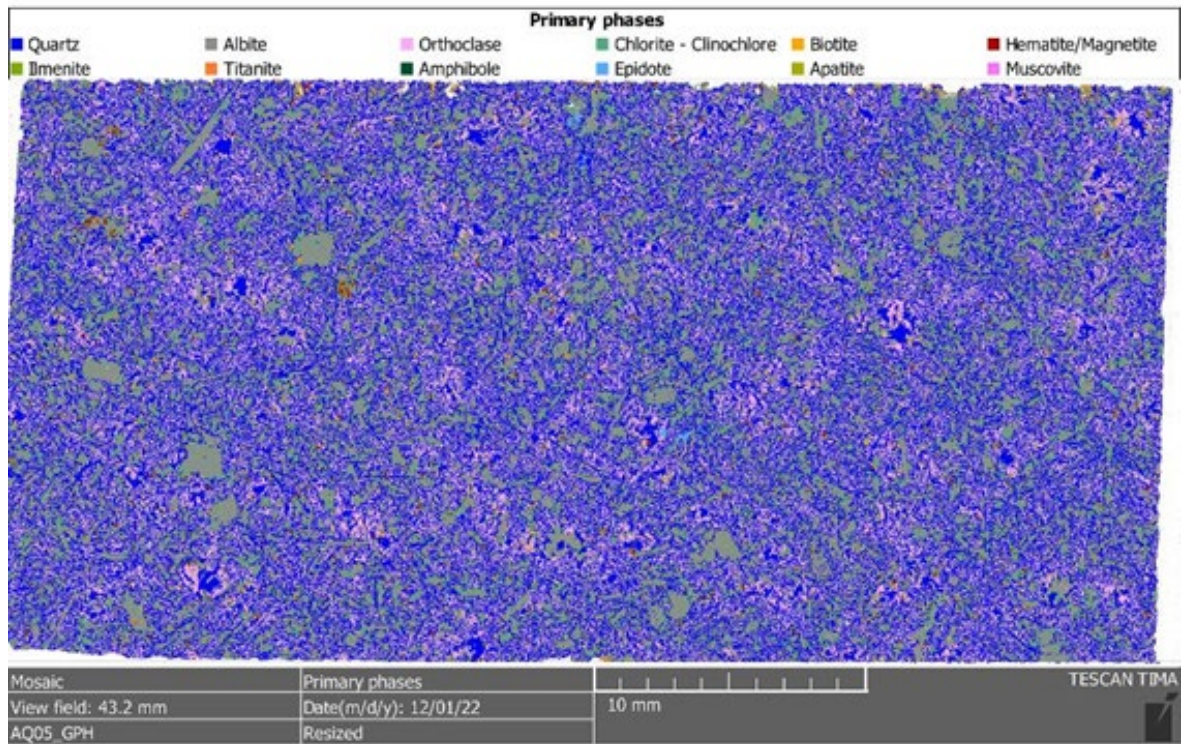


Figure C-15: Phase map of granophyre sample rock AQ05_GPH

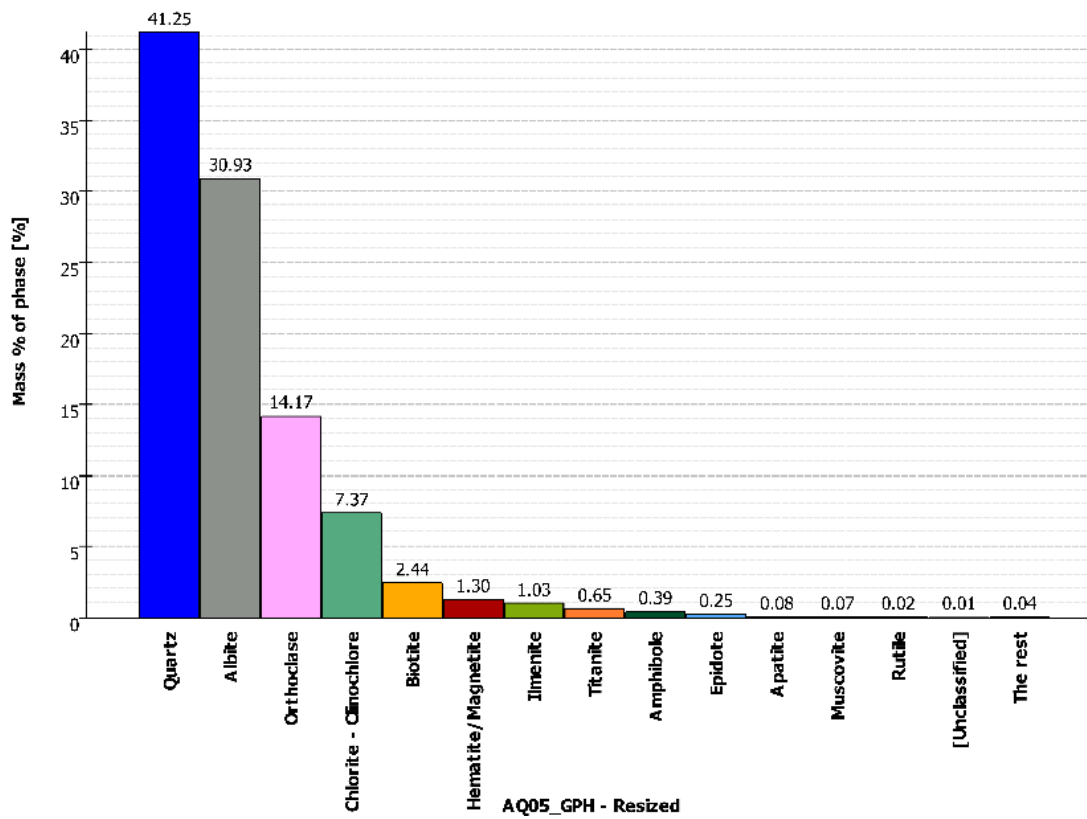


Figure C-16: Modal analysis of granophyre sample rock AQ05_GPH

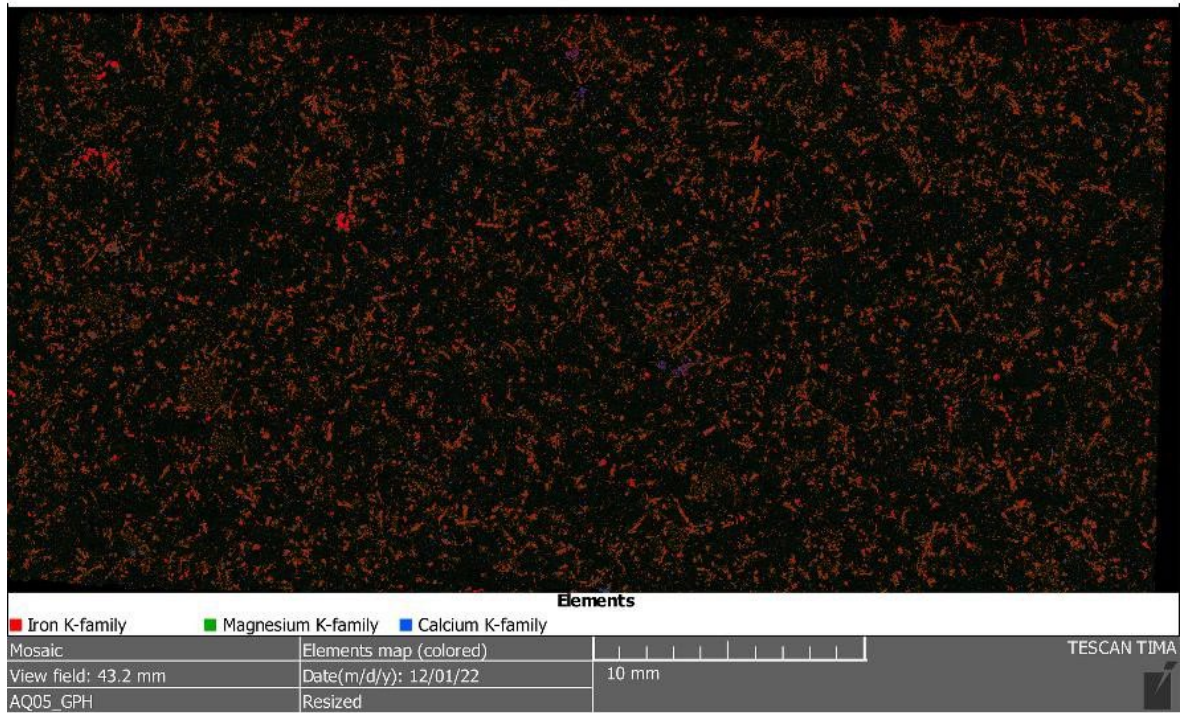


Figure C-17: Element map of granophyre sample rock AQ05_GPH

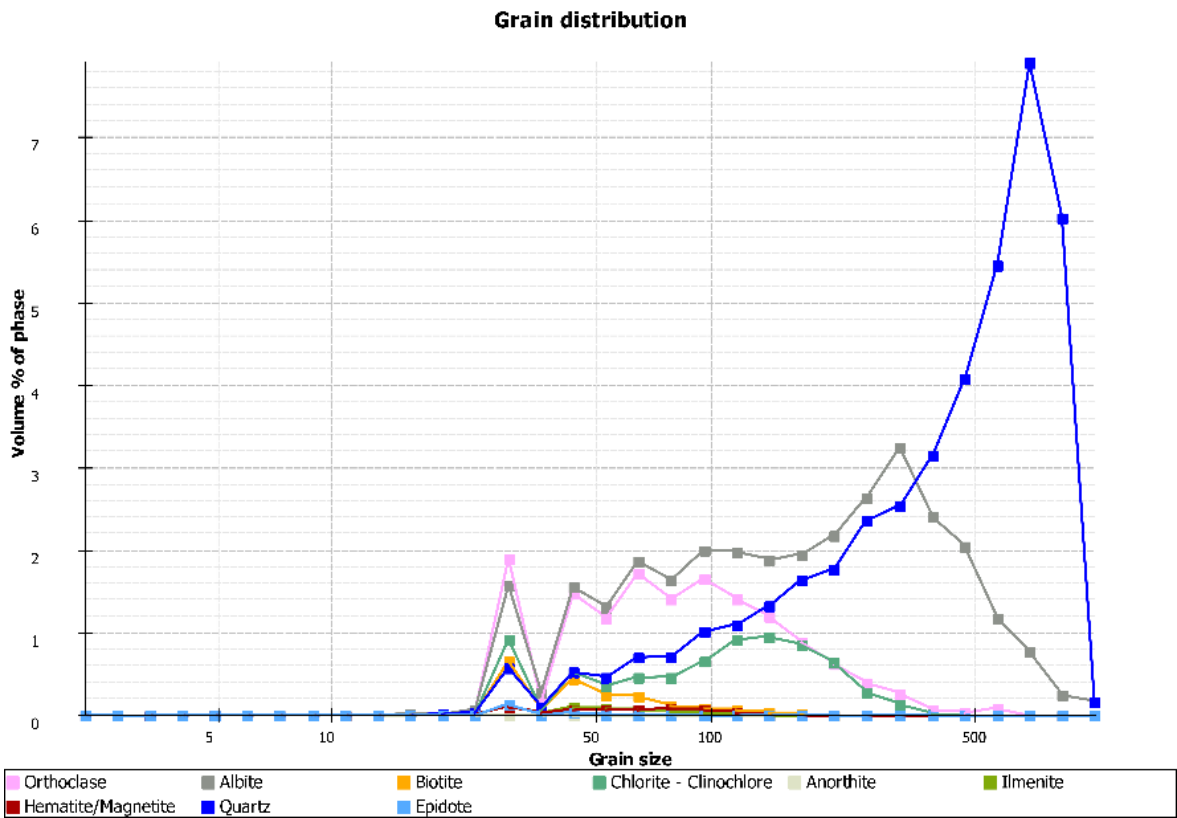


Figure C-18: Grain size distribution of granophyre sample rock AQ05_GPH

C-2-4 Sample rock AQ06_GPH



Figure C-19: Panorama image of granophyre sample rock AQ06_GPH

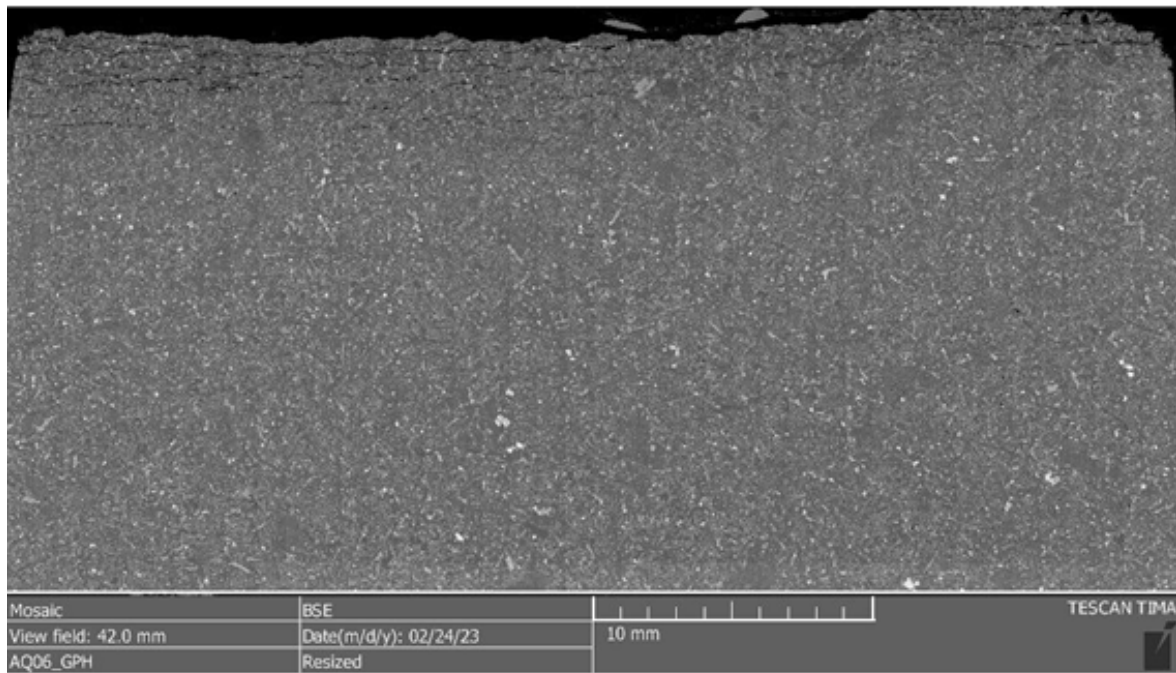


Figure C-20: BSE image of granophyre sample rock AQ06_GPH

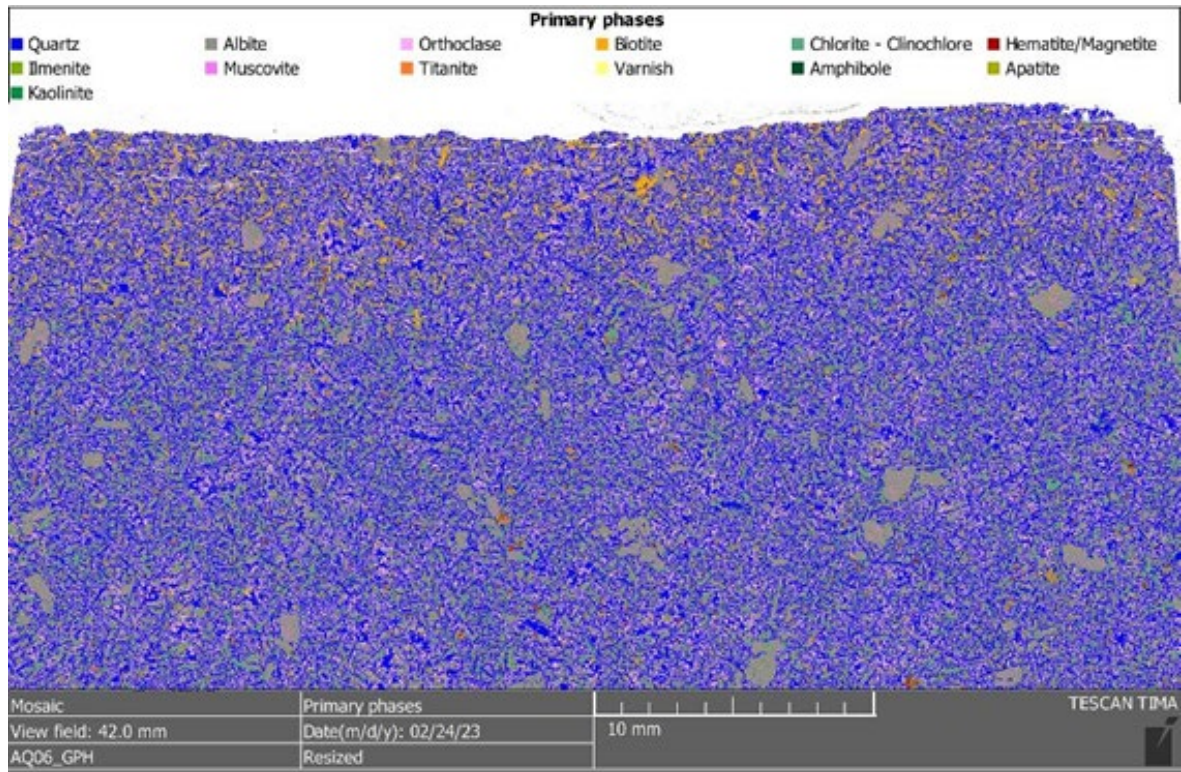


Figure C-21: Phase map of granophyre sample rock AQ06_GPH

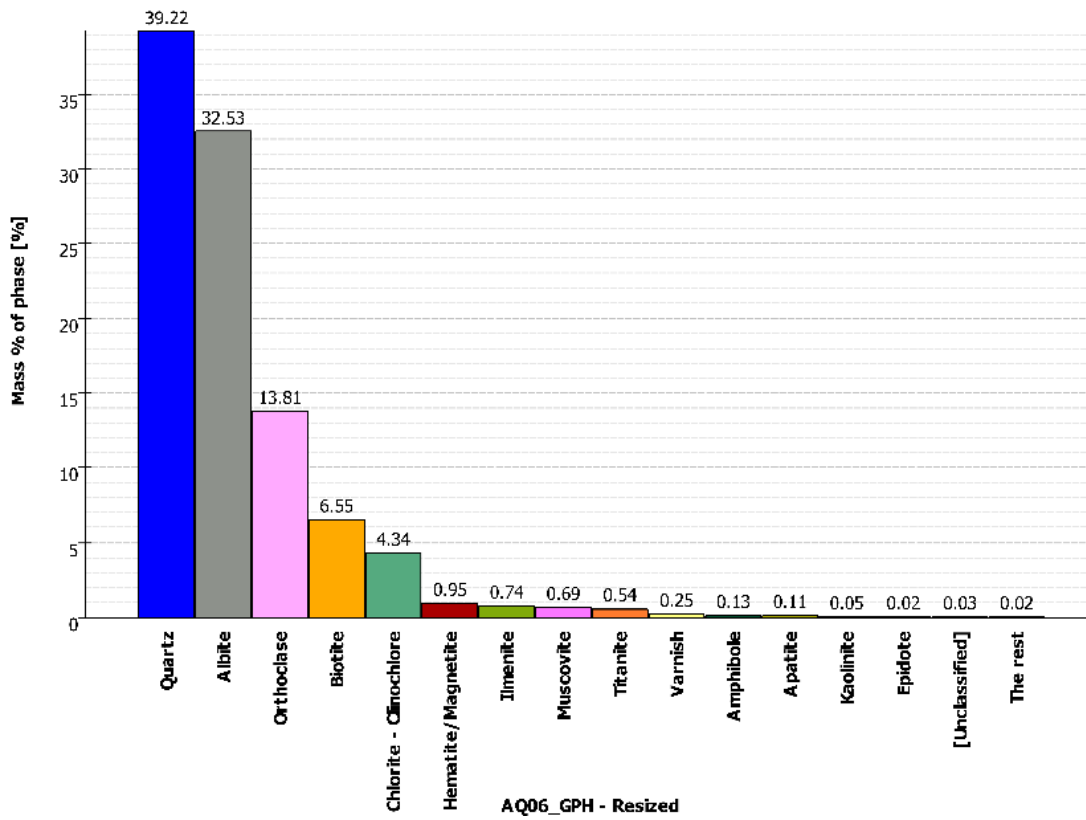


Figure C-22: Modal analysis of granophyre sample rock AQ06_GPH

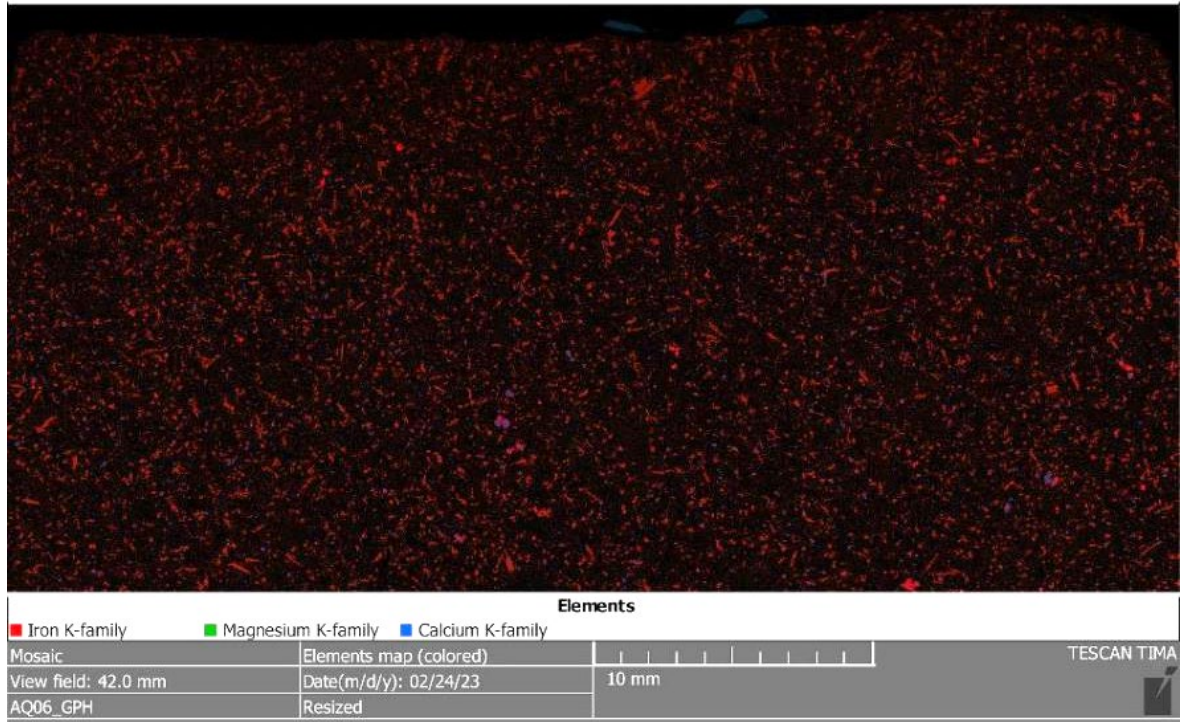


Figure C-23: Element map of granophyre sample rock AQ06_GPH

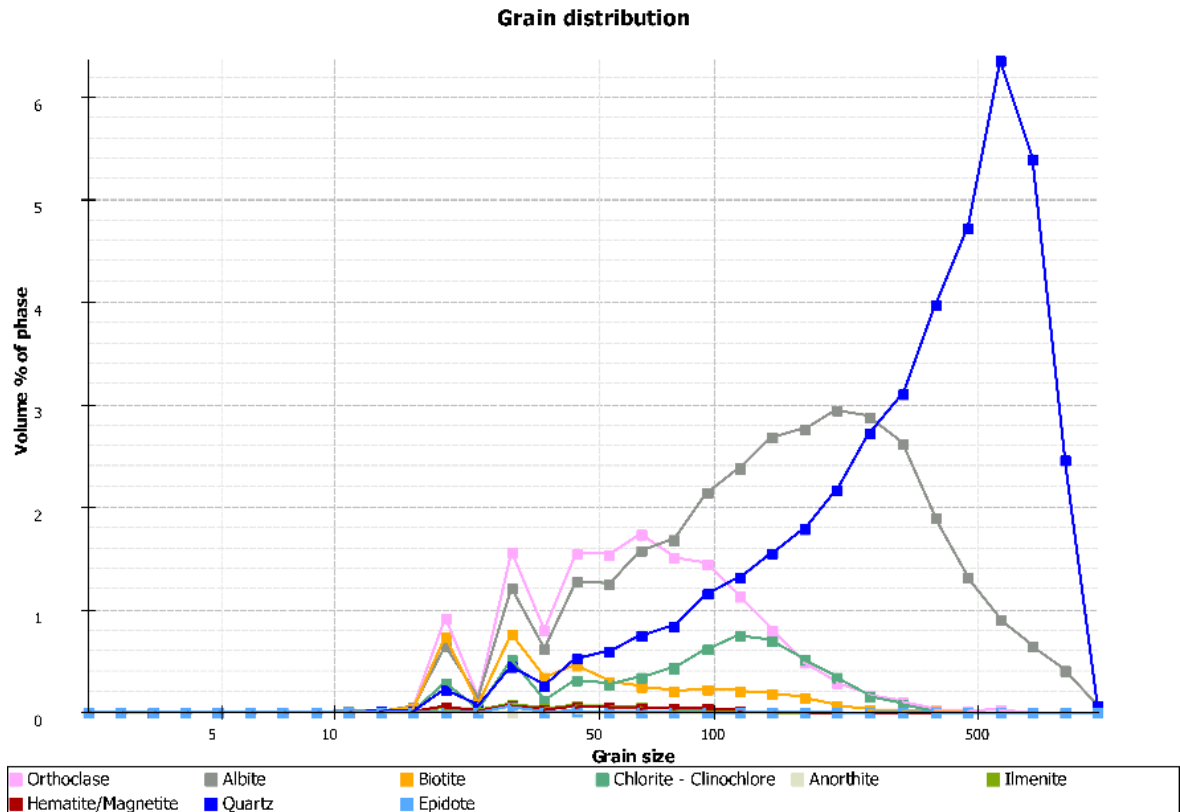


Figure C-24: Grain size distribution of granophyre sample rock AQ06_GPH

C-2-5 Sample rock AQ08_GPH



Figure C-25: Panorama image of granophyre sample rock AQ08_GPH

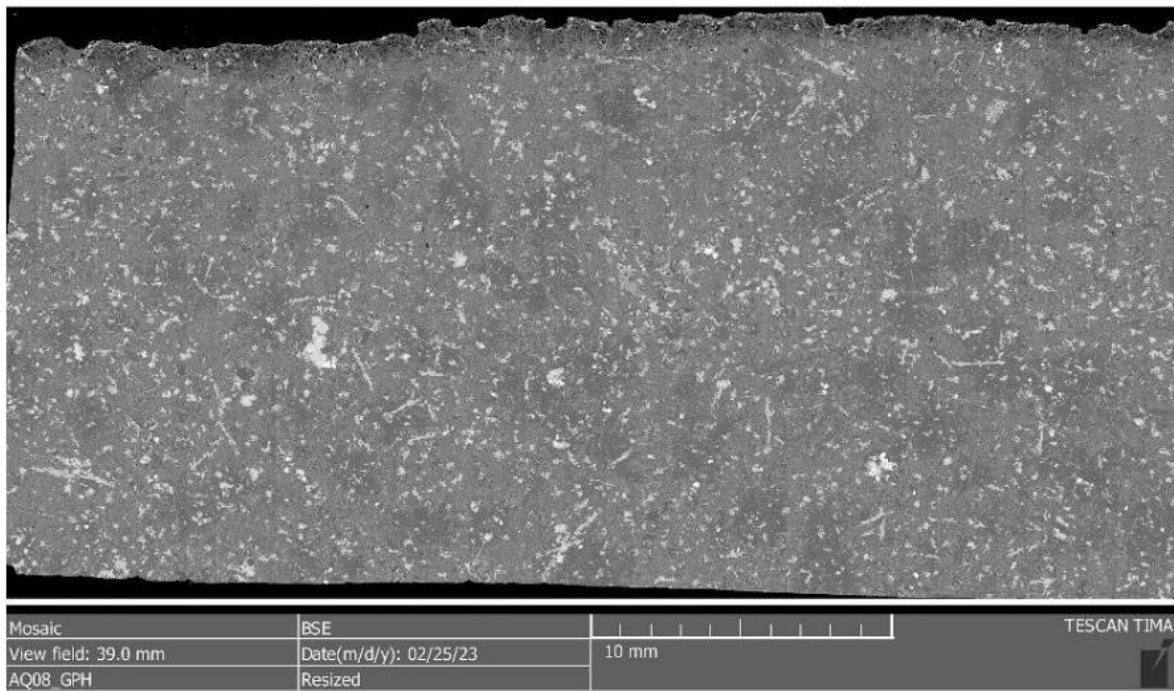


Figure C-26: BSE image of granophyre sample rock AQ08_GPH

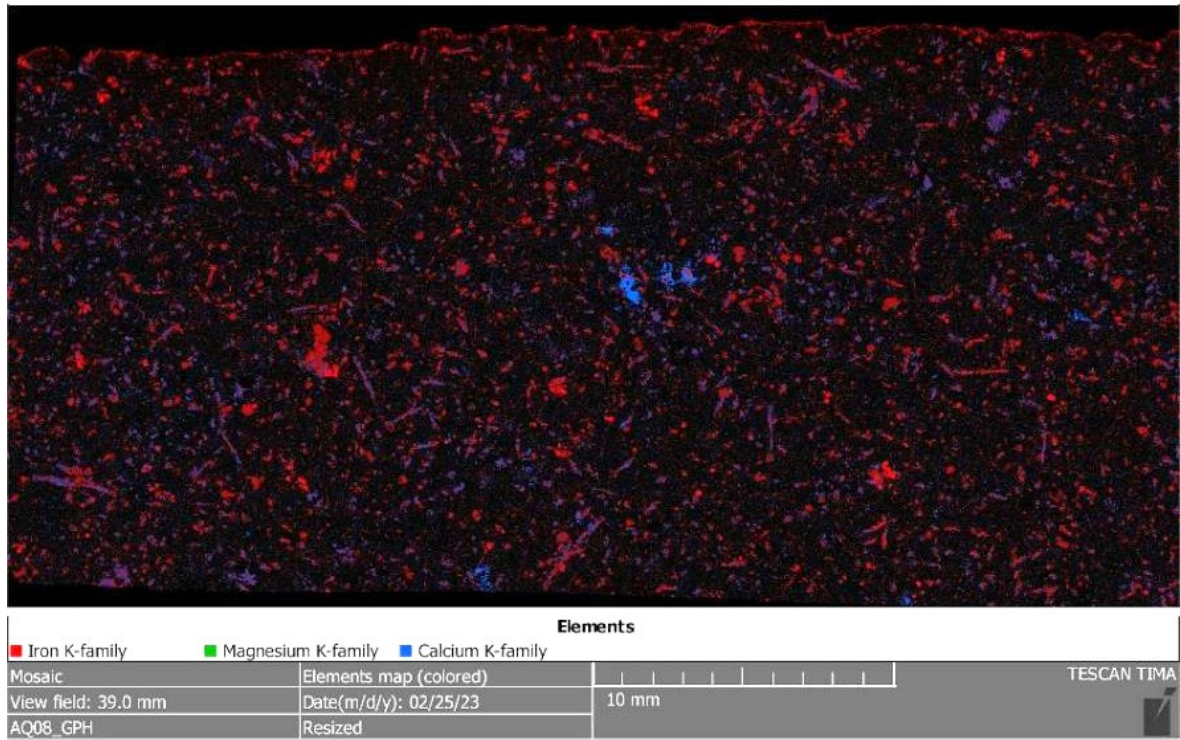


Figure C-29: Element map of granophyre sample rock AQ08_GPH

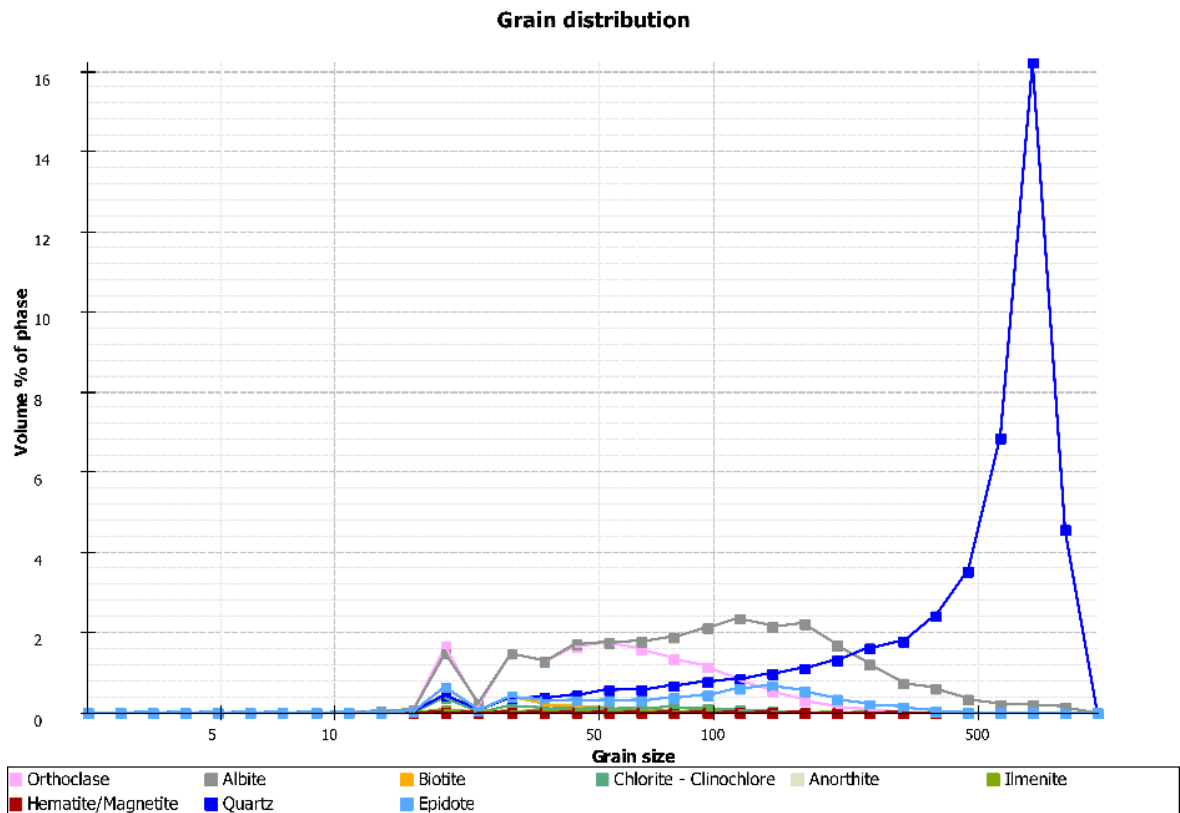


Figure C-30: Grain size distribution of granophyre sample rock AQ08_GPH

C-2-6 Sample rock AQ09_GPH



Figure C-31: Panorama image of granophyre sample rock AQ09_GPH

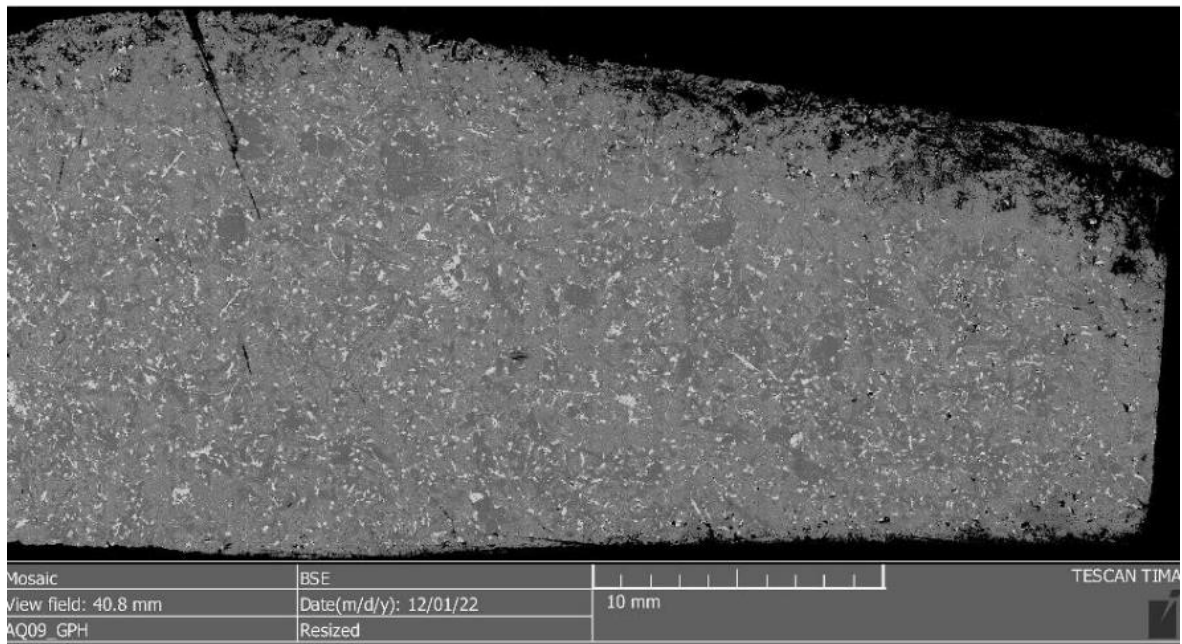


Figure C-32: BSE image of granophyre sample rock AQ09_GPH

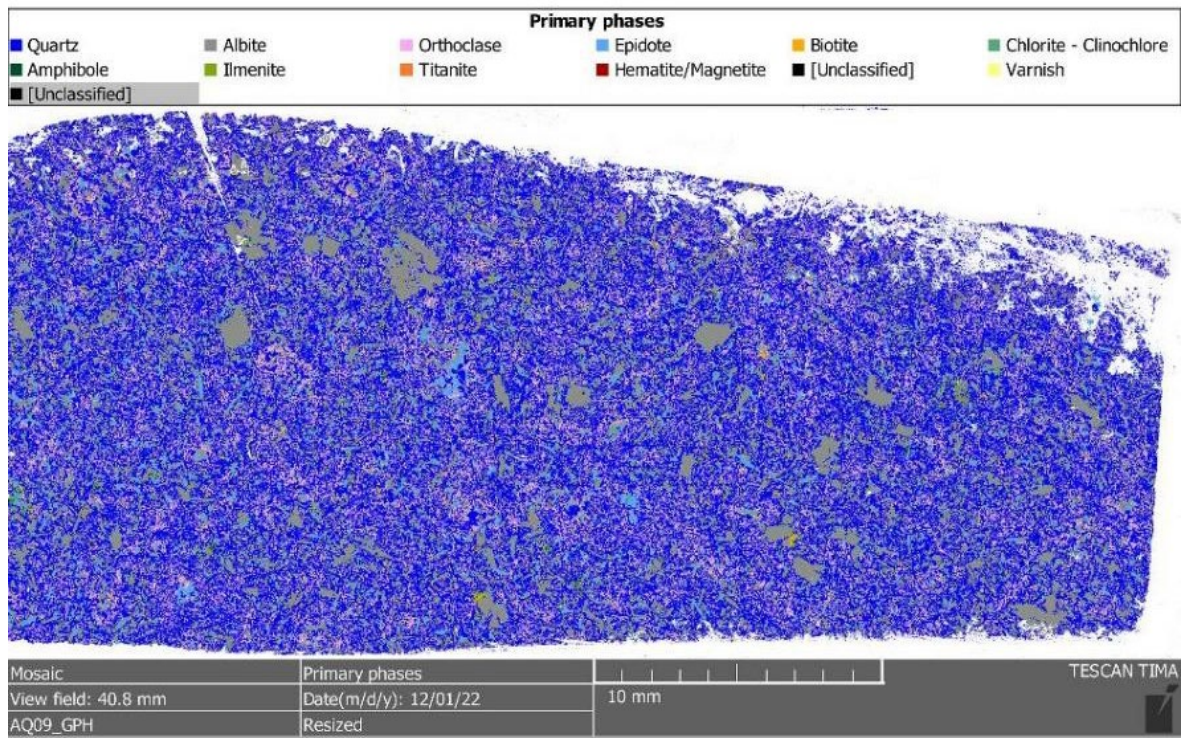


Figure C-33: Phase map of granophyre sample rock AQ09_GPH

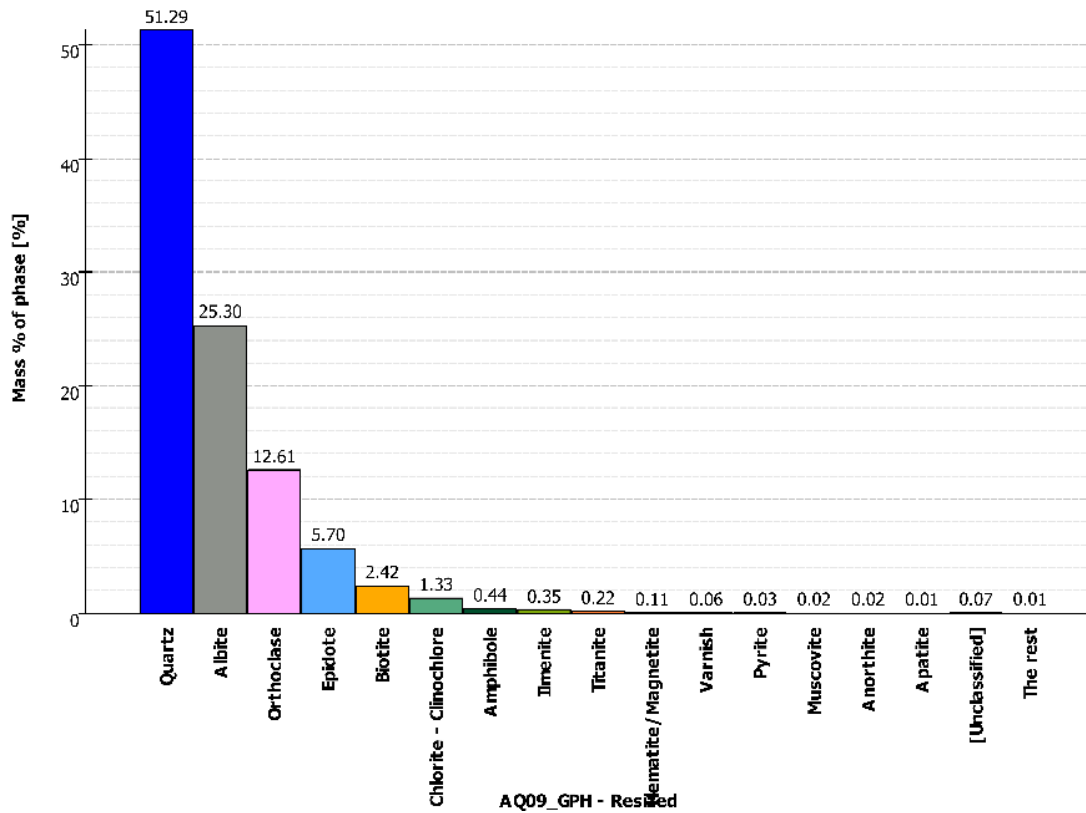


Figure C-34: Modal analysis of granophyre sample rock AQ09_GPH

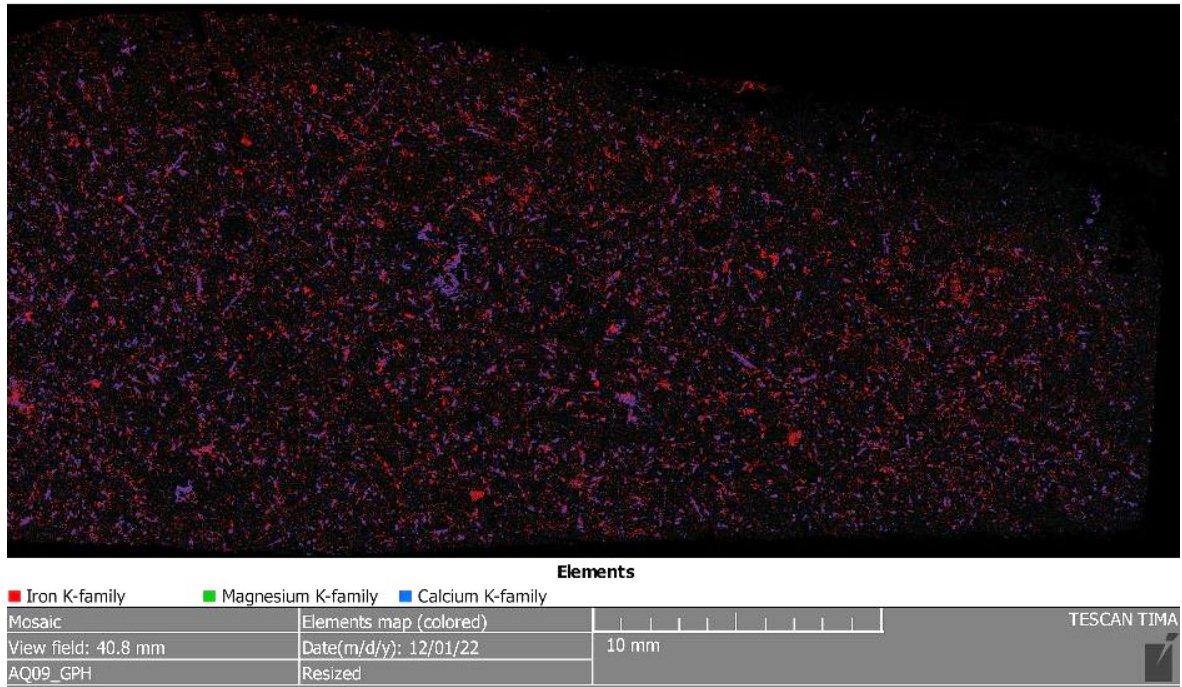


Figure C-35: Element map of granophyre sample rock AQ09_GPH

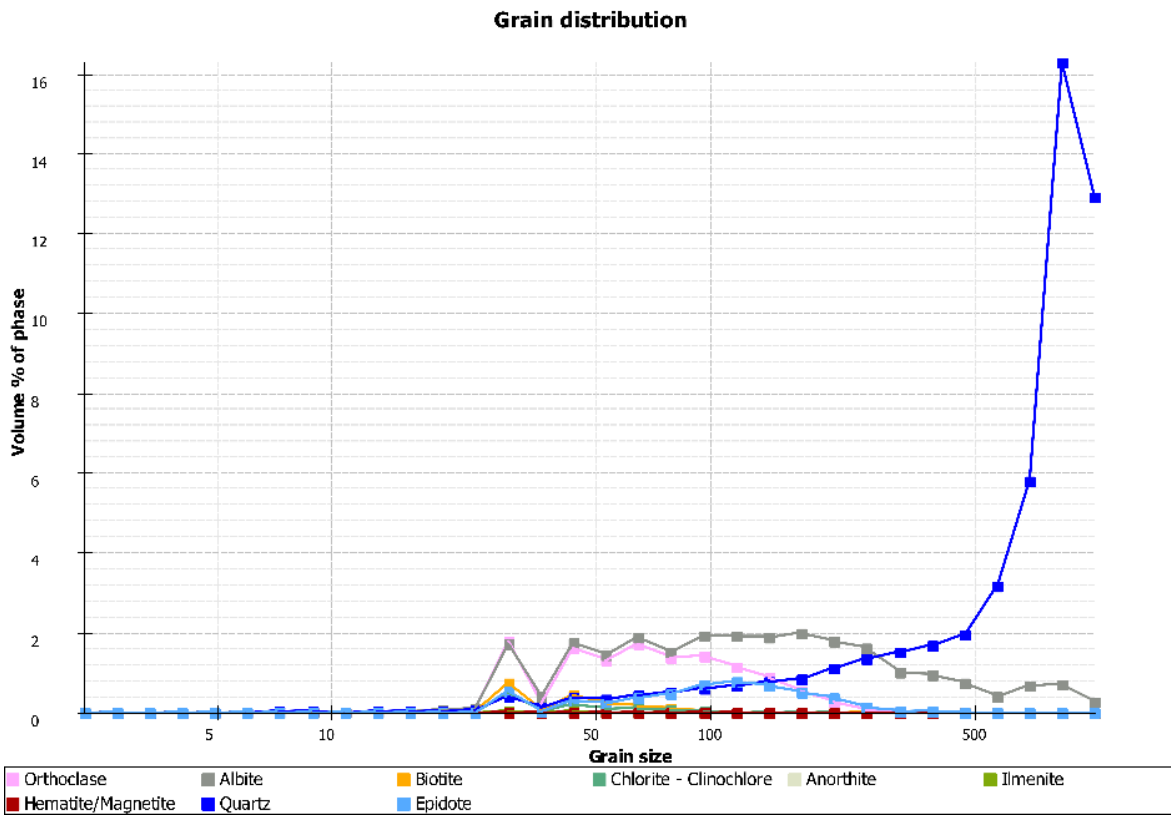


Figure C-36: Grain size distribution of granophyre sample rock AQ09_GPH

C-2-7 Sample rock AQ13_GPH



Figure C-37: Panorama image of granophyre sample rock AQ13_GPH

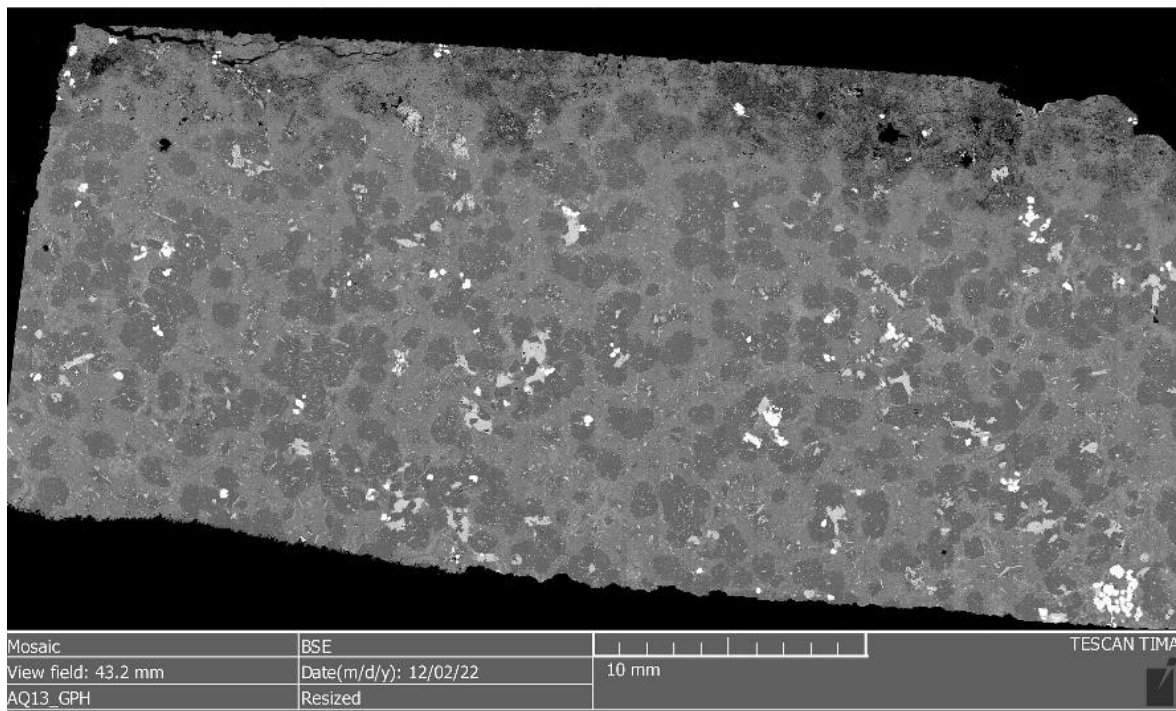


Figure C-38: BSE image of granophyre sample rock AQ13_GPH

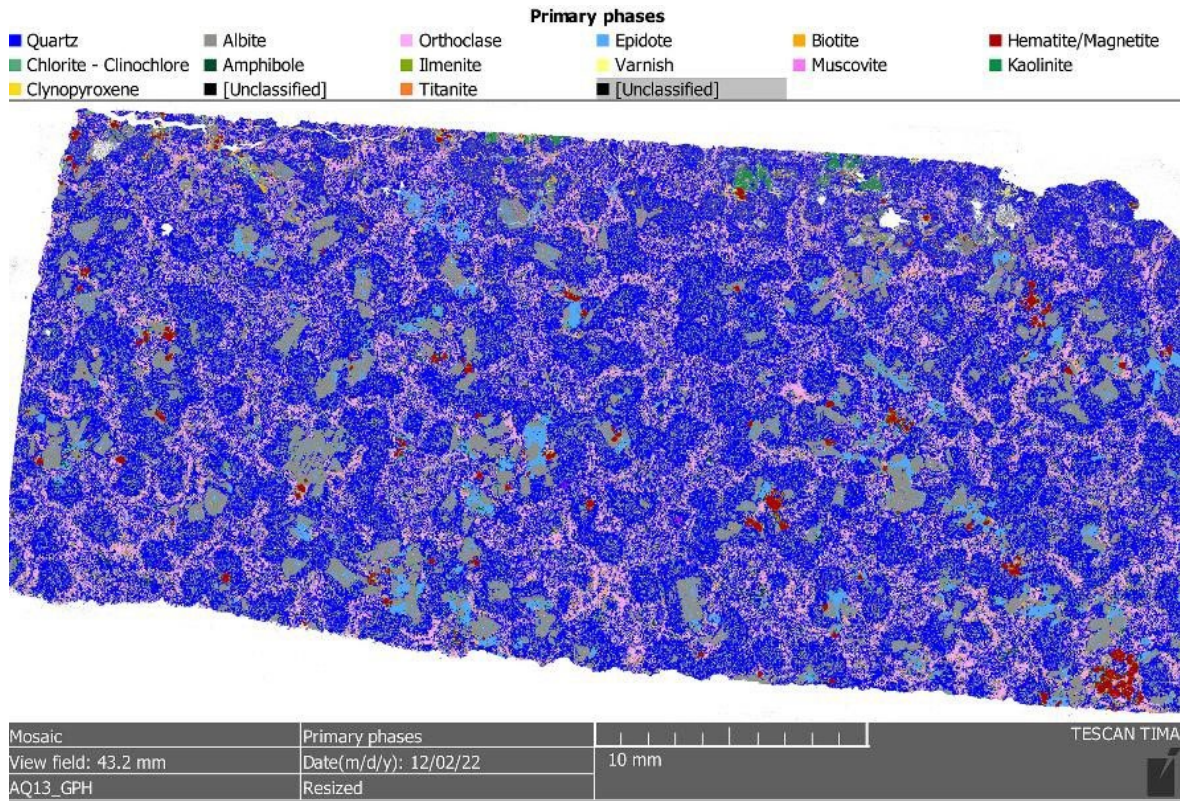


Figure C-39: Phase map of granophyre sample rock AQ13_GPH

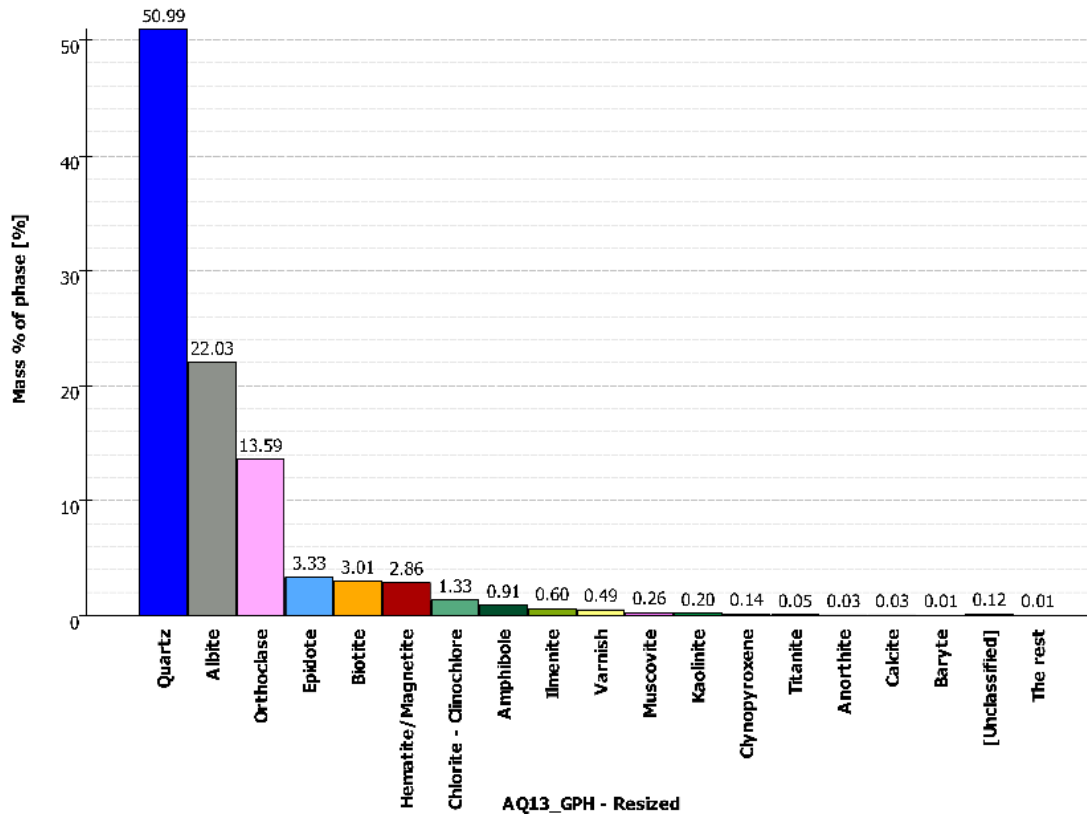


Figure C-40: Modal analysis of granophyre sample rock AQ13_GPH

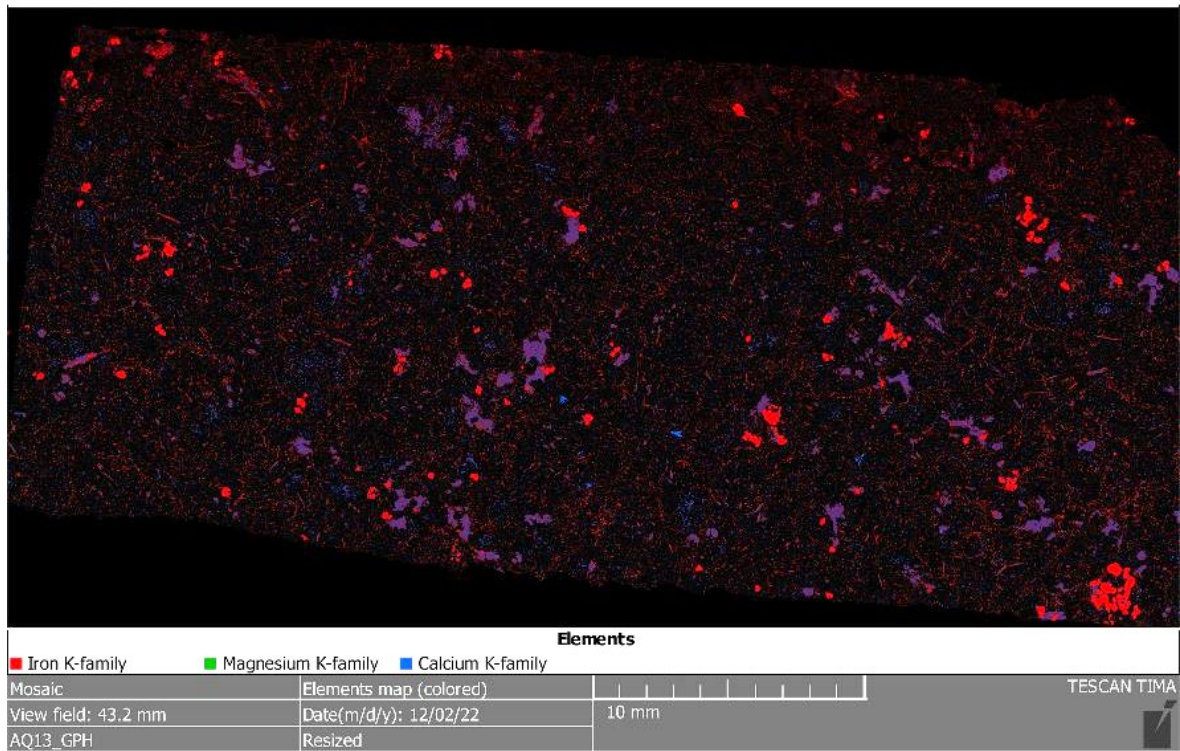


Figure C-41: Element map of granophyre sample rock AQ13_GPH

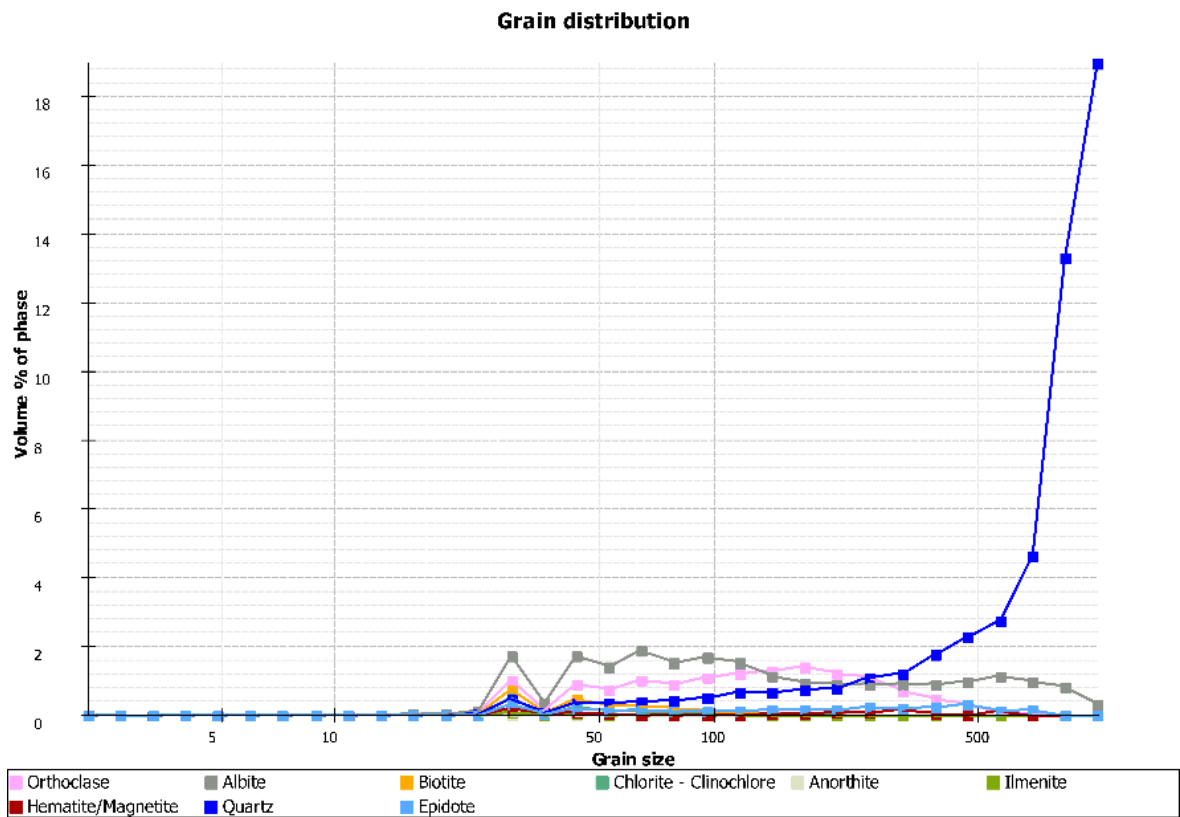


Figure C-42: Grain size distribution of granophyre sample rock AQ13_GPH

C-2-8 Sample rock AQ14_GPH



Figure C-43: Panorama image of granophyre sample rock AQ14_GPH

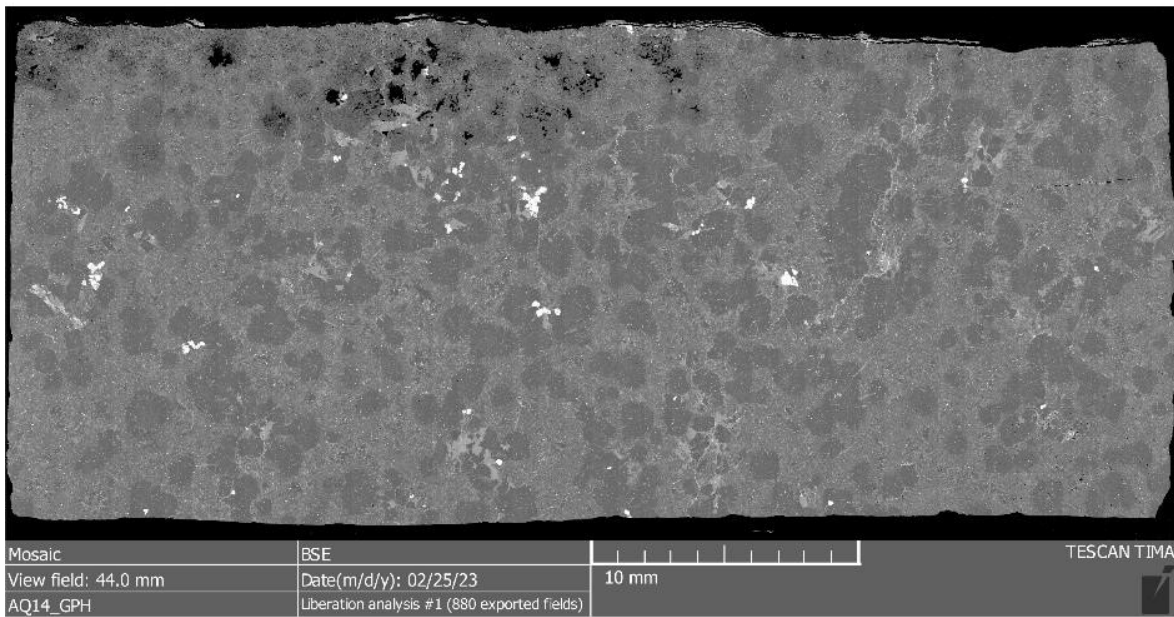


Figure C-44: BSE image of granophyre sample rock AQ14_GPH

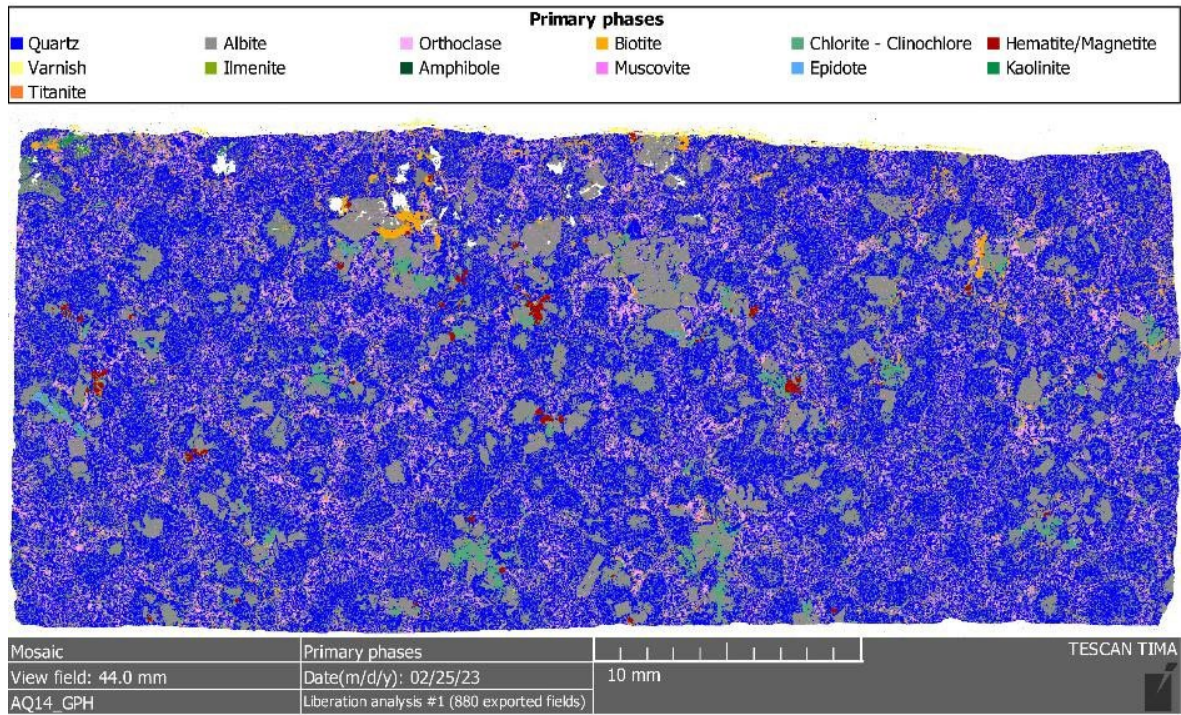


Figure C-45: Phase map of granophyre sample rock AQ14_GPH

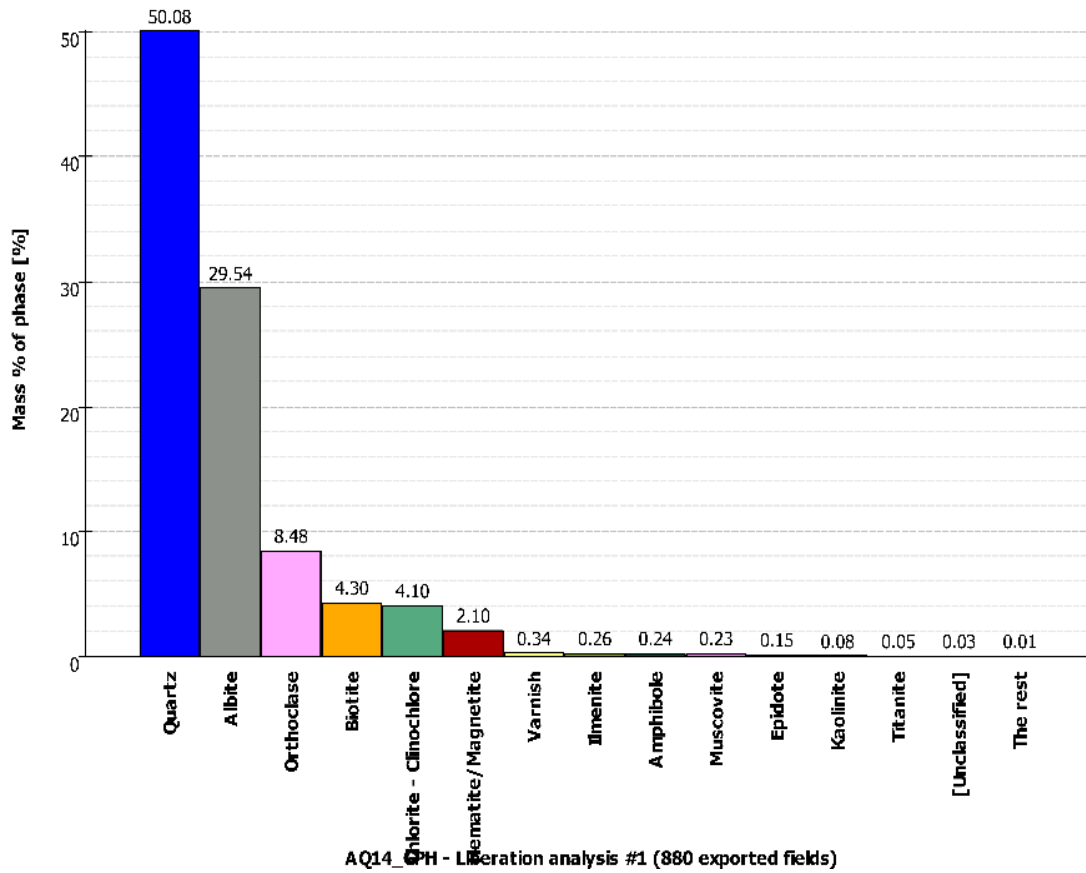


Figure C-46: Modal analysis of granophyre sample rock AQ14_GPH

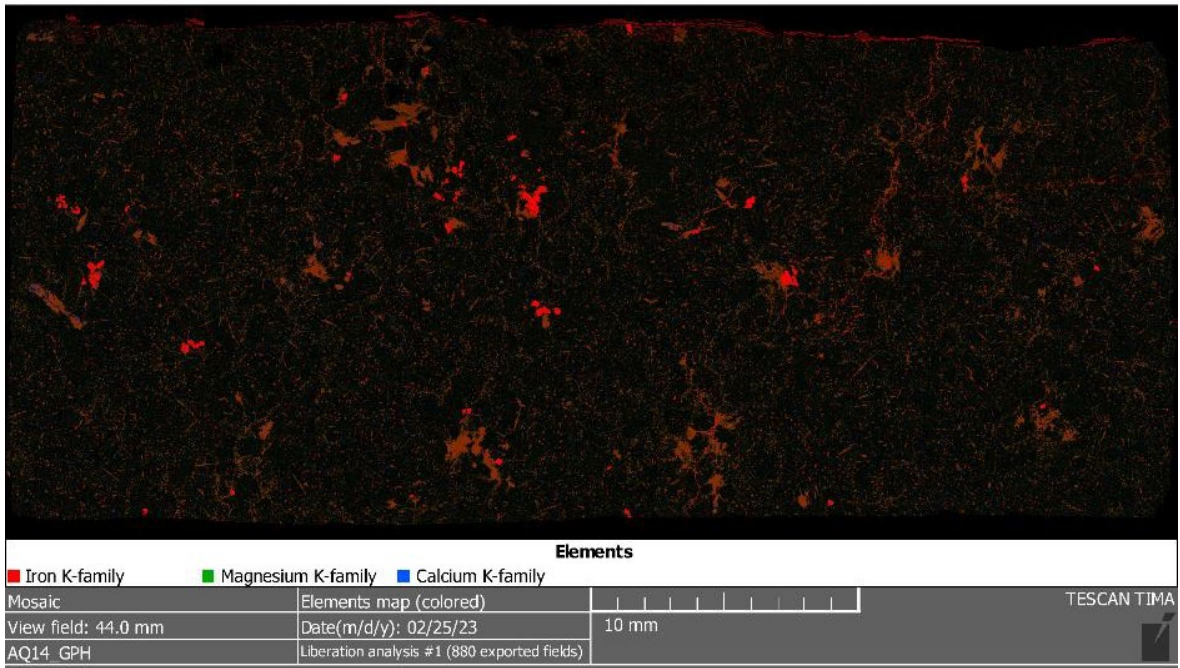


Figure C-47: Element map of granophyre sample rock AQ14_GPH

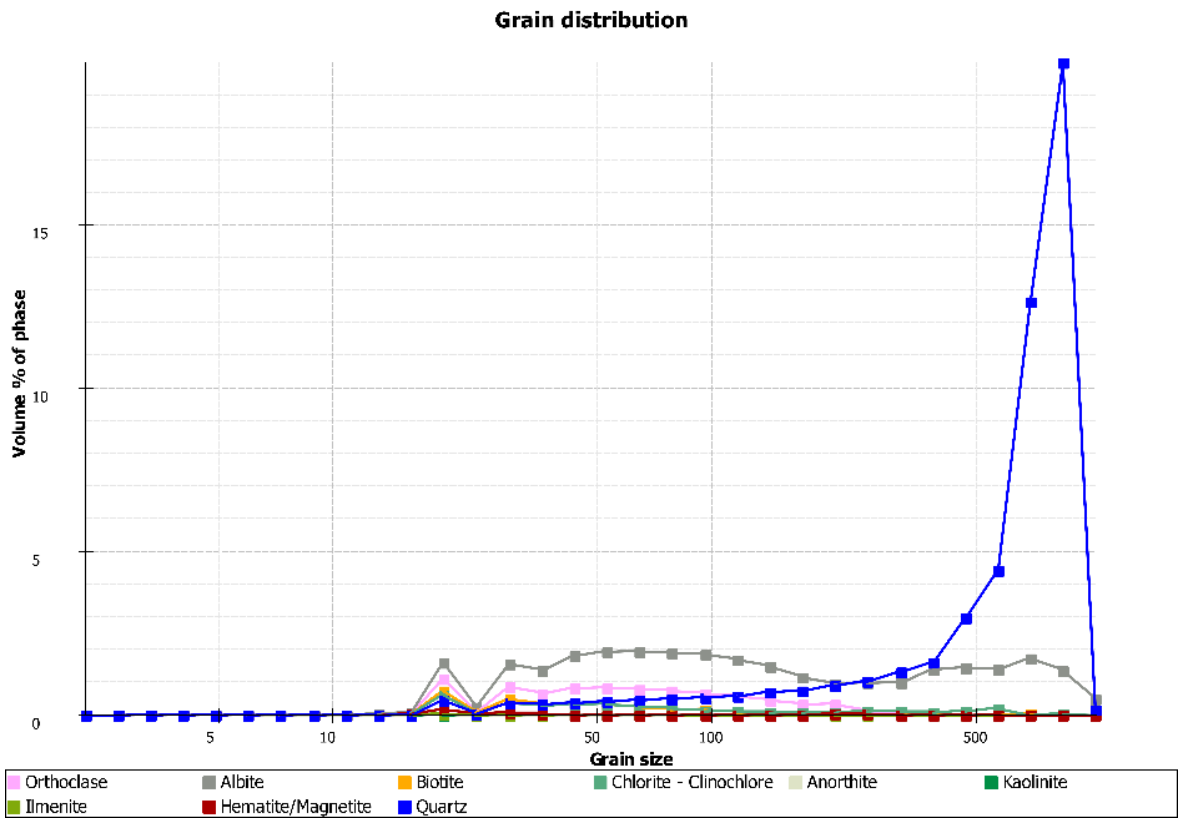


Figure C-48: Grain size distribution of granophyre sample rock AQ14_GPH

C-2-9 Sample rock EX02_GPH



Figure C-49: Panorama image of granophyre sample rock EX02_GPH

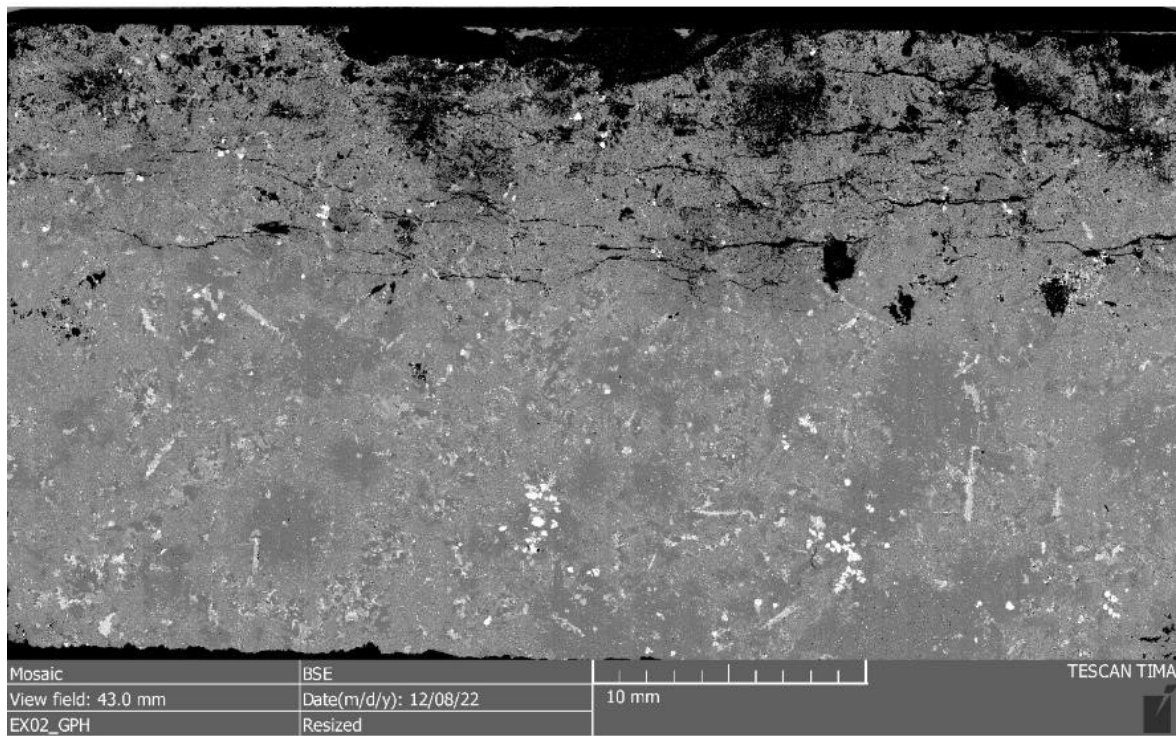


Figure C-50: BSE image of granophyre sample rock EX02_GPH

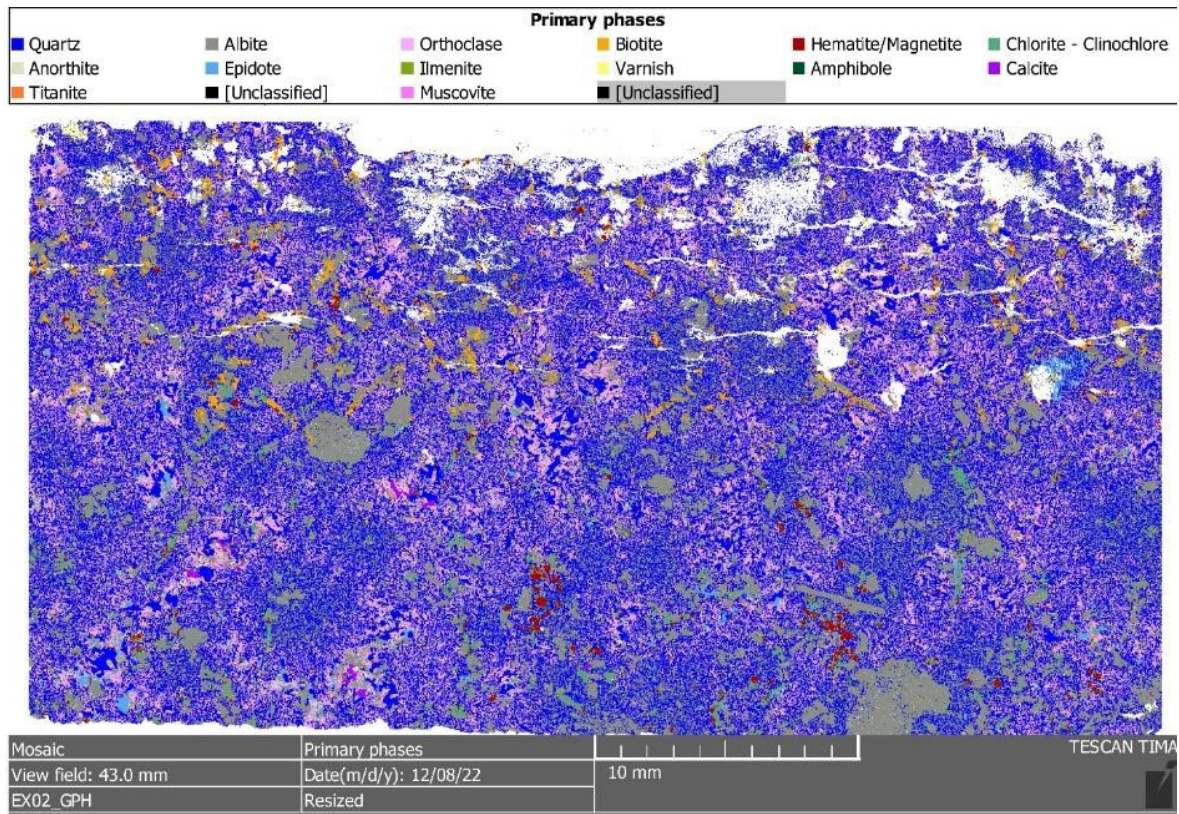


Figure C-51: Phase map of granophyre sample rock EX02_GPH

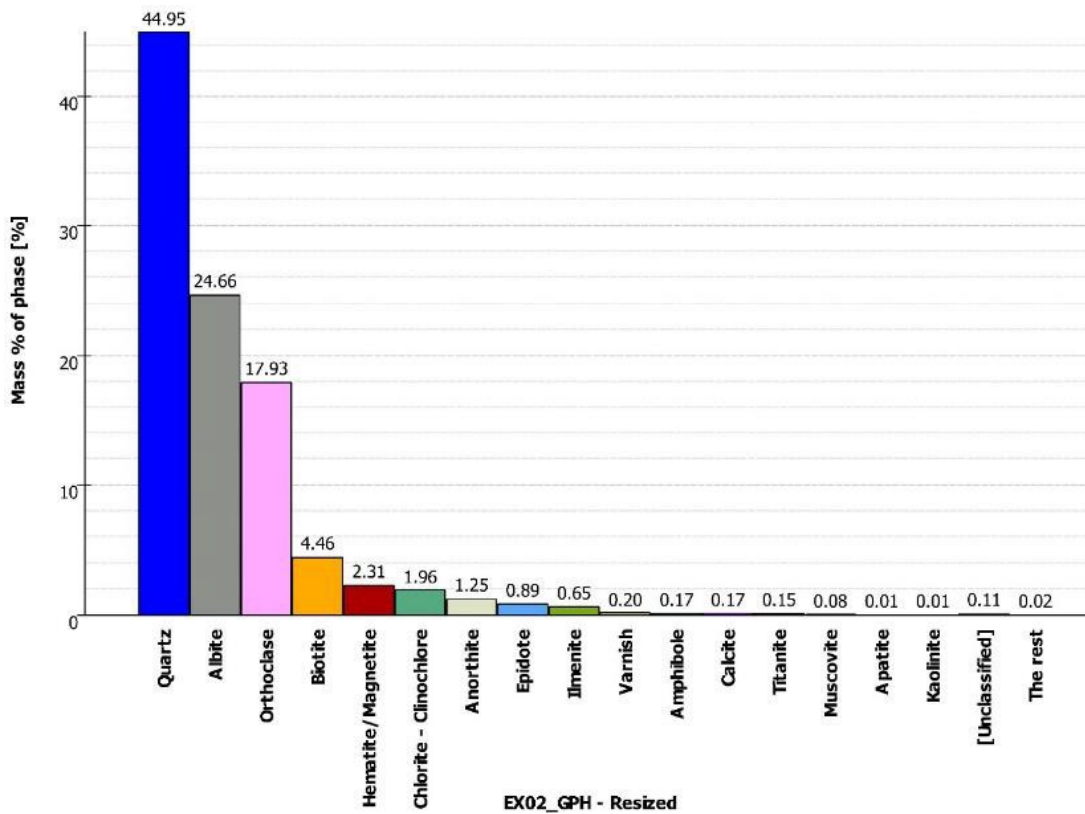


Figure C-52: Modal analysis of granophyre sample rock EX02_GPH

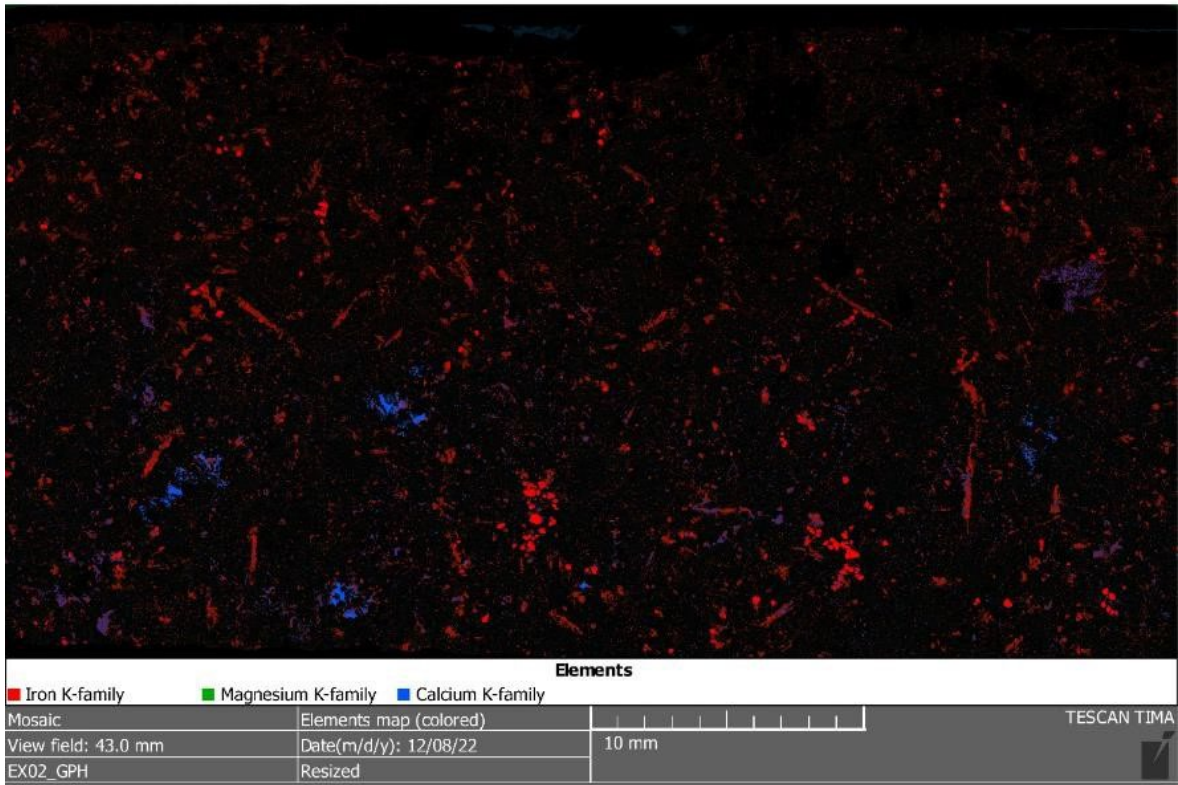


Figure C-53: Element map of granophyre sample rock EX02_GPH

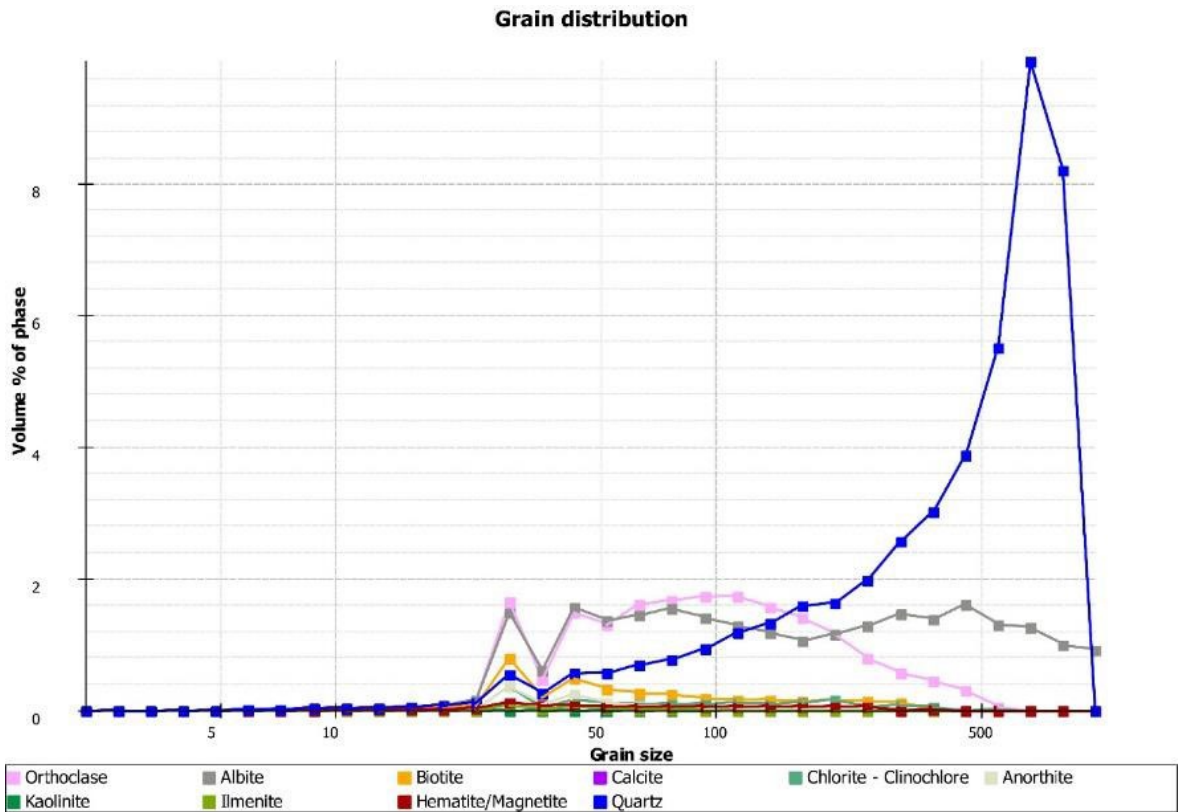


Figure C-54: Grain size distribution of granophyre sample rock EX02_GPH

C-2-10 Sample rock EX03_GPH



Figure C-55: Panorama image of granophyre sample rock EX03_GPH

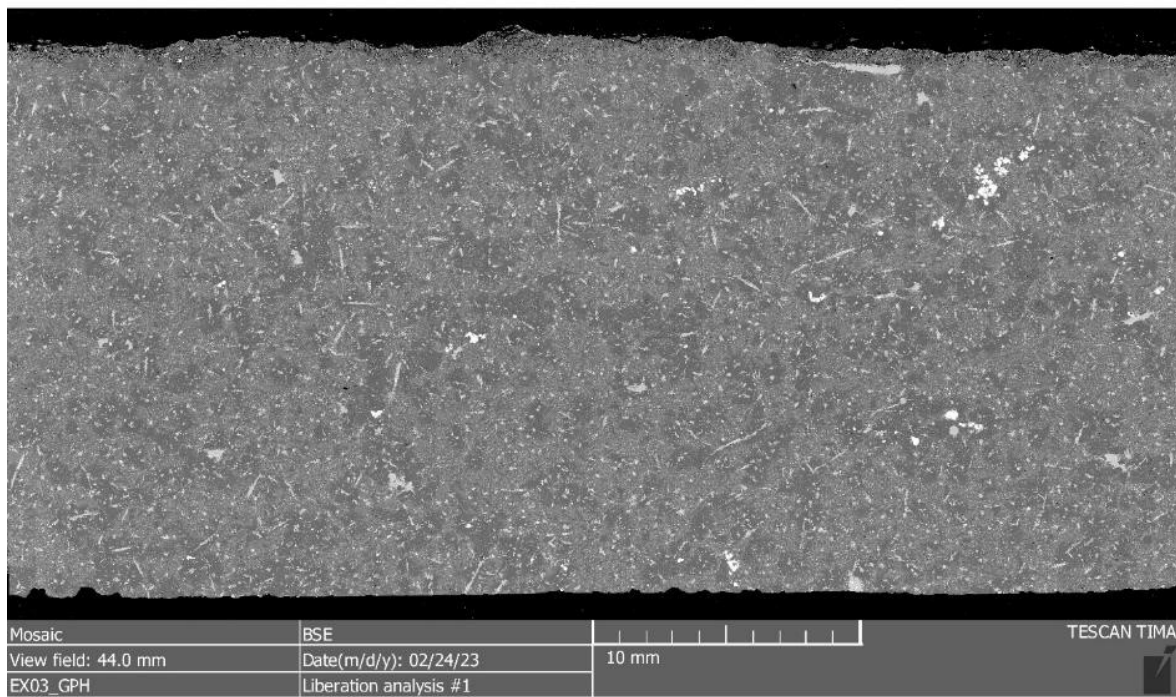


Figure C-56: BSE image of granophyre sample rock EX03_GPH

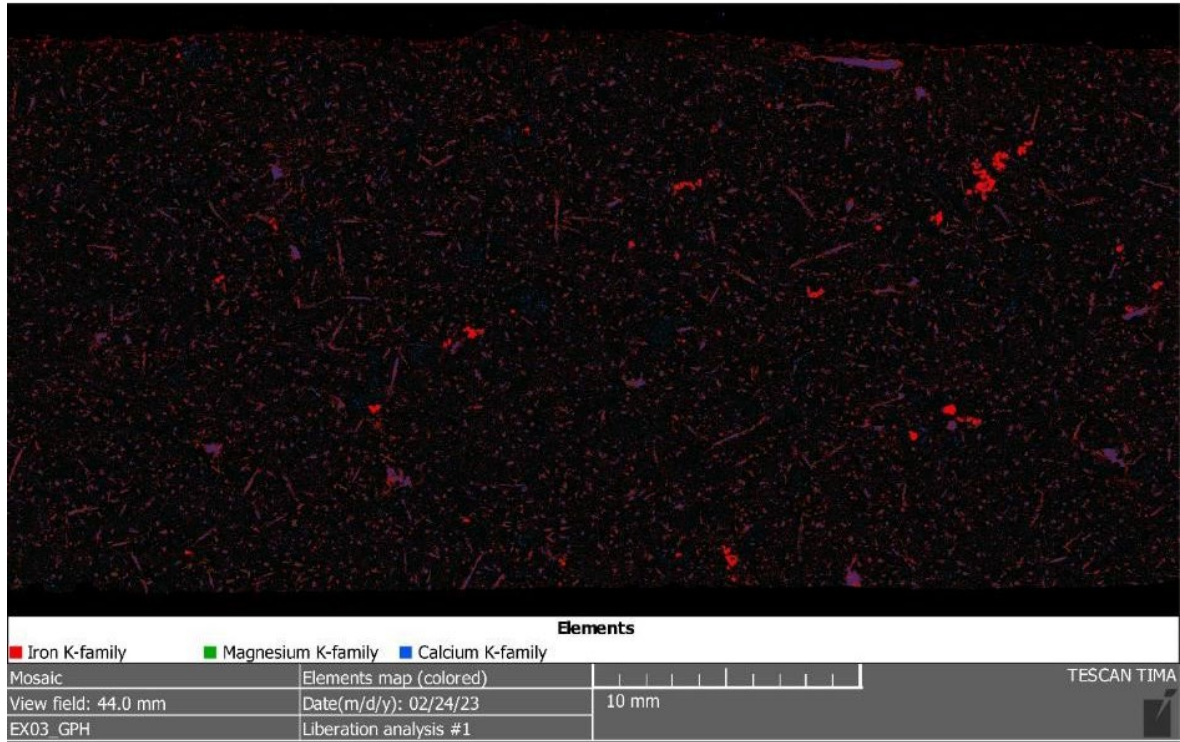


Figure C-59: Element map of granophyre sample rock EX03_GPH

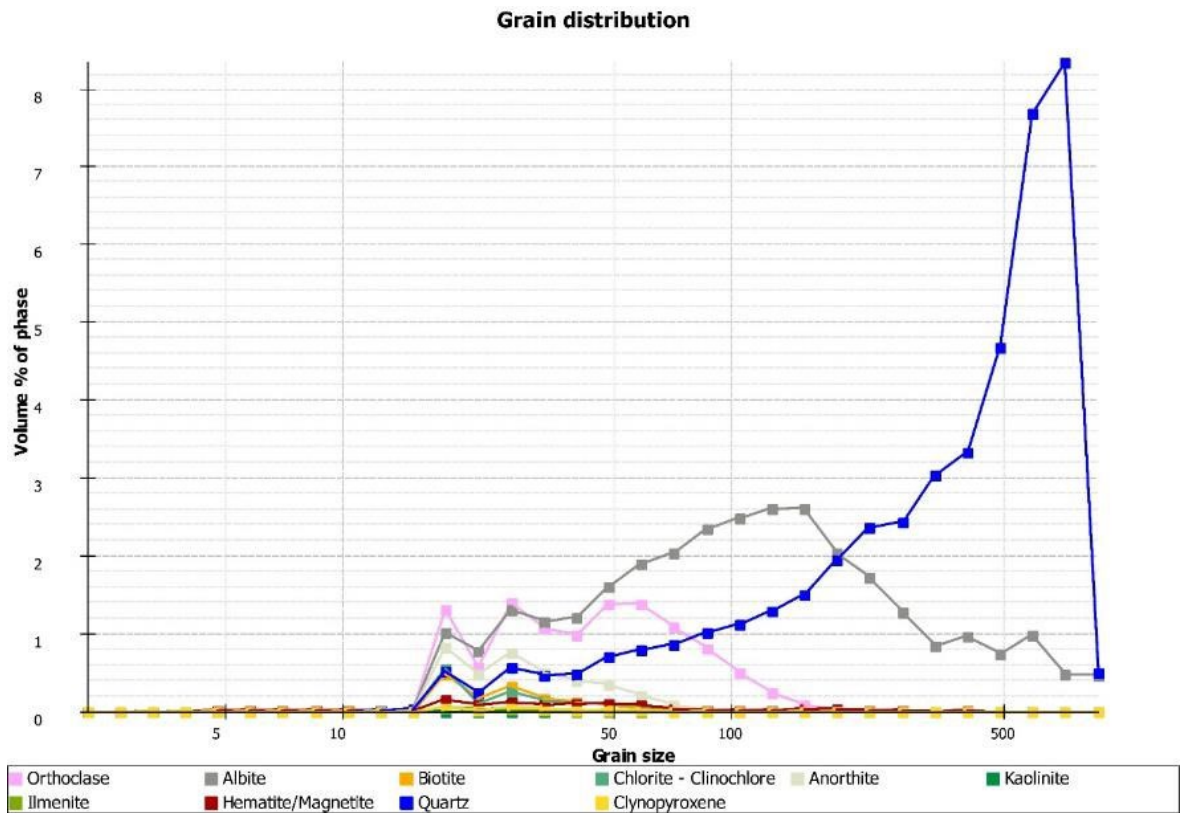


Figure C-60: Grain size distribution of granophyre sample rock EX03_GPH

C-2-11 Sample rock EX05_GPH



Figure C-61: Panorama image of granophyre sample rock EX05_GPH

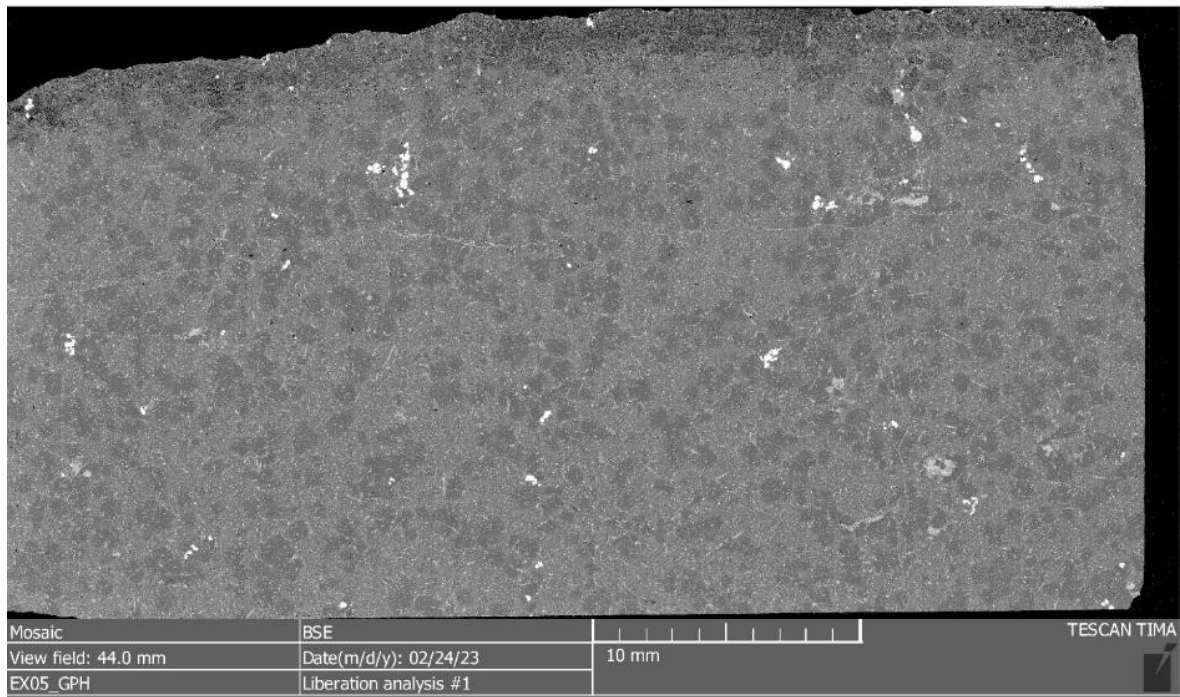


Figure C-62: BSE image of granophyre sample rock EX05_GPH

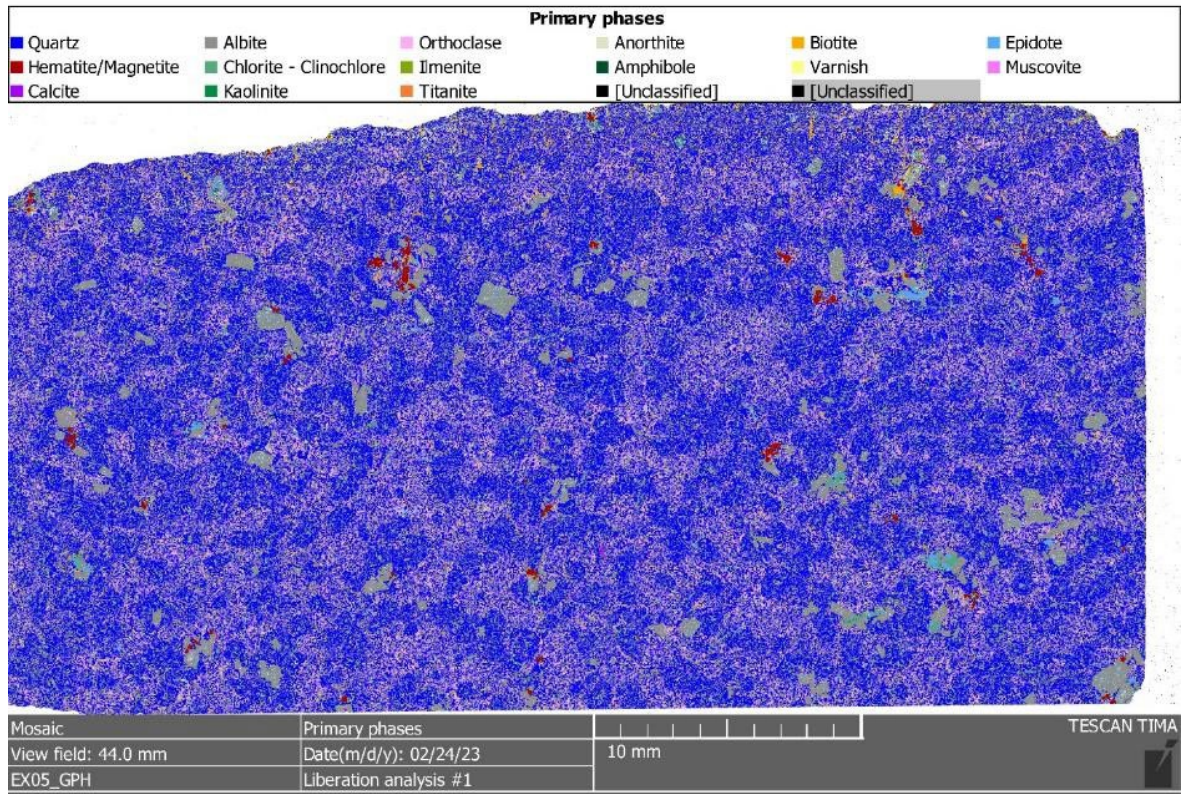


Figure C-63: Phase map of granophyre sample rock EX05_GPH

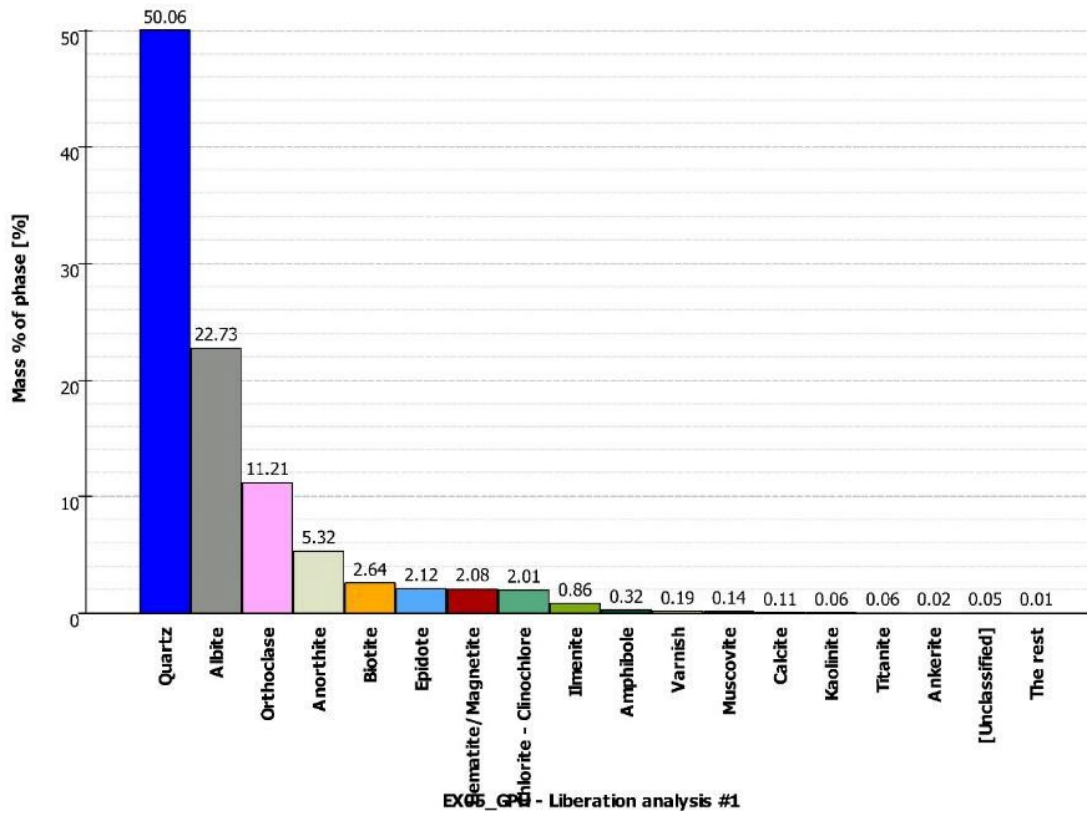


Figure C-64: Modal analysis of granophyre sample rock EX05_GPH

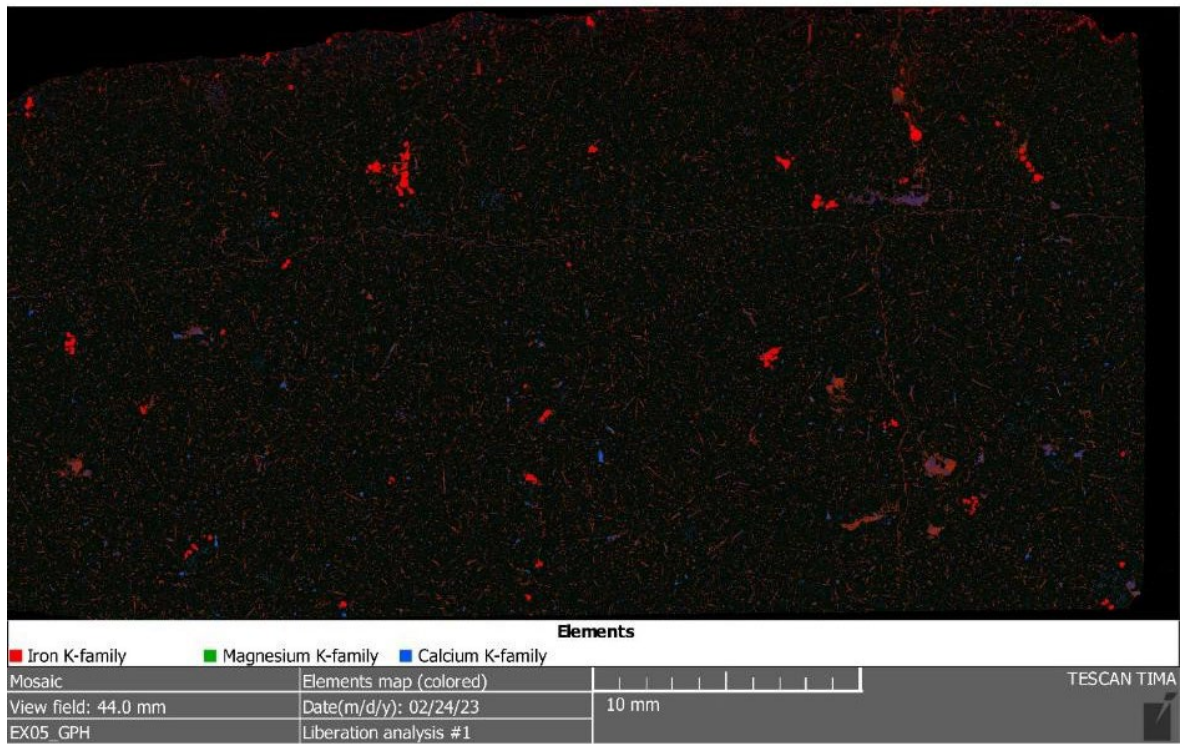


Figure C-65: Element map of granophyre sample rock EX05_GPH

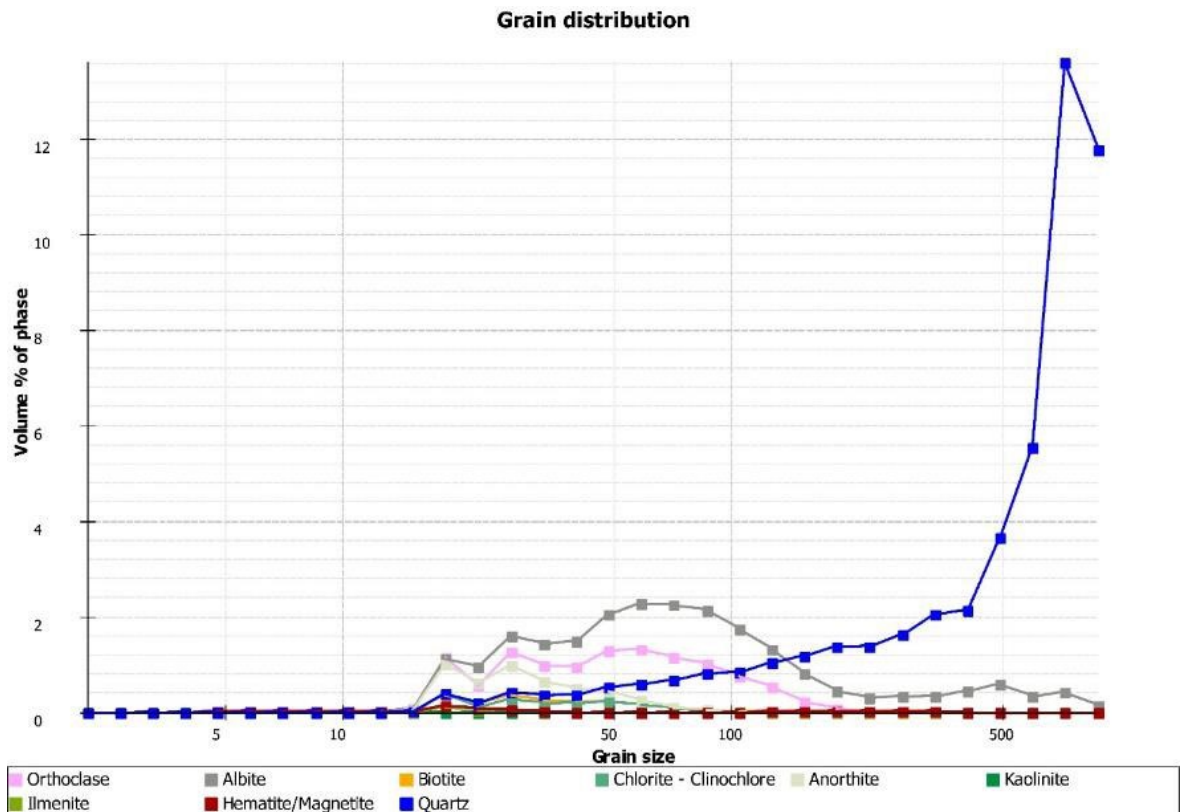


Figure C-66: Grain size distribution of granophyre sample rock EX05_GPH

C-2-12 Sample rock EX06_GPH



Figure C-67: Panorama image of granophyre sample rock EX06_GPH

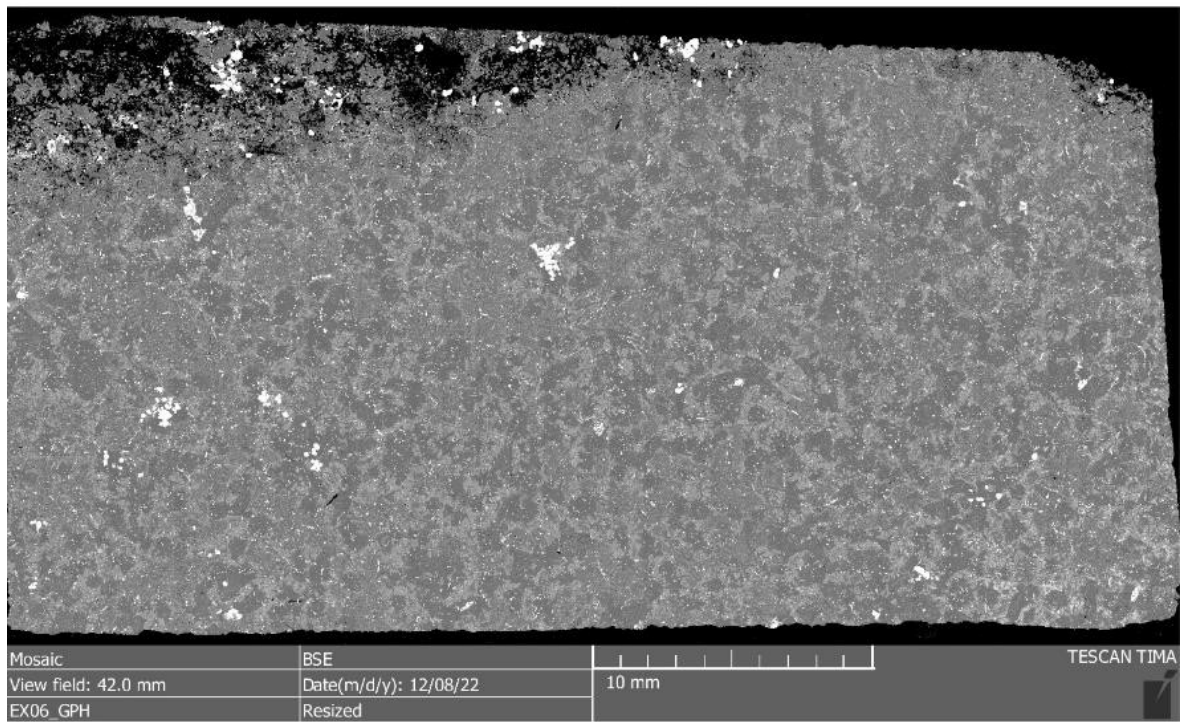


Figure C-68: BSE image of granophyre sample rock EX06_GPH

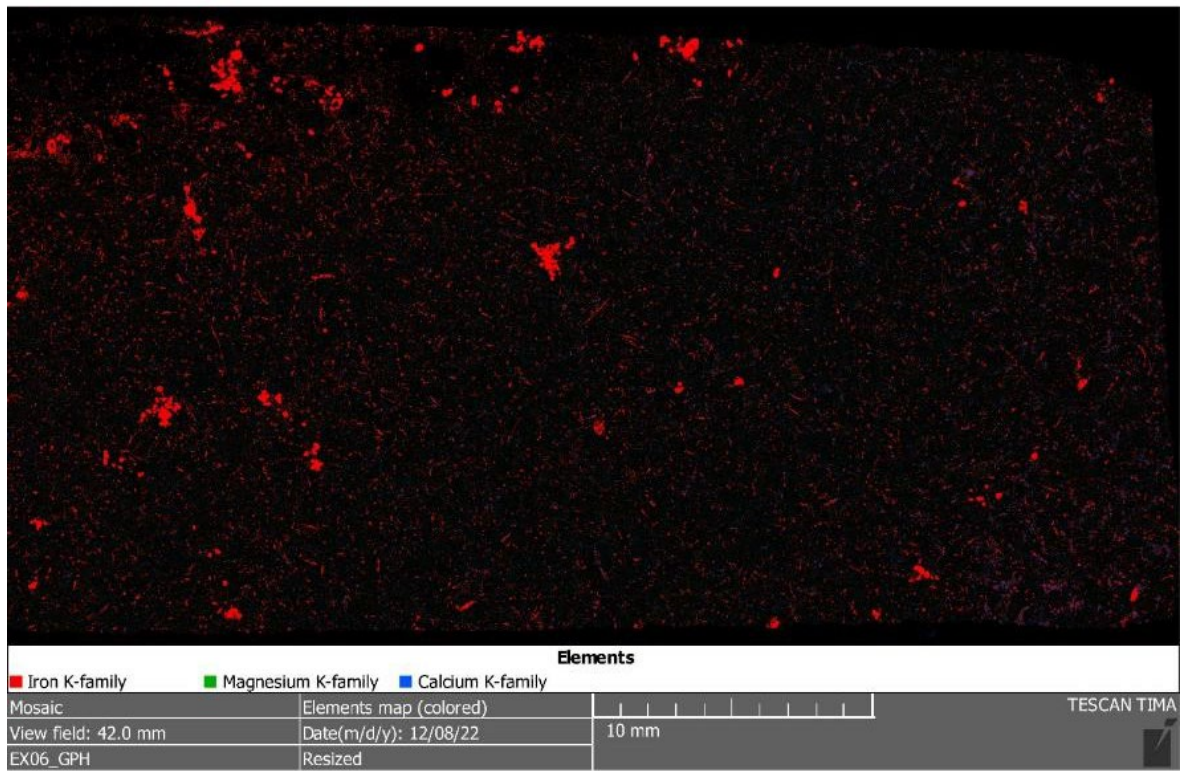


Figure C-71: Element map of granophyre sample rock EX06_GPH

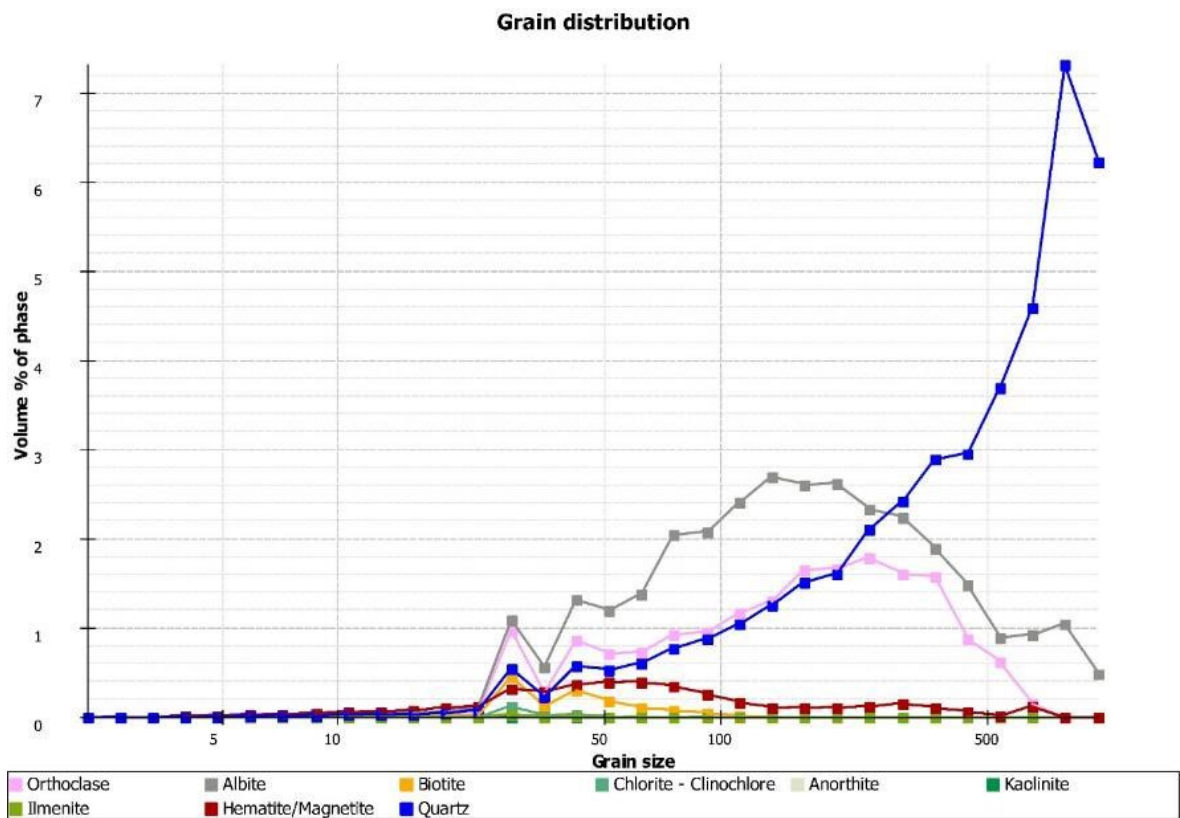


Figure C-72: Grain size distribution of granophyre sample rock EX06_GPH

c-2-13 Sample rock EX08_GPH



Figure C-73: Panorama image of granophyre sample rock EX08_GPH

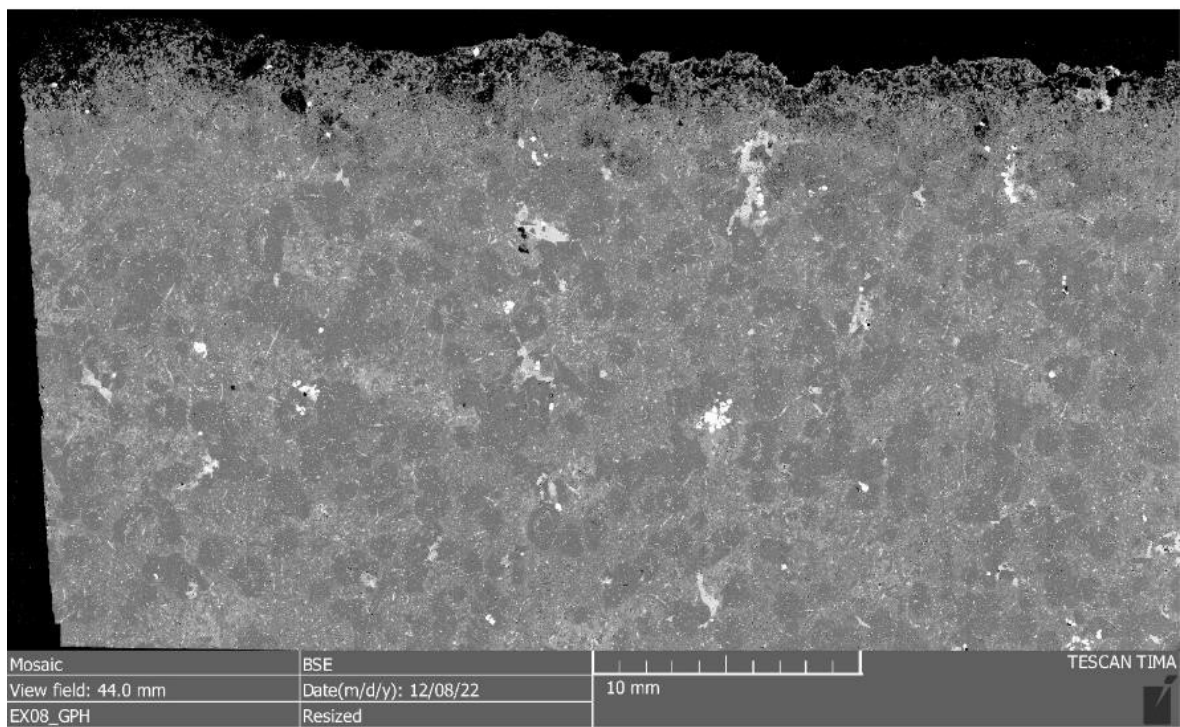


Figure C-74: BSE image of granophyre sample rock EX08_GPH

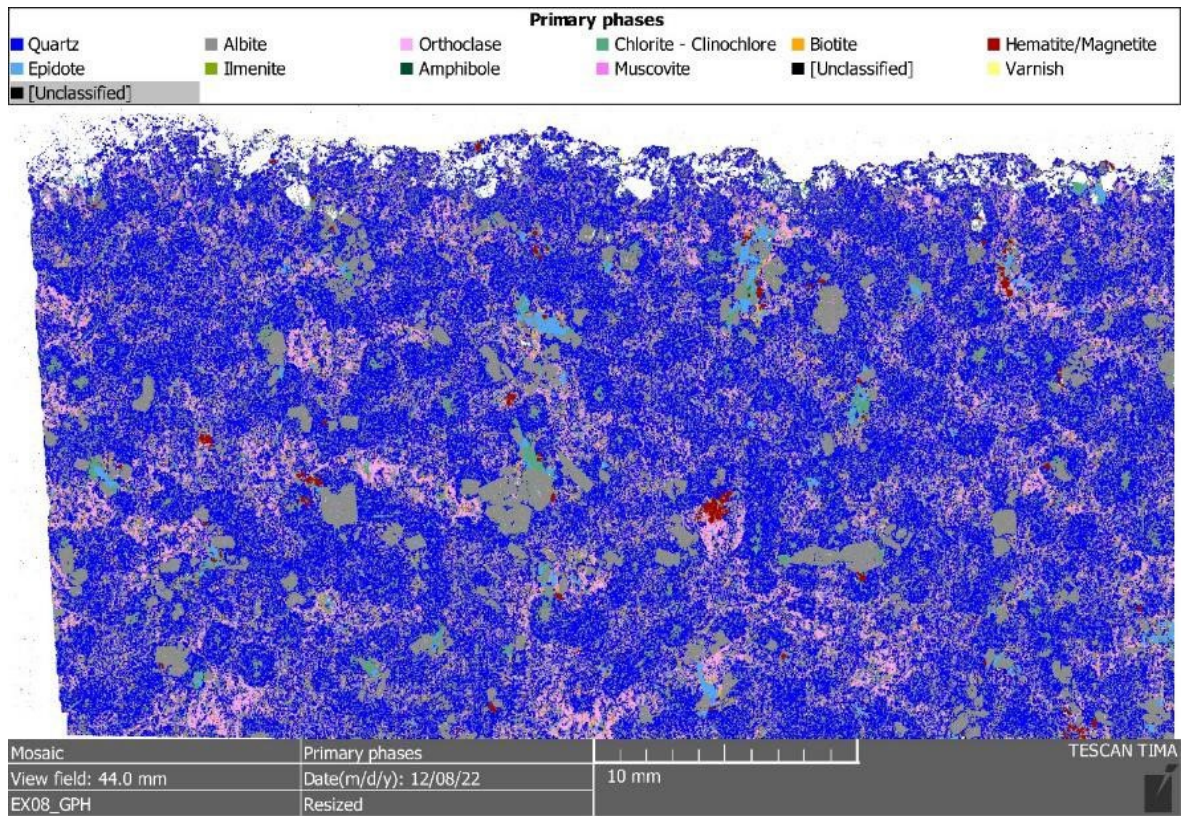


Figure C-75: Phase map of granophyre sample rock EX08_GPH

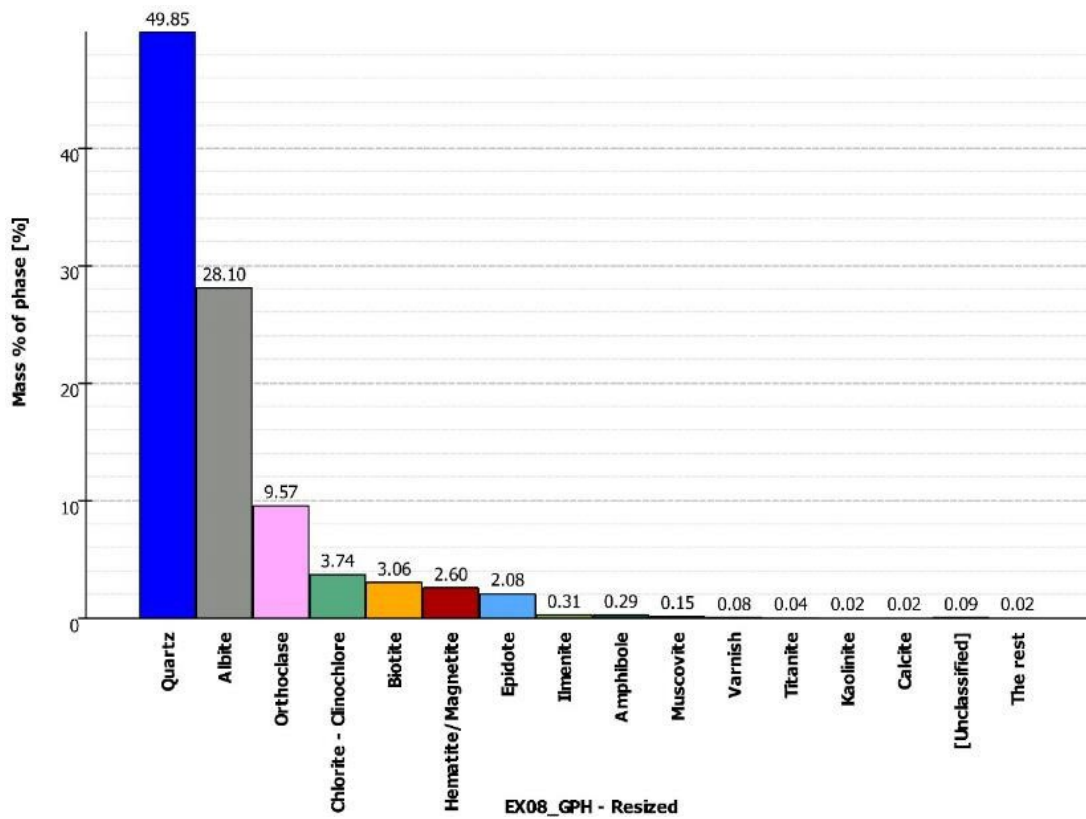


Figure C-76: Modal analysis of granophyre sample rock EX08_GPH

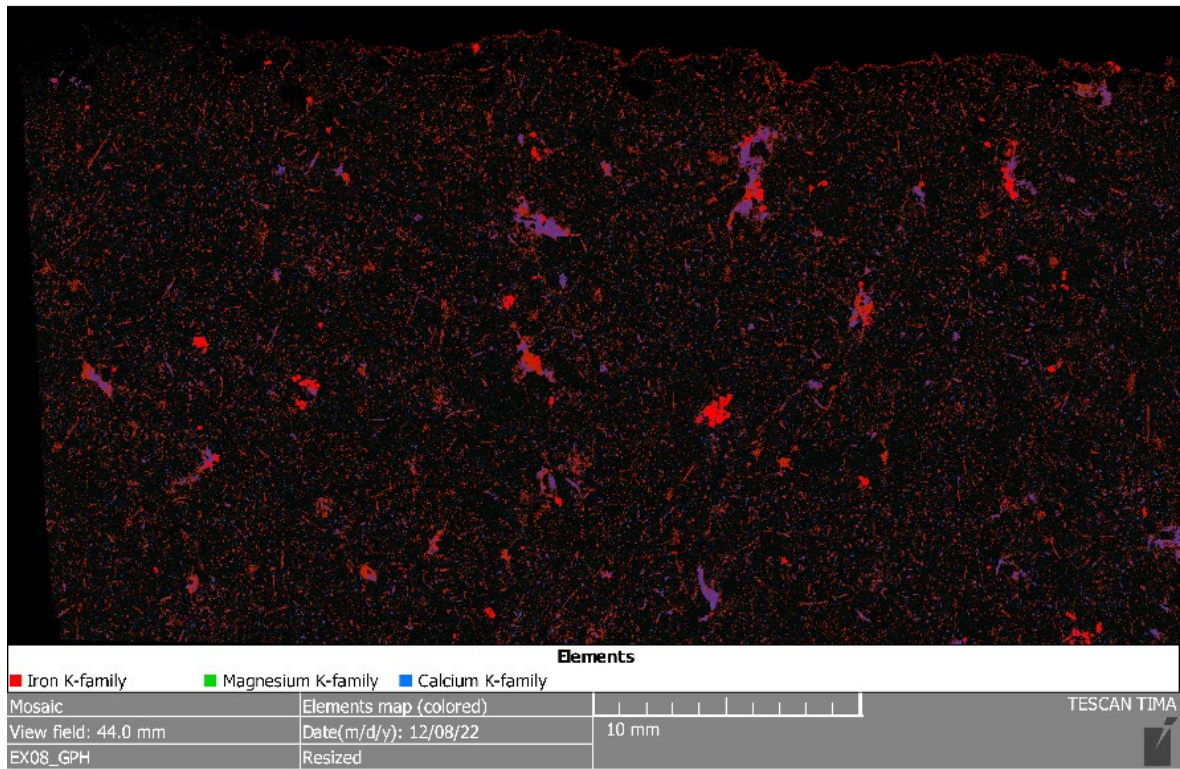


Figure C-77: Element map of granophyre sample rock EX08_GPH

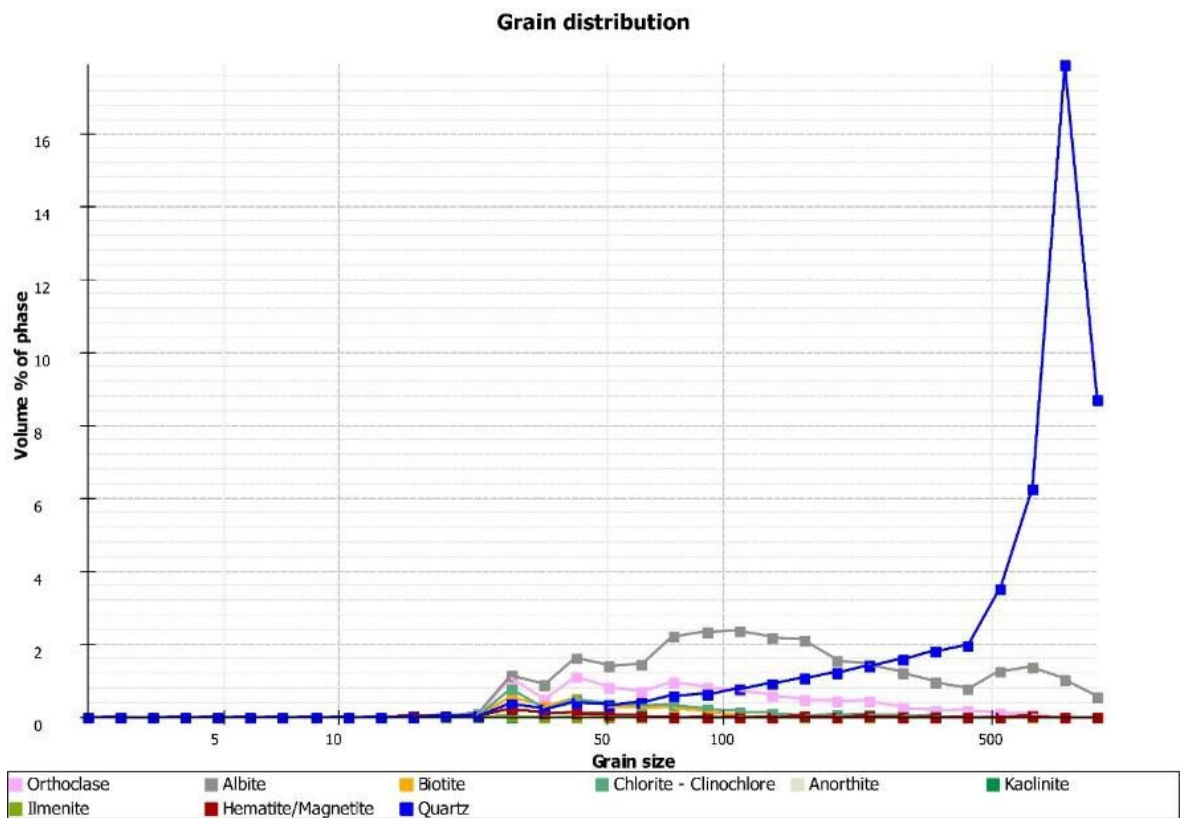


Figure C-78: Grain size distribution of granophyre sample rock EX08_GPH

C-2-14 Sample rock EX09_GPH



Figure C-79: Panorama image of granophyre sample rock EX09_GPH

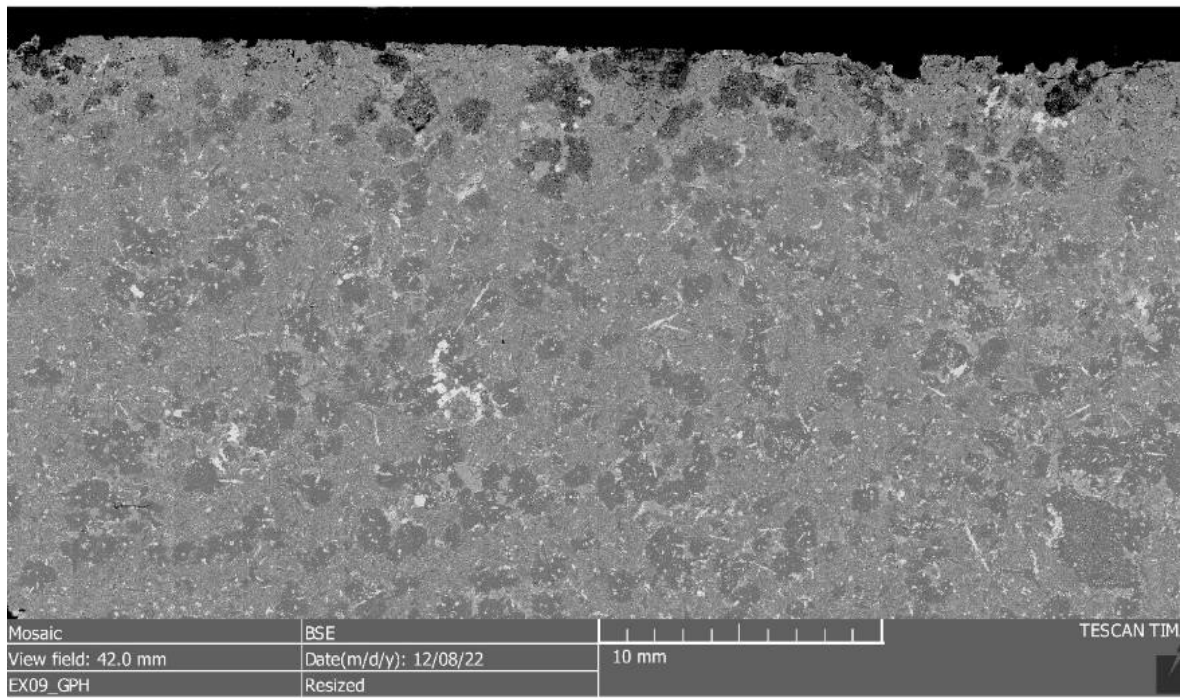


Figure C-80: BSE image of granophyre sample rock EX02_GPH

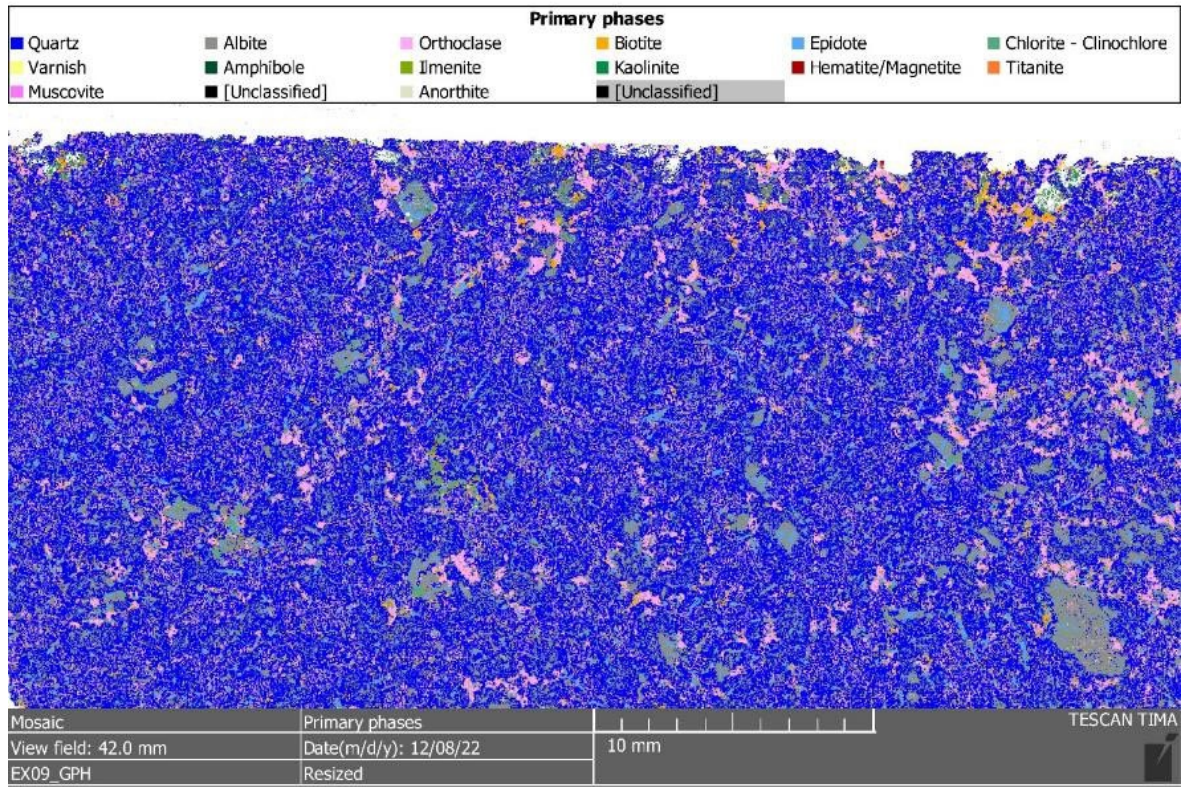


Figure C-81: Phase map of granophyre sample rock EX09_GPH

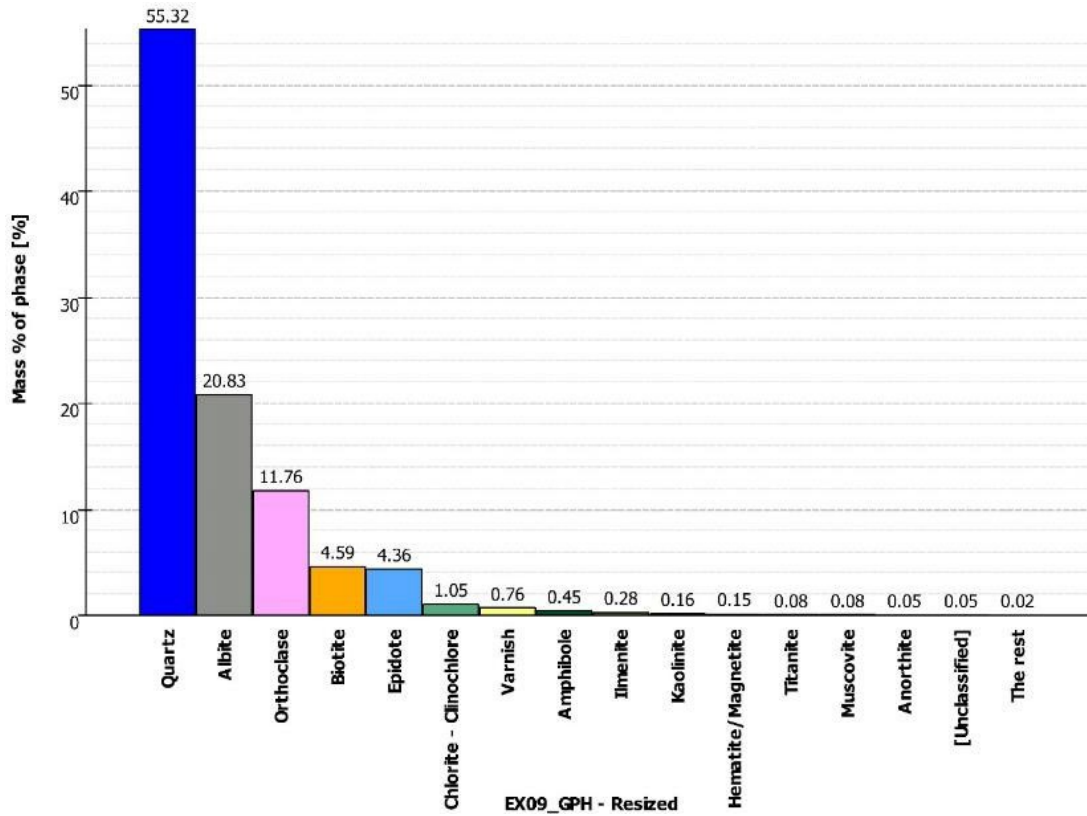


Figure C-82: Modal analysis of granophyre sample rock EX09_GPH

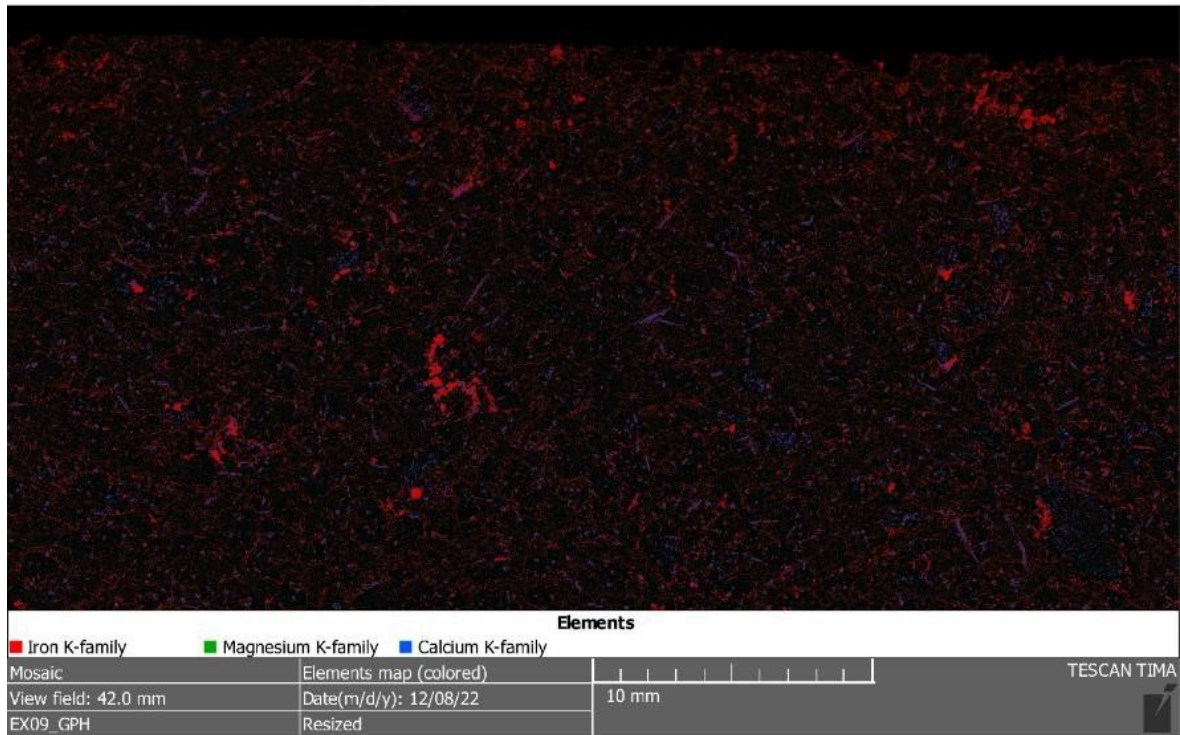


Figure C-83: Element map of granophyre sample rock EX09_GPH

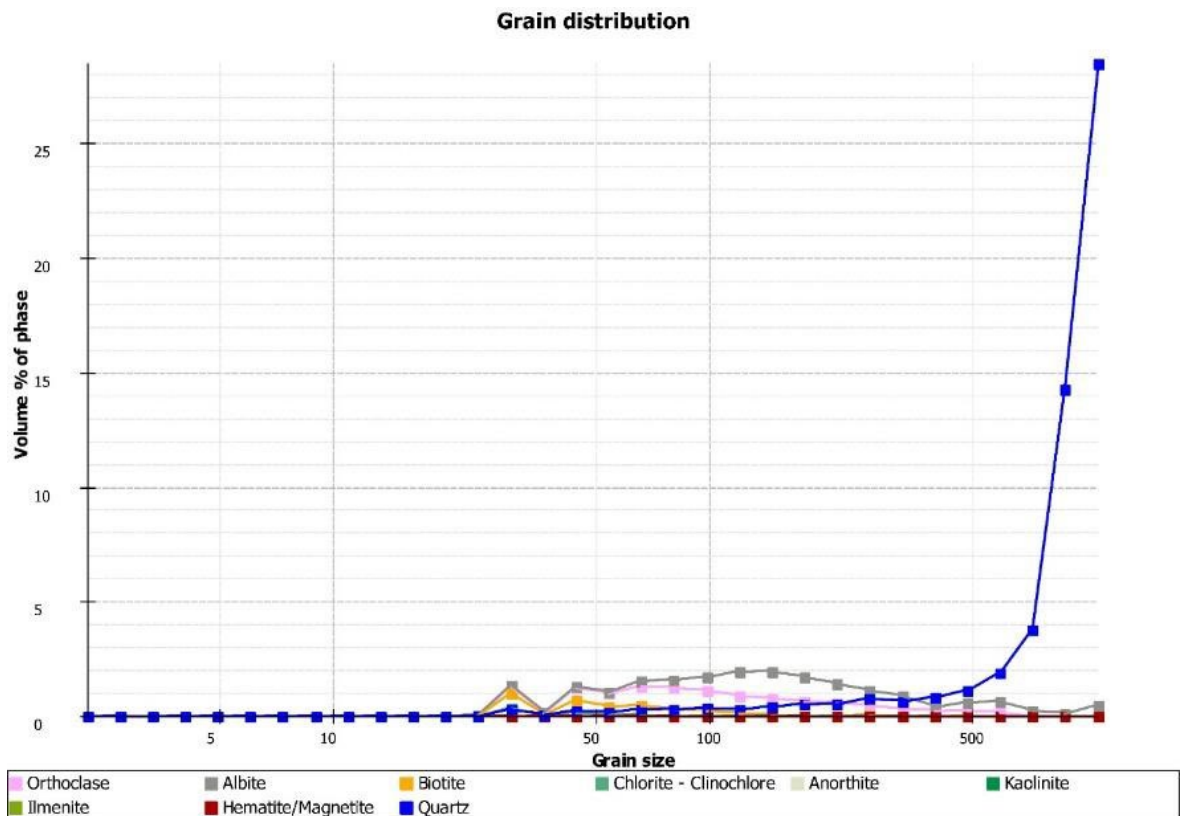


Figure C-84: Grain size distribution of granophyre sample rock EX09_GPH

C-2-15 Sample rock RS01-GPH



Figure C-85: Panorama image of granophyre sample rock RS01_GPH

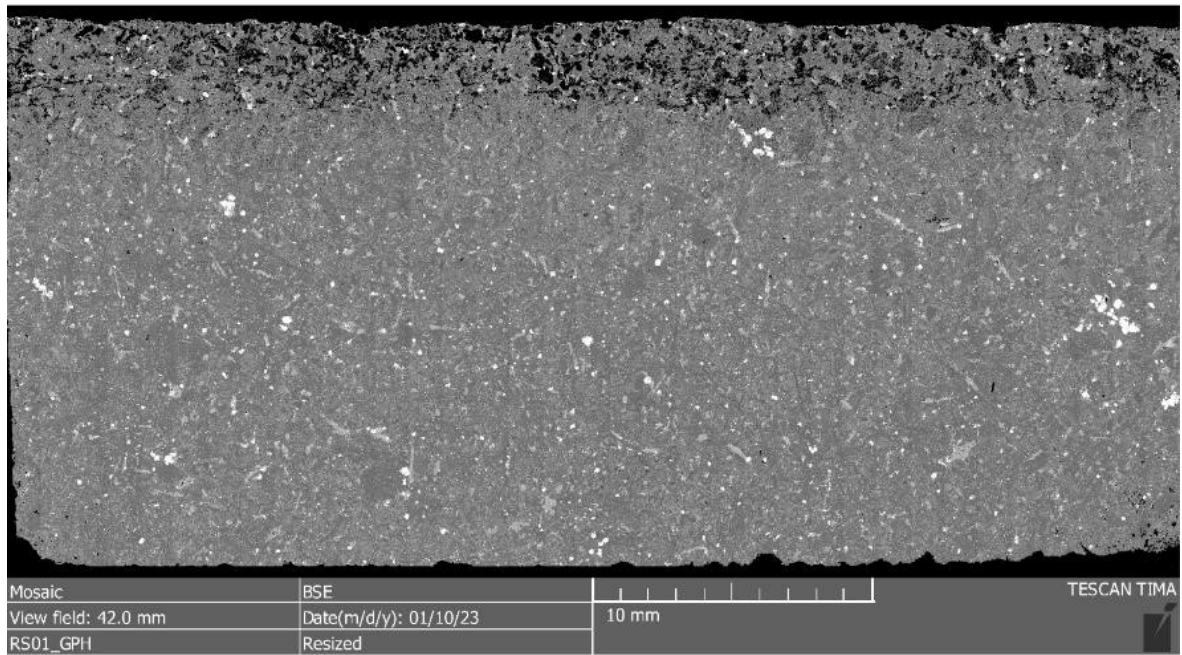


Figure C-86: BSE image of granophyre sample rock RS01_GPH

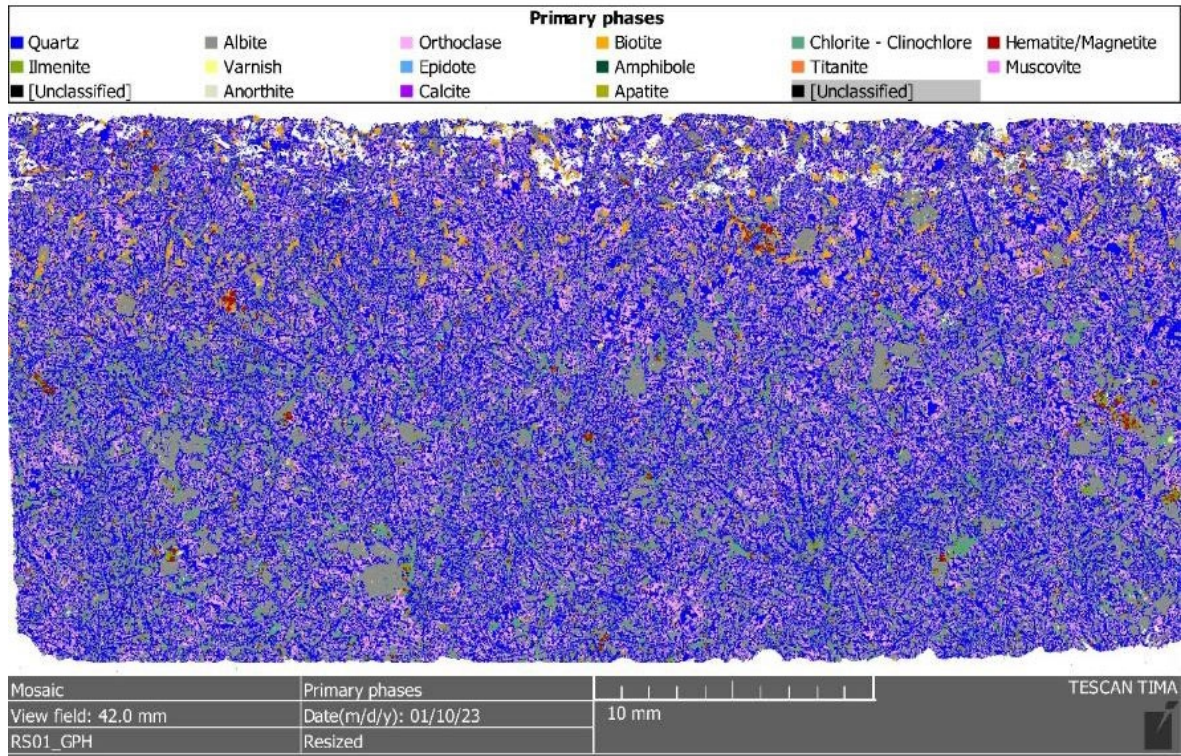


Figure C-87: Phase map of granophyre sample rock RS01_GPH

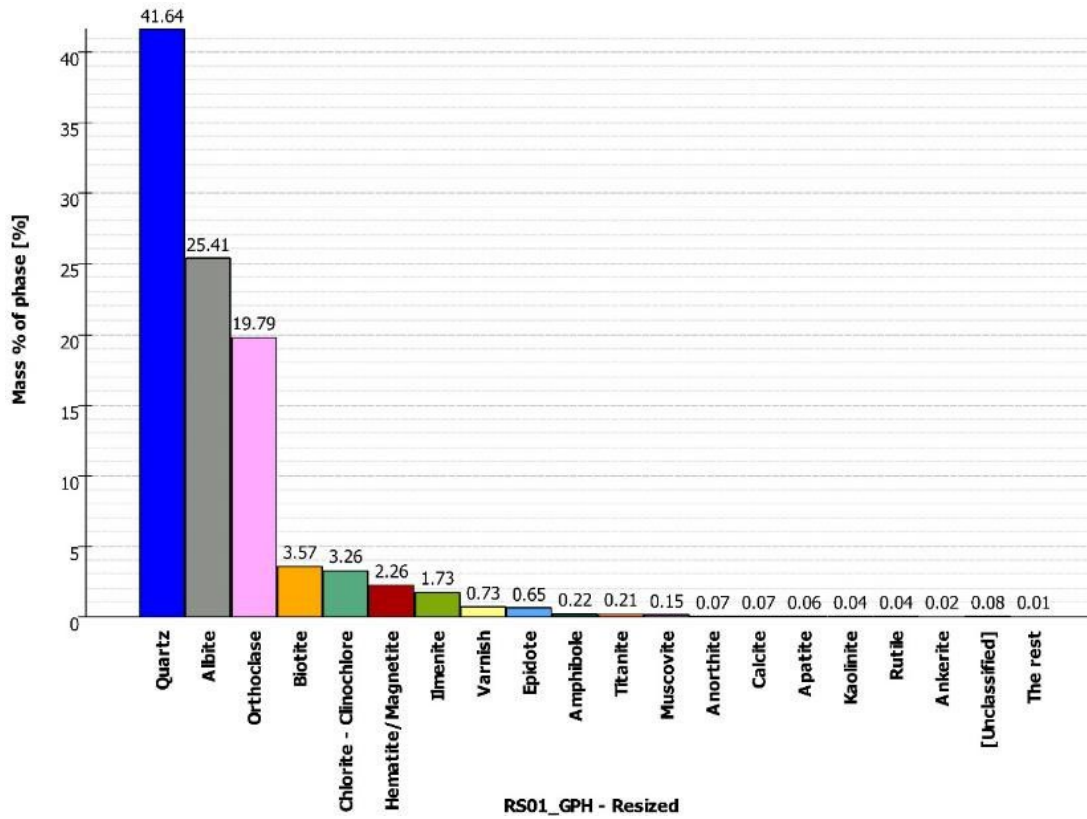


Figure C-88: Modal analysis of granophyre sample rock RS01_GPH

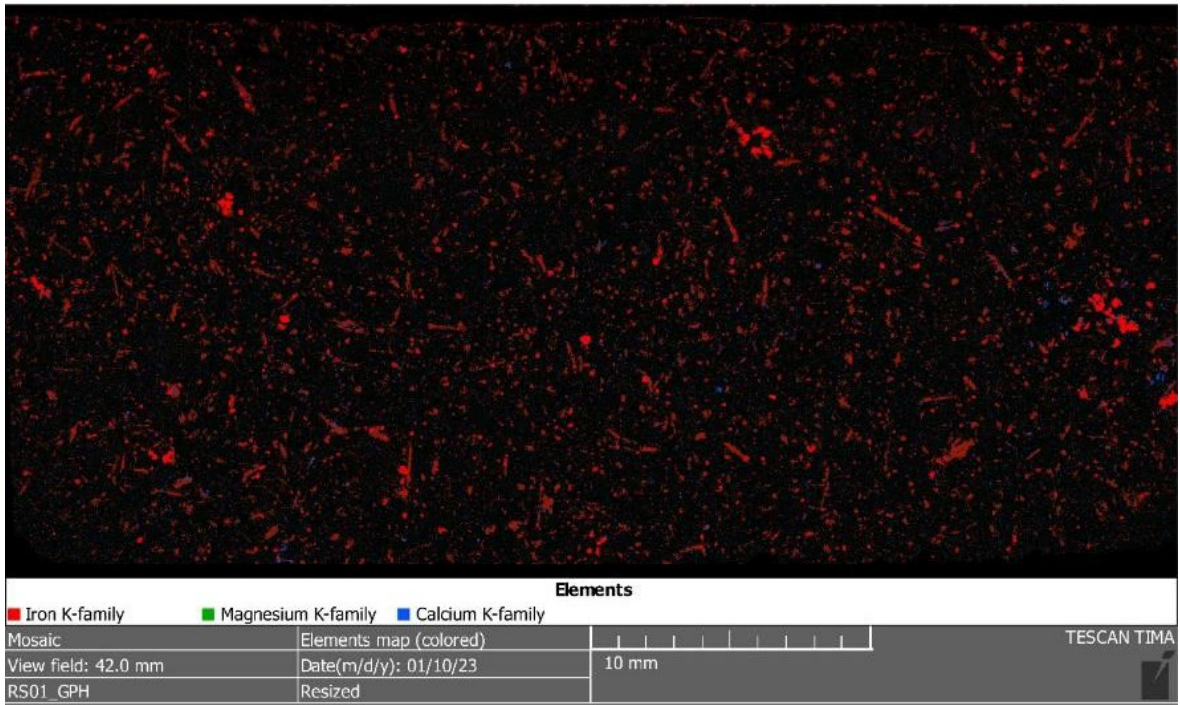


Figure C-89: Element map of granophyre sample rock RS01_GPH

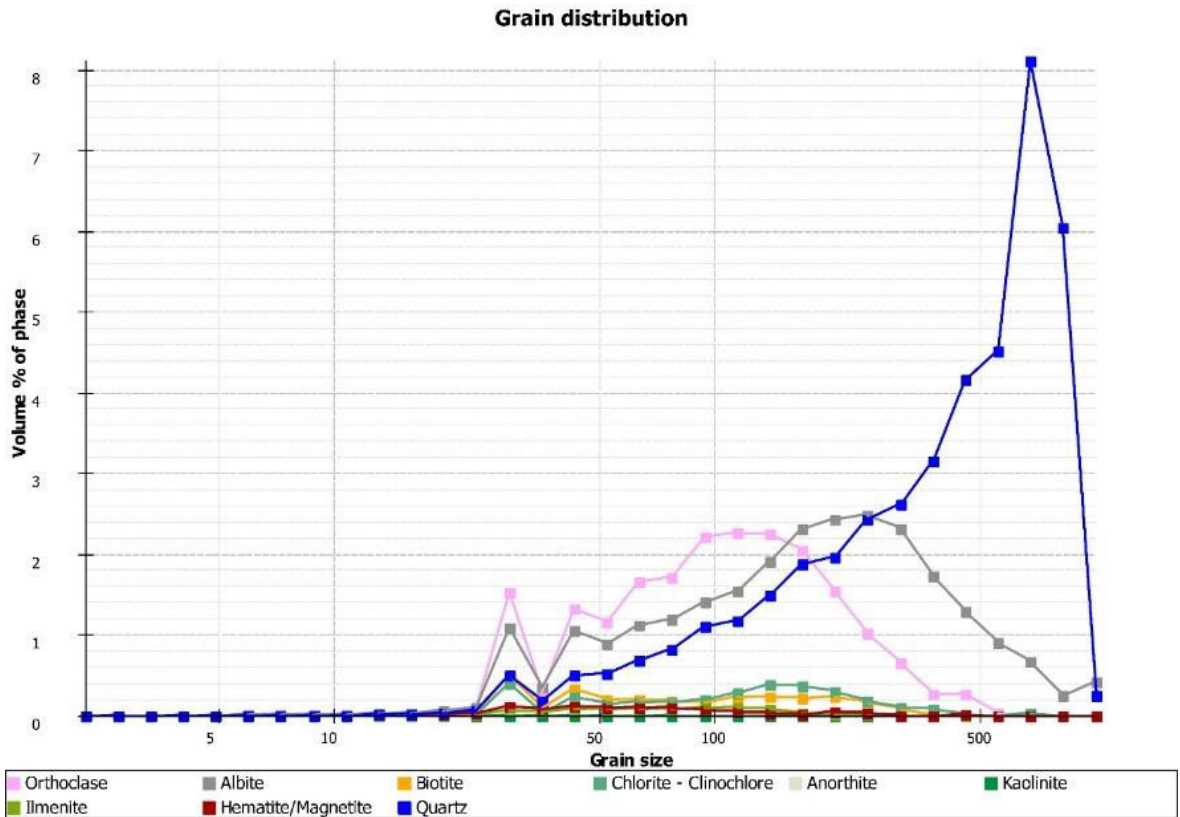


Figure C-90: Grain size distribution of granophyre sample rock RS01_GPH

C-2-16 Sample rock RS04_GPH



Figure C-91: Panorama image of granophyre sample rock RS04_GPH

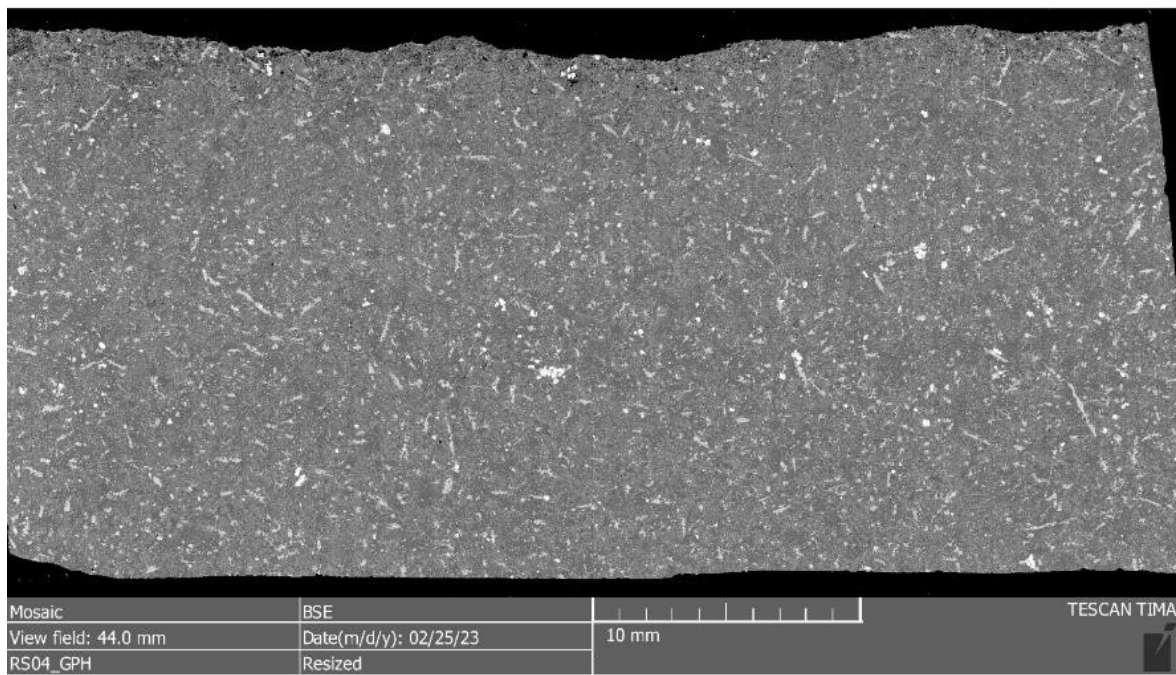


Figure C-92: BSE image of granophyre sample rock RS04_GPH

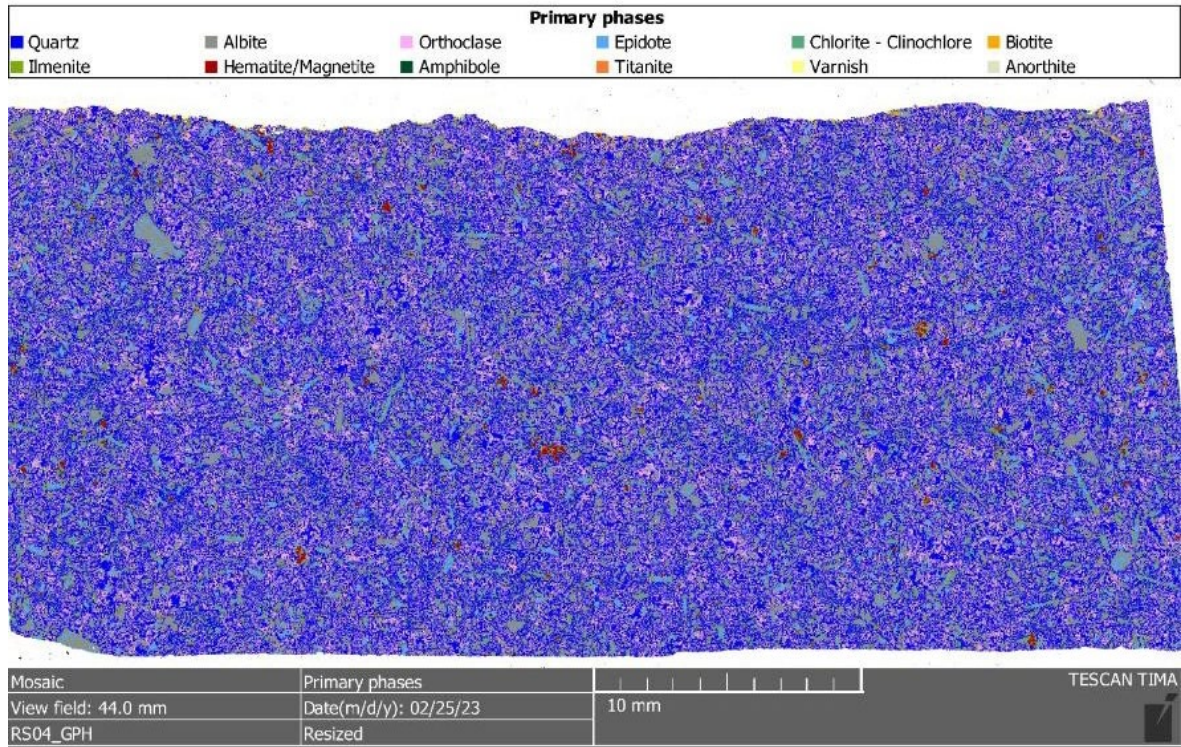


Figure C-93: Phase map of granophyre sample rock RS01_GPH

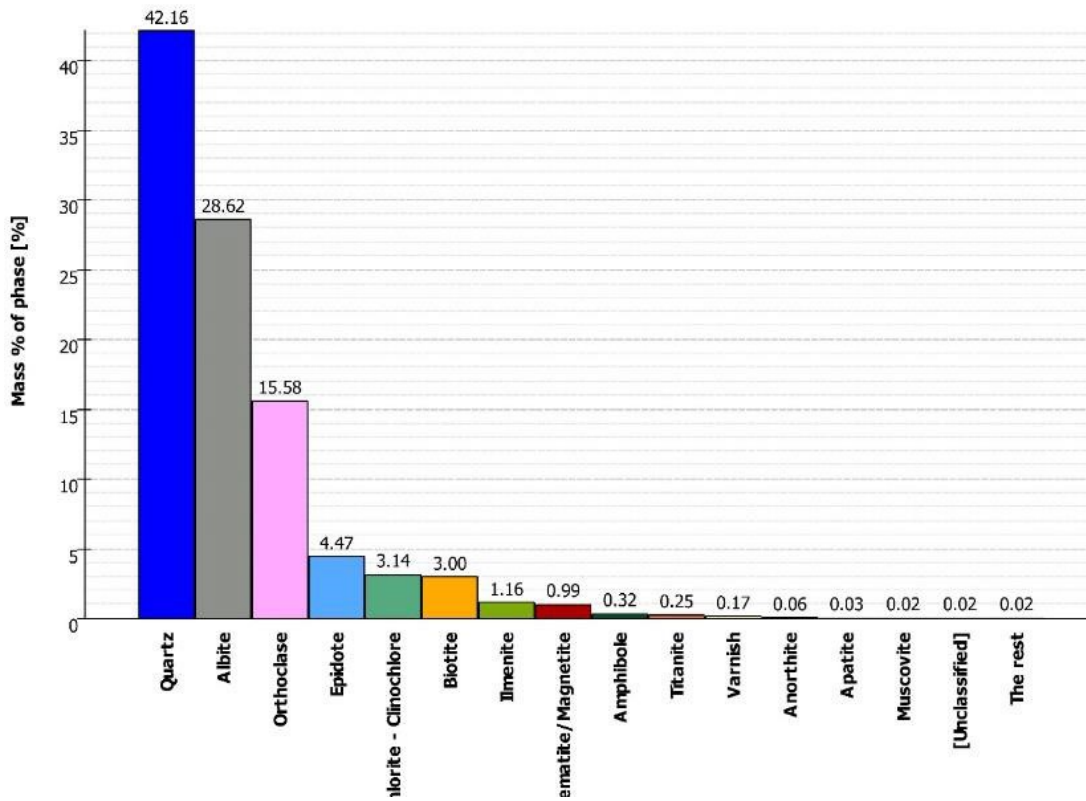


Figure C-94: Modal analysis of granophyre sample rock RS04_GPH

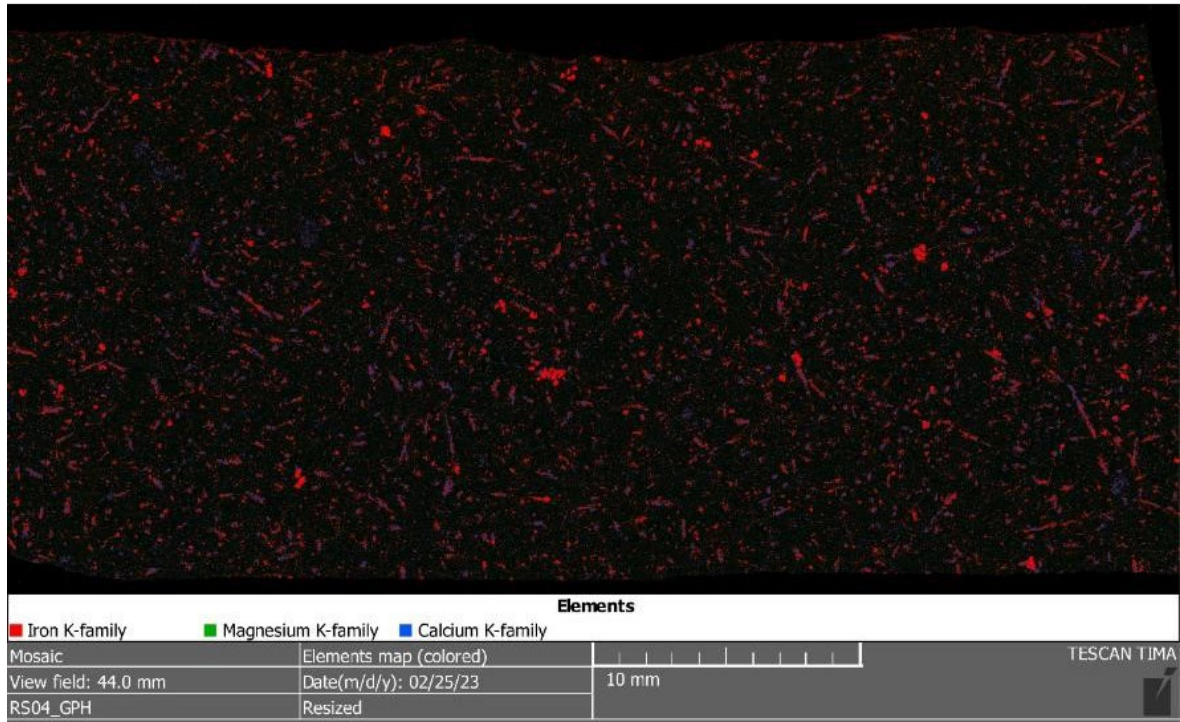


Figure C-95: Element map of granophyre sample rock RS04_GPH

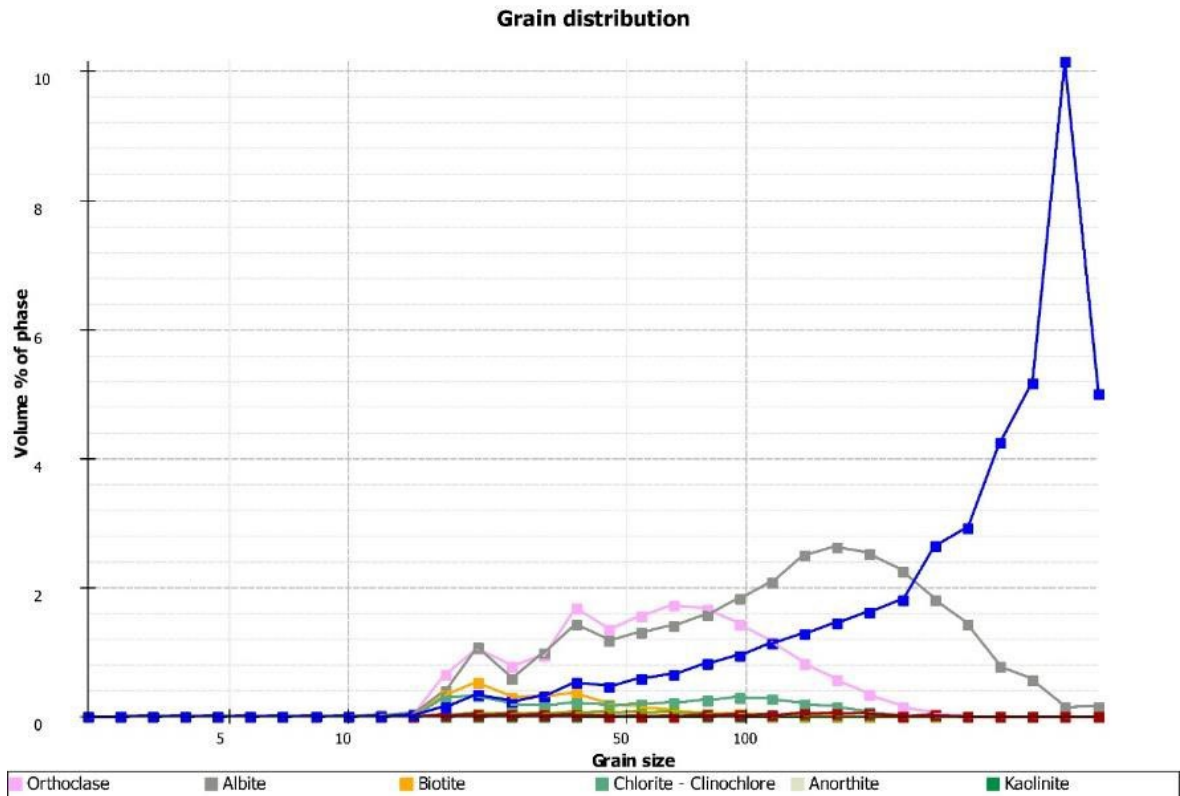


Figure C-96: Grain size distribution of granophyre sample rock RS04_GPH

C-2-17 Sample rock RS05#1_GPH



Figure C-97: Panorama image of granophyre sample rock RS05#1_GPH

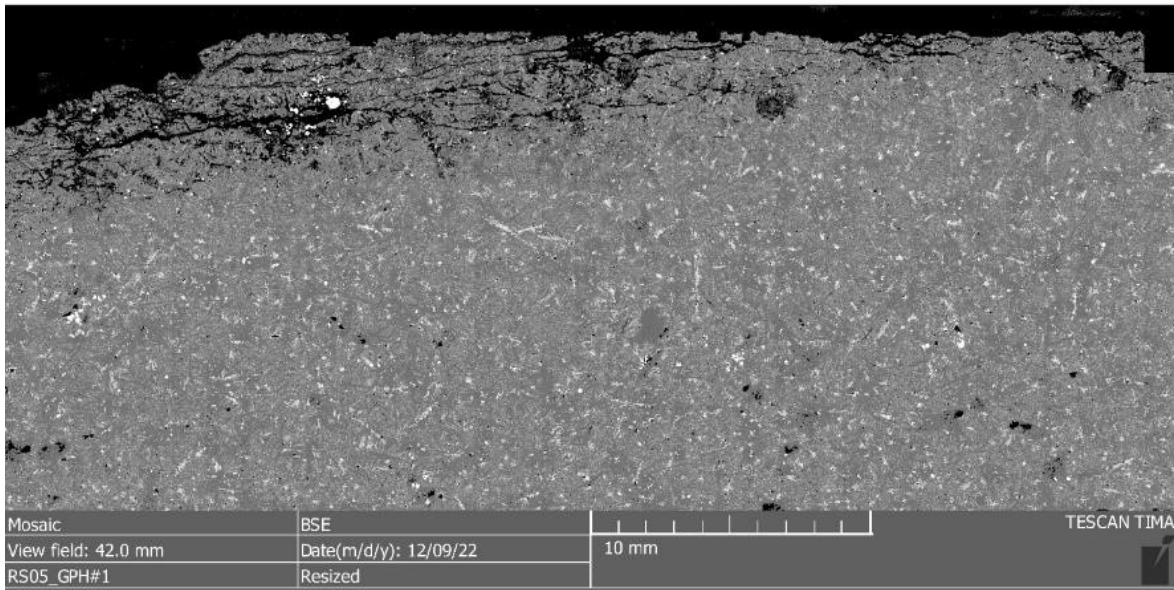


Figure C-98: BSE image of granophyre sample rock RS05#1_GPH

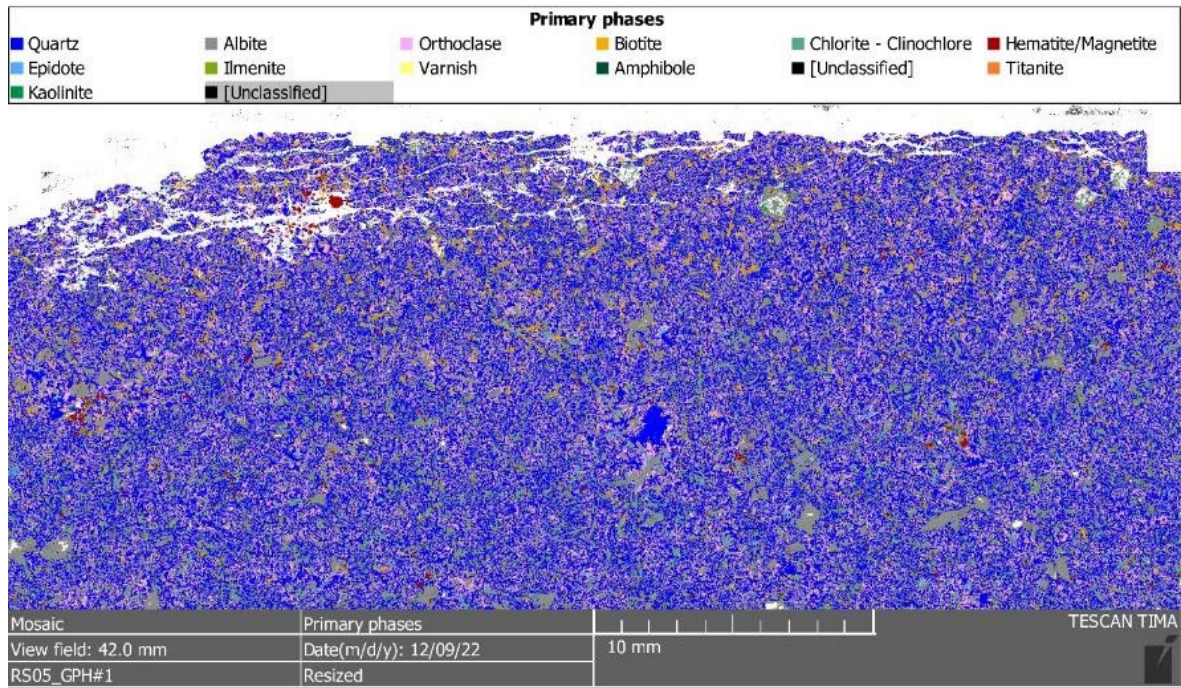


Figure C-99: Phase map of granophyre sample rock RS05#1_GPH

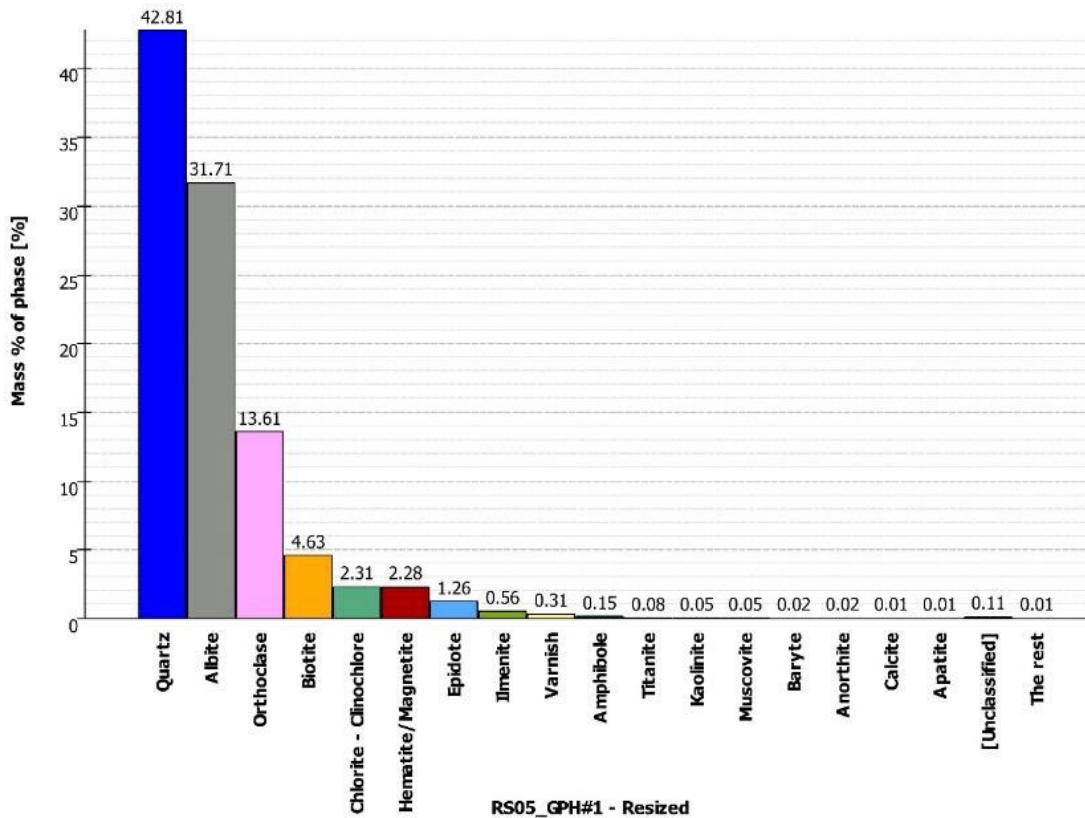


Figure C-100: Modal analysis of granophyre sample rock RS05#1_GPH

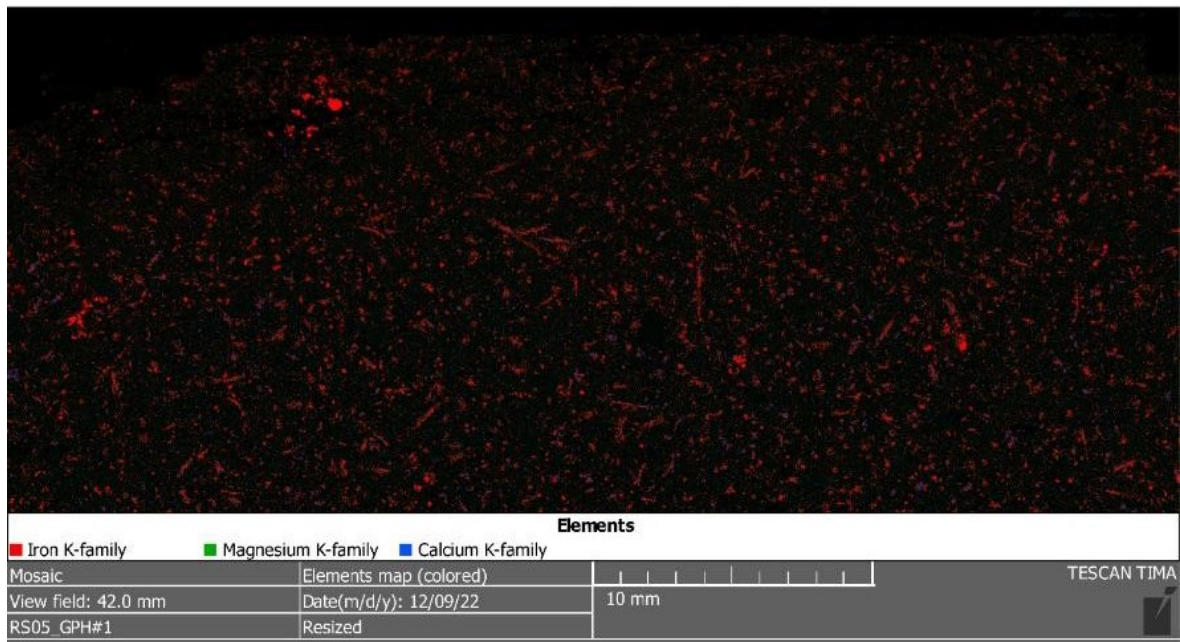


Figure C-101: Element map of granophyre sample rock RS05#1_GPH

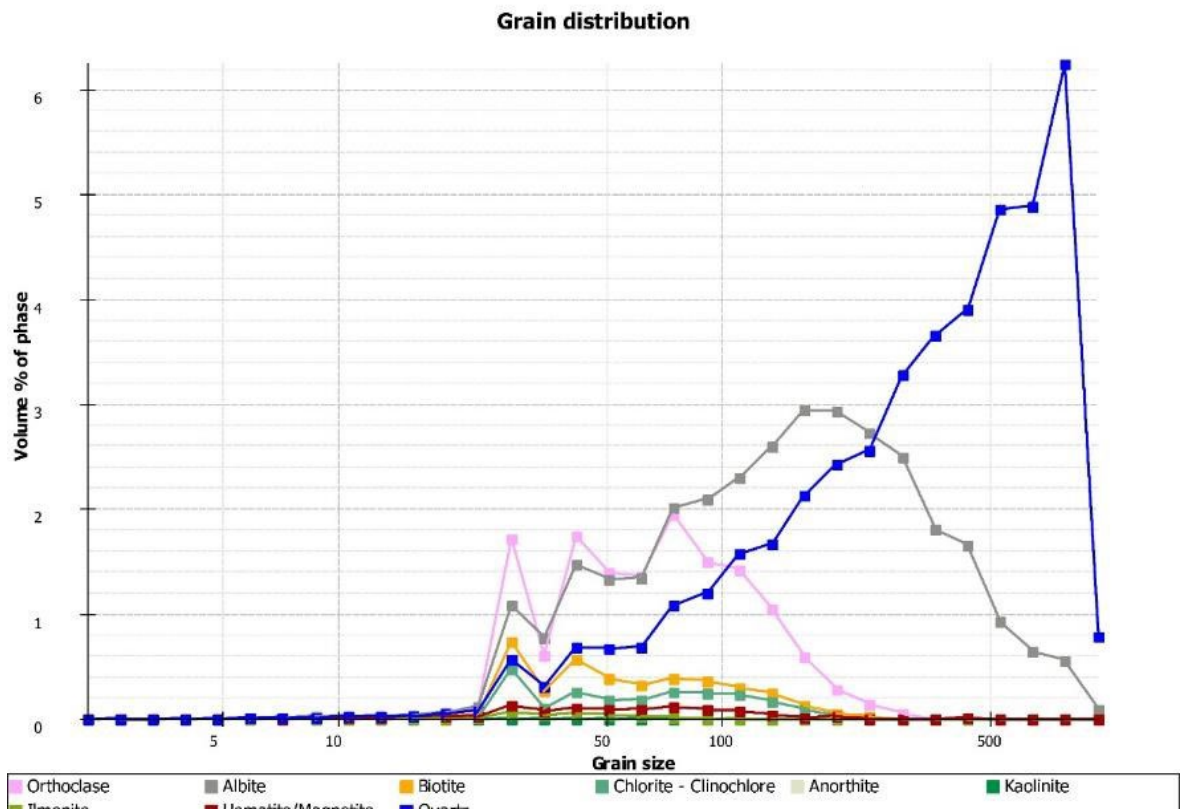


Figure C-102: Grain size distribution of granophyre sample rock RS05#1_GPH

C-2-18 Sample rock RS06_GPH



Figure C-103: Panorama image of granophyre sample rock RS06_GPH

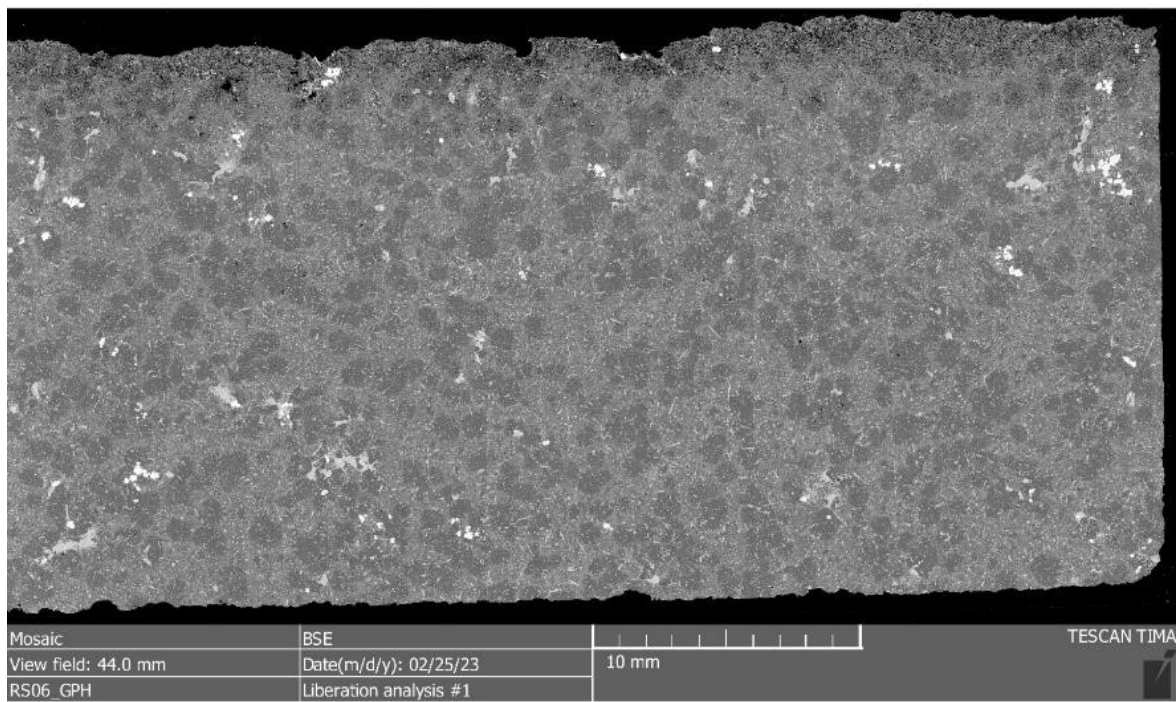


Figure C-104: BSE image of granophyre sample rock RS06_GPH

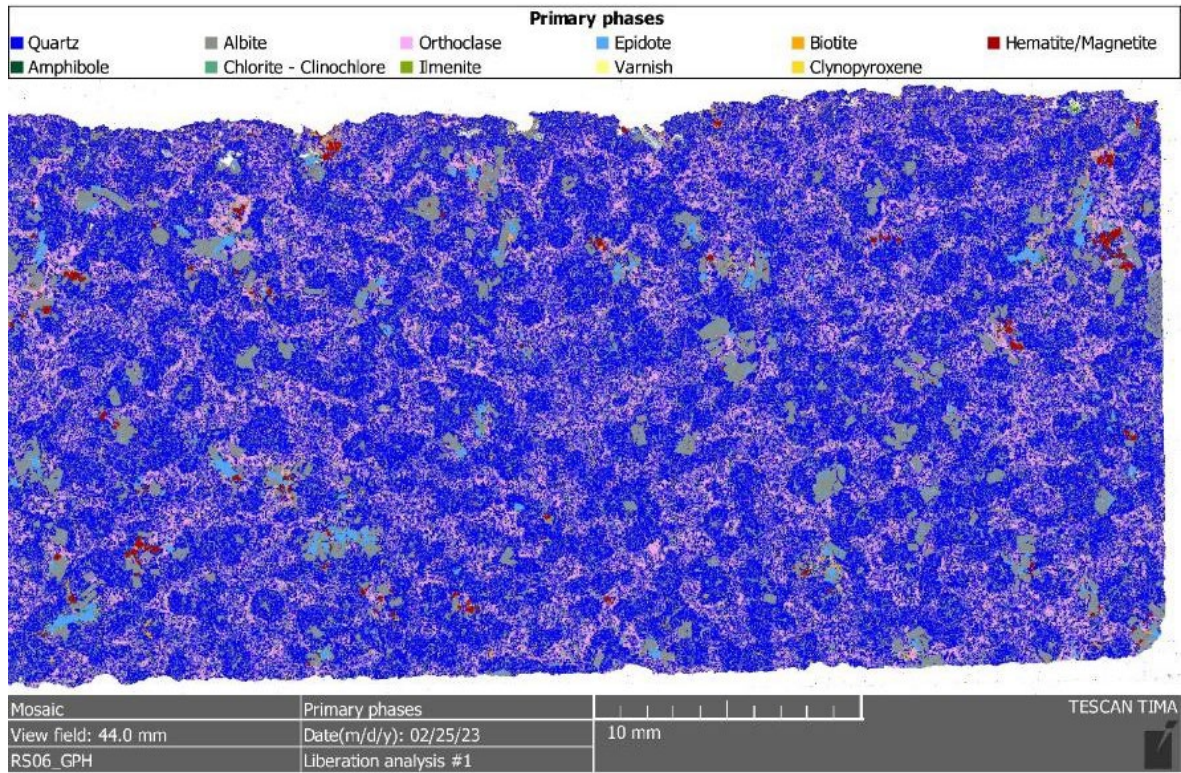


Figure C-105: Phase map of granophyre sample rock RS06_GPH

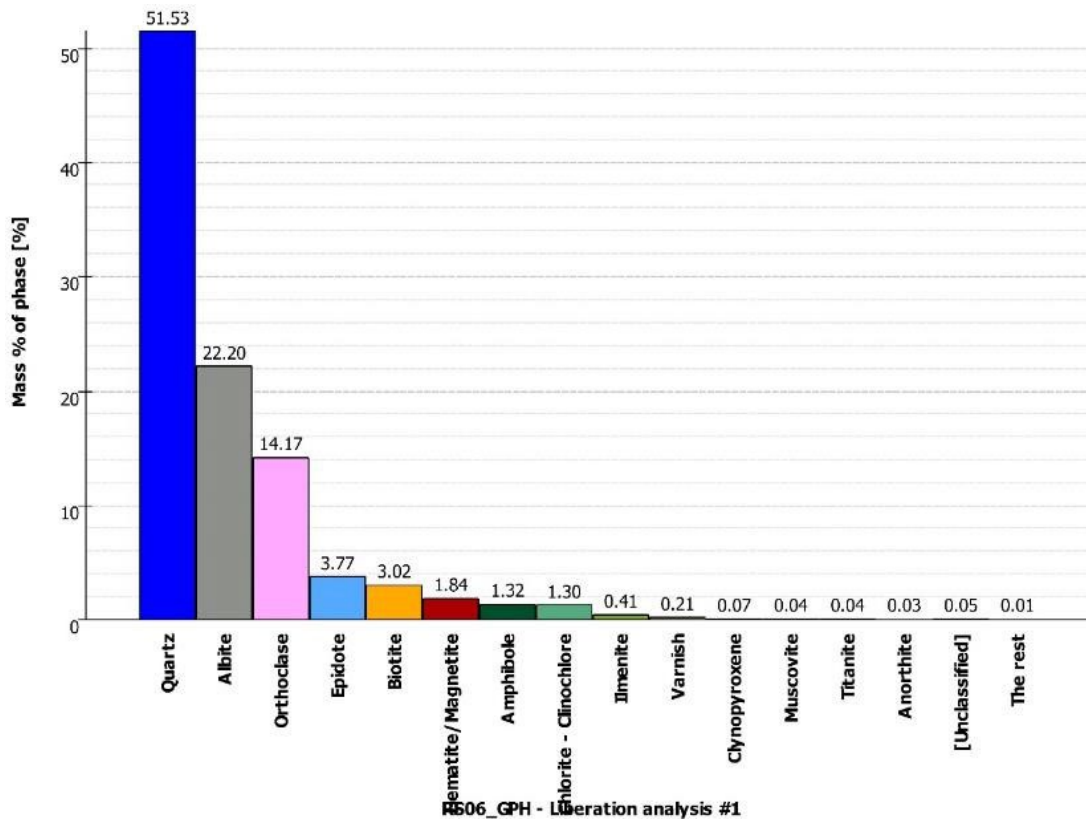


Figure C-106: Modal analysis of granophyre sample rock RS06_GPH

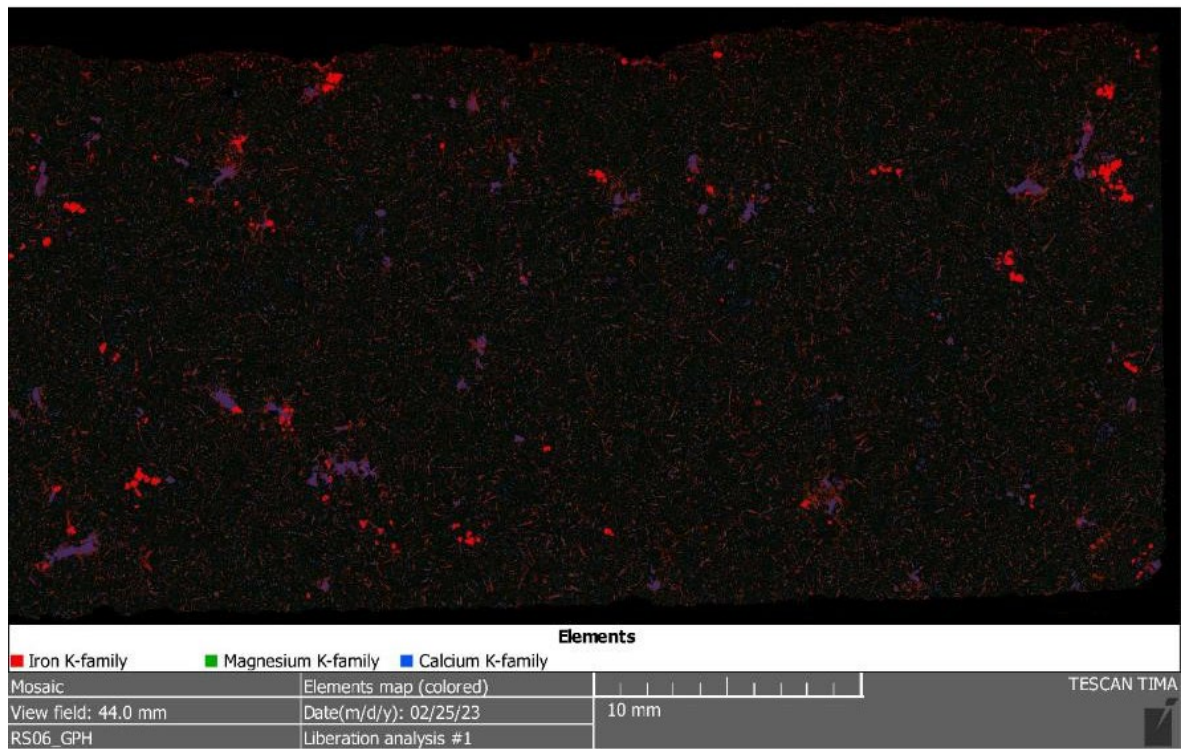


Figure C-107: Element map of granophyre sample rock RS06_GPH

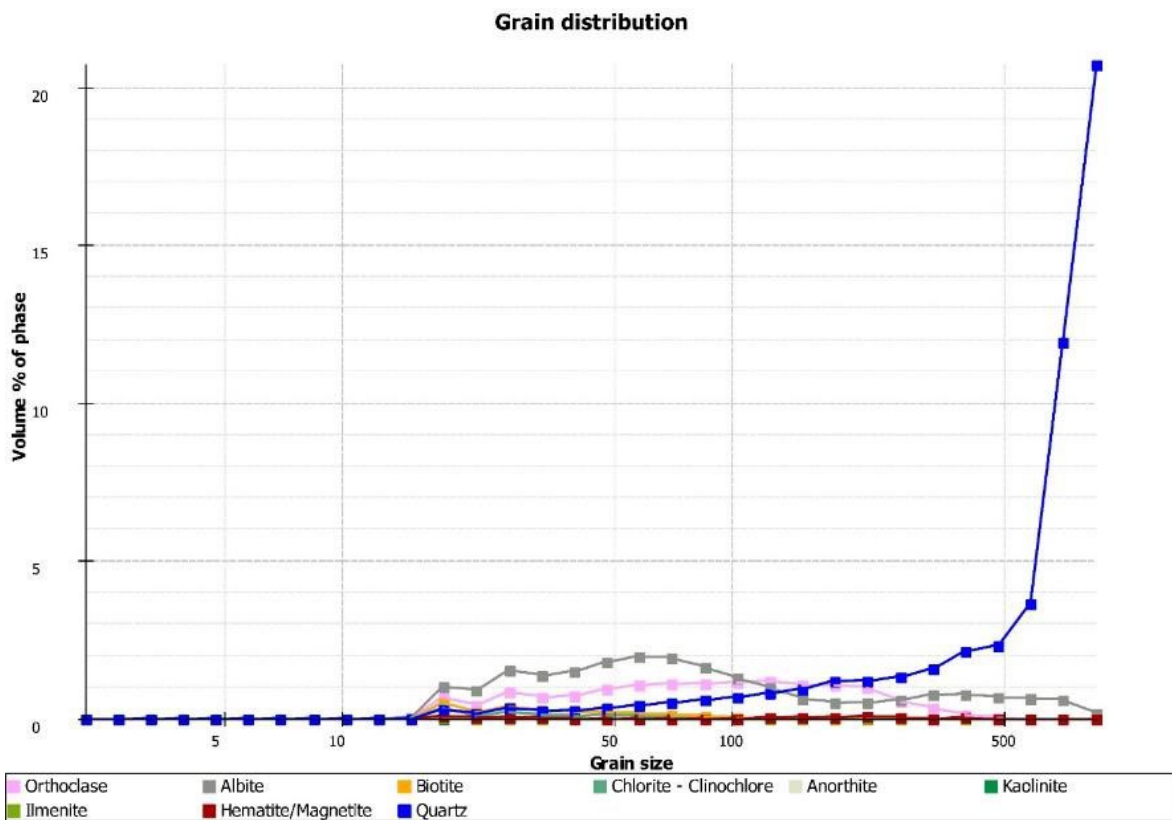


Figure C-108: Grain size distribution of granophyre sample rock RS06_GPH

C-2-19 Sample rock RS11_GPH



Figure C-109: Panorama image of granophyre sample rock RS11_GPH

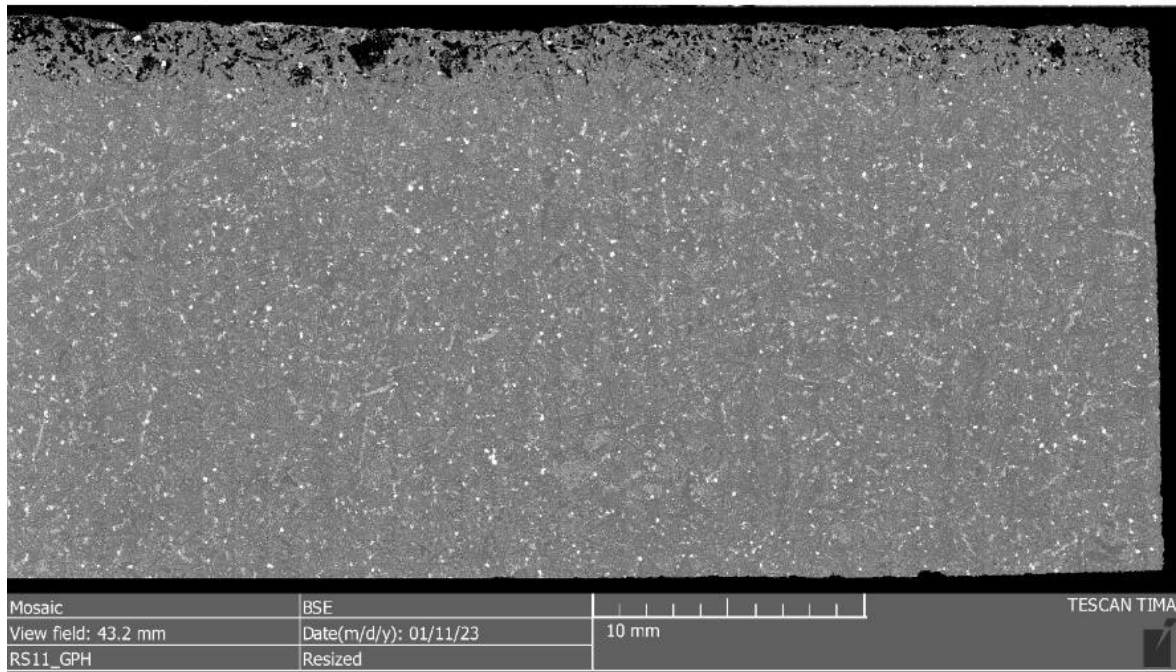


Figure C-110: BSE image of granophyre sample rock RS11_GPH

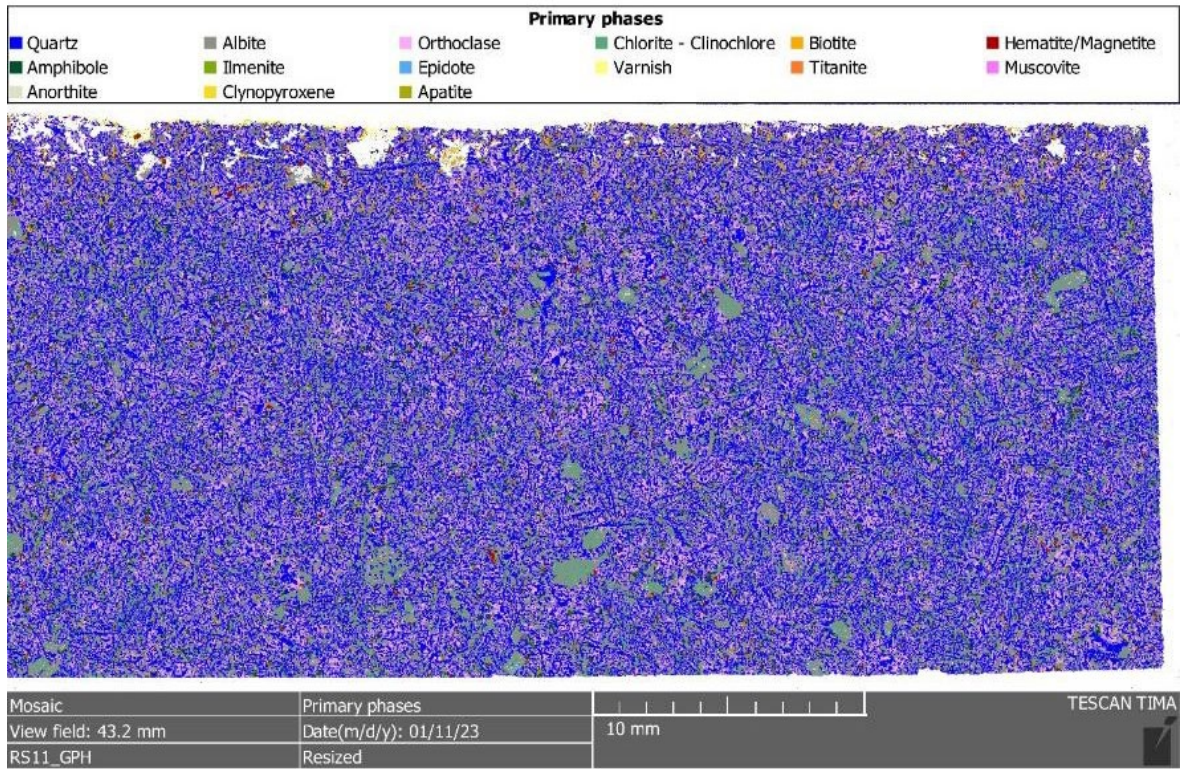


Figure C-111: Phase map of granophyre sample rock RS11_GPH

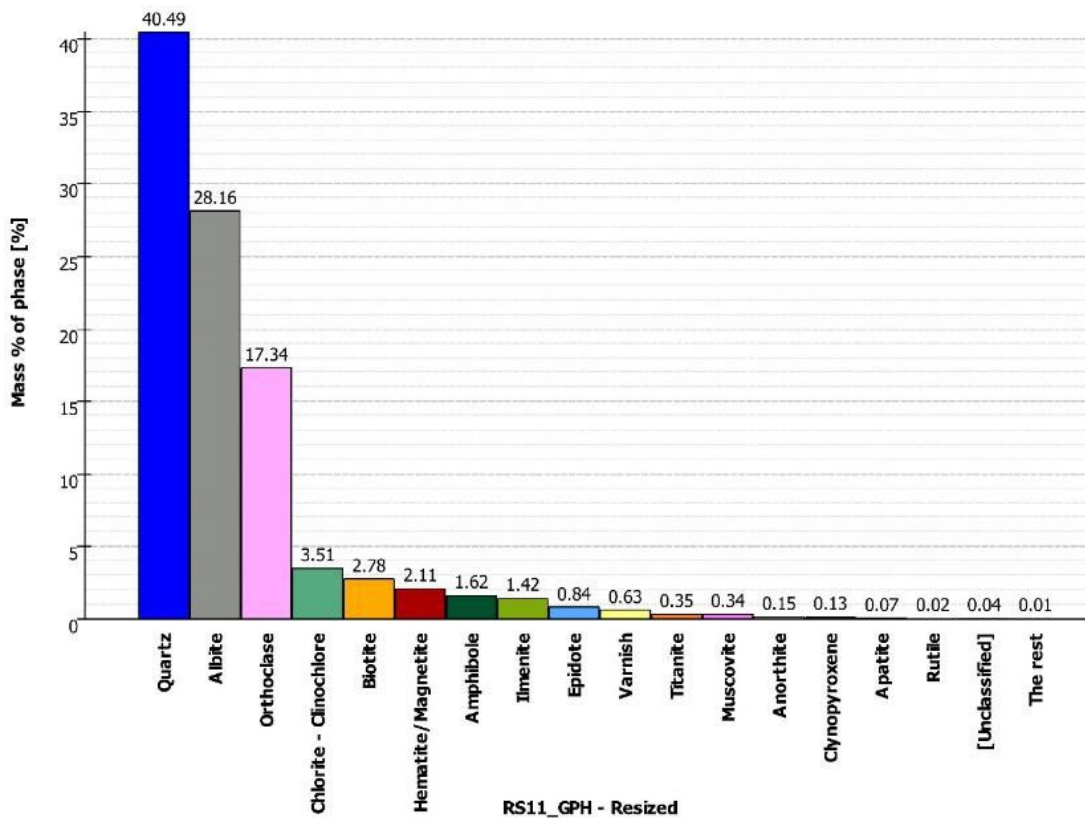


Figure C-112: Modal analysis of granophyre sample rock RS11_GPH

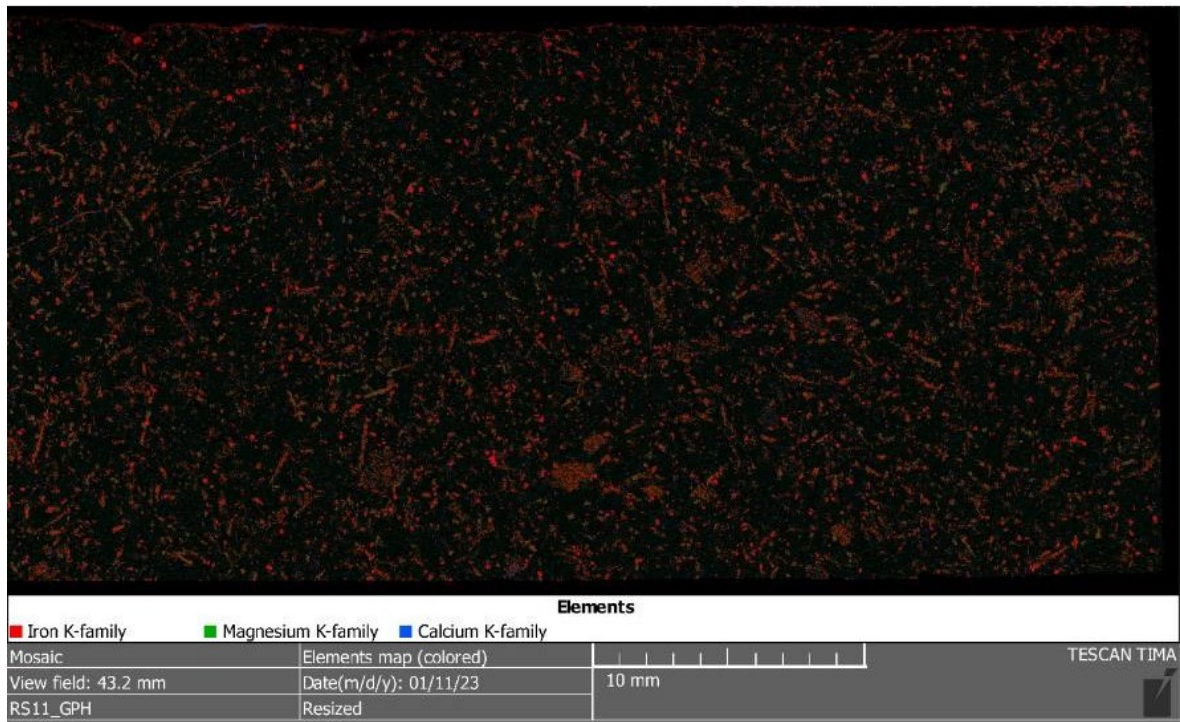


Figure C-113: Element map of granophyre sample rock RS11_GPH

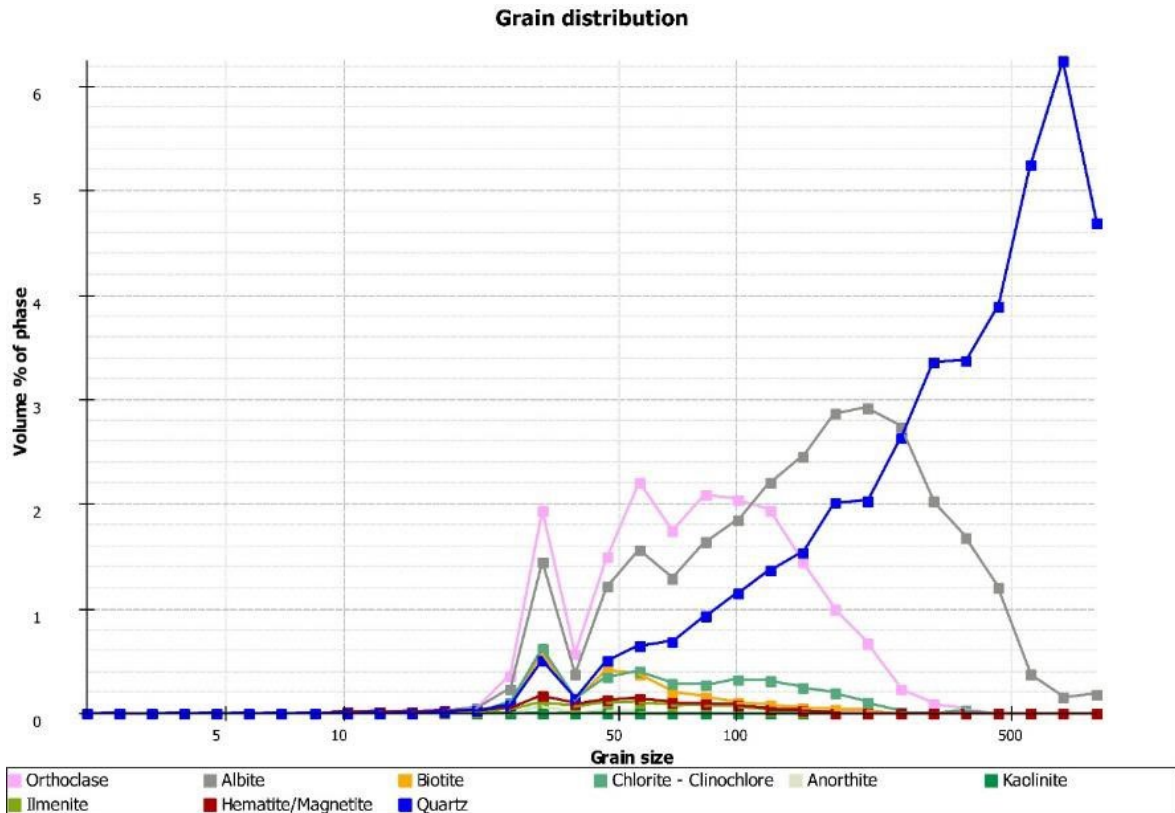


Figure C-114: Grain size distribution of granophyre sample rock RS11_GPH

Appendix C-3 Gabbro

C-3-1 Sample rock AQ03_GBR



Figure C-115: Panorama image of gabbro sample rock AQ03_GBR

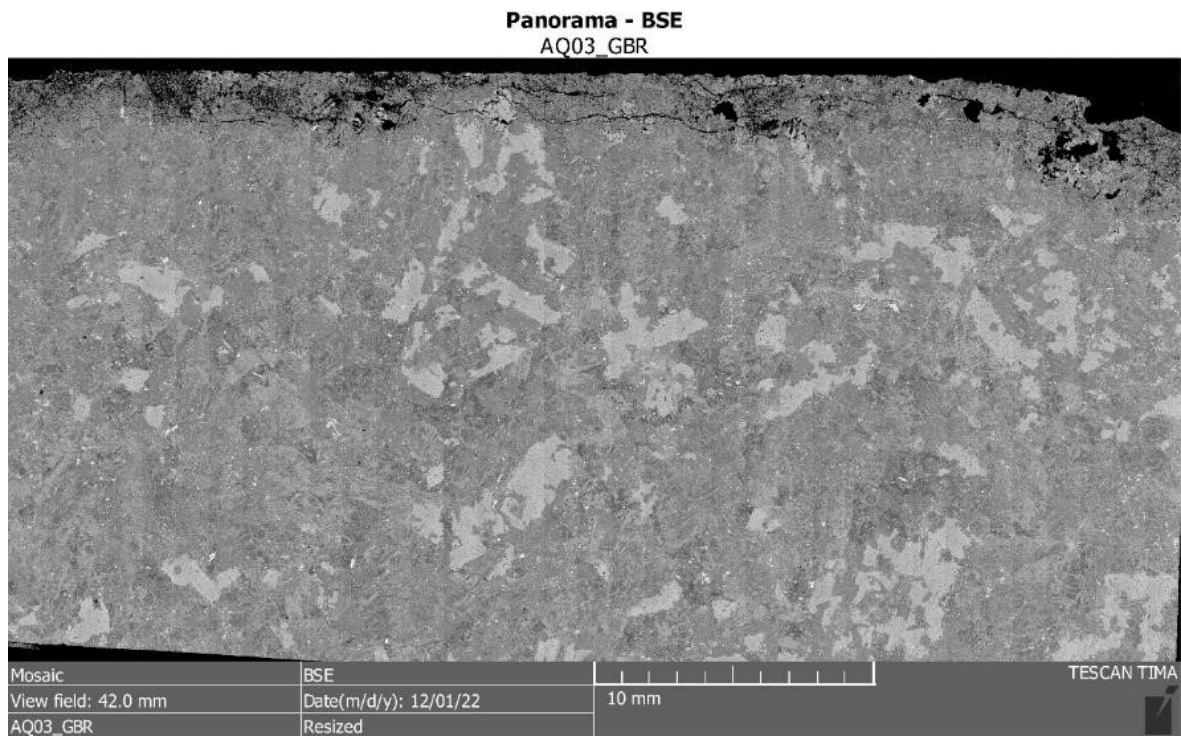


Figure C-116: BSE image of gabbro sample rock AQ03_GBR

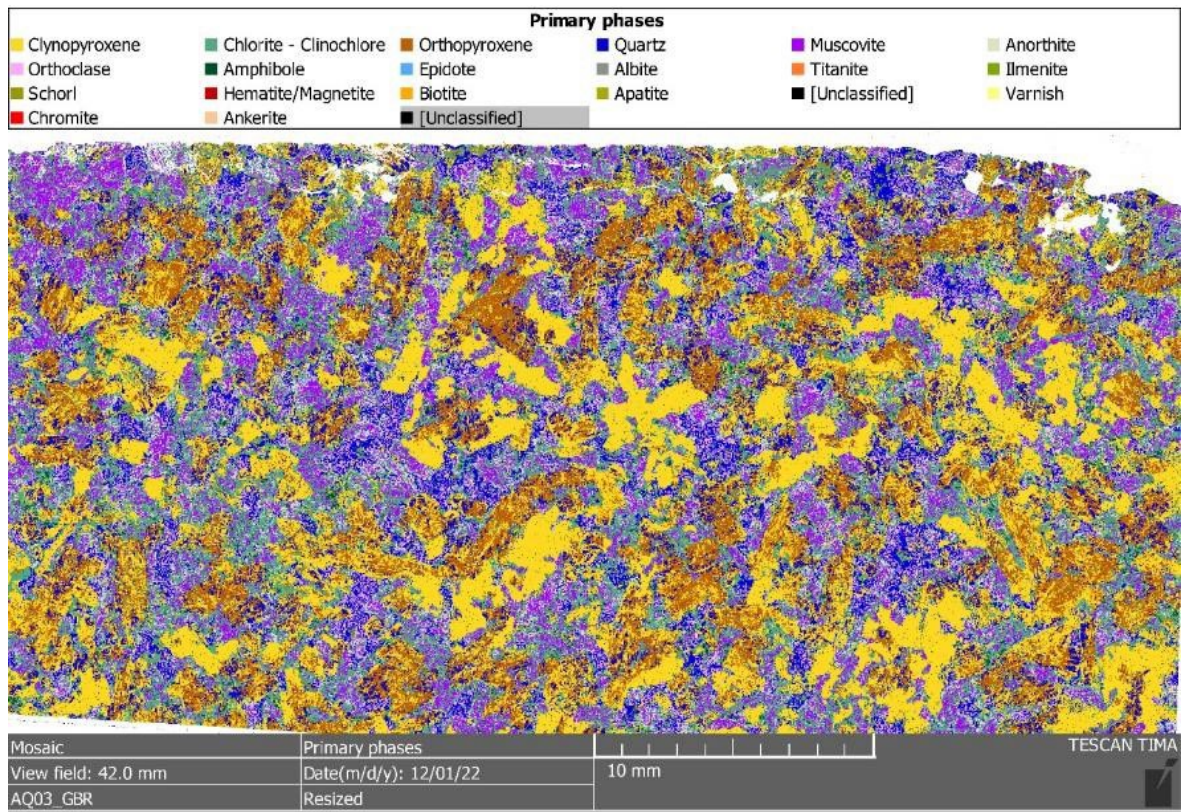


Figure C-117: Phase map of gabbro sample rock AQ03_GBR

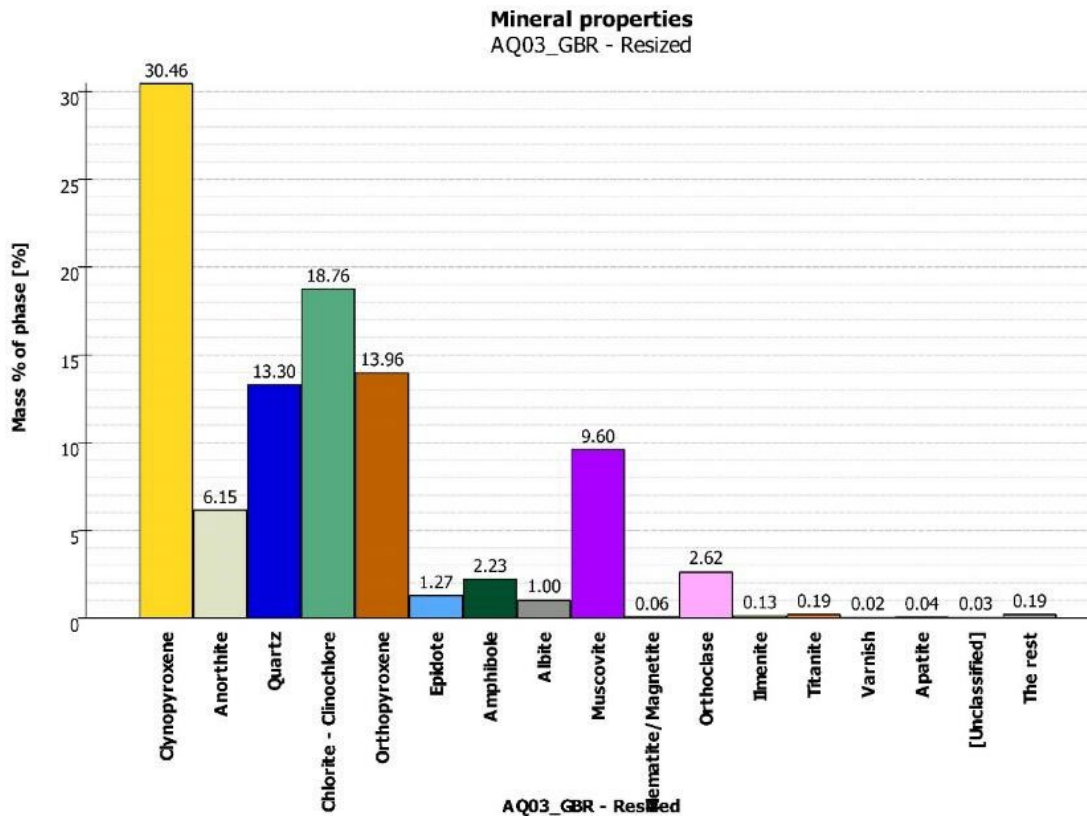


Figure C-118: Modal analysis of gabbro sample rock AQ03_GBR

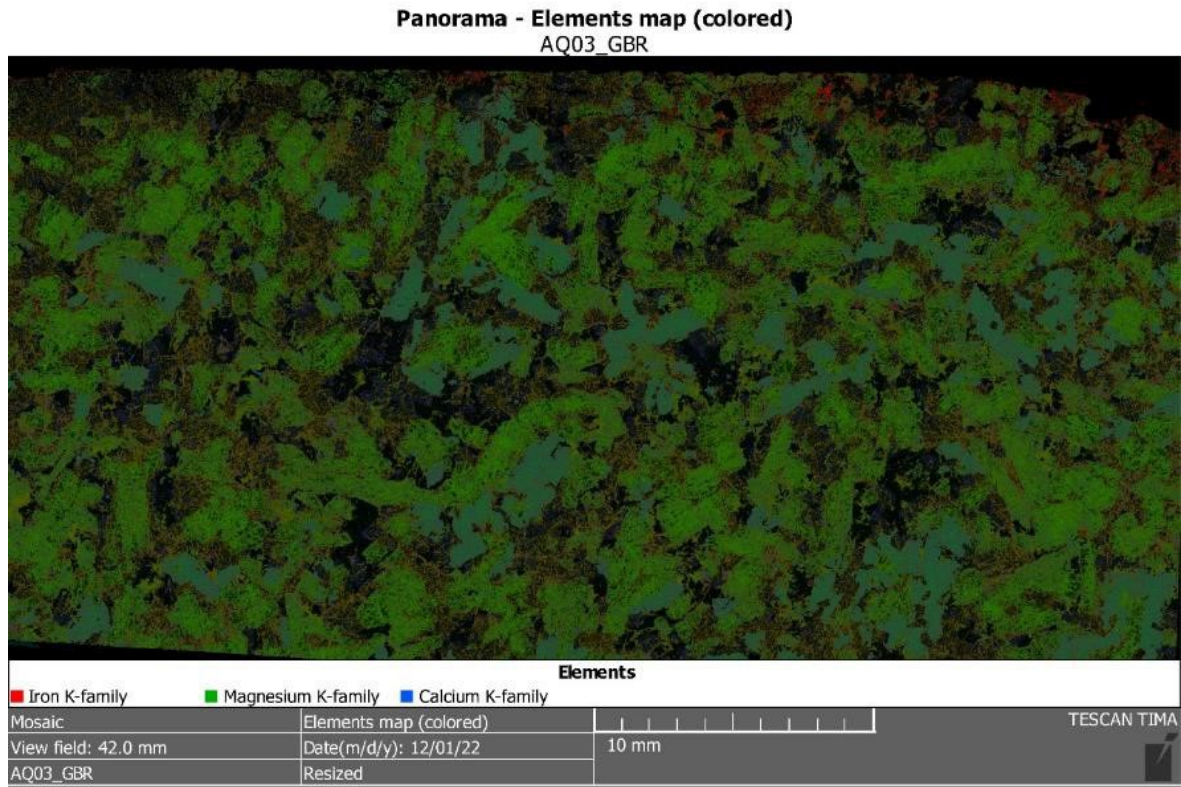


Figure C-119: Element map of gabbro sample rock AQ03_GBR

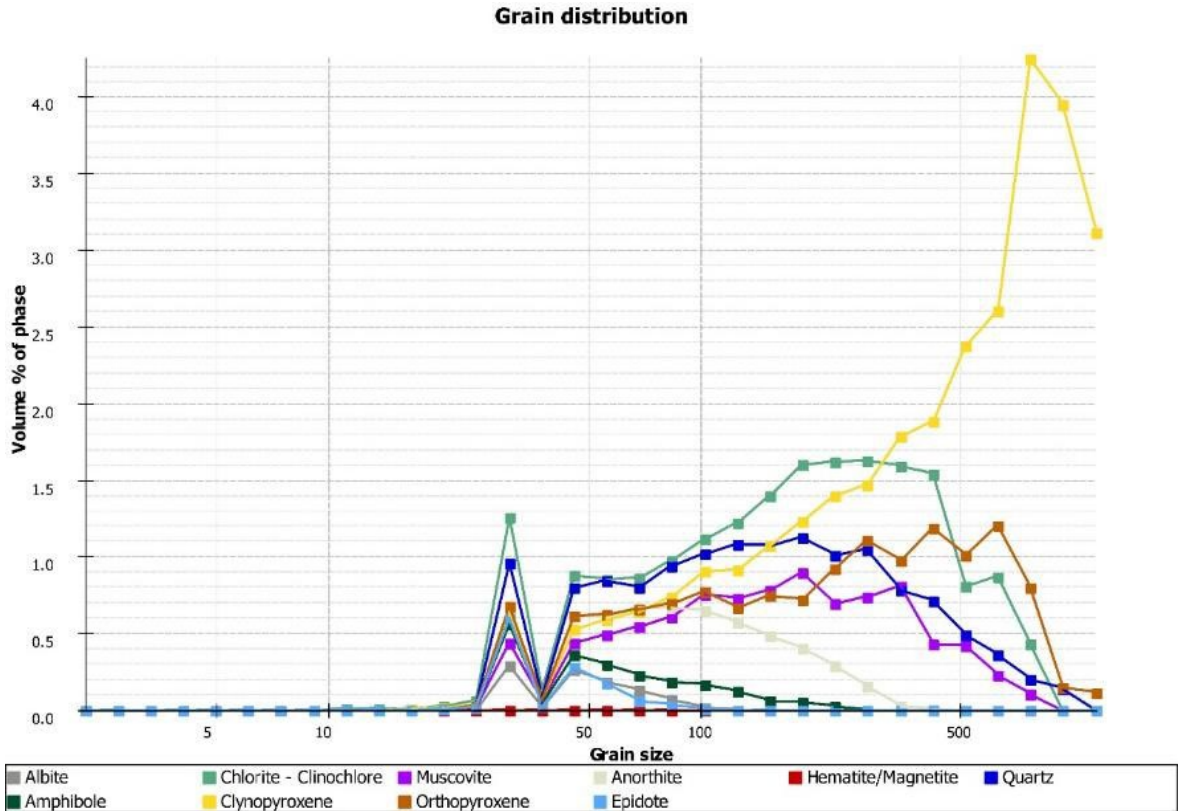


Figure C-120: Grain size distribution of gabbro sample rock AQ03_GBR

C-3-2 Sample rock AQ09_GBR



Figure C-121: Panorama image of gabbro sample rock AQ09_GBR

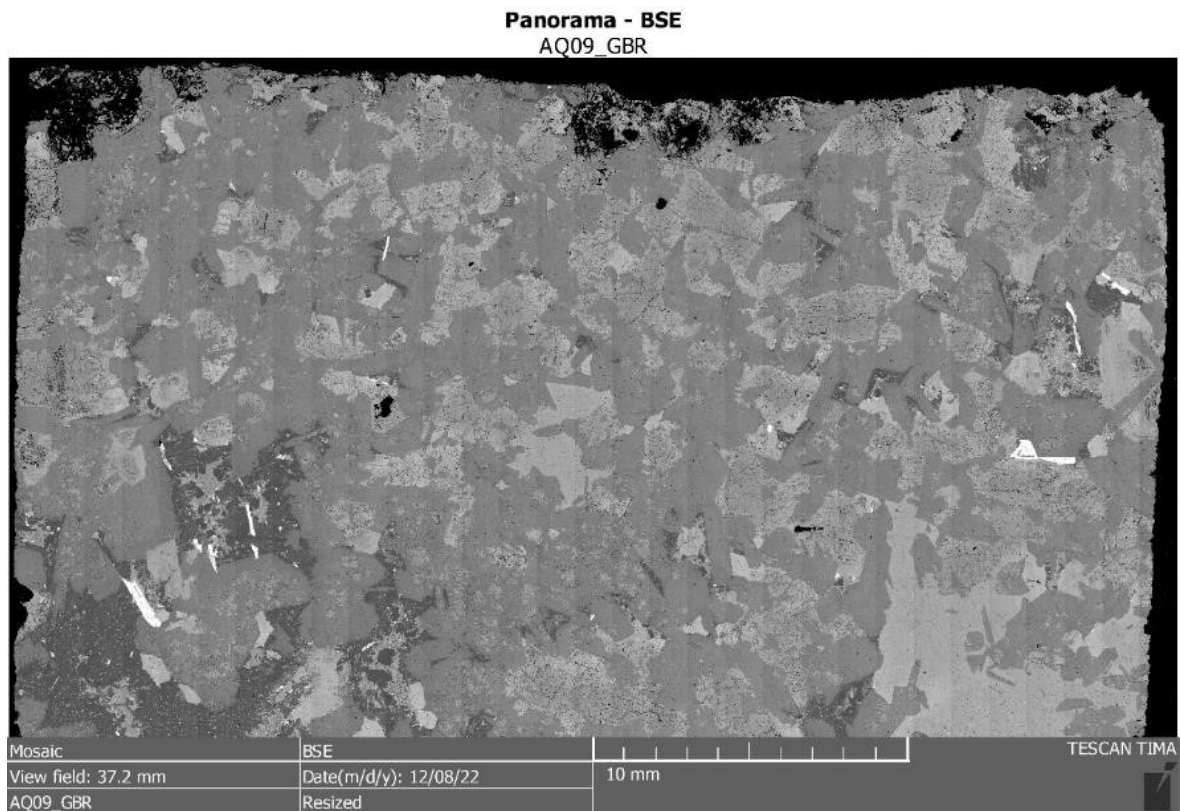


Figure C-122: BSE image of gabbro sample rock AQ09_GBR

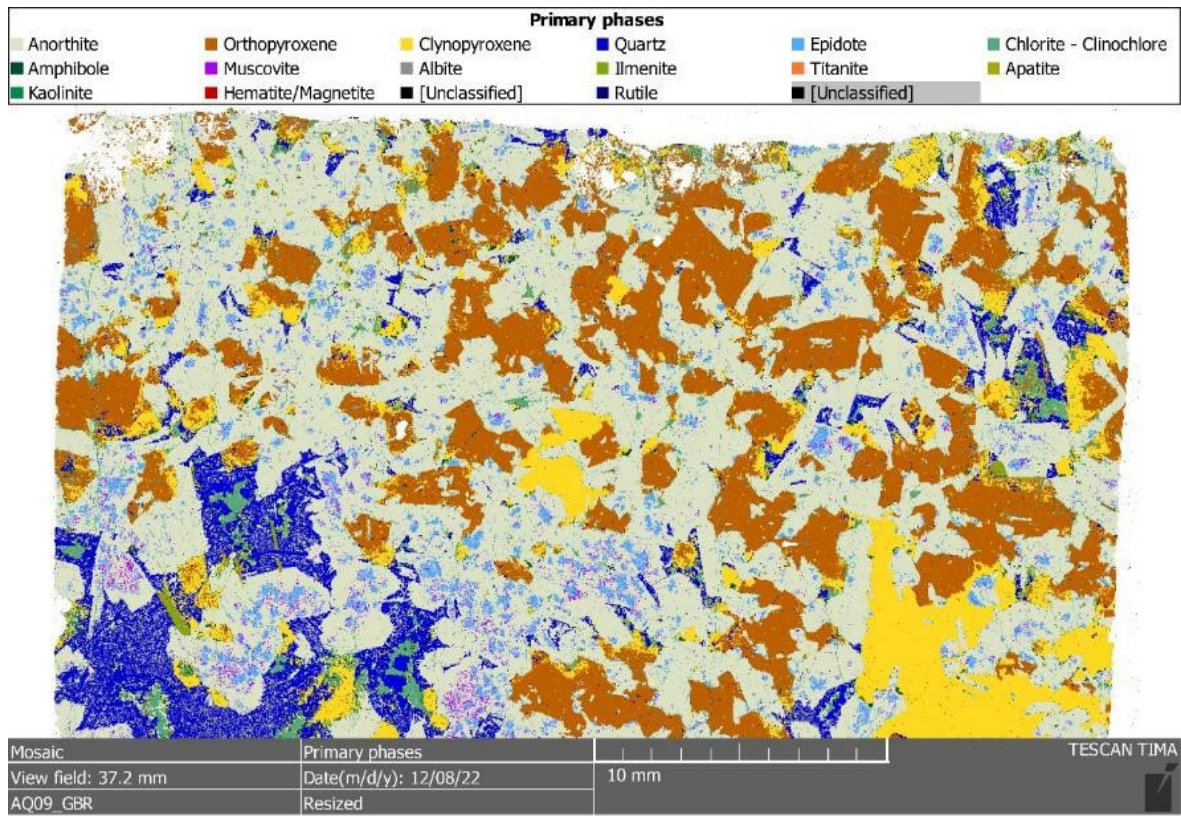


Figure C-123: Phase map of gabbro sample rock AQ09_GBR

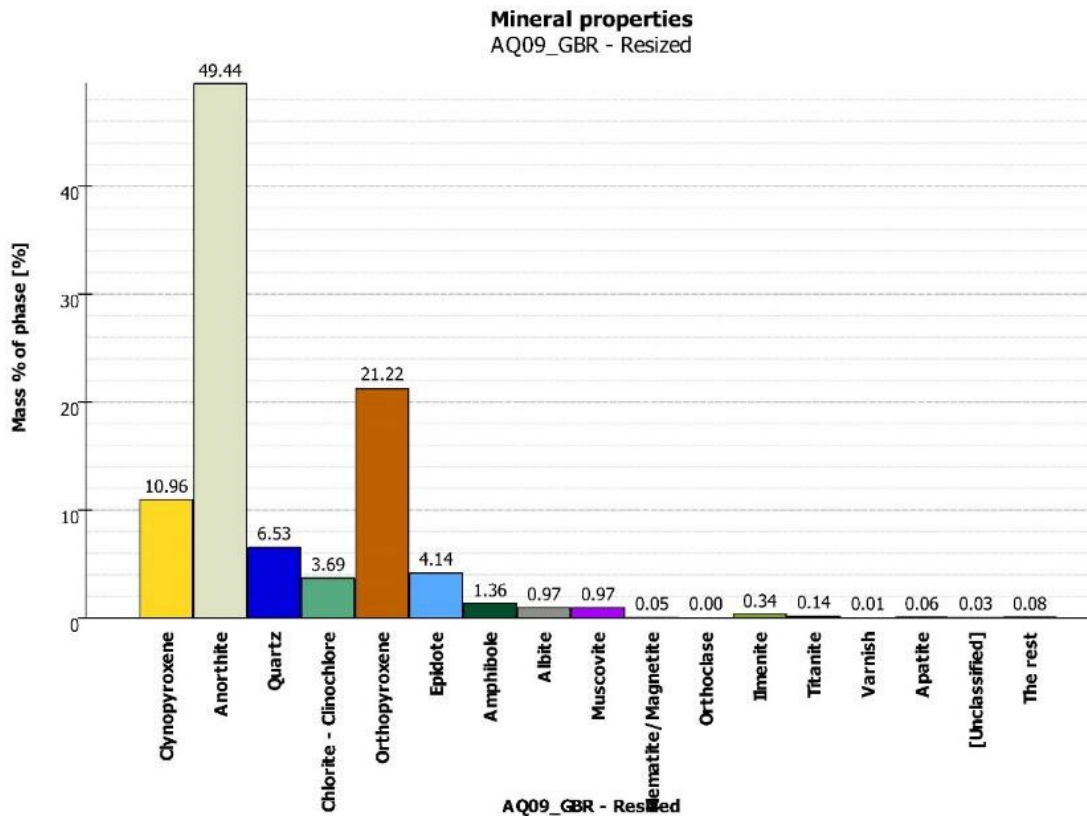


Figure C-124: Modal analysis of gabbro sample rock AQ09_GBR

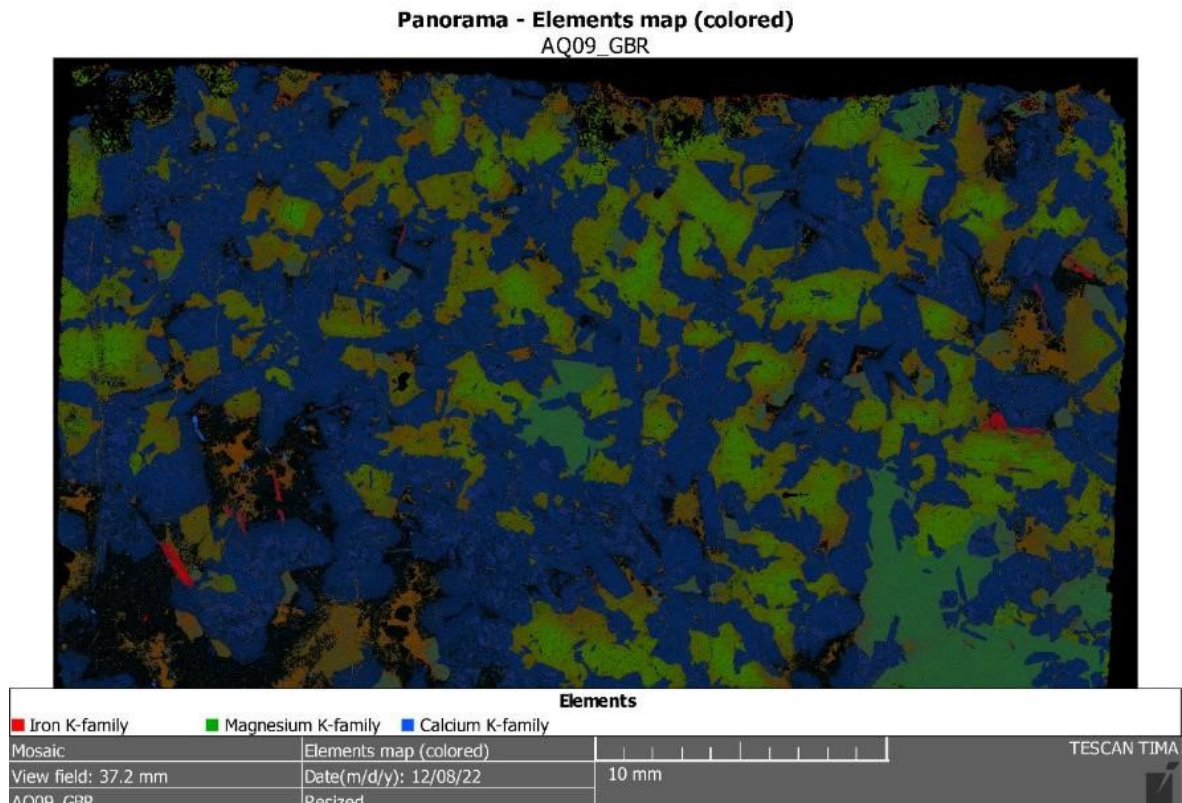


Figure C-125: Element map of gabbro sample rock AQ09_GBR

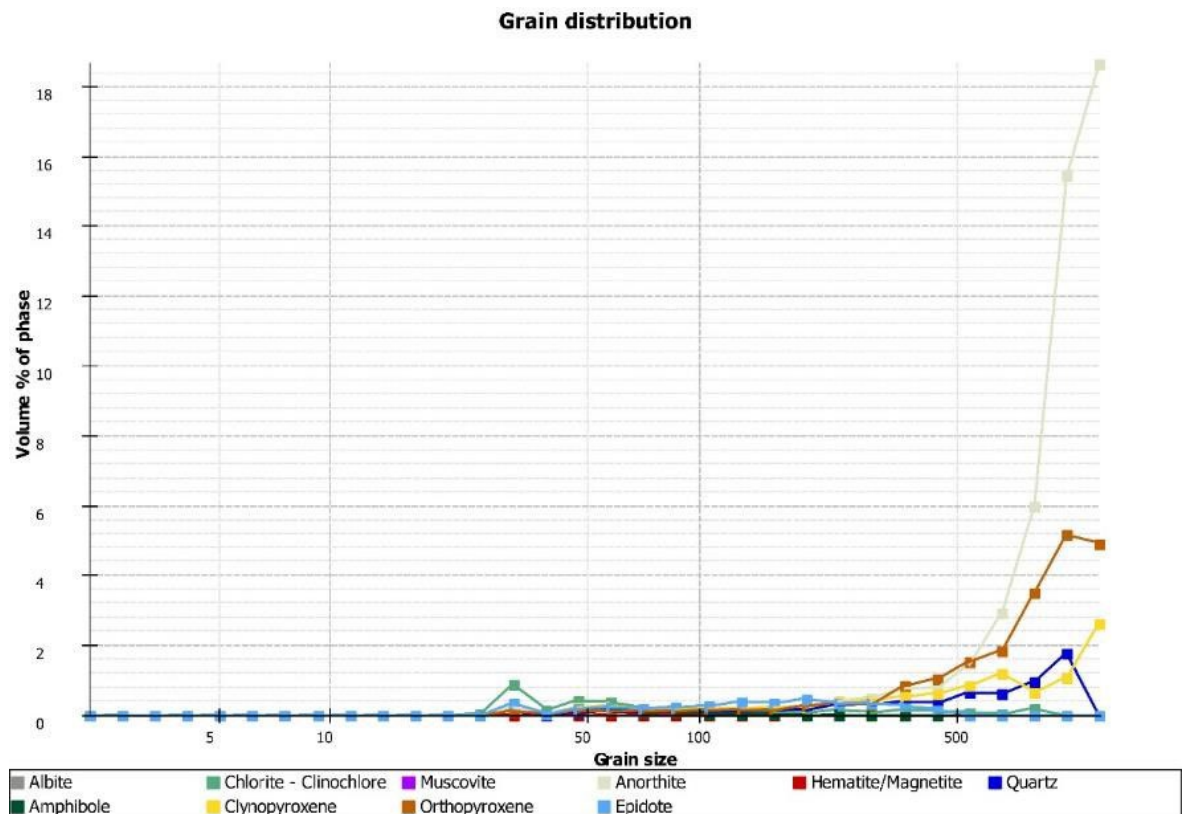


Figure C-126: Grain size distribution of gabbro sample rock AQ09_GBR

C-3-3 Sample rock AQ16_GBR

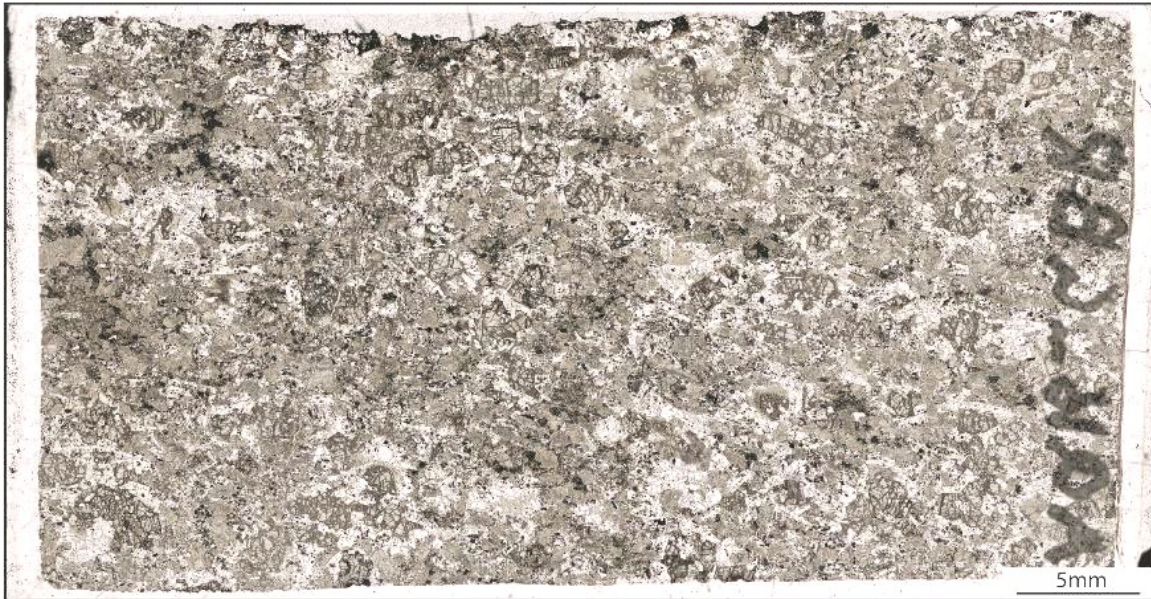


Figure C-127: Panorama image of gabbro sample rock AQ16_GBR

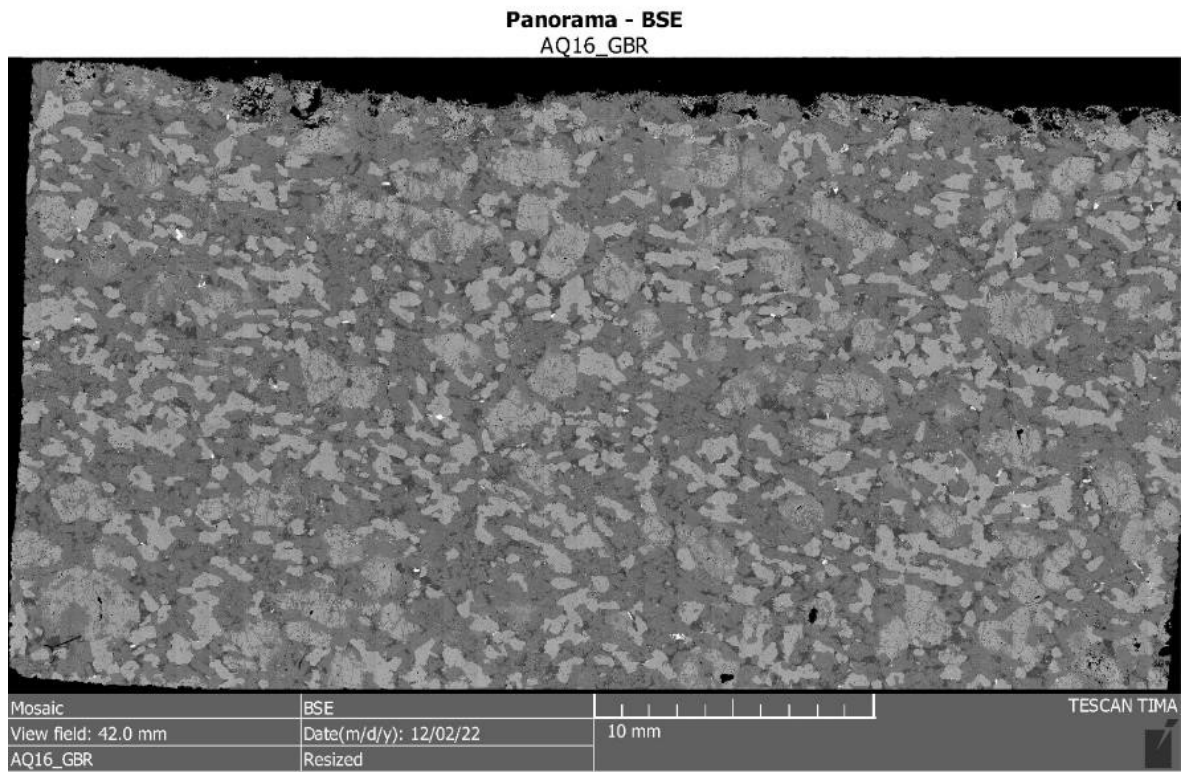


Figure C-128: BSE image of gabbro sample rock AQ16_GBR

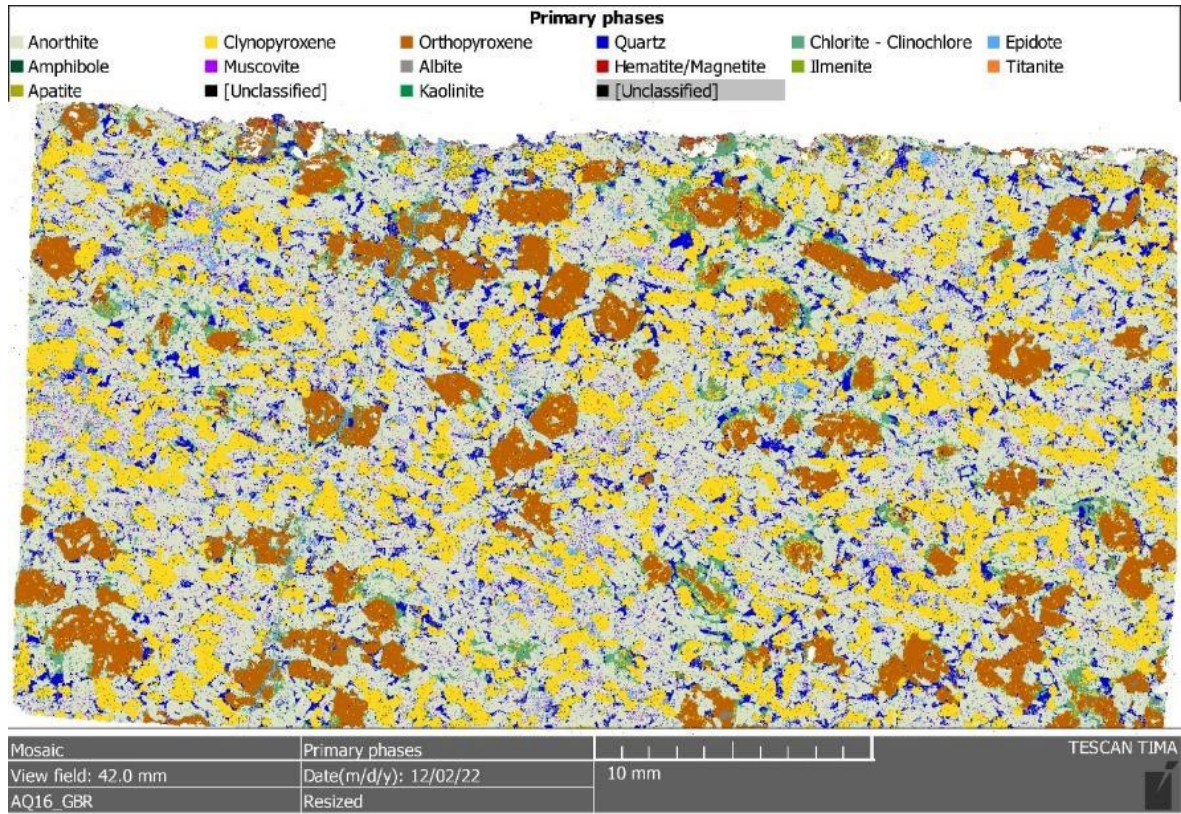


Figure C-129: Phase map of gabbro sample rock AQ16_GBR

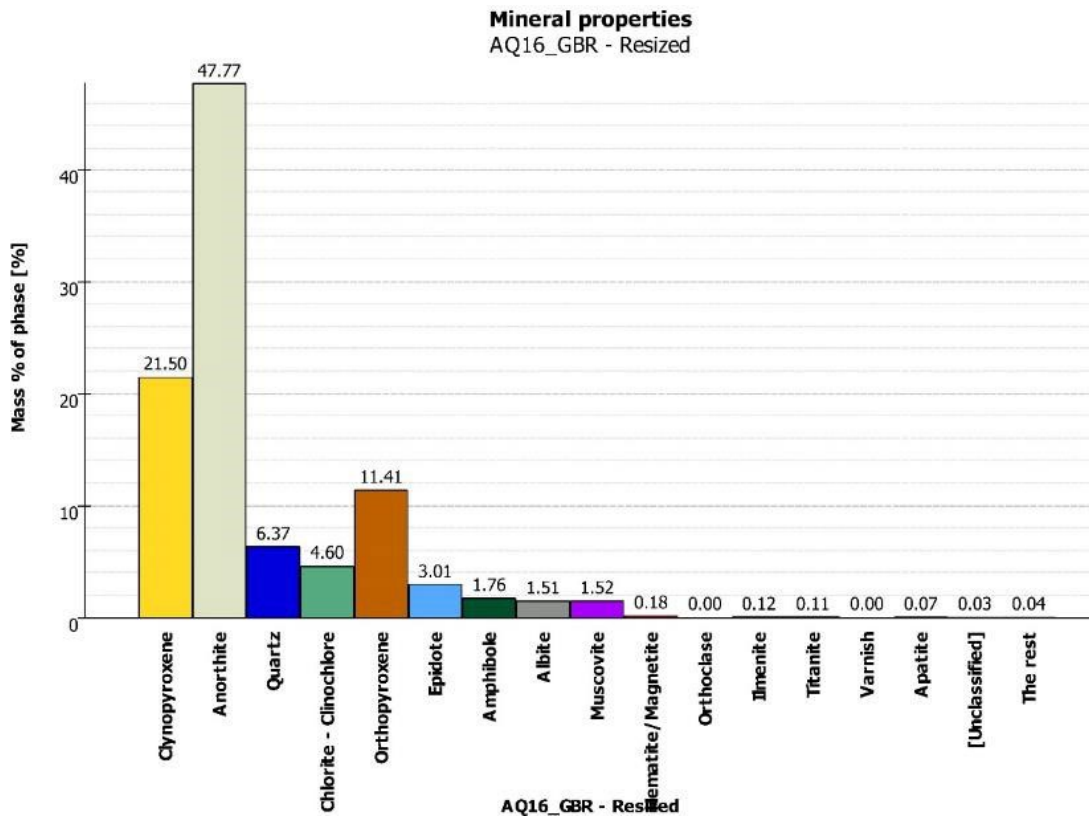


Figure C-130: Modal analysis of gabbro sample rock AQ16_GBR

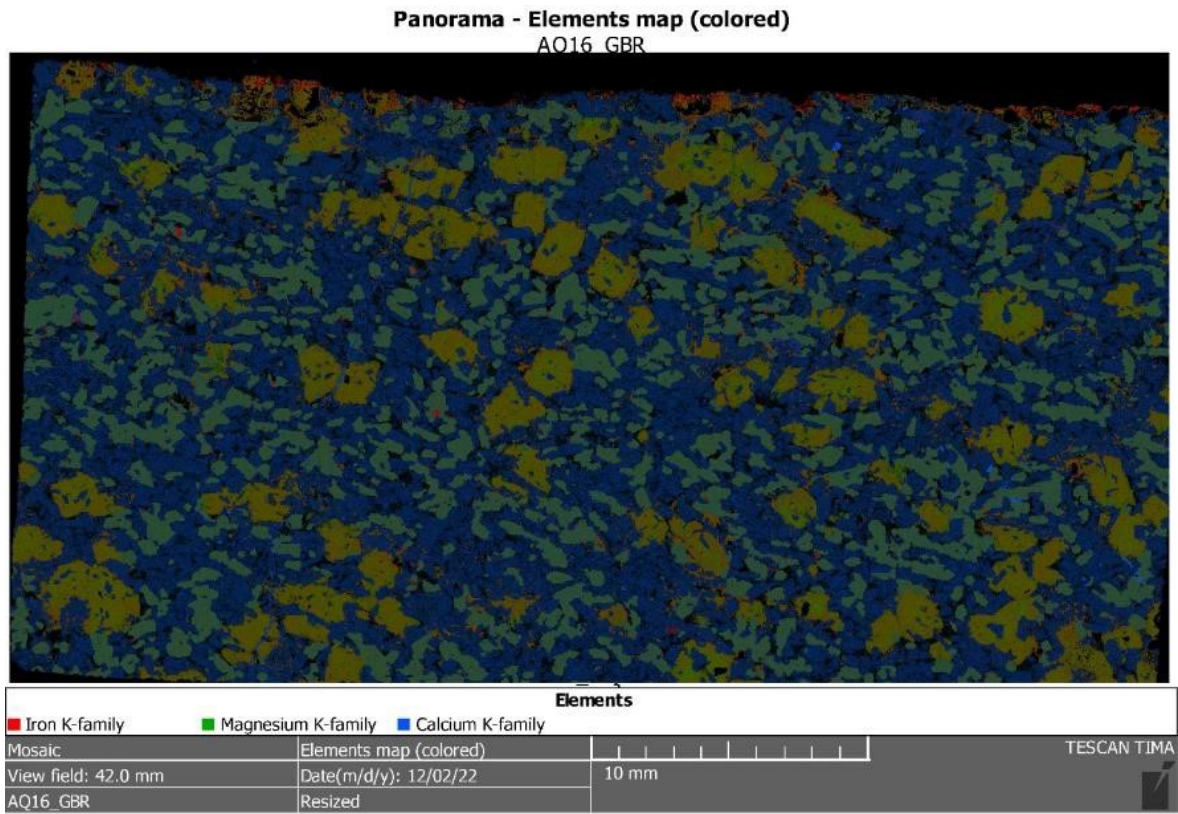


Figure C-131: Element map of gabbro sample rock AQ16_GBR

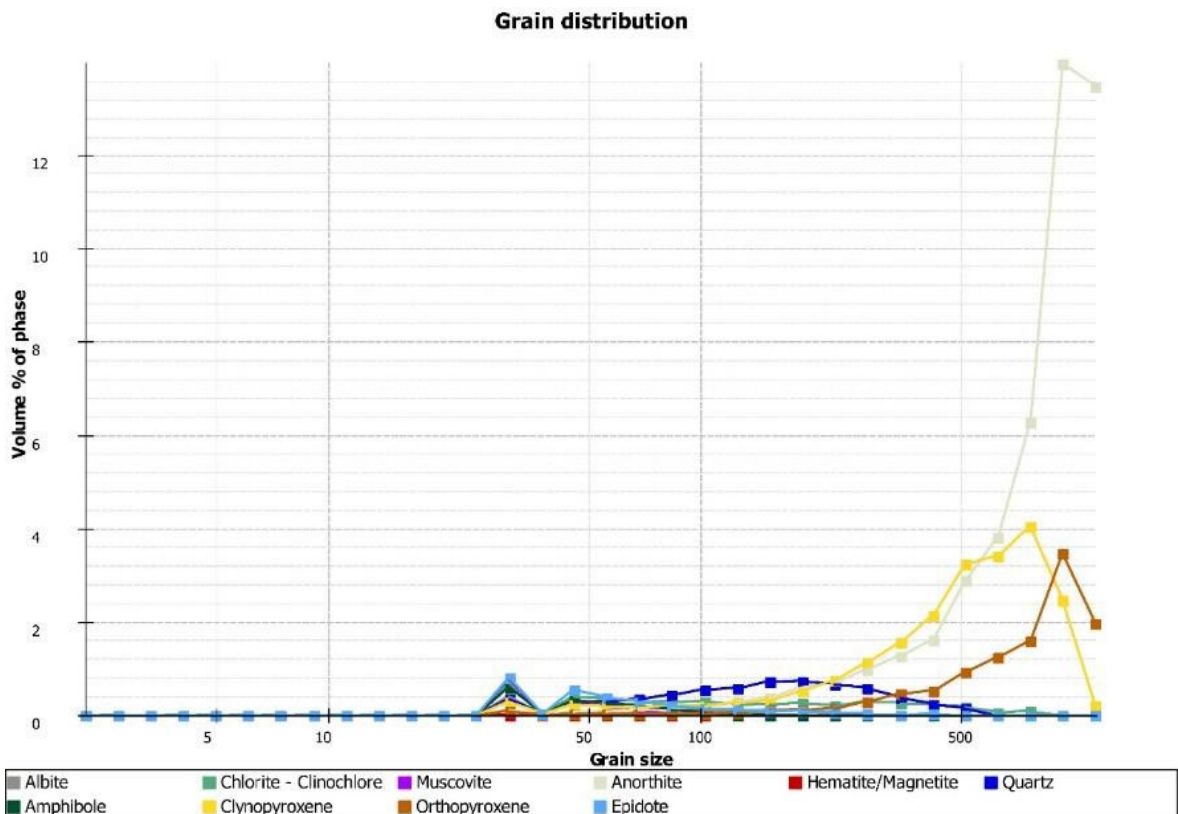


Figure C-132: Grain size distribution of gabbro sample rock AQ16_GBR

C-3-4 Sample rock EX04_GBR



Figure C-133: Panorama image of gabbro sample rock EX04_GBR

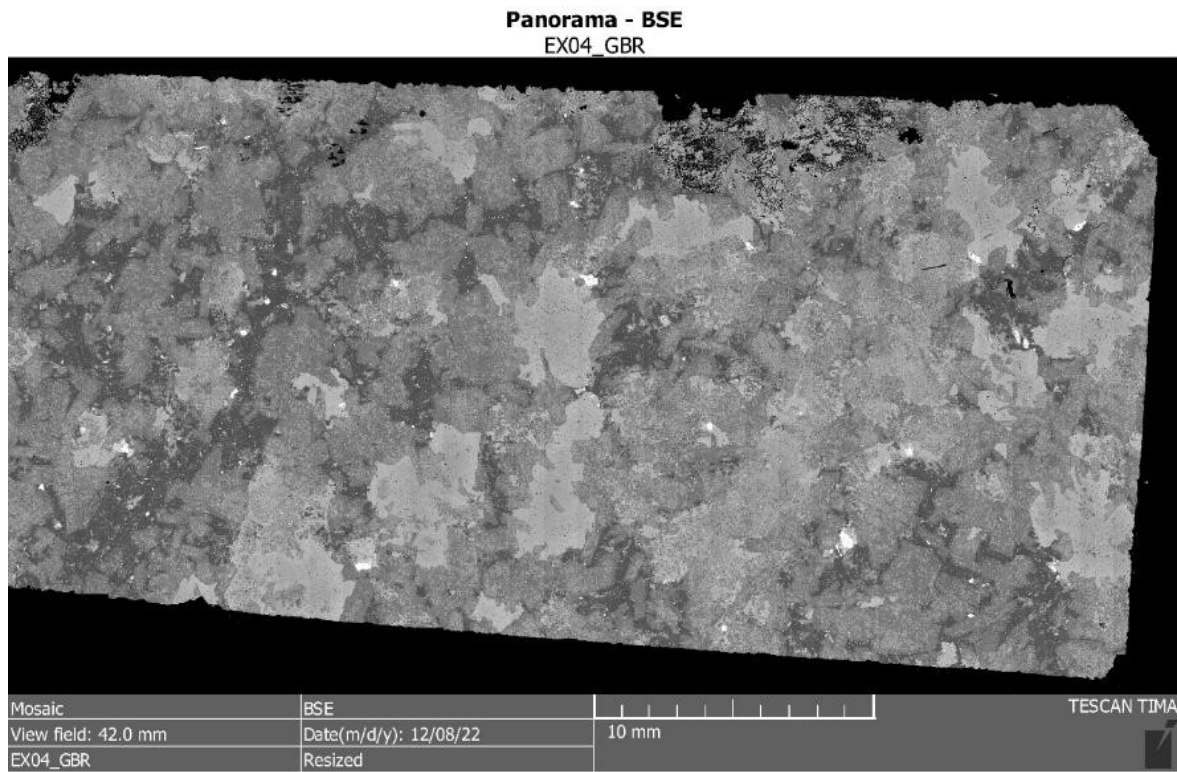


Figure C-134: BSE image of gabbro sample rock EX04_GBR

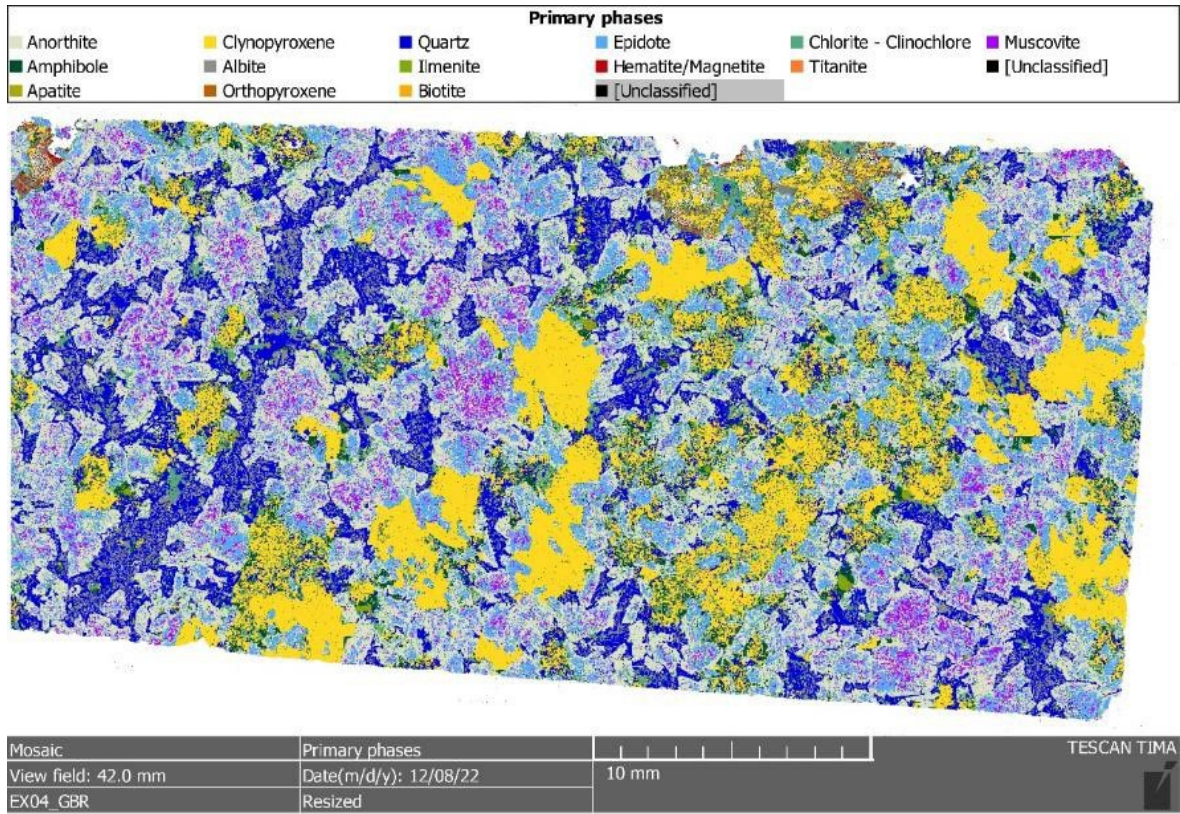


Figure C-135: Phase map of gabbro sample rock EX04_GBR

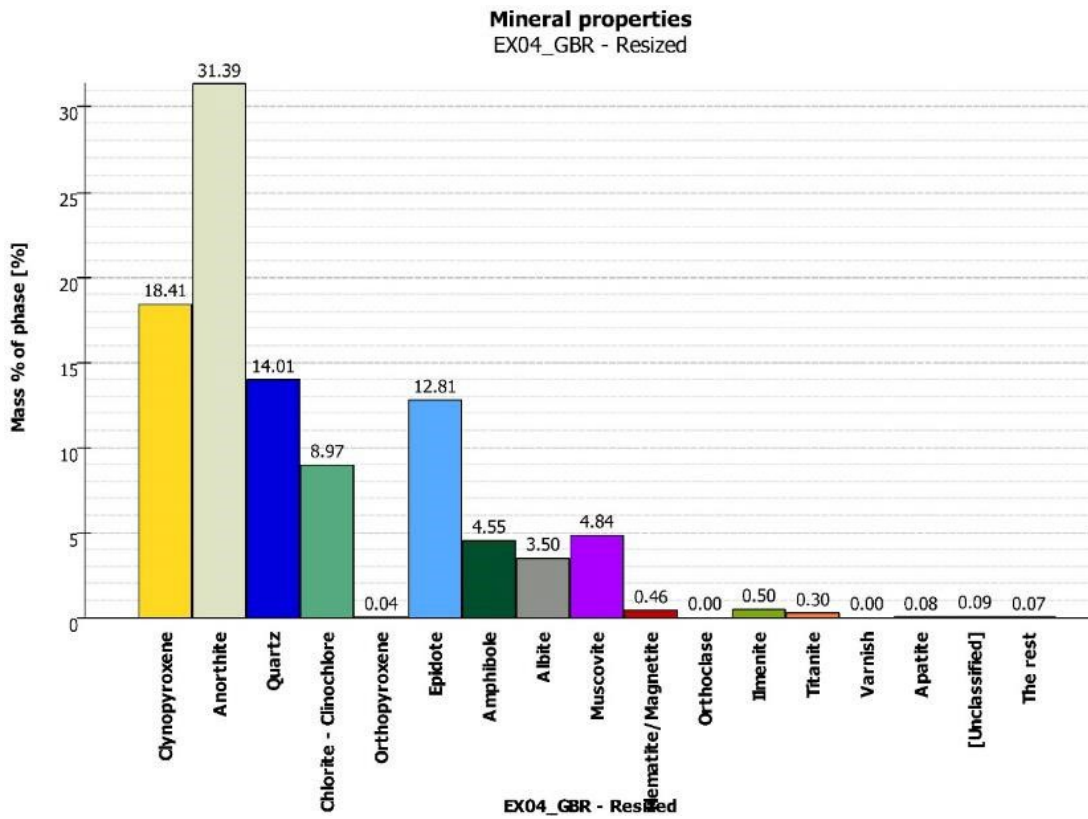


Figure C-136: Modal analysis of gabbro sample rock EX04_GBR

Panorama - Elements map (colored)
EX04_GBR

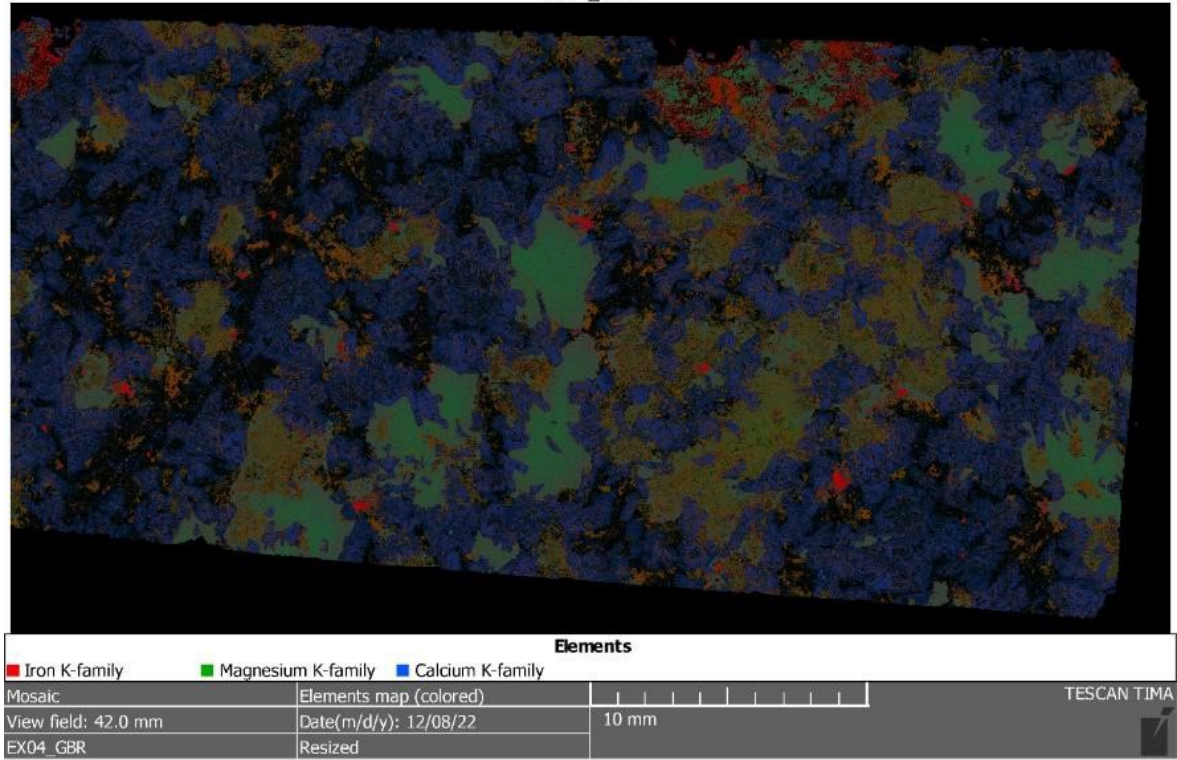


Figure C-137: Element map of gabbro sample rock EX04_GBR

Grain distribution

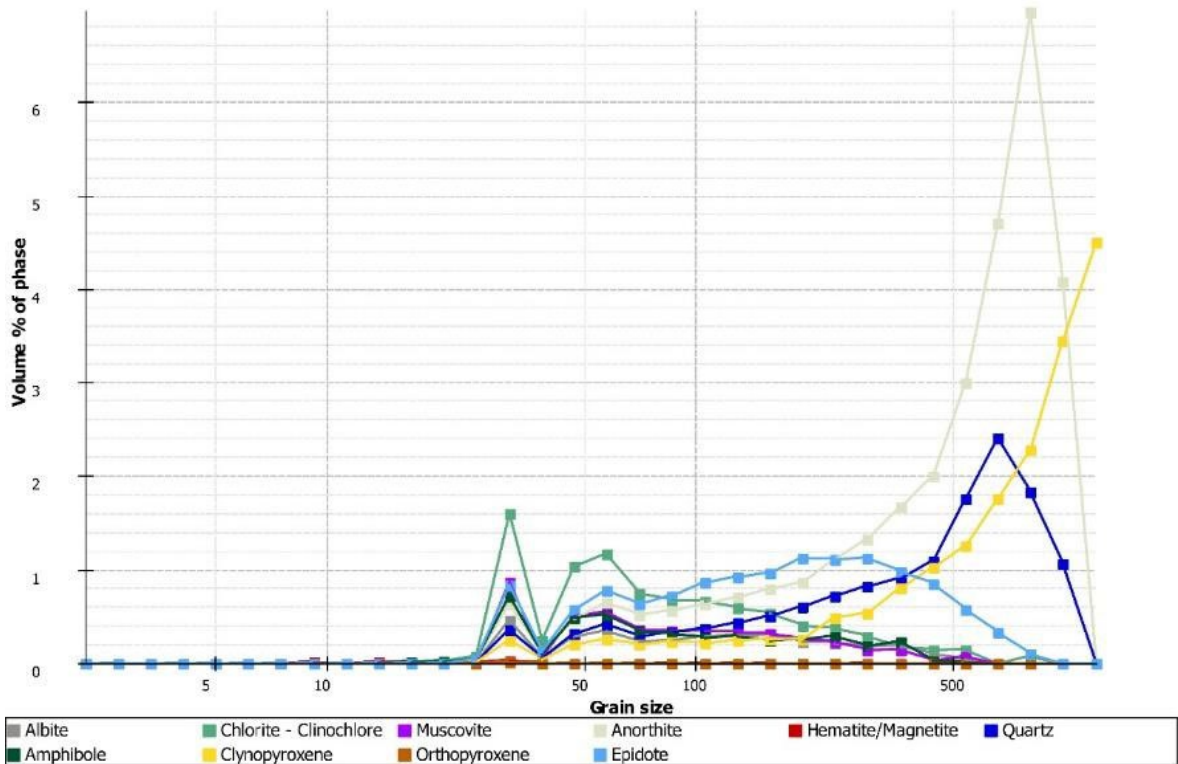


Figure C-138: Grain size distribution of gabbro sample rock EX04_GBR

C-3-5 Sample rock EX09_GBR



Figure C-139: Panorama image of gabbro sample rock EX09_GBR

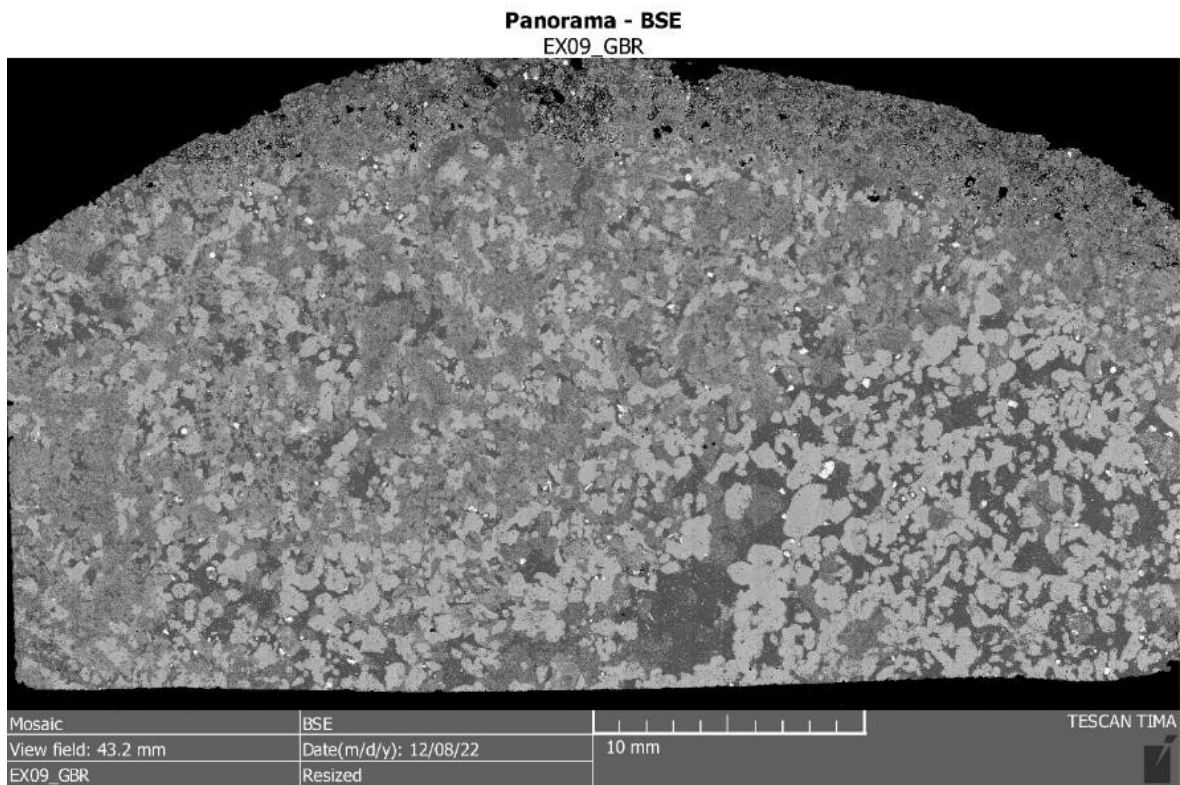


Figure C-140: BSE image of gabbro sample rock EX09_GBR

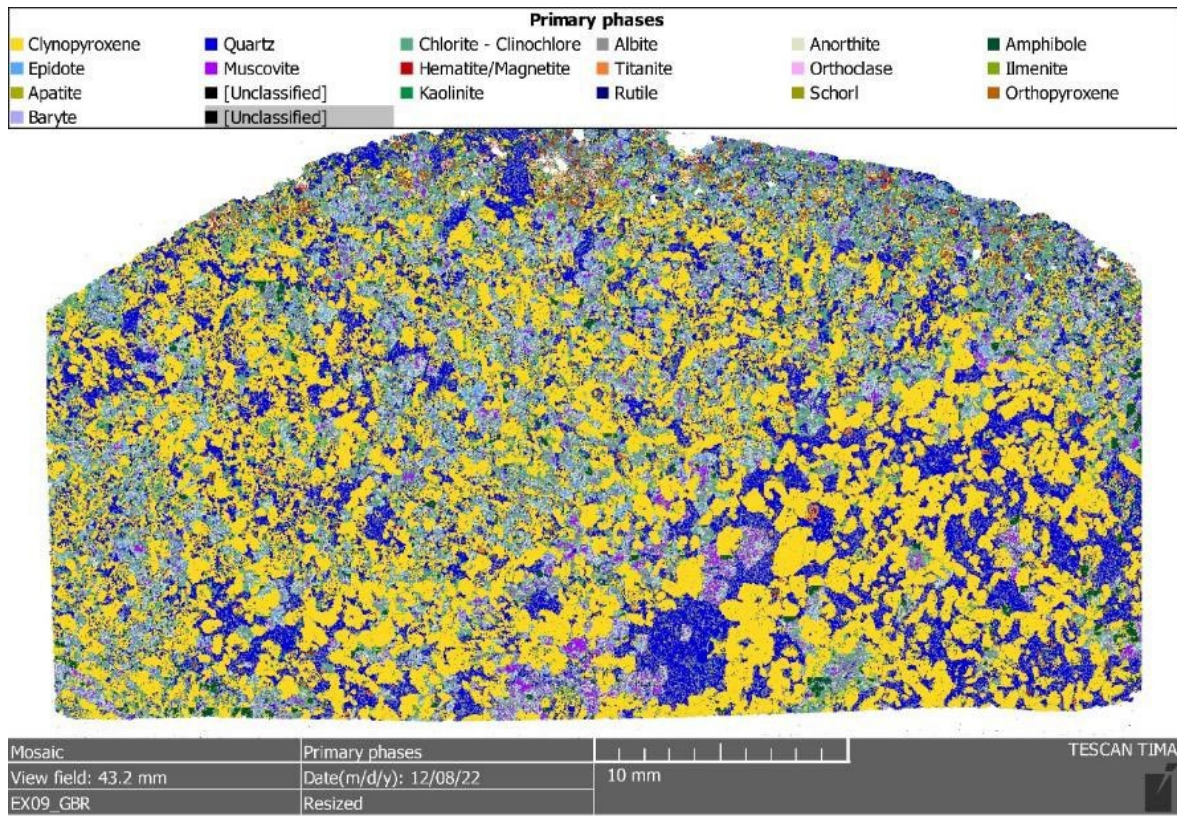


Figure C-141: : Phase map of gabbro sample rock EX09_GBR

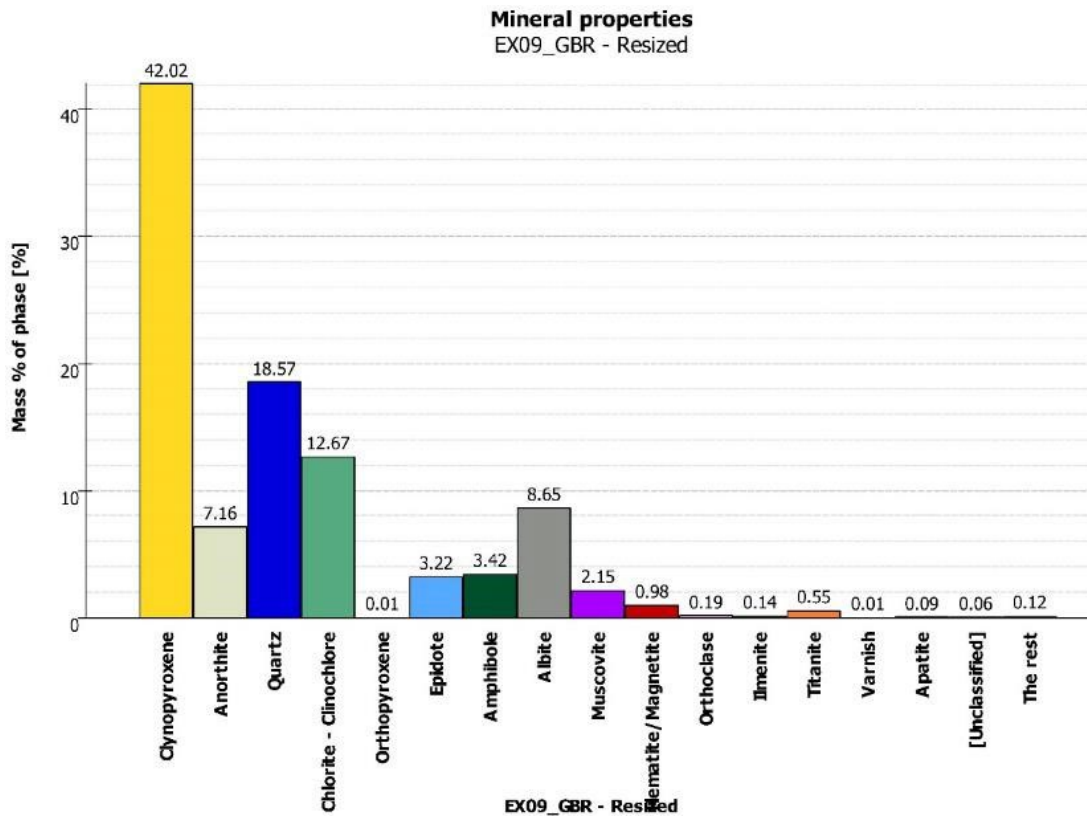


Figure C-142: Modal analysis of gabbro sample rock EX09_GBR

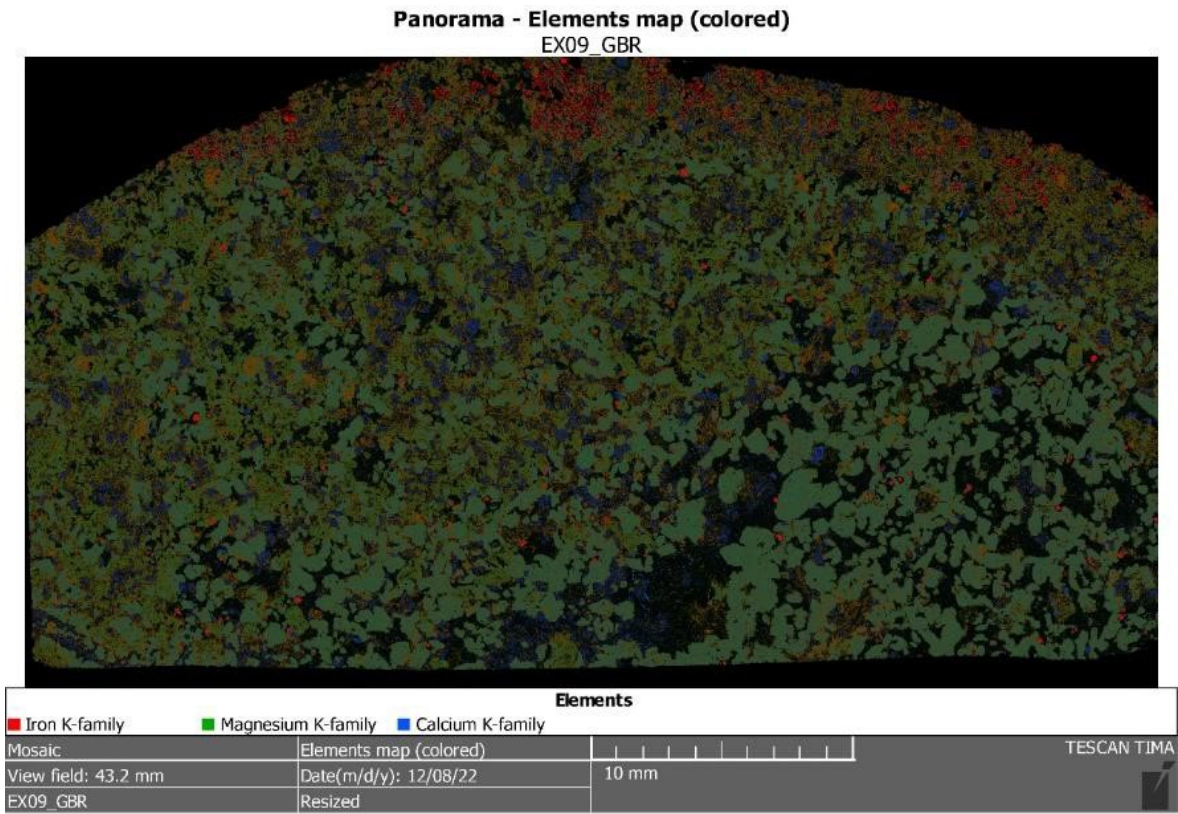


Figure C-143: Element map of gabbro sample rock EX09_GBR

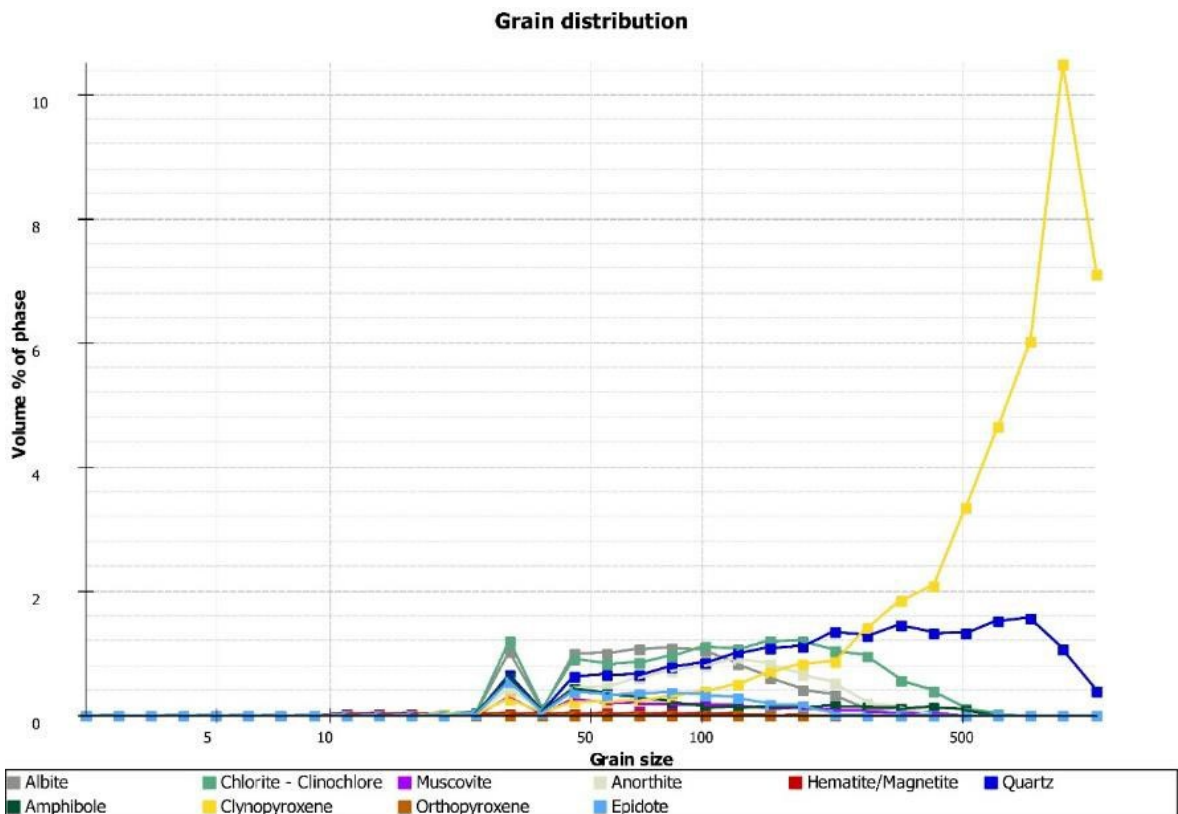


Figure C-144: Grain size distribution of gabbro sample rock EX09_GBR

C-3-6 Sample rock RS02_GBR

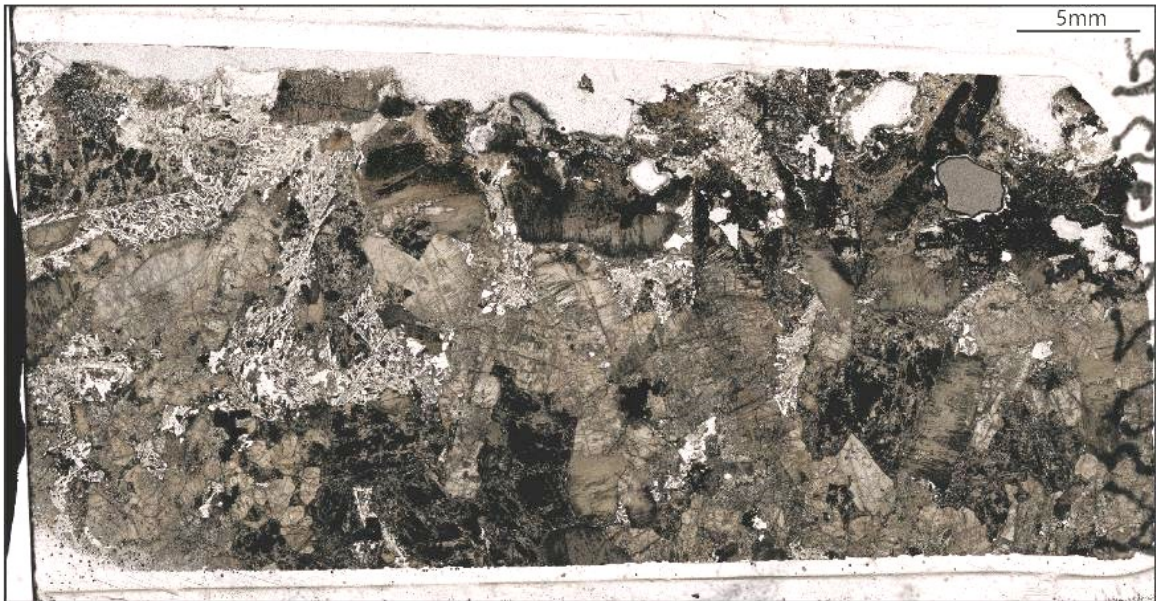


Figure C-145: Panorama image of gabbro sample rock RS02_GBR

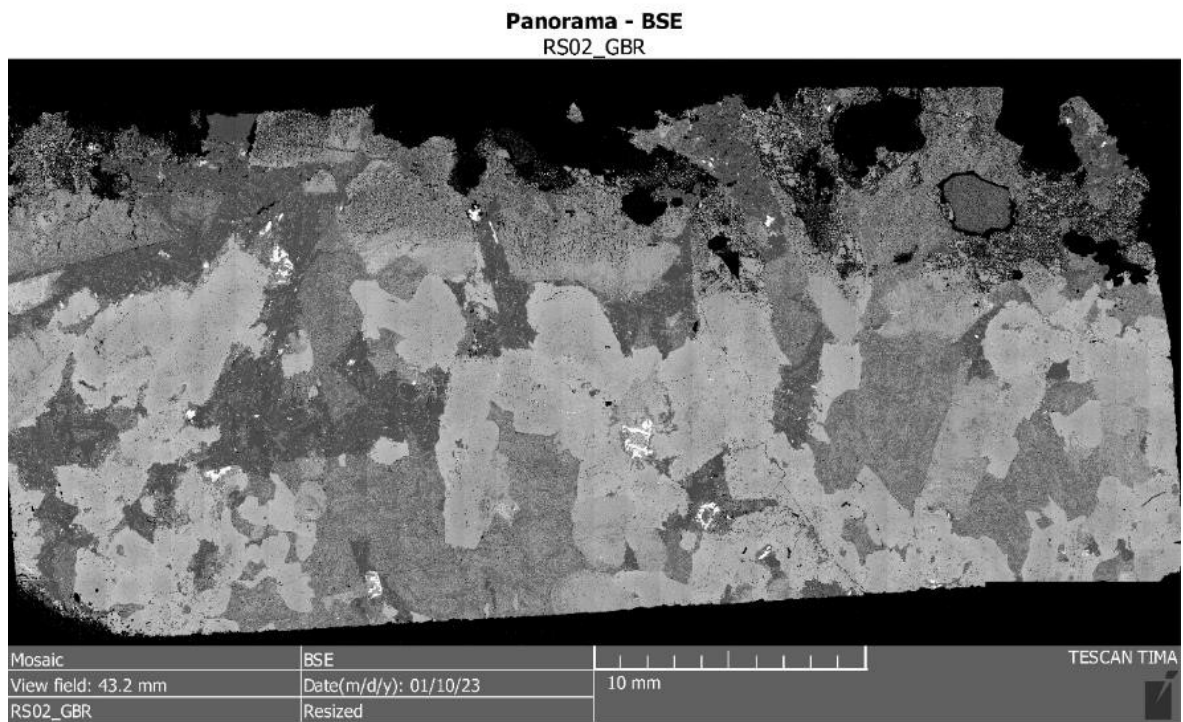


Figure C-146: BSE image of gabbro sample rock RS02_GBR

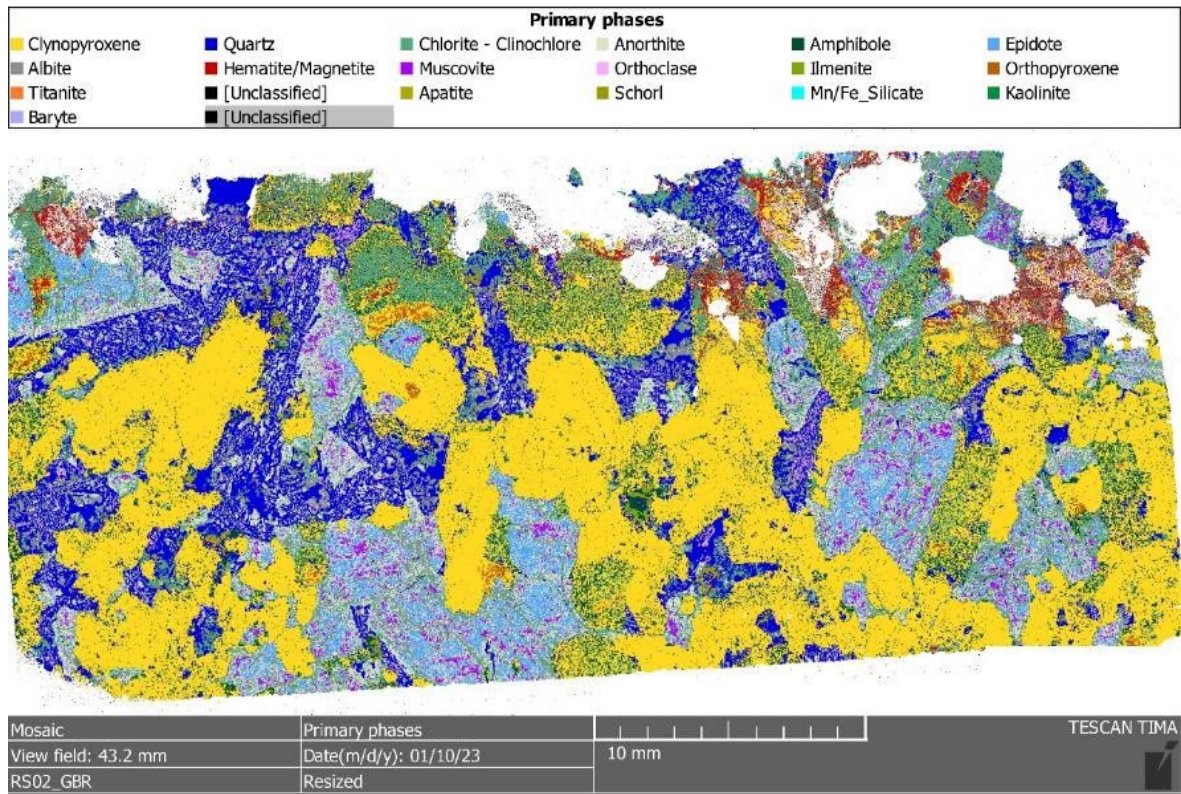


Figure C-147: Phase map of gabbro sample rock RS02_GBR

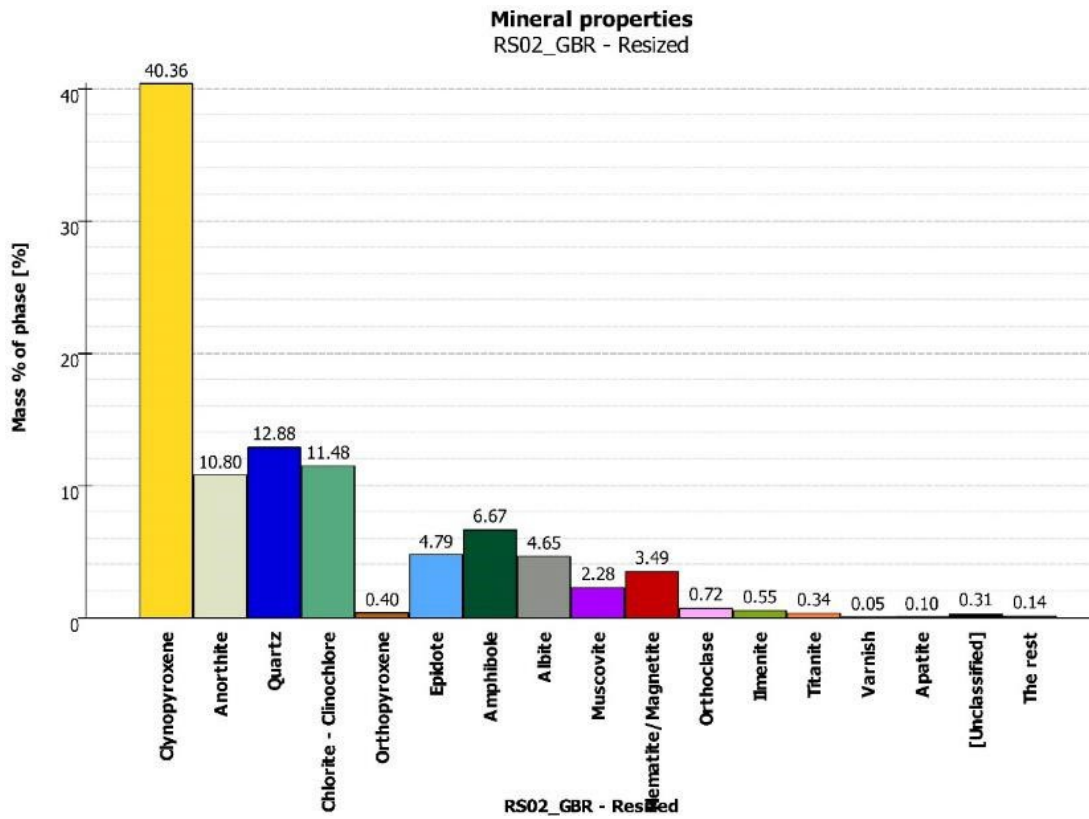


Figure C-148: Modal analysis of gabbro sample rock RS02_GBR

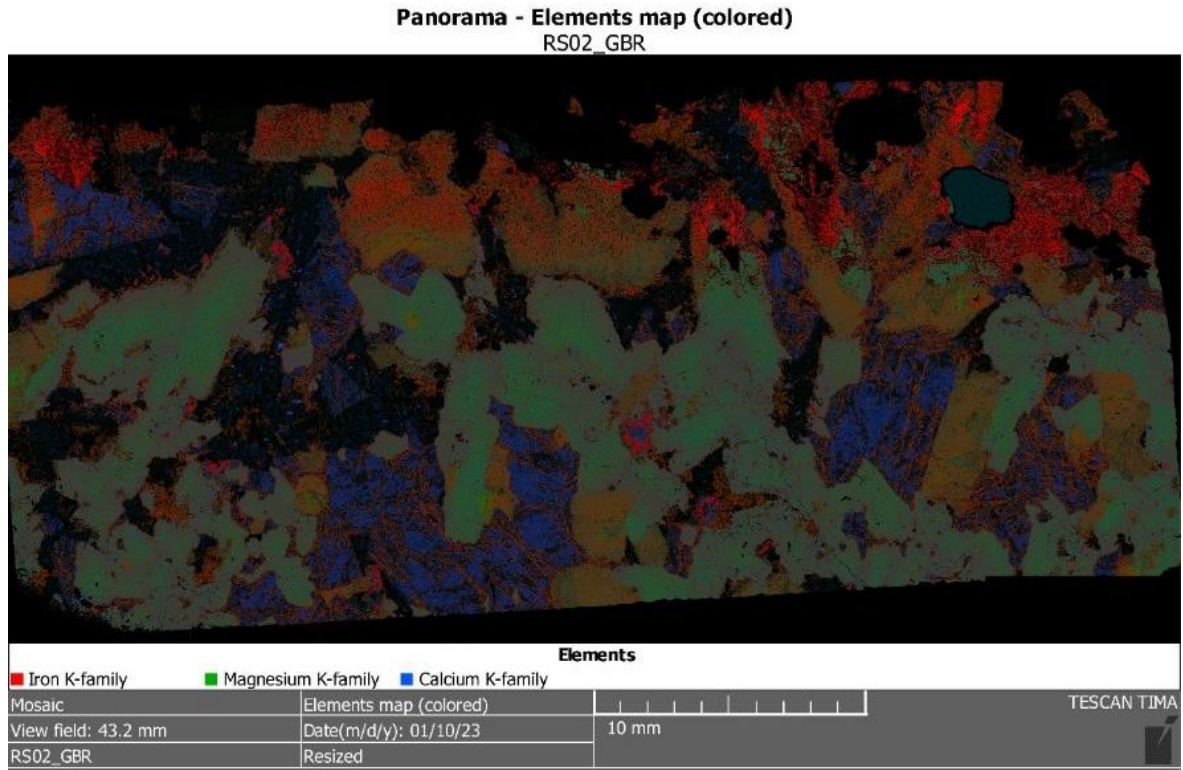


Figure C-149: Element map of gabbro sample rock RS02_GBR

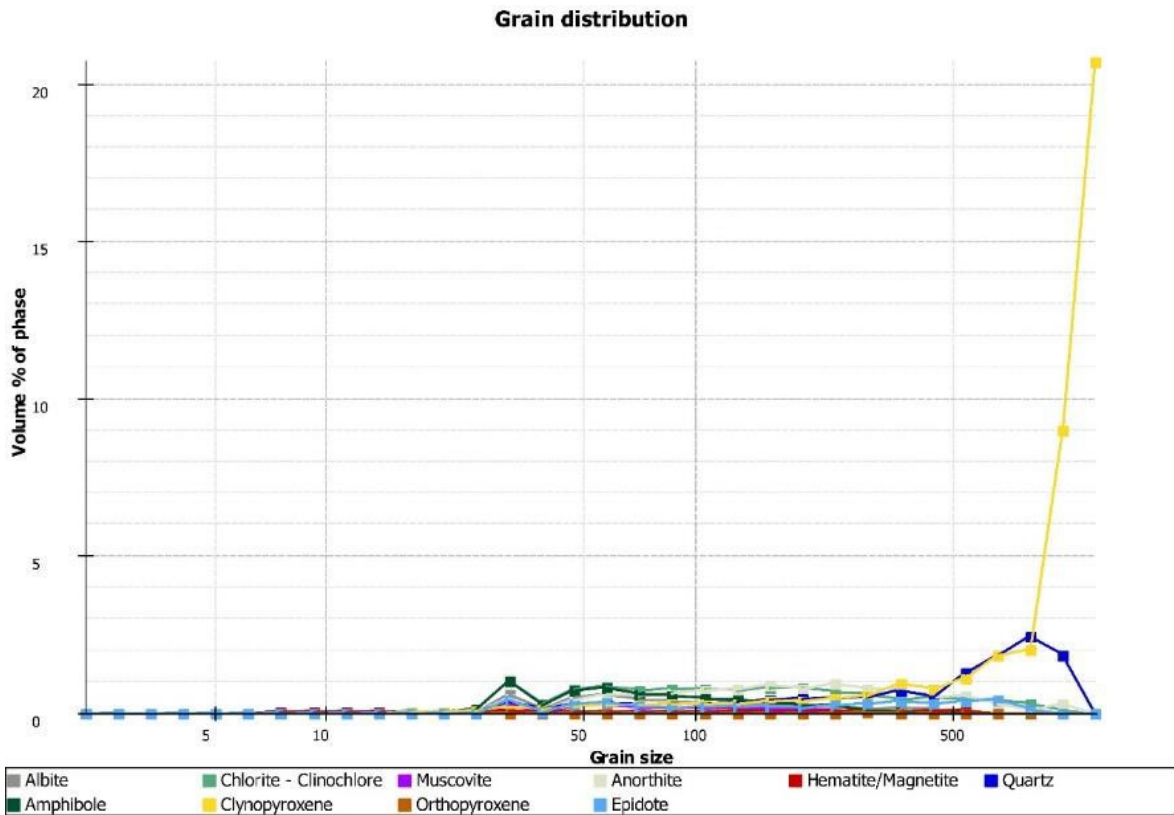


Figure C-150: Grain size distribution of gabbro sample rock RS02_GBR

C-3-7 Sample rock RS10_GBR



Figure C-151: Panorama image of gabbro sample rock RS10_GBR

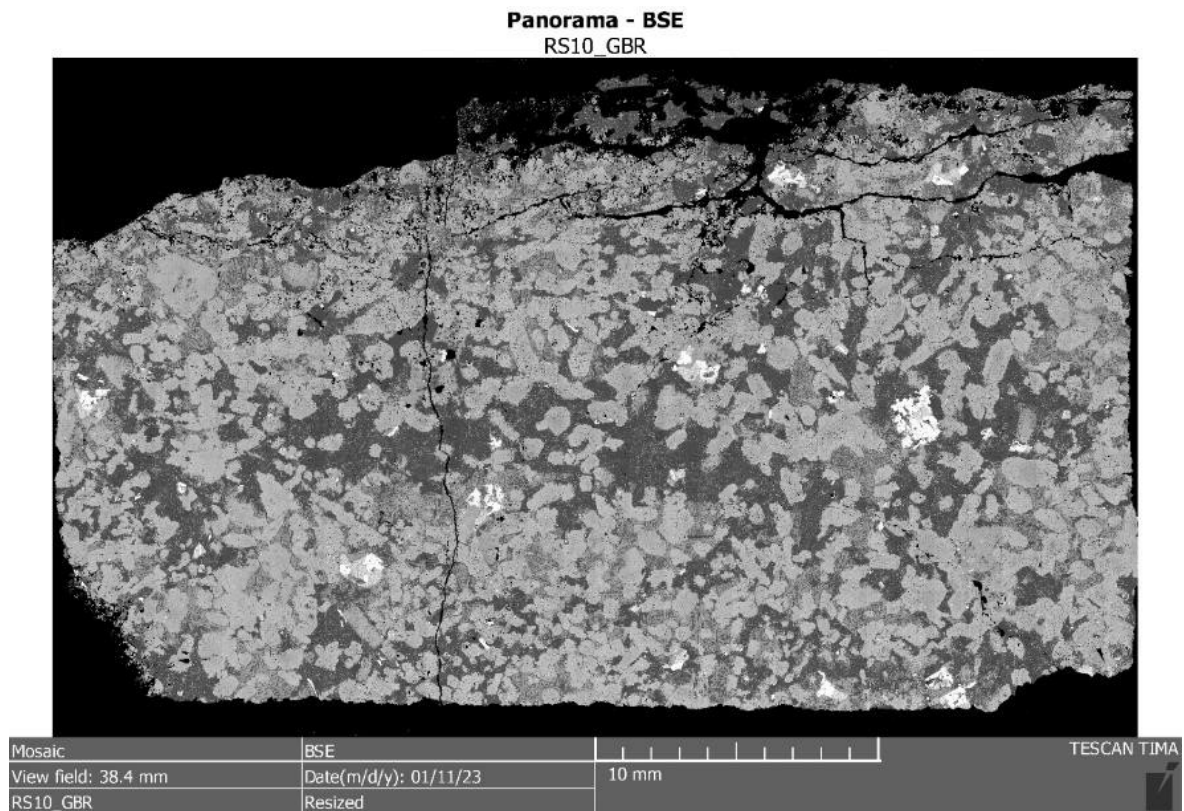


Figure C-152: BSE image of gabbro sample rock RS10_GBR

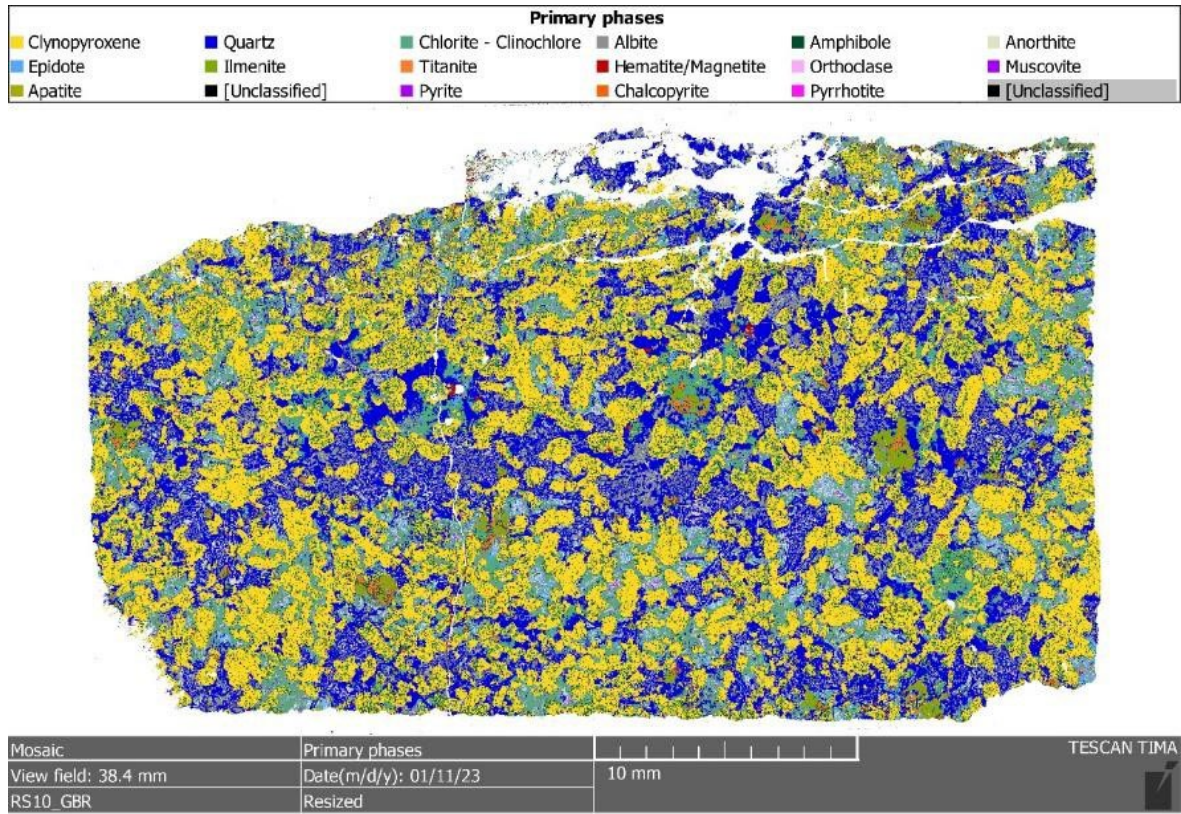


Figure C-153: Phase map of gabbro sample rock RS10_GBR

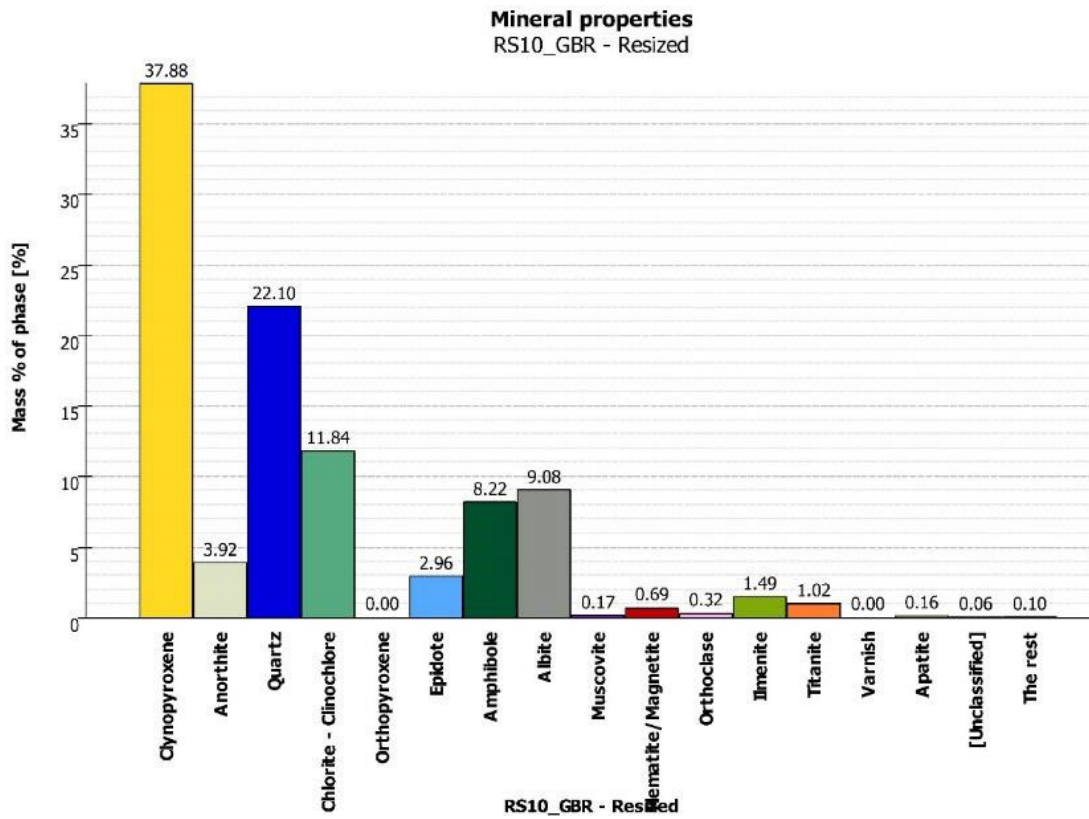


Figure C-154: Modal analysis of gabbro sample rock RS10_GBR

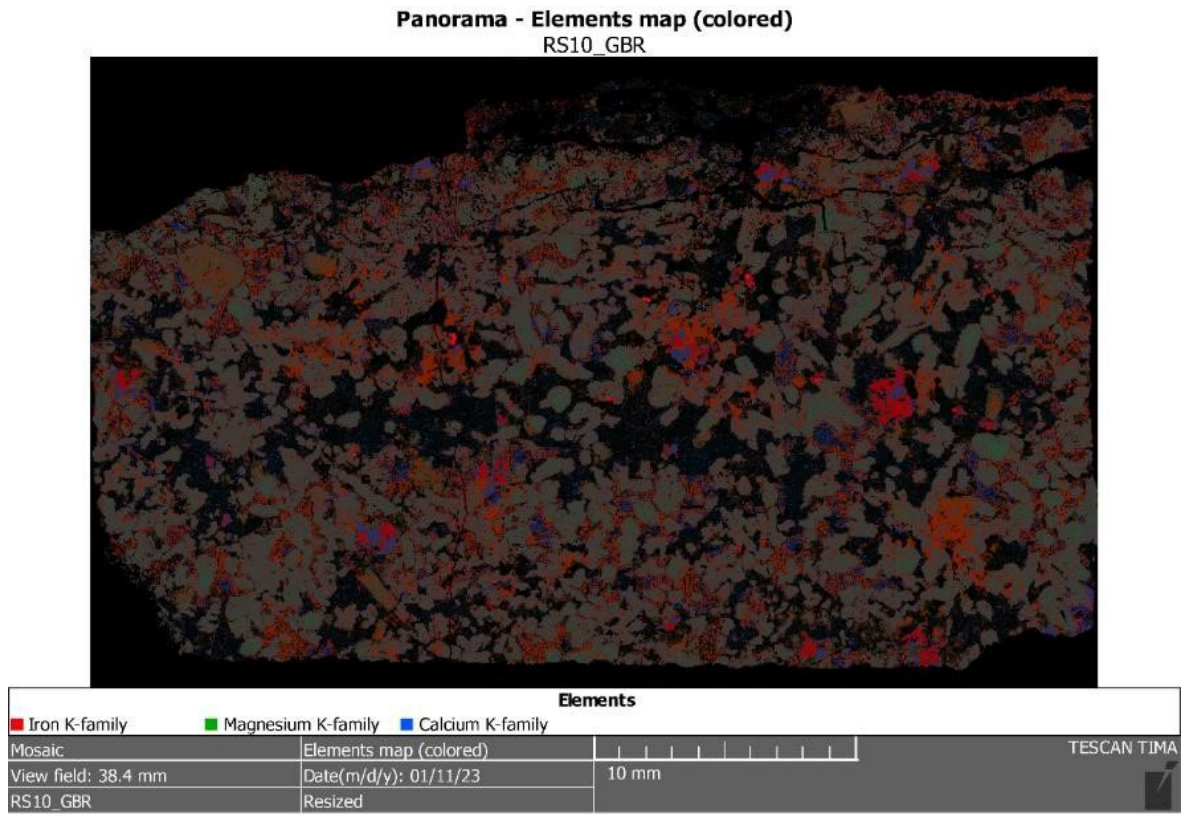


Figure C-155: Element map of gabbro sample rock RS10_GBR

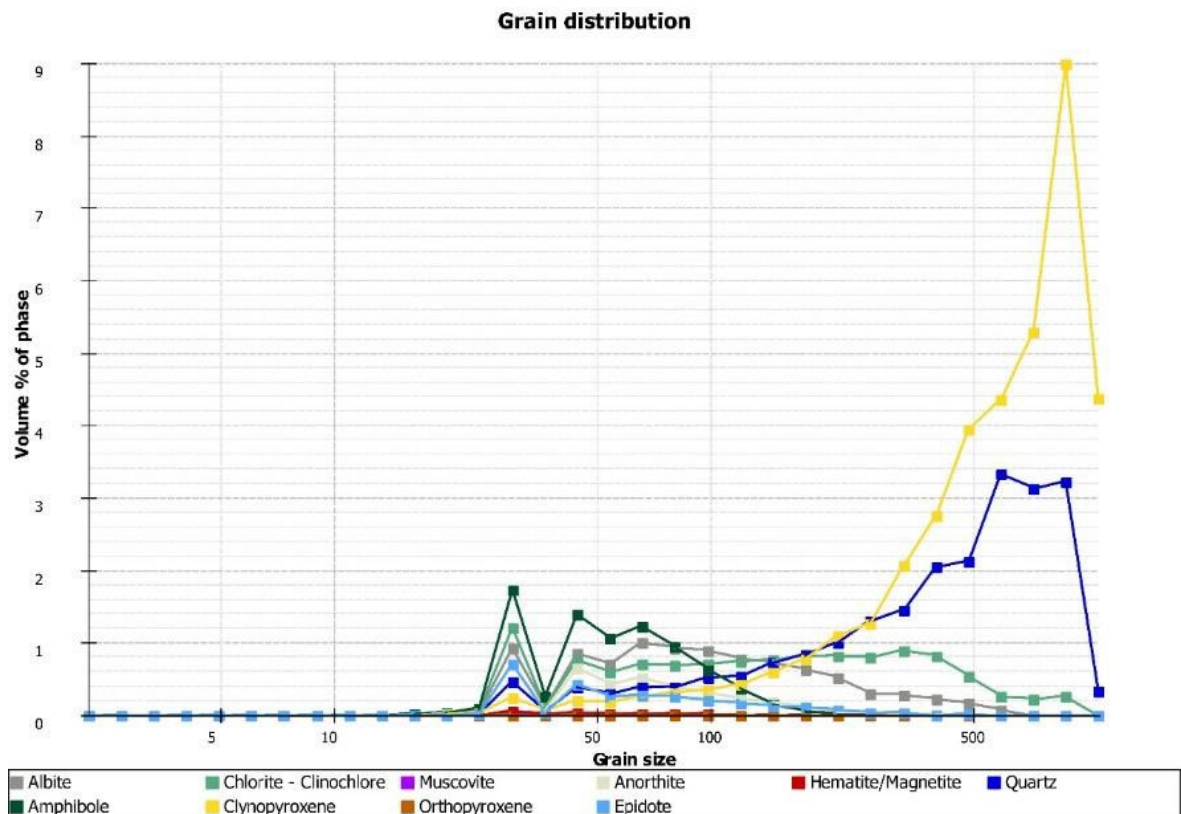


Figure C-156: Grain size distribution of gabbro sample rock RS10_GBR

C-3-8 Sample rock RS16_GBR

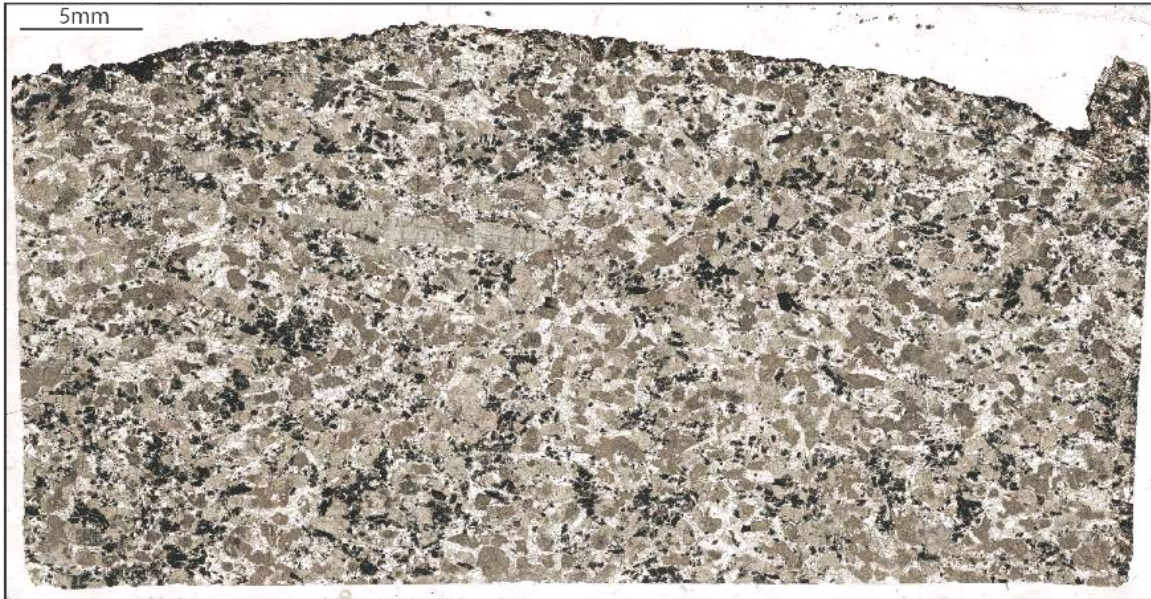


Figure C-157: Panorama image of gabbro sample rock RS16_GBR

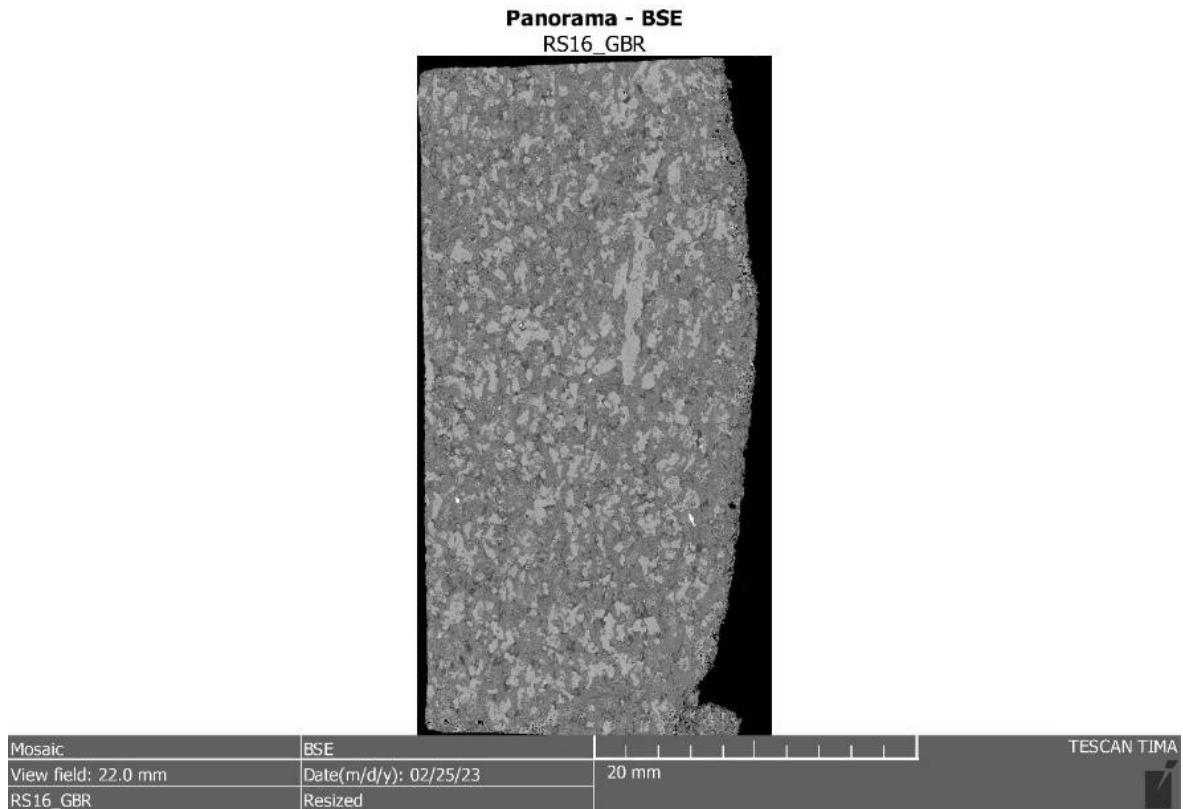


Figure C-158: BSE image of gabbro sample rock RS16_GBR

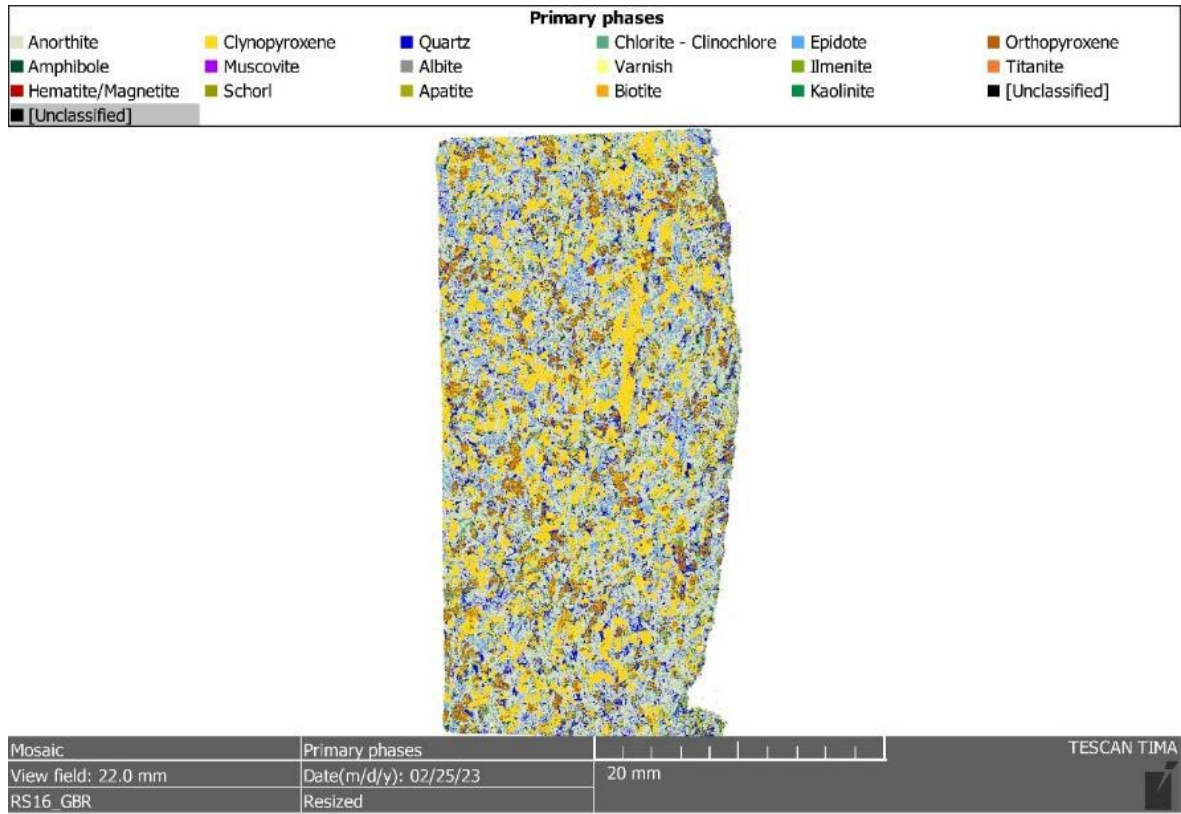


Figure C-159: Phase map of gabbro sample rock RS16_GBR

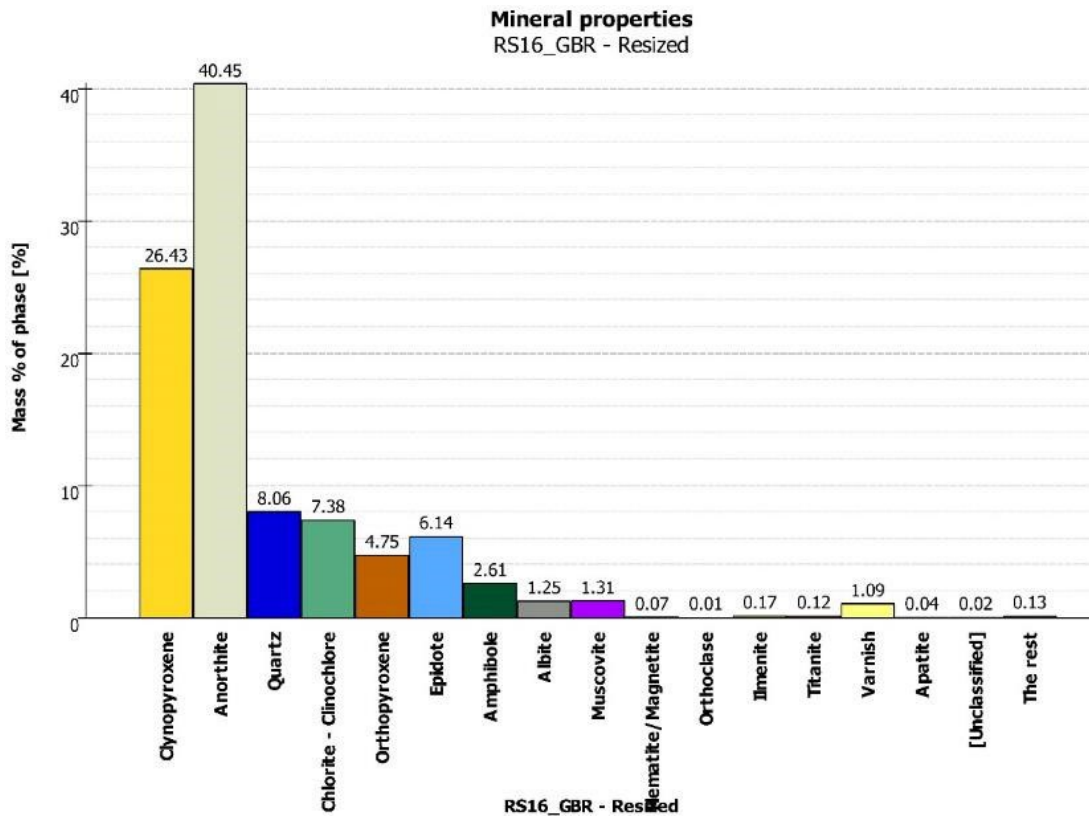


Figure C-160: Modal analysis of gabbro sample rock RS16_GBR

Panorama - Elements map (colored)
RS16_GBR

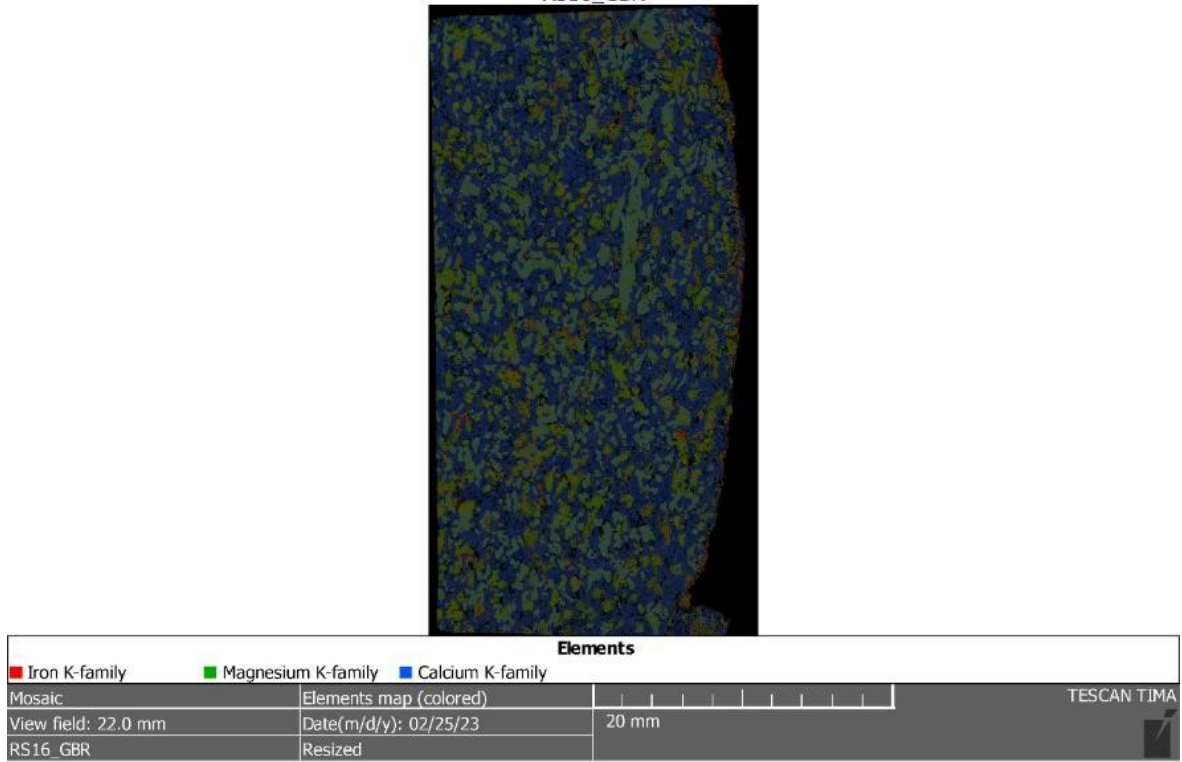


Figure C-161: Element map of gabbro sample rock RS16_GBR

Grain distribution

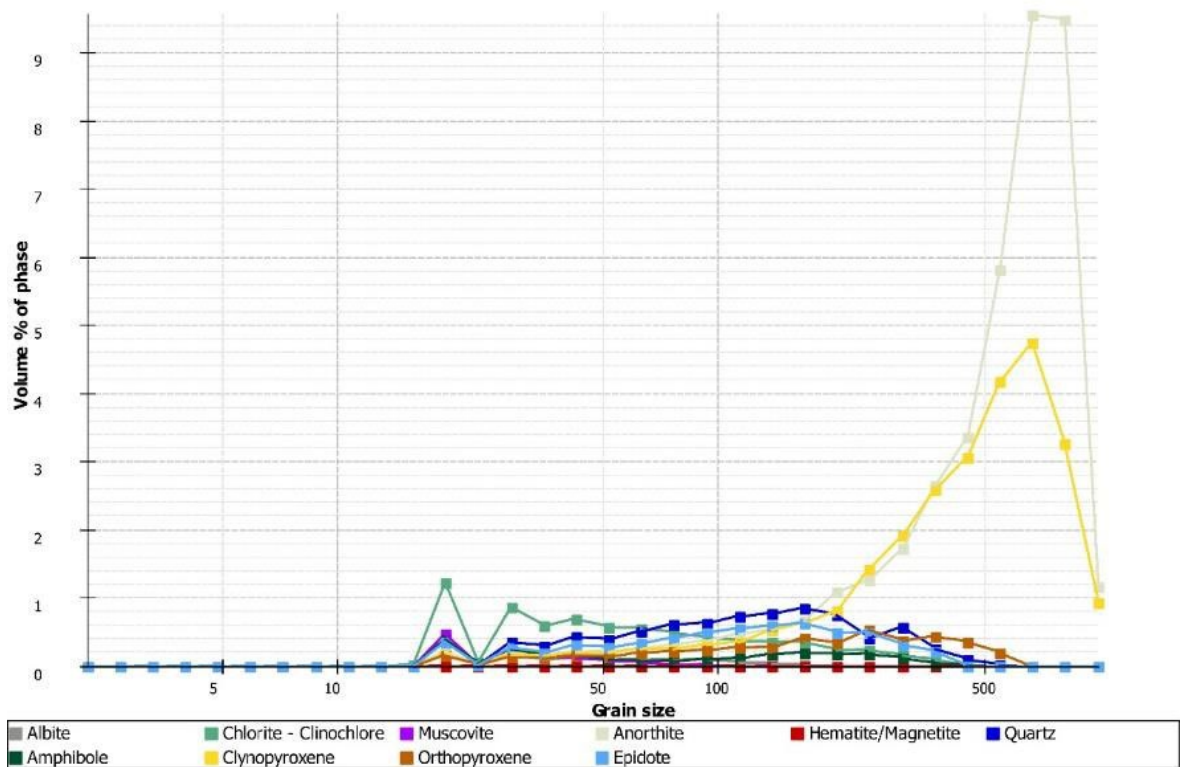


Figure C-162: Grain size distribution of gabbro sample rock RS16_GBR

Appendix C-4 Granite

C-4-1 Sample rock RS02_GRT



Figure C-163: Panorama image of granite sample rock RS02_GRT

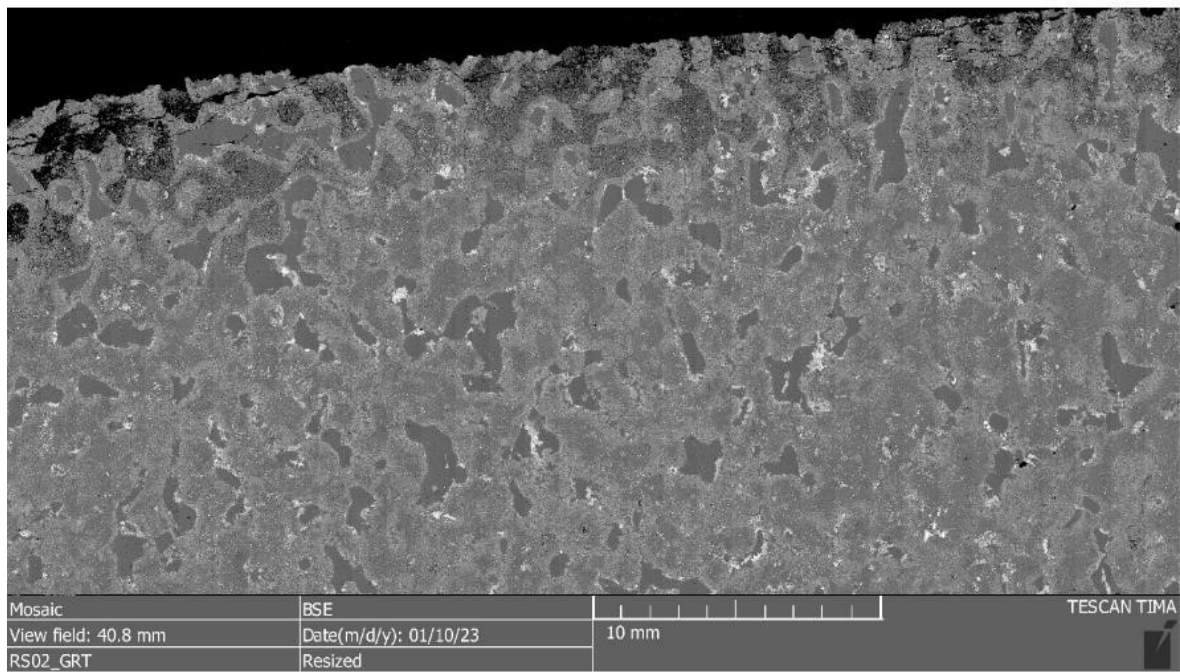


Figure C-164: BSE image of granite sample rock RS02_GRT

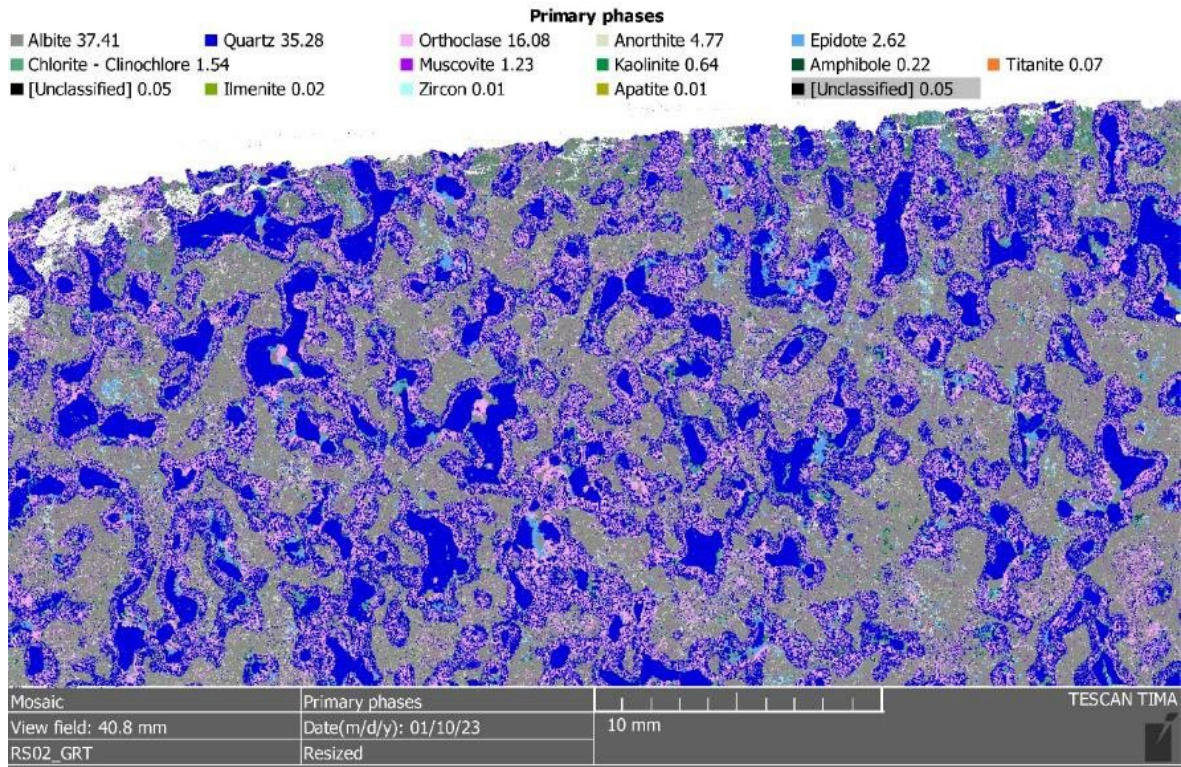


Figure C-165: Phase map of granite sample rock RS02_GRT

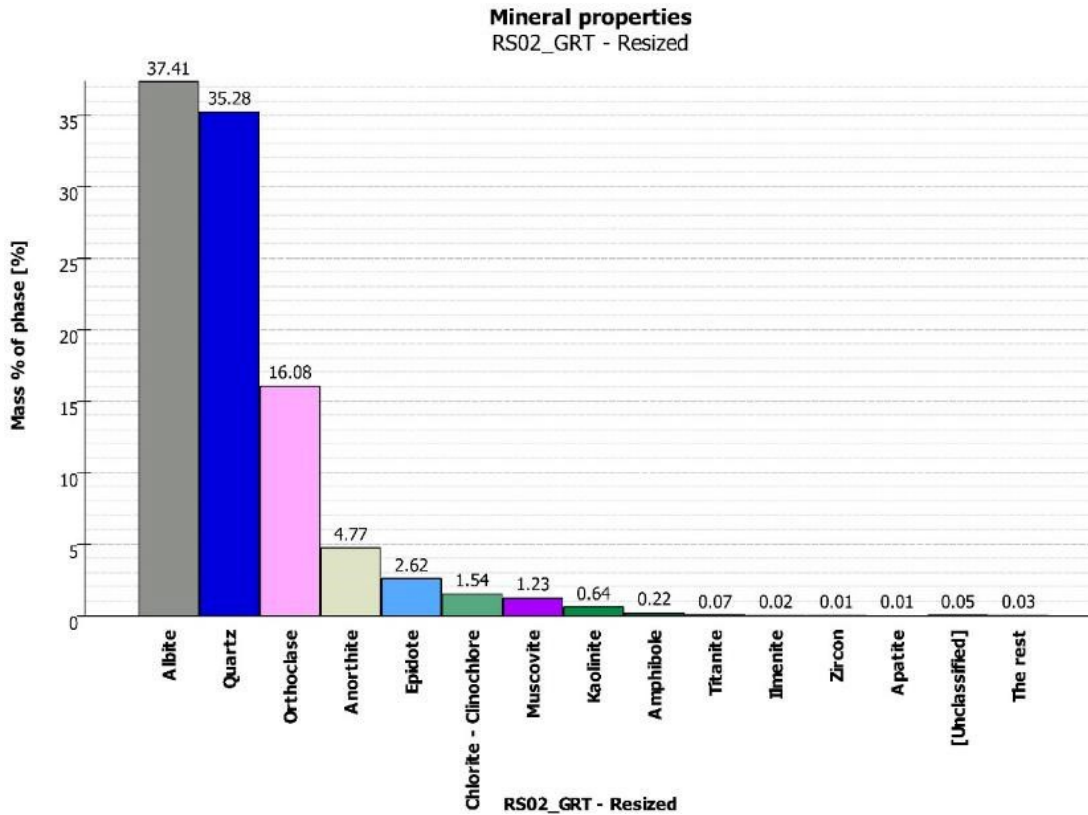


Figure C-166: Modal analysis of granite sample rock RS02_GRT

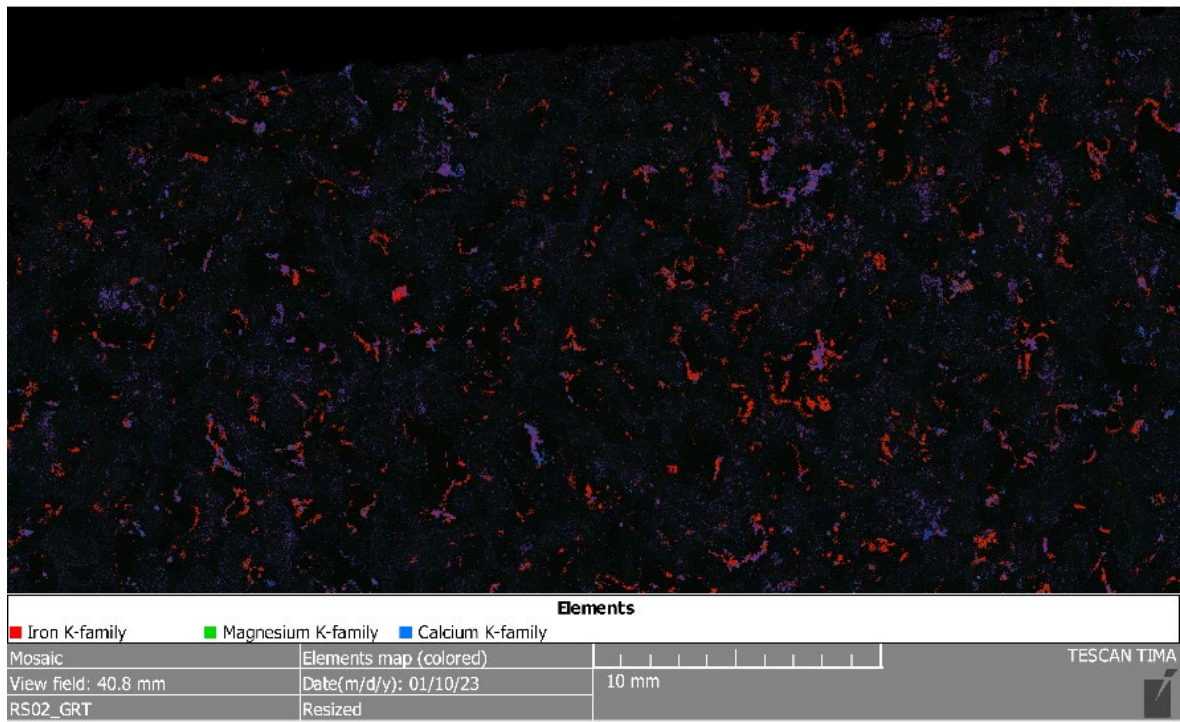


Figure C-167: Element map of granite sample rock RS02_GRT

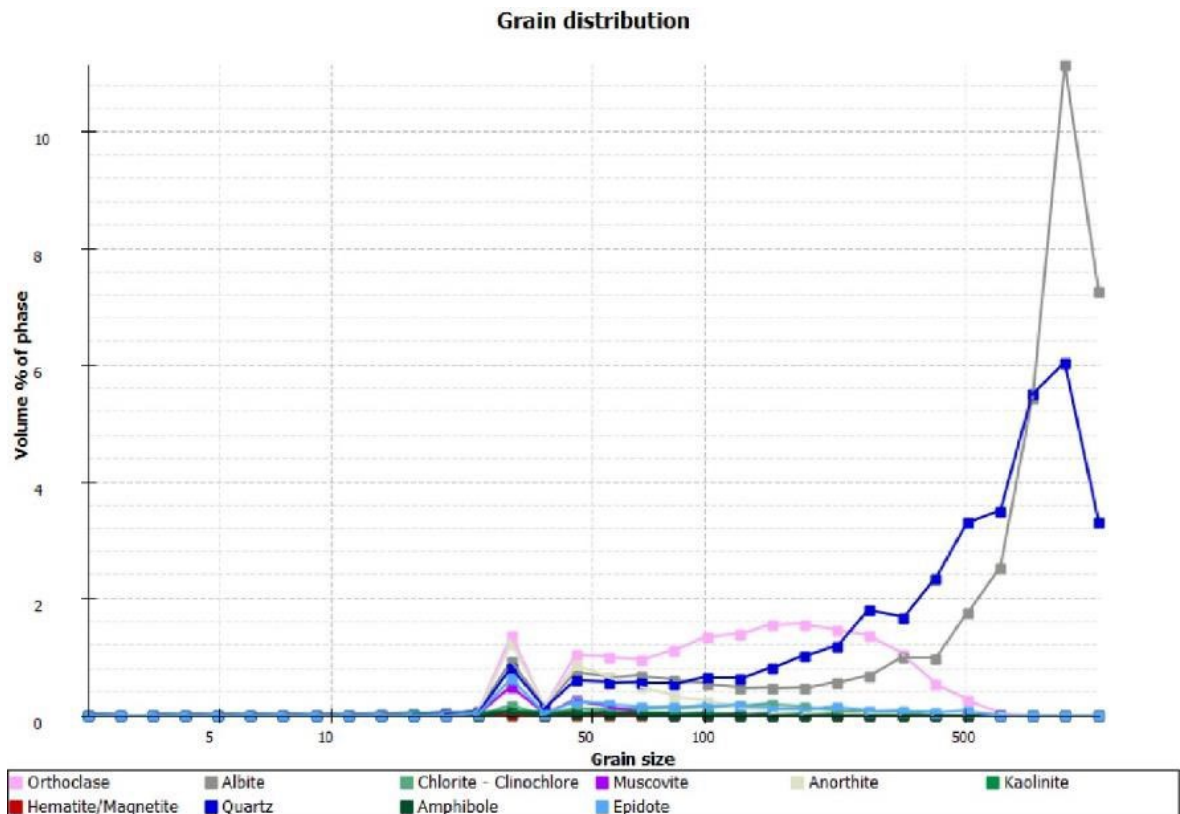


Figure C-168: Grain size distribution of granite sample rock RS02_GRT

Appendix C-5 Dolerite

C-5-1 Sample rock EX08_DOL



Figure C-169: Panorama image of dolerite sample rock EX08_DOL

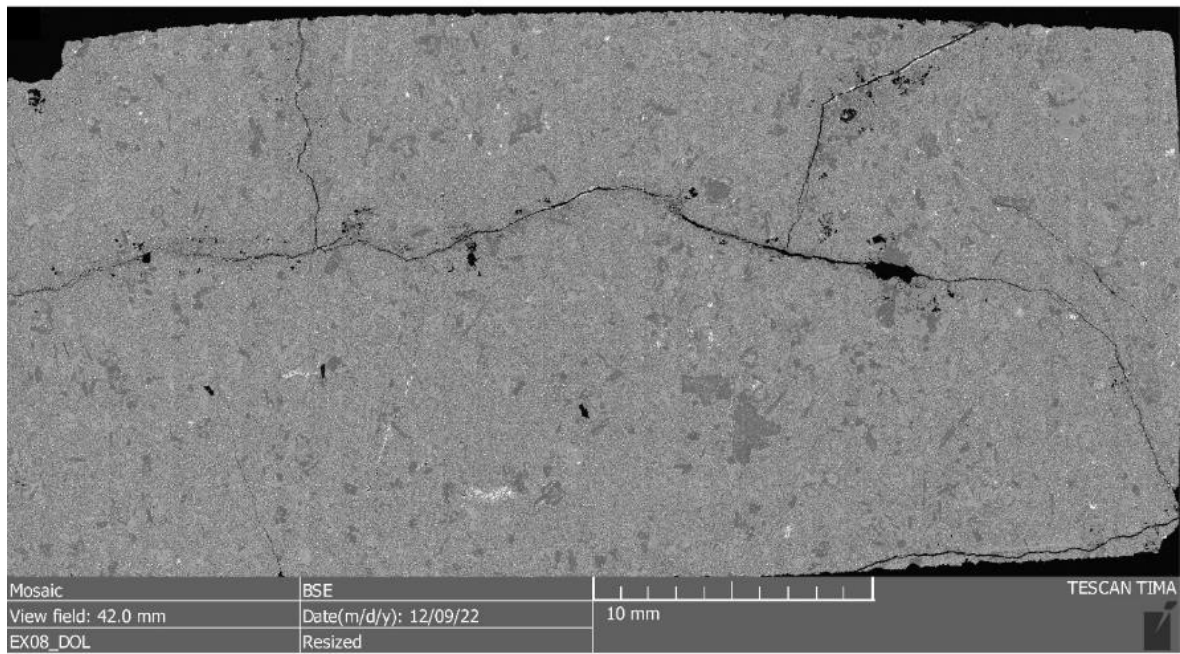


Figure C-170: BSE image of dolerite sample rock EX08_DOL

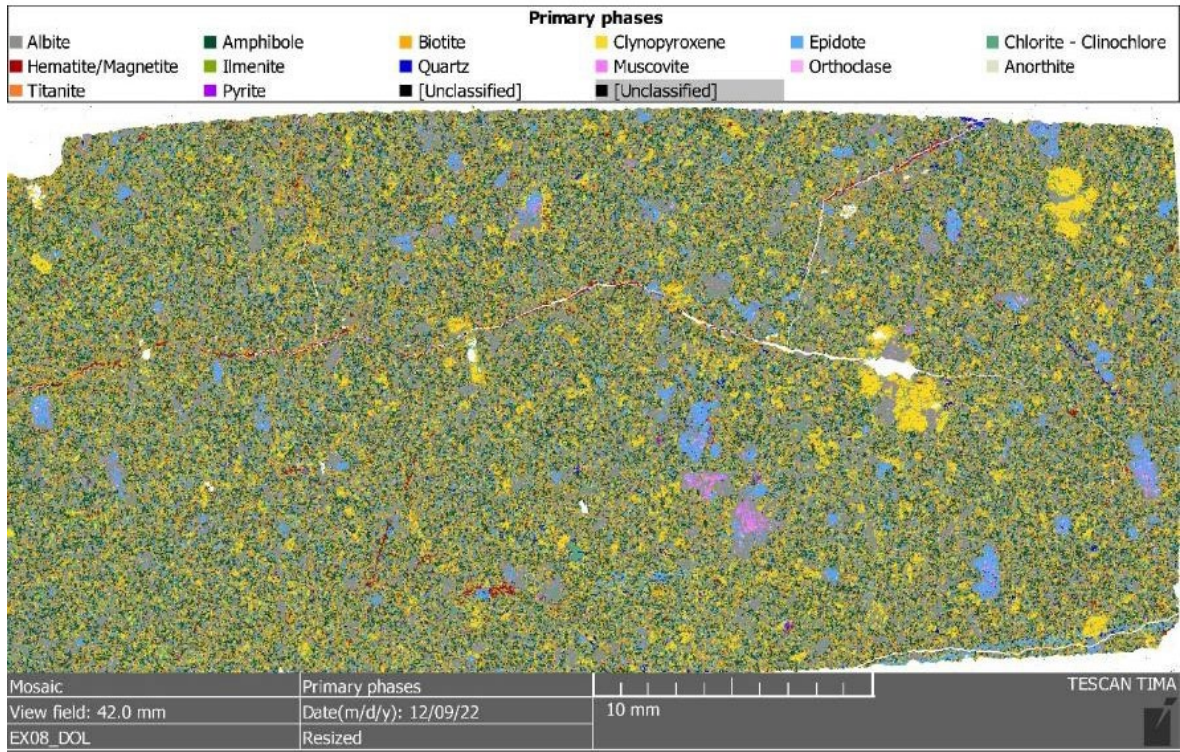


Figure C-171: Phase map of dolerite sample rock EX08_DOL

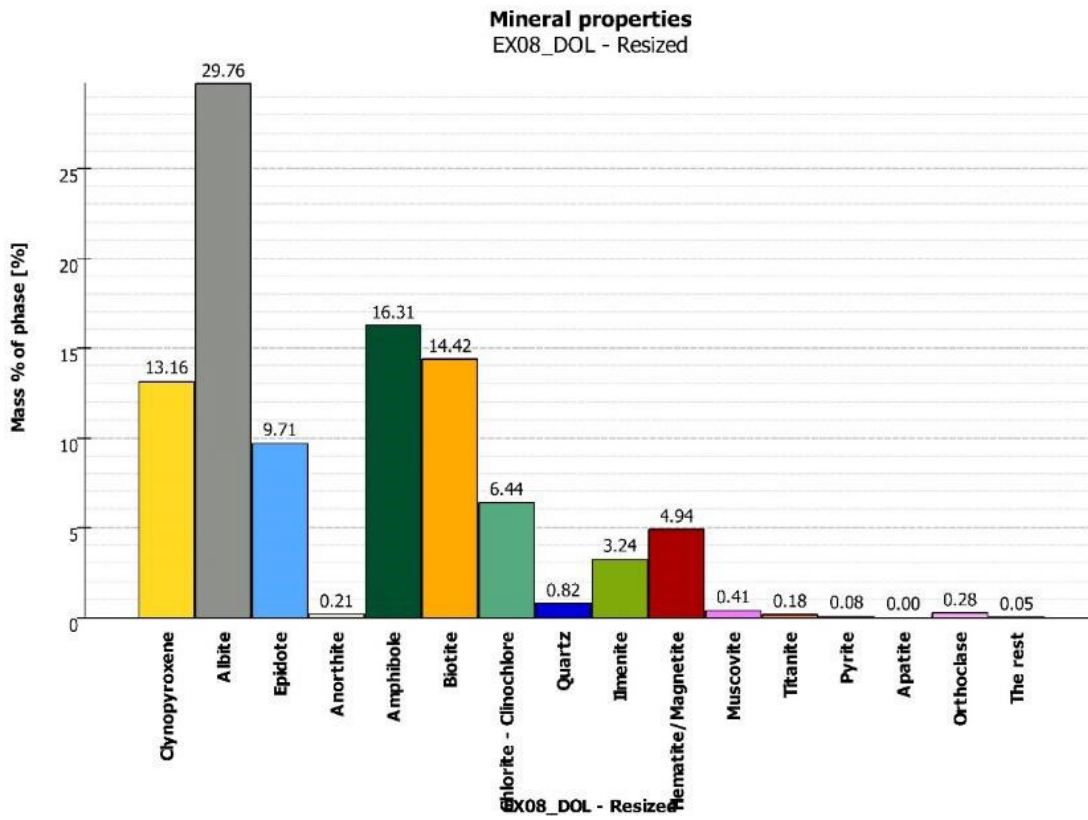


Figure C-172: Modal analysis of dolerite sample rock EX08_DOL

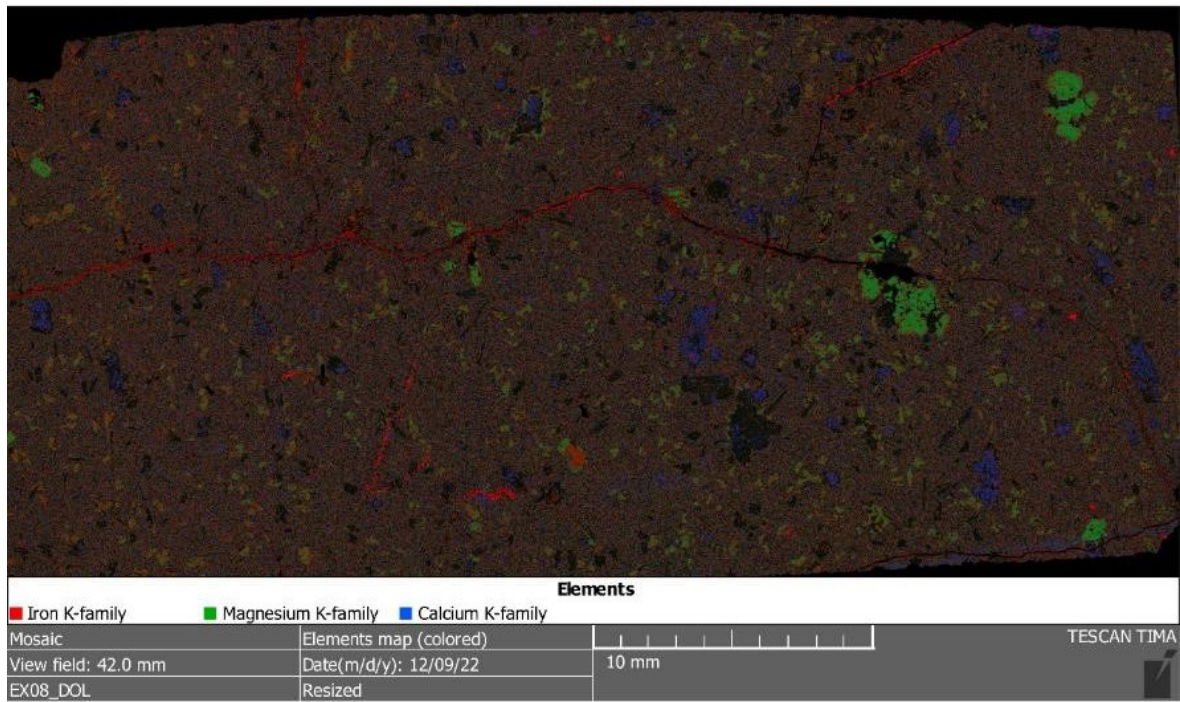


Figure C-173: Element map of dolerite sample rock EX08_DOL

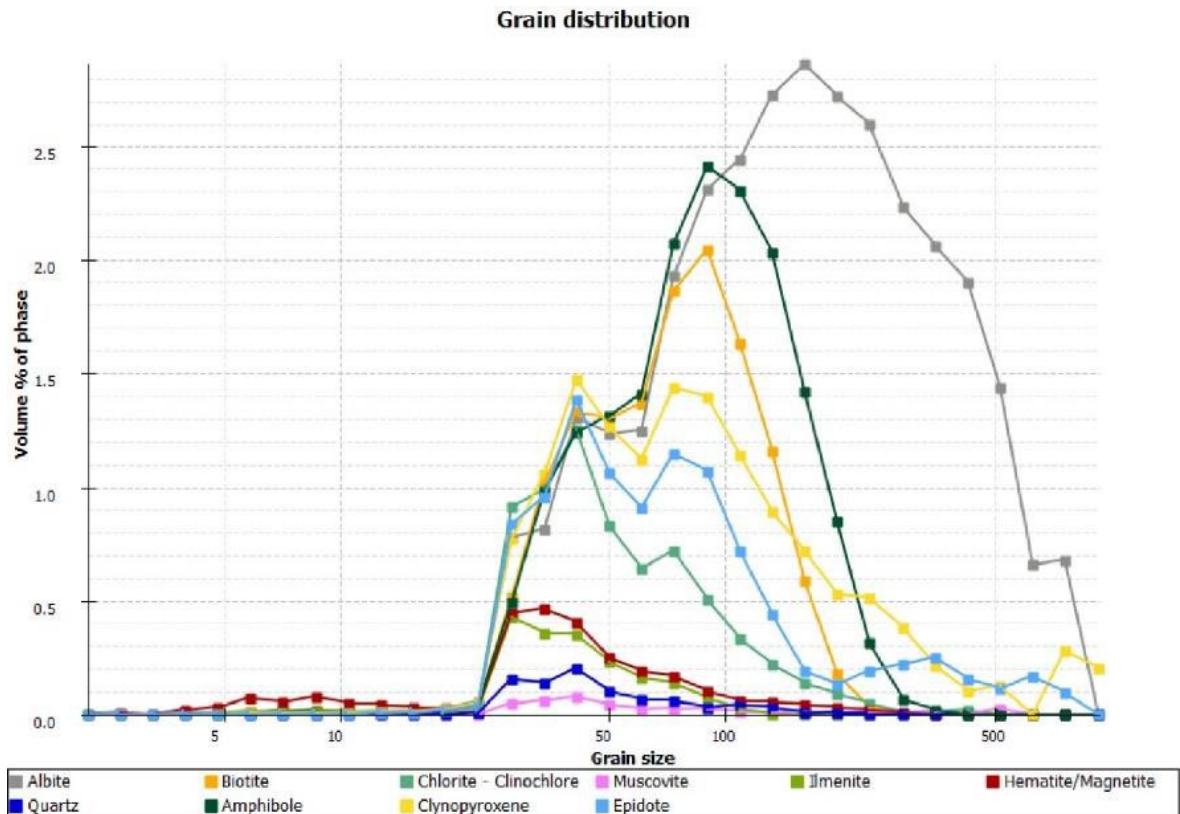


Figure C-174: Grain size distribution of dolerite sample rock EX08_DOL

C-5-2 Sample rock RS05_DOL

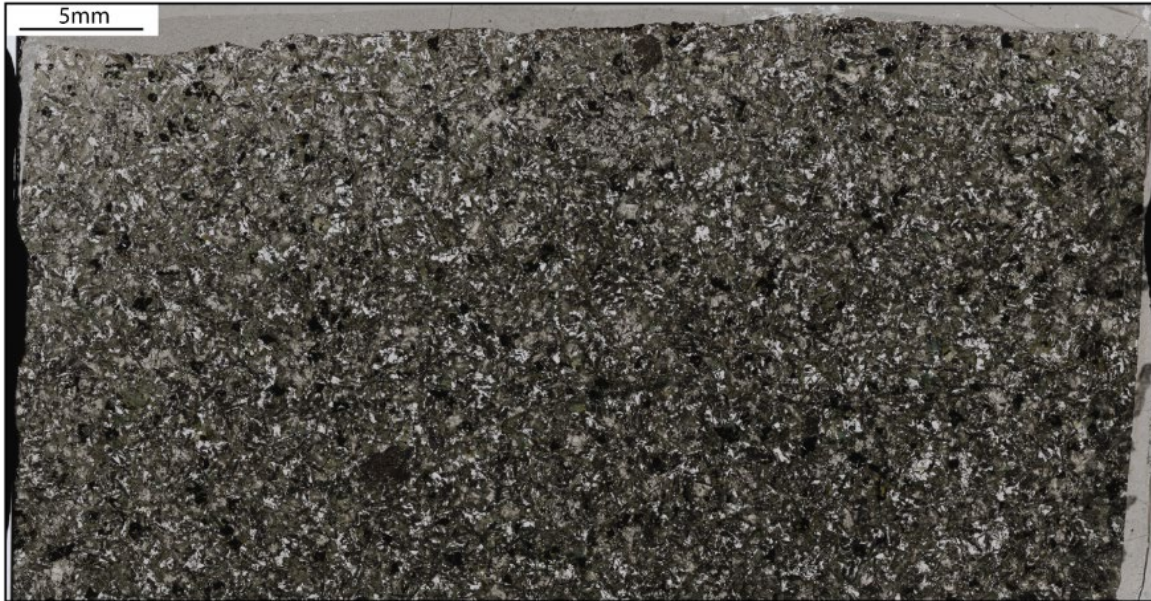


Figure C-175: Panorama image of dolerite sample rock RS05_DOL

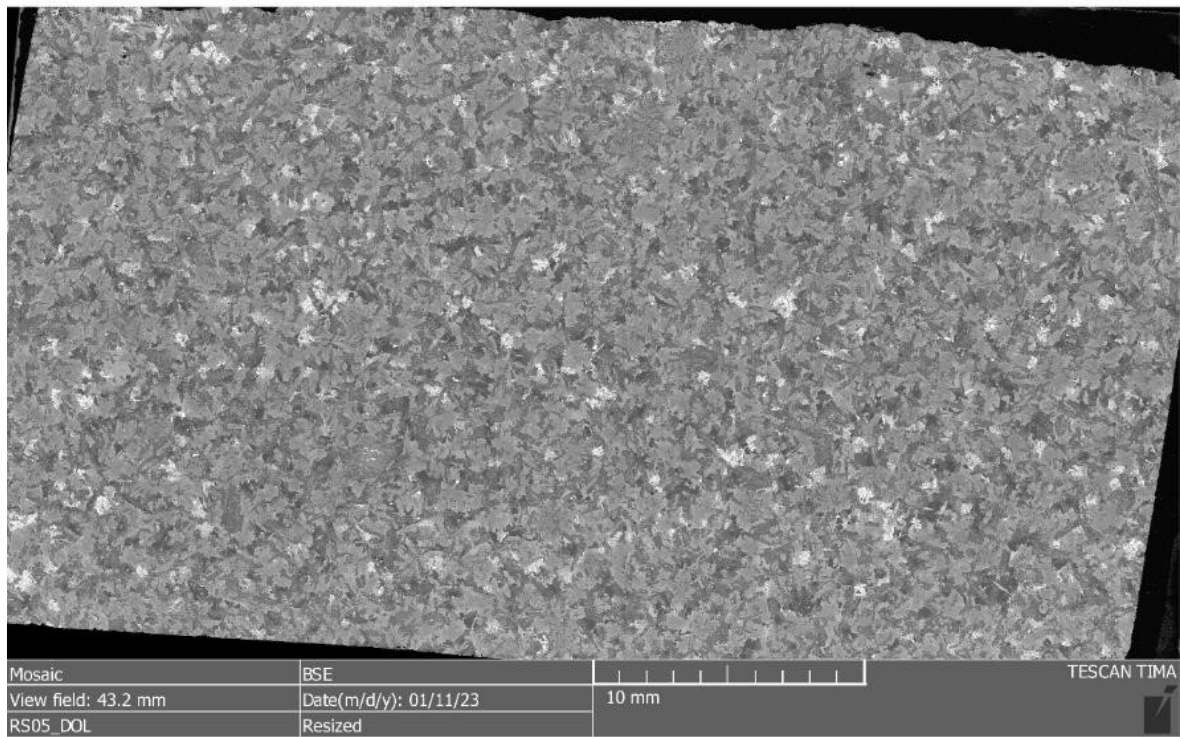


Figure C-176: BSE image of dolerite sample rock RS05_DOL

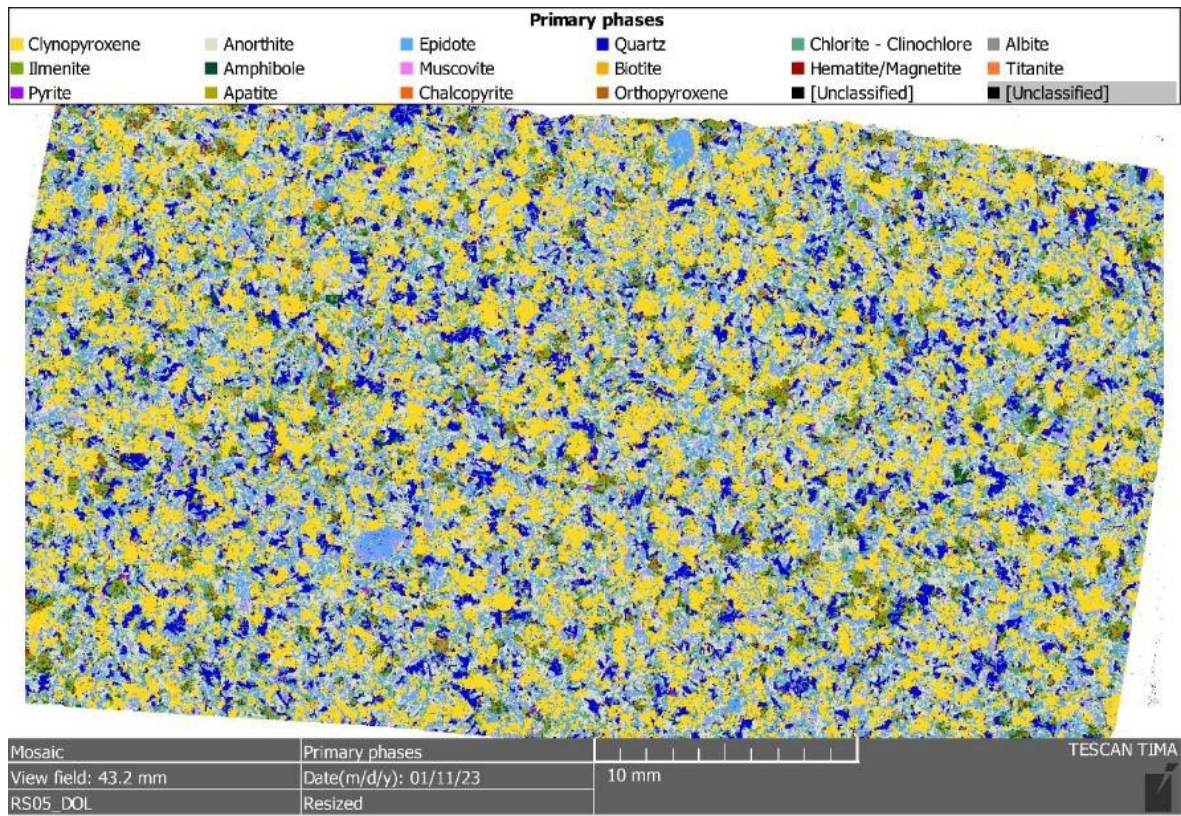


Figure C-177: Phase map of dolerite sample rock RS05_DOL

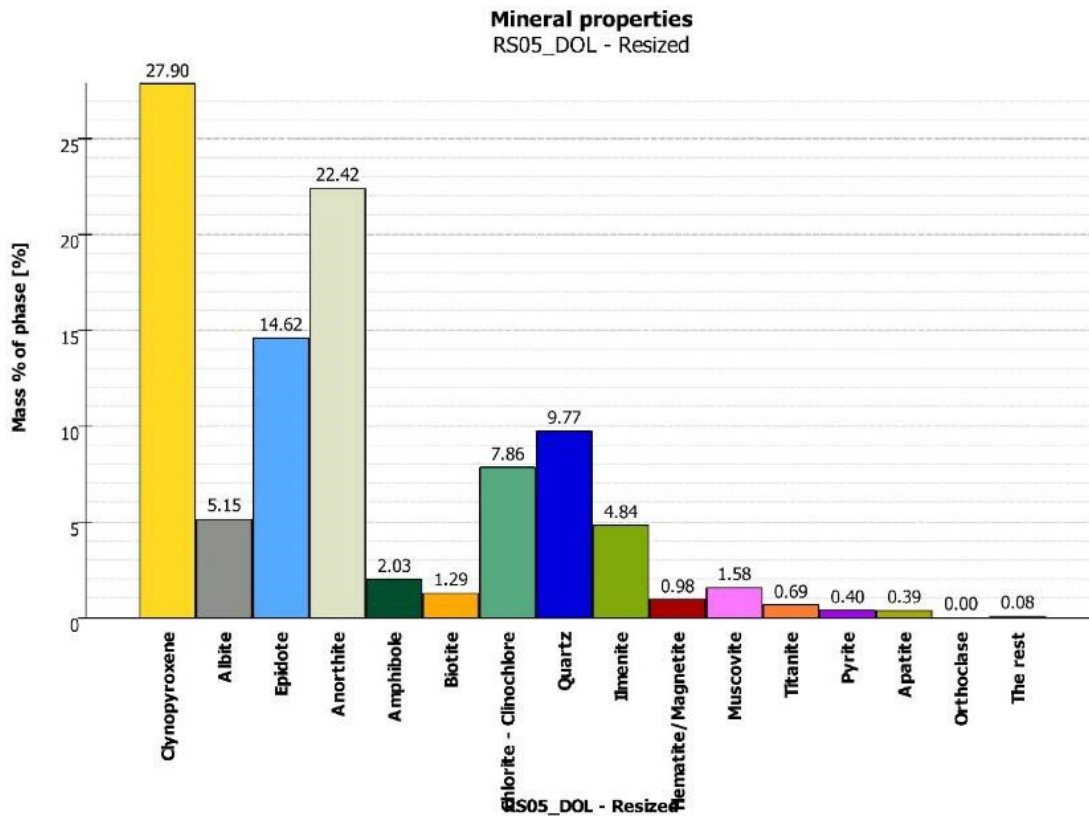


Figure C-178: Modal analysis of dolerite sample rock RS05_DOL

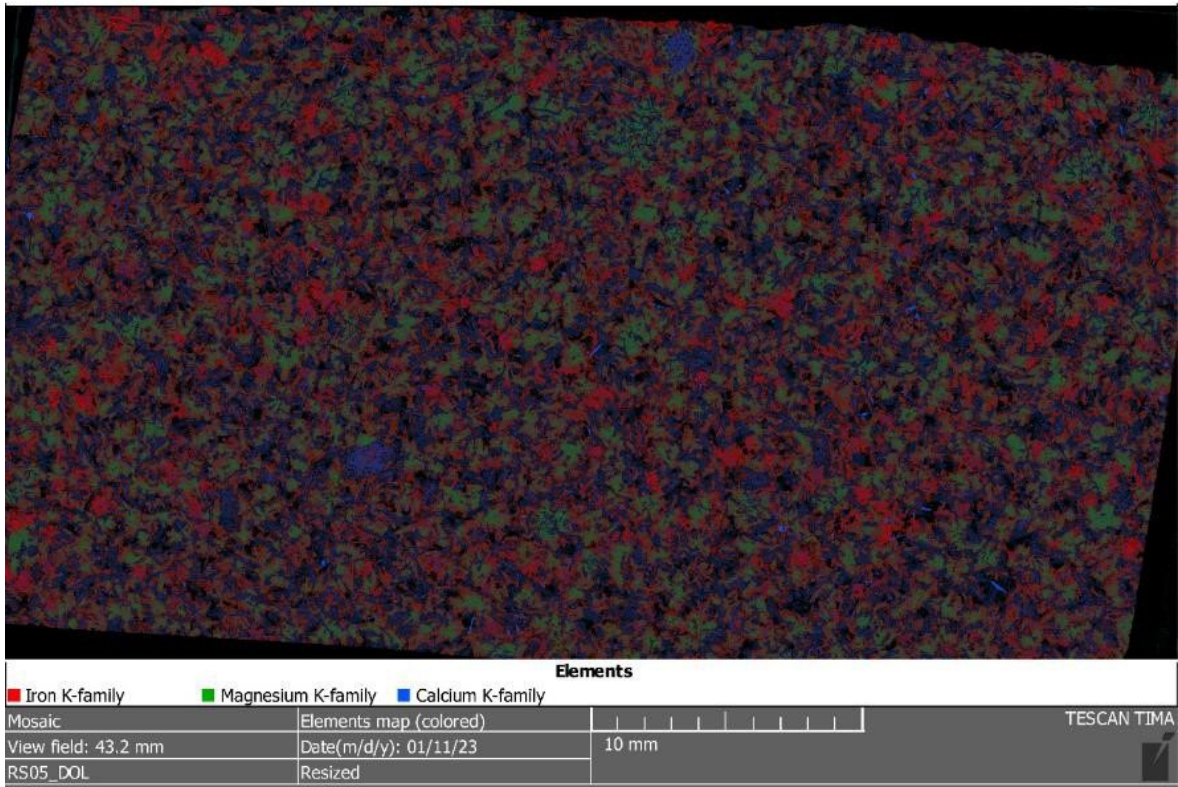


Figure C-179: Element map of dolerite sample rock RS05_DOL

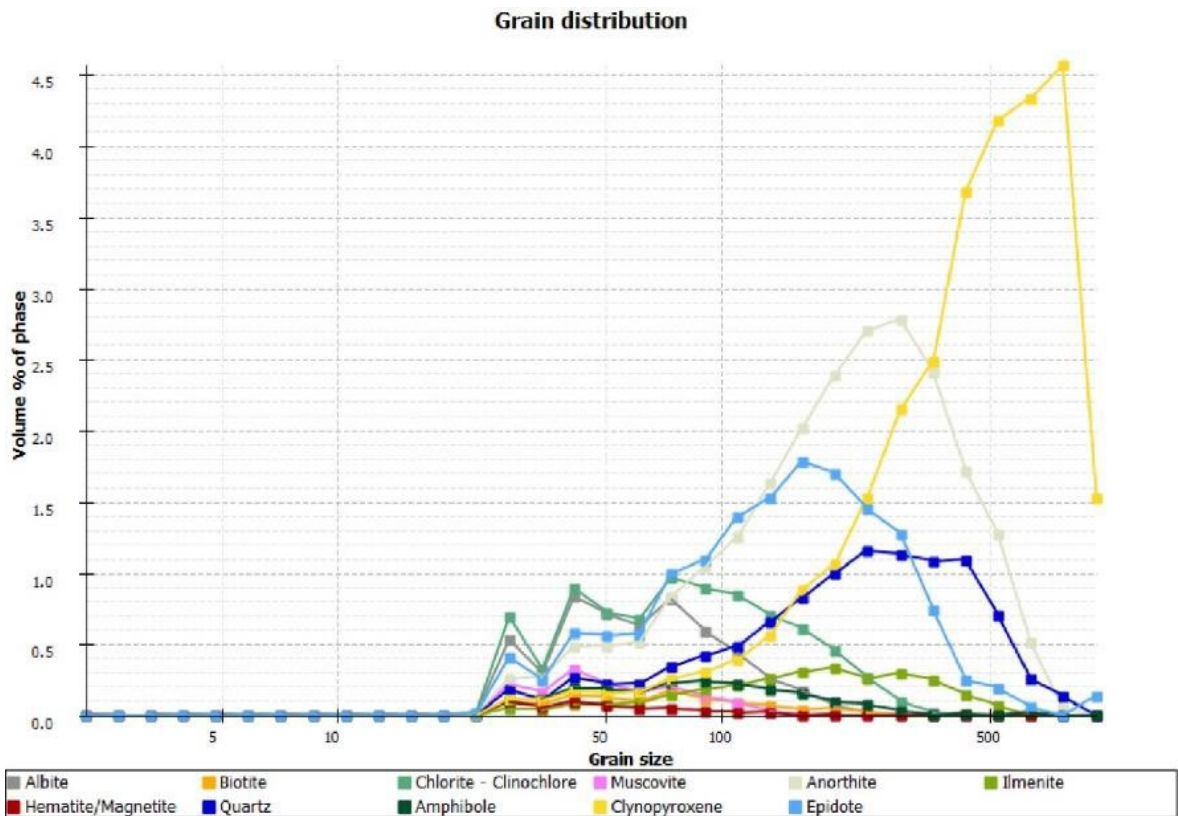


Figure C-180: Grain size distribution of dolerite sample rock RS05_DOL

Appendix C-6 Basalt

C-6-1 Sample rock AQ12_BAS



Figure C-181: anorama image of basalt sample rock AQ12_BAS

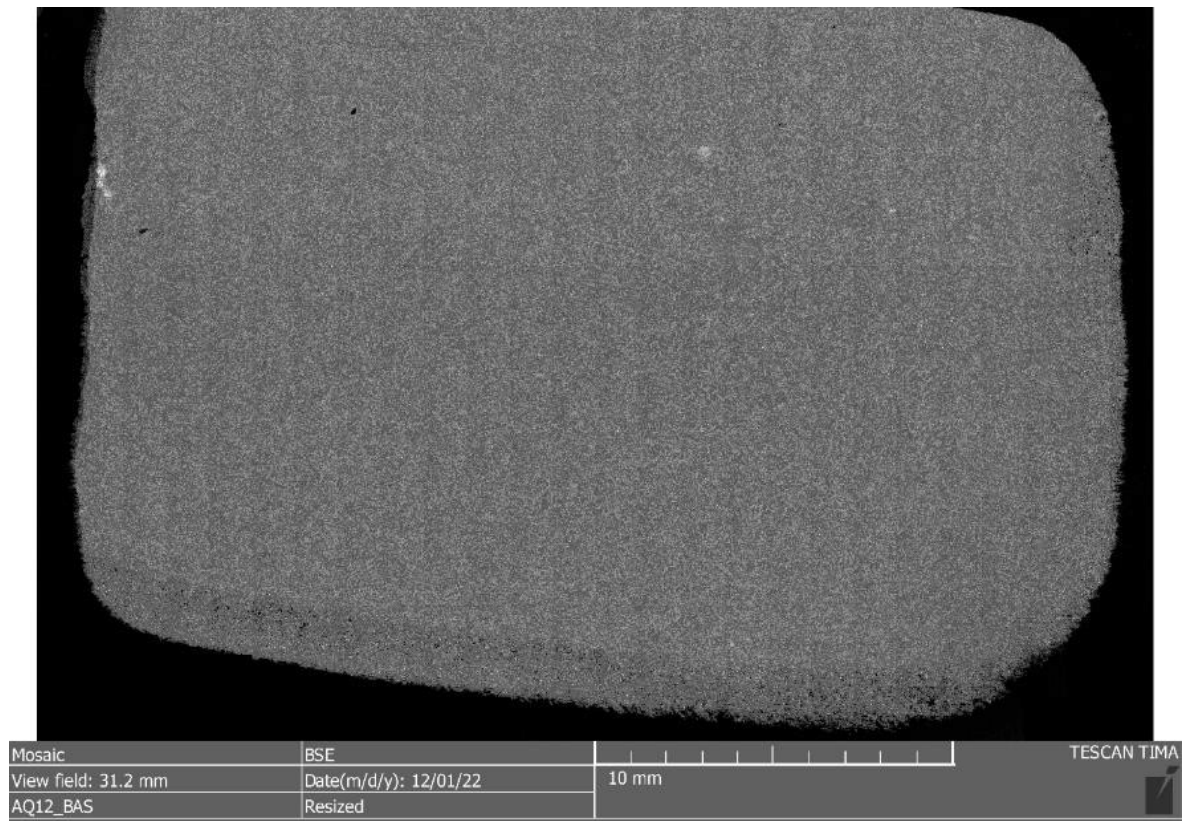


Figure C-182: BSE image of basalt sample rock AQ12_BAS

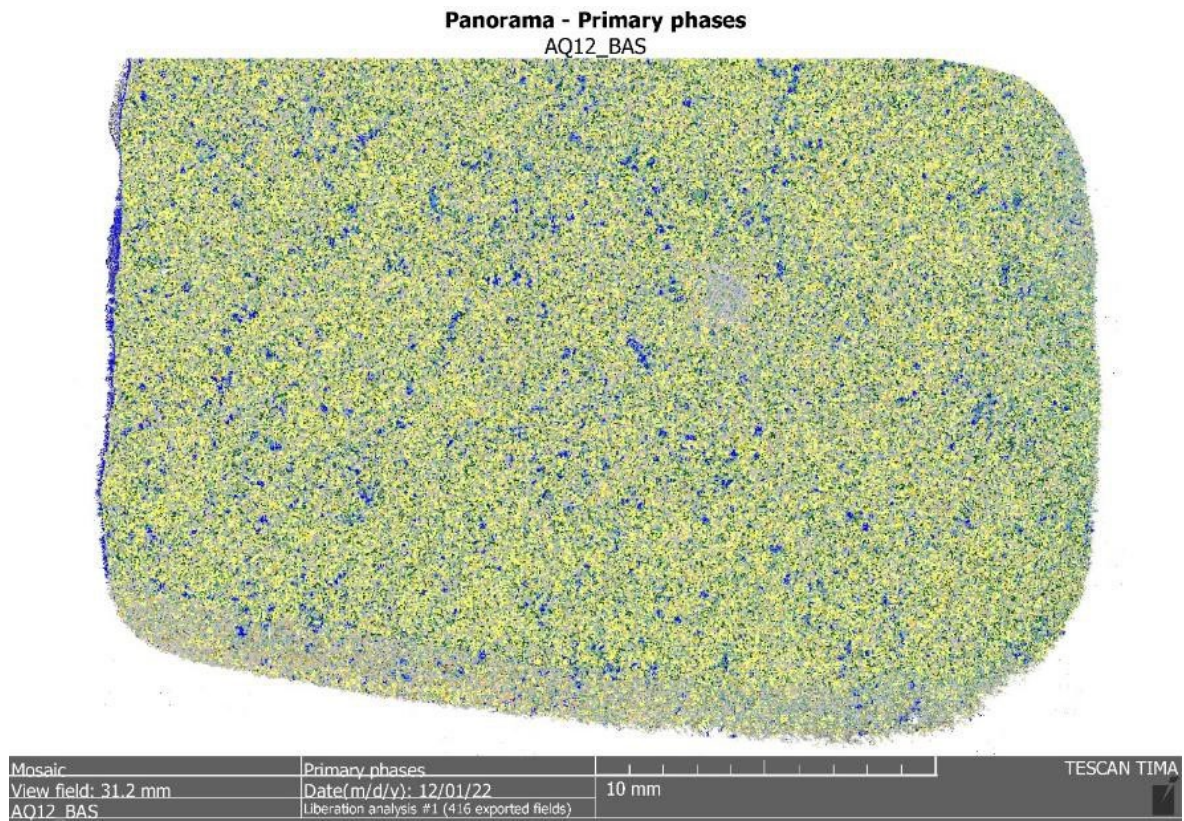


Figure C-183: Phase map of basalt sample rock AQ12_BAS

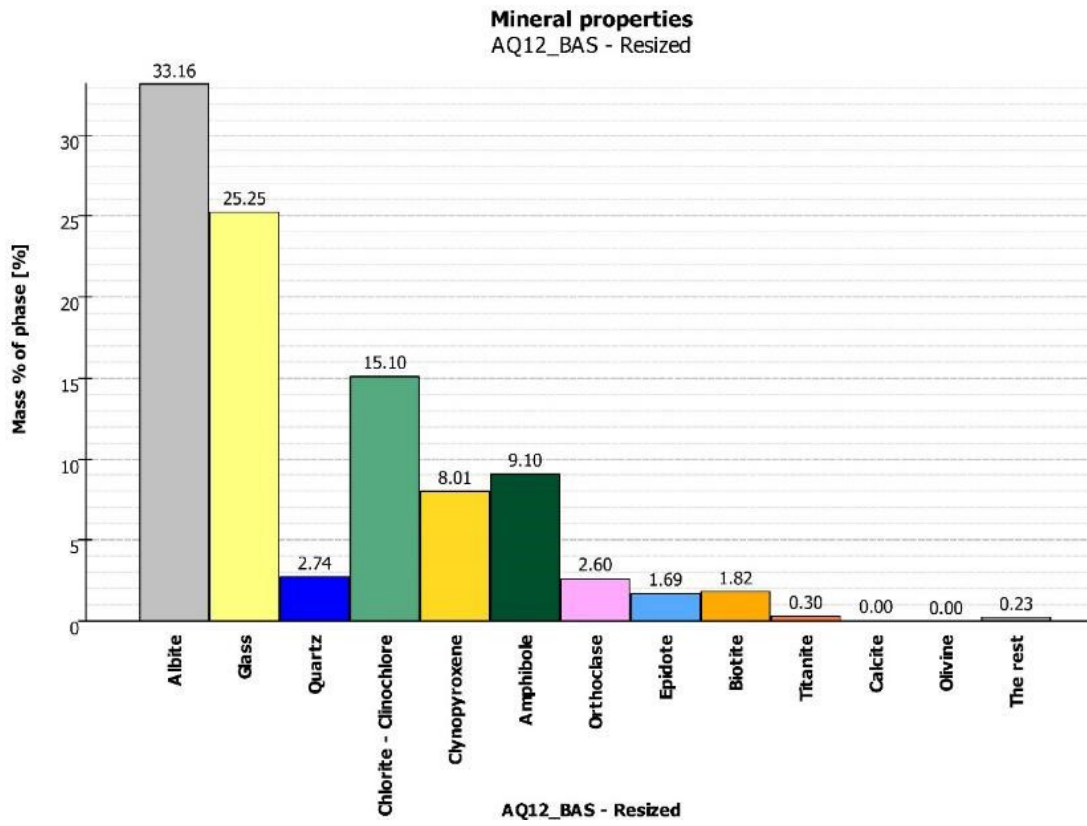


Figure C-184: Modal analysis of basalt sample rock AQ12_BAS

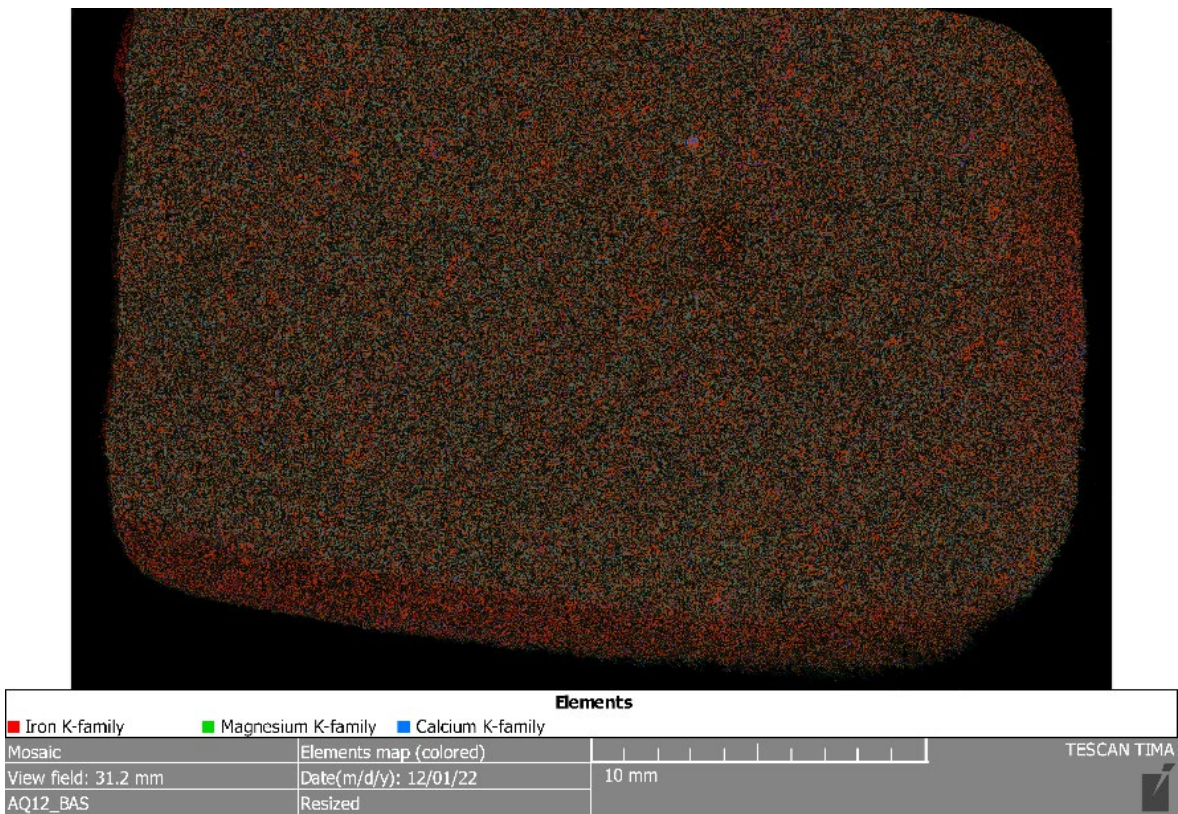


Figure C-185: Element map of basalt sample rock AQ12_BAS

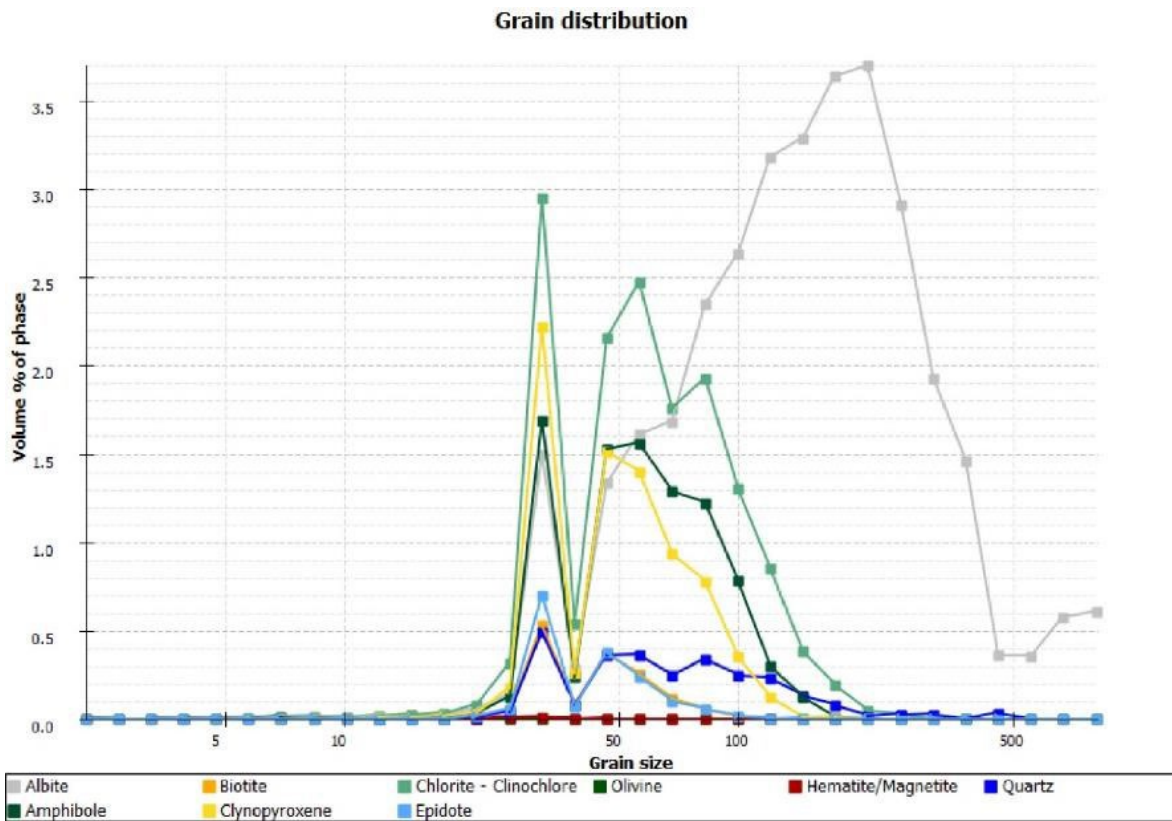


Figure C-186: Grain size distribution of basalt sample rock AQ12_BAS

C-6-2 Sample rock RS09_BAS



Figure C-187: Panorama image of basalt sample rock RS09_BAS

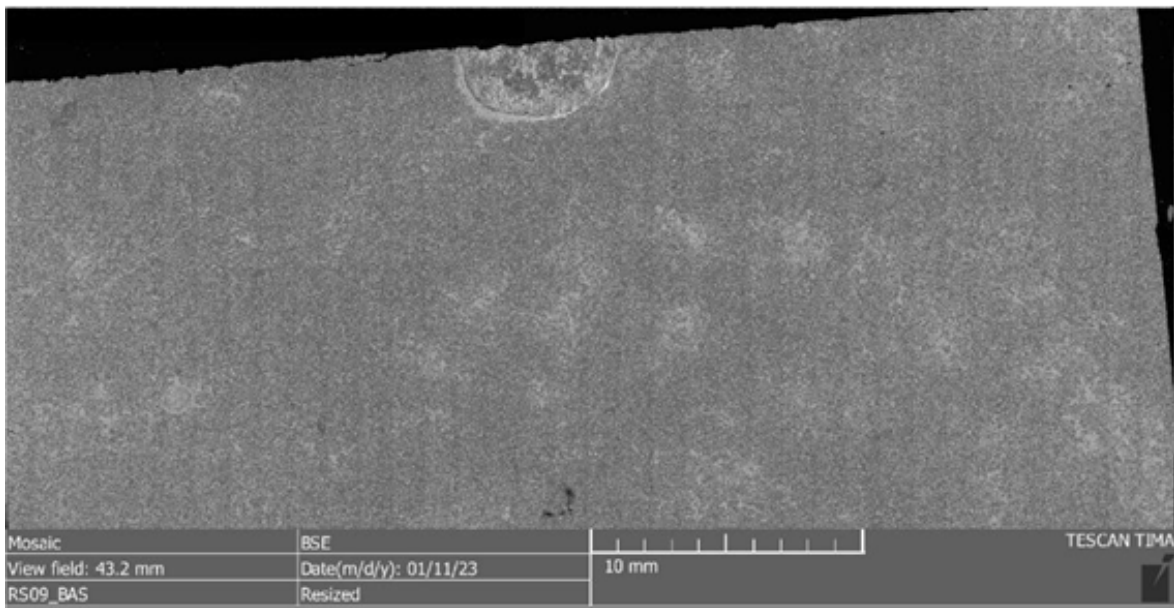


Figure C-188: BSE image of basalt sample rock RS09_BAS

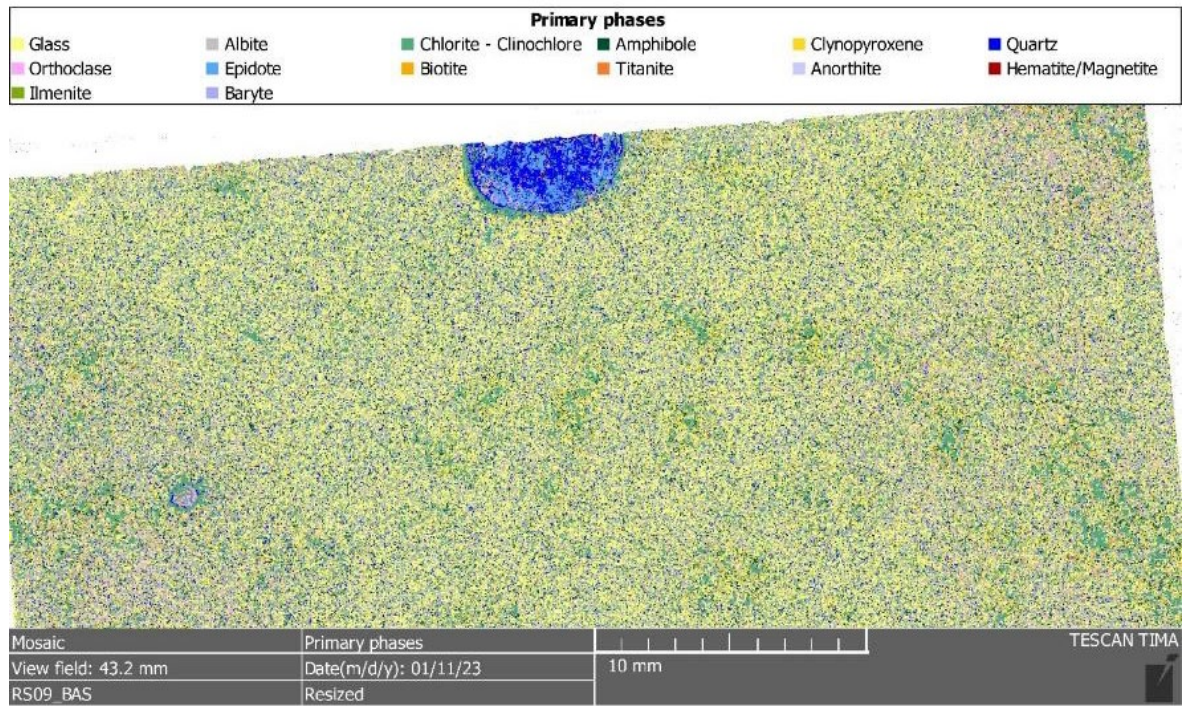


Figure C-189: Phase map of basalt sample rock AQ12_BAS

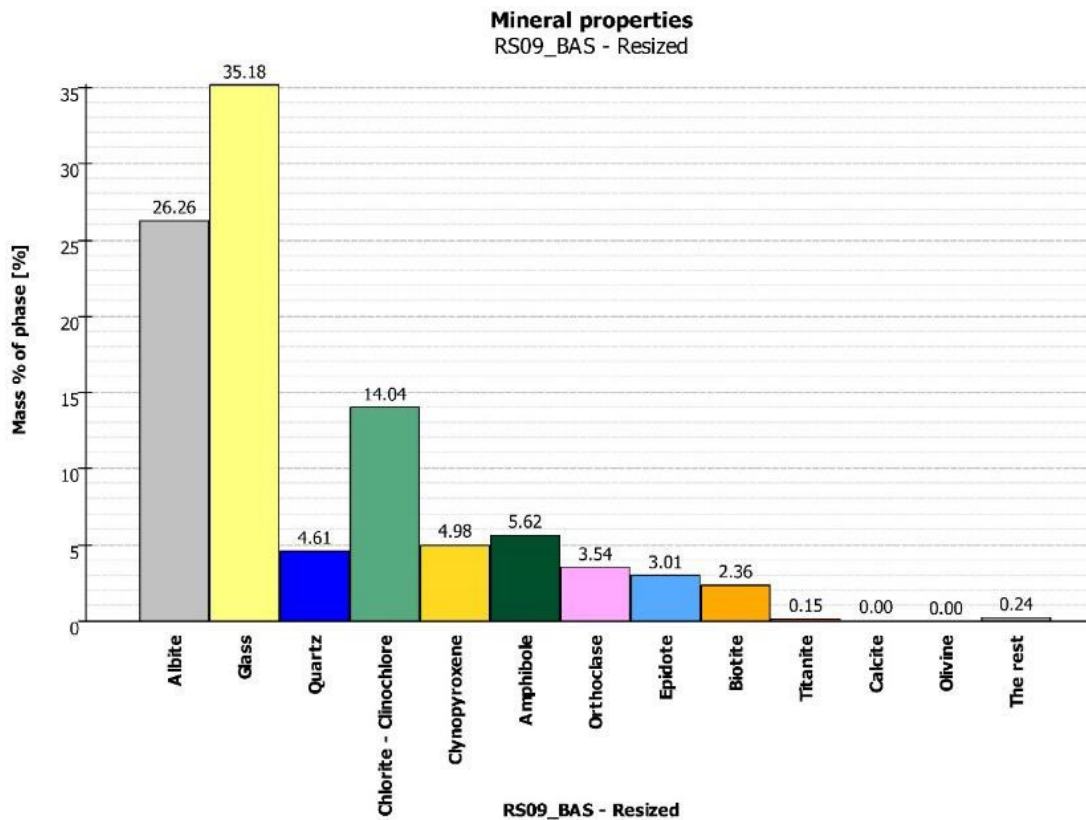


Figure C-190: Modal analysis of basalt sample rock RS09_BAS

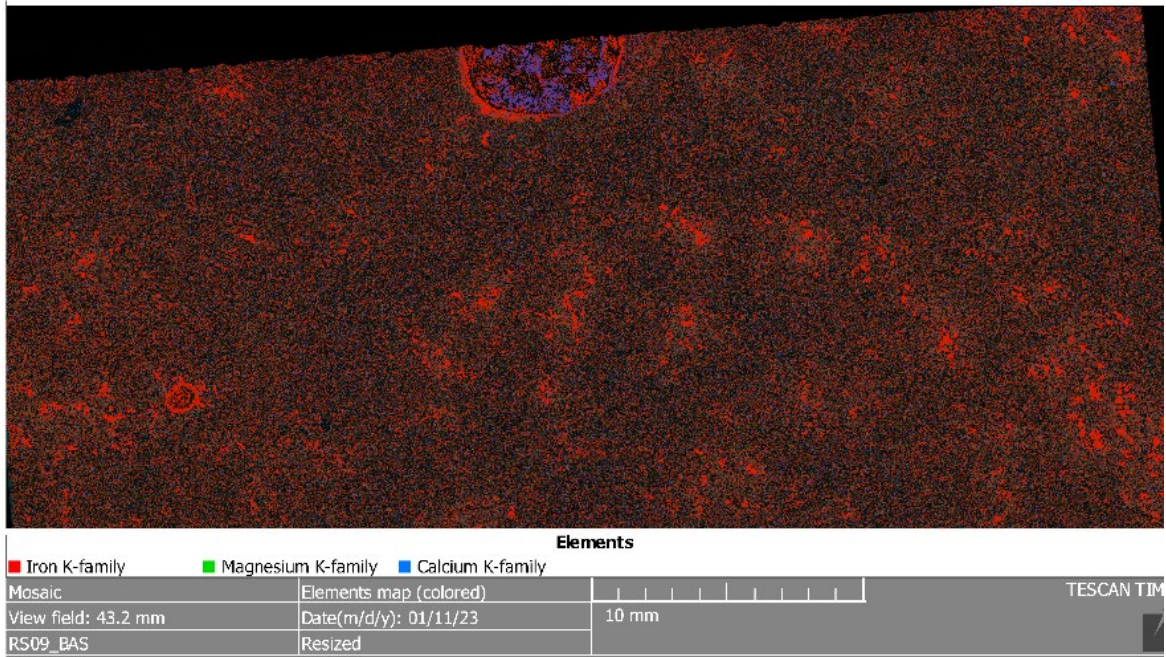


Figure C-191: Element map of basalt sample rock RS09_BAS

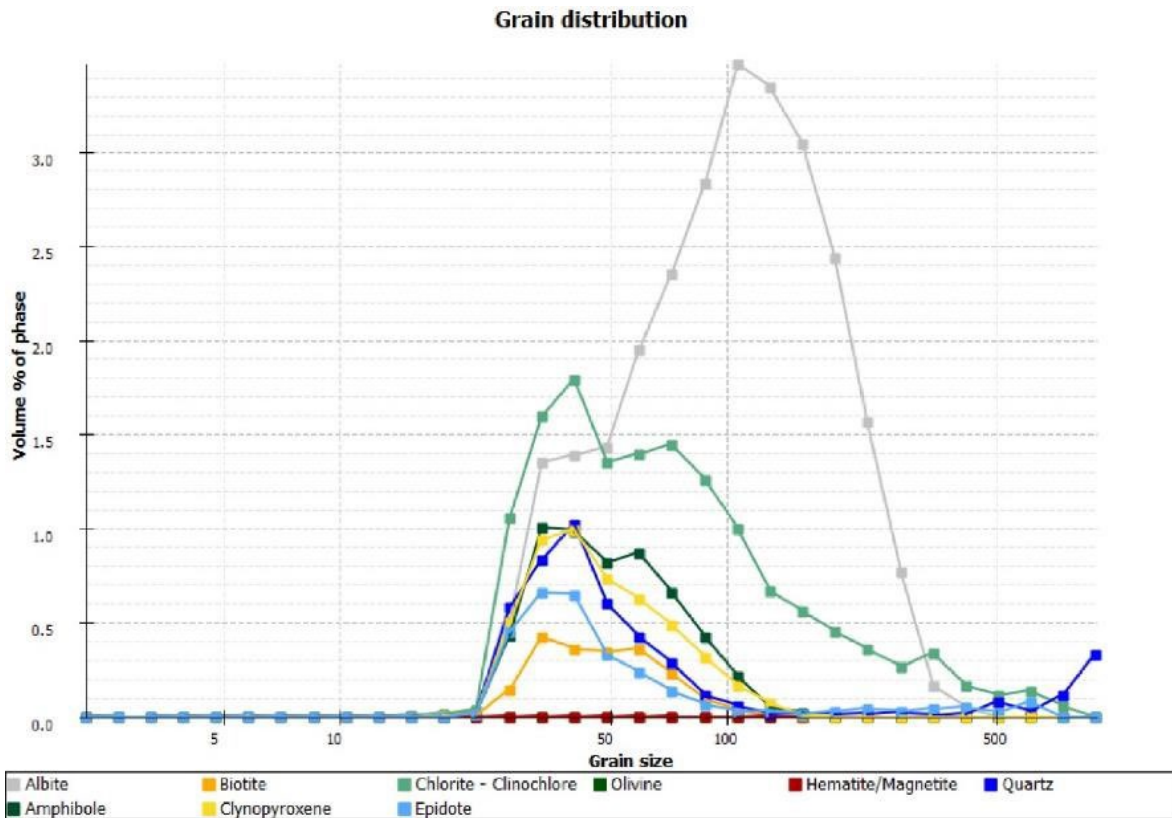


Figure C-192: Grain size distribution of basalt sample rock RS09_BAS

C-6-3 Sample rock RS12_BAS



Figure C-193: Panorama image of basalt sample rock RS12_BAS

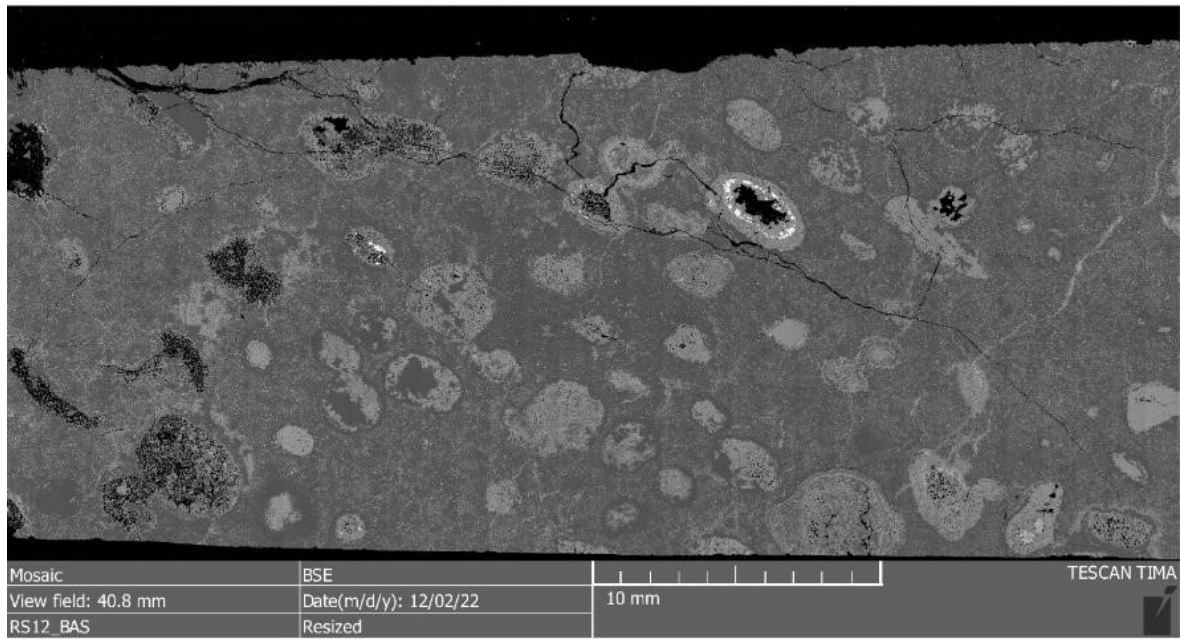


Figure C-194: BSE image of basalt sample rock RS12_BAS

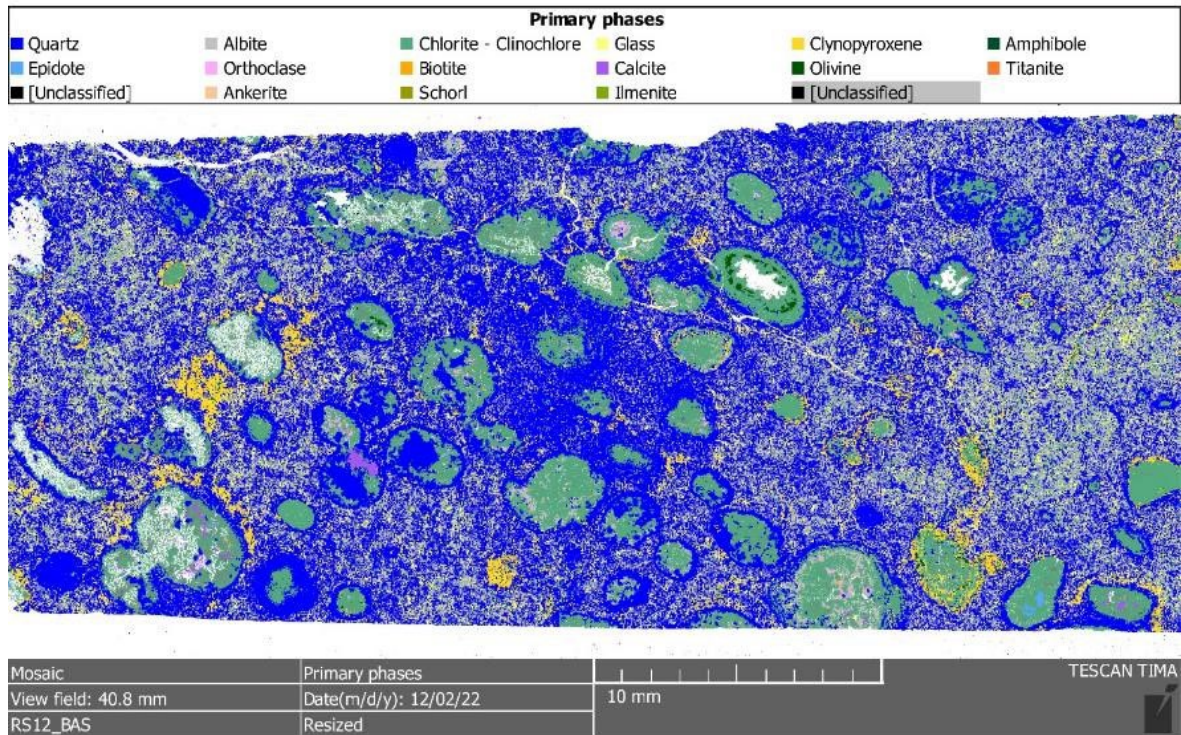


Figure C-195: Phase map of basalt sample rock RS12_BAS

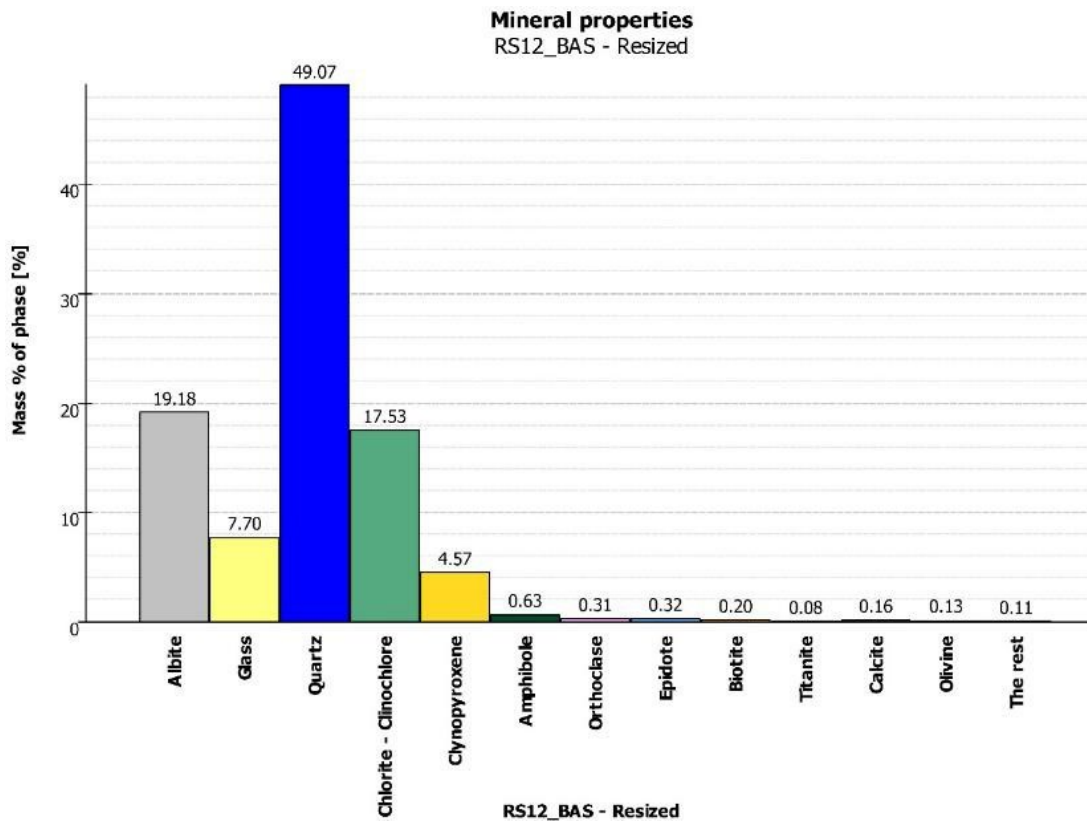


Figure C-196: Modal analysis of basalt sample rock RS12_BAS

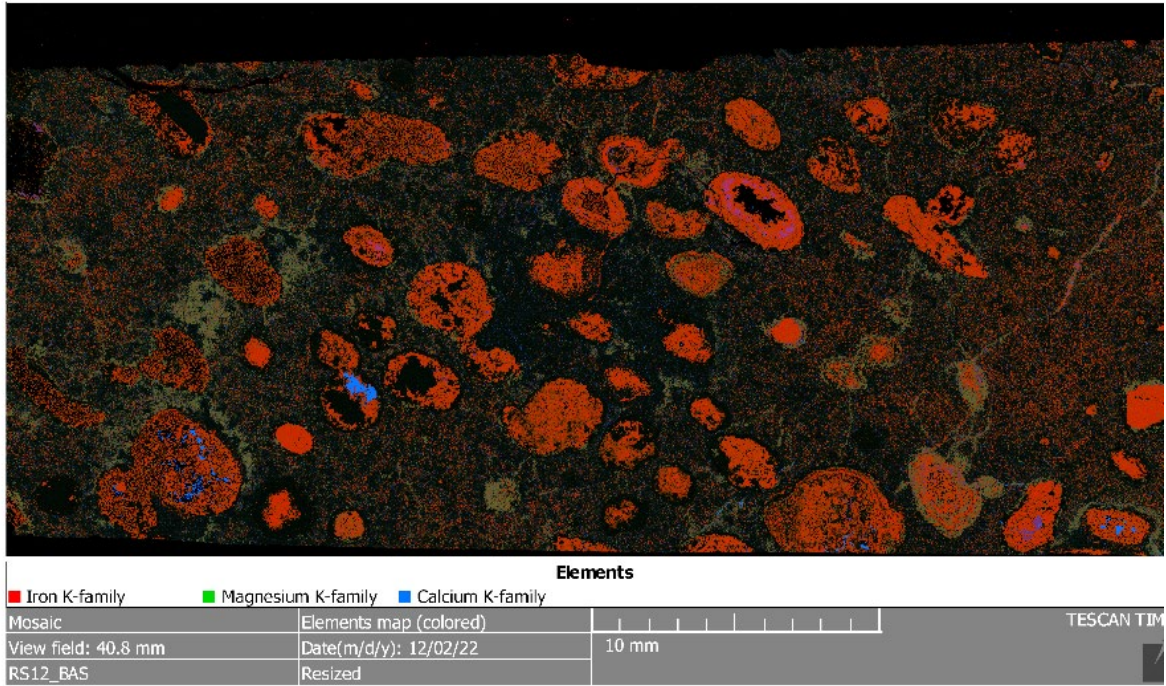


Figure C-197: Element map of basalt sample rock RS12_BAS

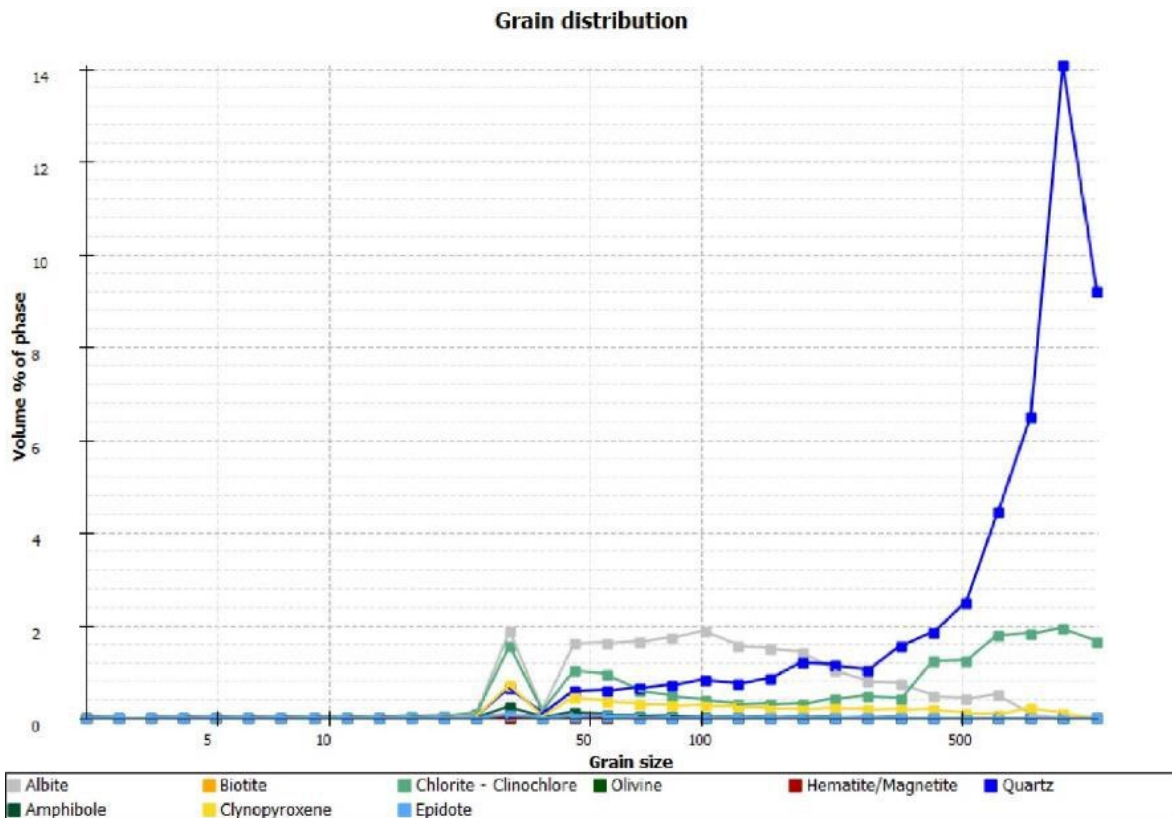


Figure C-198: Grain size distribution of basalt sample rock RS12_BAS